UNIVERSITY OF CALIFORNIA, SAN DIEGO

Seismic Behavior of Architectural Precast Concrete Cladding Panels and Connections

A dissertation submitted in partial satisfaction
of the requirements for the degree
Doctor of Philosophy

in

Structural Engineering

by

Elide Pantoli

Committee in charge:

Professor Tara C. Hutchinson, Chair
Professor William S. Hodgkiss
Professor Jose I. Restrepo
Professor David T. Sandwell
Professor Chia-Ming Uang

2016

The Dissertation of Elide Pantoli is approved, and it acceptable in quality and form for publication on microfilm and electronically:

_____

_____

_____

_____

_____

Chair

University of California, San Diego

2016

DEDICATION

To my parents Donatella and Luigi who taught me the importance of education.

To my sisters and brother Giulia, Michela, David, Laura, Maddalena, Sophia and Sanny who inspire me to be the best person I can be.

EPIGRAPH

"Always aim high, work hard, and care deeply about what you believe in.

And, when you stumble, keep faith.

And, when you're knocked down, get right back up

and never listen to anyone who says you can't of shouldn't go on"

Hillary Rodham Clinton

TABLE OF CONTENTS

LIST OF ABBREVIATIONS

ACI	American Concrete Institute
APC	Architectural Precast Concrete
ASCE	American Society of Civil Engineering
BI	Base Isolated
BNCS	Building Nonstructural Components and Systems (project)
F	Force
FA	Floor acceleration (general)
FB	Fixed Base
ID	Interstory Drift
IDR	Interstory Drift Ratio
IP	In-plane
NCSs	Nonstructural Components and Systems
NEES	Network for Earthquake Engineering Simulation
OP	Out-of-plane
PCI	Precast Concrete Institute
PIDR	Pak Interstory Drift Ratio
PFA	Peak Floor Acceleration
PPA	Peak Panel Acceleration
PSD	Power Spectral Density
SDOF	Single degree of freedom
SJSU	San Jose State University
UCSD	University of California, San Diego

LIST OF SYMBOLS

A	Area
a_i	Acceleration at floor i
a_p	Component amplification factor
a_s	Structure amplification factor
A_x	Torsional amplification factor
C_d	Deflection amplification factor
$C_{Lc/d,d}$	Configuration in the component test on sliding connection
C_p	Seismic force coefficient
d	Diameter
d_b	Longitudinal bar diameter
D_p	Relative seismic displacement
D_{95}	Earthquake duration
E	Young modulus
f	Natural frequency (Hz)
f'_c	Unconfined compressive strength of concrete
f'_{cc}	Confined compressive strength of concrete
$FA^{floor,corner}$	Floor acceleration at a certain floor and corner
F_c	Force in the connection
f_c	Cutoff frequency of a filter
F_L	Force activation sliding of a sliding tieback connection
F_{max}	Maximum theoretical force in the ductile fuse connection
F_p	Design force
F_y	Force producing yielding in the rod of a sliding tieback connection
F_u	Ultimate force
f_y	Yield stress

f_u	Ultimate stress
k	Stiffness
h	Height of the structure respect to the ground
I	Moment of inertia
$ID^{[corner\ name]}$	Interstory drift at a corner
ID_w	Interstory drift in the Westward direction
IP_h	In-plane horizontal
IP_v	In-plane vertical
I_p	Importance factor
$k_{IP,h}$	Stiffness connection in the in-plane horizontal direction of the panel
$k_{IP\text{-}v}$	Stiffness in the in-plane vertical direction of the panel
k_{OP}	Stiffness in the out-of-plane horizontal direction of the panel
l	length
L_c	Clear length (sliding rods)
L_f	Free length (flexing rods)
l_p	Plastic hinge length
m	Mass
M#	Name of input motions in the component test on sliding connections
$M_{p\text{-}expected}$	Maximum flexural capacity
M_u	Ultimate moment
M_w	Moment magnitude
M_y	Yield moment
$PA^{panel\ name}$	Acceleration in the panel
Psa	Pseudo spectral acceleration
Psv	Pseudo spectral velocity
Pm	Permanent misalignment

R	Response modification factor
R_p	Component response modification factor reduction factor,
R_{rup}	Distance from the point of rupture
R_y	Ratio of expected yield to the specified yield force
S_{D1}	Spectral response at one second
S_d	Spectral displacement
S_{DS}	Short period spectral acceleration
S_s	Spectral acceleration at short periods
T	Period
V_{30}	Shear wave velocity of the soil
Z	Plastic section modulus
z	Height of attachment of a nonstructural component with respect to the ground
W_p	Weight of a component
Δ_c^{panel}	Displacement absorbed by the connection in a panel
Δ	Displacement applied during the component test on flexing connection
Δ_y	Yield displacement
Δ_u	Ultimate displacement
ε_{cc}	Strain of confined concrete at the peak stress
ε_{cu}	Ultimate strain of confined concrete
ε_{oh}	Strain at the onset of hardening
Ω_0	Amplification factor to account for overstrength
σ	Stress
χ_y	Yield curvature
χ_u	Ultimate curvature

LIST OF FIGURES

LIST OF TABLES

ACKNOLEDGEMENTS

I would like to gratefully acknowledge all the people who contributed to this dissertation and my life in the past six years. First of all, I want to thank all my financial sponsors, including the Jacob Fellowship, Powell Fellowship, Departmental dissertation fellowship, National Science Foundation, Precast/Prestressed Concrete Institute, Charles Pankow foundation, and Gordon leadership center.

I am very grateful for the members of my defense committee Professors Tara Hutchinson, Jose Restrepo, Chia-Ming Uang, William Hodgkiss and David Sandwell. I am particularly grateful to my advisor, Professor Tara Hutchison, who supported my though this journey. She has been an incredible mentor both from an academic and personal point of view.

I would also like to thank everyone who contributed to make the BNCS project a success. First of all the students who shared with me the fun and the hard work of the project: Michelle Chen, Consuelo Aranda, Rodrigo Astroza, Hamed Ebrahimian, Elias Espino, Giovanni De Francesco, Jin-Kyung Kim, Steven Mintz, Hae-Jun Park, and Francesco Selva. None of this would also have been possible without the incredible contribution of the NEES@UCSD and NEES@UCLA staff. I am particularly grateful for the help and constant support of Robert Beckley, Andrew Gunthardt, Darren McKay, Steve Morris, Dan Radulescu, Alex Sherman, and Hector.

Third, I would like to thank all amazing people in the Structural Engineering department who supported me. First of all Professor Lelli Van Den Einde who helped me discover my passion for teaching. I would like to thank all the staff of the department, and in particular Debra Bomar, Yvonne Wilson, and Lindsay Walton. I am also very thankful for Steve Porter, who can always make me feel at home. I am very thankful for all my colleagues in the department, who were always willing to help me. I would also like to thank all my former students, whose smiles gave meaning to many of my days. Last but not least I would like to thank my family and friends for all the support they provided me throughout my PhD.

Chapter 1 reproduces content and images of the material as it appears in the PCI Journal 2016. Pantoli, E., Hutchinson, T. C., McMullin, K. M., Underwood, G. A., and Hildebrand, M. J., 2016. “Seismic-drift-compatible design of architectural precast concrete cladding: Tieback connections and corner joints.” PCI Journal, July-August, 38-52. The author of the dissertation is the principal author of the

above cited paper.

Chapter 3 reproduces content and images of the material as it appears in the PCI Journal 2016 and Proceedings of the Façade tectonics conference 2014. Pantoli, E., Hutchinson, T. C., McMullin, K. M., Underwood, G. A., and Hildebrand, M. J. 2016. "Seismic-drift-compatible design of architectural precast concrete cladding: Tieback connections and corner joints." PCI Journal, July-August, 38-52. Pantoli, E., Hutchinson, T. C., Underwood, G. A., and Hildebrand M., 2014. "Seismic behavior of sliding push-pull connection in architectural precast concrete panels." Proceedings, Façade Tectonics, January 9-12, Los Angeles, CA. The author of the dissertation is the principal author of the above cited papers.

Chapter 4 reproduces content and images of the material as it appears in the PCI Journal 2016, Proceedings of the Façade tectonics conference 2014, and Proceedings of the Compdyn Conference 2013. Pantoli, E., Hutchinson, T. C., McMullin, K. M., Underwood, G. A., and Hildebrand, M. J., 2016. "Seismic-drift-compatible design of architectural precast concrete cladding: Tieback connections and corner joints." PCI Journal, July-August, 38-52. Pantoli, E., Hutchinson, T. C., Underwood, G. A., and Hildebrand M., 2014. "Seismic behavior of sliding push-pull connection in architectural precast concrete panels." Proceedings, Façade Tectonics, January 9-12, Los Angeles, CA. Pantoli, E., Chen, M., Hutchinson, T. C., Underwood, G. A., and Hildebrand M., 2013. "Shake table testing of a full-scale five-story building: seismic performance of precast concrete cladding panels." Proceedings, Compdyn Conference , June12–14, Kos Island, Greece. The author of the dissertation is the principal author of the above cited papers.

Chapter 5 reproduces content and images of the material as it appears in the Proceedings of the PCI convention 2013. Pantoli, E., Hutchinson, T. C., Underwood, G. A., and Hildebrand M., 2013. "Shake table testing of a full-scale five-story building: seismic performance of precast concrete cladding panels." Proceedings, PCI convention, September 21-24, Grapevine, TX. The author of the dissertation is the principal author of the above cited papers.

Chapter 6 reproduces content and images of the material as it appears in the Proceedings of the ATC-SEI conference 2015. Pantoli, E., and Hutchinson T. C., 2015. "Experimental and Analytical Study of the Dynamic Characteristics of Architectural Precast Concrete Cladding." Proceedings, ACT-SEI, 2nd

conference on improving the seismic performance of existing buildings and other structures, December 10-12, San Francisco, CA. The author of the dissertation is the principal author of the above cited papers.

Chapter 7 and 8 reproduce content and images of the material currently in preparation. Pantoli, E., Hutchinson, T.C. “Seismic accelerations developed in APC cladding panels” (tentative title). The author of the dissertation is the principal author of the above cited papers.

****

My dissertation research was supported by the National Science Foundation through Grant No. CMMI-0936505, "Full-Scale Structural and Nonstructural Building System Performance during Earthquakes". Professor Tara Hutchinson is the principle investigator for this research project, and include Professor Joel Conte and Professor Jose Restrepo are the co-principle investigators. Specific to the precast concrete cladding, the author appreciates the input of Glen Underwood and Clark Pacific, Mark Hildebrand of Willis Construction, Professor Kurt McMullin of SJSU, and the PCI advisory board. My dissertation research also received partial support through a dissertation fellowship from the Department of Structural Engineering at the University of California, San Diego. The above support is gratefully acknowledged. Opinions and findings of this study are of the author and do not necessarily reflect those of the sponsors.

VITA

2007	B.S. in Civil Engineering, University of Bologna, Italy
2010	M.S. in Civil Engineering, University of Bologna, Italy
2016	Ph.D. in Structural Engineering, University of California, San Diego, USA

PUBLICATIONS

Pantoli, E., Hutchinson, T. C., McMullin, K.M., Underwood, G.A., Hildebrand, M.J. (2016). "Seismic drift-compatible design of architectural precast concrete cladding: tieback connections and corner joints." *PCI journal*, July-August, pp. 38-52.

Pantoli, E., Chen, M.C., Wang, X., Astroza, R., Ebrahimian, H., Hutchinson, T.C., Conte, J.P., Restrepo, J.I., Marin, C., Walsh, K.D. and Bachman, R.E. (2016). "Full-scale structural and nonstructural building system performance during earthquakes: Part II-NCS damage states." *Earthquake Spectra*, 32(2), pp.771-794.

Pantoli, E., Chen, M.C., Hutchinson, T.C., Astroza, R., Conte, J.P., Ebrahimian, H., Restrepo, J.I. and Wang, X. (2016). "Landmark data set from the Building Nonstructural Components and Systems (BNCS) project." *Earthquake Spectra*, 32(2), pp.1239-1259.

Pantoli, E., Hutchinson T. (2015). "Experimental and Analytical Study of the Dynamic Characteristics of Architectural Precast Concrete Cladding." *Proc., ACT-SEI, 2nd conference on improving the seismic performance of existing buildings and other structures*, December 10-12, San Francisco, CA.

Pantoli, E., Hutchinson, T., Underwood, G. A., and Hildebrand M., (2014). "Seismic behavior of sliding push-pull connections in architectural precast concrete panels." *Proc., Façade Tectonics Conference*, January 9-12, Los Angeles, CA.

Pantoli, E., Chen, M., Hutchinson, T., Underwood, G. A., and Hildebrand M. (2013). "Shake table testing of a full-scale five-story building: seismic performance of precast concrete cladding panels." *Proc., Compdyn*, June12–14, Kos Island, Greece.

Pantoli, E., Hutchinson, T., Underwood, G. A., and Hildebrand M. (2013). "Shake table testing of a full-scale five-story building: seismic performance of precast concrete cladding panels." *Proc., PCI convention*, September 21-24, Grapevine, TX.

Pantoli, E., Wang, X., Chen, M. C., Hutchinson, T. C., Meacham, B., and Park, H. J. (2013). "Shake table testing of a full-scale five-story building: performance of the major nonstructural components-egress and façades." *Proc., Structures Congress*, May 2-4, Pittuburgh, PA, pp. 1447-1459.

Chen, M.C., **Pantoli, E**., Wang, X., Astroza, R., Ebrahimian, H., Hutchinson, T.C., Conte, J.P., Restrepo, J.I., Marin, C., Walsh, K.D. and Bachman, R.E. (2016). "Full-scale structural and nonstructural building system performance during earthquakes: Part I-Specimen description, test protocol, and structural response." *Earthquake Spectra*, 32(2), pp.737-770.

Astroza, R., **Pantoli, E.**, Selva, F., Restrepo, J.I., Hutchinson, T.C. and Conte, J.P. (2015). "Experimental Evaluation of the Seismic Response of a Rooftop-Mounted Cooling Tower." *Earthquake Spectra*, 31(3), pp.1567-1589.

Wang, X., **Pantoli, E.**, Hutchinson, T., Restrepo, J., Wood, R., Hoehler, M., Grzesik, P., and Sesma, F. (2015). "Seismic Performance of Cold-Formed Steel Wall Systems in a Full-Scale Building." *ASCE J. Struct. Eng*., 141(10).

Geng, J., Melgar, D., Bock, Y., **Pantoli, E**. and Restrepo, J. (2013). "Recovering coseismic point ground tilts from collocated high-rate GPS and accelerometers." *Geophysical Research Letters*, 40(19), pp.5095-5100.

ABSTRACT OF THE DISSERTATION

Seismic Behavior of Architectural Precast Concrete Cladding Panels and Connections

by

Elide Pantoli

Doctor of Philosophy in Structural Engineering

University of California, San Diego, 2016

Professor Tara C. Hutchinson, Chair

Architectural precast concrete (APC) cladding is a type of building façade composed by concrete panels separated from each other by joints and attached to the building structure with steel connections. Seismic damage to this component has been observed in past earthquakes, it is costly and time consuming to repair, and, importantly, it can be life threatening. APC cladding is unique among nonstructural components, since its heavy concrete panels span from floor to floor. As a result, this system is uniquely sensitive to **both** interstory drifts and floor accelerations. However, only few experimental or analytical programs have specifically focused on this type of façade. Since knowledge regarding the seismic behavior of APC façades is limited, design code prescriptions are relatively qualitative and do not accurately consider the many features of the system.

The first part of this dissertation aims to provide guidance to practitioners to improve the drift-compatible design of APC cladding. Results are based on three experiments: one system level experiment in which sixteen panels were installed on a full-scale building and two component tests on tieback connections. The combination of the results from these tests provided information on the how to improve the detailing of tieback connections to create the optimal compromise between good seismic performance

and constructability. In addition, this part of the dissertation includes a one-of-a-kind study of a new type of corner system allowing for smaller corner joints thanks to a ductile fuse.

The second part of this dissertation presents an analysis of the accelerations developed in the APC cladding during seismic motions. This analysis is based on numerical models validated using data from the system level experiment. Initially, the dynamic characteristics of the APC cladding are analyzed using models of the panels and connections. Subsequently, the APC cladding is included in a building model, with the goal of determining the amplification of accelerations in the panels during service and design level motions. The study revealed issues in the way the panels are currently designed to resist seismic forces.

Chapter 1

Introduction

Architectural precast concrete (APC) cladding is a type of building façade composed of APC panels attached to the building exterior with steel connections. Individual panels are separated from each other by horizontal and vertical joints filled with flexible caulking. This type of façade has been used worldwide since the 1960s, and it can be designed using a variety of panel geometries and connection details. Its use is appealing since individual parts can be fabricated offsite and erected rapidly. In addition, it is durable and panels can be fabricated in a variety of colors, shapes and textures. In seismic areas, APC cladding is generally designed as a building nonstructural component. Since panels span generally from floor to floor, APC cladding can be considered sensitive to interstory drifts. However, differently from other nonstructural components spanning multiple levels, APC cladding is also very heavy, and thus equally sensitive to accelerations.

This introductory chapter presents first of all a description of the types of façades most commonly used, and then it focuses on the description of the main characteristics of APC cladding. Subsequently, the chapter focuses on the discussion of the issues related to the seismic behavior of precast concrete façades: the current design codes and typical practice in different countries, the damage observed in the past earthquake and the research already performed. The last part of the chapter introduced the main objective of this study and the organization of the dissertation.

1.1 Façade Systems

1.1.1 Historic Overview

Until a couple of centuries ago, façades were very different from what we find in most buildings today. In fact, for most of the history of structures, exterior walls have been an integral part of the load bearing system. However, when engineers and architects began to use structural frames to support loads, exterior walls were liberated from their previous role and this led to the necessity of providing an architectural (i.e. non-load bearing) exterior wall, more commonly façade. Early famous examples of non-loadbearing façades include the Crystal Palace in London (1851), the Reliance

Building in Chicago (1895), L'innovation department store in Brussels created by Victor Horta (1901) and the Bauhaus building (1926), which are shown in Figure 1.1. The commonplace use of modern façade systems, such as curtain walls, occurred only after World War II due to the advancement in technology and increase of material availability (Murray 2009, Crosbie 2005, Vigener and Brown 2012).

(a) **(b)**

(c) **(d)**

Figure 1.1. Examples of early façades: (a) Crystal Palace, (b) L'innovation department store, (c) Bauhaus building (CC image courtesy of Alec Luhn on Flickr), and (d) Reliance building (CC image courtesy of Steve Silverman on Flickr)

1.1.2 Function

Modern façades have to satisfy several separate goals, as reported by Arnold (2009):

1. Support their own weight;
2. Accommodate movement created by temperature variation or structural movements;
3. Provide necessary clearances and alignments that allow it to be constructed properly;
4. Provide access to the several components for maintenance and repair;
5. Resist water penetration;
6. Resist excessive air infiltration;
7. Avoid condensation on the interior surfaces;
8. Help conserve energy;
9. Attenuate sound transmission;
10. Provide nominal resistance to heat and smoke passage;
11. Protect the occupants from outside threats;
12. Be durable;
13. Look aesthetically pleasing;
14. Be relatively inexpensive.

During the design of a façade, engineers are mainly concerned with the first four goals, while goals 5 to 10 are mostly architectural considerations. The last four goals are overarching general issues that also need to be taken into account.

1.1.3 Classification

Façades are generally classified into three types: infill panels, cladding and mix systems, which are a combination of infill and cladding. The difference between infill and cladding is that while the former is constructed within the structural frame, the latter is attached outside of the structure.

Infill

Traditionally, infills have been created using masonry, and this type of technology is still popular in Europe and South America. More lightweight infill options, such as those created by steel or timber framing, are also available. Typically, infill panels are also combined with glazing (Baird et al.

2011). An example of a modern type of infill is constituted by light steel C-sections and plasterboard spanning from floor to floor (SteelConstruction.info).

Cladding

One common type of cladding is the so called "curtain walls". According to the Whole Building Design Guide (Vigener and Brown, 2012) a curtain wall is a thin and generally aluminum framed wall. The infills of this wall can be created using glass, metal panels or thin stone. Depending of their fabrication and installation, curtain walls can be divided into "stick system" or "unitized". In the former, the frame of the curtain wall and the infill are installed and connected piece by piece, while in the latter type, the wall is composed by larger units assembled in the factory and then shipped on site (Vigener and Brown 2012). Another type of cladding is known as "frameless glazing" or "spider glazing" (Figure 1.2). In this system the façade is constituted entirely by glass panels joined by steel connectors at the corners.

(a) **(b)**

Figure 1.2. Examples of spider glazing: (a) Everett Station (CC image courtesy of SounderBruce on Flickr), and at Melbourne Exhibition Center Station (CC image courtesy of Ding YangYang on WikiCommons)

"Monolithic cladding" is a type of enclosure that has a seamless appearance, usually created by applying plaster on top of a backing material. This type of cladding include also Exterior Insulation and Finish Systems (EIFS), created by metal framing, sheathing, polystyrene insulation and plaster. The type of cladding known as "masonry veneers" is created by a single layer of masonry or brick separated by the main structure. They have to support their own weight and they are typically tied to the structure to provide some out-of-plane resistance. Another type of classification of cladding can be adopted by

considering the weight of the panels composing the façade. “Lightweight panels” are composed of materials such as metal sheets, plywood and autoclaved aerated concrete, while “heavy panels” are created with stone or architectural precast concrete (Baird 2014).

1.2 Architectural Precast Concrete (APC) Cladding Technology

APC façades are completely covered by many separate panels, each one attached to the structural elements with the aid of steel connections and separate from each other by caulking-filled joints, as shown in Figure 1.3. This technology was first used in the 1920s, but it flourished only from the 1960s thanks to the new developments in transportation and lifting technology.

(a) **(b)**

Figure 1.3. Example of APC panels (a) during transportation and (b) installed on a building (Images courtesy of Mark Hildebrand)

A classic example of one of the first buildings making use of APC cladding is the Baha’I House of Worship in Wilmette, Illinois (Figure 1.4a) whose construction started in the 1920s. Many other famous buildings utilize this technology, including the TransAmerica Building in San Francisco (Figure 1.4b) the Jubilee church in Rome (Figure 1.4c), and the metronome in New York City (Figure 1.4d).

1.2.1 Benefits

The benefits of APC cladding technology include:

- *Speed of construction*. APC panels are fabricated at a precast factory and delivered to the site just prior to installation, where twenty or more panels can be installed during a working day;

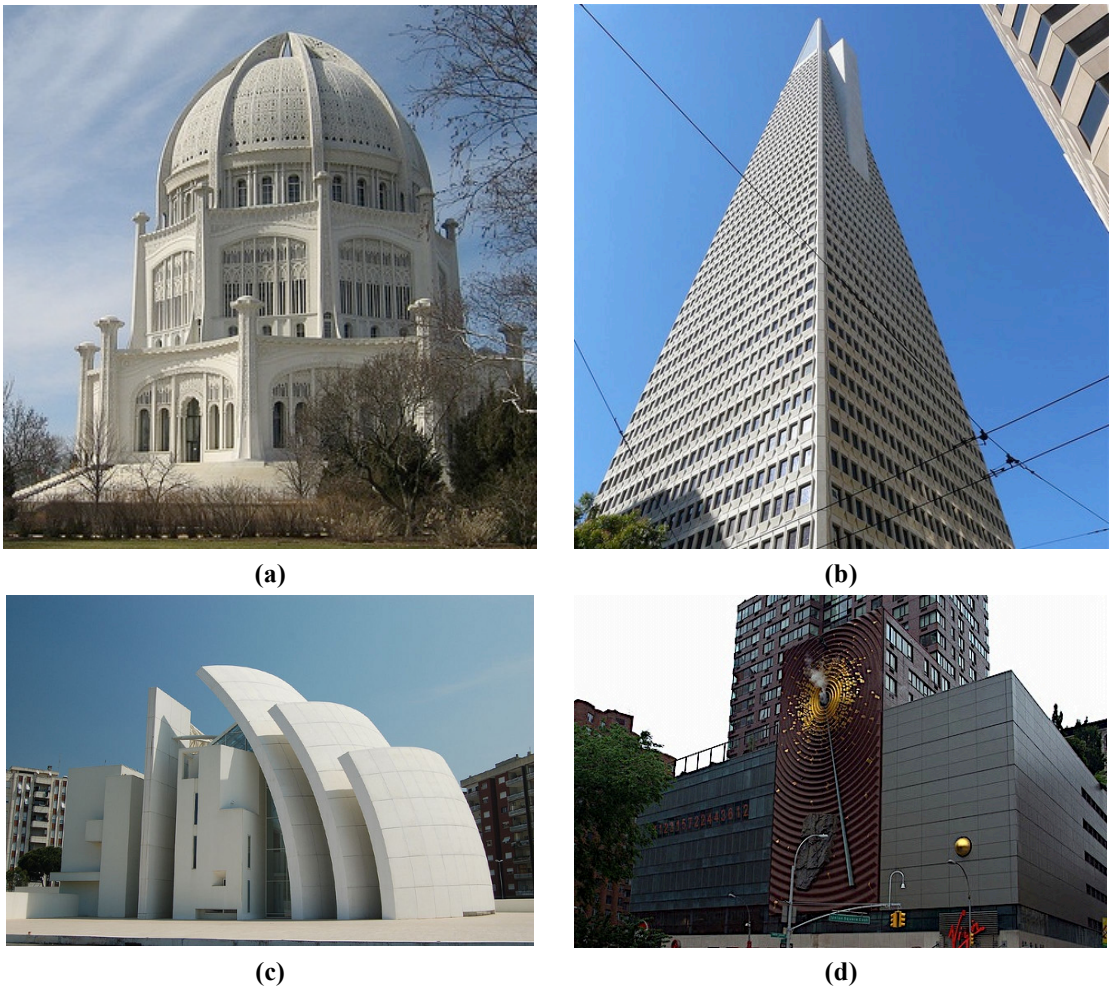

(a) **(b)**

(c) **(d)**

Figure 1.4. Photographs of buildings with APC cladding: (a) Baha'I House of Worship in Wilmette, Illinois (CC image courtesy of Chris Yutzy on Flickr), (b) TransAmerical building in San Francisco, California (CC image courtesy of Benjamin Dumas on Flickr), (c) Jubilee church in Rome, Italy (CC image courtesy of Alan Massey on Flickr), and (d) Metronome building in New York City (CC image courtesy of Charles Kaiser on Flickr)

- *Durability.* APC is resistant to impact, corrosion, weathering and abrasion;
- *Superior quality compared to poured-in-place concrete*;
- *Low life-cycle costs.* APC can be designed to match the intended life cycle of a building. In addition, it does not require painting;
- *Aesthetics.* Architectural concrete can be produced in many different colors and textures and it can mimic a wide range of materials. In addition, it can be created in many different shapes;

- *Sustainability*. Concrete is made by readily available elements, it can contribute to energy efficiency and it can include recycled materials (PCI 2007).

1.2.2 APC Panels Configurations

Panels of different geometries can be used, namely PCI (2007) identifies four commonly used types of panels:

1. *Solid wall panels*: they do not contain any opening and in seismic regions their height corresponds to the story height;
2. *Window wall panels:* these story-height panels can contain one or more window openings. When the window is roughly centered vertically, the wall panel is called "punched window", while if the window opening is at the upper edge of the panel, the panel is named "U-shaped". Building configurations using punched window and U-shaped panels are schematically shown in Figure 1.5a and b respectively;

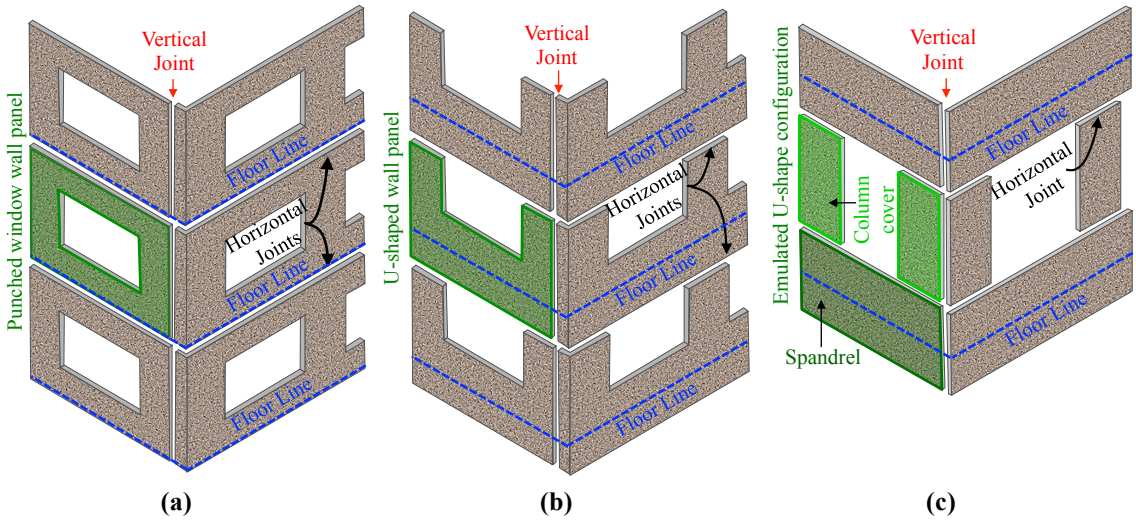

Figure 1.5. Subset of common APC cladding arrangements for building façades: (a) punched window panels, (b) u-shaped panels, and (c) emulated u-shaped panels (Courtesy of Hutchinson et. al 2014)

3. *Spandrel panels*. These are horizontal units, usually separated by strips of glass;
4. *Column covers and mullions*. These units may be broad or barely wider that the column itself and run vertically in the structure. Column covers might extend from floor to floor or between

spandrels. When column covers and spandrel panels are used together, they form a configuration that can be called "emulated U-shaped", as shown in Figure 1.5c.

The decision on which of the type of panels to select depends on architectural considerations and transportability. For example, if the story height exceeds the transportability limits for a single panel, mullions and spandrels are required.

1.2.3 Production of APC Panels

APC cladding panels are produced at a precast facility, where the typical process includes the assembly of the rebar cage, creation of the form, pouring of concrete, and finishing of the panels (e.g. with sandblasting). In the meanwhile, temporary connections are installed on the structure to prepare for the installation of the panels. Panels are then shipped on site, lifted from the truck with a crane, aligned, and attached to the building through temporary connections. In the following days, the temporary connections can be replaced with the finals ones, which usually include welding. Panels are then finished with the application of caulking in the joints.

1.3 Seismic Protection of APC Cladding

There are four possible contributions cladding can have to the seismic resistance of a building, as initially suggested by Arnold in 1989:

- *Theoretical detachment*: no contribution from the panels to the lateral stiffness of the building.
- *Accidental participation*: if the separation between cladding and structure is not effective for example due to errors during installation or unexpected development of mechanical restraints;
- *Controlled damping:* when cladding panels are used to add damping to the system through special "advanced" connections;
- *Full structural participation*: in this approach, cladding panels are designed to be an integral part of the lateral force resisting system of a building. This last one is generally not used.

The "theoretical detachment" approach is the one most common in practice, and for these reasons it will be the one examined in this research. However, some research has been performed in the past on advanced connections and the possibility of integrating cladding panels in the lateral force resisting system of the building. A literature review of all approaches is presented in subsequent

sections.

1.3.1 Current Practice

APC cladding is generally designed as a nonstructural component, meaning that during an earthquake it should support only its own seismic weight. The mechanism for the seismic protection of this façade system is provided mainly by its steel connections, which must both resist seismic forces created by the panel mass and absorb story drifts, since generally APC panels span from floor to floor. One of the key purposes of the steel connections is to detach the panel-to-building displacements in the in-plane direction. In fact, due to the high in-plane stiffness of the panels, without such a mechanism panels could start acting as structural shear walls thus attracting forces created in the structure. Separation of the in-plane displacements can be achieved by allowing the panel either to translate or to rock. *Translation* is achieved with a combination of fixed connections and connections that are allowed to slide in the horizontal direction, while *rocking* is achieved by the combination of vertical sliding connections.

1.3.2 United States

In the U.S., panels with a low height-to-width ratio (e.g. punched window wall panels) are generally allow to move with a "translation mechanism", while "rocking mechanism" is used for tall and narrow panels like column covers. A translation mechanism is created by connecting the bottom of the panel with fixed "bearing" connections and the top of the panels with "tie-back" (or "push-pull") connections, which restrain the panel in the out-of-plane direction while allowing in-plane translation. The main element of a tie-back connection is generally a steel rod that can absorb drifts by either sliding inside a slot ("sliding connections") or bending ("flexing connections"). Further details about the design of APC panels in the West Coast of the United States is presented in Chapter 2.

1.3.3 New Zealand

The technology used in New Zealand is similar to that used in the West Coast of the United States. However, bearing connections are generally placed at the top of the panels and tie-backs at the bottom. Namely, in New Zealand sliding tie-back connections are more popular than flexing connections (NZNSEE 2007).

1.3.4 Italy

In Italy, precast concrete panels are typically used to clad precast buildings, which generally have either industrial or commercial use. Colombo and Toniolo (2011) report that, until recently, the drift-compatible issues of panels were not specifically considered during the design phase. In fact, even if the panels were designed to resist forces created only by their own seismic weight, they were fixed at both floors, thus acting as structural shearwalls and attracting forces created by the seismic weight of the structure. The vulnerability of this system was revealed during the 2009 L'Aquila earthquake, during which many cases of collapse of APC cladding panels were observed (see next section). Colombo and Toniolo (2011) report three possible solutions to this issue. The first one is to keep the connections as they are but add secondary retention mechanisms to prevent the panel collapse in case of fracture of the main connections. This solution has been proposed especially for the retrofit of existing structures. The second solution is to design an integrated structure in which the panels act as structural shearwalls. This solution would require the use of new connections able to absorb the larger forces generated by the mass of the structural system. A final solution is to allow the panels to move relatively to the structure, as done in other countries such as the United States. If this latter solution is adopted, Riva et al. (2011) reports that bearing connections are generally installed at the bottom of the panels, while connections able to allow for seismic drifts at its top. For example, Figure 1.6 presents the location of these two types of connections in two horizontal (i.e spanning from column to column) panels, one resting on the ground and one at some height on the building.

There is a large variability of the detailing of both types of connections, since connection technologies are protected by patents, and thus each firm is encouraged to create their own design (Capozzi 2009). For this reason, the following discussion of connections is aimed only at providing examples, but it is not intended to be an exhaustive list of all the connections used in the Italian practice. The connections at the bottom of the panels designed to support gravity loads generally assume a shelf-type form. Figure 1.7 shows a bottom connection composed by a cantilevering shelf created by a stiffened angle that is fixed to an embed in the structural element with a bolt. This shelf supports the bottom of the panel by inserting it inside a channel of appropriated shape embedded in the

panel. Figure 1.8 presents another example of a shelf-like bottom connection.

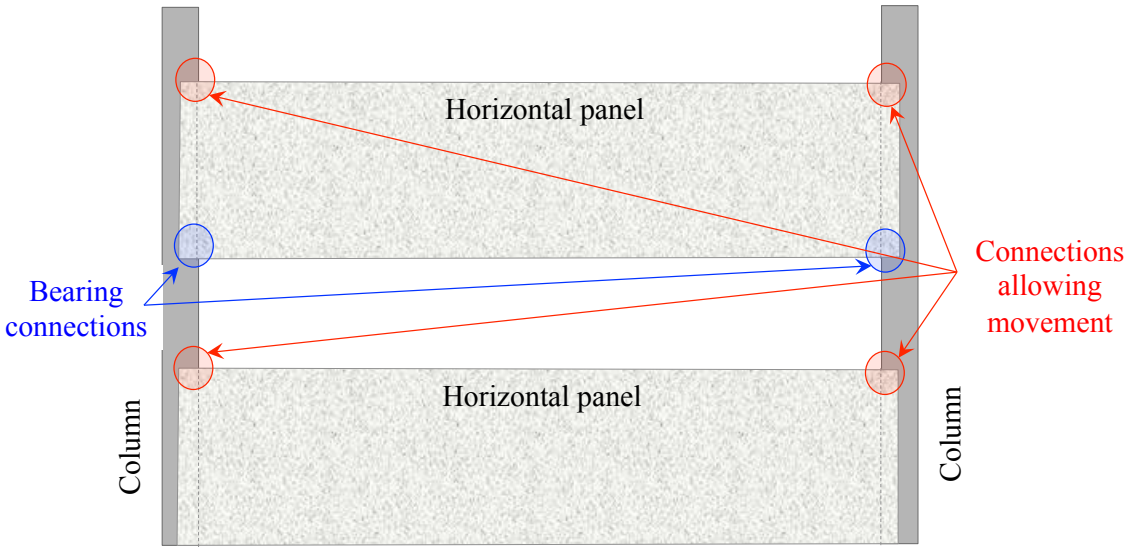

Figure 1.6. Location of connections in horizontal panels in the typical Italian practice (Image modified from Colombo and Toniolo 2011)

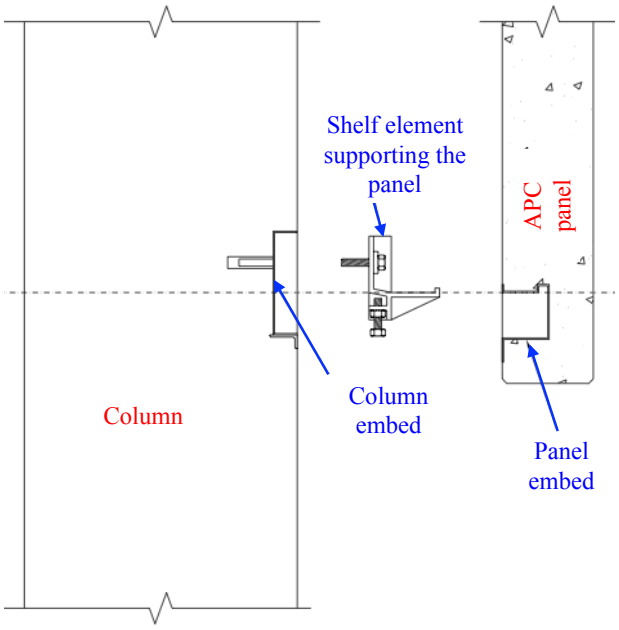

Figure 1.7. Example of bottom connections (Image modified from Mandelli Contegni et al. 2007)

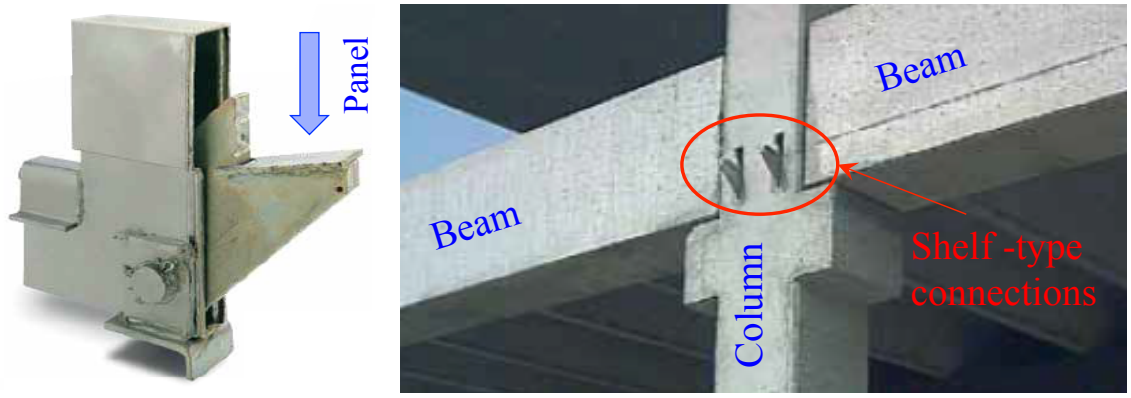

(a) **(b)**

Figure 1.8. Examples of shelf-connections typical of the Italian practice from the Ruredilbook catalogue (Courtesy of Ruredil 2014)

Typical connection designed to allow seismic movement used in Italian practice are shown in Figure 1.9. The main elements of the connection are two channel sections embedded in the panels and in the structural elements, a bolt with the head shaped specifically to match the shape of the channel, and a connector. In Figure 1.9a, the connector is in the form of a plate with one of the ends shaped to match the profile of the channel and the other having a slot. In Figure 1.9b the connector element is a reinforced angle clip, also in this case provided with a slot. Figure 1.10 shows more examples of these types of connections. The long channels in these connections have the goal of both absorbing construction tolerances and seismic drifts. However, the lack of specific detailing of this connections, especially regarding the tightening of the sliding element, could lead to an improper working of the sliding mechanism.

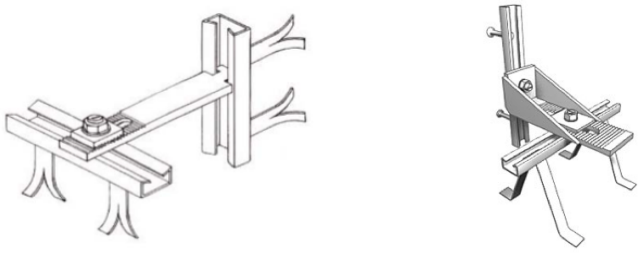

(a) **(b)**

Figure 1.9. Typical connection allowing movement utilized in the Italian practice (Courtesy of Capozzi, 2009)

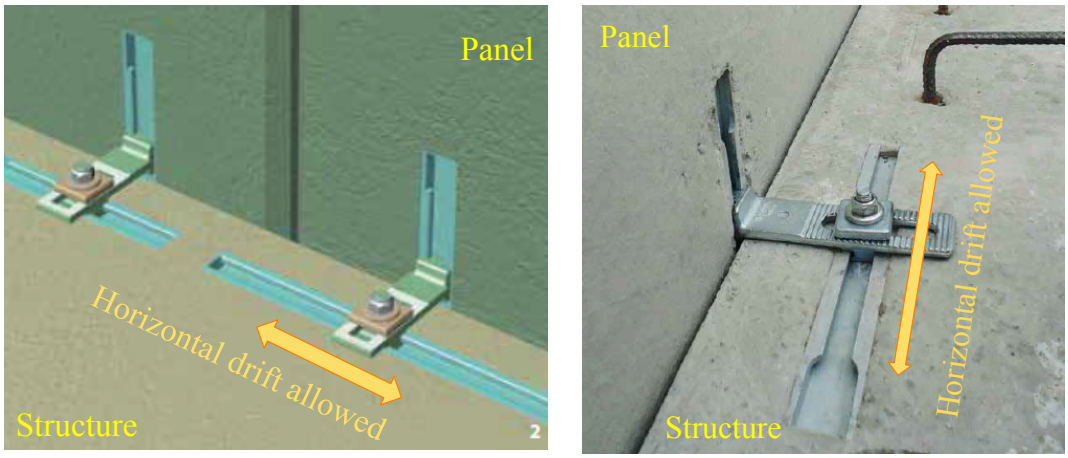

(a) **(b)**

Figure 1.10. Sliding connections allowing for horizontal drifts typical of the Italian practice (Image modified from Ruedil 2014)

Another type of panel-column connection allowing for movement and used for horizontal panels is shown in Figure 1.11. The main element is a stiffened angle, which has holes on one side for the connection to the column and a slotted hole on the other side to connection to the panel. This slot is designed to allow for construction tolerances and seismic drifts. Another variation of the sliding connection for vertical (i.e. connected to ground and beam) panels is presented in Figure 1.12.

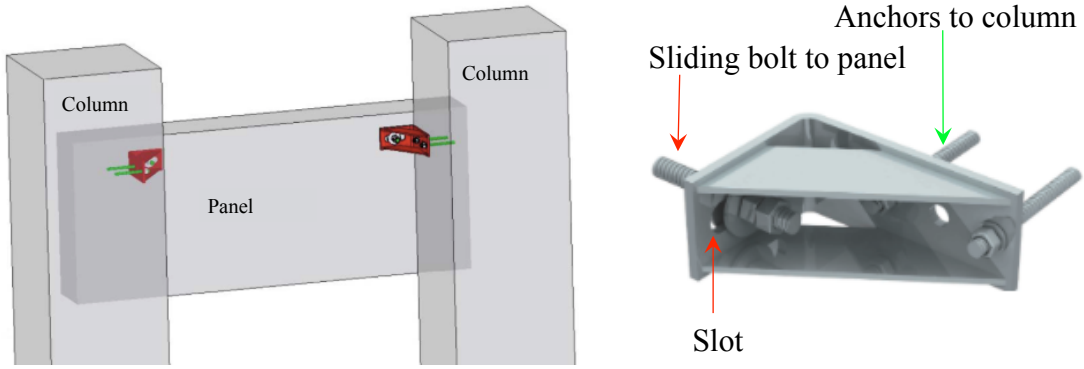

(a) **(b)**

Figure 1.11. Variation of the sliding connection in the Italian practice used for horizontal panels: (a) location and (b) details of the connections (Courtesy of prefabbricazione.web 2014a)

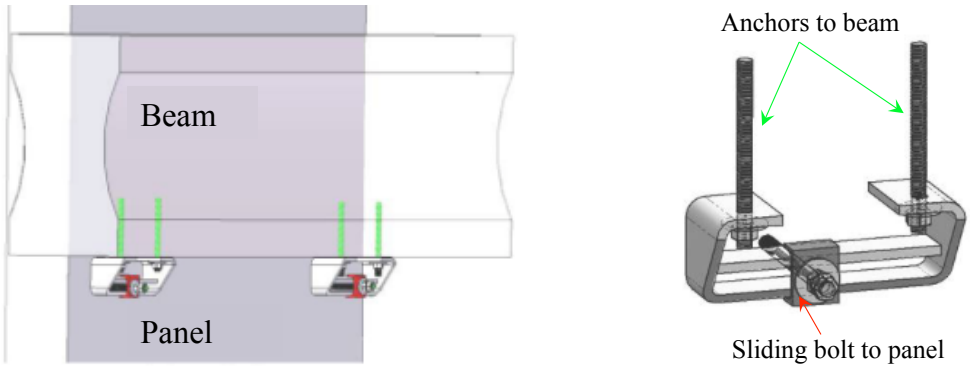

Figure 1.12. Variation of the sliding connection in the Italian practice used for vertical panels: (a) location and (b) details of the connections (Courtesy of prefabbricazione.web 2014b)

1.3.5 Japan

In 1987, Wang (Wang 1987) reported that the seismic protection of APC cladding in Japan was mostly created by allowing a rocking motion of the panels made possible by vertical sliding connections. One of the advantages of rocking motion is that the connections do not need to accommodate large distances relative to the actual story drift, depending on the horizontal distances between the connections. Rocking connections are not common in the U.S., likely because they are more expensive and more complex. This could lead to a greater chance of errors during installation.

1.4 Damage to APC Cladding During Past Earthquakes

1.4.1 Worldwide

1985 Mexico City earthquake

Goodno (1989) examined the behavior of façades in 25 buildings hit by the Mexico City earthquake. Only 4 out of these 25 reported poor performance, which included cladding failure, while 16 performed well. It is noted that many different types of façade technologies were used in the buildings affected. Some of the results reported by Goodno include:

- Two buildings with heavy cladding with a design similar to the typical U.S. practice performed well;
- Damage was observed in a façade composed by panels and infill walls. In this case, panels were attached to the infill by mortar reinforced with 1/8'' steel wires tied to 4'' nails driven

into the brick masonry. The damage observed consisted in the delamination of the panels from the mortar backing, posing danger of the panels falling from the building;

- Damage to a façade system composed by column covers and spandrel panels was observed. Column covers were attached to the building through embeds in the slabs and experienced racking at the location of the panel inserts while spandrels were not damaged;
- A building reported spandrel panels being intact, but a large amount of glass breakage;

The author reported that this damage might have been caused by lack of provisions to accommodate lateral movements. In fact, in many cases the cladding erector simply used available material and created connections out of scrap reinforcing bars.

For this same earthquake, Fintel (1986) reported good APC cladding performance. He noted that the bottom of the panels were typically connected to the slab with welded plates, while the top of the panels were connected with elements similar to short flexing connections. For the buildings he surveyed, he reported only two cases of poor performance. In the first, a number of panels pulled away several inches at the top due to bolt shear failures. Nevertheless, the lower welded connections did not fail and kept the panel attached. In the second case, some upper panels fell from a building. These panels were U-shaped and were covering two columns at an expansion joint. Apparently during the earthquake the joint opened wider than expected creating detachment of the panel.

1995 Kobe earthquake (Japan)

Horii et al. (1995) performed an inspection of 50 buildings with APC panels after the Kobe earthquake and concluded that the main cause of damage was the relative displacement imposed to the floor-to-floor panels. In fact, most of this damage was observed in wall panels, while spandrel panels behaved better. Damage observed included:

- Fallen panels;
- Damage around panel openings;
- Out-of-plane misalignment, observed in more than 50% of the buildings inspected;
- In-plane relative permanent displacements, reported for more that 70% of the cases considered;
- Corner panels movements;

- Damage to surface finishing materials;
- Damage to the connections e.g. shear failure of anchor bolts in sliding connections;
- Damage to concrete close to the connections.

2009 L'Aquila earthquake (Italy)

As explained in the previous sections, in the typical Italian practice before this earthquake, issues of drift-compatibility were not explicitly addressed. In fact, APC panels were designed as nonstructural components, however they were fixed to different floors. As expected, this lead to great amount of damage and collapse of many APC panels during L'Aquila earthquake, which affected an area with many precast structures, especially one story industrial building and two/three stories commercial buildings (Toniolo and Colombo 2012, Myamoto International 2009). Examples of damage are reported in Figure 1.13a and Figure 1.14a.

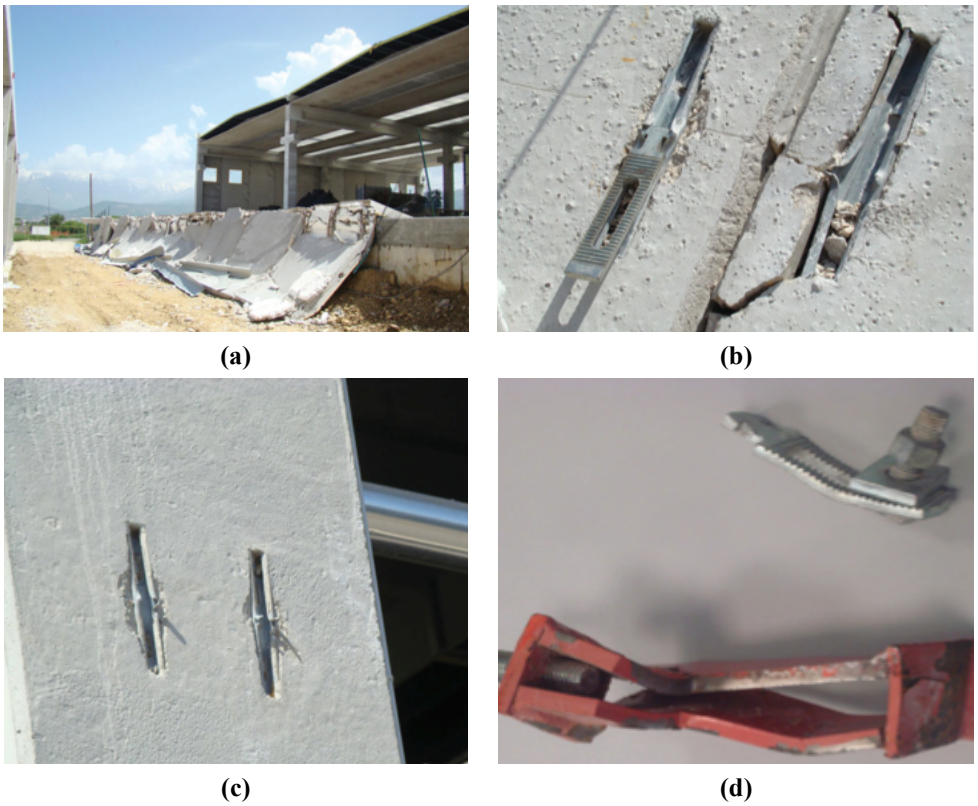

(a) **(b)**

(c) **(d)**

Figure 1.13. Damage to APC cladding during the 2009 L'Aquila earthquake (Courtesy of Toniolo and Colombo 2012)

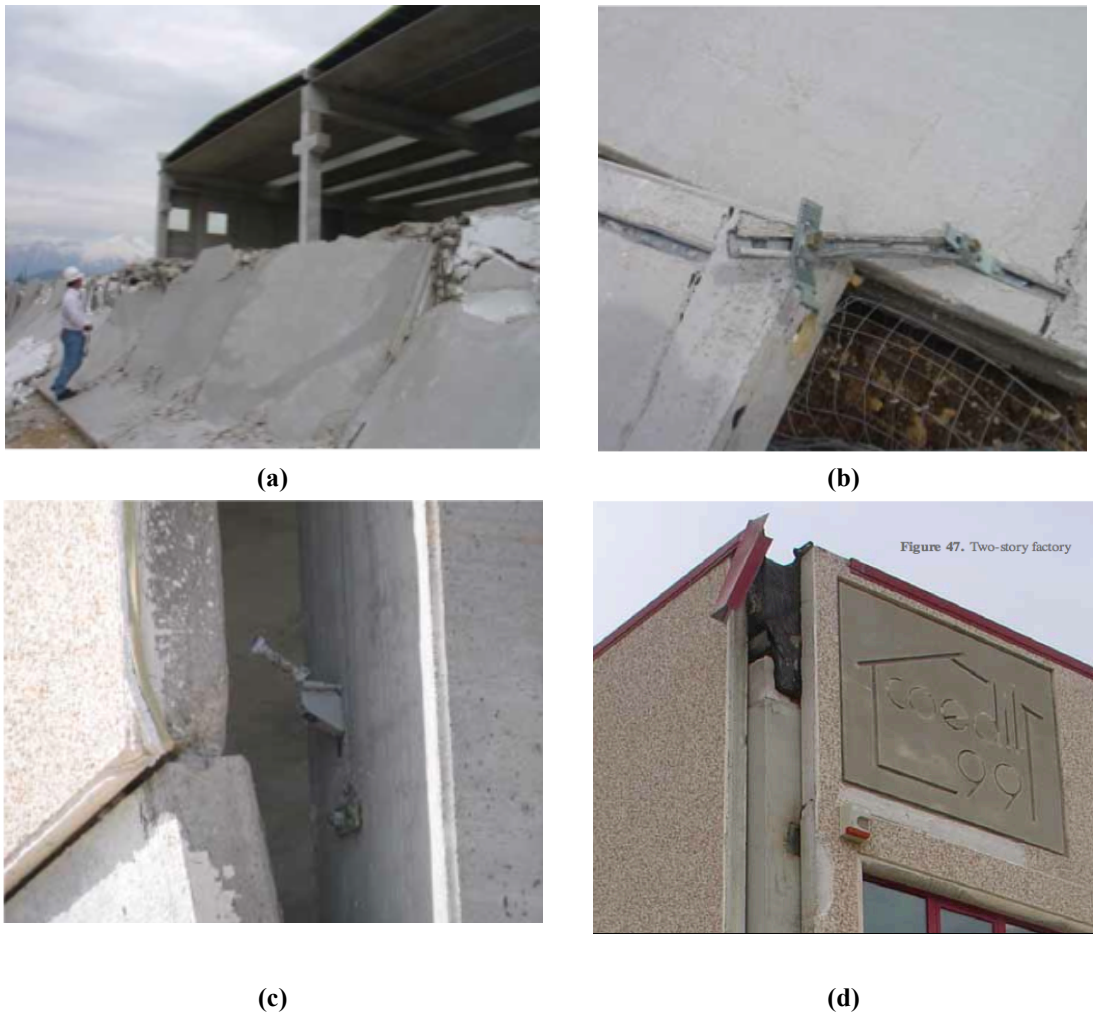

Figure 1.14. Damage to APC cladding observed after the L'Aquila earthquake: (a) collapse of APC panels, (b) failed bottom connections, (c) failed C channel connection, and (d) building showing collapsed corner panel (Courtesy of Myamoto international)

Damage was mostly caused by failure of connections created by forces larger than those considered during design, due to the fact that these very stiff panels fixed to multiple heights were acting as structural shearwalls, and attracting seismic forces created by the mass of the structure. A typical damage involved the sliding connections with channels and anchors, as can be seen Figure 1.13b-c and Figure 1.14b. Since the connection channels received large forces in the transverse direction of the panels, in many instances the head of the anchor bolt pulled out the edges of the channel. Even the bottom shelf connections underwent damage, for example pull-out of the connections from the anchoring to the panel, as shown in Figure 1.14c. As already mentioned, in the Italian practice

there is great variability of detailing in the APC cladding connections, however it was noticed that none of the different type of connections remained undamaged (Figure 1.13d), thus confirming a systematic issue in the way the connections were designed especially related to design force. Because of the lack of drift-compatibility considerations, corner panels were also particularly sensitive to damage and collapse is several cases, as shown in Figure 1.14d.

2010 El Major Cucapah, Baja California earthquake (Mexico)

EERI (2010) reports a case of minor damage to precast wall panels after the 2010 El Major Cucapah earthquake. Namely, residual offset of the walls relative to each other in both directions and spalling of concrete at a corner was reported in one of the buildings at the regional medical center and medical plaza (Figure 1.15).

(a) **(b)**

Figure 1.15. Damage to APC cladding after the El Major Cucapah earthquake: (a) relative displacement, and (b) corner crushing (EERI 2010)

2010 Maule earthquake (Chile)

In Chile, APC cladding in mostly used in industrial and low-rise office building. These building have generally performed well when requirements for seismic resistance were considered in designing and detailing. Following the 2010 Maule earthquake, in one case, a building was clad with wall panels attached to the structure with long slotted embeds oriented vertically in the columns and

horizontally in the wall panels to provide ample alignment tolerance and allow in-plane movement. Some of the cladding panels fell from the building because they were not able to withstand the large forces created by the earthquake. In fact, the lips of the channel embed deformed and allowed the bolts to pull out as shown in Figure 1.16a (Ghosh and Cleland 2010). FEMA reported that during this earthquake, damage was observed to some precast corridor and railing panels (Figure 1.16b), many of which had to be removed from the building to avoid collapse. These panels were supported by a bearing seat at the center and on steel dowels at the ends (FEMA E-74 2011).

(a) **(b)**

Figure 1.16. Damage to APC panels during the 2010 Maule earthquake: (a) damage to cladding connection (Gosh and Cleland 2010) and (b) damage to railing panels (FEMA E-74 2011)

2011 Christchurch earthquake (New Zealand)

Baird (2014) reports that little to no damage was experience by APC panels during the 2011 Christchurch earthquake. Damage consisted mainly of cracking or crushing of the concrete, probably due to pounding between adjacent elements in case of corner areas (Figure 1.17a). Another common type of damage was rupture of caulking (Figure 1.17b). It was also found that, in case the beam plastic hinges were located between APC panels connections, both APC connections and panels experience extensive damage because of the increase in length of the beam (Figure 1.17c). Only one case of collapse of panels was observed in Christchurch, where six spandrel panels fell from the upper stories of a building (Figure 1.17d-e). This failure was attributed to a construction error, in fact, the bolt of the sliding connections were welded to the clip, thus impeding any relative motion. Since the bolts were unable to slide, they failed in shear. Collapse of APC panels was also observed after the earthquake of June 2011. Each panel was fixed at its base to the structure and to other panels, but the top connections

were not able to provide any degree of lateral movement and tore out through the panel as observed in Figure 1.18 (Baird 2014).

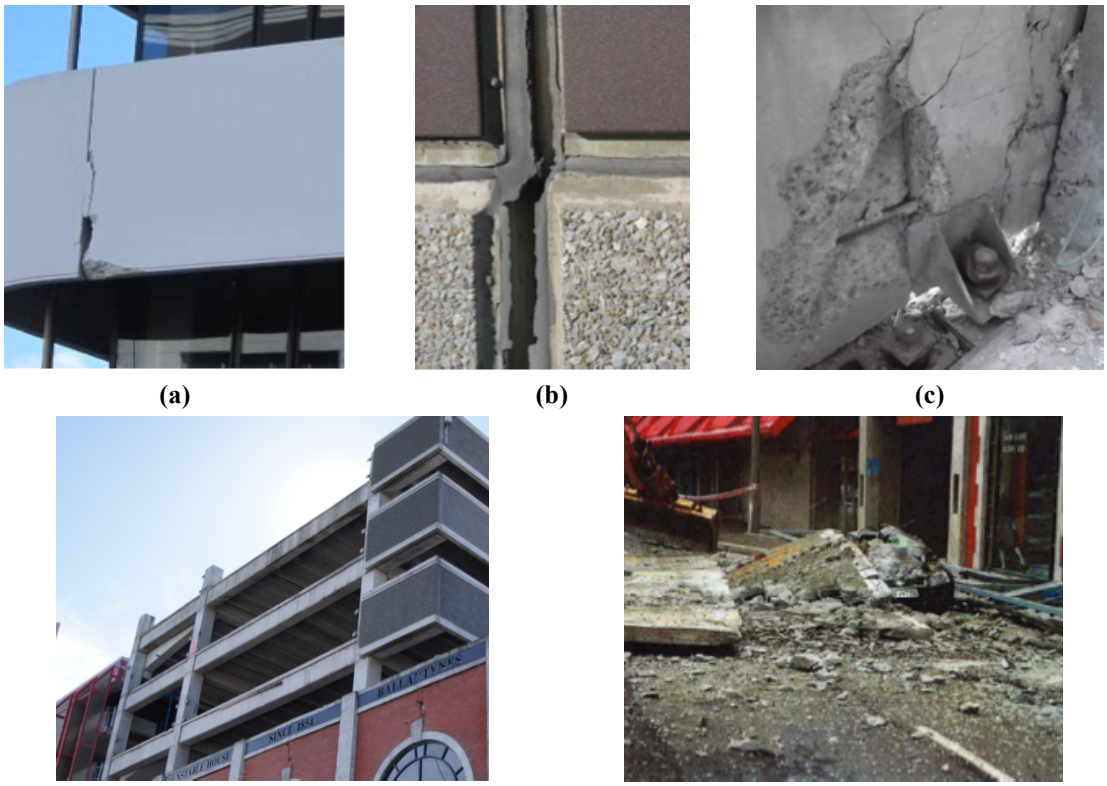

(a) **(b)** **(c)**

(d) **(e)**

Figure 1.17. Damage to APC panels during the Christchurch earthquake in February: (a) cracking and corner crushing, (b) rupture of caulking, (c) damage to connections and panels due to frame elongation, (d) building from which the panels fell, and (e) panels fallen on top of a car (Baird 2014)

(a) **(b)**

Figure 1.18. Panels collapsed during the Christchurch earthquake in June 2011 (Baird 2014)

2012 Emilia earthquake (Italy)

During the Emilia earthquake in Italy, extensive damage to APC cladding was observed. According to Belleri et al. (2014) APC panels collapsed because of their connections were inadequate to absorb the seismic loads they experienced. In fact, the connections were designed mainly to sustain gravity and wind loads. The failure of the connections was caused in most cases by the detachment of the bolts form the channels, and happened particularly at panels installed at upper levels. Magiulo at al. (2013) list the causes of the collapses observed, namely a lack of seismic design of the connections, pounding of elements, and additional forces in the connections created by panel-structure interaction. He reports cases of collapse created by failure of the connections channels (Figure 1.19a). In addition, he also presented the failure of a connection, where a steel profile was embedded in the beam, some hammer head elements were welded to this embed and then inserted in the anchor channel embedded in the cladding panels. The earthquake caused failure of the welds and consequence collapse of the panels (Figure 1.19b-c). Damage to APC panels during the Emilia earthquake is also reported by Bournas et al. (2013). He specified that in most of the buildings he inspected damage to cladding panels was observed, regardless of the presence or absence of seismic provisions during the design process. Bournas observed that collapse occurred in two cases: 1) when there were excessive drifts that exhausted the sliding capacity of the connections and 2) when the out-of-plane inertia forces were too large. Examples of buildings with collapsed APC panels are reported in Figure 1.20.

(a) **(b)** **(c)**

Figure 1.19. Connection failures after the Emilia earthquake (Courtesy of Magiulo et al. 2013)

(a) (b)

(c) (d)

(e) (f)

(g) (h)

Figure 1.20. Building that experienced collapse of roof and APC cladding during the Emilia earthquake (Ercolino et al. 2012a, Ercolino et al. 2012b, Di Croce et al. 2012)

1.4.2 United States

Although there are many existing buildings with APC cladding in the U.S., panel collapse due to earthquakes has only been reported in a few cases. It is noted that the fact that there has not been a major earthquake in recent years could have contributed to this.

During the 1964 Alaska earthquake, several panels fell form a J.C. penny store because of connections shearing, fracturing and fatiguing (Sielaff et al. 2005, Arnold 2009) as shown in Figure 1.21a. During the 1987 Whittier Narrows earthquake, a precast panel fell from a parking garage at the California State University in the Los Angeles area as shown in Figure 1.21b (Taly 1988). Although the 1989 Loma Prieta earthquake did not result in damage to the panels, reconnaissance teams speculate that if the intensity of the shaking had been higher, damage to the connections would have likely occurred (EERI, 1990; and further reported in Sielaff et al., 2005).

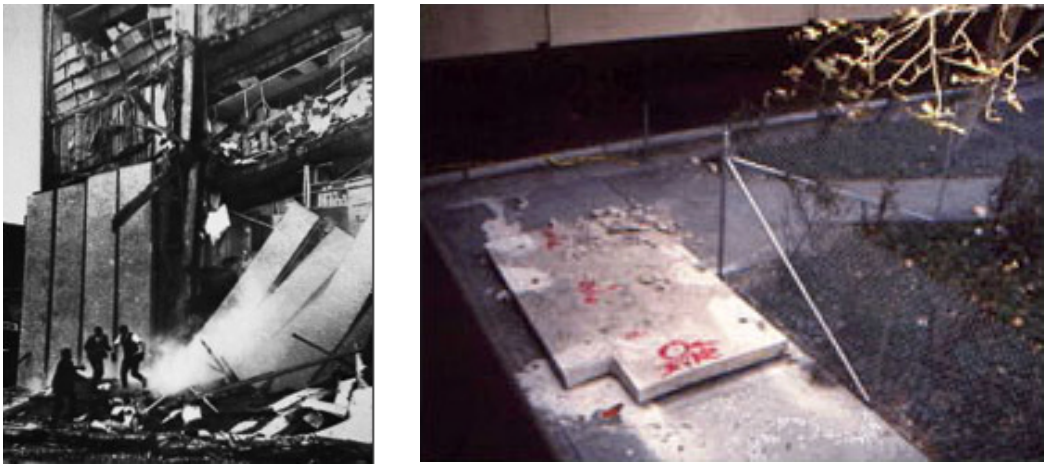

(a) **(b)**

Figure 1.21. Failed panels after the (a) 1964 Alaska earthquake and the (b) Whittier Narrows earthquake (Arnold 2009)

Iverson and Hawkins (1994) report that APC cladding behaved well during the 1994 Northridge earthquake with very few cases of damage, those that did occur were generally caused by pounding of cladding on adjacent structural elements. However, FEMA-74 (2011) reports an instance of a precast panel failing on top of a hospital building and damage to a corner panel (Figure 1.22a-b). In addition, failure of a tieback connection is also reported (Figure 1.22c).

(a) (b) (c)

Figure 1.22. Damage observed after the 1994 Northridge earthquake: (a), (b) panel failure, and (c) broken connections (Courtesy of FEMA-74 2011)

1.5 Past Research on APC Cladding

Research on the seismic behavior of APC cladding started as early as the 1970s. Initially, research was focused on the interaction between the cladding and the building, to determine the possible stiffening effects that APC panels can create on a building. A second set of studies dealt with "advanced" connections, created to add damping to the structure-cladding system. A few investigations were also conducted to study the possibility of using APC façades as a part of the load bearing system. Summaries of these studies are presented in the following sections.

1.5.1 Cladding-Building Interaction

In 1973, Uchida et al. performed the first experimental study on APC cladding with the goal of determining the effect of the panels on the vibration characteristics of buildings. This was achieved by constructing a two-story two-bay steel frame with APC cladding and subjecting it to vibrations. Uchida concluded that the stiffening effects of panels created some torsional vibrations (Uchida et al. 1973).

During the 1980s, many analytical studies about the influence of APC cladding on the seismic behavior of buildings were conducted by Goodno, Palsson and their team. In these studies, the authors considered a 25-story building with APC cladding installed using sliding connections, which was calibrated using experimental frequencies. A figure showing the building and cladding under consideration is shown in Figure 1.23. The behavior of the building-cladding system was found by

determining the inertia matrix for the building, creating a separate stiffness matrix for the panels, and finally joining them together (Pallson et al. 1984). The authors concluded that APC cladding could considerably alter the dynamic characteristics of the building and create variations in the peak displacements achieved during a seismic input motion, especially at low drifts (Goodno et al. 1980). One of the studies of this research group focused on the effect of cladding on torsional behavior, and it concluded that cladding could increase the torsional frequencies by 60%. This effect could be made even worst by failure of panels on part of the building, fact that could further affect the effects on torsional behavior.

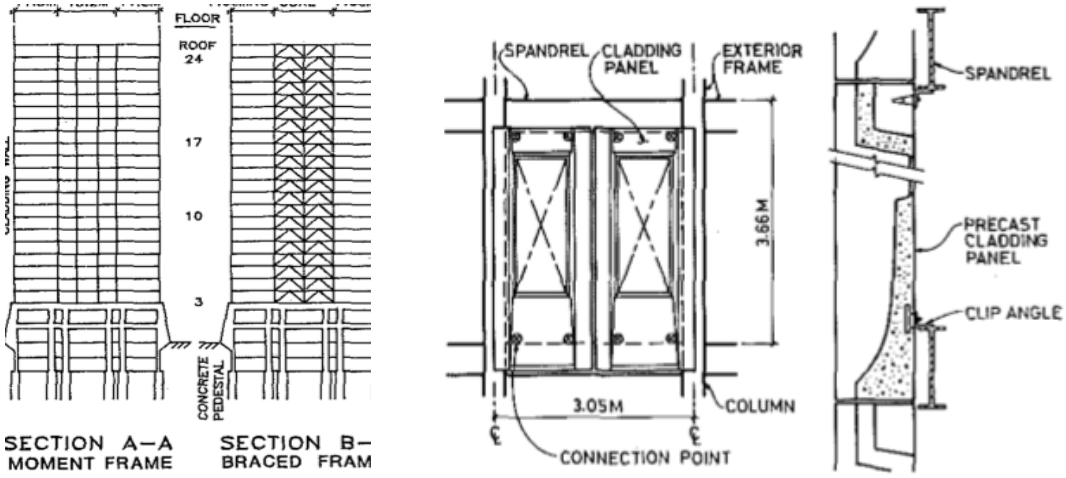

(a) **(b)**

Figure 1.23. Building and cladding modeled by Goodno and Palsson during their studies (Courtesy of Goodno and Palsson 1986)

An interesting study of the stiffening effects of cladding on moment resisting frames was conducted by Gaiotti and Smith in 1992. According to this research, some connection configurations can restrain the racking deformation of the frame thus stiffening it. To evaluate this issue, the authors selected a combination of typical frames and panels and performed an analysis of frames with and without cladding, and discovered that the interaction of the racking action of frame and panels can cause a quadruple curvature of the beam (Figure 1.24a). In a representative case, the racking stiffness of the clad frame was found to be 75 times higher that the one of the unclad frame. However, the results were influenced by both the initial stiffness of the connections and beam. To account for the stiffening of the frame created by the panels with a 1D element, an equivalent diagonal strut extending between

the locations of bearing connections was proposed (Figure 1.24b).

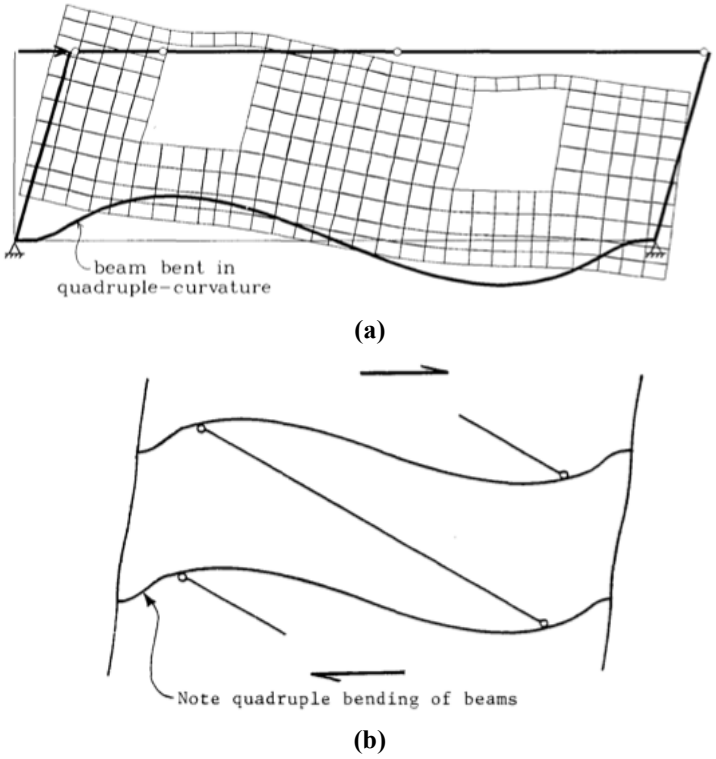

Figure 1.24. Interaction between cladding and structure presented by Gaiotti and Smith (1992): (a) deformed shape of the frame and panel, and (b) proposed modeling strategy (Courtesy of Gaiotti and Smith 1992)

In 2012, Baird built a full-scale model of a portion of a frame and installed a full-scale panel on it to understand the frame-panel interaction (Figure 1.25, Baird et al. 2012). Initially, the bare frame was subjected to quasi-static cyclic loading imposing increasing levels of drifts. Subsequently, a cladding panel was installed on the frame using bearing and tie-back connections used in current practice and the same tests were performed. The comparison of these results provided the influence of cladding on the behavior of the frame. Numerical analysis such as non-linear static pushover analysis and response history were also conduced for building with cladding. Results from this study confirmed the influence of cladding on the seismic behavior of multi-story buildings, with an increase in the initial stiffness of 30-50% of the cladded frame with respect to the bare frame and a higher strength.

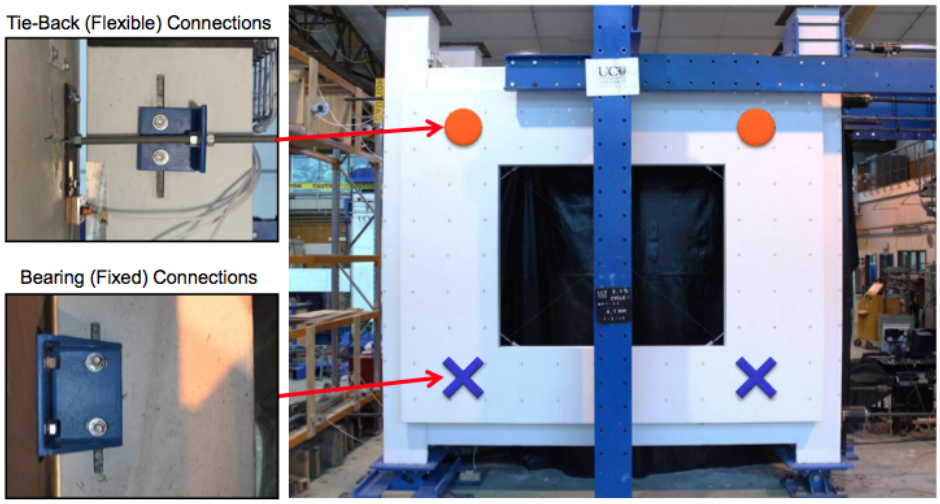

Figure 1.25. Frame and panel tested by Baird et al. (2012)

1.5.2 Dissipative "Advanced" Connections

Benefits of adding damping to the system with the use of dissipative "advanced" cladding connections include that the energy is dissipated over the whole height of the building and the structural system is protected. Dissipative devices can be additional to the normal cladding connections or can be incorporated into them. Dissipation for APC systems have been achieved through friction, yielding of a metal (steel, lead) and viscous behavior of a polymer (Thiel et al. 1986).

A first analytical study of a building using advanced connections with hysteretical damping was performed by Thiel et al. (1986). This study concluded that very stiff devices were more effective, that damping was greater at lower floors since it is dependent on interstory drifts, and that this added damping could result in more than 50% reduction in base shear and peak roof displacements. Another analytical study presenting a nonlinear dynamic analysis of buildings with and without advanced connections was performed by Goodno et al. in 1992. In this study it was shown that cladding with ductile connections could be used as an effective passive control system for buildings.

Several different types of advanced connections were proposed by different authors. For example, Pall (1989) suggested the use of friction-damped connections, created by the modification of the upper panel connections. These connections would be designed not to slip during service level conditions -thus controlling deflections- and slipping during a major earthquake to dissipate energy. A nonlinear time-history dynamic analysis was performed on a typical ten-story concrete frame, and it

was concluded that cladding installed using advanced connections could increase the torsional resistance of the building, dissipate a large amount of energy during an earthquake, decrease drifts, help preserve the structural integrity and reduce floor accelerations.

In the same year Kemeny and Lorant (1989) proposed the use elastomeric connections to attached the perimeter columns to APC panels. These connections would remain elastic for moderate loads and include the yielding of some steel parts during strong motions (Kemeny and Lorant 1989).

In 1993, Pinelli et al. tested a series of advanced connections consisting of a tapered steel element (Figure 1.26a). The connection presented a stable and large hysteretical loop, no stiffness degradation, a good fatigue behavior, and ductile failure. Data obtained from the testing of the connections were then incorporated into a building model. This study showed that, even if the increased damping generally attenuated the dynamic response, the change in stiffness created in the building might actually amplify the response, depending on the type of earthquake motion (Pinelli et al. 1995).

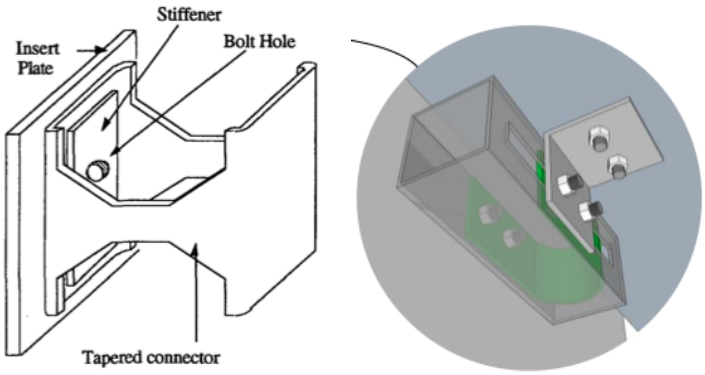

Figure 1.26. Examples of advanced connections as proposed by: (b) Pinelli et al. 1993 and (c) Baird et al. 2013

More recently, Baird et al. (2013) started a research project on a new type of advanced connections composed of U-shaped flexural steel plates (Figure 1.26b). The first part of the study consisted in a quasi-static cyclic component tests of the connection, which provided its hysteretical behavior. In the second part of the experiment, a building subassembly incorporating cladding was tested and provided the force-drift behavior of the frame. During the final part of the study, a building incorporating cladding installed with the new connection was modeled. For this case, it was concluded

that cladding with advanced connections resulted in a reduction of the drifts and an increase in the energy dissipated by the structure.

1.5.3 Full Structural Participation

Several authors over the years suggested using APC panels as part of the load carrying system of the building. The first one was Gjelvik in 1974, who suggested to utilize the panels to resist lateral loads such as wind. In 1989, Henry (Henry et al. 1989) developed a mathematical model to represent cladding panels as structural members. In 2012, Hobelman et al. suggested that using the external walls as supporting systems could be economical and feasible for constructions of 10 stories or fewer. Even if these few studies seem to suggest the feasibility of using APC cladding as part of the structural system, this never became mainstream in the United States. The situation might be different in other countries. For example, in Italy APC cladding is mostly used for short, industrial buildings, and some authors have proposed to use the panels as structural elements (Colombo and Toniolo 2011). This could be done in several ways, for example by fixing the vertical panels to both the foundation and beam, or to connect horizontal panels to the columns and to each other (Figure 1.27).

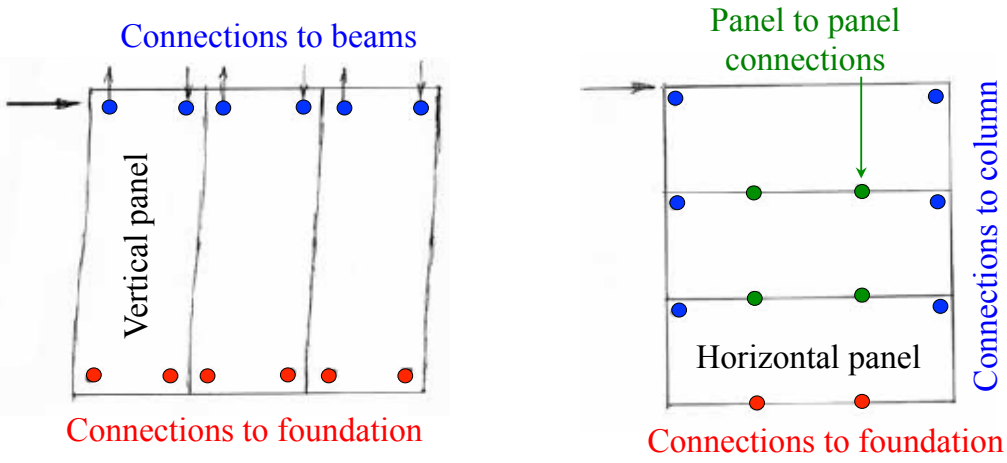

Figure 1.27. Ways to create full structural participation of the panels in the Italian practice for (a) vertical panels and (b) horizontal panels (Image modified from Colombo and Toniolo 2011)

1.5.4 Seismic Behavior of APC Cladding as Commonly Installed on Buildings

Experimental studies to evaluate the behavior of the APC cladding as installed in real buildings started in the 1980s. In 1986, Wang performed static tests imposing lateral drift on a structural frame

encased by APC panels installed according to common practice in California and Japan (Wang 1987). Conclusions and recommendation from this large study included:

- The performance of cladding connections is really sensitive to erection errors, for example premature failure of sliding connections was observed when they were tightened over specification;
- Particular attention needs to be placed on the panel and joint kinematics, and joints should be wide enough to avoid contact between adjacent panels;
- Long flexing connections proved to be able to absorb drifts really well, while sliding connections manifested possible problems both due to insufficient slot length or impedance of the sliding mechanism;
- Panels should be hung so that bearing connections are at the top.

In 1988, Rihal embarked on an experimental project that included static tests of typical flexing connections with different lengths, cyclical racking tests on full-size panels installed with bearing and flexing connections and dynamic tests on a reduced-scale model of a two-story steel moment resisting frame with and without APC panels. This experiment also included the development of several analytical models. Conclusions included:

- The load capacity of flexing connections decreases with increasing length. The behavior of a cantilevering threaded rod presents a good correlation between experimental and analytical results;
- In-plane resistance of the panels is controlled by the resistance of tieback connections, with drift ratios at failure varying from 0.68% for 6'' rods to 1.17% for 8'' rod;
- Addition of cladding has a significance influence on the fundamental frequency of a structure. In this experiment an overall decrement in natural frequencies was observed, because the effect of the added mass overcame that of the additional stiffness.

In 1988, Craig et al. performed cyclic component tests on bolt insert and "ductile rod push-pull cladding connections" (corresponding to flexing rod connections) to analyze their kinematic and constitutive properties. Push-pull connections of length of 8, 9,11 and 12'', with a diameter of 5/8'' and

using A36 steel were considered at yielded at 0.5'' of displacement. The lateral stiffness of the 12'' long rods was found to be 0.46 kips/inch. Analytical model were also developed and they proved able to predict the onset of inelastic behavior of the panels. Results seemed to indicate that commonly used connections might be susceptible to low-cycle fatigue failure. In fact, they exhibit fatigue cracking at one or both ends for displacements not exceeding those prescribed by the UBC code. In one half of the cases, complete fracture occurred.

In 1989, Sack et al. performed experimental and analytical studies on connections to determine their stiffness and understand the participation of cladding in the structural response. Several different types of inserts and connection bodies were tested to obtain the load-displacement behavior and energy dissipation capabilities. These included welded, flexing and sliding connections. Results indicated that connection stiffness was actually lower than predicted analytically. Subsequently, the team also tested a full-scale one-story single bay frame with two APC panels using earthquake loading. This test showed that flexing connections have a low stiffness and allow structural frame to deform without transferring large amounts of load. Sliding connections could also be effective in providing this dissociation if the slots are properly aligned and low friction washers are installed. In case the interstory drifts are larger than what the sliding connection can accommodate, severe impact loads are generated in the connections and in the panels. Possible issues concerning connections mentioned by these authors include a possible brittle failure of flexing connections and permanent misalignments of sliding connection after moderate earthquakes. From the analytical studies, it was also concluded that an increment of stiffness of the bare frame of 17% was observed once the panels were in place.

In 1989, Pinelli and Craig started laboratory tests on cladding connections inserts typical of Mexican practice (Figure 1.28). These inserts were tested in the laboratory to determine shear and moment capacity as well as linear and nonlinear behavior, energy dissipation properties and ductility. The inserts were tested under cyclic shear and moment loads. It was found that in many cases the failure of the insert was brittle and sudden, especially for inserts located at the corner of the specimen where concrete suffered from a lack of confinement. After the failure of the concrete, the connections started acting like pins, and failed by a total crushing of the concrete or a fracture of the weld between the steel

plate and the rebar. Inserts at the edges acted better with respect to those at the corners. The ductility changed considerably depending on the type of insert, its location, the load type and the magnitude of the load cycles. Following the experimental results, refined finite element models of the connections were also developed (Meyappa et al. 1988).

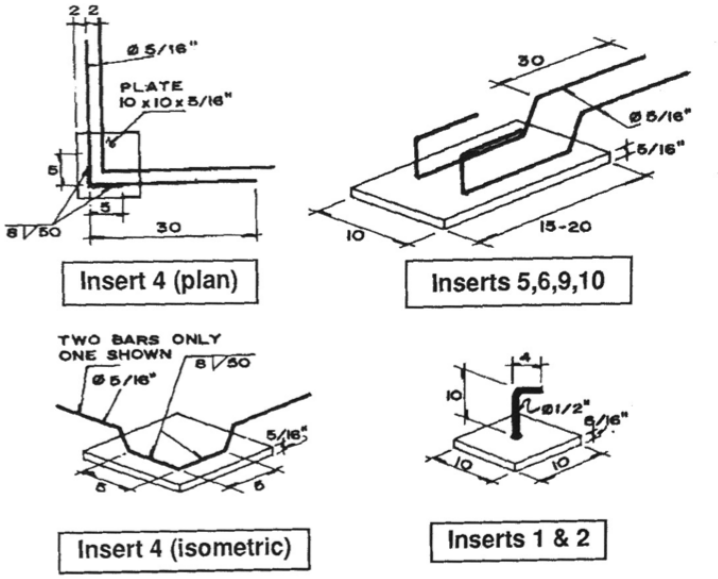

Figure 1.28. Examples of inserts tested by Pinelli and Craig (1989)

In 2004, McMullin et al. performed a series of monotonic loading tests on APC connections subjected to out-of-plane and in-plane displacement of the panel with the goal of obtaining force-displacement relationships to be used in a pushover analysis. Push-pull connections proved to be very ductile when subjected to both axial and bending load. When loaded axially, they showed stiffness lower than expected and the deflections involved also the bending of the supporting plate.

In 2009, Maneetes and Memari developed a refined model of an APC panel and connections (Figure 1.29) designed to participate in the lateral force resisting system. Their goal was to better understand the panel strength and stiffness characteristics when subjected to in-plane loading (Maneetes and Menari 2009). This panel included bearing connections with a HSS at the bottom, a friction damper and slotted tieback connections at the top. They conducted an analysis of the sources of stiffness of the panels and concluded that the concrete panels could contribute to the flexibility of the system. The use of a headed concrete anchor system could greatly reduce the lateral stiffness of the panel.

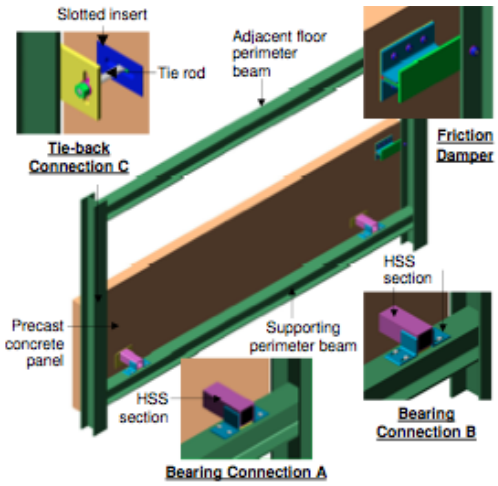

Figure 1.29. Panel modeled by Mameetes and Memari (2009)

In 2011, McMullin et al. tested two corner APC panels on a steel frame at the E-Defense facility in Kobe (McMullin et al. 2012; Hutchinson et al. 2014). The panels were designed to allow interstory drifts through a rocking motion, and were installed using slotted bearing connections at the bottom and non-bearing connections at the top. Throughout the entire test program, the APC system behaved according to design, and at the end of the test sequence no visual damage to welds, rods, panels or support plates was observed. In addition, there was no permanent misalignment. Pictures of the two panels and bearing sliding connections are shown in Figure 1.30.

(a) **(b)**

Figure 1.30. E-Defense test on corner APC panels: (a) photograph showing the two panels and (b) photograph of the lower bearing sliding connection (Courtesy of Hutchinson et al. 2014)

A test on one of a variations of the sliding connections used in the Italian practice was performed by Belleri et al. (2016). Figure 1.31 shows the test setup and details of the sliding connection

used. During this test, cladding-panel to column subassemblies were tested by imposing a quasi-static cyclic drift. This study confirmed that a key characteristic of the connections is the tightening of the sliding element. When this is to tight, it could lead to premature fracture of the connections.

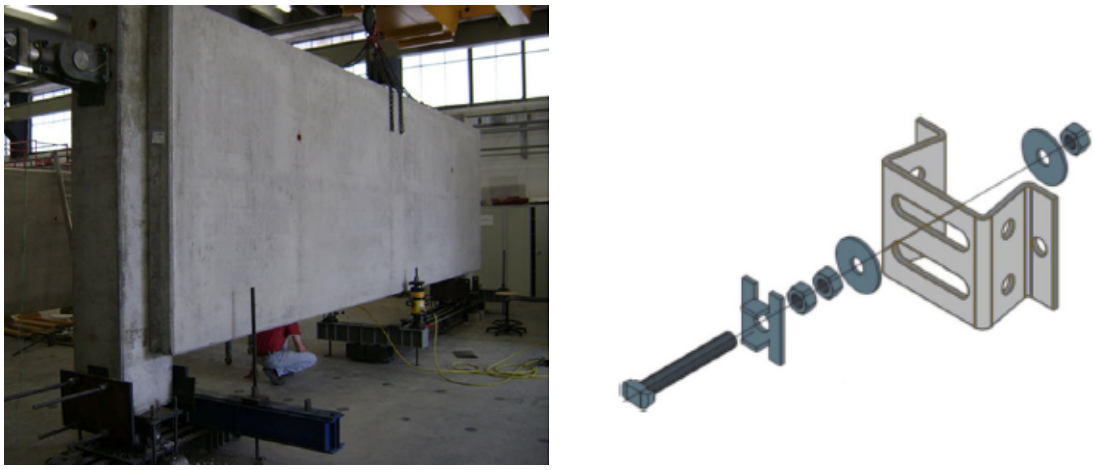

(a) (b)

Figure 1.31. Experiment conducted by Belleri et al. (2016): (a) set up of the experiment, and (b) detail of the sliding connection (Courtesy of Belleri et al. 2016)

1.6 Objectives of This Research

As seen in this chapter, APC cladding is a type of façade vastly used worldwide in many different types of buildings, and it can be constructed using a great variety of panel geometries and connection details. Damage to APC cladding façade was observed after many recent strong earthquakes worldwide, and the fact that the U.S. has been spared by such a widespread damage might be attributed to the fact that there has not been a design level earthquake in recent years. Damage to APC cladding can have life-threatening consequences due to the size of these panels. In addition, it is costly and time consuming to repair. Nevertheless, most of the past research did not specifically focus of verifying and improving the current practice for the design of this type of cladding. In fact, a large part of research efforts focused on either understanding the effect of cladding on the structural system, or on studying practices that are not commonly used, such as dissipative connections and full-structure participation. The studies conducted with the goal of understanding the seismic behavior of the panels have also many limitations. In fact, each study needs to focus on a certain type of panel geometry and connection, and it is not easy to directly extend the results to the large amount of systems used. To make things even

worst, general research on nonstructural components cannot be directly applied to this type of system. In fact, in general, nonstructural components that span from floor to floor (piping, glass façades, cold-formed steel façades etc.) are lightweight, thus mostly sensitive to interstory drifts, while heavy components are connected to only one floor, thus they are sensitive only to floor accelerations. However, since APC panels are very heavy and they might span from floor to floor, they are equally sensitive to both floor accelerations and interstory drifts.

Scope of this dissertation is to improve the understanding of the seismic behavior of the widely used punched window wall panels and connections as typically designed in the high-seismicity areas of the United States, with the goal of improving their seismic design. These panels span from floor to floor and might be very heavy (up to 30 kips), thus their design requires specific considerations relative to both drift-compatibility and seismic forces, which will both be treated in this dissertation.

1.7 Organization

The present research is divided in nine chapters: the first three introduce APC cladding, its design and the experiments performed, chapters 4 and 5 presents the results relative to the drift-compatibility issues, while chapter 6 through 8 focuses on problems related to the accelerations and forces. Finally, chapter 9 presents the conclusions of the study. It is noted that, since the panels have different issues in the out-of-plane (OP) and in-plane (IP) directions (Figure 1.32), different chapters focus on different panels. The individual chapters are summarized as follows:

- *Chapter 1* presents an overview of façade systems in general and APC cladding in particular, describes the different types of panel types and connection details used worldwide, summarizes damage to the panels observed during past earthquake and past research, and identifies the objectives and organization of this study;
- *Chapter 2* describes how APC cladding and connections are currently designed, with particular focus on the seismic design. In addition, it presents the main issues relative to the drift-compatible design and seismic forces that will be further studied in this dissertations;

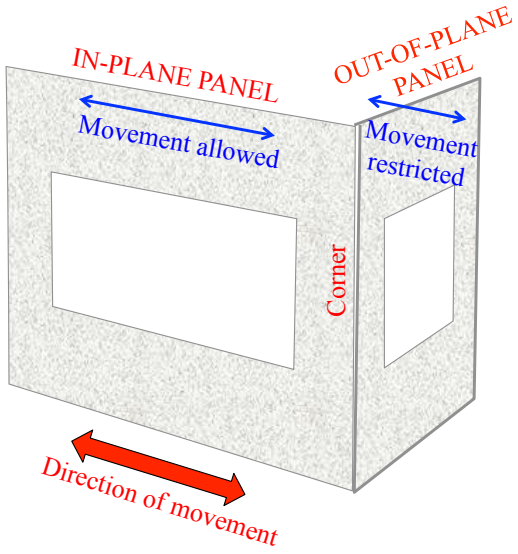

Figure 1.32. Identification of IP and OP panels

- *Chapter 3* describes of the Building Nonstructural Components and System (BNCS) experiment and the component test on sliding and flexing connections;
- *Chapter 4* presents the results relative to the IP (drift-sensitive) behavior of the tieback connections. This includes the results from the BNCS experiments and component tests on sliding and tieback connections;
- *Chapter 5* summarizes the results relative to the corner system, including those found during the BNCS experiment and those obtained by numerical analysis of the behavior of the corner system. This chapter considered the interaction between IP and OP panels;
- *Chapter 6* presents a study on the dynamic characterization of APC cladding (both IP and OP panels);
- *Chapter 7* is dedicated to the analysis of accelerations developed in the panels during a service level earthquake. This focuses on the OP panels;
- *Chapter 8* presents the same results as chapter 8 but relative to a design level earthquake in which the building behaves nonlinearly. As seen from the previous chapter, also this chapter focuses on the OP panels;
- *Chapter 9* summarizes the conclusions and design recommendations.

- Appendix A contains further information on the input motions used in the analyses in chapter 7 and 8;
- Appendix B contains calculations relative to the nonlinear model in chapter 9.

ACKNOLEDGEMENTS

Chapter 1 reproduces content and images of the material as it appears in the PCI Journal 2016. Pantoli, E., Hutchinson, T. C., McMullin, K. M., Underwood, G. A., and Hildebrand, M. J., 2016. "Seismic-drift-compatible design of architectural precast concrete cladding: Tieback connections and corner joints." PCI Journal, July-August, 38-52. The author of the dissertation is the principal author of the above cited paper.

Chapter 2

Seismic Design of Punched Window Wall Panels

The goal of this chapter is to present in detail the current practice for the design of APC cladding in the West Coast of the United States and its main issues and criticisms. This discussion includes first of all general considerations important during the design of panels and connections, such as how to select the panel type and geometry, and the type of tieback connection. The second section presents details on the seismic design of the cladding, including the calculations of seismic forces, the design of the tieback connections to accommodate seismic drifts and the sizing of the critical corner joints. The final section summarizes the open issues and criticisms related to the current design process, both in terms of drift compatibility and seismic forces.

2.1 General Design Considerations for APC Cladding

2.1.1 Selection of Panel Type

The selection of the type of panel is dictated by both transportability limitations and architectural constraints. Namely:

- If the story height of the building is less than the maximum panel height that can be transported, wall panels are used. *Punched window wall panels* (Figure 1.5a) are preferred when horizontal joints at the floor level are acceptable. The main advantage of this configuration is that the top connections can be located above the ceiling where they are easily concealed. In addition, these panels may be pre-glazed. In contrast, *u-shaped wall panels* (Figure 1.5b) may be required if a horizontal joint at the floor is architecturally unacceptable. As a result, the top connections will be made at or below the ceiling and may be restricted in their size and location. In addition, this type of panel is more difficult to pre-glaze;
- If the story height is greater than the transportability limit for the panels, the façade system has to be broken into smaller components. By combining *spandrels and column covers*, a u-shape can be emulated (Figure 1.5c);

  As previously stated, this research work focuses on punched window wall panels, and only the

design of this type of panel will be further considered. This choice was made since this type of panel is very common and it presents specific issues, due to its geometry and the fact that it spans from floor to floor.

2.1.2 Loads Acting on Panels and Connections

According to PCI 2007, during the design of APC cladding, engineers need to consider the forces created by:

- The APC panel itself. This include self-weight;
- Handling, transportation and erection;
- Externally applied loads or loads transmitted to the unit by the supporting structure, including wind, seismic, snow, blast loads;
- Restrained volume change. Volume changes are caused by variations in temperature, shrinkage and creep, but usually this last effect is minimal for APC panels. These forces can be reduced when most of the volume change takes place before the installation of the final connections. Differential temperature between the inside and outside of the building may cause bowing of the panels. This could lead to hairline cracking radiating from the corners of the openings depending of panel restraints. The tendency of shrinkage to create cracking can be reduced with sufficient reinforcement, but might be exacerbated in case of complex shapes.

2.1.3 Design of Panel Geometry and Reinforcement

The general rule to decide the size of APC panels is to produce panels as large as possible without creating special handling requirements or losing repetition (PCI 2007). For punched window wall panels, the geometry is determined by the following considerations:

- *Height*. The height of the wall panel is the same as the story-height of the building they are installed on and, in addition, is limited to the transportability of the panels. Typically, panel heights can be between 10 and 15 feet;
- *Length*. Usually the length of a panels corresponds to the structural bay width and may be as large as 30 feet;

- *Thickness*. A panel thickness of 5 to 6 inches allows adequate strength, space for reinforcement, and durability. When choosing the thickness, it is important to remember that a panel that is too thin may bow or deflect excessively, creating cracking and caulking problems at the building corners and leakage at the windows.

Each panel may be solid of have one or more punched openings for windows. The panel weight will depend on its geometry, and when window openings are present it will naturally be reduced. A large panel (e.g. 15' x 30' x 6'') constructed of normal weight concrete absent window openings would weigh a minimum of 36 kips.

Mild reinforcement typically Grade60 A706 is used in these panels to help supporting loads and preventing cracking that could be created by handling, transportation, and erection and by deformation imposed by volume changes and loads such as wind. In addition to reinforcing steel, other steel parts are cast into the panel, such as inserts necessary for the handling of the panels and connection embeds. It is noted that additional mild reinforcement is usually placed in areas that need more strength or are more prone to cracking, such as around the openings, inserts and embeds. An example of reinforcement placed in an average size APC panel unit is shown in Figure 2.1. Figure 2.2 presents a summary of the criteria for the selection and general design of APC cladding.

2.1.4 Design of Connections

According to PCI 2007, connections must satisfy the following criteria:

1. *Strength*. A connection must have the strength needed to carry the loads imposed during its lifetime. The imposed loads include self weight, seismic, wind, forces created by volume change, and loads imposed from adjacent materials such as windows;
2. *Ductility*. This is generally achieved by designing the steel components to yield before the failure of concrete;
3. *Volume change accommodation*;

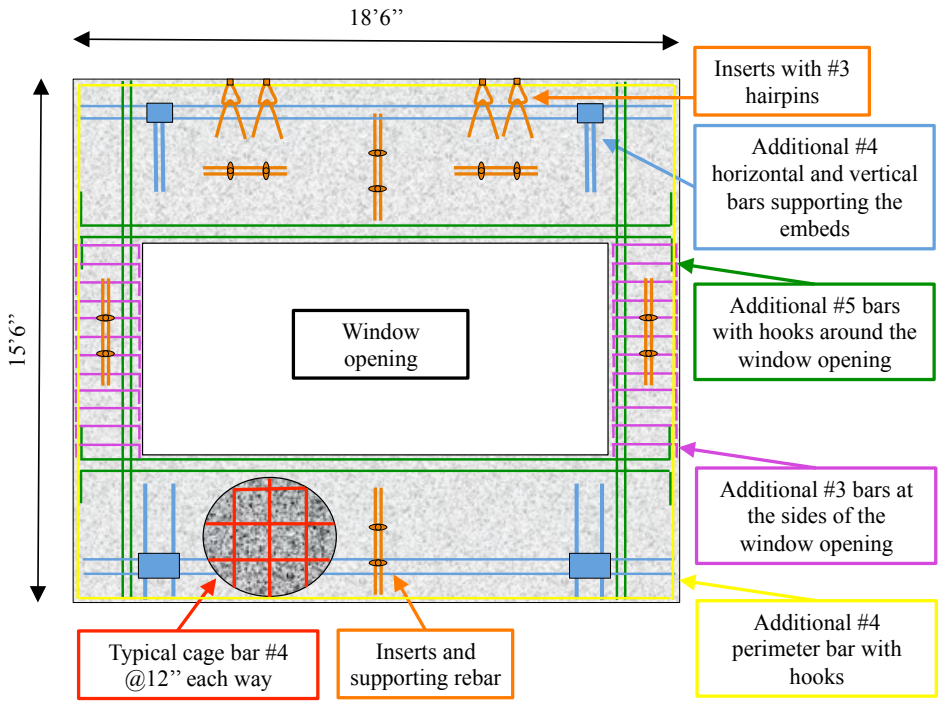

Figure 2.1. Typical reinforcement of an average size APC panel (Modification of construction drawings provided by Clark Pacific)

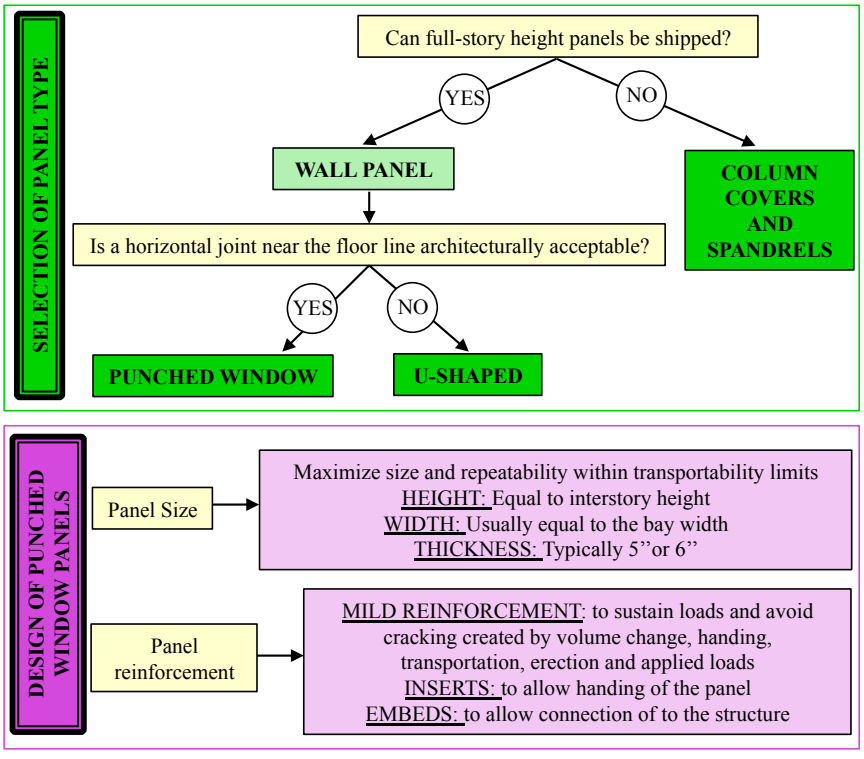

Figure 2.2. Summary of considerations to be made in the selection of the type of APC panel and in the design of punched window wall panels

4. Durability. Depending on the type of environment they are used in, connections should be adequately protected;
5. Fire resistance;
6. *Constructability and economy*;
7. *Wind considerations*;
8. *Seismic considerations*;
9. *Blast resistance*. This is considered for buildings that can be a potential target of attack.

Even though all these considerations are important, this chapter focuses on constructability and seismic consideration. The considerations reported in the following sections were discussed with U.S. designers, and thus can be considered typical of the West Coast practice. However, it is noted that detailing could certainly vary in different areas.

Bearing Connections

Bearing connections fix the bottom of the panel to the structure. They have to resist forces in the three directions: in-plane longitudinal, in-plane vertical, and out-of-plane or transverse. Figure 2.3 shows a sketch and a photograph of a typical bearing connection. A typical bearing connection is composed by:

- *A panel embed created with an angle clip welded to anchoring bolts*. The width of the bearing angle usually varies from 6'' to 12'' and its thickness from ¾'' to 1'';
- *A bearing bolt*. This needs to be placed on top of the bearing surface but not too far from the panel, to avoid large eccentricities. A typical bearing bolt has a diameter of 1-1 1/4'';
- *Angle clips welded to the panel and the structure embed*. These clips are typically 4''x4''x3/8'' and are 3 ½ or 4'' tall. In the case shown, the clips are welded to a supporting plate, which is then welded to the structure embed, thus reducing eccentricities.

Loads from the panel are transmitted through the panel embed to the bearing bolt and the clip angles, which are then transmitting the loads to the structure embed through welds. The bearing bolt supports mainly the vertical loads, while the angle clips have the goal of providing resistance in the longitudinal and transverse direction of the panel.

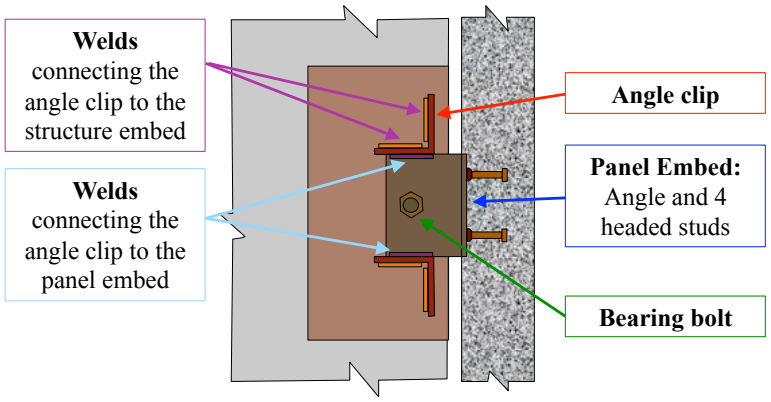

(a)

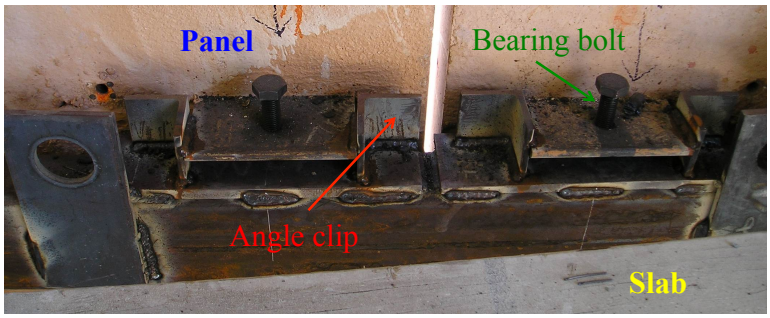

(b)

Figure 2.3. Typical bearing connections: (a) schematic plan view showing the different parts of the connection, and (b) photograph (Photograph provided by Glen Underwood at Clark Pacific)

Sliding Tieback Connections

The main elements of sliding tieback connections are:

- *A panel embed*. This is created with a plate roughly 8''x8''x1/2'' that has a hole in the middle and it is welded with four anchors and one nut;
- *A threaded rod or a bolt*. This usually has a diameter of ¾'' or 1'';
- *A slotted clip welded to structure or a structural embed*. Typically, the thickness of the clip is from ½ '' to ¾ '', while the two legs are 6 to 8'' long;
- *Two plate washers and nuts*. The plate washers are typically around 3/8'' to 1/2'' in thickness, and they need to be large enough to cover the slot and avoid getting stuck inside it during the movement of the building.

The threaded rod is connected to the panel through the nut in the panel embed. It then extends through the slotted clip and is held into position by the plate washers and nuts. IP displacements are

allowed by the sliding of the threaded rod inside the slotted clip. To facilitate sliding it is important for the nuts to be no more than finger tight to avoid the creation of excessive frictional resistance. Out-of-plane (OP) forces created in the panel are transmitted to the structure through tension or compression in the rod and then bending of the slotted clip. Note that the two plate washers are denoted "tension" and "compression" depending on the type of axial force developed in the rod during their action. In case the distance between the sliding surface and the panel (denoted as clear length L_c) is zero, the configuration is called "snug" and a sliding bolt is used instead of a rod. Figure 2.4a-b shows a schematic plan view of a sliding connection during its initial configuration and intended behavior, while Figure 2.4c-d show a sliding connection with L_c different than zero and a snug configuration.

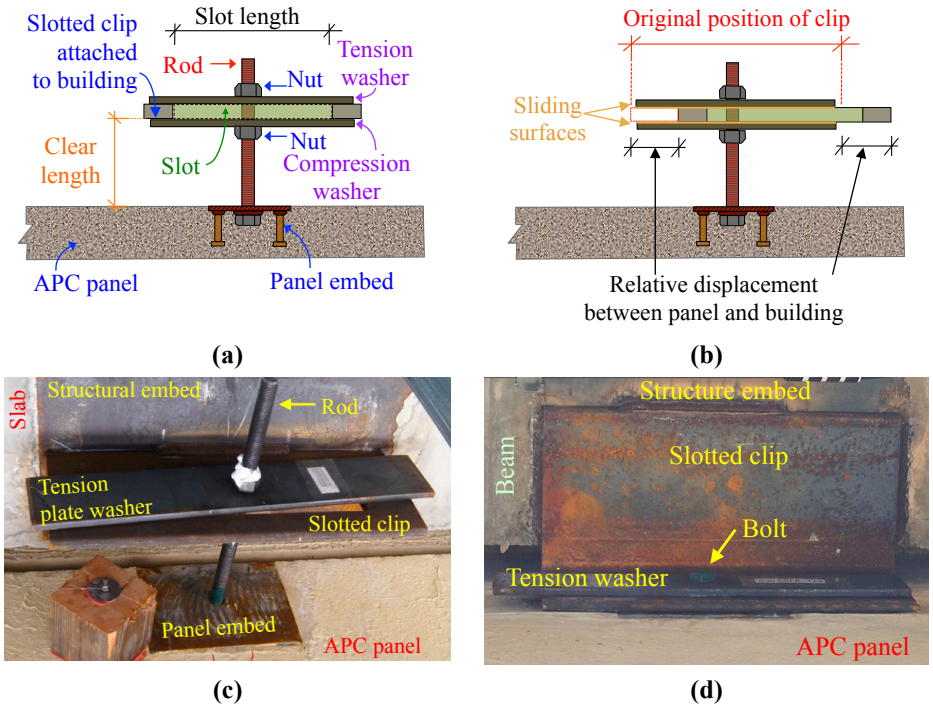

Figure 2.4. Sliding connections: (a) schematic of original configuration and (b) intended behavior during building movement in plan view, (c) photograph of a sliding connection with L_c different than zero and (d) photograph of a snug configuration (view looking up)

Flexing Tieback Connections

A typical flexing connection involves similar components as used in sliding connections, with exception for the rod, which is longer, and the angle clip which is shorter. Typically, these angle clips can be 4''x6''x1/2'' and 7'' long to accommodate a 3'' diameter hole, which is oversized to account for construction tolerances. Flexing connections allow IP displacement through elastic and plastic bending

of this relatively long threaded rod. Figure 2.5a and b shows a schematic of the initial configuration and intended behavior during motion for this type of connections in plan view, while Figure 2.5c shows a photograph of a typical flexing connection.

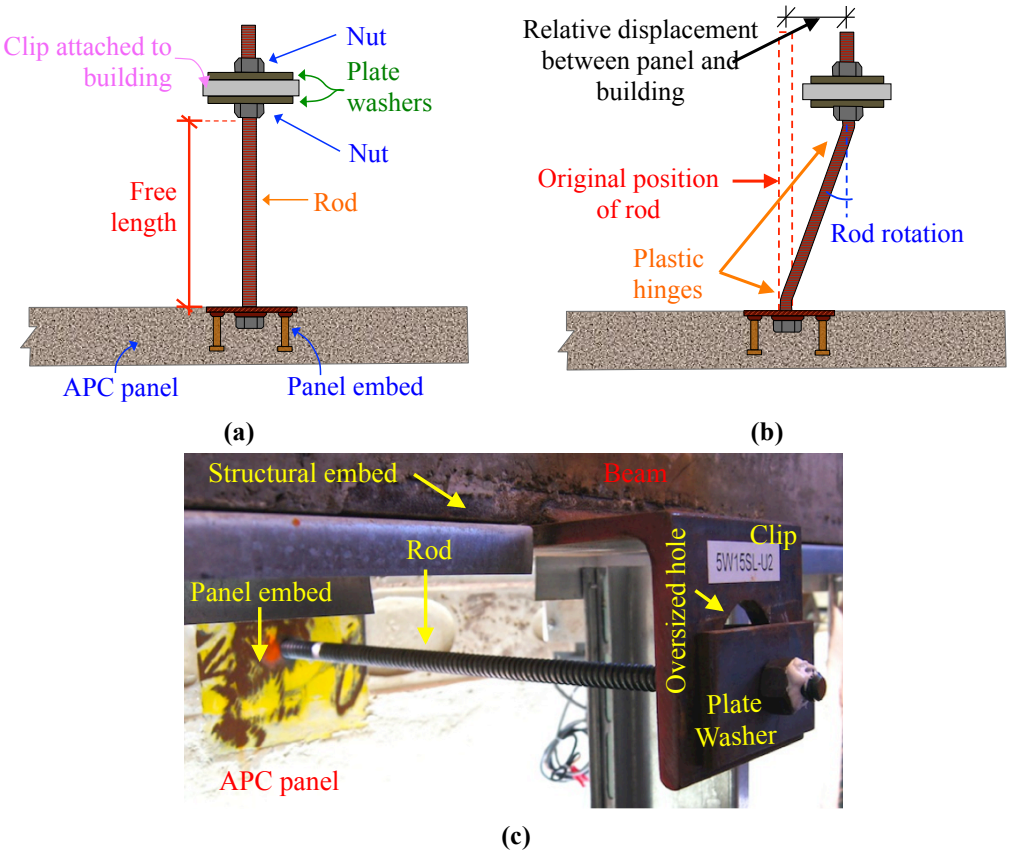

Figure 2.5. Flexing connections: (a) photograph, (b) and (c) schematic of original configuration and intended behavior during building movement

2.1.5 Selection of Tieback Connections

Designers have to make several decisions regarding the tieback connections. First of all, they must decide the location of the connections, which is generally selected to facilitate installation. For example, cladding connections are generally located at the bottom of a slab or a beam or the side of a column. Connections located in tight spaces between the back of the panel and face of a beam or column are difficult to access and are only used if no alternative can be found. After the selection of the location of the connection, designers have to decide the type of tieback to be used. The choice between sliding and flexing connections is affected by many factors, namely:

- *Time and ease of installation.* Connections should be simple enough to be easily assembled by an ironworker wearing gloves. In addition, effective connections can be also used to facilitate the installation of the panels. In fact, during the typical erection process of an APC panel, the final alignment is done after the panel has been released from the crane and the connections are holding it on the building with the goal of speeding up the time of installation. An efficient connection must be able to be assembled when the panel is not yet in its final position and be used to bring the panel into alignment. From this point of view, long rods, such as those used in flexing connections or in sliding connection with some free rod length, are preferrable, since the same rod serves both in the final connection and to ease installation. When long rods are not provided, such as for snug sliding tiebacks, the use of some temporary connections during the installation of the panels is required adding material and time to the erection process. In addition, all sliding connections have the additional requirement of being only "finger" tightened, thus necessitating more attention from the ironworker and allowing more room for error;
- *Cost.* Flexing rod connections are generally considered less expensive. In fact, sliding connection require larger angle clips, plate washers and welds;
- *The distance between the back of the panel and the attachment point to the structure*. In case this distance is short, both connections can be used, while in case of long distances only flexing rods are acceptable. The configurations available depend usually on whether the structure is steel or concrete. In concrete structures, beams and slabs are generally very close to the back of the panel, while in steel buildings there is usually more space between the structure and the façade system. In fact, the perimeter beams can be centered 1.5 to 3 feet back from the face of the APC panel;
- *Architectural constraints on the back of the panel*. In many cases, architectural interior finishes impose a limitation on the length of the rod. In the finishes are very close to the back of the panel, engineers might have not choice but sliding connections.

  In summary, costs, ease and time of installation would drive the engineer to opt for flexing

connections. These are generally feasible for many concrete and steel structures. However, it is often the presence of architectural finishes close to the façade that dictate the real restriction. They limit the space available on the back of the panel and may force the designer to choose the more expensive and less efficient sliding connections. A survey by the authors of fourteen precast producers and designers revealed that 93% use sliding connections, while only 29% use flexing connections.

2.2 Seismic Design Considerations for APC Cladding

Design of APC cladding is based on considerations of different nature, such as transportability limitations for the panels, architectural constrains imposed by the building shape and its finishes (e.g. ceilings) and seismicity of the area. In the high-seismicity regions of the U.S., APC panels and connections must be designed in accordance with the following model code provisions and reference standards:

- International Building Code (IBC 2012);
- ASCE/SEI 7 Minimum Design Loads for Buildings and Other Structures (ASCE 2010);
- ACI 318 – Building Code Requirements for Structural Concrete (ACI 2011);
- AISC 341 – Seismic Provisions for Steel Buildings (AISC 341 2010);
- PCI MNL 120 – PCI Design Handbook (PCI 2010);
- PCI MNL 122 – Architectural Precast Concrete (PCI 2007).

This chapter presents an overview of the design process for panels, connections and joints, with particular emphasis on seismic considerations.

2.2.1 Accommodation of Seismic Displacements

In terms of accommodation of seismic displacements, ASCE 7-10 Section 13.5.3 requires that connections and panel joints should:

1. Allow for the story drift caused by seismic displacements;
2. Allow movement by either a sliding or bending of steel;
3. Have sufficient ductility and rotation capacity to preclude fracture of the concrete or brittle failures at or near welds.

These design provisions addressing drift compatibility are intentionally broad and qualitative

but provide no specific guidance to design professionals detailing these systems. Consequently, engineers are left to their own devices when faced with the design of some of the key parameters of the connections, which require a compromise between the optimization of the performance of the connection and architectural/practical considerations.

Sliding Tieback Connections

The key drift-sensitive parameters to be designed in a sliding connection are the slot and rod lengths. The slot length is determined by adding two times the expected story drift to the rod diameter and erection tolerance (which is usually 1”). As for the rod length -which is usually considered as the clear length L_c (a)- a compromise needs to be found between issues of different nature. On one side, practical considerations -such as the time of installation (section 3.5.2)- encourage engineers to design connection with some free rod length. However, if the rod is excessively long (i.e. flexible) it could start bending well before sliding can occur. As of today, no recommendations about the maximum length allowed for the rods of sliding connections is provided.

Flexing Tieback Connections

For flexing connections, the primary displacement-sensitive design parameter is the free rod length L_f, corresponding to the total length of the rod that is actually going to bend, as shown in a. As seen for sliding connections, different considerations need to be taken into account when designing the rods: a rod too long might not fit due to architectural constraints (section 3.5.2), but a rod too short may fracture due to excessive cycle rotations. Unfortunately, no current recommendations are given about the range of length that would allow for a good seismic performance. Figure 2.6 presents a summary of the considerations engineers make to design connections.

Design of Joints

Horizontal and vertical joints between panels usually have a thickness of 3/4’’ or more, with the exceptions of corner joints, which will be discussed in the following section. Joints need to be sealed in order to prevent water and air penetration through the building envelope and they are required to accommodate changes in the wall or structure dimensions caused by variations in temperature, moisture content or deflection from applied loads.

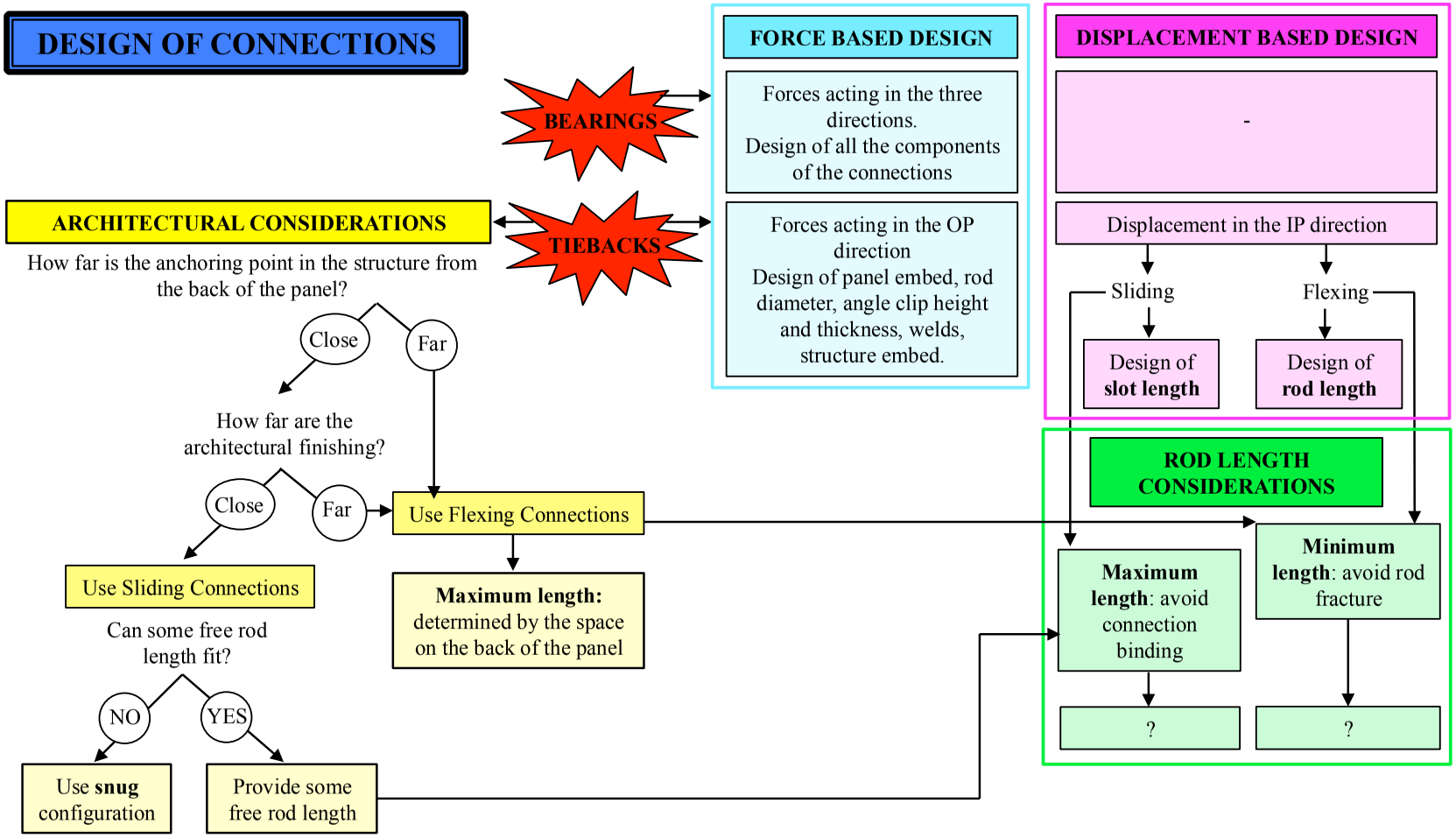

Figure 2.6. Summary of considerations to be made in the design of APC cladding connections

Vertical corner joints of APC cladding constitute a particularly critical location in the system because this is the point where panels moving in-plane and out-of-plane have to interact. As already mentioned, when a panel moves in the IP direction, ideally it displaces rigidly with the bottom slab. In the OP direction panels are allow to deform or tilt, thus moving at their bottom with the bottom slab and their top with the top slab. Clearly, in the absence of a gap as large as the story drift, the top of the two corner panels will impact during motion (Figure 2.7a-b). This collision could result in connection failure and disengagement of the panel from the structure.

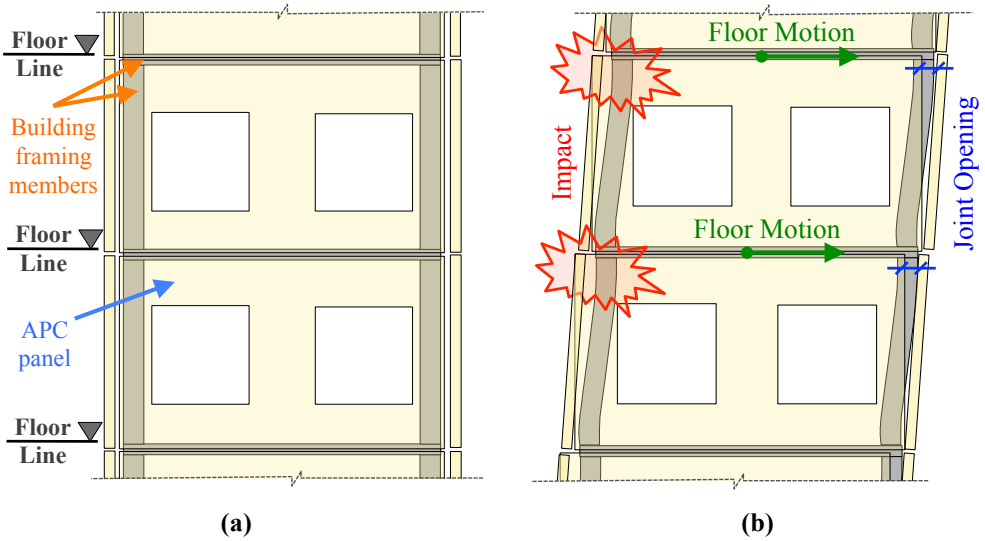

Figure 2.7. APC cladding attached to a building frame as (a) undeformed and (b) deformed during seismic displacement (Courtesy of Hutchinson et al. 2014)

For corner joints, until the 1990s, a ¾-inch joint at this intersection was expected to perform suitably, however, code changes have resulted in seismic joint widths that match the maximum expected inelastic drift of the structure. Namely, per ASCE 7 Section 13.5.3 (a): "Connections and panel joints shall allow for the story drift caused by relative seismic displacements (D_p) determined in Section 13.3.2, or 0.5 in. (13mm), whichever is greatest". As a result of this code provision, joint widths of 3-½" are not uncommon. This type of large joint running vertically at each corner of the building –as shown in Figure 2.8 -is architecturally undesirable and could make the market for precast concrete cladding less desirable when compared with other façades, such as steel stud systems. However, the current state of knowledge prevents reducing the joint back to its' ¾-inch size.

(a) **(b)**

Figure 2.8. Variation in reveal at the exterior of various APC cladding for (a) a miter joint and (b) a butt-return joint (Images provided by Glen Underwood at Clark Pacific)

2.2.2 Accommodation of Seismic Forces

Seismic Weight

The first step to find the seismic design force in the connections is to estimate the inertial forces, i.e. seismic weight and accelerations. This section illustrates these steps and calculates the forces for a double-symmetric panel with weight W, mass M and the simple geometry shown in Figure 2.9. The first step to is the calculation of the panel weight and center of gravity, considering both the weight of the panel and glazing. The second step consists in the calculations of the reactions in each connection. In this phase both gravity and seismic load in the three directions must be found. The connection reactions created by these loads are determined by statics. For the case of a horizontal acceleration a_h and the geometry of the panel presented Figure 2.9, the forces in the connections are presented below for each load:

- *Gravity load.* The vertical component of the gravity load (z-direction) is distributed among the bearing connections and is clearly –W/2. Due to the horizontal eccentricity between the center of gravity of the panels and the center of the supports (e_h), a moment around the y-axis is also created, and it is resisted by transverse forces in the bearing and tieback connections. The

magnitude of this moment is We_h, and due to the symmetry in the panels this creates an equal force of $+We_h/2D$ in each of the tieback connections and $-We_h/2D$ in each of the bearings;

- *Out-of-plane (OP) seismic load (x-direction).* The OOP seismic acceleration creates an equal seismic force of +/- $Ma_h/4$ in the four connections, where a_h is the acceleration in the horizontal direction and M is the mass of the panel;

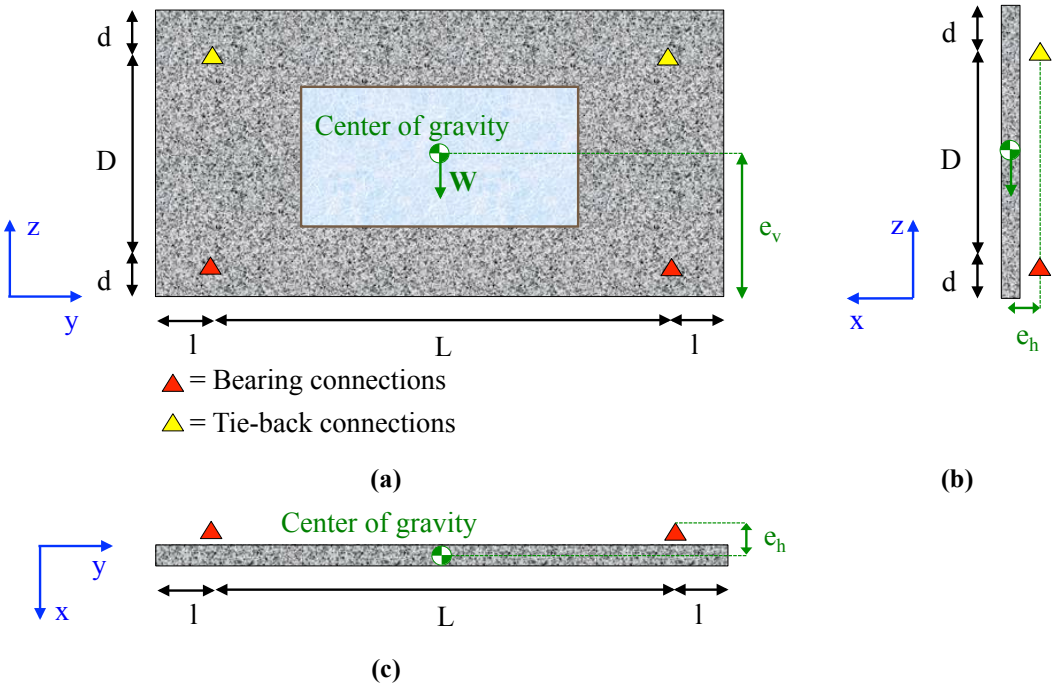

Figure 2.9. Geometry of the sample panel considered: (a) elevation, front view, (b) elevation, lateral view, and (c) plan view

- *In-plane (IP) seismic load (y-direction).* The IP force is distributed equally between the two bearing connections -since tiebacks cannot absorb forces in this direction- and it is equal to +/- $Ma_h/2$. Due to e_h, a moment around the vertical axis is also created, with transverse forces absorbed by bearing and tieback connections. The magnitude of this moment is equal to Ma_he_h, and thus the force created on each side of the panel is Ma_he_h/L, which creates a force on each connection of +/- $Ma_he_h/2L$. In addition, due to the vertical eccentricity of the load e_v, a moment around the x-axis is also created. This moment has a magnitude of Ma_he_v, and creates a vertical force of +/- Ma_he_v/L in each bearing connection;

- *Vertical seismic load (z-direction)*. Vertical forces created by this load are equally distributed between the two bearing connections and it will be equal to +/- $Ma_v/2$. In addition, the vertical load is also going to create a transverse force in both the bearings and tieback connections equal to +/- $Ma_ve_h/2D$.

Table 2.1 clearly shows that forces in the connections are dependent upon the eccentricity of the mass of the panel. Efficient connection design results from keeping this eccentricity to a minimum.

Table 2.1. Summary of the forces in the connection created by the loads for the sample panel under consideration

Connection	Force direction	Gravity	Seismic OOP (x)	Seismic IP (y)	Seismic Vertical (z)
Bearing	Vertical (z)	-W/2	-	+/- Ma_he_v/L	+/- $Ma_v/2$
	Horizontal OOP (x)	$-We_h/2D$	+/- $Ma_h/4$	+/- $Ma_he_h/2L$	+/- $Ma_ve_h/2D$
	Horizontal IP (y)	-	-	+/- $Ma_h/2$	-
Tieback	Vertical (z)	-	-	-	-
	Horizontal OOP (x)	$+We_h/2D$	+/- $Ma_h/4$	+/- $Ma_he_h/2L$	+/- $Ma_ve_h/2D$
	Horizontal IP (y)	-	-	-	-

Seismic Forces

The forces previously calculated need to be converted into seismic design forces that must be carried by the body and fasteners of connections. This can be done using Equation 13.3-1 in ASCE-7 (2010):

$$F_p = \frac{0.4 a_p S_{DS}}{\frac{R_p}{I_p}} \left(1 + 2\frac{z}{h}\right) W_p \qquad \text{Eq. 2.1}$$

Where:

- S_{DS}: spectral acceleration for short period;
- a_p : component amplification factor, as found in Table 13.5-1 of ASCE 7-10;
- I_p: component importance factor, varying from 1 to 1.5;
- W_p: component operating weight, previously found for each connection;

- R_p: component response modification factor;
- z: height of the structure of point of attachment of component respect to the base;
- h: average roof height of structure with respect to the base.

The subscript "p" denotes "parts and portions of a structure". ASCE-7 specifies also the maximum and minimum values of F_p as equal to $1.6S_{DS}I_pW_p$ and $0.3S_{DS}I_pW_p$, respectively. The upper bound accounts for the fact that the structure is supposedly responding in a non-linear way to a design earthquake event, which would limit the floor accelerations. This section of the code further specifies that the seismic design force F_p needs to be applied in at least two orthogonal horizontal directions in combination with service loads. For cantilevering systems, the force F_p is assumed to act in any horizontal direction, and the element must be designed also to resist a concurrent vertical force of +/- $0.2S_{DS}W_p$. The coefficients a_p and R_p to be used are specified for "exterior nonstructural wall elements and connections" in Table 13.5-1 of ASCE-7. Namely, for body of the connection a_p and R_p can be taken as 1.0 and 2.5 respectively, while for the fastener elements for the connection system, they are equal to 1.25 and 1. It should be noted that these values provide a force more than 3 times larger for fastener components of connections, in an effort to prevent brittle failure modes. The higher force level is intended to maintain the response of these elements in their elastic range. Also, this amplified force level satisfies the exception to the following ductility provisions of ACI (2011) Appendix D for anchorage to concrete:

- D3.3.4.3d: "The anchor or group of anchors shall be designed for the maximum tension obtained from design load combinations that include E, with E increased by Ω_0."
- D3.3.5.3c: "The anchor or group of anchors shall be designed for the maximum shear obtained from design load combinations that include E, with E increased by Ω_0." Where Ω_0 is the amplification factor to account for overstrength of the seismic-force-resisting system.

If the dynamic characteristics of the structure are known, the code provides an alternative way to determined the design forces through the following formula (where a_i is the acceleration at level i obtained by modal analysis and where A_x is the torsional amplification factors:

$$F_p = \frac{a_i a_p W_p}{\left(\frac{R_p}{I_p}\right)} A_x \qquad \text{Eq. 2.2}$$

Load Combination

The load combinations to be considered are presented by ASCE-7 section 2.3.2:

- Load combination #1: 1.4D. In this case the forces for the body and fasteners of the connection are the same;
- Load combination #5: 1.2D + 1.0E. This combination needs to be considered separately for IP and OP forces and in both cases it needs to be combined with the effects of vertical accelerations;
- Load combination #7: 0.9D +1.0E. This load combination is applied as the previous one.

From the load combinations, the maximum forces in the directions to be considered is found and it is this forces that will be used during design of the connections.

Forces in Bearing Connections

As seen in the previous part of this section, bearing connections are designed to resist forces in the three directions. Namely:

- *Panel embed*. The anchors and their welds have to be designed to resist axial forces and moments and they are considered as fastener elements. The free leg of the angle clip is also acting both axially and in bending and it can be considered as body of the connection;
- *Bearing bolt*. The bolt is designed to be able to transmit the maximum vertical force in the connection and it is considered a body element.
- *Angles clips and their welds*. Goal of this part of the connection is mainly to resist OP and IP forces. Namely, the welds in the IP direction are designed to absorb the maximum IP force, while the OP welds are designed to be able to transmit the maximum OP force. While clips can be considered as body elements, welds are clearly to be designed with fastener forces.

Forces in Tieback Connections

The following elements need to be designed to resist those forces:

- *Panel embed*. The anchors and their welds have to be designed to resist forces in the OP direction. Concrete breakout and welds checked against fastener forces, while failure of steel anchors is checked with body forces. The embed plate is also checked in for bending using body forces;
- *Rod*. Both flexing and sliding rods need to be checked in compression and tension and are considered as fastener;
- *Plate washers*. These are checked in bending as body elements;
- *Angle clip*. This is designed for bending considering the body forces;
- *Welds form the clip to the structure embed*. Clearly, welds must be designed to resist the maximum OP force calculated for fasteners elements.

2.2.3 Current Practice

A survey addressing questions about the detailing of tiebacks and corner joints was conducted among 13 precast producers and/or designers. This survey indicated that engineers certainly realize that building displacements affect panel joint size and configuration. To define the joint width and design the connections, the designer typically uses either the displacement values given by the structural engineer of record or maximums allowed by the code (ASCE 2010). More than 90% of the respondents to this survey use sliding connections to accommodate this drift, with the slots designed to take the maximum expected displacement, with nominal extra space to account for fit up tolerances. Only about 25% of respondents, however, indicated that they use flexural yielding of steel to accommodate drift even though this is expressly permitted by the code.

2.3 Criticism to the Current Design Code

2.3.1 Drift-Sensitive Design of Connections and Corner Systems

Tieback Connections

In current design codes such as ASCE7-10 (ASCE 2010), provisions addressing drift compatibility of cladding panels are either too vague or overly qualitative to provide specific guidance to design professionals. This leaves the detailing of key parts of the connections, such as the rod length, up to the discretion of the designer. This issue is made more complicated by the conflicting interests a

designer needs to face. In the case of sliding connections, practical considerations, such as allowance for construction tolerances, architectural finishes and the speed of installation, tend to encourage designers to detail sliding connections with a larger rod length. However, if the rod is excessively long (i.e. flexible) it will have a tendency to bend well before sliding can occur. Thus, a key unresolved issue in the design of sliding connections is the maximum length that can be provided to obtain a satisfactory seismic performance. Similar consideration can be made for flexing connections. However, in this case, a rod too long might not fit due to architectural constrains, but a rod too short may fracture due to excessive cycle rotations. The outstanding question for the design of flexing connections is the minimum length that can be used to avoid fracture of the rod during seismic motion. Goal of this research is to provide the designers with the maximum length for a sliding connections and minimum length of a flexing connection to ensure a good seismic performance.

Corner Joints

Another issue created by the drift of the panels is related to the corners of the system. This is the point where panels moving in-plane and out-of-plane interact. When a panel moves in-plane, ideally it displaces rigidly with the lower slab. In the out-of-plane direction, panels are allowed to deform or tilt, thus moving at their bottom with the bottom slab and their top with the top slab. Clearly, in the absence of a gap as large as the story drift, the top of the two corner panels will impact. This collision could result in connection failure and disengagement of the panel from the structure. Until the 1990s, a ¾'' joint at this intersection was expected to perform suitably, however, code changes have resulted in seismic joint widths that match the maximum expected inelastic drift of the structure. As a result, joint widths of 3-½" are not uncommon. These large joints running up each corner of the building are architecturally undesirable and can make the market for APC cladding less desirable when compared with other façades. Goal of my research is to identify a possible solution to this system, meaning a corner system allowing for smaller corner joints but still ensuring a good seismic performance.

2.3.2 Seismic Accelerations and Forces

While the criticisms relatively to the drift-compatibility are well defined, recognizing the issues relative to the calculations of seismic forces requires an understanding of how nonstructural components have been analyzed in the past, the origin of the different parameters in the design formula, and the criticism to this formula made by other researchers.

Seismic Response of Nonstructural Components

Villaverde (1997, 2009) notes determining the seismic response of nonstructural elements can be particularly challenging, since it depends on many factors, such as the response and the dynamic characteristic of the structure, and the location of the element within the structure. The following factors can also create some complications:

- The response of the nonstructural components depends both on the ground motion and the structural response to that motion, thus adding a secondary level of uncertainly;
- The motion of the nonstructural element may modify the motion of the structure, which can then modify the motion of the element;
- Since the input to the nonstructural element depends on the location of the element, identical elements installed at different locations can have a completely different response;
- If the nonstructural element is connected to the structure at more than one point, the supports of the elements might be excited by motions that are out of phase;
- The response of the nonstructural components is influenced by the possible inelastic behavior of both the structural and the nonstructural component itself;

Much effort has been devoted since the 1960s to develop a method for the seismic analysis for NCSs. Initially, this efforts were focused on ensuring the survivability of critical equipment in nuclear power plants (e.g. Villaverde 1997). The first way used to understand the seismic behavior of nonstructural components was performing a combined analysis of the structure-nonstructural system. The idea of determining the response of NCSs considering the analysis of the compound system it forms with the building is conceptually simple, but it presents problems during its implementation. In fact, the composite system has a large number of degrees of freedom, yet with large variance in masses,

stiffness and damping of structural and nonstructural components. This can create problems with conventional methods of analysis. For example, modal analysis might present difficulties in the computation of natural frequencies, while a step-by-step integration might become sensitive to the integrations time step (Villaverde 1997, Soong 1995). In addition, this so-called "primary-secondary system" has four major dynamic characteristics that require special attention (Igusa and Der Kiureghian 1985):

- Tuning: coincidence of the frequencies of the primary and secondary subsystems;
- Interaction: the feedback between the motion of the two subsystems;
- Non-classical damping: which occurs when the damping characteristics of the two subsystems are different;
- Spatial coupling: the effect of multiple support excitation of the secondary system, which is influenced also by the location of support points and the stiffness of connecting elements.

Another alternative is to use the modal synthesis method. In this method, the response of secondary systems is still calculated on the basis of a modal analysis of the combined systems, but the dynamic properties of this system are obtained in terms of the dynamic properties of the components considered independently (Villaverde 2009). This strategy is uncoupled and it requires subsequently, or cascade analysis i.e. first a structural analysis and then the analysis of NCSs.

The final and probably more popular method used for the analysis of the response of NCSs is the floor response spectrum method. In this method, the dynamic response of the structure at the point of attachment with the nonstructural component in its absence is found, and then used to calculate the response of a SDOF system representing the nonstructural component. This method ignores the interaction between the structure and nonstructural components, and for this reason they can constitute a good approximation only in case of nonstructural components with small masses and natural frequencies far from those of the building. In addition, this method cannot be rationally applied for the analysis of nonstructural elements with multiple points of attachment. A third limitation is that this method is valid only for linear systems.

Summary of the Origin of the Code Design Formula Parameters

The design of "part and portions of the buildings", or nonstructural components, is explicitly addressed in the design code since the 1927 version of the Uniform Building Code (UBC) (ICBO 1927). Since the 1935 edition of the UBC (ICBO 1935), the design force for these components is set equal to the weight multiplied by a seismic coefficient, which depended on the seismicity on the area in which the building was constructed. In addition, larger forces were attributed to elements whose damage during an earthquake could be particularly dangerous.

The formula got more elaborated throughout the years. For example, the ATC 3-06 document published in 1978 (ATC 3-06 1978) introduced the first version of both the component amplification factor and the structure amplification factor. The values of the component amplification factor depended on the ratio between the main natural period of the component and building. If this was less than 0.6 or larger than 1.4, the amplification factor was 1, while it was set to 2 when this ratio was in between 0.6 and 1.4, i.e. close to resonance. The tri-service manual published by the Department of Defense in 1982 (Department of defense tri-service seismic design committee 1982) started recognizing the difference between "rigid" and "flexible" nonstructural components. In case of flexible equipment (i.e. with a natural period of more than 0.05 seconds) the formula included a component amplification factor whose value depended on the period of the building and period ratio, and could reach a maximum value of 5. It is noted that an explicit rational for the numerical values adopted was not presented. The 1988 UBC provisions (ICBO 1988) adopted the distinction between rigid and flexible elements, even if they set the limit between the two at a natural period of 0.06 seconds.

A criticism to the provisions came from Soong et al. 1993. This report is very important, since introduced values and concepts still used today. First of all, it proposed a variation of the component amplification factor between 1 and 2.5, which are the values currently is use. However, in this case the exact values depended on the ratio between the natural period of the building and components. It is noted that the formulas provided in this report were largely based on either analytical work or engineering judgment, since the experimental work available at the time was very limited. The main experimental study cited was a 1982 experiment conducted by Kelly (Kelly 1982) in which a one-third

scale building model with three oscillators attached was subjected to several scaled earthquake motions. During this experiment, the amplification factors of the oscillators varied from 1.91 to 2.99. This report introduced also the concept of component response modification factor. The value attributed to this factor for exterior non-bearing walls was 3, very similar to what is still used today. It is important again to notice that the numerical values of the component response modification factors were arbitrary, and a value of 3 only meant that the committee in charge to assigning this value judged that this component had "some minimal level of energy absorption capabilities" (Drake and Bragagnolo 2000).

The 1994 NEHRP (BSSC 1994) provisions adopted many of the recommendations proposed by Soong et al. 1993, however in a simplified version. For example, the component amplification factor was set to either 1 or 2.5 for different type of components, while the dependency from the building-component period ratio was eliminated. This version of the code also reintroduced the linear variation of the structural amplification factor.

The current design formula appeared for the first time in the 1997 edition of the NEHRP provisions (BSSC 1997). In this formula, the structure amplification factor was set to vary linearly from 1 at the base of the building to 3 at the roof. The studies on which these findings are based were mostly analytical studies or empirical studies of earthquake in California, which did not undergo significant nonlinear deformations (Kehoe and Freeman 1998).

Criticisms to the Structural Amplification Values in the Design Formula

Many criticisms to the current design formula, and especially to the values of the structure amplification factor were made throughout the years. Early criticism came from Rodriguez et al. 2002. The authors of this study performed a non-linear time-history dynamic analysis to determine the horizontal floor accelerations. This investigation found that the maximum magnification of floor accelerations occurs always at the uppermost floor, and that, when the building response is inelastic, the floor accelerations are reduced at the uppermost floor. A method named "first mode reduced" was proposed to find the amplification of accelerations at different floors. This method assumes that only the first mode is affected by the ductility and proposes a floor acceleration magnification of 1 at the first floor and constant in the upper floors.

In 2003 Horne and Burton investigated the seismic forces in hospital equipment and compared them to the code requirements. They particularly criticized the fact that the component amplification factor a_p provided by the code does not take into account the dynamic properties of neither the equipment nor structure. They proposed to change the formula to calculate F_p to:

$$F_p = a_p \left(\frac{F_i}{W_i} \right) \left(\frac{R/I}{R_p/I_p} \right) W_p \qquad \text{Eq. 2.3}$$

Where the value of a_p follows the distribution shown in Figure 2.10.

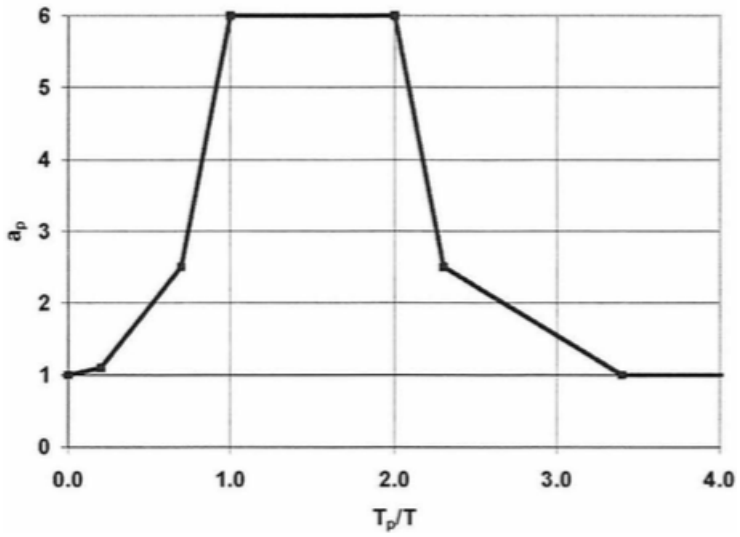

Figure 2.10. Values of a_p as function of T_p/T proposed by Horne and Burton 2003. (Courtesy of Horne and Burton 2003)

In 2004, Chaudhuri and Hutchinson performed a study to find the distribution of the magnification of floor accelerations along the height of a building for a broad range of seismic hazard levels. The study was based on the analysis of eight steel moment resisting frame buildings with a variety of natural periods. They found significant scatter in the results, and determined that the code limits was generally conservative at the upper floors of flexible buildings, while it could under-predict the accelerations at the lower stories of rigid buildings. Using a probabilistic approach they found the values of the amplification coefficient along the height of the building at different confidence levels. Selected results are presented in Figure 2.11.

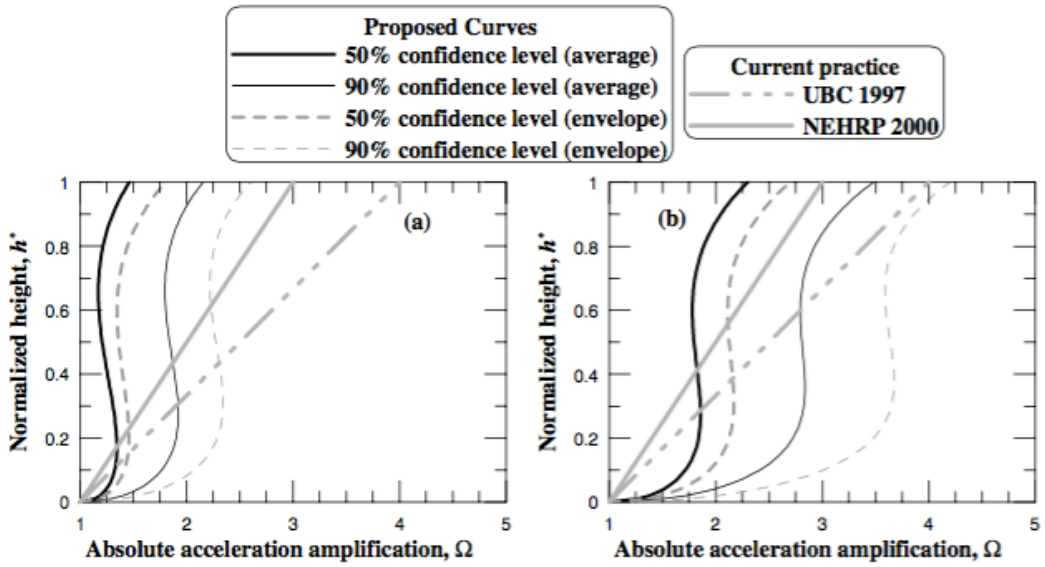

Figure 2.11. Distribution of floor acceleration amplification along the normalized height for flexible and rigid buildings proposed by Chaudhuri and Hutchinson 2004 (Courtesy of Chadhuri and Hutchinson 2004)

In 2005 Miranda and Taghavi proposed a simplified method to estimate floor accelerations demands for linear buildings. These were found using approximations of the first three modes of vibration of the building, which was modeled as a cantilever flexural beam connected laterally to a cantilever shear beam. Another study was performed by Medina et al. (2006), who examined the response of light components installed on moment resisting frames. In the analysis they considered a variety of stiff and flexible frames, subjected them to a series of earthquakes and then used the accelerations response at floors as input to the nonstructural components, which were modeled as a SDOF. The study found that a wide range of amplification of the components were possible depending on several factors, first of all the natural frequency of the component itself. Hence, the authors identified a need to understand the dynamic behavior of NCSs. Other factors relevant for the behavior of the NCSs were:

- The natural periods of the supporting structure;
- The location of the component in the building, with maximum component accelerations generally larger at the top of the building;
- Height of the supporting structures;
- Stiffness distribution in the supporting structure;

- Strength of the supporting structure;
- Damping of the NCSs. The authors used 0.01%, 2% and 5% as possible values.

The authors found that, for values of $T_c/T_{builiding}$ between 0 and 0.5, the amplification factor for elastic frames is always larger than the unit due to the effect of higher modes (Figure 2.12). The authors end the paper with recommendations on how to estimate the peak component accelerations. Another study conducted by Dowell at al. 2008 also concluded the relevance of higher mode of the structure, which are not considered in the current design code.

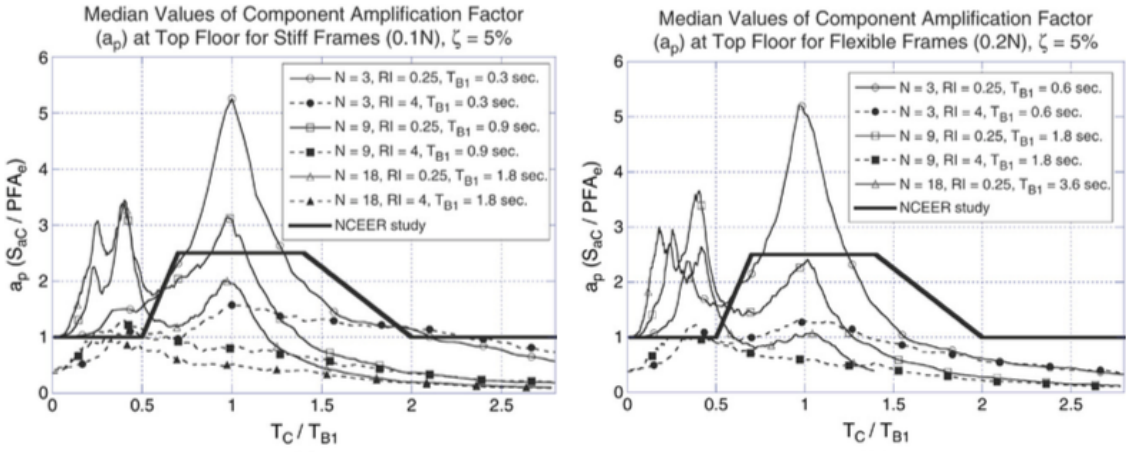

(a) **(b)**

Figure 2.12. Values of the a_p found by Medina et al. 2006 for the component located at the top of (a) stiff and (b) flexible frames [RI=relative intensity]. (Courtesy of Medina et al. 2006)

In 2006, Singh and co-authors wrote two companion papers presenting criticism for the formula to calculate F_p, one for flexible and one for rigid components. In the paper about rigid components (Singh et al. 2006a), Singh identifies three different issues in the definition of the force: the fact that F_p is independent from the dynamic characteristics of a building, the fact that the coefficient varies linearly with the height of the building, and the way in which a_p is defined. Some of the criticisms were:

- The code does not consider the height of the building. The authors of the study proposed a new formula, in which the main difference is in the definition of the component acceleration coefficient C_z. This can be assumed as in the code definition if the building period is unknown. However a new formulation is proposed in case the period is known. In this case,

different values of C_z are prescribed for short (number of stories ≤8) and tall (number of stories >8) buildings. In fact, their study reveled that for short buildings the variation of accelerations with height is almost linear. For taller buildings however the accelerations remains almost constant for the middle stories and then increases sharply close to the roof. This is attributed to the whiplashing effect of higher modes;

- The code ignores higher modes of the building. This be acceptable for lower buildings, but not for tall ones. In fact, the authors' analysis showed that the difference in acceleration when higher modes and considered and are not considered can be up to 6.6 times for tall buildings;
- 5% damping is assumed. However, the level of damping could be higher during a strong ground motion, while lower during low-level excitation;
- Irregularities in buildings can cause difference in the response.

A companion paper (Singh et al. 2006b) examined the behavior of flexible components, and proposed several formulas for the calculations of F_p in case the building and component natural periods are known or unknown. One of the final remarks of this paper is related to the fact that tuning of the component frequency to one of the higher modes could provide even higher forces than when the component motion is tuned with the main frequency. It is noted that, even if the floor acceleration may be reduced with the structure yields, the component acceleration may mot be reduced. In fact, past studies (Sewell et al. 1986, Singh et al 1993) seem to show that the response of a flexible components in a yielding structure could be even larger.

In 2009, Miranda and Taghavi compared the response of building responding elastically and nonlinearly, and reported that the floor amplifications generally decrease with the increase in nonlinearity. The values of amplification of acceleration in the floors along the normalized height of the building is shown in Figure 2.13.

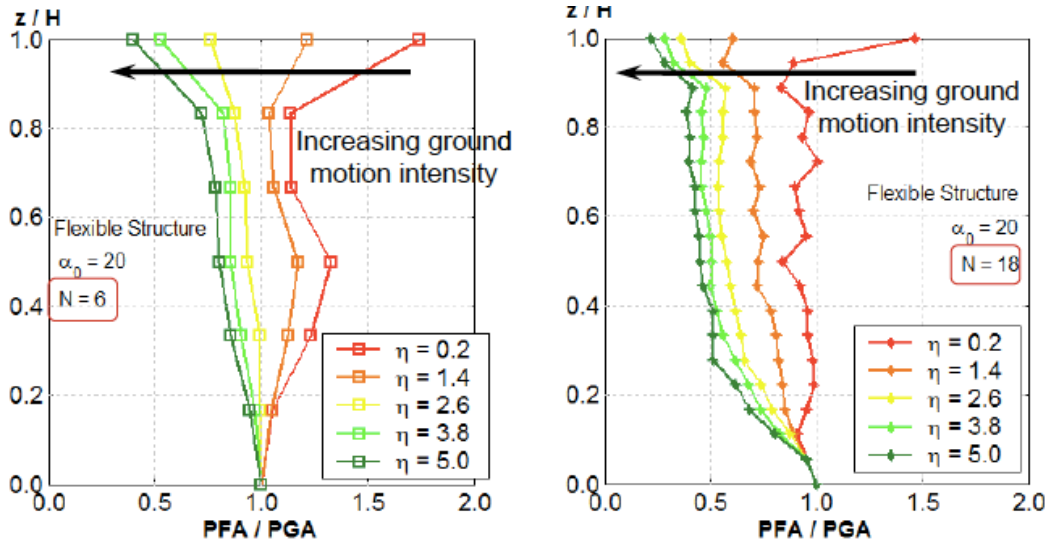

Figure 2.13. Variation of peak floor acceleration (PFA) divided by the peak ground acceleration (PFA) as reported by Miranda and Taghavi in 2009 (Courtesy of Miranda and Taghavi in 2009

In 2011 Fathali and Lizundia analyzed the data from 37 set of earthquake records obtained from 16 fixed-base building at least 15 story tall. Data considered were recorded during the 1997 Whittier and 2009 Inglewood earthquake, with PGA varying from 0.003g to 0.523g and PFA varying from 0.007g to 0..653g. The study focused on the calculation of the ratio PFA/PGA at different floors of a building. Linear regression was used to find the best fit for the PGA/PFA versus z/h. Results indicate that the profile is different from a straight line, and a nonlinear equation can better represent the behavior as:

$$\frac{PFA}{PGA} = 1 + \alpha\left(\frac{z}{h}\right)^{\beta} \qquad \text{Eq. 2.4}$$

The study examined also the component amplification factor a_p. It was noted that a_p can exceed the code value for range on component periods between 0.1 and 0.75 seconds. The mean plus one standard deviation reached a maximum of 3.3. For larger periods, the code might overestimate the actual a_p. These results are shown in Figure 2.14.

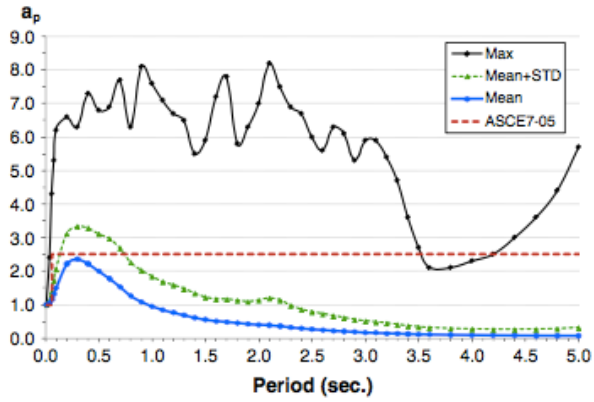

Figure 2.14. Values of a_p found by Fathali and Lizundia 2011 (Courtesy of Fathali and Lizundia 2011)

In 2012 Lepage et al. tried to find the response on NCSs for a nonlinear response of buildings (Figure 2.15). The data for the building response used in this study were derived from shake table test data on the nonlinear seismic response of multistory reinforced concrete structures from a series of experiments conducted at the University of Illinois on small scale structures. Additional data from real earthquakes were also considered. Models of regular-shapes RC buildings of 6 and 12 story were created in SAP2000 and subjected to a suite of motions, during with the building had to respond nonlinearly (design event) and linearly. The value of the effective response modification coefficient for the structure R' was derived as the ratio of the maximum base shear in the linear and nonlinear response. The value of amplification of the structural response from the linear and nonlinear case is reported in the figure. Based on the experimental and analytical data, the authors proposed to define the acceleration demand on the nonstructural components as:

$$A_{pi} = A_0 \left(1 + \frac{3}{R'} \frac{h_i}{h_r}\right) a_p \qquad \text{Eq. 2.5}$$

Where A_{pi}=maximum acceleration of the nonstructural component at floor i.

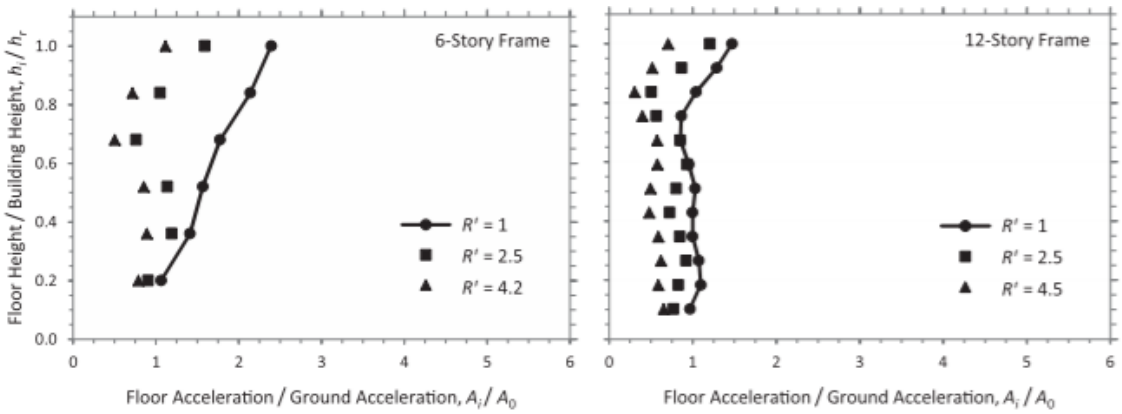

Figure 2.15. Amplification of accelerations along the height of the building for different nonlinear levels reported by Lepage et al 2012 (Courtesy of Lepage 2012)

In 2013 Wieser et al. performed an investigation on the floor acceleration of yielding special resisting frame building. This study was based on a suite of 21 far-field ground motions on 3D models in Opensees. They concluded that the current code equations overestimate PFA/PGA ratio in elastic building with natural periods between 1 and 4 seconds by as much as 4 times. The also commented that the component amplification factor a_p is not constant along the height of the building, since it is related to the floor to which it is attached.

A recent critic to code formulas for the design of nonstructural components came from Kehoe in 2014. The author pointed out that the behavior of nonstructural components is very complex, and the actual dynamic characteristics depend on the detail of the construction and possible additional mass added by content. However, the values of a_p prescribed by the code do not take into account the characteristics of the component, but they are associated by the generic component, and come mostly form engineering judgment more than from methods on analysis. The single values provided for a_p implies also that the behavior of the component is the same in both directions, this is clearly not the case for walls, where the out-of-plane and in plane behavior are generally very different. The values of amplification of the response on nonstructural component does not also take into account possible amplification created by higher modes of the structure. Kehoe proposes to use a different approach to determine the dynamic characteristics of the NCSs, based on tables providing the stiffness of the elements depending on typical values of the geometry. The author states also that the conditions of attachment of the nonstructural component to the structure should be considered.

In 2014 Qu et al. published a paper with a review of the formula for the calculations of forces in NCSs. They used data from instrumented buildings in California (50 reinforced concrete concrete shear wall building, 50 steel moment frames, 27 steel braced frame spanning from low-rise to high rise). According to this study, the code captures the vertical distribution of peak floor accelerations but does not predict them with the same confidence at each level. The formula also completely ignores any possible torsional response of the building, which could create non-uniform acceleration in the floor plan. Additional amplifications could also be caused by diaphragm flexibility. Another criticism to the code is the fact that it does not consider properly the effect of the vertical ground motion. The authors found that the peak vertical floor acceleration is not constant with the height of the building, and actually could increase linearly. If the vertical period of nonstructural component aligns with that of the supporting structure, the response could be amplified in this direction. In 2014 Wang et al. published a case study in which the seismic demands on acceleration sensitive non-structural components were examined. They considered two case studies for experimental for building which response with different levels of nonlinearity.

Summary of the Issues Relative to the Calculations of Seismic Forces in APC Cladding

From the discussions in the previous sections, it is possible to identify issues in the formula for the calculation of the seismic force F_p when applied to APC cladding connections. In terms of *component amplification factor* a_p it was found that many of the past analytical studies to determine a_p were based on the floor response spectrum method, which provides good results for lightweight components attached to one floor, thus the results cannot be extended to APC cladding panels. The values of the component amplification factors of 1 and 2.5 for "rigid" and "flexible" components was introduced in the early 1990s, when a very limited number of experiments were available, thus there are great uncertainties in these numbers. In addition, the code classifies all the exterior walls as rigid elements, thus attributing them an a_p of 1. While this hypothesis might be reasonable for many types of lightweight façades, this might not be the case for APC cladding. In fact, cladding panels combine a very large mass with low stiffness in the OP direction. A final criticism is that the code formula provides a single value of a_p for a single component. However, for components attached to two floors

there should be two different a_p: one relative to the bottom floor ($a_{p,bottom}$) and one relative to the top floor ($a_{p,top}$), see Figure 2.16.

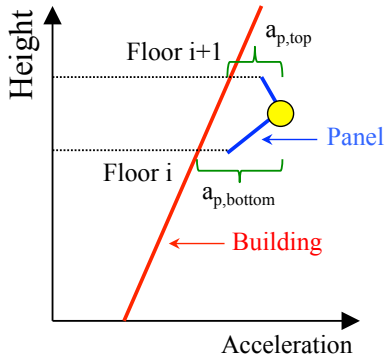

Figure 2.16. Schematic showing $a_{p,top}$ and $a_{p,bottom}$

The concept *of component response modification factor* R_p was introduced in the early 1990s, and the numerical values are completely arbitrary. Dividing the estimate of acceleration in the APC cladding by an arbitrary value of 2.5 could create issues during lower level earthquake. For example, this could lead to yielding of some components during a service level motion;

The linear variation of the *structure amplification factor* a_s re-introduced in the code in the late 1990s is based on either analytical studies or studies of past earthquakes in California, which were not large enough to produced a significant inelastic response of the structure. This factor has been criticized by many researchers and practitioners since its introduction.

The main goals of this research relative to the calculations of seismic design forces are:

- Identify the dynamic characteristics of APC panels, and determine if they can be really considered rigid or not;
- In case they cannot be considered rigid, determine the real component amplification factor during design level motions.
- Determine the consequences of the presence of the arbitrary R_p in terms of performance during service and design level motions.

Chapter 3

Description of the Experimental Projects: BNCS and Component Tests

The main goal of this chapter is to present details on the three experiments performed on APC cladding whose results are analyzed in the following chapters. The three experimental studies include one system level experiment herein short named the Building Nonstructural Components and Systems (BNCS) project[1] and two component tests on sliding and flexing rod connections performed at UCSD and San Jose' State University (SJSU), respectively. In the case of the component tests, this chapter presents only the description of the experiments themselves, while the results are presented in Chapter 4. However, for the BNCS project this chapter presents both the description of the project and the description of physical damage. Further elaborations of the results from the BNCS project are presented in the appropriate chapters throughout this dissertation (chapter 4 for the results relative to flexing connections, chapter 5 for the results concerning corner joints, chapters 6,7,8 for results relative to

[1] This research project, coined Building Nonstructural Components and Systems (BNCS), is discussed in detail within a series of four technical reports:

BNCS Report #1: Full-scale structural and nonstructural building system performance during earthquakes and post-earthquake fire – specimen design, construction, and test protocol. SSRP-2013/09, Department of Structural Engineering, University of California, San Diego, La Jolla, CA.

BNCS Report #2: Full-scale structural and nonstructural building system performance during earthquakes and post-earthquake fire – test results. SSRP-2013/10, Department of Structural Engineering, University of California, San Diego, La Jolla, CA.

BNCS Report #3: Full-scale structural and nonstructural building system performance during earthquakes and post-earthquake fire – camera and analog sensor details. Structural SSRP-2013/11, Department of Structural Engineering, University of California, San Diego, La Jolla, CA.

BNCS Report #4: Full-scale structural and nonstructural building system performance during earthquakes and post-earthquake fire – construction details and technical specifications of specific subsystems.SSRP-2013/12 , Department of Structural Engineering, University of California, San Diego, La Jolla, CA.

In addition, a complete set of high-quality test data from this research project is archived and publicly available in the NEES data repository (DOI: 10.4231/ D38W38349).

accelerations).

3.1 Building Nonstructural Components and Systems (BNCS) Project

3.1.1 Overview

Central to the BNCS project was the construction and testing of a full-scale five-story building on the large high performance outdoor shake table at the George E. Brown Jr. Network for Earthquake Engineering Simulation at the University of California, San Diego (NEES@UCSD). This shake table is unidirectional, with motion applied at the table plate in the east-west direction. Notable to this building was an array of nonstructural components and systems, which included stairs, a functional passenger elevator, partition walls and, ceilings, gas piping, electrical conduits and roof mounted equipment. Two different types of exterior façade were utilized: cold-formed steel balloon framed walls at the three lower levels and APC cladding at the two upper levels. This second type of façade is the subject of this dissertation. A picture of this test specimen is shown in Figure 3.1a.

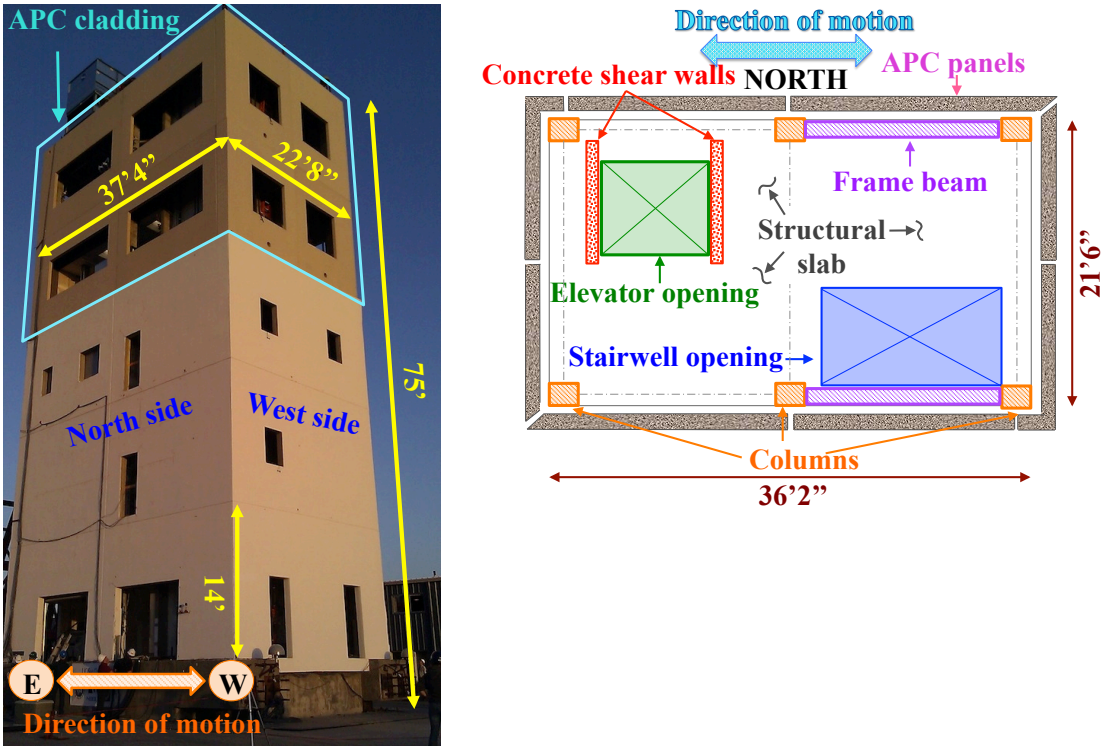

(a) (b)

Figure 3.1. BNCS building: (a) picture from the northwest corner, and (b) plan view of a typical floor

The overall height of the reinforced concrete building, including its foundation, was 75', with 14' story height and a slab of 36'2'' by 21'6''. Figure 3.1b shows the plan view of the slab at a typical floor, which was characterized by the presence of six columns, two walls spanning in the north-south direction and openings for the elevator and stairs. The total weight of the building was 1410 kips, of which 1100 kips accounted for the structural components. This weight includes the 420 kip foundation. The lateral seismic resisting system of this building was provided by a pair of identical one-bay special reinforced concrete moment resisting frames in the northeast and southeast bays. While the capacity of the beams was roughly the same at each floor, the technology used at each floor was different, and it included the use of high-strength steel and ductile connections. The building was instrumented with more than 500 analog sensors and more than 80 cameras monitoring structural components, nonstructural components and shake table.

Initially, the building was tested while isolated from the shake table with four high-damping rubber bearings installed at each of the four corners of the structure. Following the seven base isolated motions (named BI1 through BI7), the foundation was fixed to the table and the building underwent six seismic motions while in a fix base configuration (FB1 through FB6). The initial motions were intended to be serviceability level and some had long duration, while the final motions in the fixed-base configuration were intended to reach the design level earthquake and surpass it. In some cases the actual motion was used as the target, while in other cases the original motion was spectrally matched to the ASCE 7-05 (ASCE 2005) design spectrum assuming a high seismic zone in Southern California (site class D). The full test protocol, including the name of each test, is shown in Table 3.1. It is noted that white noise and pulse base excitation were input before and after earthquake motions. After the seismic test phase, fire tests were also performed at the third floor of the damaged specimen (Kim et al. 2013). More detailed information about this project is presented in a series of reports and papers (Chen et al. 2016, 2013a-b; Hutchinson et al., 2013; Pantoli et al. 2016, 2013a-b).

3.1.2 Overview of APC Cladding Installed on the BNCS Building

Geometry and Nomenclature

The two upper floors of the BNCS building were enclosed by APC cladding that was designed,

Table 3.1. Seismic test protocol

Base	Station-scale (Earthquake)	Name	Type	Notes
Isolated (BI)	Canoga Park-100% (1994 Northridge earthquake)	BI1	Spectrally matched	Serviceability level
	LA City Terrace-100% (1994 Northridge earthquake)	BI2	Spectrally matched	Serviceability level
	LA City Terrace-100% (1994 Northridge earthquake)	BI3	Spectrally matched	Serviceability level
	San Pedro-100% (2010 Maule-Chile earthquake)	BI	Actual motion	Long duration
	ICA-50% (2007 Pisco-Peru earthquake)	BI5	Actual motion	Long duration, multiple runs
	ICA-100% (2007 Pisco-Peru earthquake)	BI6	Actual motion	Long duration, multiple runs
	ICA-140% (2007 Pisco-Peru earthquake)	BI7	Actual motion	Long duration, multiple runs
Fixed (FB)	Canoga Park-100% (1994 Northridge earthquake)	FB1	Spectrally matched	Serviceability level
	LA City Terrace-100% (1994 Northridge earthquake)	FB2	Spectrally matched	Serviceability level
	ICA-50% (2007 Pisco-Peru earthquake)	FB3	Actual motion	Long duration, multiple runs
	ICA-100% (2007 Pisco-Peru earthquake)	FB4	Actual motion	Long duration, multiple runs
	Pump Station #9-67% (2002 Denali eq.)	FB5	Spectrally matched	~Design Earthquake
	Pump Station #9-100% (2002 Denali eq.)	FB6	Spectrally matched	~>50% larger than Design Earthquake

installed and instrumented in collaboration with precasters and an advisory board within the Precast Concrete Institute (PCI). Two punched window panels per side of the building were installed at each floor, resulting in a total of 16 panels. Since the movement of the shake table was in the east-west direction, the eight panels in the south and north faces experienced mainly building motion in the in-

plane direction (IP panels), while the eight panels in the west and east sides experienced predominantly out of plane motions (OP panels).

All the panels had the same thickness of 5''. The height of the panels installed on the fourth floor was 13'11'' while the panels on the fifth level were 15'5'' tall. The IP panels had width between 18'8'' and 16'11'' and a weight between 10.7 kips and 13 kips, while the OP panels were smaller, with a width of 11'4'' (not including the returning corner) and a weight between 8.1 and 9.5 kips.

Connection of the panels to the building skeleton were facilitated by steel embeds installed in the slab, beams and columns. The panels were supported by two bearing connections at the bottom and tieback connections at the top, two for the smaller OP panels and four for the larger IP panels. The exact geometry of the panels in the south and east face and the location of connections are shown in Figure 3.2. It is noted that the geometry of the panels in the north and west side is mirrored respect to the one of the south and east sides, respectively.

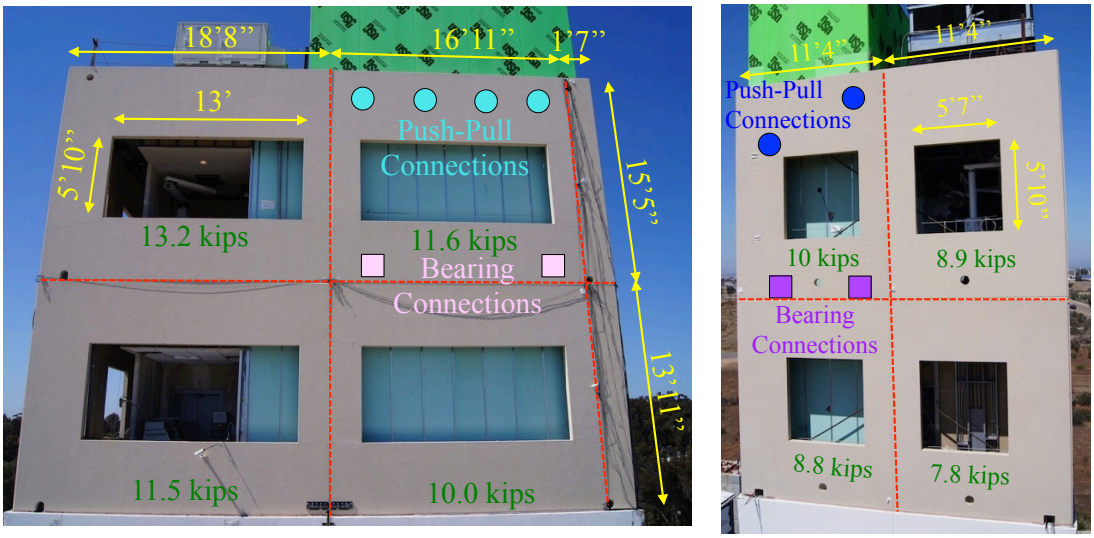

(a) **(b)**

Figure 3.2. View of the APC panels installed in the BNCS building, showing the geometry and the typical location of connections: (a) IP panels on the south side and (b) OP panels on the east side

Figure 3.3 presents a summary of the name of the panels and their nomenclature. The name of each panel is composed by three digits, indicating the level number and the side of the building onto which the panel is installed. Normal weight concrete with a 28-day design compressive strength f'_c = 5 ksi were used in the fabrication of these panels. The bearing connection supporting the panels had a

geometry slightly different from what is seen commonly in buildings. Namely, due to the presence of the upturn beam and the fourth level, which increased the distance from the point of attachment to the panel, some bearing connections had to be reinforced by a haunch (Figure 3.4a). These hunched connections were installed on the IP panels in the eastern side of the building at both floors, while all the OP panels had bearing connections without haunches (Figure 3.4b). Since these connections were not one of the points of attention of the test, they will not be further discussed. Tieback connections will be discussed further in the following sections.

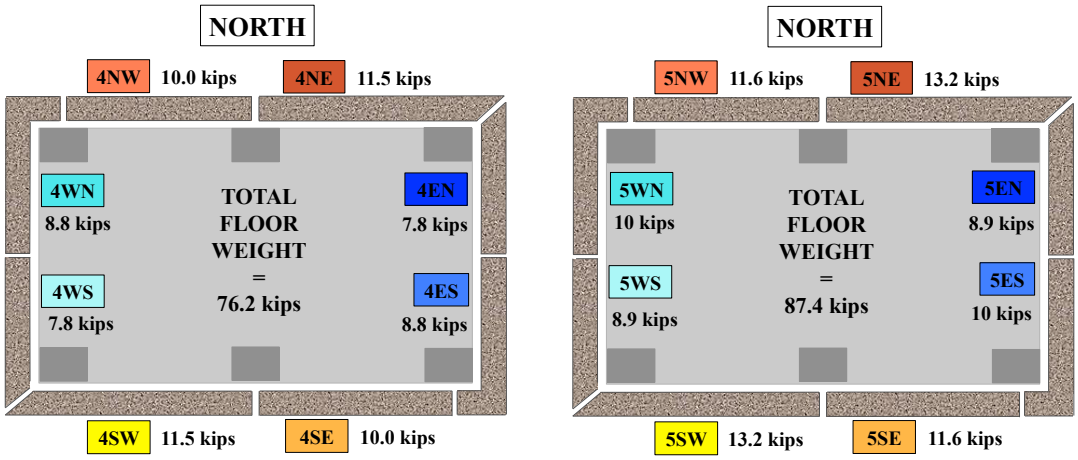

Figure 3.3. Summary of weights of panels and nomenclature of panels for (a0) the forth level and (b) the fifth level

Design

Panel design, construction, and installation were performed by a U.S. West-Coast precaster with expertise in precast concrete cladding systems. Structural design criteria and detailing conformed to requirements of ASCE 7-10, ACI 318-08, PCI MNL 120-04 and ANSI/AISC 360-05 for regions of high seismicity. Nonlinear time history analyses of the building were conducted and used to predict interstory drift ratios (IDRs) anticipated during design and maximum credible earthquake events and were used to size the joints and design the slotted and flexing rod connections. The expected peak drifts were 2% and 1.1% at the fourth and fifth level, respectively. In terms of forces, the preliminary analysis predicted a short period spectral acceleration S_{DS} of 2.33 g, 1.60 g and 2.84 at the fourth floor, fifth floor, and roof respectively.

(a) **(b)**

Figure 3.4. Bearing connections used in the BNCS building: (a) hunched, and (b) not-hunched

Installation

Panels were cast off-site at a precast plant and shipped to the NEES@UCSD facility on the day of installation. In total, the installation of the 16 panels on the building was performed during approximately five days, with the following activities performed each day:

- Day one: All connections were prepared, including welding of connection angles to the structural embeds and placement of the rods (Figure 3.5.a);
- Day two and three: Eight panels per day were installed on the building (Figure 3.5.b and c);
- Day four and five: Welding of all connections to the embeds in the structural slab and frame was completed (Figure 3.5.d).
- Finally, several days were needed to place caulking in the joints.

Instrumentation

A total of 65 analog sensors monitored the behavior of the cladding panels. The main goals were to monitor:

- The displacement at the top of the panel relative to the structural skeleton. In particular the in-plane movement of the IP panels and the out-of-plane movement of the OP panels were closely

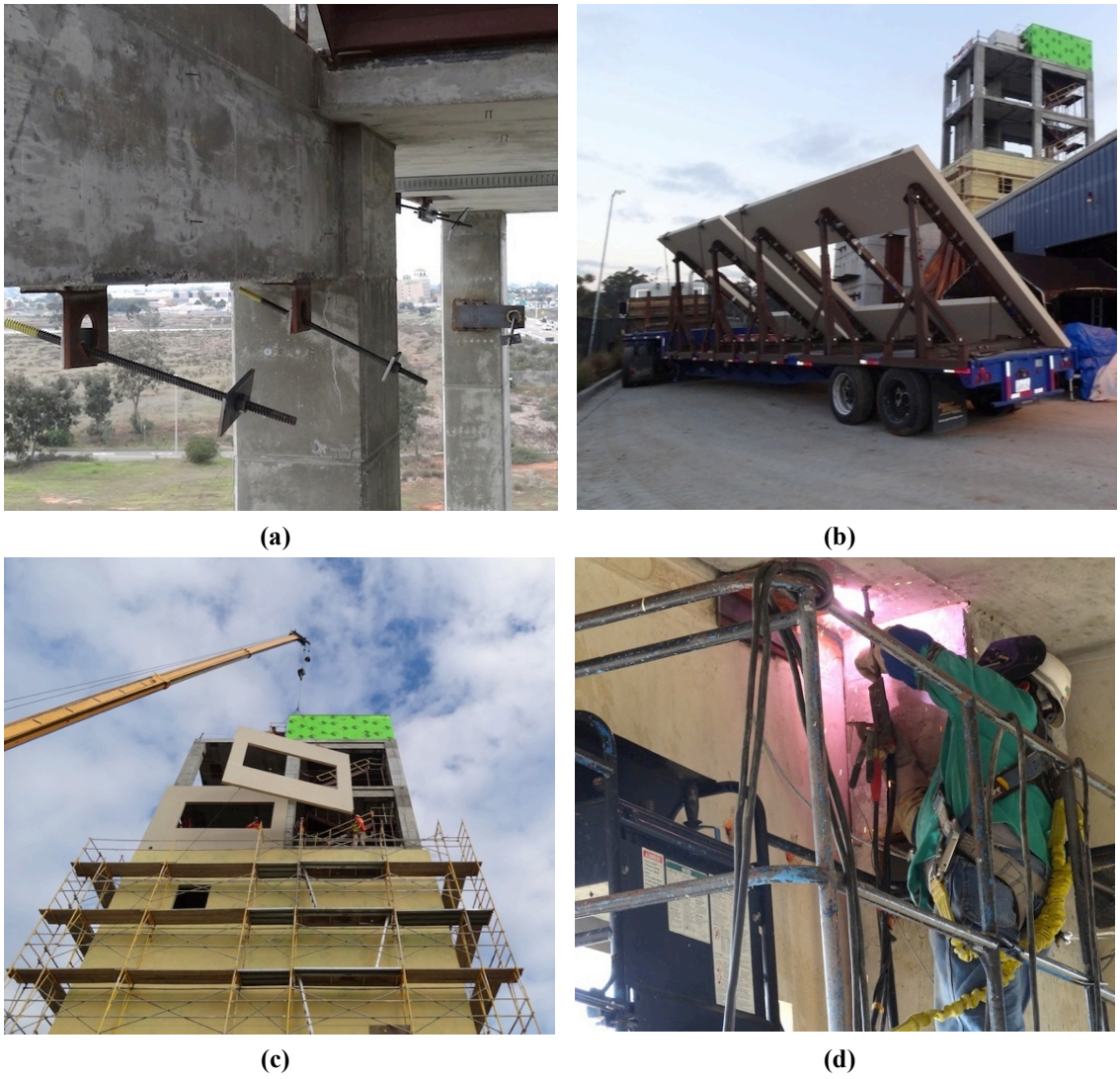

Figure 3.5. Installation phases during the BNCS project: (a) installation of temporary connections, (b) transportation of the panels on site, (c) lifting of the panels, and (d) welding of the final connections (Courtesy of Chen et al. 2013a)

monitored. String potentiometers and linear potentiometers were used for this goal;

- The east-west and vertical acceleration in both IP and OP panels.

Force in the connection rods, especially for the corner connections in the OP panels. Due to the large number of panels and connections compared to the number of sensors available, measurement locations were concentrated in the southeast corner of the building. In addition to the analog sensors, four video cameras were installed to monitor the behavior of the panels during the FB testing: these recorded the behavior of the two types of corner joints, namely a corner connection and a flexing rod

connection. It is noted that data about the structural behavior were also available. The global behavior of the structural system was also monitored with accelerometers installed at the corners of each floors stab. Thanks to these accelerometers, it was possible not only to obtain the time history of accelerations, but also the drifts through double integration of accelerations.

Tieback Connections

Both flexing and sliding tieback connections were installed in the IP panels. The main variable for these connections was the length of the rod. In fact, rods considered "long", "medium" and "short" were installed, as summarized in Table 3.2 and Table 3.3. It is noted that the definition of clear length L_c and free length L_f was presented in Chapter 3, while d is the diameter of the rod, which was 0.75'' for connections in the IP panels.

Table 3.2. Summary of L_f and L_f/d for flexing tieback connections during the BNCS experiment

Short rod		Medium rod		Long rod	
L_f (inch)	L_f/d	L_f (inch)	L_f/d	L_f (inch)	L_f/d
10.9	14.5	14.9	19.8	18.9	25.2

Table 3.3. Summary of of L_c and L_c/d for sliding tieback connections during the BNCS experiment

Short rod		Medium rod		Long rod	
L_c (inch)	L_c/d	L_c (inch)	L_c/d	L_c (inch)	L_c/d
0 ["snug"]	0	3.5	4.7	7	9.3

The location of each type of connection at the fourth and fifth level is shown in Figure 3.6. The flexing rods were coil rods ASTM A108 with minimum values of f_u and f_y at 80 and 60 ksi, respectively. The sliding connections rods were a UNC threaded rods ASTM A572 Grade 50. Tension tests on rods from two batches of the sliding rods were performed, and they revealed an average f_y of 65 ksi, an f_u of 82 ksi, and an elongation at fracture of roughly 14%. . More detailed information about these tests can be found in Hutchinson et al. 2014.. The structural shapes and plates used were ASTM A36 Grade 50. The name of each connection is shown in Figure 3.7. In this nomenclature E, W, N and S stand for east, west, north and south respectively, while C stands for central.

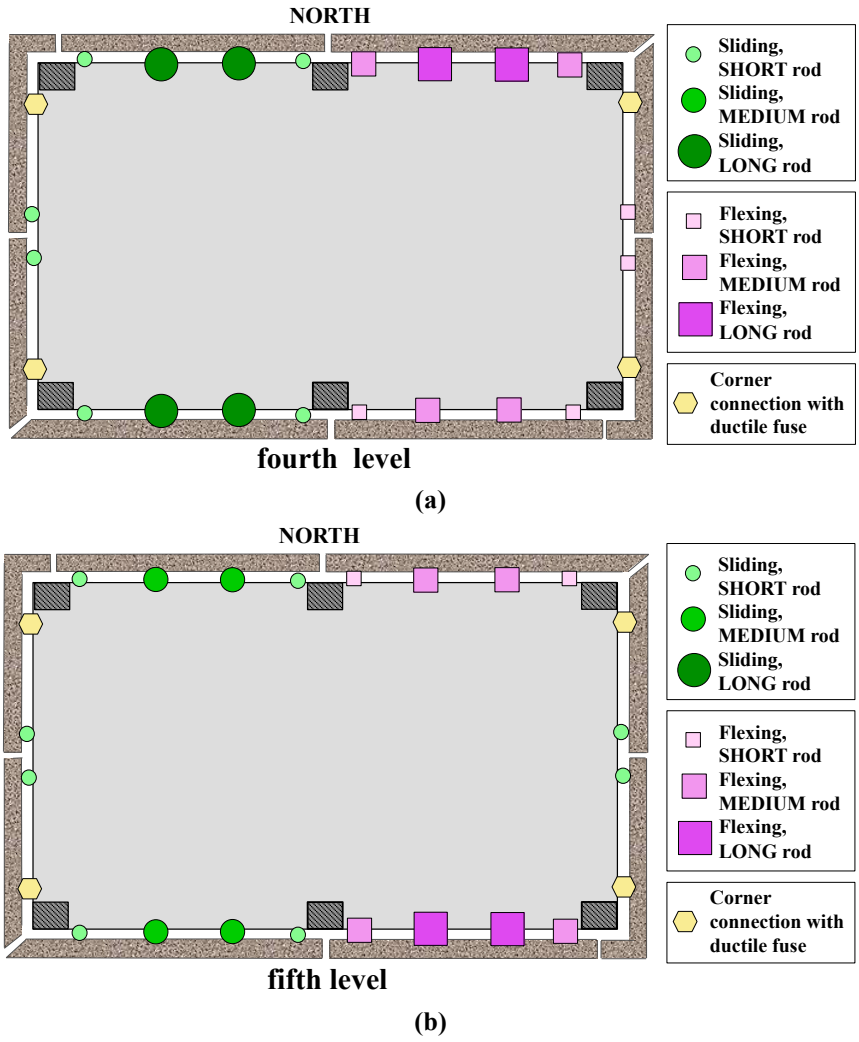

Figure 3.6. Plan view showing the location of each type of connection for the (a) fourth and (b) fifth levels

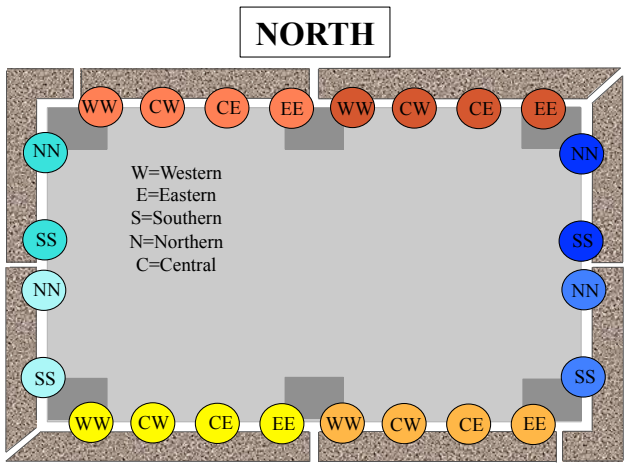

Figure 3.7. Name of tieback connections

Type of Corner Joint

Miter corner joints were installed in the southwest and northeast corner of the building, while butt-return corner joints were utilized at the northwest and southeast corners. Pictures of the two corner joints at the roof are shown in Figure 3.8. The joint size was 1'' for the butt-return joint and ¾'' for the miter joint, which allowed a movement of 1.06'' due to the inclination. All the joints were filled with caulking.

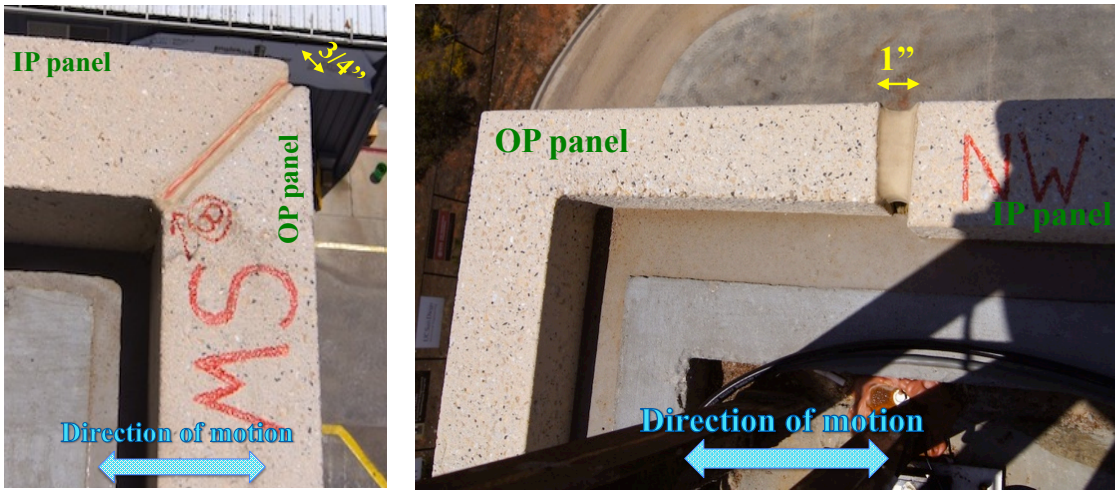

(a) **(b)**

Figure 3.8. Photographs of (a) miter and (b) butt-return corner joint as seen from the roof

Corner Connections

During this experiment, a new connection with a ductile fuse allowing for smaller corner joints was explored and installed at each corner in the OP panels. In this new corner system the interstory drifts are (ideally) absorbed as follows:

- Elastic drifts are absorbed by the closing of the vertical corner joint, with the joint sized sufficiently to avoid impact; and
- Inelastic drifts are larger than the vertical corner joint and therefore intended to result in collision of the corner panels. However, upon impact the ductile fuse is designed to prevent connection overload through the fuse mechanism, ensuring that the panels remain attached to the building after the event. In this work, the ductile fuse was in the form of a cantilevering bending plate that deformed during impact. At the same time, it was sized to avoid damage to

the other parts of the panel/connection. A picture of this connection is shown in Figure 3.9a. A schematic of the corner system during inelastic drift demands for the southeast corner is shown in Figure 3.9b and c.

The geometry of the ductile plate used in the BNCS project is shown in Figure 3.9a. Namely, the plate was 7'' high, ¾'' thick and created an arm for the rod on 9''. The rod itself was a coil rod 1''

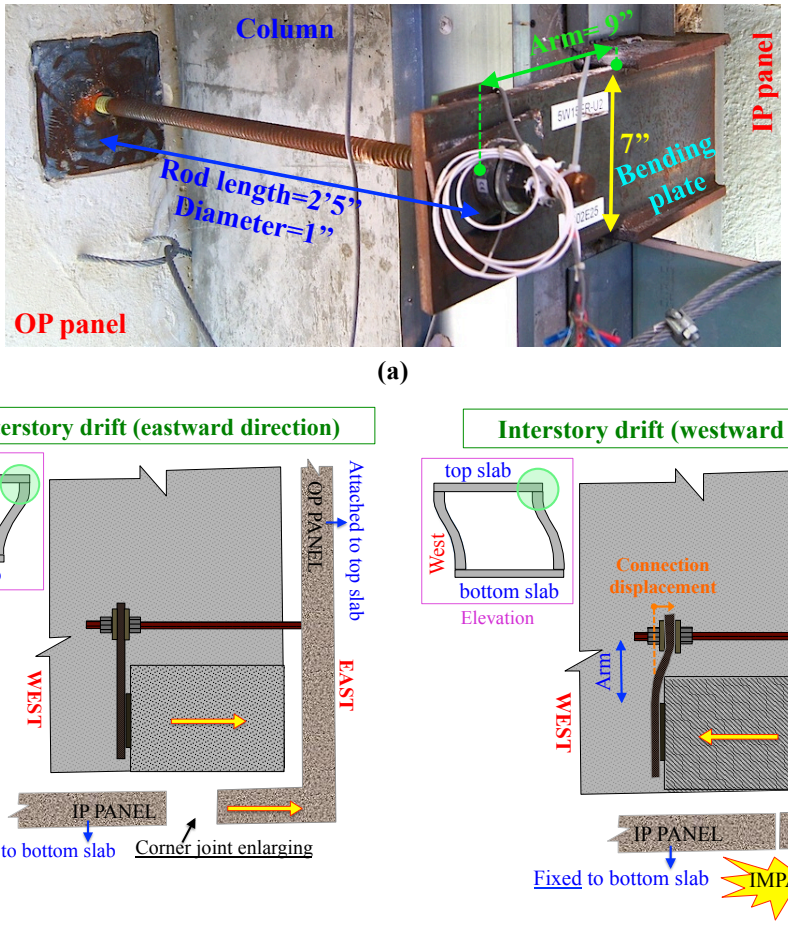

Figure 3.9. Corner connection with ductile fuse on the OP panels (a) photograph, (b), (c) conceptual schematic showing the desire behavior of a corner connection in panel 4ES during eastward and westward motion. Note: the circle in the elevation schematic of parts b and c denotes the corner considered in the respective plan views; yellow arrow denotes direction of movement of OP panel and top of column.

in diameter and 2'5'' long. In this specific case, the design drift at the fourth floor was 3.4''. With the ductile fuse design method, the joint is sized for elastic drifts. Therefore, the design inelastic drift predicted was reduced by dividing the drift by the code deflection amplification factor C_d (=5.5 for

special moment concrete frames), resulting in a minimum gap size of 0.5''. Both types of corner joints were sized to allow 1'' drift. The design of the new corner connections with ductile fuse used the ASCE-7 (ASCE, 2010) equation 13.3.1 for estimating the design force F_p (see discussion in Chapter 3).

For example, for the corner connection of panel 4ES (z = 56', h = 70', S_{DS}=1.6 g, a_p = 1.0 for bodies of connection and 1.25 for fasteners of the connection, R_p = 2.5 for bodies of connection and 1.0 for fasteners of the connection, I_p = 1.0, and W_p = 3.26 kips) the F_p for the body and fasteners of the connection can be calculated as 2.17 kips and 6.78 kips, respectively. The maximum flexural capacity of the cantilevering plate $M_{p\text{-expected}}$, including strain hardening effects and expected material over strength values, may be estimated as:

$$M_{p-\exp ected} = 1.1 \cdot R_y \cdot f_y \cdot Z = 56.6 kips \cdot inch$$

Where:

- R_y= Ratio of expected yield stress to the specified yield stress (e.g. AISC 341, Table A3.1 for various materials, or for A36 Hot-rolled shapes and bars, R_y = 1.5);
- f_y = yield strength (= 35 ksi) ;
- Z = plastic section modulus = $(7*(0.75)^2/4)$ = 0.98 $inch^3$;

The maximum value of the force in the rod is then obtained by dividing the moment by the arm (9''), for this example resulting in an F_{max} = 6.28 kips. Ductility is provided by ensuring the expected plastic flexural capacity of the plate is less than the capacity of the welds, the rod in tension, and the concrete anchorages of the embeds in the column and the panel itself. A full example of this kind of design is presented in Hutchinson et al. 2014.

3.1.3 Observation of Physical Damage

Observed damage in the cladding included that in the joints, connections and panels. Damage to the tieback connections manifested in permanent bending of the steel i.e. plastic bending of the rods or the plate used in the corner connections with ductile fuse. No damage to the bearing connections-such as weld fracture of permanent deformation-was observed. The panels manifested some visible surface cracking, tearing of caulking, or permanent misalignments precipitated by plastic bending of connection rods or plates. When describing damage to panel and connections, the nomenclature used

will be the one presented in Figure 3.3 and Figure 3.7.

Inspection Timeline

A total of 11 inspection phases were scheduled during the test program. Inspections of the building were generally performed after each test, except after some of the first BI tests. The following types of inspections of the cladding panels were performed:

- Basic interior inspection. This was performed from floor level and it allowed close observations of the bottom of the panels. Permanent deformations of damaged rods were visible and its amount could be estimated, but it was not possible to measure it directly. From the roof it was also possible to inspect the upper edge of the corner joins in the southwest and northwest corners;
- Exterior inspection. This inspection had to be performed using a man-lift;
- Interior inspection of the upper part of the panels. Due to safety reasons, inspection of the upper parts of the panels was mostly performed with the man-lift while performing the exterior inspection;
- Localized inspections. These were inspection of an upper area of the panel, which was observed to have cracked during the basic inspection.

Basic interior inspections were performed before the beginning of testing and at every inspection phase. Unfortunately, due to time constrains, it was not possible to perform other types of inspections after each motion. It should also be noted that it was not possible to inspect the interior of the eastern panels on the south side of the building due to the presence of the stairwell walls. The connections were visible through access holes but a slight bend in the rod would not probably have been visible. A summary of the inspections performed is presented in Table 3.4.

Initial Damage and BI Test Phase

Few very thin cracks were found before the beginning of test. These cracks were spanned from the bottom corners of windows to the edge of the panel and they were mostly concentrated in the OP panels. During BI tests, the development of few other very thin cracks was observed. The most part of them was either close to pre-existing cracks or continuing them.

Table 3.4. Summary of inspections performed on APC cladding

Inspection Phase	Test performed	Basic interior inspection	Complete Exterior inspection	Upper interior inspection	Localized inspection (location)
0	None	X			
1	BI1 BI2	X			
2	BI3 BI4	X			
3	BI5	X			
4	BI6	X			
5	BI7	X			
6	FB1	X			4SW and 5SW
7	FB2	X			
8	FB3	X	X	X	
9	FB4	X	X	X	
10	FB5	X			
11	FB6	X	X	X	

Damage After FB1

After FB1, two sliding rod connections were damaged, namely the long sliding rod in connection CW of panel 4SW was permanently bent 1'' eastward (Figure 3.10a) while the medium sliding rod in connection CW in panel 5SW was permanently bent 0.08'' westward (Figure 3.10b). The rods in both central connections in panels 4SW and 5SW were replaced after this test.

Damage After FB2

Three of the four sliding rod connections at the fourth floor showed plastic deformation after this earthquake. Namely, the two central connections in panel 4SW had a permanent deformation of 1'', while connection CE in panel 4NW was permanently bent 1.2''. The connections on the northern panel bent westward while the one in southern panel bent eastward. It is noted that the two connections in panel 4SW had just been replaced. In addition to damage in the connections, caulking in the miter corner joint in the southwest side of the building started to bulge slightly. Due to time constrains, none

of the connections that got damaged was repaired after this earthquake.

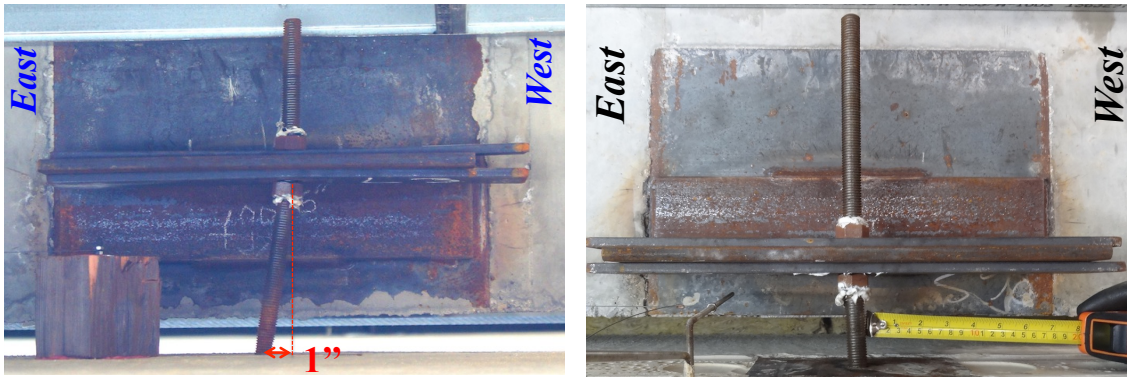

(a) **(b)**

Figure 3.10. Damage to connections after FB1: (a) connection CW in panel 4SW, and (b) connection CW in panel 5SW

Damage After FB3

The three connections that got damaged during FB2 and could not be repaired bent further, for a total plastic displacement of 2.4’’ for connection CE in panel 4NW, 2’’ for connection CE in panel 4SW and 2.25’’ for connection CW in the same panels. In this last connection, the plate covering the slot moved inside the slot itself (Figure 3.11a). During the operation of repair of the rods in these two panels it was noted that the two panels had been dragged inward during the earthquake because of the bending of the rod. For the panel 4SW it was possible to roughly estimate that the panel had been dragged inward 0.3’’. After cutting the bent rods the panel got back to its normal position. Moreover, a similar patter of cracks developed in each on panel 4SW and 4NW and include a series of vertical cracks running down from the damaged connection and close to it (Figure 3.11b).

After this test, all the connections in the IP panels were replaced. Exception was made for connection EE in panel 4SW and 5SW because they were inaccessible because of the presence of partition walls. In the sliding connections with long rods, the outside nut and plate were not installed, making these connections acting in tension only. After FB3 the first exterior inspection of the panels was performed. A typical patter of cracks was found in most of the IP panels: these cracks started from the bottom corners of the window opening (or really close to it) and developed either horizontally or slightly inclined downward all the way to the edge of the panel. In some cases this same type of cracks was observed to start from the upper corners of the window opening. The panels on the fifth floor

showed in general more cracking. It should be noted that this was the first exterior inspection performed, meaning that these crack could also have developed during the installation of the panels.

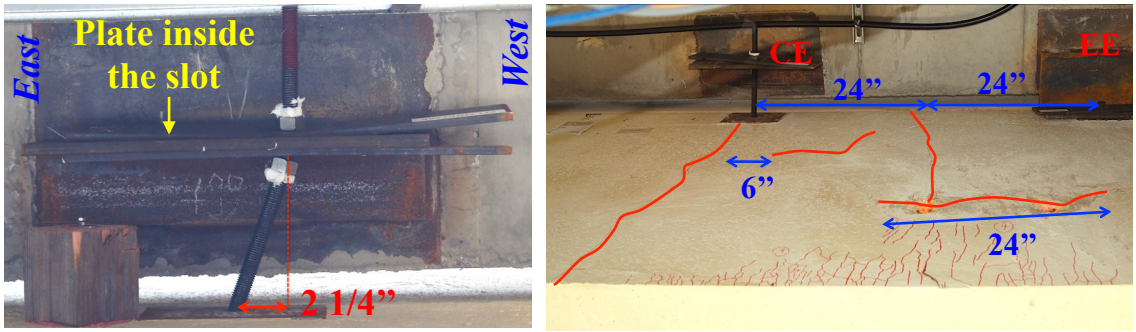

(a) (b)

Figure 3.11. Damage observed after FB3: (a) connection CW in panel 4SW and (b) cracks in panel 5NW

Damage After FB4

The fact that sliding rods were replaced without placing the outside nut and plate did not prevent them from getting damaged. In fact, connection CW in panel 4NW permanently bent roughly 0.4’’ westward. It was decided not to replace the rod in this connection. A vertical crack in the panel developed between this connection and the upper side of the window opening. During this test, one of the medium sliding rods got also damaged (CW connection in the 5SW panel), showing a permanent deformation of 1’’ eastward (Figure 3.12a). The rod of this connection was replaced after this test.

After FB4, distinct crack patterns were observed to develop in the panels: several vertical and inclined cracks formed close to one of the bearing connection in the panel 4ES, two vertical cracks developed in the bottom west quadrant of panel 4SW (Figure 3.12b), and several diagonal cracks formed close to the embed of connection SS in panel 4WS. These cracks were 0.008’’ thick and run from the upper corner of the window opening either to the panel embed or to the top of the panel. This same type of crack pattern but less developed was observed in panel 5WS. An exterior inspection was performed after this earthquake, revealing only few new cracks in the IP panels. These cracks were following the same patter already observed during the previous inspections. A summary of the cracks observed on the outside of panels 4SE and 5SE, and representative of what was observed in other IP panels, is presented in Figure 3.13.

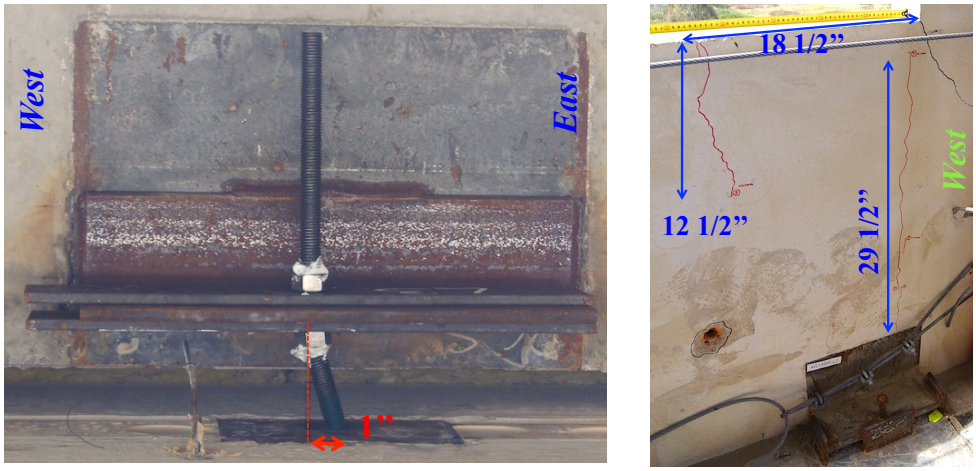

(a) (b)

Figure 3.12. Damage observed after FB4: (a) plastic deformation of connection CW in panel 5SW and (b) cracks at the bottom west side of panel 4SW

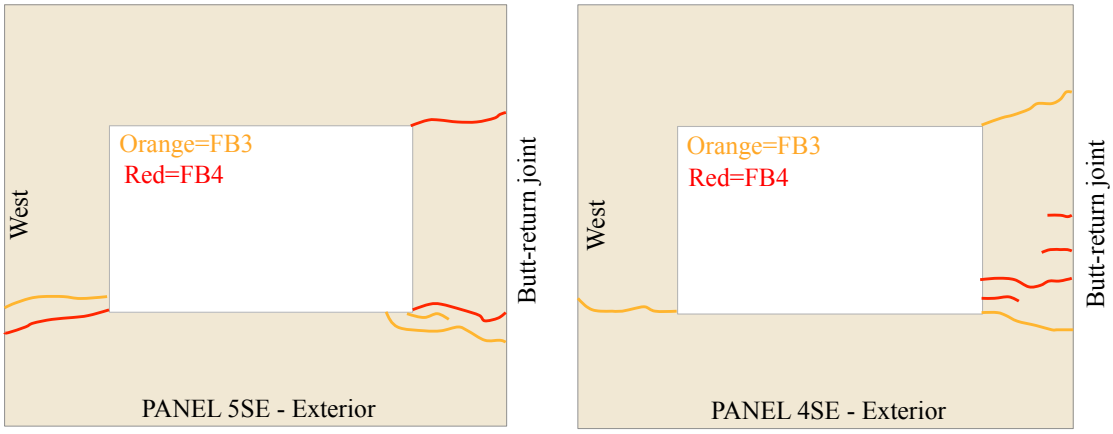

(a) (b)

Figure 3.13. Pattern of cracks observed in the exterior of the panels after FB3 and FB4 for (a) panel 4SE and (b) panel 5SE

Damage after FB5

The damage to long sliding rods observed after FB5 included the straightening of the rod in connection CW in panel 4NW (which got bent after the previous motion) and a 1'' westward permanent deformation of connection CE in panel 4SW. This motion saw the beginning of plastic deformation of flexing rods: in fact, the medium length rods in connections EE and WW of panel 4NE had a residual westward deformation of 1.6'' and 1.2'', respectively. The corner connection with ductile fuse also started to exhibit plastic deformation, with the connection NN in panel 4WN showing a plastic bending of the plate of 0.4''. Moreover, further cracks developed close to the SW corner of the building at the

fourth level, including vertical cracks starting from the western bearing connection in panel 4SW and a diagonal crack connecting the bottom southern connection to the corner of the window in panel 4WS.

Damage After FB6

The long sliding rods in connections CW and CE in the 4NW panel got permanently bent of 0.2'' eastward and 1'' westward, respectively. It is noted that connection CW was already damaged from the previous tests. The same type of rod in connection CE in panel 4SW showed a permanent deformation of 2.5'' (Figure 3.14a). In both of these panels, new vertical cracks formed close to the centerline of the panels. The two medium flexing connections in panel 4NE that had already permanently bent had further damage. Connection WW (which was bent 1.2'' westward) was permanently bent only 0.8'' westward after this test. Connection EE showed a permanent bending of 1.6'' westward (Figure 3.14b), equal to the same already seen after the previous test. Connection EE in panel 5NE bent 1'' eastward. One of the flexing rod connections with long rods got also damaged, bending 1.6'' eastward.

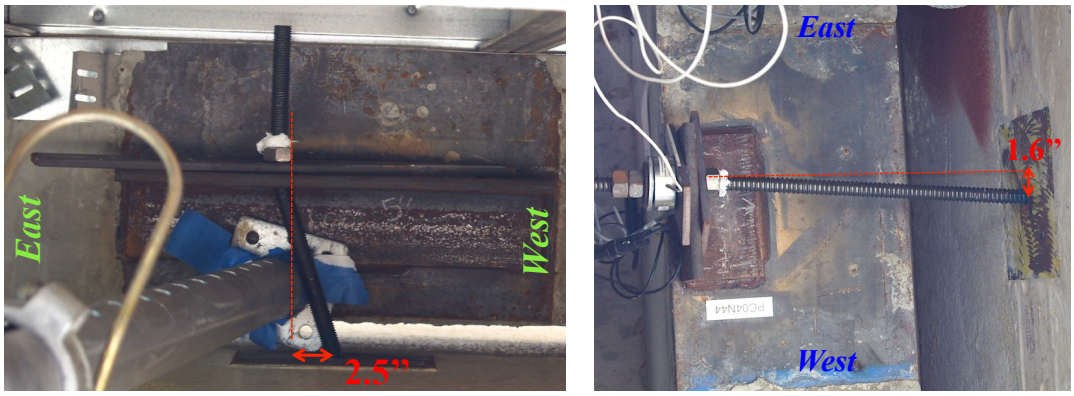

(a) **(b)**

Figure 3.14. Damage to tiebacks after FB6: (a) connection CE in panel 4SW and (b) connection EE in panel 4NE

The corner connection with ductile fuse in the north edge of panel 4WN showed further plastic deformation (Figure 3.15a) while the crack pattern close to the embed of connection SS in panel 4WS extended. A similar pattern of cracks, but of a lesser extent, developed close to connections NN in panel 4EN, NN in panel 5EN and SS in panel 5WS. Moreover, almost all the OP panels developed cracks in their inner side. These crack (or cracks) started from the corner of the window opening and developed toward the edge of the panels in an inclined direction (Figure 3.15b). Figure 3.16 summarizes the final

damage for panels 4WS and 4WN, while Figure 3.17 does the same for panels 4NW and 4SW. It is noted that these were the most damaged panels.

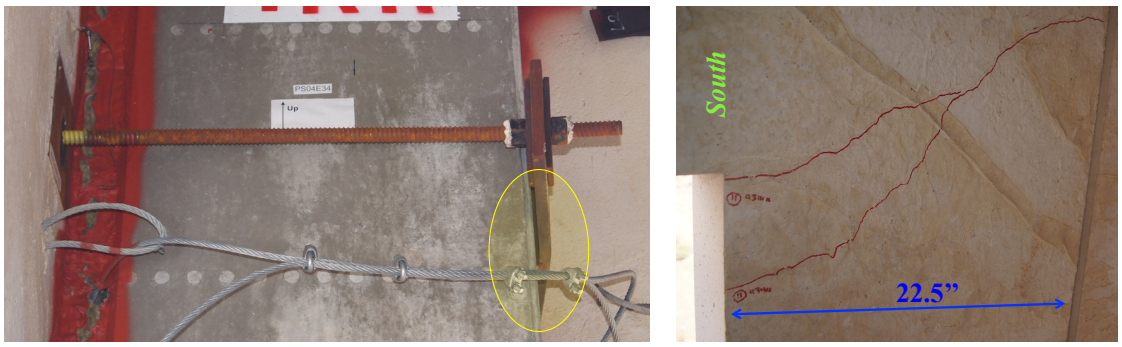

(a) (b)

Figure 3.15. Damage after FB6: (a) corner connection in panel 4WN showing plastic deformation of the ductile plate and (b) typical cracking pattern in the inner side of OP panels, example for panel 4WS

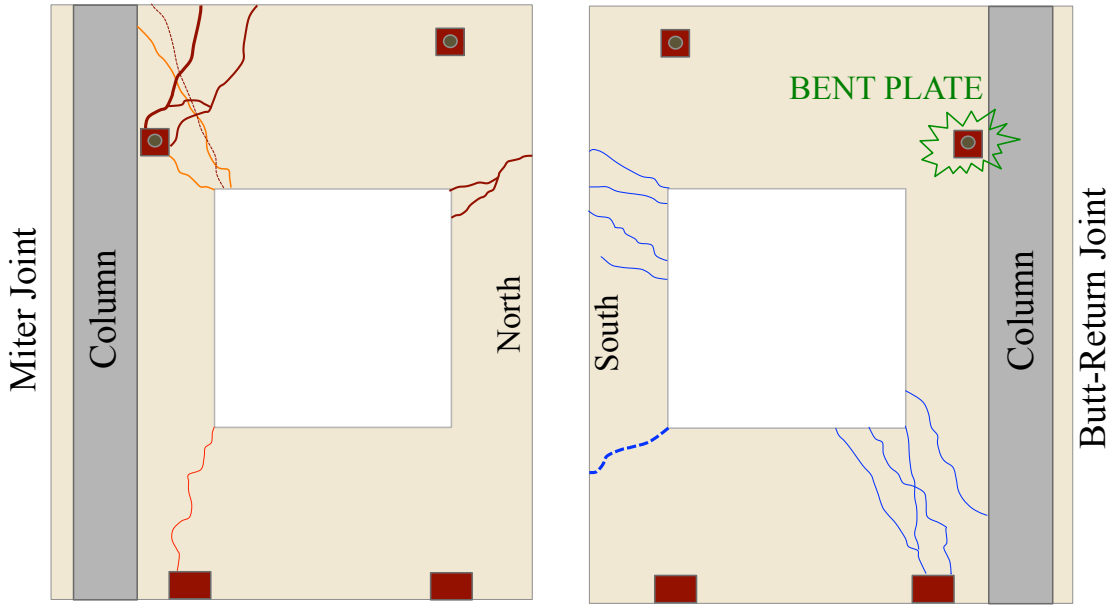

(a) (b)

Figure 3.16. Final patter of cracks in the most damaged OP panels: (a) panel 4WS and (b) panel 4WN

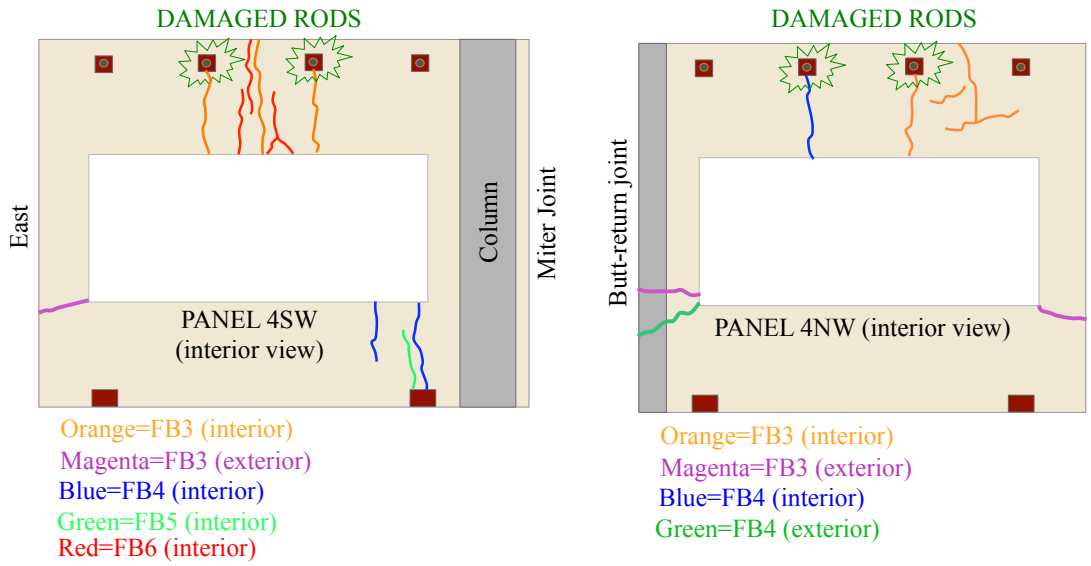

(a) **(b)**

Figure 3.17. Pattern of cracks in the most damaged IP panels: (a) panel 4SW and (b) panel 4NW

After this last earthquake, several panels acquired also a permanent misalignment (Figure 3.18). The top of panels 4WS and 4WN were permanently moved 1'' and 1.6'' westward, respectively. Panel 4SW moved 0.6'' inward respect to the bottom of the upper panel and 0.8'' outward respect to panel 4SE at top. The inspection of the exterior of the building revealed extensive damage to caulking. Tearing of vertical caulking was found in many instances, especially close to the butt-return joins in the fourth floor (Figure 3.19). Extensive damage to horizontal caulking was found between the top of panel 4SW and the bottom of panels 5SW, where it was completely teared off for a length of 5' from the corner.

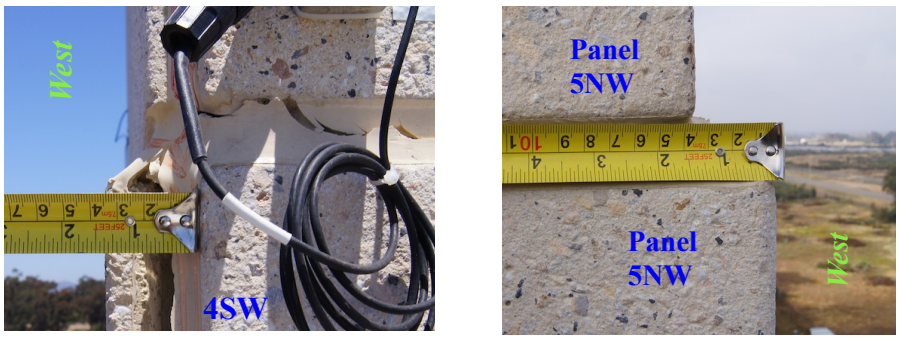

(a) **(b)**

Figure 3.18. Misalignments of the panels at the fourth level in the (a) SW and (b) NW corners

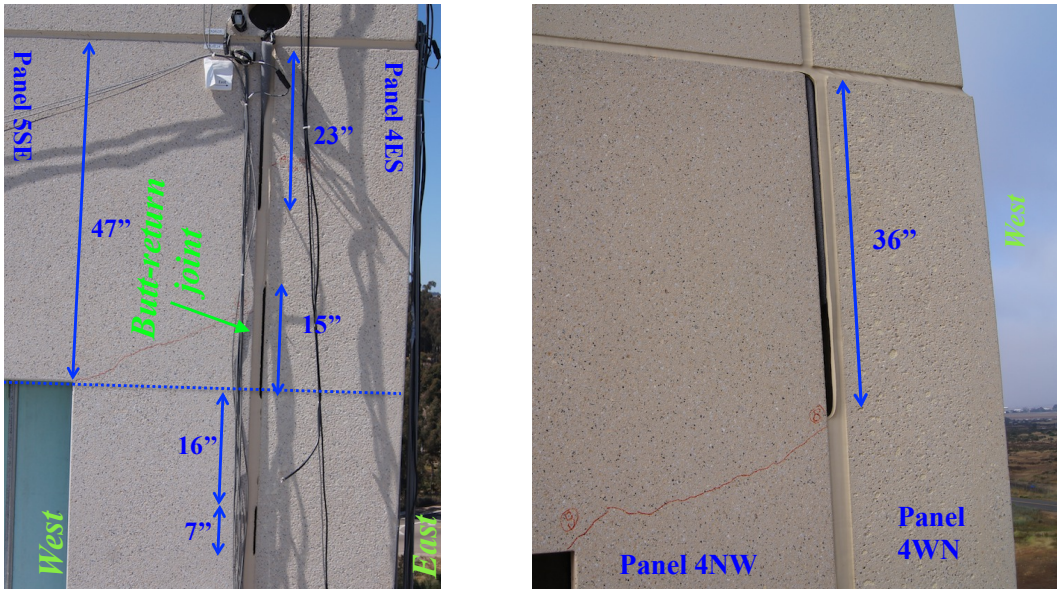

(a) **(b)**

Figure 3.19. Damage to caulking in vertical joint at the fourth level in the (a) SE and (b) NW corners

Damage States

Damage states for panels and connections were determined. As already mentioned, damage to the panels manifested as either visible surface cracking (Cr) or tearing of caulking (Ca). Plastic bending of connection rods also results in the panel permanent misalignments (Pm). A summary of damage to the fourth and fifth level panels and connections can be found in Table 3.5 and Table 3.6, respectively. It is noted that when damage level is not available because no inspection was performed, N/A is used. The damage description corresponding to different damage states is presented below:

- Sliding/flexing connections in IP panels. Moderate damage: permanent deformation of the rod;
- Corner connection with ductile fuse in OP panels. Minor: cracking of the panel or minor plastic deformation of the ductile plate. Moderate: significant plastic deformation of the ductile plate;
- Permanent misalignment. Minor: Permanent misalignment smaller than 1’’; Moderate: Permanent misalignment large or equal to 1’’;
- Tearing of caulking. Minor: Restricted to small areas. Moderate: complete tearing of a significant length of caulking (>4’’);

- Cracking. Minor: Mostly hairline cracks. Moderate: Cracks thicker than 0.02’’.

Table 3.5. Performance of the APC cladding in the BNCS building at the fourth level

Test	PIDR fourth level (%)	PFA fourth floor (g)	Connections					Panels		
			IP				OP-Corner	Pm	Ca	Cr
			Flexing		Sliding					
			medium	long	short	long				
BI7	0.15	0.24	None	None	None	None	None	None	None	None
FB1	0.24	0.31	None	None	None	Mod.	None	None	None	Minor
FB2	0.26	0.32	None	None	None	Mod.	None	None	None	Minor
FB3	0.43	0.43	None	None	None	Mod.	Minor	None	None	Minor
FB4	0.74	0.50	None	None	None	Mod.	Minor	None	None	Minor
FB5	1.09	0.70	Mod.	None	None	Mod.	Minor	N/A	N/A	Minor
FB6	1.29	0.65	Mod.	Mod.	None	Mod.	Mod.	Mod.	Mod.	Mod.

Note: Mod.=Moderate

Table 3.6. Performance of the APC cladding in the BNCS building at the fifth level

Test	PIDR fifth level (%)	PFA fifth floor (g)	Connections					Panels		
			IP				OP-Corner	Pm	Ca	Cr
			Flexing		Sliding					
			short	medium	short	medium				
BI7	0.09	0.24	None	None	None	None	None	None	None	None
FB1	0.13	0.35	None	None	None	None[1]	None	None	None	Minor
FB2	0.14	0.35	None	None	None	None	None	None	None	Minor
FB3	0.23	0.47	None	None	None	None	None	None	None	Minor
FB4	0.36	0.57	None	None	None	Mod.	None	None	None	Minor
FB5	0.54	0.68	None	None	None	None	None	N/A	N/A	Minor
FB6	0.66	0.65	None	Mod.	None	None	None	None	Minor	Minor

Note: Mod.=Moderate

3.2 Component Test on Sliding Connections

The experiment on sliding connections was conducted at the Powell Laboratories at UCSD. It consisted in the application of controlled earthquake-type displacement to two tieback connections via a shake table. The configuration of the connections was rotated 90 degrees, resulting in the two rods

being vertical. At the top, the rods were held by a fixed slotted section, while at their bottom a concrete mass was hang on them to apply controlled tensile load. This same block was then fixed to the shake table, and imposed the horizontal north-south motion to the connections. Figure 3.20 shows the complete configuration, which was composed of:

- A hollow steel tube (HSS) member with two slotted holes. This simulated the two slotted angles and was welded to a frame fixed to a reaction wall;
- Two threaded rods with nuts and oversized sliding plate washers. Each rod was inserted in its own slot in the HSS section. All rods were A36 with national coarse threads. The mill certificates reported for both rod diameters a yield stress between 45 ksi and 55 ksi and a tensile strength between 69 ksi and 75 ksi. Tension tests on the !'' and the 1'' diameter rods were performed. For the 3/4'' diameter the average f_y was 59.6 ksi the average f_u was 72.5 ksi, while the elongation varied from 16 to 19%. For the 1'' diameter rods the average f_y was 58.6 ksi, the average f_u was 79.2 ksi and the elongation varied from 24 to 26%;

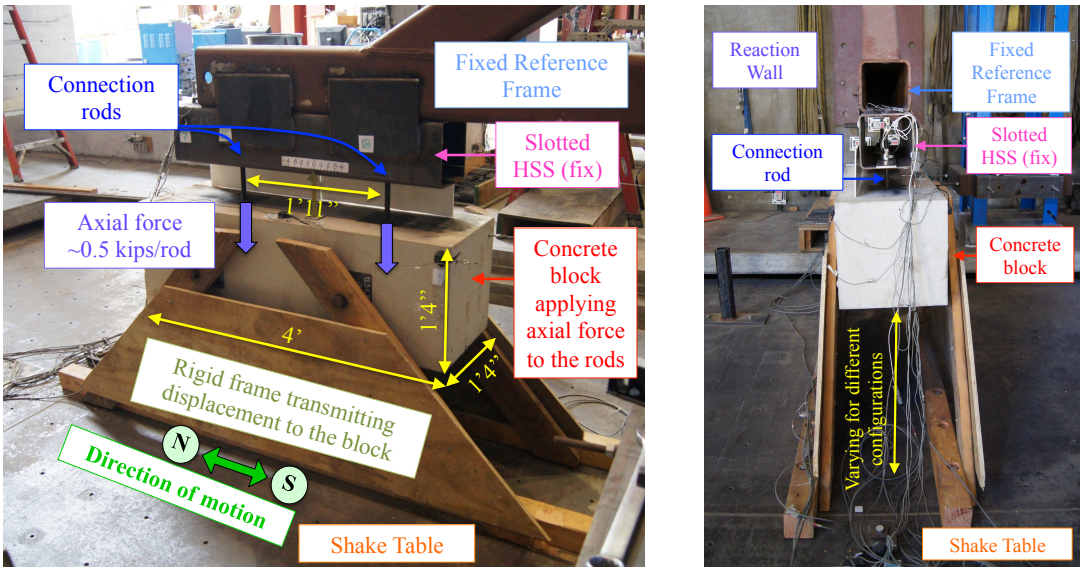

(a) **(b)**

Figure 3.20. Setup of the component test on sliding connection: (a) side view and (b) front view

- A concrete block with two threaded embeds. The rods were threaded into the embeds allowing the block to hang and apply an axial static tensile force of roughly 0.5 kips to each rod; and
- A wooden frame fixing the concrete block to the shake table. This allowed transfer of the

dynamic loads from the shake table to the connections. The direction of motion was longitudinal (north-south).

A set of twenty analog sensors and three cameras were utilized during the experiment. The types of analog sensors installed were:

- String potentiometers. They monitored the displacement of the concrete block and shake table;
- Accelerometers. Six accelerometers were installed on the block to obtain its six degrees of movement. Additional accelerometers were installed on the shake table and fixed support; and
- Load cells. During the first phase of testing, two load cells per rod were installed, one between the upper sliding plate and nut and one between the bottom sliding plate and nut. During the second phase, only the load cells between the upper sliding plates and nuts were maintained.

Figure 3.21 presents sketches showing the locations and names of accelerometers and string potentiometers and a photograph showing the location of some of them. The three cameras caught one frontal view, one lateral view and one angles view. Screenshots from each of them are presented in Figure 3.22.

The experiment was divided into two phases, each one testing the sensitivity of the connections to a different parameter:

- Phase one. During this phase, the sensitivity of the connection to the normal compressive force applied to the sliding surface was investigated. The diameter of the rods d was 0.75" and the clear length L_c was 2.5" (i.e. $L_c/d=3.3$). The input motion was sinusoidal and two tests in total were performed. It is noted that during this initial phase, the connection of the block to the table and location of cameras varied slightly compared to what was previously presented; and
- Phase two. The goal of this phase was to study the performance of rods with different L_c/d ratios. During this second phase, the compression sliding plate-located at the bottom of the HSS section in this case- was removed because even a small tightening of the bottom nut caused the connection to fail. Six different configurations were tested, as summarized in Table 3.7. The six configurations differed in terms of L_c/d ratio (3.3, 5.3 or 7.3) and rod diameter (0.75" or 1"). This table also summarizes for each configuration the effective diameter of the

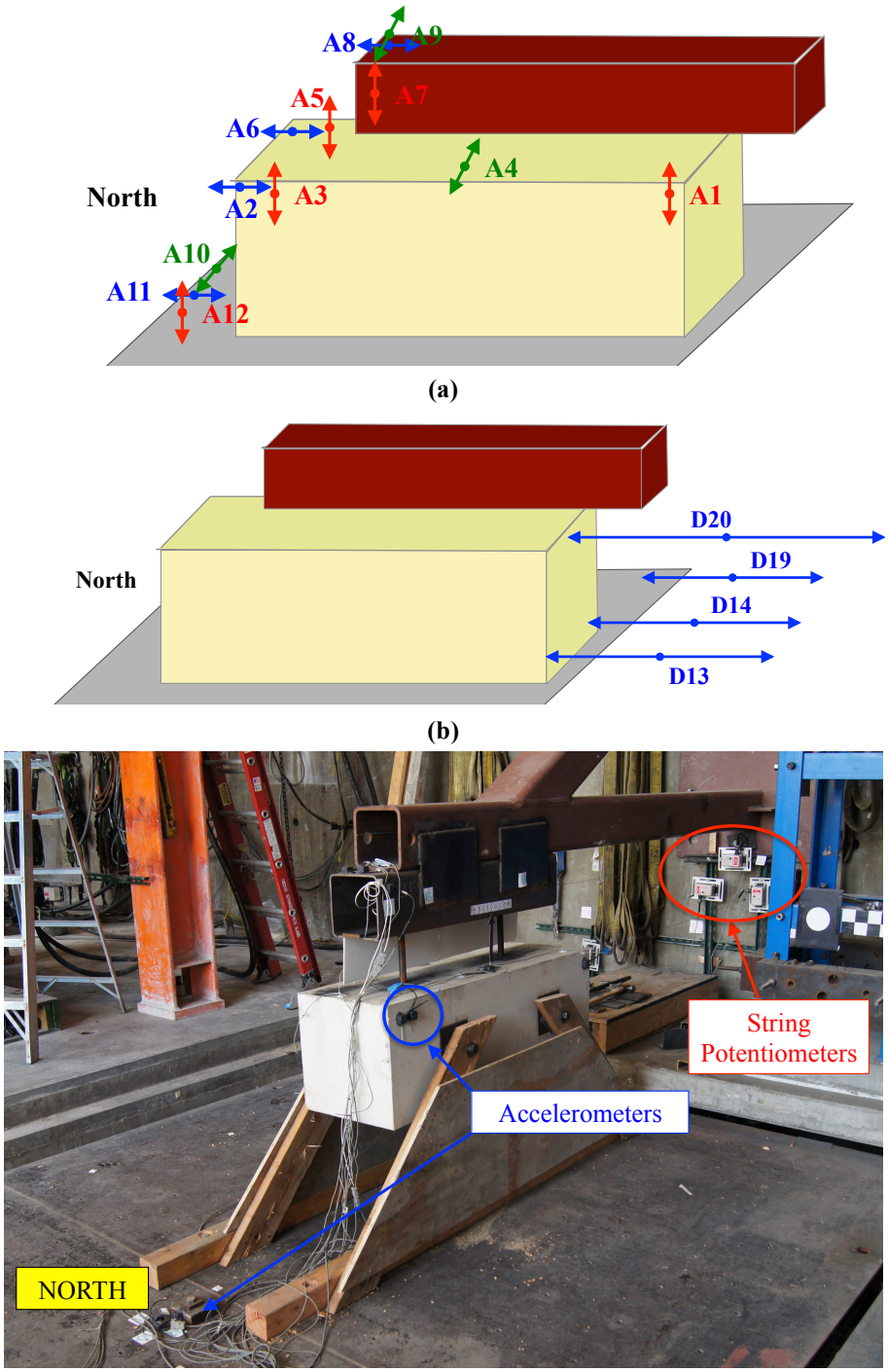

Figure 3.21. Schematic and photograph showing the location of accelerometers and string potentiometers

(a)

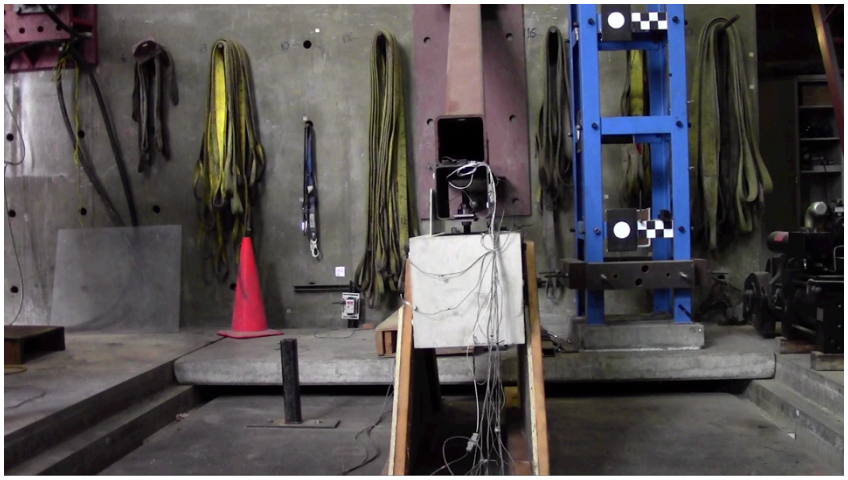

(b)

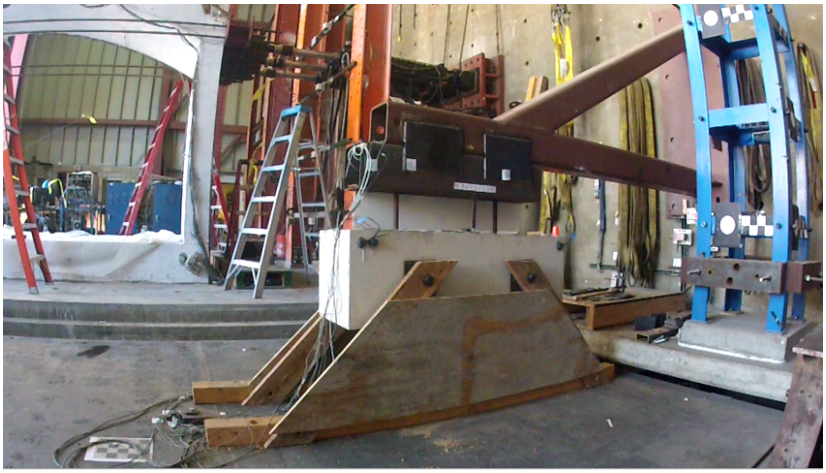

(c)

Figure 3.22. Screenshots from the three cameras deployed during this test: (a) frontal view, (b) side view and (c) angled view

Table 3.7. Summary of characteristics of the six test configurations (C)

	Configurations					
	$C_{3.3,\ 0.75}$	$C_{3.3,\ 1}$	$C_{5.3,\ 0.75}$	$C_{3.3,\ 1}$	$C_{7.3,\ 0.75}$	$C_{7.3,\ 1}$
L_c/d ratio	3.3	3.3	5.3	5.3	7.3	7.3
Nominal d (inch)	0.75	1	0.75	1	0.75	1
Effective d (inch)	0.65	0.88	0.65	0.88	0.65	0.88
L_c (inch)	2.5	3.3	4	5.3	5.5	7.3
Flexibility (Nominal d) (inch/kip)	0.003	0.002	0.019	0.008	0.030	0.022
Flexibility (Effective d) (inch/kip)	0.005	0.003	0.021	0.014	0.054	0.038

rods (i.e. the minimum diameter considering the thread), the clear length of the rod L_c, and the theoretical flexibility ($=L_c^3/12EI$) calculated with the nominal and the effective diameter. It is important to note that for the configurations with the same L_c/d, the flexibility of the rod was actually smaller for the rod with the larger diameter, since the flexibility is proportional to the cube of the length and to the inverse of the fourth power of the diameter.

For each configuration, five tests with different input motions (M) were run. The input motions were direct displacement measurements from one of the IP panels with sliding connections (4SW) recorded during the BNCS experiment. Three records from the BNCS project were selected because of their different features:

- Ica record from Pisco earthquake, Peru', 2007. This motion was characterized by a long duration;
- Canoga Park record from Northridge earthquake, California, 1994. This was characterized by a lower period and a short duration; and
- Denali record from Denali earthquake, Alaska, 2002. This motion presents a higher period and a medium duration.

The protocol begins with the Ica motion run three times with three different amplitude scale factors, creating a peak drift of 0.5'', 2.1'' and 4.1'', respectively. Considering the story-height of 168''

form the BNCS building, this displacement corresponded to drift ratios of 0.81%, 1.3% and 4.1%, respectively. Subsequently the Canoga Park and Denali motions were run with the amplitude scaled to obtain the same maximum drift of 4.1''. The entire test protocol is presented in Table 3.8, which shows for each motion the scaling factor used to modify the motion from the original BNCS measurements, the target peak drift in inches, the same target input drift in %, and the strong motions duration.

Table 3.8. Summary of characteristic of the five input motions (M)

	Motions				
	M1	**M2**	**M3**	**M4**	**M5**
Input motion	Ica	Ica	Ica	Canoga Park	Denali
Scaling Factor (%)	37	160	300	900	140
Maximum Drift (inch)	0.5	2.1	4.1	4.1	4.1
Maximum Drift Ratio (%)	0.81	1.3	2.4	2.4	2.4
Strong Duration (sec)	116	116	116	21	57

Figure 3.23a shows the displacement spectra for the achieved table acceleration during the first configuration for motions M3 (Ica 300%), M4 (Canoga Park 900%) and M5 (Denali 140%). Figure 3.23b shows the acceleration spectra normalized by the zero period acceleration for the same tests for relevant periods. It is noted that low period acceleration content was introduced to the original motions during these tests due to the shake table. It is noted that, during the BNCS project, the Canoga Park and Denali motions were scaled using spectral matching, while the Ica motion was used directly and only amplitude scaled.

3.3 Component Tests on Flexing Connections

Component tests on flexing connections were performed at SJSU by McMullin (2014), with the goal of determining the number of cycles at fracture for rods with different lengths and diameters, and the typical force-deformation behavior of flexing connections. The test configuration was similar to the one already described for the tests on sliding connections, meaning that the rod -one in this case- was rotated 90 degrees and a mass was hung from it to create a controlled axial load of 300 pounds (Figure 3.24). Tests were conduced using commercially available A36 steel coil rods of either ¾'' or 1''

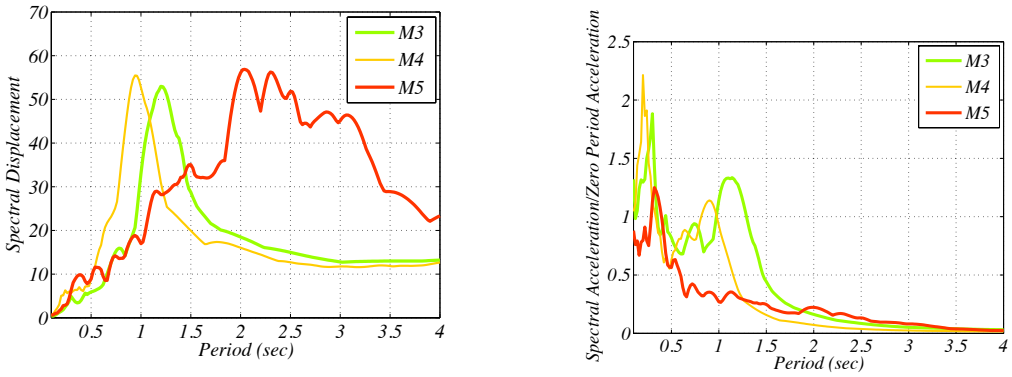

(a) **(b)**

Figure 3.23. Elastic response spectra for achieved accelerations during the first configuration: (a) displacement and (b) acceleration normalized by zero period acceleration

diameter with free lengths L_f varying from 10.9'' to 18.9'' (i.e. L_f/d from 10.9 to 25.2). During each test, a pseudo-static cyclical displacement targeted to achieve either a constant or increasing amplitude was applied to the rod until it fractured.

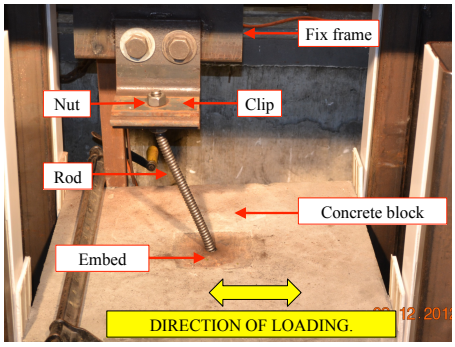

Figure 3.24. Picture of the test set-up for component test on flexing connections

ACKNOLEDGEMENTS

Chapter 3 reproduces content and images of the material as it appears in the PCI Journal 2016 and Proceedings of the Façade tectonics conference 2014. Pantoli, E., Hutchinson, T. C., McMullin, K. M., Underwood, G. A., and Hildebrand, M. J. 2016. "Seismic-drift-compatible design of architectural precast concrete cladding: Tieback connections and corner joints." PCI Journal, July-August, 38-52. Pantoli, E., Hutchinson, T. C., Underwood, G. A., and Hildebrand M., 2014. "Seismic behavior of sliding push-pull connection in architectural precast concrete panels." Proceedings, Façade Tectonics, January 9-12, Los Angeles, CA. The author of the dissertation is the principal author of the above cited papers.

Chapter 4

Drift-Compatible Design of Tieback Connections

This chapter presents the results relative to the two different types of tieback connections considered in the study (sliding and flexing). Results obtained from both the BNCS test and from component tests are presented.

4.1 Sliding Connections

4.1.1 Results From the BNCS Project

To understand the performance of the sliding tieback connection installed in the APC cladding, it is essential to understand the building response at the upper stories of the BNCS building, since this provides the input motions to the panels. Figure 4.1 shows the peak floor accelerations (PFA) and peak interstory drift ratios (PIDR) of the fourth and fifth level of the building. The accelerations reported are calculated as the average of those measured at each corner. The values of the PIDR and PFA were quite small for all BI tests, with PIDRs smaller than 0.15% at the fourth level and PFA no greater than 0.24 g on the fifth floor during motion BI7. The first two FB motions, which were scaled to achieve serviceability demands within the building, reported peak accelerations and interstory drifts only slightly larger then those obtained in the final BI motion. The maximum value of PFA was obtained during motion FB5, when the structure observed considerable plastic deformation. The PFA at fifth floor was 0.68 g, while 0.99 g was measured at the roof slab. The largest PIDR was observed during the final motion FB6, with almost 1.3% and 0.7% attained on levels four and five, respectively. These values were lower anticipated, as a soft story mechanism developed in the lower levels of the building, with PIDRs approaching 6% for the first two floors. The period of the building varied from 2.5 seconds during BI phase to 0.9-1.2 seconds during FB phase. Further information about the structural behavior can be found in Chen et al. 2016. While the complete description of damage observed during the BNCS project to the cladding system is presented in the previous chapter, this section summarizes the damage only to sliding connections, and it links it with the structural performance.

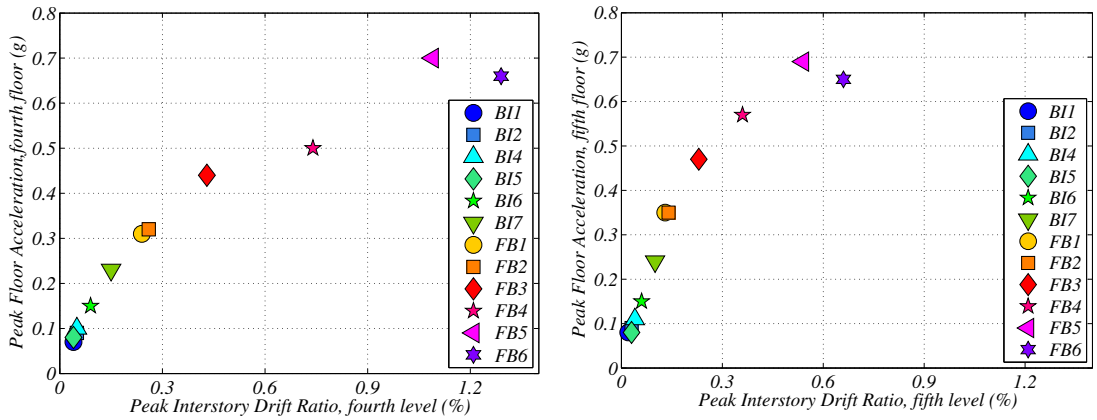

(a) **(b)**

Figure 4.1. Peak interstory drift ratio versus peak floor acceleration for the (a) fourth level, (b) fifth level

Summary of Damage to Sliding Connections

As seen in the previous chapter, damage to connections manifested primarily as a permanent bending of the rods, while none of the rods actually fractured. This is partially due to the fact that the drift imposed at the upper stories were smaller than the design ones. The sliding snug connections performed very well, in fact no damage to this type of connection was observed either during testing or during demo of the panels. Medium rod length sliding connections developed plastic yielding during progressively increasing interstory drift demands. Table 4.1 summarizes the physical observations on medium length rods, including noting when the rods were replaced. The first notable damage to these connections was observed following motion FB1 (Figure 4.2a). The plastic bend of the connection was barely visible and it was measured after the rod was removed. Subsequently, no additional visible damage to these connections was noted until motion FB4, during which one of the rods was permanently bent (Figure 4.2b). The PIDR during this motion was only 0.35%. Interestingly, the residual deformation of the rod of 1'' was greater than the PID of 0.6'', suggesting that the connection accumulated drift deformations through a ratcheting mechanism as the connection cycled back and forth, binding in one direction, while sliding in the other. This connection was replaced and was not damaged further, despite the much larger PIDR in subsequent motions. This confirms the fact that the behavior of sliding connections is more difficult to predict, due to the uncertainties intrinsic in the prediction of friction mechanism.

Table 4.1. Residual deformation in sliding connections with medium length rods (Green=no damage, Red=damage) [*=rod replaced]

Test	PID (PIDR) fifth level	Panel 5SW		Panel 5NW	
		Connection CW Inch (°)	Connection CE Inch (°)	Connection CW Inch (°)	Connection CE Inch (°)
BI	0.17'' (0.1%)	None	None	None	None
FB1	0.22'' (0.13%)	0.08''(1) *	None	None	None
FB2	0.23'' (0.14%)	None	None	None	None
FB3	0.38'' (0.23%)	None*	None*	None*	None*
FB4	0.60'' (0.36%)	1''(16)*	None	None	None
FB5	0.91'' (0.54%)	None	None	None	None
FB6	1.11'' (0.66%)	None	None	None	None

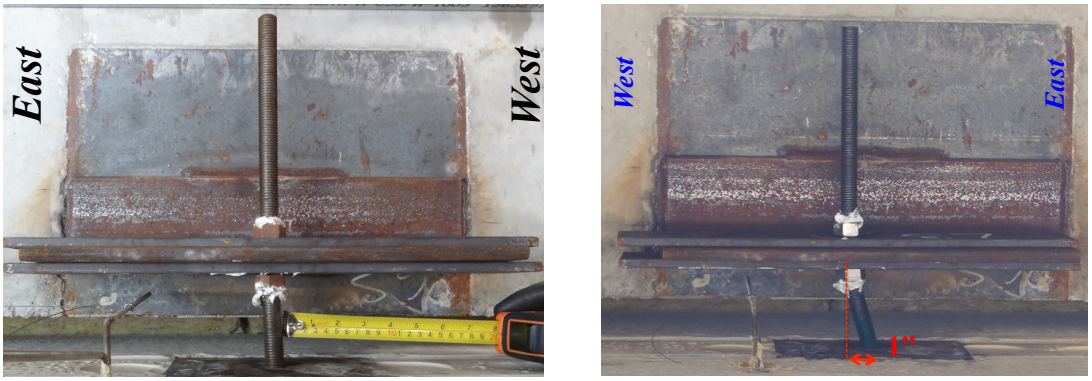

(a) **(b)**

Figure 4.2. Damage to medium length sliding connections observed after (a) FB1 and (b) FB4

Table 4.2 presents the progression of damage for the sliding connection with long rods and their associated times of replacement. Similarly, these connections were not damaged during the BI tests, however, significant permanent deformation was observed during the FB motion sequence. In particular during FB2, when a PIDR of only 0.2% was reached, three of four connections were observed with permanent bends during post-event inspection. As it was clear that this configuration was not optimal, during replacement of these rods, the outside nut was not reinstalled to allow the rod to only carry tension, and to alleviate binding from clamping of the plate washers during rotation. During motion FB4 only one connection was slightly damaged. However, during motions FB5 and FB6, these

connections were severely plastically bent again, demonstrating the difficulty of utilizing a very long rod for this type of connection. Examples of the physical damage to the sliding connections with long rods are shown in Figure 4.3.

Table 4.2. Residual deformation in sliding connections with long rods (Green=no damage, Red=damage) [*=replaced, **=replaced with no compression washer]

Test	PID (PIDR) fourth level	Damage to panel 4SW		Damage to panel 4NW	
		Connection CW Inch (°)	Connection CE Inch (°)	Connection CW Inch (°)	Connection CE Inch (°)
BI	0.25'' (0.15%)	None	None	None	None
FB1	0.40'' (0.24%)	1 (8) *	None	None	None
FB2	0.44'' (0.26%)	1 (8)	1 (8)	None	1.2 (10)
FB3	0.72'' (0.43%)	2.2 (18)**	2 (16)**	None**	2.4 (20)**
FB4	1.24'' (0.74%)	None	None	0.4(3)	None
FB5	1.83'' (1.09%)	None	1(8)	0(0)	None
FB6	2.17'' (1.29%)	None	2.5(21)	0.2(1)	1(8)

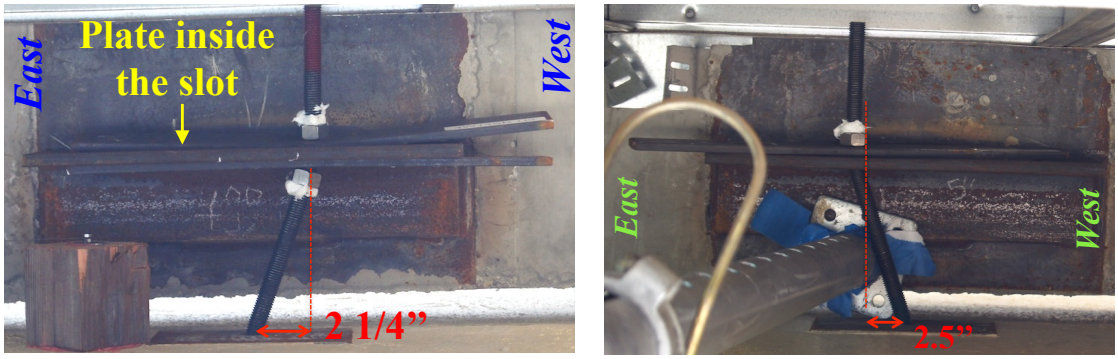

(a) **(b)**

Figure 4.3. Damage to long sliding connections observed after (a) FB3 and (b) FB6

Comparison Between Displacements in the Connection and Interstory Drifts

In each of the eight IP panels, the in-plane displacement absorbed by the tieback connections at the top of the panels (Δ_c) was measured by a string potentiometer connected to the panel and the slab. In this case, the ID considered is the theoretical one at the location of the centerline of the panels, calculated as the weighted average of the ID at corners. From these measurements, it was clear that the

behavior of panels with sliding and flexing connections was different.

Figure 4.4 shows the time histories of Δ_c and ID for panel 4SW –which had sliding connections- and panel 4SE –which had flexing connections- for three different tests. During the final BI motion (Figure 4.4a) Δ_c was smaller than ID in both cases. However, while at the panel with sliding connections Δ_c was quite similar to ID, in the panel with flexing rod connections Δ_c was half of the total ID, meaning that in this panel half of the drift was absorbed by a deformation of the panel itself.

The behavior changed during the FB phase of testing. Figure 4.4b shows that, even for the small FB1 record, Δ_c was slightly larger than ID for the panel with sliding connections, while it still was smaller that the ID for the panel with flexing connections. The behavior of the sliding connection can be understood considering the force-displacement behavior of a frictional system: once the value of the force in the connection reaches the value necessary to activate motion, the sliding is activated and the displacement can increase without increment in force until the force goes back to be less that threshold force and the mechanism locks. The behavior is of course different when the movement is controlled by bending of the steel such as occurs in the flexing connections. In this case, resistance of the steel can limit the displacement, especially if the steel is elastic or only slightly plastic. This behavior observed in FB1 continued up to FB4, with the difference between Δ_c and ID increasing for the panel with sliding connections and decreasing for panel with flexing connections. During the last two motions, the amplitude of Δ_c for the panel with flexing rod connections approached the ID.

Figure 4.4c shows an asymmetric behavior of the panel with flexing rod connections, namely, Δ_c was larger than ID for the movement in the positive direction (eastward), while it was still smaller than the ID for movements in the negative direction (westward). The asymmetry in the behavior might be due to some permanent deformation of the flexing rod (as observed in the inspection phases), which initiated exactly during the design motion FB5.

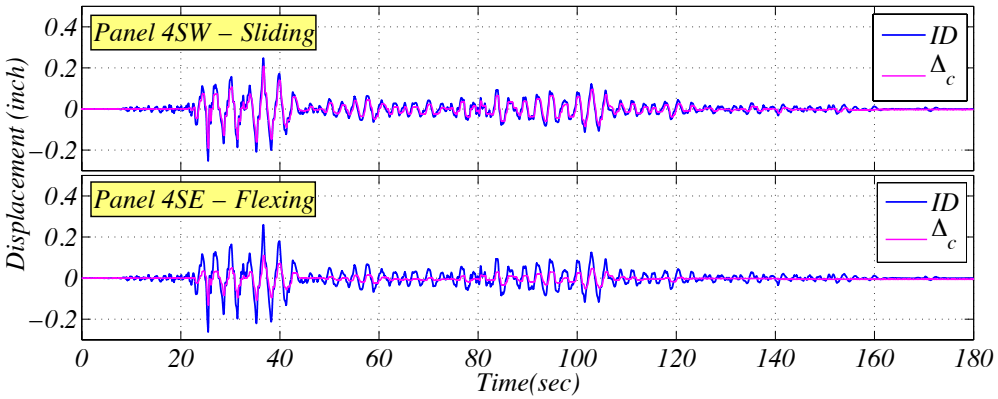

(a)

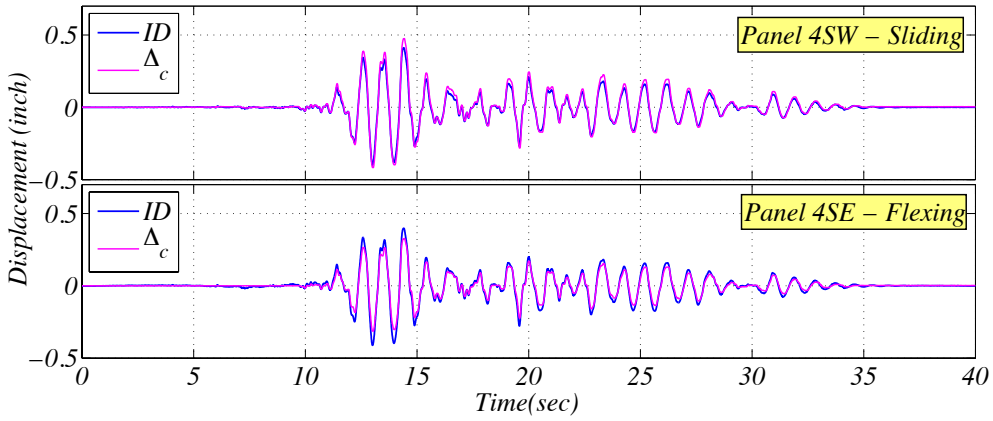

(b)

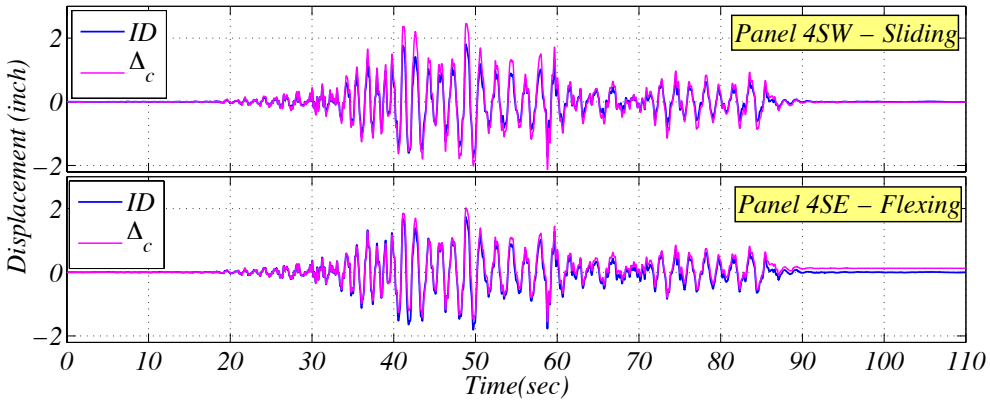

(c)

Figure 4.4. Time histories of ID and Δ_c for panel 4SW (sliding connections) and 4SE (flexing connections) during: (a) BI7, (b) FB1, and (c) FB5

Scatter plots summarizing the peaks of ID versus the peaks of Δ_c for each motion are presented in Figure 4.5. Results for the panels at the fourth level (respectively moving in the eastward/positive direction and in the westward/negative direction) are presented in Figure 4.5a and b. As already

observed from the time histories, the displacement Δ_c was always smaller than ID during the BI motions. In addition, the panels with sliding connections had a Δ_c greater than the ID for all of the FB motions. It can be also observed that the increment of Δ_c with respect to the ID followed a specific trend, which was more pronounced in the eastward direction than in the westward direction.

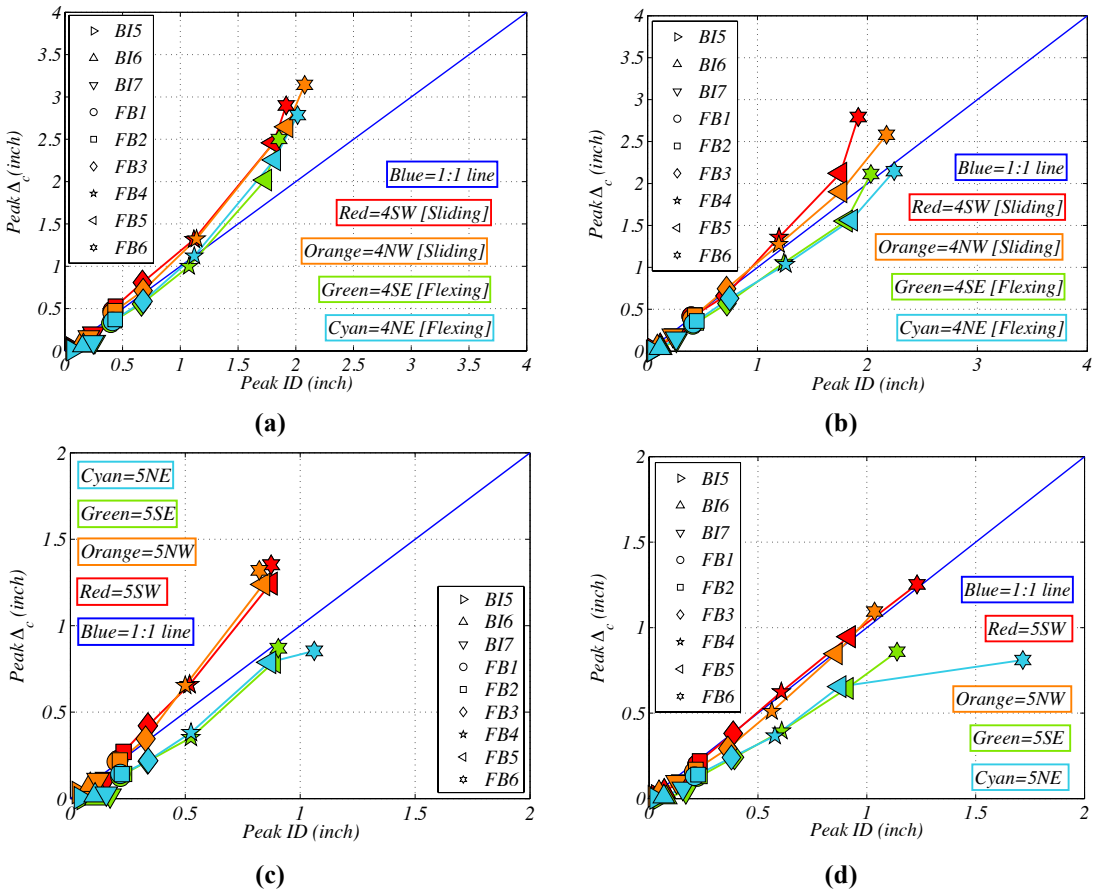

Figure 4.5. Peak ID versus peak Δ_c: (a) panels on the fourth floor-eastward displacement, (b) panels on the fourth floor-westward displacement, (c) panels on the fifth floor-eastward displacement, (d) panels on the fifth floor-westward displacement

The displacement of the panels with flexing connections was asymmetric. Namely, it followed the same trend as the sliding connection in the eastward direction, while in the westward direction the Δ_c was mostly smaller than the ID, though it approached a 1:1 line during the last motion. The behavior of the panels on the fifth level can be seen in Figure 4.5c (eastward movement) and d (westward movement).

The behavior of the panels with sliding connections in the eastward direction was similar to that observed on the fourth level. For the westward movement Δ_c was initially smaller than ID and then

it kept really similar to it. In this case, the panels with flexing rod connections showed a Δ_c smaller the ID for all the cases. A summary of these results is presented in Pantoli et al. 2013c.

4.1.2 Results From the Component Test

Variation of the Connections Performance with Change in the Axial Force

Table 4.3 summarizes the values of the pre-test static forces applied on each sliding surface for the two tests performed and their variation from test 1 to 2. As can be observed, forces applied during both tests were within a reasonable range and the increment of forces from test 1 to 2 was relatively small. During test 1, both connections worked as desired and no damage was observed. However, test 2 resulted in binding of both connections during the very first cycles of motion and as a result the test could not be completed.

Table 4.3. Summary of static forces measured by the load cells

	Pre test axial force (kips)			
	South rod, bottom	South rod, top	North rod, bottom	North rod, top
Test 1	0.08	0.42	0	0.76
Test 2	0.1	0.57	0.08	0.93
Variation	+0.02	+0.15	+0.08	+0.17

Post-processing of video data revealed the following sequence of events:

- During the first (northward) excursion, the southern connection slid while the northern connection did not slide and its rod bound up in the northward direction (Figure 4.6a). Forces both at the top and bottom of the northern rod reached values larger that 10kips –the maximum that the load cells could measure- while forces in the southern load cells remained small;
- During the second (southward) excursion the southern connection did not slide and the rod bound up in the southward direction while the rod in the northern connection straightened up (Figure 4.6b). During this second cycle forces measured in the southern load cells both exceeded 10 kips while the ones in the northern load cells decreased; and
- During the third (northward) excursion the southern connection slid and the rod remained

bound in the southward direction while the northern connection rod bent back in the northward direction (Figure 4.6c). Forces behaved roughly similar to the first cycle.

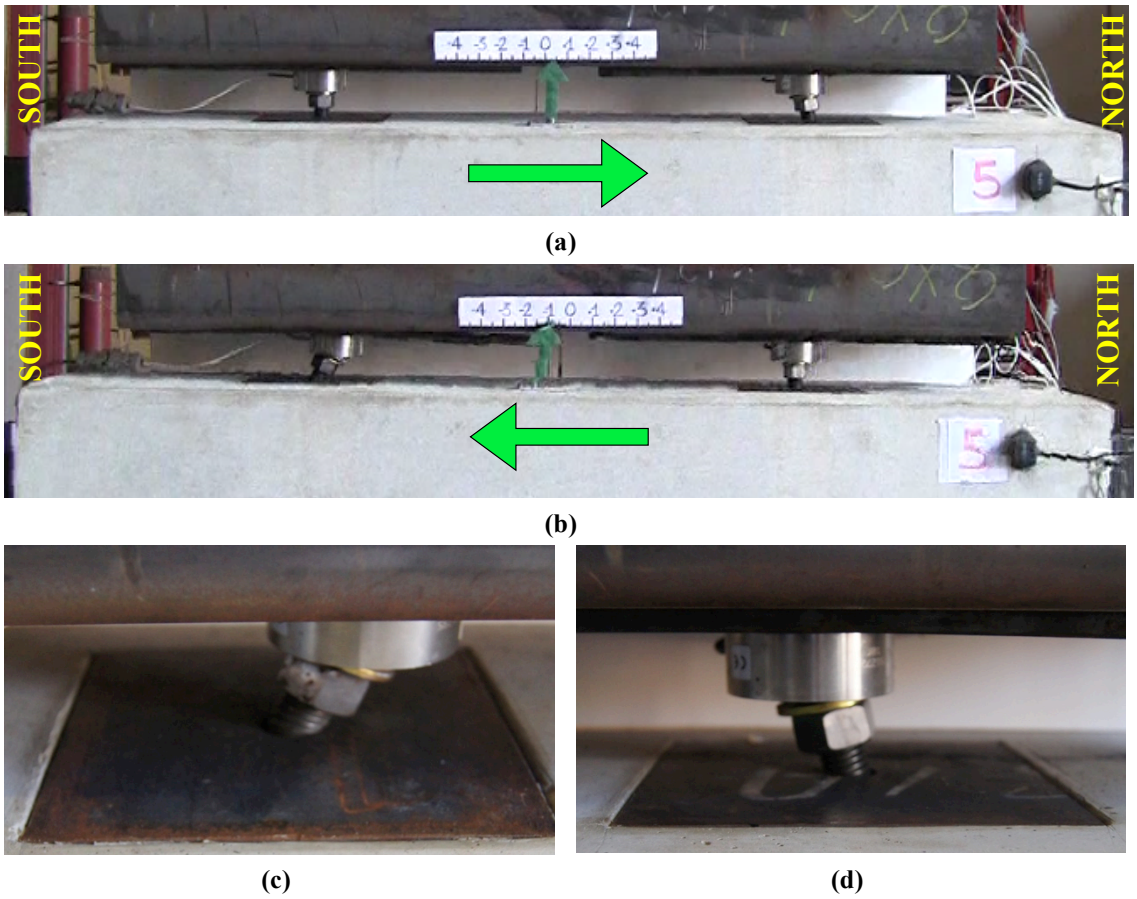

(a)

(b)

(c) (d)

Figure 4.6. Damage progression during test 2 (a) after the first (northward) cycle, (b) after the second (southward) cycle, and (c), (d) after the third and final (northward) cycle.

At the end of testing the bottom load cells were damaged, and as a result their measurement was not considered reliable. The top load cells measured a residual force of 3 kips and 6 kips in the north and south rods, respectively. This first phase of testing showed how sensitive this type of connection might be to the applied normal force. In addition, the behavior of the southern connection showed that resistance to sliding could be different in the two directions.

Variation of the Connections Performance with Change in Rod Length and Diameter

Phase one showed that it was extremely difficult to obtain a consistent behavior of the rods when the compression (bottom) plate was installed, since even small changes in the applied normal force could lead to unpredictable binding of the connections. Therefore, in phase two, the compression

plate and nut were eliminated.

In these tests, damage to the rods (in the form of plastic bending) was classified as either minor or moderate according to the following criteria:

- Minor. Plastic bending ≤ 2°. This type of damage was observed only during the post-processing of the video data. As a consequence, rods showing minor damage were not replaced prior to continued testing; and
- Moderate. Permanent bending > 2°. This damage was visible during and/or immediately after testing, therefore, the rods were replaced prior to subsequent tests.

It is noted that fracture of the rods was not observed during these tests, however, this type of damage would have been classified as severe. Figure 4.7a shows the damage level versus the measured peak drifts for each of the tests performed. From this figure it is possible to observe how damage generally increased with increments in the L_c/d ratio of the rods and motion amplitude. No damage was observed during the two configurations with the lowest L_c/d ratio (3.3). When L_c/d was increased to a 5.3, minor damage was observed during motion M5 for both diameters.

During the configurations with the largest L_c/d ratio (7.3), minor damage was observed even during the low amplitude motions and moderate damage was reached in several cases. Rods in the configuration $C_{7.3,\,0.75}$ attained minor damage during M1 and M3 and moderate damage during M2 and M4 (Figure 4.7b). During the tests of the configuration $C_{7.3,1}$ damage remained mostly minor. Moderate damage was attained only during M4 while no damage was observed during M5. For this second phase of testing, with the bottom plate removed, it can be concluded that an L_c/d ratio less than or about 5.3 results in more reliable connection performance, compared with the larger L_c/d ratios tested. In addition, for connections with larger L_c/d ratios, a larger rod diameter demonstrated better performance due to its lower flexibility.

Understanding the transient values of the axial forces in the rod is important because the axial force in the rod directly determines the friction force, which resists sliding. Figure 4.8a and c presents the static value of the forces prior to each motion for each test configuration measured in the northern and southern load cell, respectively.

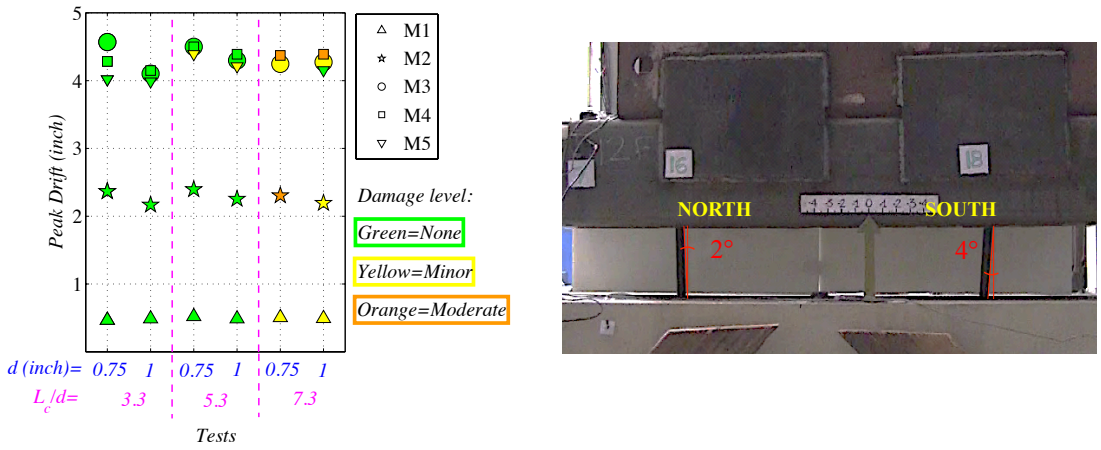

(a) (b)

Figure 4.7. (a) Summary of damage states, and (b) photograph of the damage observed during the configuration $C_{7.3,\,0.75}$ after M2

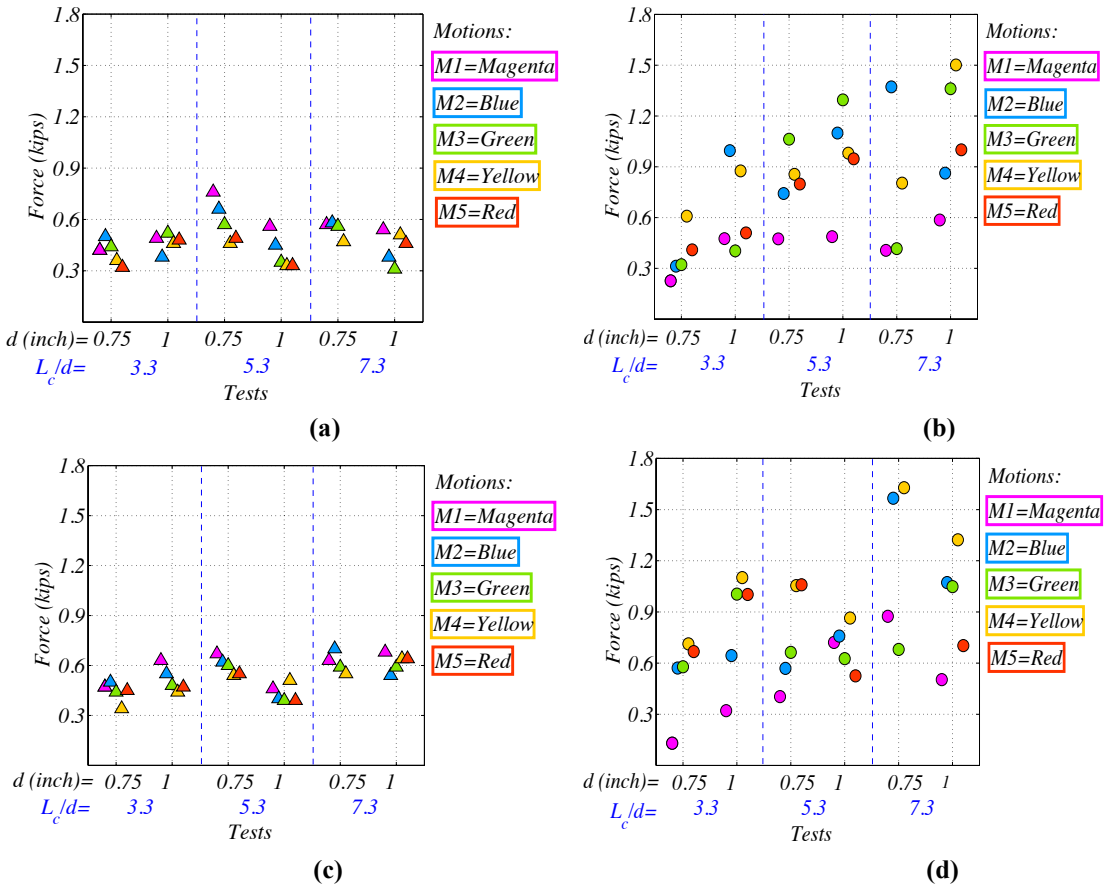

(a) (b)

(c) (d)

Figure 4.8. Summary of pre-test and maximum tensile forces recorded in (a),(b) north rod and (c),(d) south rod

This plot shows that these forces tend to be within a reasonable range (0.30-0.76 kips). It is also noted that the difference between the pre- and the post- test value of forces was generally small, meaning that very little force redistribution occurs during the seismic test. To facilitate a comparison between different tests, the maximum forces presented in Figure 4.8b and d refer to the dynamic component of the forces only, i.e. the initial static value of the force was removed before extracting the maximum. An analysis of the trends of the maximum forces recorded during the six configurations reveals that:

- Generally ,especially in the northern load cell, maximum forces increased from configuration to configuration. This means that for configurations with the same diameter, forces were larger for larger L_e/d ratios and for the configurations with the same L_e/d ratio, forces were larger for larger diameters (i.e. longer rod). This can be understood by considering that increments in the length of the rod determine increments in the moment generated by the horizontal acceleration, which is in turn resisted by axial forces in the rods. However, there are exceptions to this trend possibly because of differences in the pre-test static values of forces;
- Tests where moderate levels of damage occurred also generated the largest maximum forces for that configuration. Namely, this is the case for motions M2 and M4 for the configuration $C_{7.3,\,0.75}$ and M4 for the configuration $C_{7.3,1}$; and
- For almost all configurations, the lowest amplitude motion M1 tended to generate the smallest maximum forces. However, motion M2, with an amplitude roughly half the amplitude of M3, M4 and M5 created maximum forces generally similar or even larger than the forces generated during the three larger motions. This implies that the peak forces are not strictly related to the peak displacements imposed on the connections. It is also noted that larger accelerations generated larger forces, therefore potentially greater friction and this could have degraded the sliding performance.

It is clear that the input displacement is absorbed by the connections via either or both of the following mechanisms:

- Flexing of the rod. This mechanism was the first one activated and the only one contributing

during small input displacements. Figure 4.9a shows a simplified constitutive law for this mechanism; and

- Sliding of the plates. A typical constitutive behavior for a frictional mechanism is shown in Figure 4.9b.

When the sliding could start easily, meaning that the limit force F_L activating the sliding was lower than the force F_y yielding the rod, rods remains elastic during testing and the response of the connection was similar to that shown in Figure 4.9c. When F_L was larger than F_y, the rod yielded in bending, and plastic deformation of the rod developed prior to initiation of sliding (Figure 4.9a d). In general, this situation can occur if F_L becomes large (due to high instantaneous normal forces, rough sliding surfaces etc.) or F_Y becomes small (smaller diameter, longer free length of the rod).

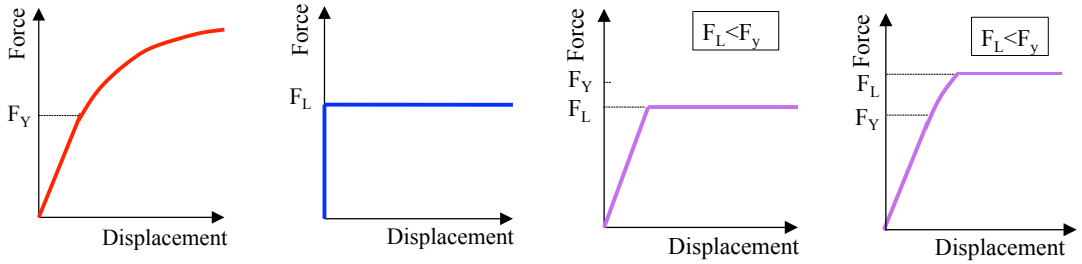

Figure 4.9. Simplified force-displacement monotonic response of sliding connections considering various dominant mechanisms: (a) steel rod yielding alone, (b) sliding mechanism alone, (c) sliding and bending combined when $F_L<F_y$, and (d) sliding and bending combined when $F_L>F_y$

A series of string potentiometers installed during phase two of the experiment allowed measurement of:

- The total displacement absorbed by the connection. This was measured as the relative displacement between the fixed slotted section and the top of the moving concrete block;
- The displacement absorbed by the sliding mechanism. This corresponds to the relative motion between the sliding plate and the fixed support; and
- The portion of the displacement absorbed by the bending of the rod. This was determined as the difference between total displacement and sliding displacement.

Figure 4.10a shows an example of the time histories of these three displacements for the configuration with $C_{3.3,1}$ subjected to M2. Interestingly, it can be noted that during the portions of test

when imposed displacements were small, the bending of the rods absorbed the entire drift, while the plates were not sliding. This can be observed in Figure 4.10a at time prior to 15 sec, between 45 and 58 sec and after 120 sec. Only when the imposed displacements become larger than a critical value (~0.3'' in this case), the sliding was activated. The peaks of the bending displacement remained almost constant at every cycle, and the time history ended up looking almost like a sinusoidal function. As expected, the maximum drift that the rod can absorb before the sliding is activated is a characteristic of its length and diameter (i.e. stiffness).

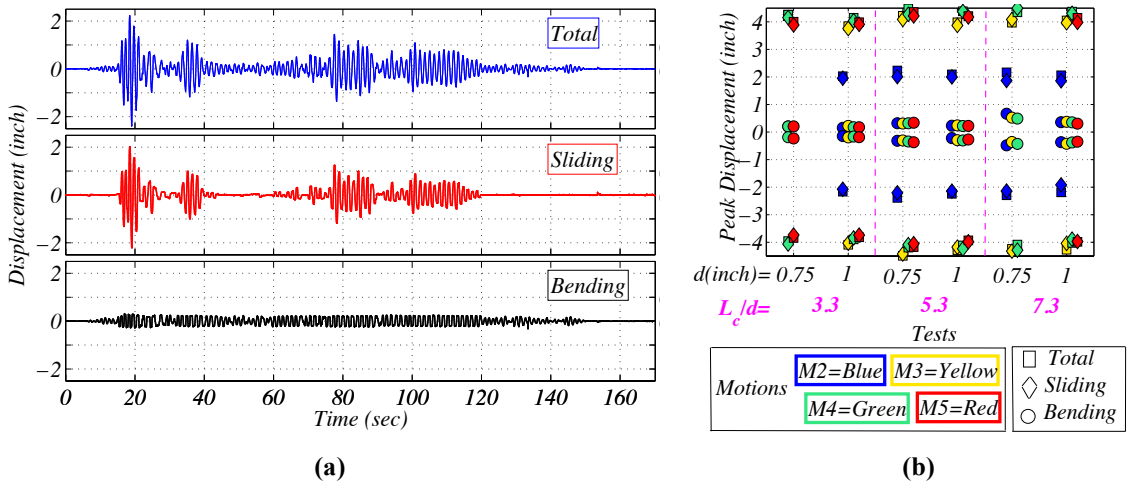

(a) (b)

Figure 4.10. (a) Time histories of the total, sliding and bending displacements during configuration $C_{3.3,1}$ and (b) summary of peak displacements during each test

Figure 4.10b summarizes the peak displacements (total, sliding, bending) observed during each test. For each configuration, the peak displacement absorbed by bending remained quite constant from motion to motion while it was different for different configurations. As the figure shows, during tests with the same Lc/d ratio, the bending displacement decreased with increasing diameter. For the configurations using the same diameter, the peak bending displacement increased with increment in the rod length. This confirms the dependency of the peak bending displacement on the flexibility of the rod. The only case in which peak bending displacements did not follow this trend was for the configuration C7.3,1 during motion M2 and, in fact, more substantial damage was observed during that test. Unfortunately, peaks for motion M1 are not shown in Figure 4.10b, since the data quality from the sensor measuring the sliding displacement during this motion was poor due to its small amplitude. However, videos show that the behavioral trend was similar to that of other motions, meaning that

imposed displacements were absorbed by bending of the rods up to a critical value, and only after this was sliding of the plate initiated. The tendency of the rods to bend before activation of sliding can have practical consequences. First of all, this bending can contribute to the creation of additional forces on the sliding surfaces (see next section). In addition, over time it could lead to accumulation of stresses in the location of maximum moment of the rod, this in turn may lead to damage of the rod itself.

One of the most important practical conclusions of phase one of testing was the sensitivity of sliding connections to binding. This issue could be better understood considering the results from phase two. In fact, during this phase, it was clearly observed that connection rods always bend and tens to bind prior to activation of sliding. This bending is not accounted for during the design phase, however it can have negative effects on the connections. In fact, when the rod bends and initiates hinging at the interface with the compression nut, a compression force is generated on one side of the rod and this is then transmitted to the outer sliding surface. This force increases the normal compressive force already acting on this surface and consequently the resistance to sliding of the plates and the tendency to bind (Figure 4.11a and b). When the compression plate is not installed, the compression force generated by the rotation of the rod does not occur (Figure 4.11c and d). It is observed that another difference between the configurations with and without the compression plate is the effective length of the rod that bends, which is larger for the configuration without the bottom plate (Figure 4.11a and c).

4.1.3 Summary of the Results and Practical Applications

The following practical conclusions were drawn from the results of these tests:

- Sliding rod connections with nuts and washers on both sides of the slotted element tend to:

  Bend and subsequently respond in a binding mode instead of sliding. Due to the flexibility of this connection, the rod bends prior to the activation of the intended sliding motion. If the bending-induced rotations are large enough, a clamping force is created between the sliding plates and the slotted angle, which makes sliding less likely. This can happen even on relatively short, stiff rods. Connection rods that are designed to slide but instead deform in a bending mode can reach moderate damage at low drift magnitudes. It is hypothesized that severe damage ,in the form of fracture of

the rods, is likely if the imposed displacements reach large values;

- Be unreliable. The sliding mechanism is highly sensitive to the amplitude of frictional force on the sliding surface, and if clamping forces develop during flexing of longer rods, this leads to an unreliable response. Indeed, the frictional resistance depends on the frictional coefficient between the sliding surfaces and the normal force applied to the surface, both of which have a large variability, particularly during dynamic loading, as occurs during seismic motion.

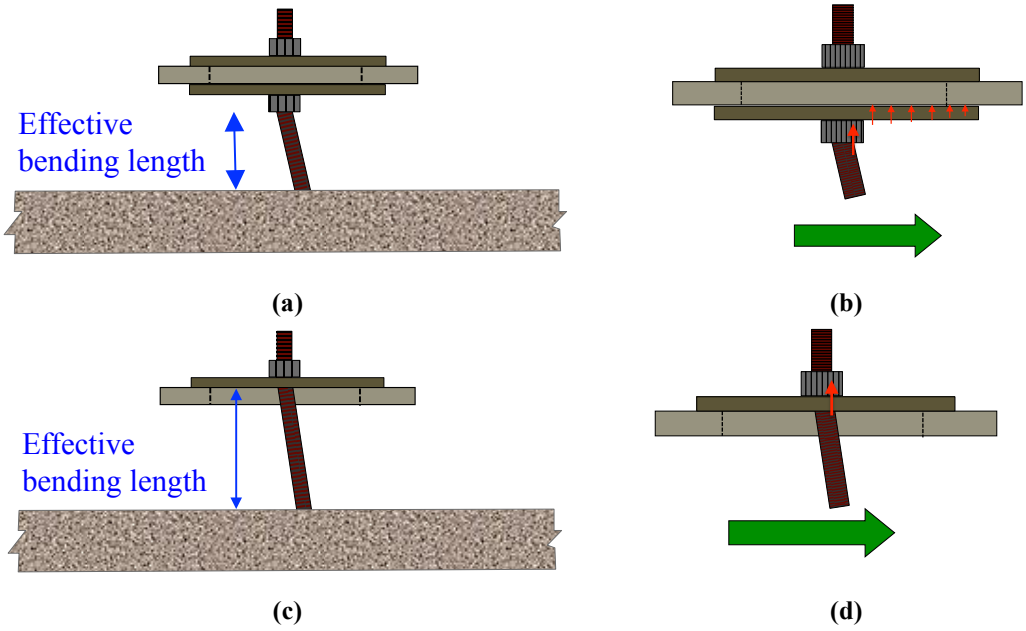

Figure 4.11. Bending behavior of the rod (a) in presence of the bottom plate, (b) force developed in presence of the bottom plate, (c) in absence of the bottom plate, and (d) force developed in absence of the bottom plate

There are several ways to improve the performance of sliding connections:

- Eliminate the free rod length. Snug sliding connections consistently demonstrated good performance (as demonstrated in the BNCS experiment);
- Eliminate the compression plate. The elimination of this plate makes it impossible for the clamping force to develop. Sliding connections without the compression plate responded with a sliding mechanism for all L_c/d ratios tested. However, due to the permanent plastic rotations required to initiate sliding it is recommended that the L_c/d ratio be limited to 5.3. It is noted that removing the compression plate obviously makes the connection a tension connection

only. The compression element will have to be replaced with some other mechanism or connection,like a push only connection separate from the tension rod. Some precasters have achieved this by welding an angle clip to the structure that rests against the back of panel after panel alignment. More information about these results are presented in Pantoli et al. 2014.

4.2 Flexing Connections

4.2.1 Damage Observed During the BNCS Test

A synthesis of visible damage to the flexing rod connection is presented in Table 4.4 and

Table 4.5, with example photographs shown in Figure 4.12. Damage was manifested via plastic hinging of the rod at the nut location. Residual damage to the flexing rod connections with short rods was not detected. It should be noted that inspection of these connections was possible only on the fifth floor, noting that this level attained smaller PIDRs. The flexing rod connections with a medium length rod on the fourth floor were permanently bent during motions FB5 and FB6 at the fourth floor while only during FB6 did they plastically yield at the fifth floor. Flexing rod connections with long rods exhibited residual damage only after motion FB6, and only at the panel on the fourth floor.

Table 4.4. Residual deformation in flexing connections with medium rods (Green=no damage; red=damage) [*=rod replaced]

Test	PID (PIDR)	Panel 4EN		PID (PIDR)	Panel 5NE	
	Fourth level	Connection WW Inch (°)	Connection EE Inch (°)	Fifth level	Connection WW Inch (°)	Connection EE Inch (°)
BI	0.25'' (0.15%)	None	None	0.17'' (0.1%)	None	None
FB1	0.40'' (0.24%)	None	None	0.22'' (0.13%)	None	None
FB2	0.44'' (0.26%)	None	None	0.23'' (0.14%)	None	None
FB3	0.72'' (0.43%)	None*	None*	0.38'' (0.23%)	None*	None*
FB4	1.24'' (0.74%)	None	None	0.60'' (0.36%)	None	None
FB5	1.83'' (1.09%)	1.2(4)	1.6(6)	0.91'' (0.54%)	None	None
FB6	2.17'' (1.29%)	0.8''(3)	1.6(6)	1.11'' (0.66%)	None	1(3)

Table 4.5. Residual deformation in flexing connections with long rods (Green=no damage; red=damage) [*=rod replaced]

Test	PID (PIDR) Fourth level	Panel 4NE	
		Connection CW	Connection CE
BI	0.25'' (0.15%)	None	None
FB1	0.40'' (0.24%)	None	None
FB2	0.44'' (0.26%)	None	None
FB3	0.72'' (0.43%)	None*	None*
FB4	1.24'' (0.74%)	None	None
FB5	1.83'' (1.09%)	None	None
FB6	2.17'' (1.29%)	1.6(5)	None

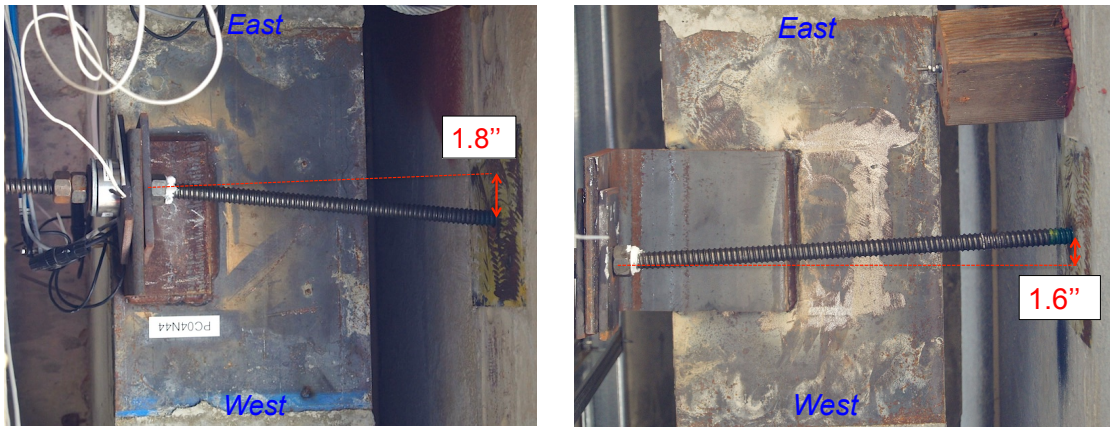

(a) **(b)**

Figure 4.12. Damage to flexing connections: (a) connection EE in panel 4NE after FB5, (b) connection CW in panel 5NE after FB6

4.2.2 Results From Component Tests and Correlation With the Results From the BNCS Test

Key observations from these tests include the following:

- Good correlation between the number of cycles of constant displacement applied at fracture, herein denoted as Δ, and the ratio $(L_f/d)/\Delta$ is observed, with less than two cycles associated with fracture for $(L_f/d)/\Delta = 1.4$ and roughly 9 cycles needed to achieve fracture for $(L_f/d)/\Delta = 2.5$ (Figure 4.13b). It is noted that these results were created by applying a constant (target)

amplitude displacement, which is clearly a simplification compared with real earthquake histories, as was applied during the BNCS test program;

- The ability to resist several cycles of large displacement is related to prior load history;
- The fracture zone was restricted to a small length of the rod; and
- The rods continued to resist several cycles of large amplitude inelastic displacement, indicating good ductility of the material.

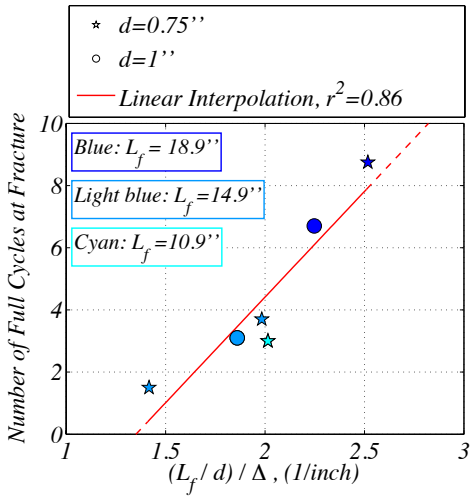

Figure 4.13. Results obtained during the component test on flexing connections: number of cycles to fracture versus (L_f/d)/Δ (Courtesy of Hutchinson et al. 2014)

Results from these component tests were compared to the observations of flexing connections during the BNCS project. Namely, Figure 4.14 shows a summary of the results from the BNCS and SJSU tests in terms of damage observed for the different rod lengths. In both plots, the y-axis shows the total number of cycles creating a displacement in the rod Δ larger than the theoretical yield displacement calculated considering the rod hinging at both ends ($\Delta_y^{theor.}$). For the SJSU tests, this corresponds to the total number of cycles, while for the BNCS experiment the number of cycles was calculated using the rainflow counting algorithm, a commonly adopted method in fatigue calculations. The x-axis of the plot shows the average rotation angle for all cycles in which the displacement exceeded the theoretical yielding displacement. For the data relative to the BNCS project, two data points are presents at each location since each panel had two connections with the same length and diameter. The two datasets are binned first by limit state achieved (Figure 4.14a) and subsequently by

L_f/d ratio (Figure 4.14b). It is noted that rods achieving fracture carried far fewer theoretical plastic excursions, but to very large rotations (red stars). It is also important to note that no apparent trend is evident when analyzing these data with regard to L_f/d.

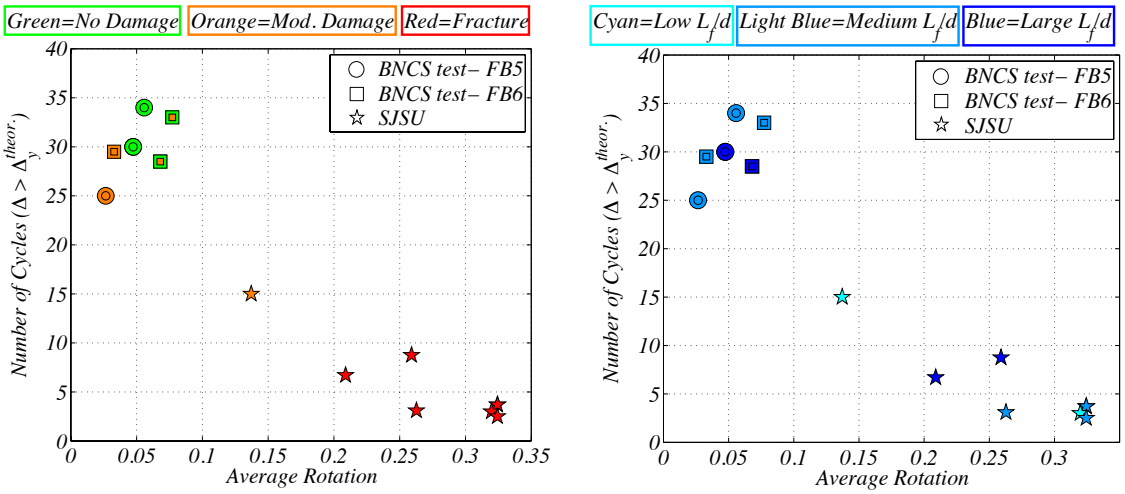

(a) **(b)**

Figure 4.14. Number of cycles with a peak-to-peak displacement greater than twice the theoretical yield displacement versus average rotation of the connection: (a) binned by limit state and (b) binned by L_f/d ratio (Courtesy of Hutchinson et al. 2014)

4.2.3 Summary of the Results and Practical Applications

Several observations were made related to the behavior of the flexing rod, particularly when the results were combined with the experimental data collected during the BNCS experiments:

- Rods with free lengths of 14.9 inches or longer are able to accommodate deflections of 5.0 inch or more;
- The ability to resist several cycles of high displacement is related to the prior load history. Rods that were tested by initially applying small displacements and then continued with many cycles of increasing displacement were unable to resist as many cycles of large displacement;
- The number of cycles of constant rotation of the plastic hinges of the rod appears to be inversely related to the applied rotation. The limit appears to be independent of rod diameter as the ¾-in and 1-in rods tested showed comparable number of cycles prior to failure. As would be expected, if the rods are not loaded past their yield displacement, they should be able to accommodate a significant number of cycles of loading; and

- The inelastic region of the rods as observed during fracture was over a short length, approximately one to two diameters of the rod. If the rods were loaded in pure tension, the inelastic region may be expected to extend nearly the full free length of the rod. The relatively localized yielding may be due to multiple reasons, including the large moments developed at the ends of the rods, the geometric complexity of the threads, and the effect of cold-working of the steel. However, even though the inelastic region of the rod was small, the rods did resist several cycles of inelastic loading and displacements far above the yield displacement, indicating good ductility of the material.

ACKNOLEDGEMENTS

Chapter 4 reproduces content and images of the material as it appears in the PCI Journal 2016, Proceedings of the Façade tectonics conference 2014, and Proceedings of the Compdyn Conference 2013. Pantoli, E., Hutchinson, T. C., McMullin, K. M., Underwood, G. A., and Hildebrand, M. J., 2016. "Seismic-drift-compatible design of architectural precast concrete cladding: Tieback connections and corner joints." PCI Journal, July-August, 38-52. Pantoli, E., Hutchinson, T. C., Underwood, G. A., and Hildebrand M., 2014. "Seismic behavior of sliding push-pull connection in architectural precast concrete panels." Proceedings, Façade Tectonics, January 9-12, Los Angeles, CA. Pantoli, E., Chen, M., Hutchinson, T. C., Underwood, G. A., and Hildebrand M., 2013. "Shake table testing of a full-scale five-story building: seismic performance of precast concrete cladding panels." Proceedings, Compdyn Conference , June12–14, Kos Island, Greece. The author of the dissertation is the principal author of the above cited papers.

Chapter 5

Behavior of Corner Joints and Connections

The goal of this chapter is to present the analysis on a new type of corner system, which allows for smaller corner joints. In this system, the corner joint is sized to avoid impacts between panels when the building remains elastic, while collision of corner panels is allowed for interstory drifts creating plastic deformation in the building. These impacts could potentially produce large forces, and thus a ductile fuse is introduced in the corner connection to limit them. Such corner system was tested in the BNCS building in combination with the commonly used miter and butt-return joints. Screenshot of cameras capturing the collision of the corner panels at the upper stories of the BNCS building is presented in Figure 5.1 and Figure 5.2. It is noted that, because the upper stories underwent drifts smaller than expected, the panels impacted only in the last two FB tests.

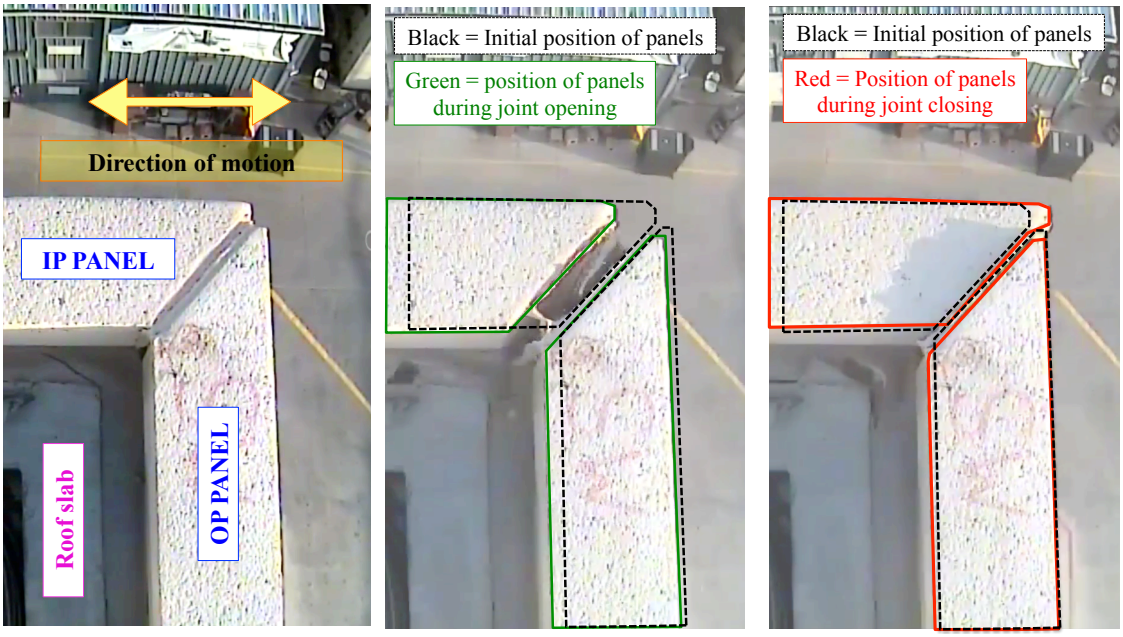

(a) (b) (c)

Figure 5.1. Screenshots from videos of the corner joints view from the roof (view looking down) during FB6 for the miter joint in the southwest corner showing (a) original position, (b) joint opening and (c) joint closing (Courtesy of Hutchinson et al. 2014)

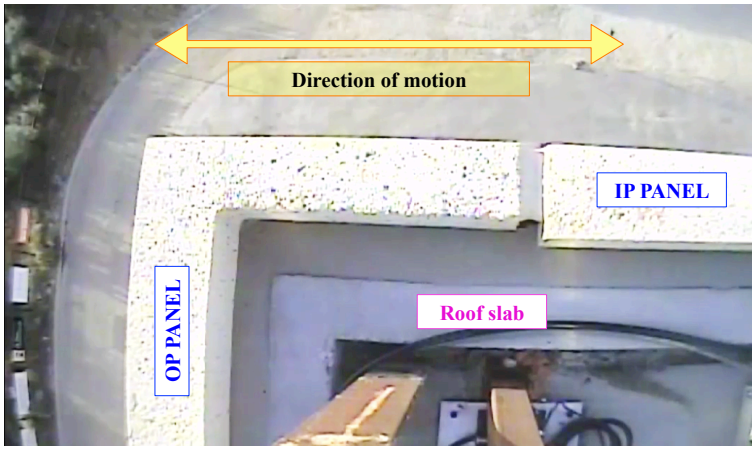

(a)

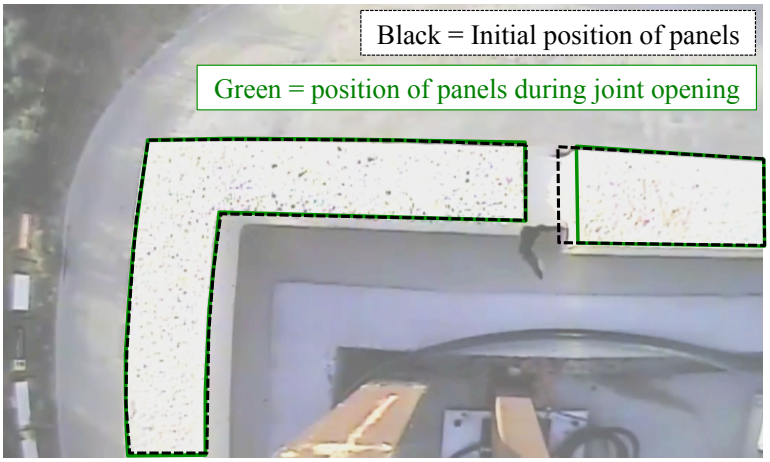

(b)

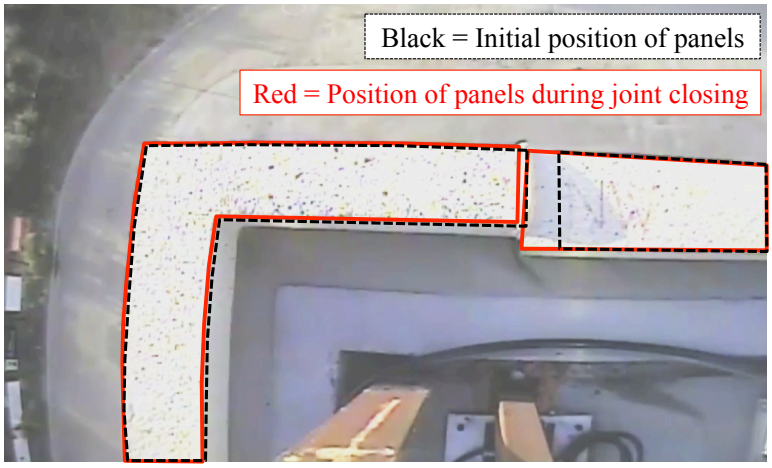

(c)

Figure 5.2. Screenshots from videos of the corner joints view from the roof during FB6 for the butt-return joint in the northwest corner showing (a) original position, (b) joint opening and (c) joint closing (view looking down) (Courtesy of Hutchinson et al. 2014)

This chapter starts by presenting the correlation between interstory drifts in the BNCS building and forces and displacements in the corner connections. Large spikes in the forces in the corner connection rod were recorded for interstory drifts larger than the joint gap, thus confirming the impact between the panels. The second section of this chapter presents a study on the different behavior of miter and butt-return corners joints, both in terms of observed damage and measured results. The following section examines another variable influencing the behavior at corners: the type of tieback connection in the IP panels. Finally, the results of a computer model simulating the collision of panels is presented. Goal of this model is to determine the effects of the collision of the panels in all the connections of the OP and IP panels.

5.1 Relationship Between Interstory Drifts and Forces in the Corner Connection

In the corner connections of the eastern panels, both forces and displacements were measured. On the western side of the building the northern panel was instrumented with a displacement potentiometer while the southern one was not instrumented. Forces were measured with a load cell installed between the outside washer and nut (Figure 5.3a). This load cell measures only tension in the rod. The displacement of the connection was recorded with a string potentiometer measuring the relative displacement between the column and the panel close to the connection embed (Figure 5.3b).

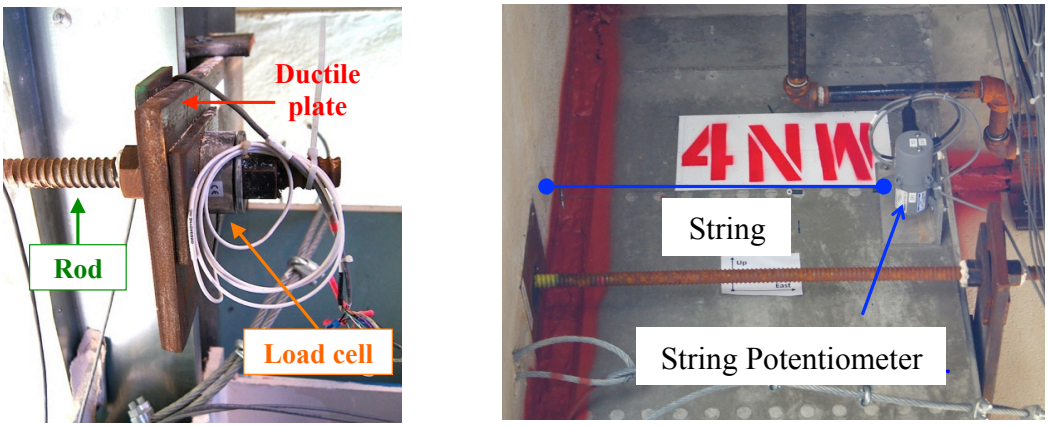

(a) (b)

Figure 5.3. Sensors monitoring the behavior of the corner connections: (a) load cell, and (b) string potentiometer

The large difference between the forces developed with and without collision of the panels is clearly shown in Figure 5.4. These plots present the time histories recorded during FB3 and FB5 of the interstory drift recorded at the southeast corner of the fourth level (ID); the floor acceleration in the southeast corner of the fifth floor slab (FA); the displacement of the panel 4ES with respect to the column as measured by the string potentiometer (Δ_c); and the tension in the connection rod of the corner connection of the same panel (F_c).

From the time histories recorded during FB3 (Figure 5.4a and b) the forces and displacements in the corner connection remain small. The difference in behavior during the eastward and westward motion can be clearly seen: when ID is in the eastward direction (positive) the building pushes the panel, thus creating compression in the rod which cannot be recorded by the sensor, while when ID is directed westward (negative) the building pulls the panel and this peak tensile forces and positive displacements are recorded. The collision between panels that characterized FB5 can be seen Figure 5.4c and d: during this test both time histories of F_c and Δ_c exhibit large spikes in the positive direction created when the joint gap closes and the IP and OP panels push against each other. These same spikes were recorded also during FB6.

To assess it the large spikes in the recorded forces were due to the interstory drifts, the correlation between the measured and the theoretical force in the corner connection was examined. The measured force is the one recorded by the load cell, while the theoretical force is calculated by multiplying the tributary mass of the connection (3.26 kips in this case) by the acceleration measured in the panel. The comparison for FB5 is shown in Figure 5.5a. At the beginning of the motion, for low levels of accelerations and drifts, the correlation between the amplitudes of theoretical and measured force is really good (Figure 5.5b). However, during the strong part of motion, many large spikes in measured force are observed, while these peaks were not present in the theoretical force (Figure 5.5c). The onset and end of these extra forces can be defined as the points in which the measured forces starts and ceases being larger than the theoretical force. Using this definition it is possible to find the duration of these spikes, which varies between 0.2 and 0.5 seconds. This duration confirms that these peaks in forces are not high frequency. Figure 5.6 presents the correlation between the beginning and end of

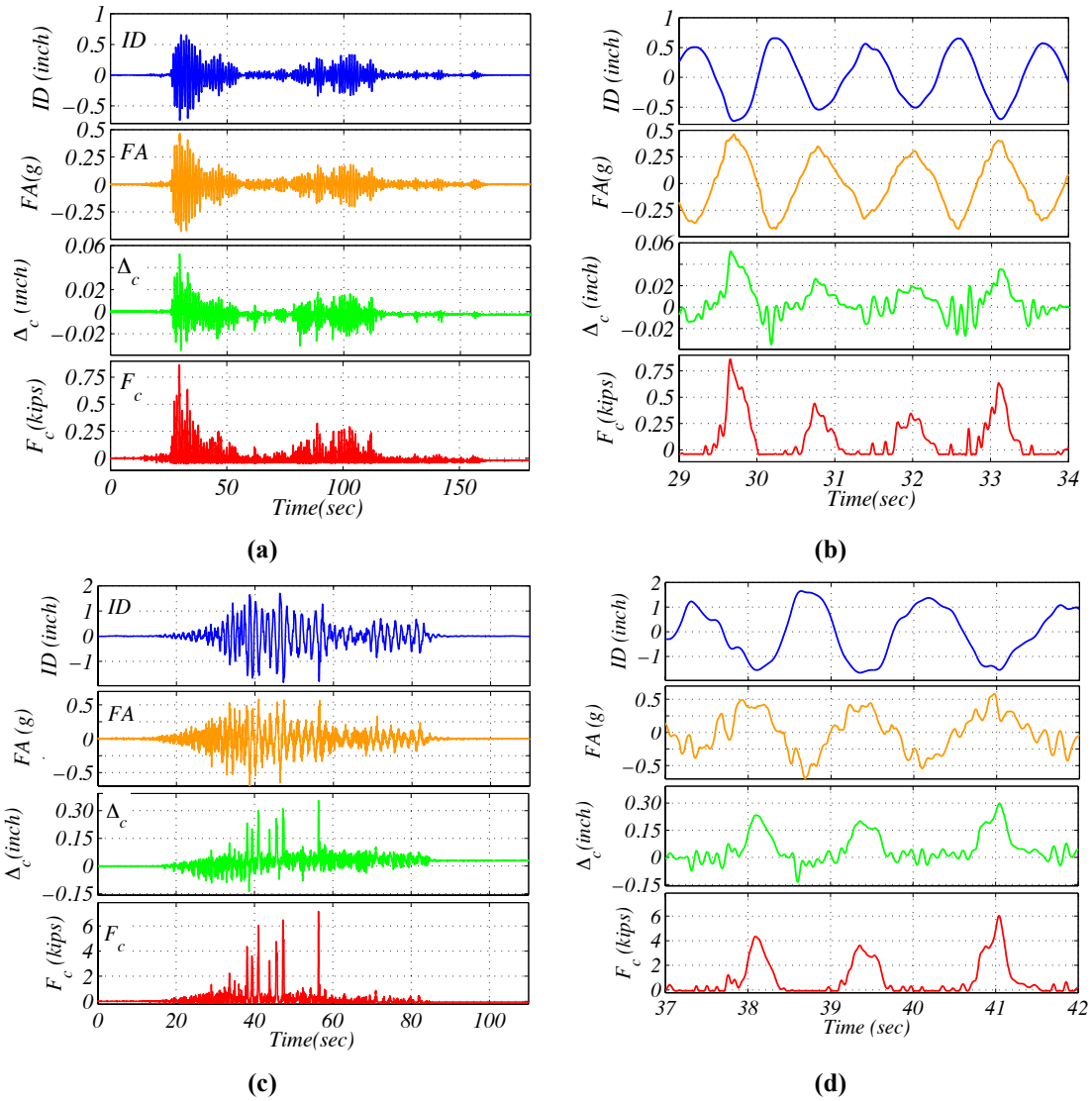

Figure 5.4. Time history of ID, FA (in the southeast corner), Δ_c and F_c in connection SS of panel 4ES recorded during (a), (b) FB3 (entire time history and zoomed view of strong motion period), and (c),(d) FB5 (entire time history and zoomed view of strong motion period)

each spike found as explained above and the time history of the interstory drifts during FB5. Clearly, the spikes start if and only if the interstory drift gets larger than the joint size (1'' corresponding to a drift of 0.6%). Similar results can be found for FB6 (Figure 5.7a), with the difference that two initial collisions at around second 39 and 44 create plastic deformation of the plate and opening of the joint. After this initial impact, the threshold of the interstory drift creating a spike in the force increases from 0.6% to 0.8% (Figure 5.7b). It is noted that results are not completely consistent since, according to this explanation, the spike at second 85 should not have been generated.

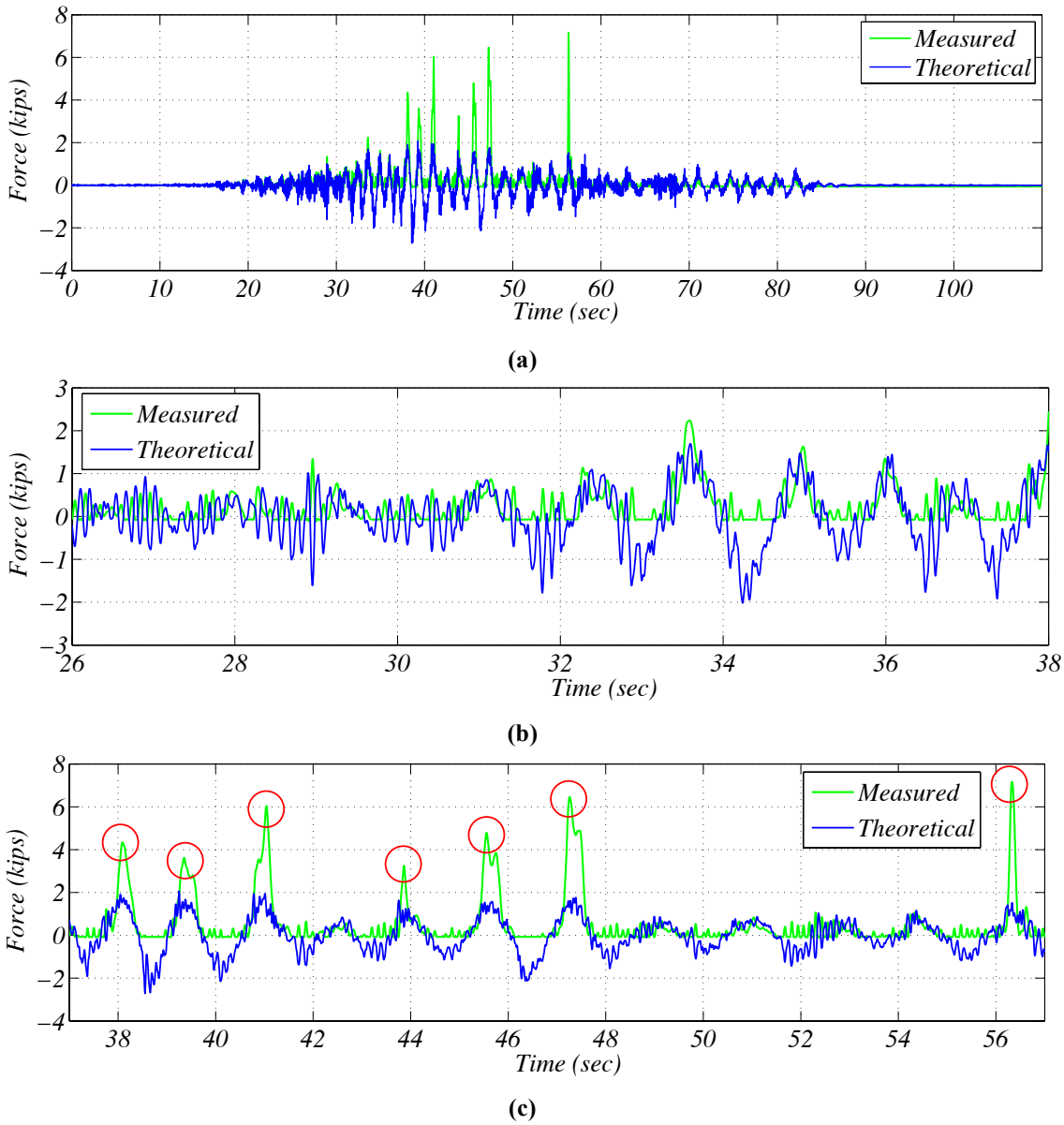

Figure 5.5. Comparison of measured and theoretical force in the corner connection during FB5: (a) full time history, (b) zoom on the low amplitude initial part of motion and (c) zoom on the strong part of motions showing spikes in measured force

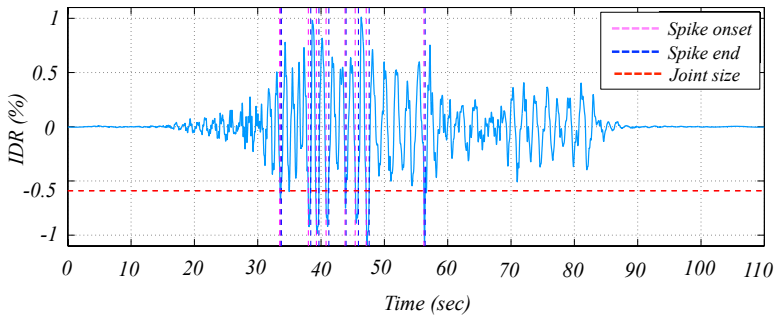

(a)

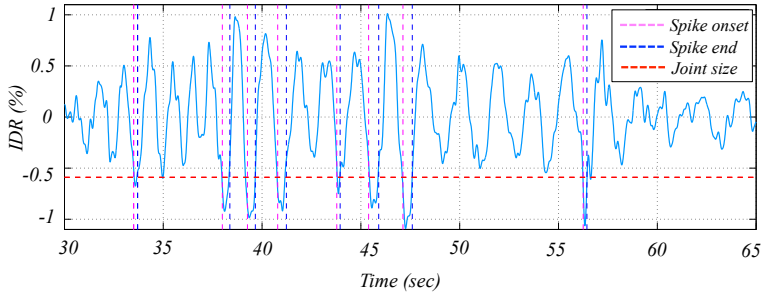

(b)

Figure 5.6. Correlation of interstory drifts and time of spikes during FB5: (a) full time history and (b) part of the time history with impacts

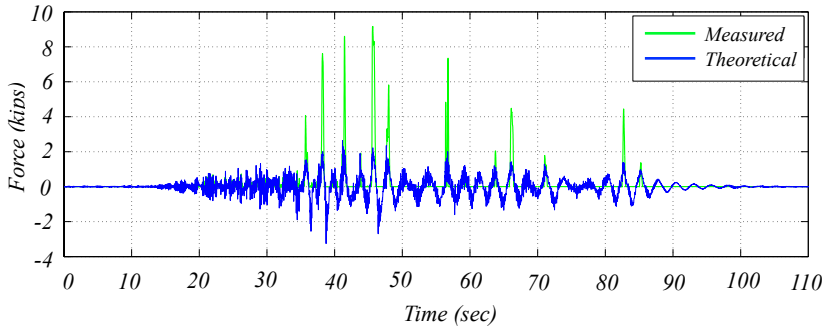

(a)

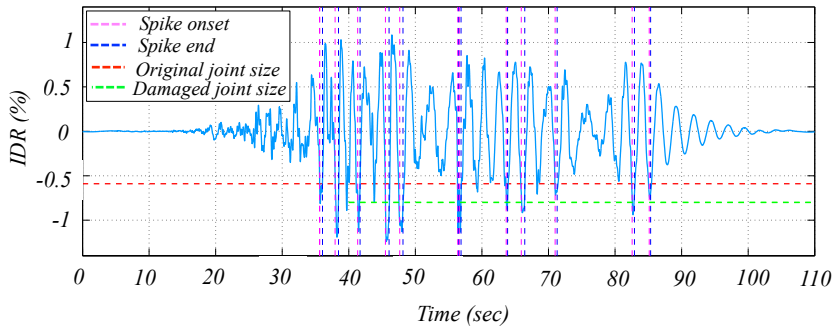

(b)

Figure 5.7. (a) Time history of measured and theoretical force in connection SS in panel 4ES during FB6 and (b) correlation between interstory drifts at the fourth level, time of spikes and joint size during FB6

5.2 Differences in the Behavior Between Miter and Butt-Return Joints

5.2.1 Observed Damage

The difference in damage pattern observed during the BNCS project in panels with miter and butt-return corner joints proves right away the difference in the behavior of the two systems. In fact, in panels with a miter joint, damage consisted mainly in a network of cracks forming close to the corner connection panel embed. These cracks were particularly developed for panel 4WS (Figure 5.8a). However, after the last motion, this same type of cracks (but much thinner and less developed) was observed almost in every OP panel close to a miter joint, while it was never observed in an OP panel close to a butt-return joint. None of the ductile plates in the corner connection of OP panels with miter joints showed any plastic deformation.

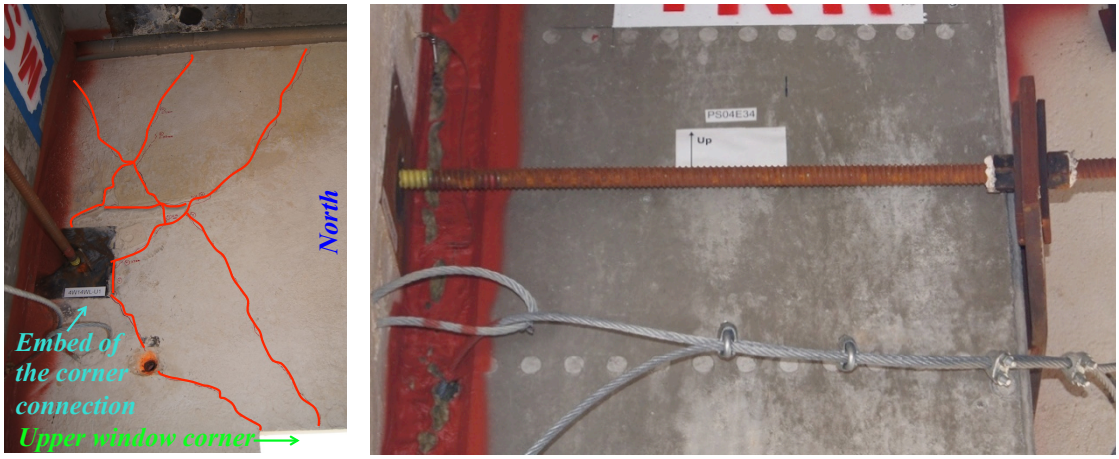

(a) (b)

Figure 5.8. Final damage to the corner connection area for (a) panel 4WS (with miter joint) and (b) connection of panel 4WN (with butt-return joint)

Panels with a butt-return joint did not exhibit cracks in the corner connection embed area, and in panel 4WN, plastic deformation of the ductile plate was observed. The first permanent deformation was observed after FB5, and it developed further after FB6 (Figure 5.8b). The complete pattern of damage in panels 4WS and 4WN was presented in Chapter 4. The difference in observed behavior is attributed to the fact that the presence of a butt-return joint gives stiffness to the corner, thus reducing flexural distortion in the panel and forcing the ductile fuse in the connections to absorb the imposed deformation. On the other side, in the panels with miter joints, the most flexible part of the corner

system is not the ductile fuse but the corner of the panel itself, which ends up distorting and getting damaged.

5.2.2 Measured Response

Peak Drifts

The comparison of the behavior of connections close to a butt-return and miter joint was made possible by the sensors installed in panels 4ES (butt-return joint) and 4EN (miter joint). For each of the two panels examined the value of the displacement at the connection (Δ_c) and westward interstory drift (ID_W) at the corresponding corner of the building were measured. These two values allowed calculation of the portion of drift not absorbed by a displacement in the connection, i.e. ID_W - Δ_c. This drift represents the displacement absorbed by other deforming mechanisms, such as through the kinematics of the joint (vertical joint closure) and deformation of the OP and IP panels. A value of ID_W -Δ_c smaller than ~1'' indicates that likely no collision occurred while a value much larger indicates that contact between the two panels occurred. Another important parameter is the residual Δ_c at the end of testing, as this indicates the final deformation of the connection.

The residual Δ_c and the peak values of Δ_c, ID_W and ID_W -Δ_c recorded during each motion for the two corners under consideration are shown in Figure 5.9. The peak values of ID_W and Δ_c confirm that during the first three motions no impact occurred as peak Δ_c was of the order of 0.04''. A small collision probably occurred during FB4, in fact ID_W reached more than 1.2'' and a Δ_c of 0.15-0.2'' was recorded in both connections. During FB5, the ID recorded was roughly twice the gap size (2'') confirming the inevitability of impacts between panels. The peak connection displacement Δ_c reached 0.35'', but it remained mostly elastic for both connections. During the last motion the total ID_W in the south side of the building was 2.1''. For panel 4ES (with butt-return joint) it can be assumed that 1'' (=47%) was absorbed by the closing of the corner joint, 0.43'' (~20%) was absorbed by the elastic deformation of the plate, 0.16'' (7%) by the plastic deformation of the plate and 0.51'' (26%) by other mechanisms. In panel 4EN (miter joint) the total 2.28'' of displacement were absorbed as follows: ~1.06'' (46%) by the closing of the gap, 0.39'' (17%) by elastic deformation of the plate and 0.04'' (2%) by a plastic deformation of the plate, leaving 0.79'' (35%) to be absorbed by other mechanisms.

This plots also confirms that the maximum elastic deformation of the connection was 0.39''.

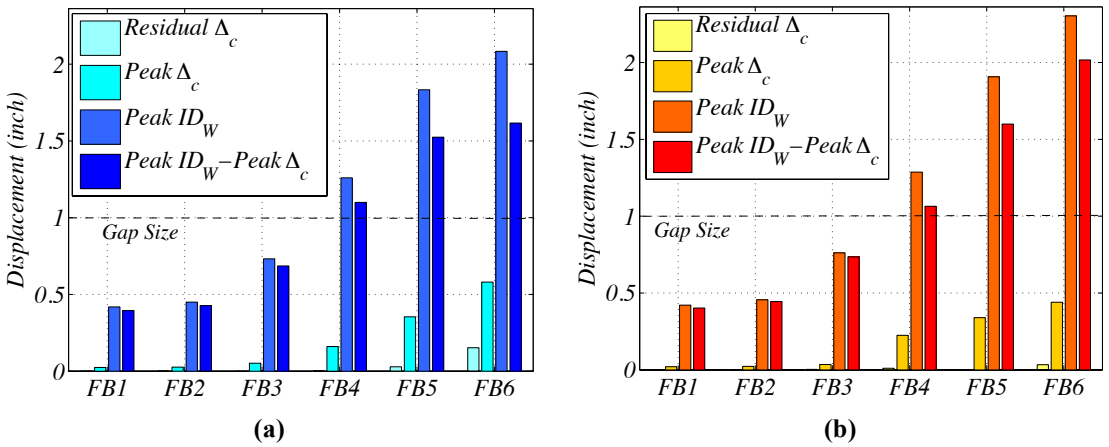

Figure 5.9. Residual Δ_c, peak Δ_c peak ID_W and peak ID_W-Δ_c recorded in all the FB motions in the (a) 4ES panel and (b) 4EN panel

Hysteretic Behavior on the Corner Connection

In addition to the analysis of the difference in the behavior of panels with miter and butt-return joint in term of displacement, it is also possible to study their difference in terms of hysteretic behavior thanks to the combined analysis of data from string potentiometers and load cells. The force-displacement behavior recorded in the last three motions for the corner connection in panel 4ES (butt-return joint) and 4EN (miter joint) is shown in Figure 5.10. During motion FB4 (Figure 5.10a and b), the connection of the panel with butt-return joint showed an almost perfect linear behavior while that of the panel with miter joint presented a bi-linear behavior with a change in stiffness at a displacement of 0.04'' and force of 0.7 kips. Figure 5.10c and d show the displacement versus force recorded during FB5. In this case, both connections recorded large collision forces and showed a nonlinear behavior: the connection in panel 4ES shows hardening, especially when displacements were larger than 0.24'', while the connection in panel 4EN (miter joint) still showed softening behavior for displacements larger than 0.2''. This softening behavior of the panel-connection with miter joint was attributed to the formation of cracks in the corner of the panel, while the stiffening behavior in the panel with butt-return joint was more likely caused by the nonlinear behavior of the steel connection (the connection deformed 0.35'' with 0.03'' of residual displacement). During the final motion, even larger impacts were recorded and the behavior of the two connections more significantly diverged. In fact, in the connection of the

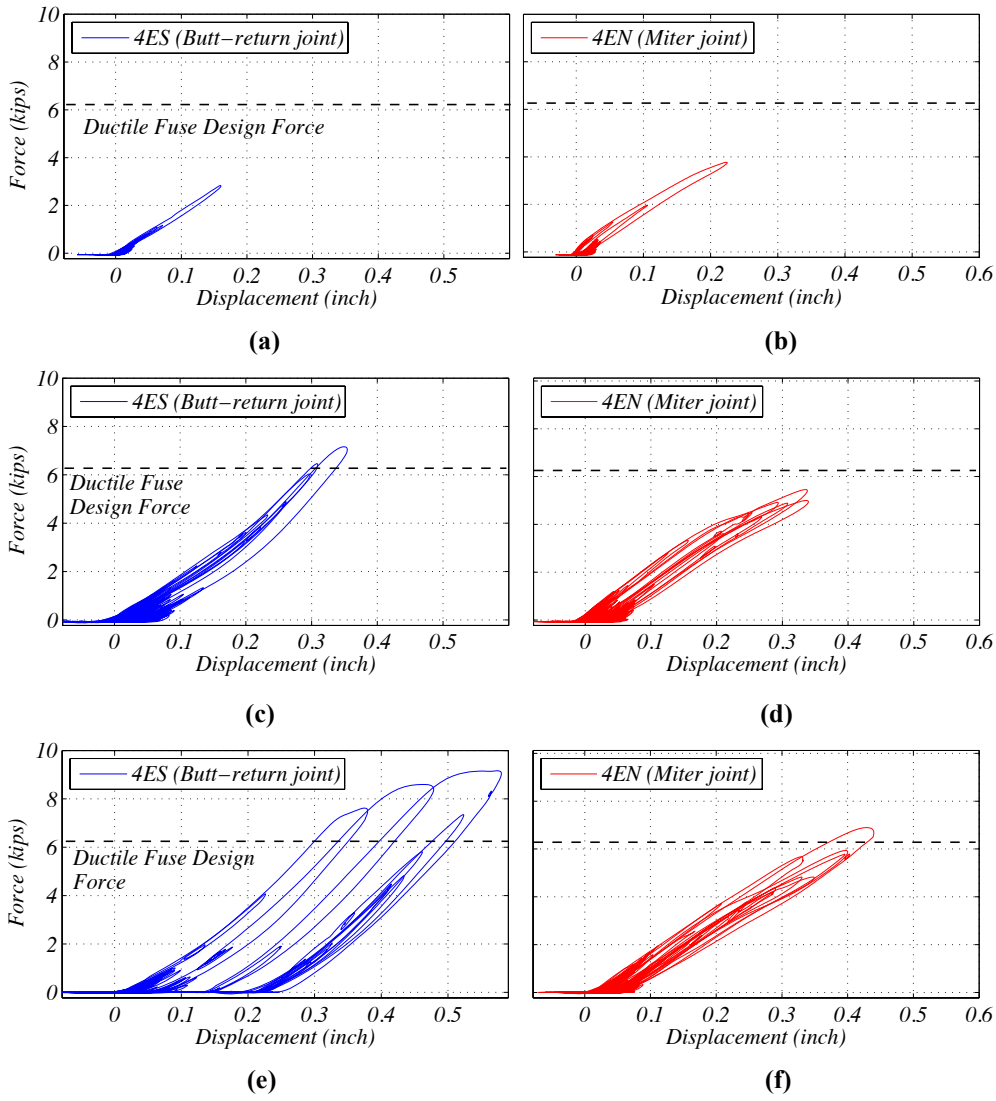

Figure 5.10. Force-displacement response recorded in the 4ES and 4EN panels during (a),(b) FB4, (c),(d) FB5 and (e),(f) FB6

panel with butt-return joint, the ductile plate developed plastic bending, as confirmed by a 0.16'' residual displacement. Several broad hysteresis loops show the dissipation of energy through continued plastic rotation of the plate. On the other hand, the connection in the northern panel (with miter joint), observed smaller displacements and also did not exhibit broad hysteresis but rather a nearly linear force-displacement. This was likely due to the fact that sources of inelastic behavior in this panel-connection were limited to crack development in the panel, and this had occurred, and stabilized, in prior motions. The smaller connection displacement can be attributed to the fact that the plastic displacement of the panel was above the connection level. These results are presented also in Pantoli et

al. 2013d.

5.3 Influence of the Type of Tieback Connection on Corner Behavior

The goal of this study is to understand why the panels on the west side of the building underwent a larger amount of damage despite similar interstory drifts. To achieve this goal, the behavior of the southeast and northwest corners was examined, since both areas were characterized by the presence of a butt-return joint. Namely the following drifts are considered:

- ID recorded at that corner;
- Displacement of the corner connections in the OP panels; and
- Displacement of the IP panel connection in that corner.

A summary of these displacements is presented in Figure 5.11.

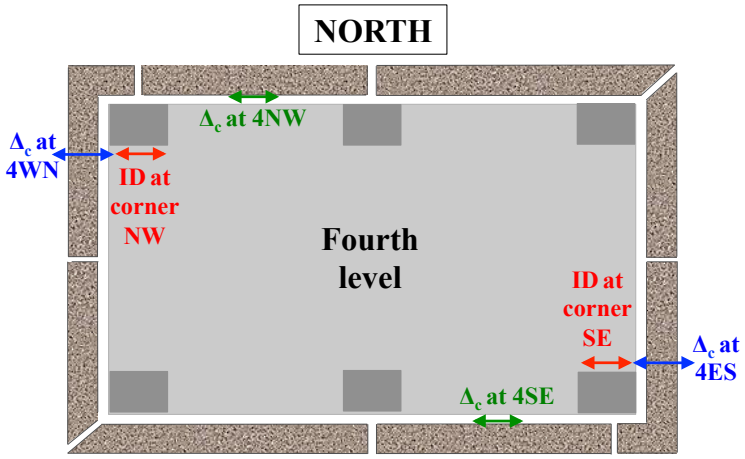

Figure 5.11. Summary of monitored displacements

Figure 5.12a and b show the behavior in the northwest corner. No displacement in the corner connection was recorded before the joint gap closed. The first movement of the connection was at second 33, when the ID was equal to 1'' (exactly the gap size for the butt-return joint). Up to this point, Δ_c and ID were very similar. The first permanent bending of the corner connection in the OP panel occurred at second 38 when ID reached 2'': at this point the corner connection absorbed 0.8'' of total displacement (0.4'' elastic and 0.4'' plastic). The pushing action of the OP and IP panels against each other affected also the movement of the IP panel, since its eastward movement became larger than ID. This might have been caused by a plastic deformation of the rods in the sliding connections.

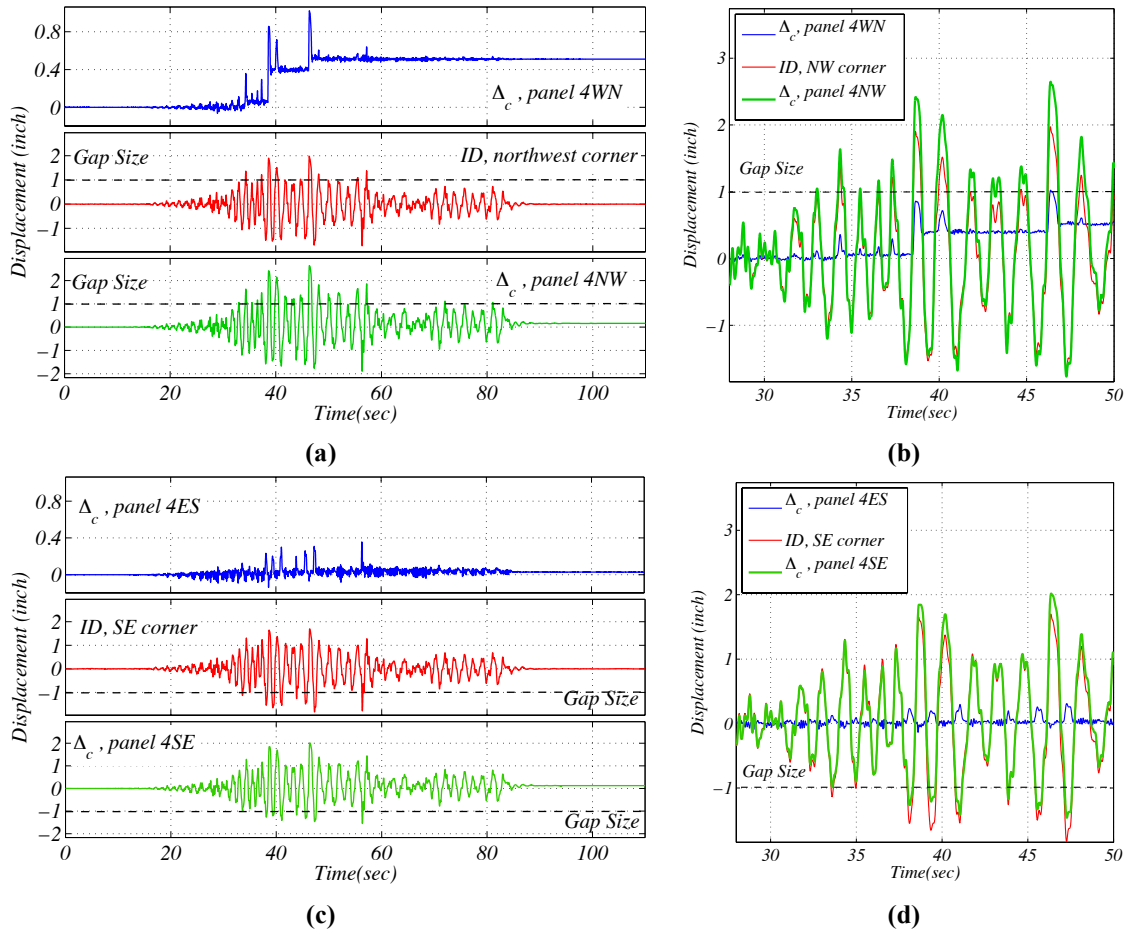

Figure 5.12. Displacements recorded at the corners during FB5: (a),(b) close to the northwest corner at the fourth level (entire time history, zoomed view, (c),(d) close to southeast corner at the fourth floor (entire time history, zoomed view)

The same plots for the southeast corner are shown in Figure 5.12c and d. In similar fashion, no deformation of the corner connection was recorded until the gap in the joint closed completely (ID = -1''). Even if IDs were similar, the behavior in this corner was completely different: in this case, when the OP panel collided with the IP panel (when the building was moving westward), the effect was a deformation of the IP panel. In this case Δ_c remained smaller than 0.35'' and was mainly elastic. The different damage level and recorded behavior of the OP panels in the west and east side of the building can be explained considering the type of IP panel installed on each side: panels with sliding connections were installed on the west side while flexing connections were installed on the east side. Impacts between OP panels at the corner occurred on both sides but only panels on the west side got damaged. A hypothesis for this behavior is as follows:

- West side: collision between OP panels and IP panels with sliding rod connection. In this case, OP panels absorbed the deformation and got damaged, meaning that the deformation mechanism in the IP panels was stiffer than the one in the OP panel. This could have two explanations: either the activation of the sliding mechanism in the IP panel was very stiff or the mechanism was not working properly. This latter explanation seems plausible, since extensive damage to the sliding connections of the fourth floor was reported and showed sliding rods behaving similar to very short ,i.e. stiff, flexing rods;
- East side: impact between OP panels and IP panels with flexing rod connection. In this second case, IP panels ended up absorbing part of the deformation while the OP panel did not get damaged. This demonstrated that the IP panels deformation mechanism was less stiff than that of the OP panels.

These results are presented also in Pantoli et al. 2013d.

5.4 Numerical Analysis of the Corner System Behavior During Collisions Between Panels

A numerical model of a slice of the BNCS building and two corner panels was created in SAP2000 (CSI 2013) to investigate the consequence of the collision of the panels. The main goal of this model was to understand the development of forces in all of the connections in the IP and OP panels due to the variation of several parameters, such as the peak interstory drift and gap size. A number of assumptions regarding the constitutive models of the steel in the connections and concrete in the panels were adopted. For this reason, the study has the goal of providing information only on the order of magnitude of the forces involved, and pointing out issues deserving future investigation.

5.4.1 Past Models of Cladding-Building Systems

This section presents a summary of how past researchers modeled APC cladding panels and connections to be incorporated in a building model. The first numerical models of panels and connections were characterized by a greater level of simplifications. For example, Henry and Roll (1986) created a two-element model, each with four nodes. The connections were modeled as beam elements with three degrees of freedom at each node (two translations and one in-plane rotation).

Another early study incorporating numerical models of the panels and connections is the one conducted by Sack (Sack 1989), which had the goal of analyzing the interaction between cladding and frame. In this study, the structural frame was idealized with beam, truss and spring elements while the façade was idealized as two dimensional panels elements supported at four discrete points. In this case, all the flexibility of the system was localized at the connections, since the panel was assumed to be rigid while only the connections could deform. The stiffness of the connections was determined by experimental data.

In 1989, Raths and Mulholland studied the shearwall effect of precast concrete non-loadbearing panels on a thirty-three story building. The study was divided into two stages. Initially, a refined model of the panel using thin shell elements with six degrees of freedom at each node was used to determine the stiffening effect of the cladding on the frame for a two-story subassembly. Information from this initial study were used to create a simplified "cross" of stick panels models (Figure 5.13).

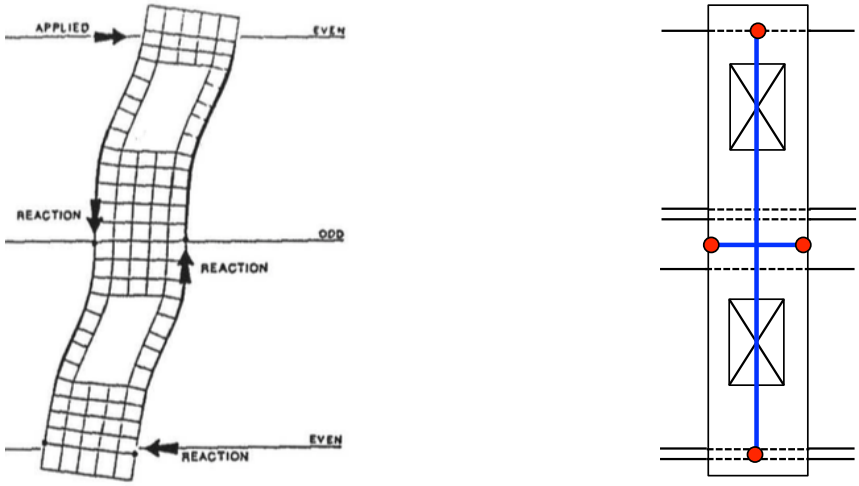

(a) **(b)**

Figure 5.13. Numerical models created by Raths and Mulholland (1989): (a) original refined model and (b) simplified model (Image modified from Raths and Mulholland 1989)

Gaiotti and Smith (1992) created a detailed model of a panel with membrane finite elements. These panels used bearing and sliding connections, which were represented by links having a stiffness calculated theoretically. The stiffness of bearing connections was assumed to be large, while a zero stiffness value was assigned to the sliding tiebacks in the direction of the slot. The authors found that

the stiffening effects of cladding in a bay could be modeled through a strut elements extending diagonally in the space of the panel.

In 2010, Cheung (Cheung 2010) performed a pushover analysis of a one story cladding system. The model was created in SAP2000 and included APC panels, steel connections (panel-to-panel, panel-to-building, panel-to-foundation) and panel joints (Figure 5.14). The APC panels were modeled with thin shell elements, while connections and joints were modeled as linear or nonlinear link elements. The force-relationship assigned to connections was determined experimentally (Figure 5.15a and b). For tieback connections, the force displacement relationship was assigned both in the in out-of-plane and in-plane directions. It is noted that this latter is not intended by design, but still possible. The slotted connections between the top of the cover panel and the spandrel panels had 4'' slots. These were assumed to have the force-displacement behavior shown in Figure 5.15c in the direction of the slot (in-plane horizontal) and to be fixed in the other directions. In addition to model the connections, also the gaps were modeled, namely no interaction was assumed till the gap closes and the adjacent panel touch. Figure 5.15d shows the force-displacement relationship for 0.75'', where the stiffness after the gap closes is assumed to be 160 kips/inch. For the 2'' vertical seismic gap it was assumed that after the gap closed a stiffness of 100 kips/inch was achieved. Bearing connections were modeled as linear connections.

Mohammadi (2014) created a model of APC panels as installed on the BNCS building (Figure 5.16). Namely the author represented the cladding panel, the structural frame and six link elements for the connections. The panel itself was modeled with twenty thin shell elements while the structural frame was modeled using rigid beam elements. Flexing rods were modeled as nonlinear links, defined as multi-linear plastic elements with kinematic hysteretic behavior. The nonlinear behavior was modeled mirroring results from experiments. Bearing connections were modeled as pin connections. To do this, the stiffness assigned to the link elements was very large (10000 kips/inch in all the three translation directions). The pushover analysis allowed determining the maximum forces experienced by the connections as a maximum interstory drift of 3.2'' (2%). Dynamic analyses were run and the amplification ratios of accelerations were determined for several periods of the input sinusoidal motion.

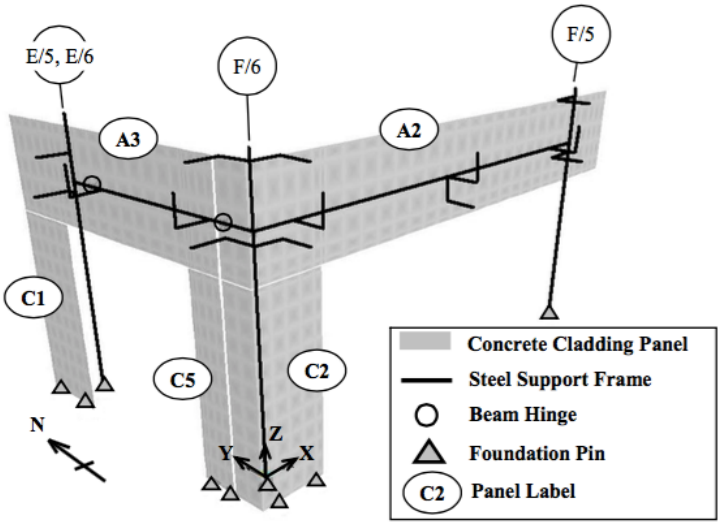

Figure 5.14. Model created by Cheung (2010)

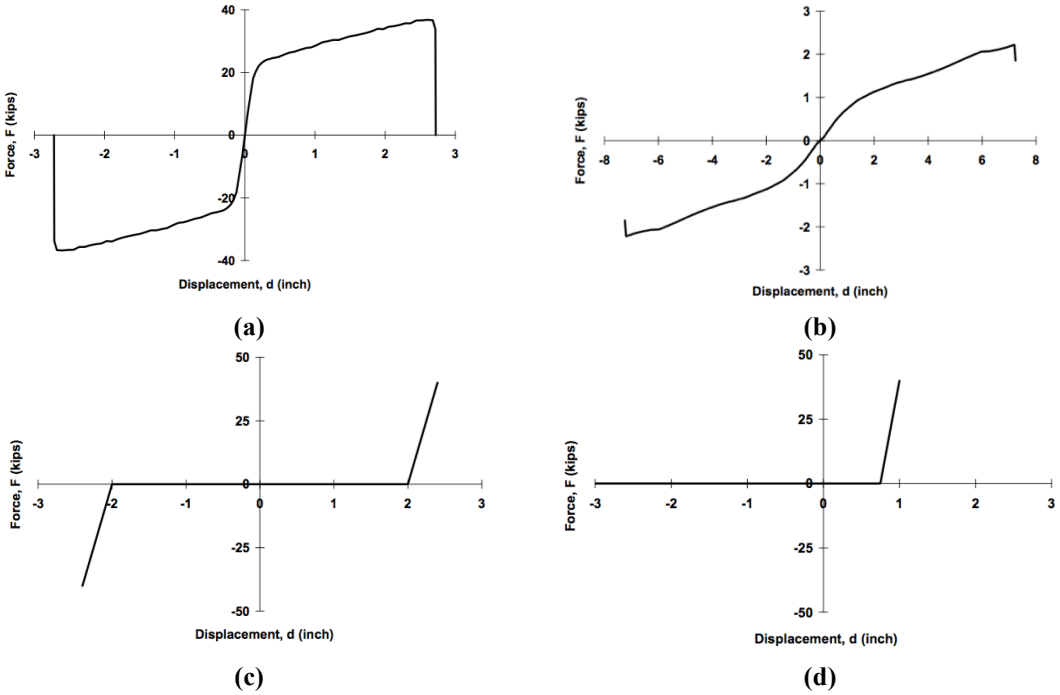

Figure 5.15. Force displacement models reported by Cheung: (a) experimental for the out-of-plane push-pull connections, (b) experimental for the in-plane push-pull connections, (c) model of the 4'' slotted connection, (d) model of the 0.75'' gap (Courtesy of Cheung 2010)

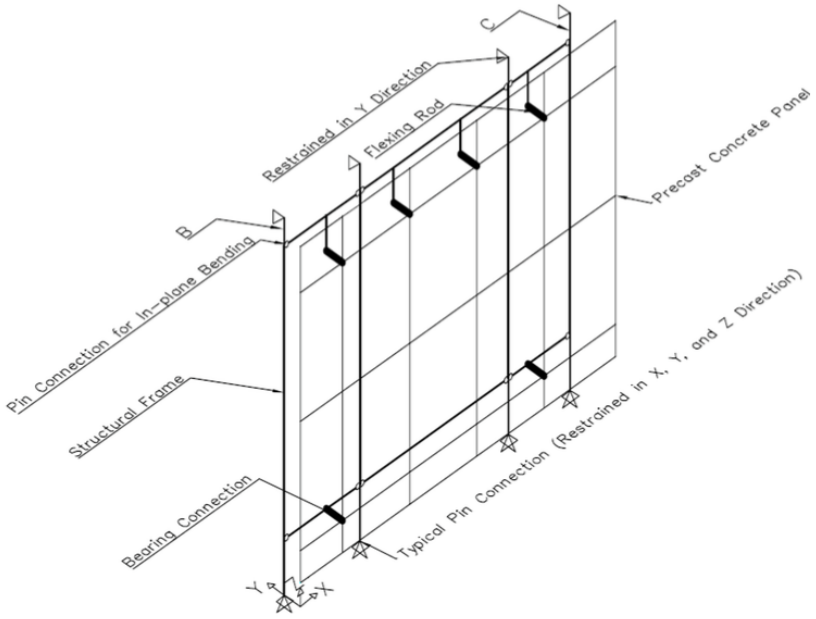

Figure 5.16. Model of the APC panel created by Mohammadi 2014

Baird (2012) created a model of cladding in Ruomoko and integrated it within a frame model. The panel was modeled with quadrilateral elastic elements while the connections were considered as springs attached to points along the beams (Figure 5.17a). Connection springs were characterized by elasto-plastic behavior. The fame elements were represented by elastic elements with inelastic behavior concentrated in the plastic hinge regions. The hysteretic behavior of the model was validated with experimental data, as shown in Figure 5.17b.

5.4.2 Description of the Model

The model used for this analysis included a chunk of a building and two corner panels. The panels were modeled similarly to what was done in several studies performed in the past and described in the previous section: using thin shell elements for the panel and spring (link) elements for the connections and joints. This numerical model was created in SAP2000 and reproduced only the south-eastern side of the fourth story of the BNCS building (Figure 5.18). This location was selected due to the increased availability of experimental data in this area during the BNCS experiment. The structural elements included in the model are the slab at the top and bottom floors, the four columns in the center and eastern edge of the building, two structural beams per floor and the two eastern beams supporting

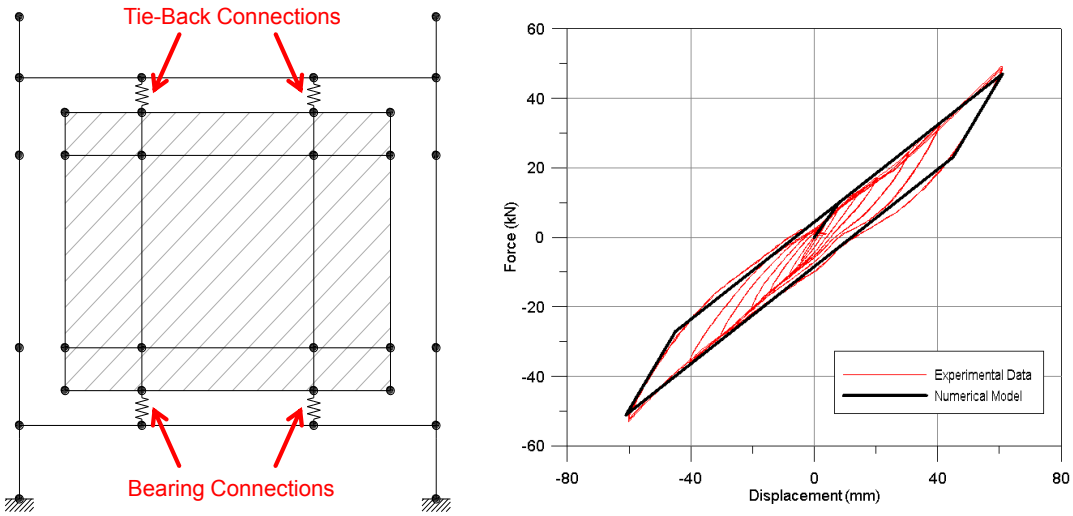

Figure 5.17. Model created by Baird (2012): (a) frame and panel model, and (b) hysteretic behavior

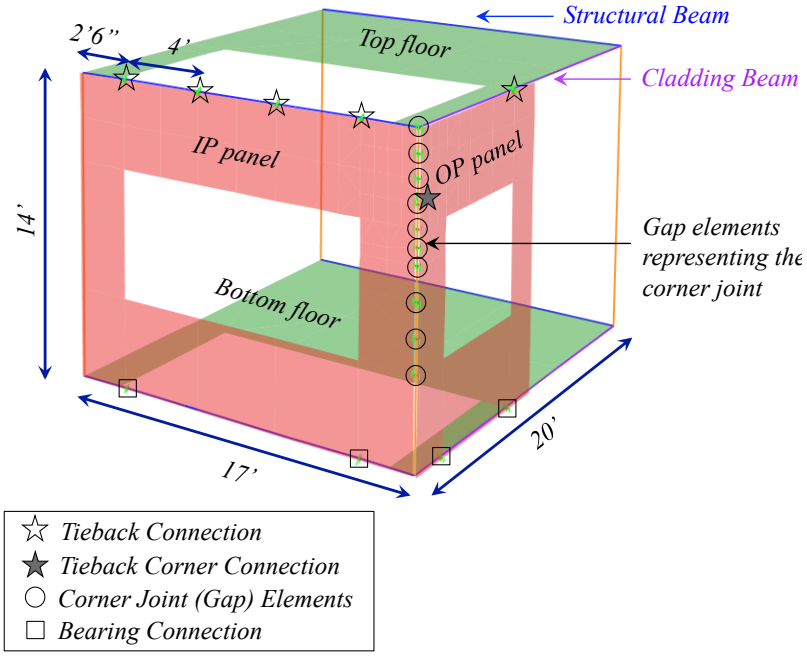

Figure 5.18. Model of the chunk of the building considered and panels

the cladding. The slab was modeled with this shell elements (8'' thick) while the beams and column with frame elements. The geometry of the elements and material properties reproduces the real one, as described in Chapter 7. Two APC cladding panels are included in the model: the southern panel of the

eastern side and the western panel on the southern edge. The panels are modeled with thin shell elements. The tieback and bearing connections are modeled as link elements with an assigned stiffness or force-displacement behavior. The corner joint is modeled as a gap element. Further details about the models of panels and connections are reported in the following sections. This model is composed by 277 nodes, 29 frame elements, 207 thin shell elements, and 22 links.

Panels

The panels were modeled with the actual geometry of the panels installed on the fourth story of the BNCS building. It is noted that it was not possible to model the return in the OP panel, since the return spanned over the depth of the column, which is not present in the model since the column is reproduced as a frame element. Results can still be considered reliable since the main effect of the return was to stiffen the corner of the OP panel and avoid excessive cracking at that location. However, the model in SAP2000 does not reproduce the cracking of the concrete and thus it is considered appropriate to omit the presence of the return. The concrete used in the panel was a 5000 psi concrete mix (E=4030 ksi). It was considered to behave linearly, with a stiffness reduction factor applied to the Young modulus of the material equal to 0.7, as suggested by the ACI manual for un-cracked walls in compression. In this case the wall is not in compression, but this factor was used since it was the highest one, but still reduces the stiffness due to some cracking probably present in the panels. E was reduced from 4030 ksi to 2821 ksi. Since the cracking of the panels is not directly considered, this model cannot be extended to panels with miter joints, since they experienced considerable cracking of the panels.

Corner Joint

The corner joint was modeled using an array of gap element links connecting the IP and OP panels and acting axially. The opening of the gap was assigned to be 1'' as the nominal opening of the gap, while the non-linear stiffness after the gap closes was assumed to be 1000 kip/inch. This number was chosen because very large but still small enough not to create numerical instabilities of the model. Twelve gap elements were distributed throughout the length of the corner joint, each one having the same constitutive behavior.

Bearing Connections

Bearing connections in both the IP and OP panels were assumed to behave linearly, with the stiffness of the connection determined through detailed numerical models (see Chapter 6). Three different values of stiffness had to be assumed in the three directions: in-plane vertical (k_{IPv}), in-plane horizontal (k_{IPh}) and out-of-plane (k_{OP}). For the connections in panels 4ES, the stiffness used was k_{IPh}=9600 kips/inch; k_{OP}=11000 kips/inch; k_{IPv}=1690 kip/inch; while for the connections in panel 4SE the vales of stiffness were k_{IPh}=9600 kips/inch; k_{OP}=11000 kips/inch; k_{IPv}=507kip/inch.

Corner Connection with Ductile Fuse

The corner connection with ductile fuse was formed by two elements in series: a 29'' long 1'' diameter rod and a bending plate acting as ductile fuse. The flexibility of the system is dominated by the rod in the IP_v and IP_h directions and by the plate in the OP direction. The IP_v and IP_h behaviors are in this case not relevant since there is no input to the connection in these direction. For this reason the connection was assumed to be linear elastic in these two directions. The values of stiffness in these two direction $k_{IP,h}$ and $k_{IP,v}$ was found with easy theoretical calculations on the bending rod:

$$k_{IP,h} = k_{IP,v} = \frac{3EI}{L^3} = 0.1 kips/inch$$

More relevant in this case is the behavior in the OP direction, which is simplified as multi-linear elastic. Since experimental data were available only for low levels of displacement, the total force-displacement curve was obtained by matching the experimental values at low drifts and with theoretical calculations at large drifts. The experimental force-displacement in the connection measured during FB6 and the force-displacement behavior adopted in the model can be seen in Figure 5.19. It is noted that the initial segment of lower stiffness is probably created by the concrete, while from a force of around 2 kips the behavior appears to be dominated by the steel of the ductile fuse.

The ultimate force and drift F_u and Δ_u were found with theoretical calculations by determining the behavior of the bending plate only, since the rod acting axially can be considered rigid. Figure 5.20a shows the geometry of the plate. The steel utilized was A36 Grade 50 (f_y=50 ksi, f_u= 65 ksi, ultimate elongation=17%). However, the actual properties are specified to be 1.25 times the nominal ones. Thus the f_y and f_u used in the model were 62.5 and 81.2 ksi, respectively. Figure 5.20b presents the moment

curvature diagram of the cross section created with the section designer tool in SAP2000.

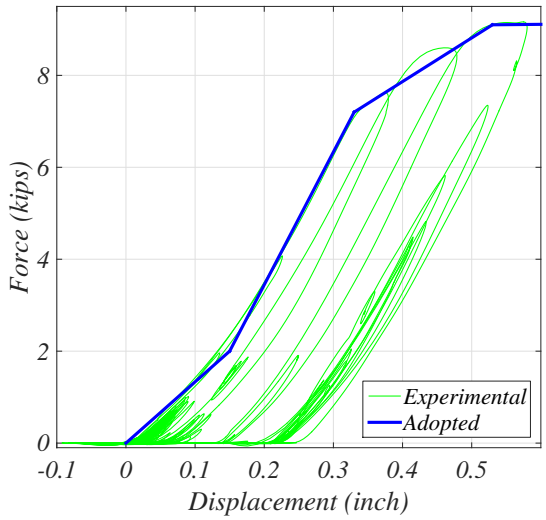

Figure 5.19. Comparison between experimental and adopted force-displacement behavior for the corner connections for FB6 for small displacements

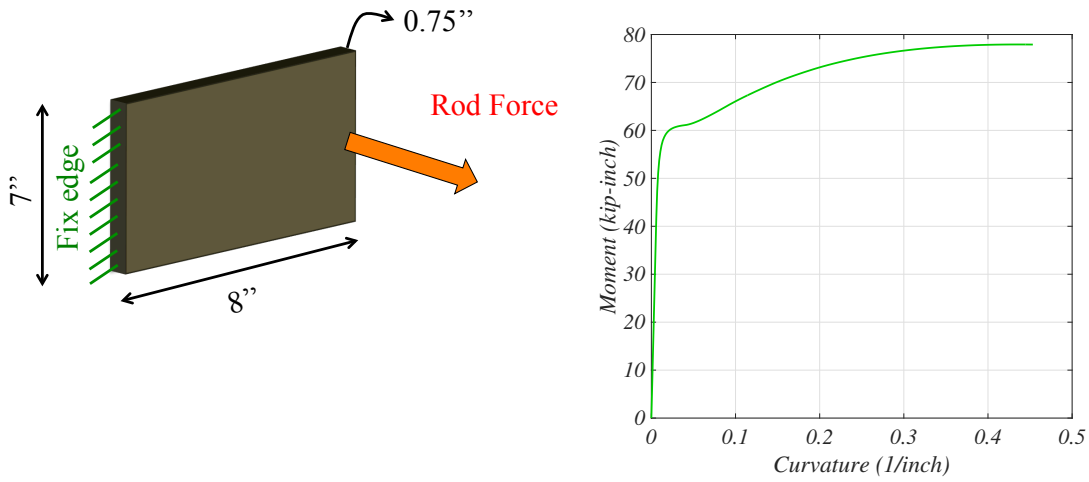

(a) **(b)**

Figure 5.20. Corner connection in the OP panel: (a) geometry of the ductile fuse and (b) moment-curvature behavior of the fuse

The theoretical values of the yield and ultimate moment can be found to confirm those found with SAP2000 as:

$$M_y = f_y \cdot \frac{Area}{2} \cdot \frac{Thickness}{2} = 62.5 \cdot \frac{7 \cdot 0.75}{2} \cdot \frac{0.75}{2} = 61.5 kip \cdot inch$$

$$M_u = f_u \cdot \frac{Area}{2} \cdot \frac{Thickness}{2} = 81.2 \cdot \frac{7 \cdot 0.75}{2} \cdot \frac{0.75}{2} = 80.0 kip \cdot inch$$

The other relative quantities found theoretically include the yield force F_y and the ultimate force F_u, which can be easily found since the arm is known:

$$F_y = \frac{M_y}{8"} = 7.7kips$$

$$F_u = \frac{M_u}{8"} = 10kips$$

The yield curvature χ_y and the ultimate curvature χ_u were found in the section designer tool in SAP2000 (Figure 5.20b) as:

$$\chi_y = 0.02\frac{1}{inch}$$

$$\chi_u = 0.45\frac{1}{inch}$$

The yield displacement Δ_y, the length of the plastic hinge l_p the plastic drift Δ_y and the ultimate drift Δ_u and are found using the classic theory for plastic behavior of steel (Bruneau et al. 1998):

$$\Delta_y = \frac{\chi_y \cdot l^2}{3} = 0.42inch$$

$$l_p = l \cdot \frac{M_u - M_y}{M_u} = 1.85inch$$

$$\Delta_p = \left(\chi_u - \chi_y\right) \cdot l_p \cdot \left(l - l_p\right) = 4.89inch$$

$$\Delta_u = \Delta_y + \Delta_p = 6.74inch$$

These theoretical calculations predict the yield force at 7.7 kips, which is close to the experimental values of the initial yielding shown in Figure 5.19. However, the theoretical calculation slightly over predicts the yield displacement. The complete force-displacement behavior of the connection as created by the following four segments (Figure 5.21):

1. Displacement: 0'' to 0.15''; Force: 0'' to 2 kips: (k=13.3 kips/inch);
2. Displacement: 0.15'' to 0.33''; Force: 2 kips to 7.2 kips: (k=29 kips/inch);

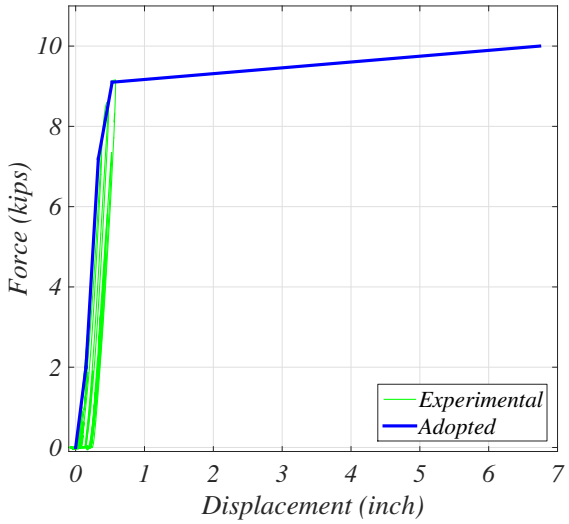

Figure 5.21. Comparison between experimental and adopted force-displacement behavior for the corner connections for FB6 (entire curve)

1. Displacement: 0.33'' to 0.53''; Force: 7.2 kips to 9.1 kips: (k=9.5 kips/inch);
2. Displacement: 0.53'' to 6.74''; Force: 9.1 kips to 10 kips.

After this behavior was identified, it was decided to compare this force-displacement curve with the hysteresis loop developed during FB5, and this is shown in Figure 5.22. Figure 5.22a shows that the initial stiffness was slightly larger for FB5, confirming the hypothesis that the initial stiffness of the connection of dominated by concrete. However, the global force-displacement plot (Figure 5.22b) shows that the adopted behavior is a good approximation overall.

Tieback Connections - OP Direction

In the OP direction, the tieback connections were assigned a multi-linear elastic behavior, whose force-deformation behavior was found with theoretical calculations. In this direction, the flexibility of the connection is provided by two elements in series: the 12'' rod deforming axially and the vertical leg of the connection angle, which is bending. Due to the large difference in stiffness of these two elements, it is assumed that the OP flexibility of the connection is completely provided by the bending angle. This angle had a cross section of 7'' by 0.5''. The assumed length of the leg was equal to the distance between the edge of the angle and the theoretical location of the rod, which was 2.75'' below the point of attachment (Figure 5.23a). The properties of the steel of the angle were found in the

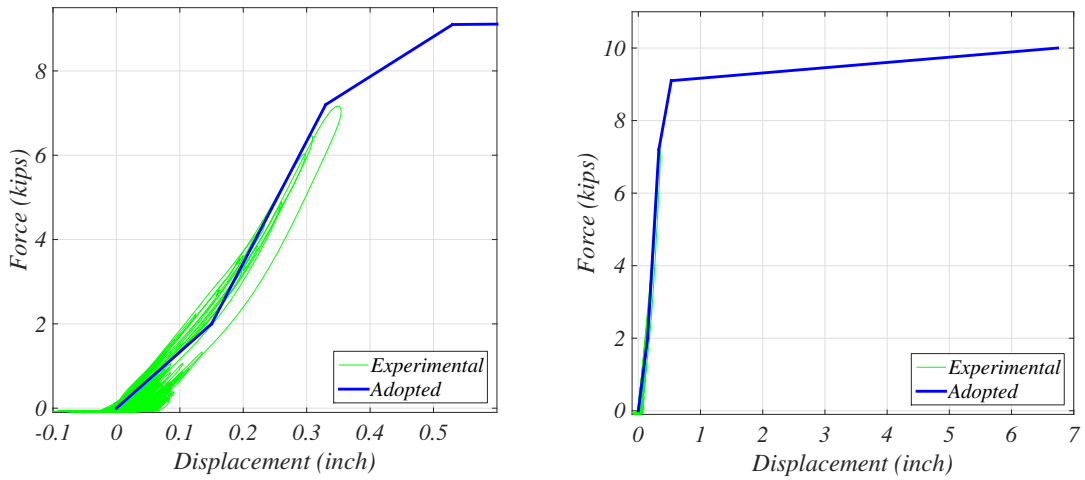

Figure 5.22. Comparison between experimental and adopted force-displacement behavior for the corner connections during FB5 (a) for low drifts and (b) for all drifts

construction drawings as those of ASTM A572 Grade 50 steel (typically f_y=50 ksi, f_u= 65 ksi, ultimate elongation=17%). The moment curvature behavior of the leg was determined in the Section Designer tool in SAP2000 and it is shown in Figure 5.23b. The values of the yield and ultimate moment M_y and M_u can be confirmed with theoretical calculations:

$$M_y = f_y \cdot \frac{Area}{2} \cdot \frac{Thickness}{2} = 50 \cdot \frac{7 \cdot 0.5}{2} \cdot \frac{0.5}{2} = 21.9 kip \cdot inch$$

$$M_u = f_u \cdot \frac{Area}{2} \cdot \frac{Thickness}{2} = 65 \cdot \frac{7 \cdot 0.5}{2} \cdot \frac{0.5}{2} = 28.4 kip \cdot inch$$

These values are clearly very similar to those found in SAP2000. Since the plate is a cantilever, and the length of the arm is known, it is possible to find the values of the yield and ultimate force F_y and F_u:

$$F_y = \frac{M_y}{2.75"} = 7.9 kip \cdot inch$$

$$F_u = \frac{M_u}{2.75"} = 10.3 kip \cdot inch$$

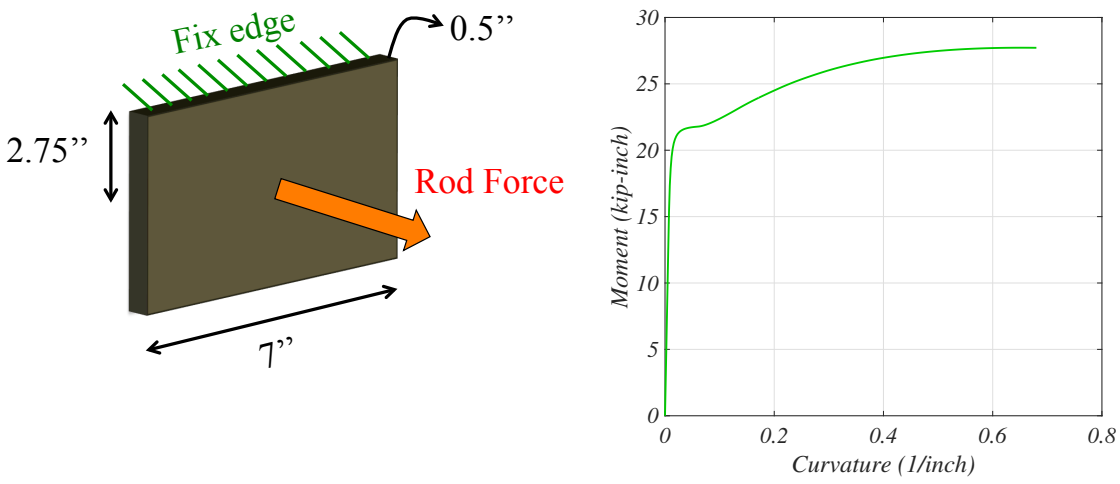

(a) **(b)**

Figure 5.23. Inner connection in the OP panel: (a) geometry of the flexing leg of the angle and (b) moment-curvature behavior of that leg

The values of the yield and ultimate curvature χ_y and χ_u found from the Section Designer tool in SAP2000 were used to determine the yield displacement Δ_y and the ultimate displacement Δ_u. These were found though the values of the plastic hinge length l_p and plastic displacement Δ_p using the classic theory for plastic behavior of steel:

$$\chi_y = 0.0282 \frac{1}{inch}$$

$$\chi_u = 0.68 \frac{1}{inch}$$

$$\Delta_y = \frac{\chi_y \cdot l^2}{3} = 0.07 inch$$

$$l_p = l \cdot \frac{M_u - M_y}{M_u} = 0.63 inch$$

$$\Delta_p = \left(\chi_u - \chi_y\right) \cdot l_p \cdot \left(l - l_p\right) = 0.87 inch$$

$$\Delta_u = \Delta_y + \Delta_p = 0.94 inch$$

The values of F_y, F_u, Δ_y and Δ_u were used to define the properties of the axial behavior of this connection. As a final check for this behavior, the axial stress and elongation of the 12’’ rod at the forces F_y and F_u were checked:

$$\sigma_{@PlateYield} = \frac{F_y}{A} = \frac{7.9}{0.332} = 23.8ksi$$

$$\sigma_{@UltimateStrenghtPlate} = \frac{F_u}{A} = \frac{10.3}{0.332} = 31.0ksi$$

Hence the rod does not yield at the limit states of the plate. At those values of forces the elongations of the rod are:

$$\Delta_{@PlateYield} = \frac{F_y L}{EA} = \frac{7.9 \cdot 12}{29000 \cdot 0.332} = 0.01inch$$

$$\Delta_{@UltimateStrengthPlate} = \frac{F_u L}{EA} = \frac{10.3 \cdot 12}{29000 \cdot 0.332} = 0.012inch$$

Clearly these values are negligible, and the presence of the rod can be ignored.

Tieback Connections : IP Direction

The rods dominate the behavior of the connections in this direction. During the BNCS test it was observed that there are three possible behaviors of the flexing rod in the IP direction (Figure 5.24):

1) The rod remains elastic. This is plausible especially for the long rods installed at the upper floors, where displacements were small;
2) The rod undergoes some type of plastic deformation, but then it bends back to its original position. This possibility is confirmed by the fact that no residual displacement in the IP panels was observed. This effect is created by the inertia mass of the panel, which is rocking on the two vertical flexible connections. Since those connections generally remain elastic, they bring the panel back to its original position, and no residual deformation of the rod is observed;
3) The rod undergoes some type of plastic deformation, it slides inside the over-sizes installation hole, and residual bending is observed after the earthquake. This sliding can happened while the rod is still elastic or already in the plastic zone, with the latter behavior considered more plausible. The unloading can present some level of sliding back or not.

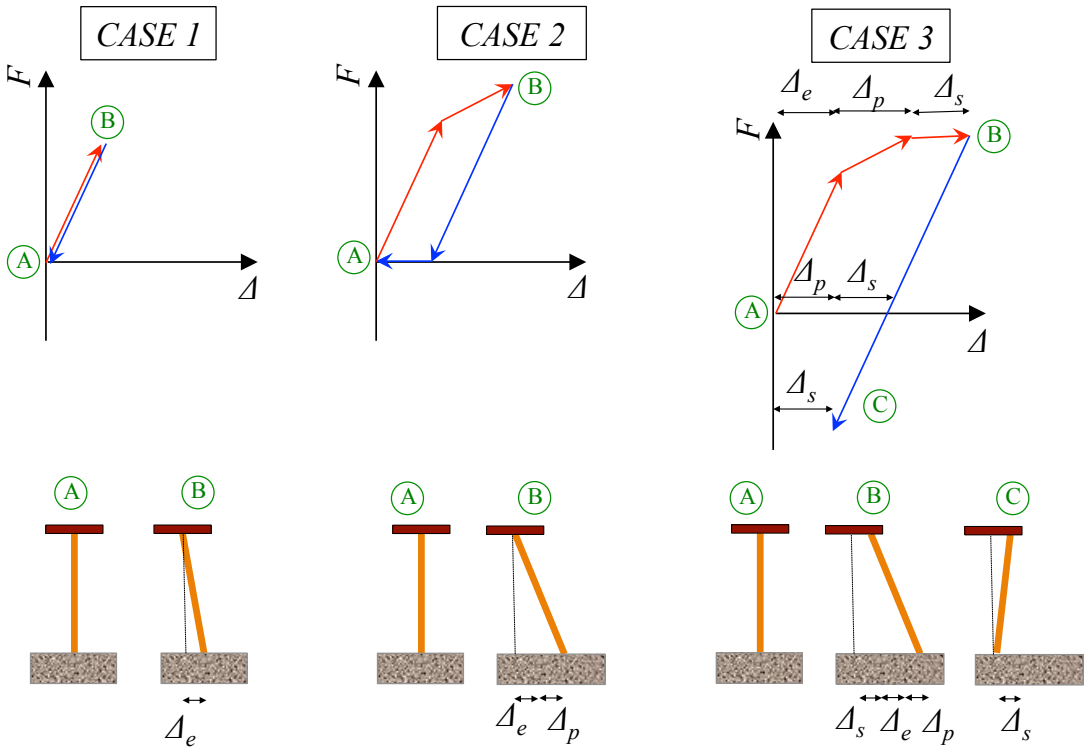

Figure 5.24. Summary of the possible behaviors of tiebacks in the IP panels

Since SAP2000 offers a limited choice of constitutive behaviors for link elements, it was decided to consider either the multi-linear elastic of the multi-linear plastic. Both behaviors ignore the sliding, which happened only in some cases and it is very difficult to characterize. The multi-linear elastic behavior was selected since it did not present residual deformation on the panels at the end of the earthquake, as in reality. However, it did not consider the dissipation of energy in the connection.

The next step was to define the force-displacement behavior of the three types of flexing rods. Force-displacement experimental data obtained from a cyclic test on the same type of rod were available thanks to the series of tests on flexing connections performed at SJSU and presented in Chapter 3. Unfortunately, those data had two main limitations: they were available only for 16'' and 20'' long rods, and they did not provide information on the ultimate values of force and displacement. Thus theoretical calculations had to be performed to find those missing pieces of information.

The values of the yield force and displacement of the 12'' long rod were estimated starting from the values of F_y and Δ_y found experimentally for the longer rods. The force-displacement plot for

the first cycle of the test and their multi-linear simplification is presented in Figure 5.25. From these plots it is possible to identify the values of the yield force and displacement at 1.45 kips and 2.1'' and 1.05 kips and 2.6'' for rods 16'' and 20'' long, respectively.

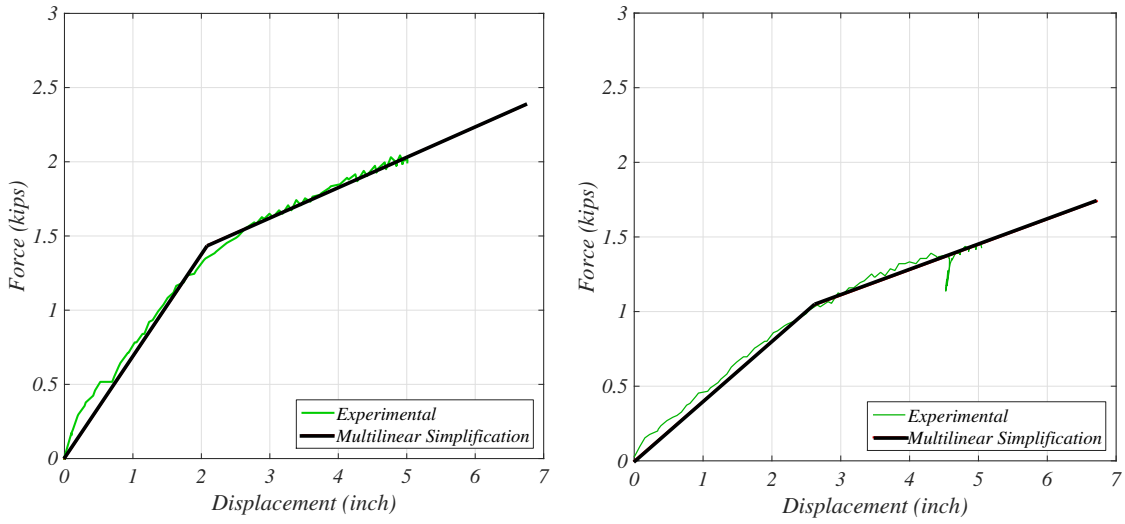

(a) **(b)**

Figure 5.25. Force-displacement experimental results for (a) a 16'' long rod and (b) a 20'' long rod

The yield force for a 12'' long rod was estimated by calculating the experimental yield moment for the longer rods considering fix-fix boundary conditions:

$$M_{y,16} = \frac{F_y L}{2} = 11.6 kip \cdot inch$$

$$M_{y,20} = \frac{F_y L}{2} = 10.5 kip \cdot inch$$

As expected, the two values are similar. The M_y for the 12'' long rod was assumed to be the average of the ones previously found (11 kip•inch) and thus it was possible to calculate the value of the yield force as:

$$F_{y,12} = \frac{2M_y}{L} = 1.8 kips$$

To find the yield displacement, it was first noticed that theoretical formulas applied to the experimental values were able to predict the values of Δ_y starting from F_y. Namely:

$$\Delta_{y,16} = \frac{F_y l^3}{12EI} = \frac{1.45 \cdot 16^3}{12 \cdot 29000 \cdot 0.0087} = 2.0"$$

$$\Delta_{y,20} = \frac{F_y l^3}{12EI} = \frac{1.05 \cdot 20^3}{12 \cdot 29000 \cdot 0.0087} = 2.8"$$

Thus the yield displacement for the unknown case was found applying the same formula:

$$\Delta_{y,12} = \frac{F_y l^3}{12EI} = \frac{1.8 \cdot 12^3}{12 \cdot 29000 \cdot 0.0087} = 1.0"$$

A similar approach was used to determine the post-yield stiffness of the short rods: in this case it was assumed that the ratio of the pre-yield and post-yield stiffness would remain roughly the same. The values of pre-yield and post yield stiffness were 0.69 kips/inch and 0.19 kips/inch for the 16'' long rod and 0.40 kips/inch and 0.17 kips/inch for the 20'' long rod. The ratio of the post-yield versus the pre-yield stiffness was 0.41 and 0.28 respectively. For the short rod, the ratio between the two stiffnesses was assumed to be the average of those previously found (0.35 kips/inch). With a pre-yield stiffness of 1.8 kips/inch, the post-yield stiffness was found to be 0.63 kips/inch. It was assumed that none of the rods reached fracture, and that the maximum displacement in the connection was the one corresponding to a drift of 3% (5''). The final force-displacement values for the three connections are shown in Figure 5.26. The reason why the 12'' long rod appears much stiffer than the other two is that, in the calculations of Δ_y, the length of the rod is cubed, and thus the results are very different.

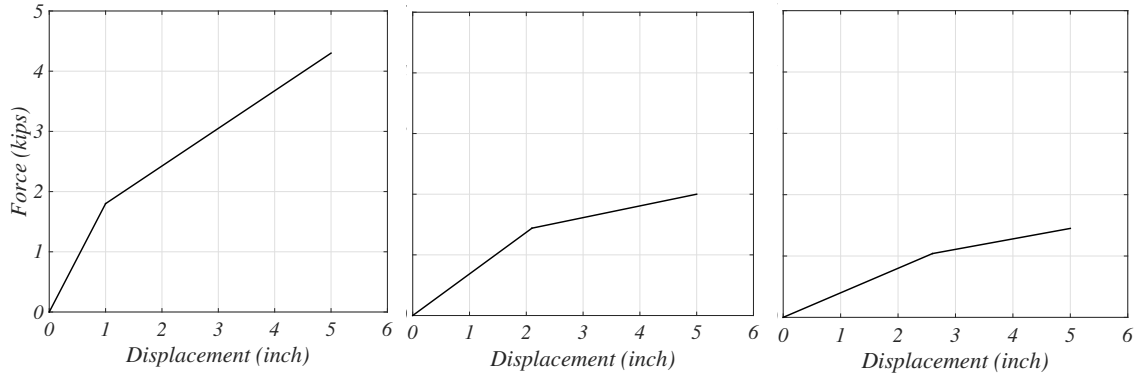

Figure 5.26. Force-displacement behavior up to a displacement of 5'' for rods (a) 12'' long, (b) 16'' long and (c) 20'' long

Type of Analysis

A nonlinear dynamic analysis was run. The loading applied was an interstory drift, which was imposed at the top of the four columns, while the bottom of the columns were considered fixed (Figure 5.27). The solution was found through direct integration solved with Newmark method (γ=0.5; β=0.25). The solution parameters were varied to have a good compromise between having stable results and reducing the solution time. The step size was fixed to 0.002 seconds, with a relative iteration tolerance of 0.005.

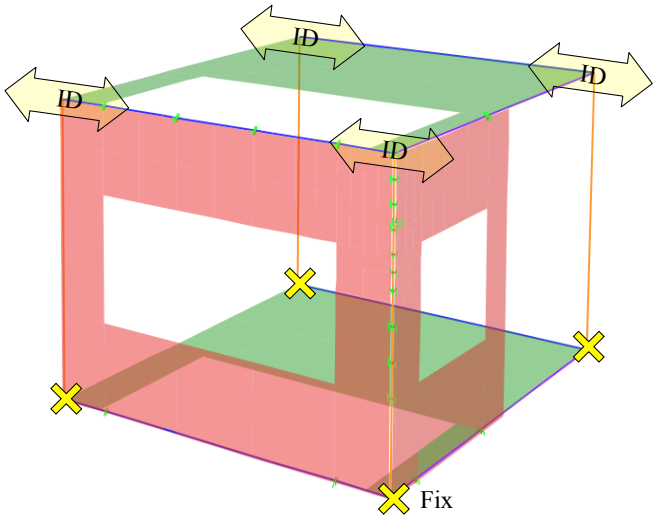

Figure 5.27. Loading applied to the model

5.4.3 Validation of the Model

Numerical and Experimental Forces in the Corner Connection

Impact forces in the corner connections (for panels with butt-return joints) were measured only in panel 4ES during FB5 and FB6, and for this reason only the data relative to those tests could be used to validate the numerical model. The first quality-check of results from the model consisted in the comparison of the time histories and peaks of the forces in the corner connection in the OP panels. Figure 5.28 and Figure 5.29 present the time history of the forces in the corner connection and the comparison of the peaks larger than 2 kips for FB5 and FB6, respectively. These plots show that the model does generally a good job predicting the forces in the connections. Results are slightly better for FB6 than for FB5, probably because the force-displacement behavior of the corner connection was

defined based on the hysteresis loop developed during FB6. Figure 5.30 presents the comparison of experimental and numerical values of the displacement in the connection (Δ_c) for FB5 and FB6. The comparison is good in both cases, however it is clear that the model cannot capture residual deformations, since the connection is modeled as elastic.

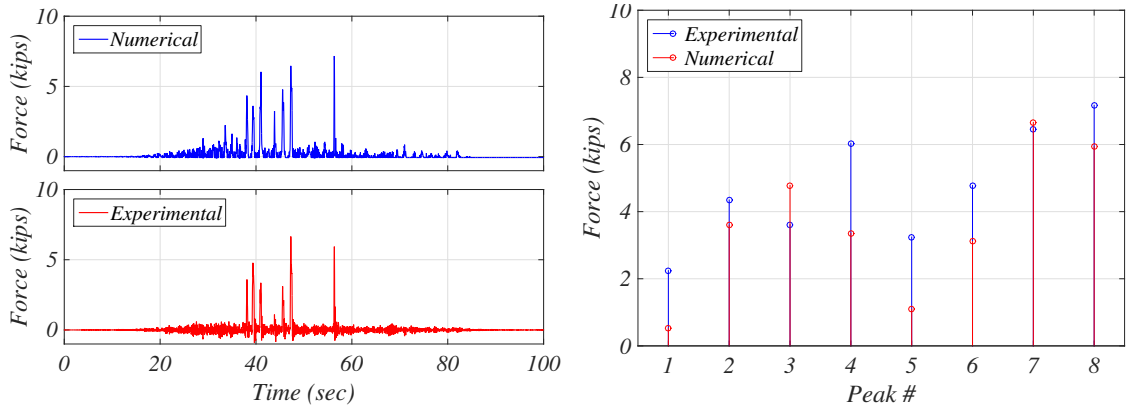

Figure 5.28. Comparison of the numerical and experimental values for FB5: (a) time history and (b) peaks

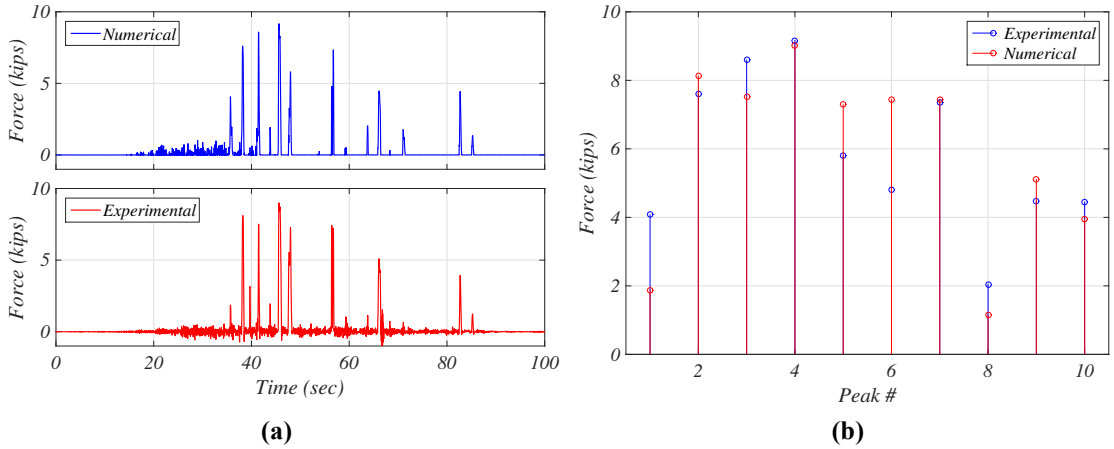

Figure 5.29. Comparison of the numerical and experimental values for FB6: (a) time history and (b) peaks

Frequency Content of Collision Forces

A second quality-check for the results of the numerical model was performed by filtering the time history of the forces with 4th order low-pass Butterworth filters with different corner frequencies f_c, to make sure the contact between the panels in the numerical model did not create instabilities and high-frequency peaks. The comparison of the time histories and peak of forces filtered at different

frequencies is presented in Figure 5.31. These plots clearly show that there is a minimal effect of high frequencies in the results. However, the filter at 10 Hz attenuates the few numerical problems created by the collision, such as those seen after the impact at second 66. For this reason, the low-pass filter with f_c at 10 Hz is used in the rest of the analysis.

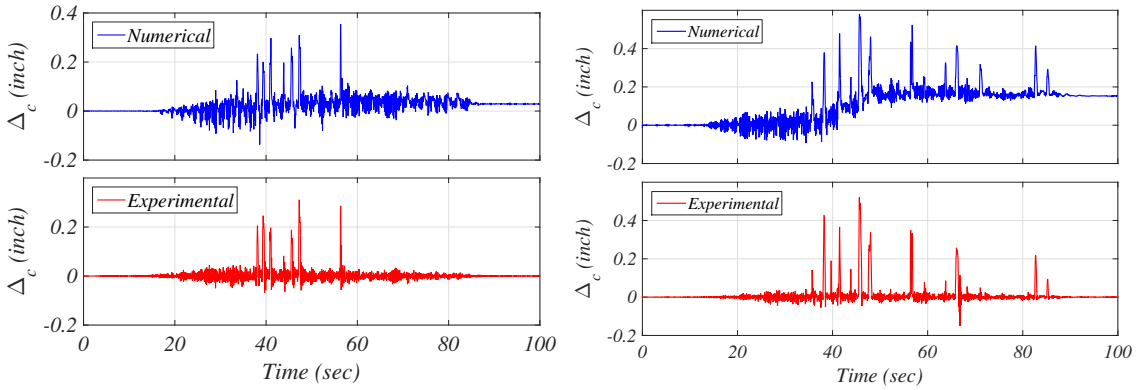

Figure 5.30. Comparison of experimental and numerical values of the displacement in the corner connection Δ_c for (a) FB5 and (b) FB6

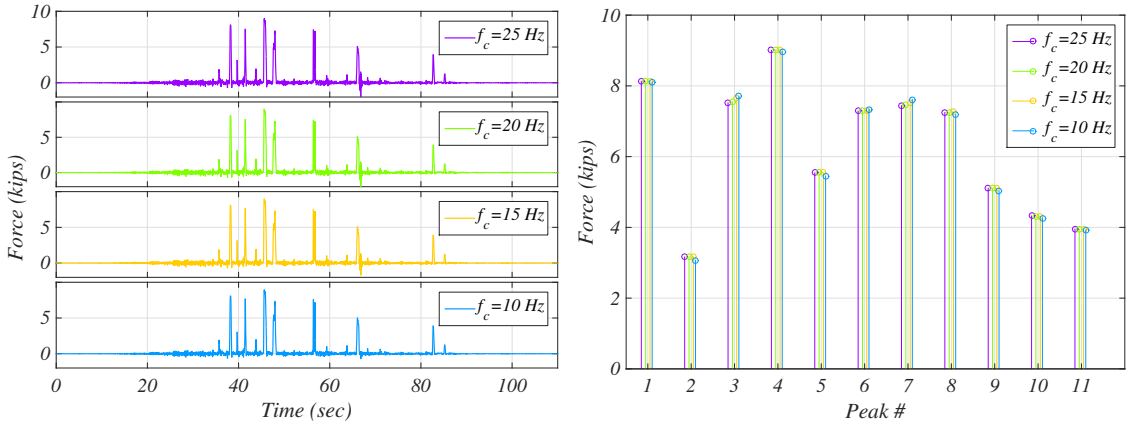

Figure 5.31. Comparison of numerical results filtered with low-pass filters with different corner frequencies

5.4.4 Forces Developed in the Connections During FB6

OP Panel

This analysis uses as input the interstory drift at the fourth level during FB6, and has the goal of understanding the magnitude of forces developed in all the connections during impacts. The geometry of the OP panel, location and nomenclature of the four connections is presented Figure 5.32.

Figure 5.33 shows the time history of the forces in the four connections during FB6. The largest forces are created in the corner connection, since this is closer to the location of the impact. The spikes in forces F_A, F_B and F_C are positive, meaning that there is tension in the connections during the impact. However, the force in the connection in the lower northern corner (F_D) has negative spikes, meaning that the impact is creating compression in this corner.

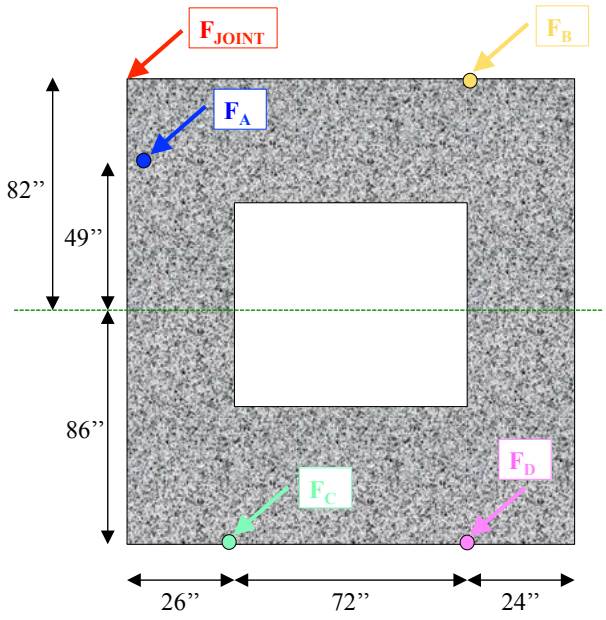

Figure 5.32. Geometry of the panel and location of the forces from the connections

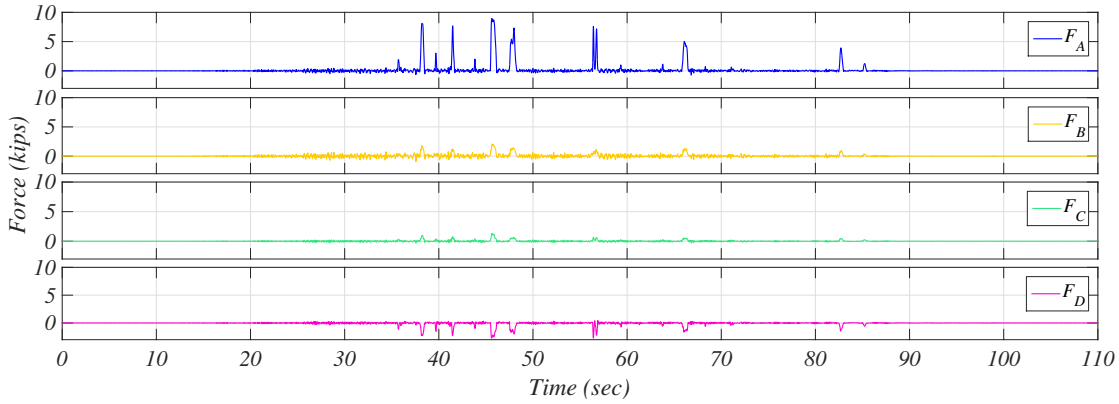

Figure 5.33. Forces in the four connections in the OP panel during FB6

The hysteretic behavior of the two tiebacks is shown in Figure 5.34. This plot shows that, while the corner connection yields, the forces and displacements in the inner tieback connection remain small and within the elastic range. It is noted that the two plots have the same scale.

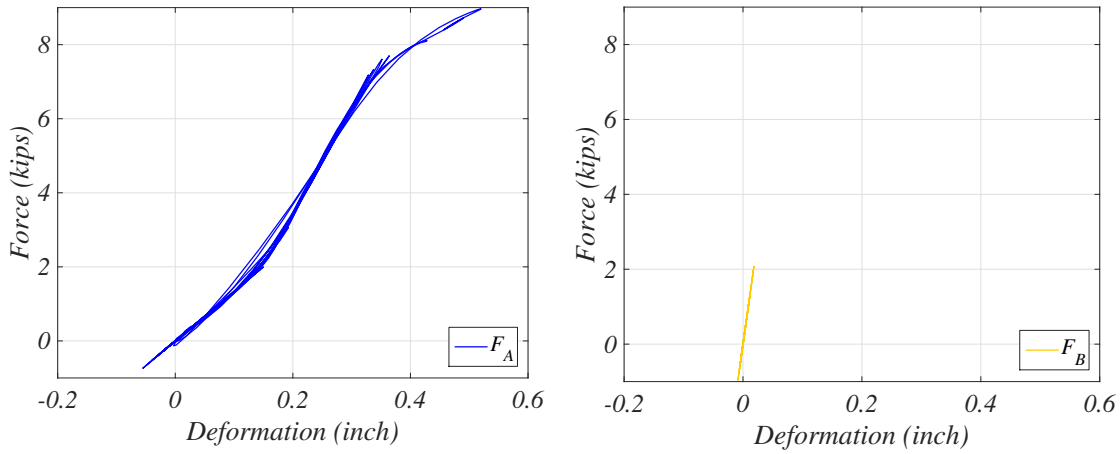

Figure 5.34. Force-deformation of the tieback connections in the OP panel: (a) F_A, and (b) F_B

IP Panel

Figure 5.35 shows the geometry of the IP panels and the location and nomenclature of the forces applied by connections and corner joint. Figure 5.36a presents the time history of horizontal forces in the bearing connections. These forces are in the same direction, and their magnitude is quite large, reaching a peak of 8.9 kips.

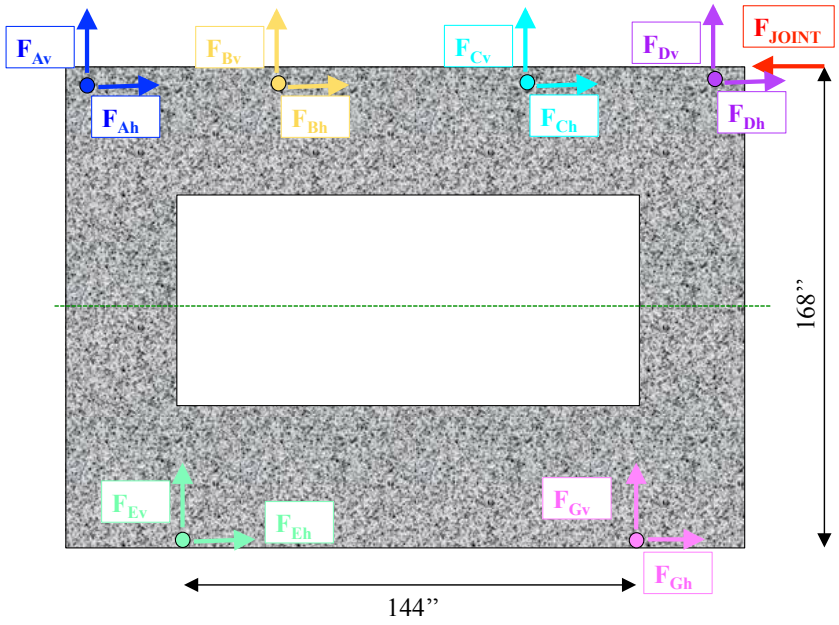

Figure 5.35. Geometry of the panel and nomenclature of forces in the IP panel

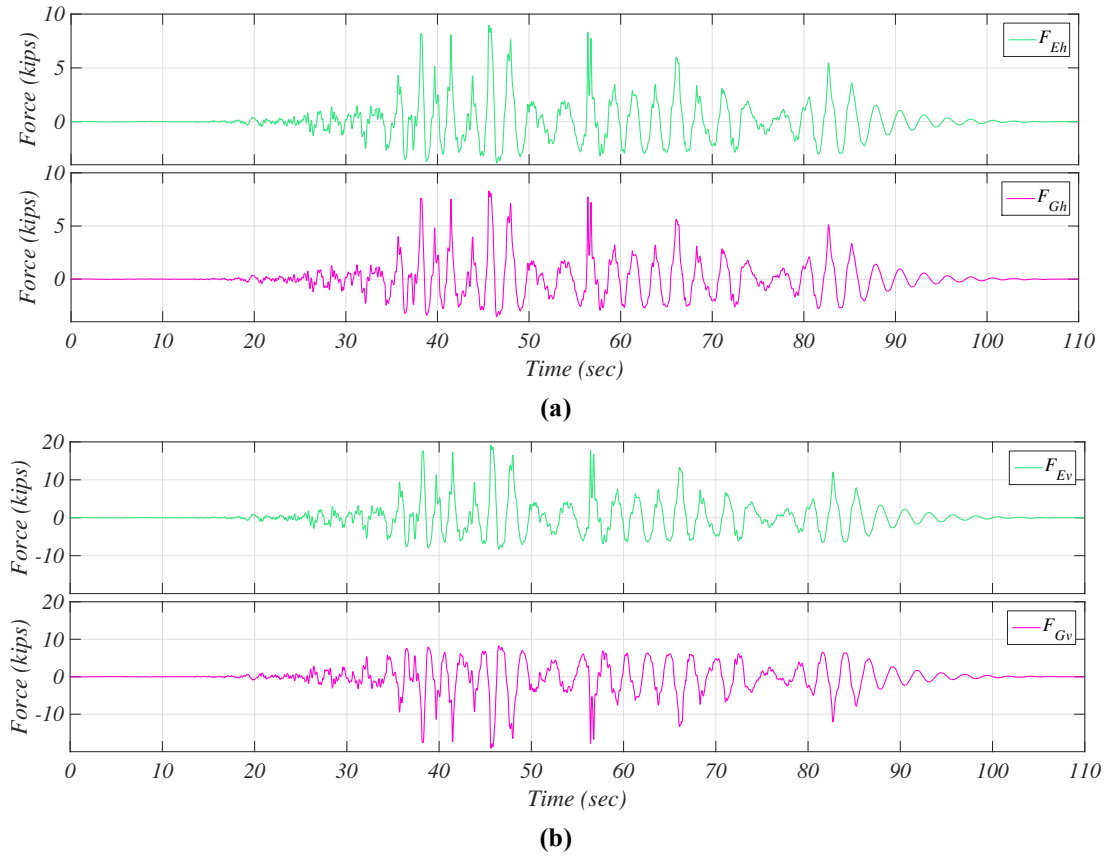

Figure 5.36. Force in the IP bearing connections during FB6 in the (a) horizontal direction and (b) vertical direction

The time history of the vertical forces in the bearings is reported in Figure 5.36b. In this case the direction of the force in the two bearings is opposite, due to the rocking of the panel. Dynamic forces in the vertical direction are large, reaching peaks of 19.1 kips. This value is even larger than the total weight of the panel. These large values of forces might be caused by the fact that bearing connections are modeled as linear, however nonlinearities might occur and limit the peak forces. Figure 5.37a and b presents the forces in the tieback connections in the horizontal and vertical directions, respectively. Forces are larger in the outer connections, which have shorter rods and thus are stiffer. Imposed displacements in the horizontal directions are large enough to create yielding in the rods, while displacement and forces remain small in the vertical direction. Forces in the tiebacks appears to be dominated by the movement of the panel and not by the collisions. Thus, it can be assumed that the extra forces created by the collisions are mostly taken by the bearings. The hysteretic behavior of the four tiebacks in the IP panel is presented in Figure 5.38. Only the two short connections in the outer

edge of the panels reached yielding during FB6, while the inner connections remained elastic.

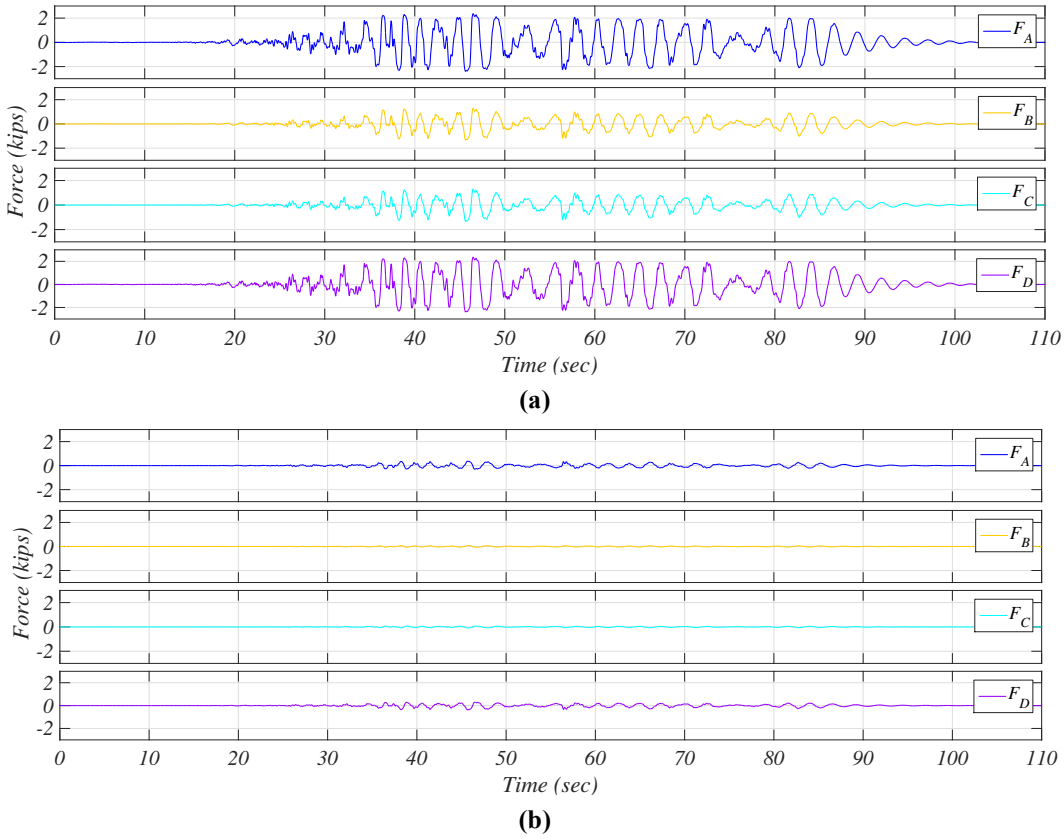

Figure 5.37. Force in the IP tieback connections during FB6 in the (a) horizontal direction and (b) vertical direction

5.4.5 Variation of the Forces in the Connection With Change in Interstory Drift

In this analysis, the drifts recorded at the fourth story during FB6 were scaled to achieve peak interstory drift ratios varying from 0.5% to 3%, while all the other parameters were kept the same. Figure 5.39 shows the variation of the peak forces in the connections in the OP panel with the variation of the PIDR. Peaks for the ductile fuse connection force F_A clearly show that the yielding of the fuse mostly in the linear range, in fact it reaches a maximum of 8 kips for drifts of 3%. The yielding of this connection happens with a force of 7.9 kips. The force F_C is small for drifts of 0.5% and 1%, while for larger drifts it increases linearly to reach a maximum of 9.4 kips. The force F_D also increases linearly and it reaches a maximum of 11.2 kips.

Figure 5.40a shows the variation of horizontal and vertical forces in the bearings of the IP panels. The magnitude of the vertical forces is the same in both connections and it reaches very large

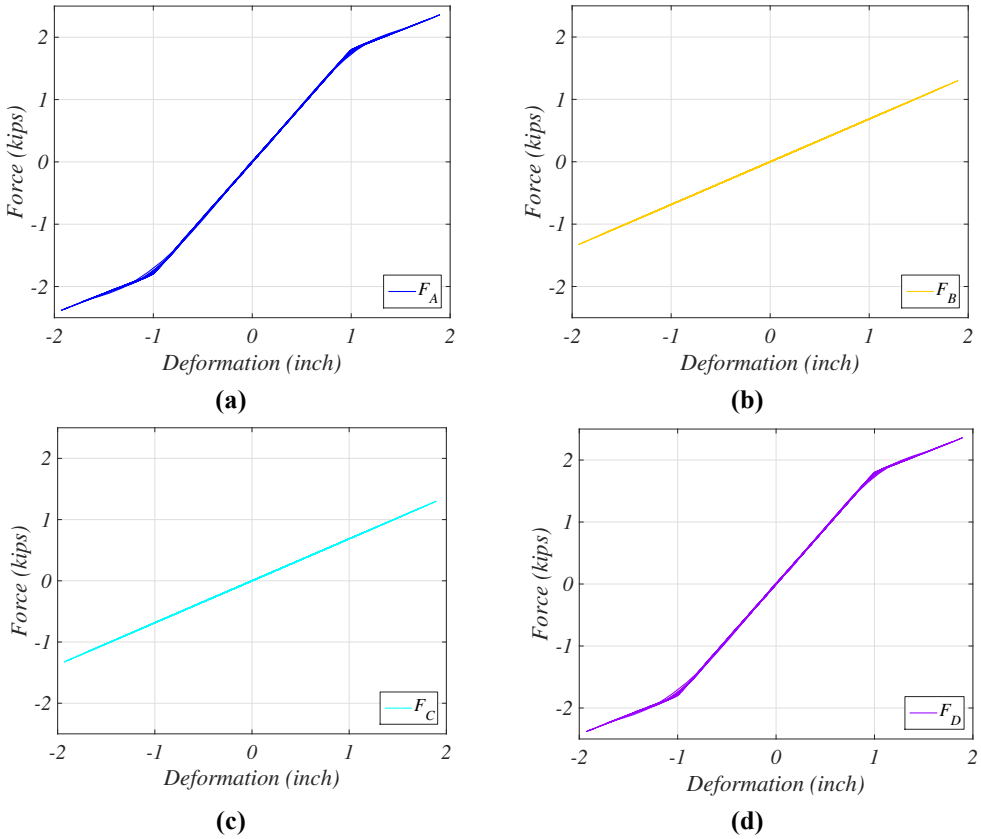

Figure 5.38. Force-deformation of the tieback connections in the IP pane: (a) F_A, (b) F_B, (c) F_C and (d) F_D

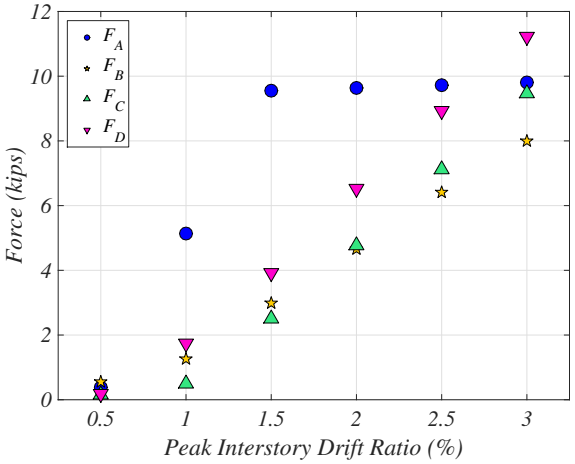

Figure 5.39. Variation of peak forces in the connections in the OP panel with the variation of peak interstory drift ratio

values (~32 kips). Forces in the horizontal directions are also very large, reaching a maximum of 15 kips. The magnitude of the force in the two connections is similar. Results for the horizontal forces in

the tieback connections are shown in Figure 5.40b. In this case large forces are reached in the stiffer outer connections, while they remain lower in the inner connections, which are softer.

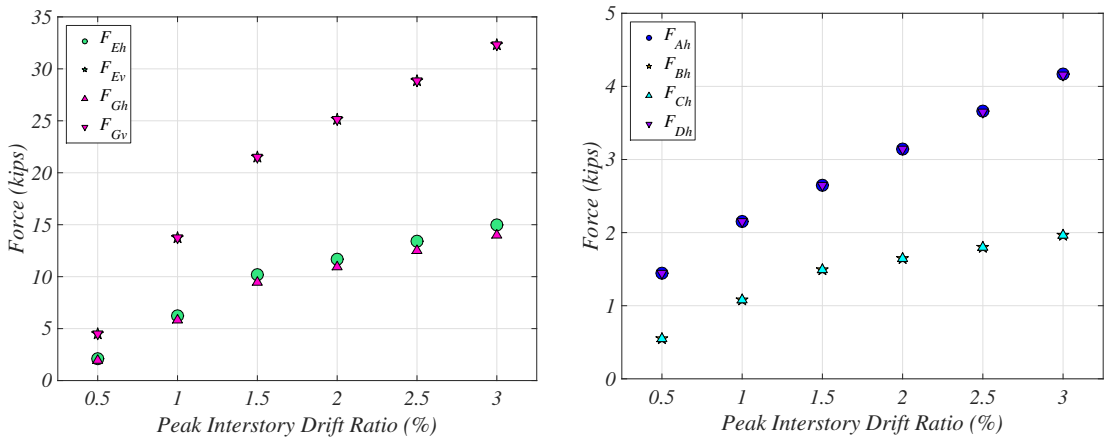

(a) **(b)**

Figure 5.40. Variation of peak forces in the connections in the IP panels with the variation of PIDR: (a) bearing connections and (b) tieback connections.

5.4.6 Variation of the Forces in the Connection With Change in the Gap Opening

Figure 5.41 presents the variation of the peak forces in the connections in the OP panel with the variation of gap opening for the FB6 motion scaled to reach a PIDR of 2.5% PIDR. The force in the corner connections with ductile fuse F_A increases sharply when the gap gets smaller than 4 inches (2.4% drift). For large gap opening F_B is the largest among the forces in the connections of the OP panel. The forces in these connections increases linearly as the gap size decreases, and it reaches a peak of 7.4 kips, still in the elastic range. The force in the bearings also increases linearly as the gap size decreases, reaching a maximum of 10.3 kips. Figure 5.42a presents the same results for the forces in the bearing connections of the IP panels. The magnitude of the vertical forces in the two bearings remains equal, and it reaches a peak of 30 kips, while that in the horizontal direction it has a maximum of 14 kips. Figure 5.42b shows that for every value of the gap opening the maximum forces in the tiebacks remain similar, and close to the yield force. In fact, the maximum force in the tiebacks depends primarily on the imposed drift, which was larger that the yield drift.

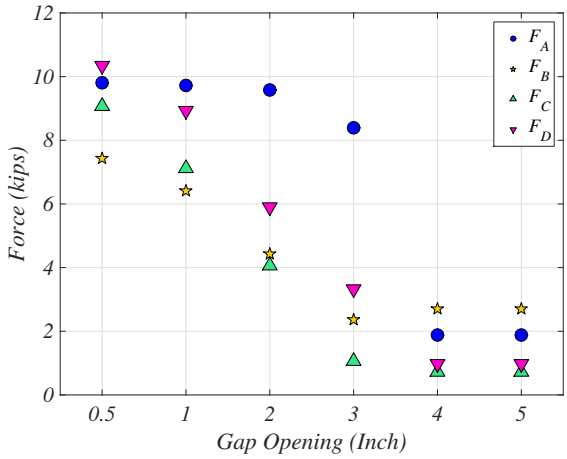

Figure 5.41. Variation of peak forces in the connections in the OP panel with the variation of gap opening (PIDR=2.5%)

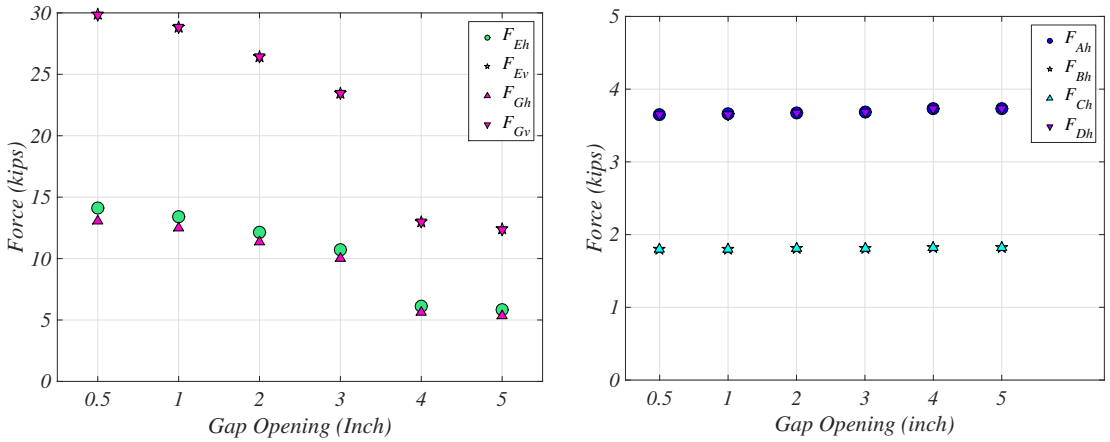

(a) **(b)**

Figure 5.42. Variation of peak forces in the connections in the IP panels with the variation of gap opening: (a) bearing connections and (b) tieback connections (PIDR=2.5%)

5.5 Practical Applications and Conclusions

The analysis of the corner tested within the BNCS project led to the following conclusions:

- Panels with butt-return joints on the west side of the building activated the newly designed ductile mechanism, resulting in visible plastic deformation of the plate due to corner panel impact, while in the panels with miter joints the plate did not visibly bend and much of the deformation was absorbed instead by the panel bending and cracking. Damage to the panel in the case of the butt-return joint was likely avoided likely due to the additional stiffness of the panel created by the return;

- Damage to OP panels was more pronounced on the west side of the building. This was (possibly) due to the different types of IP panels installed at corners, namely a flexing connection installed on the east side absorbed a portion of the deformation created between OP and IP panels thus avoiding damage to the OP panels, while the stiffer and severely damaged sliding connections on the IP panels on the west side were not able to absorb the deformation caused by the impact that resulted in damage to OP panels;
- Displacements in the connections remain elastic i.e. no permanent displacements are observed until the gap in the corner joint closes; and
- The force-displacement response measured in the ductile fuse connection observes a softening where miter joints are located, probably caused by the formation of cracks. In contrast, corners with butt-return joint showed a stiffening behavior, probably caused by stiffening in the steel of the connection. Maximum forces and displacements recorded confirmed the presence of nonlinearities during testing.

The intended goal of the ductile connection was to develop plastic deformation upon impact of corner precast concrete panels, while protecting (limiting the force transmitted) to other elements of the connection. Results from these full-scale system tests successfully confirm that these objectives were achieved when butt-return joints were used.

Results from the numerical study show that large forces in connections further from the corner joint can also be generated. The magnitude of the forces found in the investigation are specific to the geometry of the panels, but some general conclusions can be drawn:

- Upon impact, the OP panel folds outward, creating tension in the connections close to the corner, and compression in the connection further from it. Forces in the connections increase considerably with the increment of PIDR and reduction of the corner joint gap size. In the cases considered, they reached peaks similar to the yield force in the corner connection with ductile fuse (~10 kips). Forces could be smaller in case of further concrete cracking of yielding of bearing connections, which is not considered in the model;
- The forces in the tieback connections in the IP panels are controlled by the imposed drifts, and

not related to the impact between the corner panels. In fact, the collision forces created by the collisions are absorbed mainly by the bearing connections;

- The largest forces created by the collision of the panels are those generated in the bearing connections in the IP panel, since this remains rigid. In the case considered, and with the assumption of linear connections, the IP_h forces reached peaks of ~15 kips while the IP_v forces were as large as 33 kips. Yielding of the connections in this case is considered plausible. This will limit the amount of force and dissipate energy, but also create permanent damage to the bearings;

5.5.1 Limitation of the Numerical Model

The principal limitations of the model presented in this section are:

- The force-displacement behavior of the tieback connections are found by making several assumptions, since experimental data were available only for the corner connection with ductile fuse at low drifts and two types of flexing connections;
- The tieback connections were modeled as multi-linear elastic links, thus ignoring plasticity of the material;
- The model does not consider any possible softening of the steel connections due to cyclic load, nor fracture of the rods;
- Bearing connections were modeled as linear elastic springs. Due to the large forces predicted by the model in these connections, it is possible to have yielding on the materials, possibility which was not considered;
- The elastic stiffness of the bearings was found through computer models and did not have experimental validation (except for $k_{IP,v}$, see Chapter 7);
- The concrete was assumed to be linear elastic with a stiffness reduction factor of 0.7. This does not take into considerations cracking and further loss of the stiffness of the concrete. Reduction of stiffness in the concrete, especially when localized, could decrease the amount of forces in the connections or change the distribution of forces amongst the connections;
- The results are very specific to the panels geometry considered, and cannot be directly

extended to other panel configurations.

ACKNOLEDGEMENTS

Chapter 5 reproduces content and images of the material as it appears in the Proceedings of the PCI convention 2013. Pantoli, E., Hutchinson, T. C., Underwood, G. A., and Hildebrand M., 2013. “Shake table testing of a full-scale five-story building: seismic performance of precast concrete cladding panels.” Proceedings, PCI convention, September 21-24, Grapevine, TX. The author of the dissertation is the principal author of the above cited papers.

Chapter 6

Dynamic Characterization of APC Cladding

ASCE-7 (ASCE 2010) provides different values of component amplification factor a_p for elements with natural frequencies larger and smaller than 16.7 Hz (defined "rigid" and "flexible" components, respectively). Exterior walls are considered rigid elements, thus their a_p is set to 1.0, which means that they are not expected to amplify building accelerations during an earthquake. While this assumption might be correct for several types of façades, which are very light and stiff, it is not clear if it holds for APC cladding. In fact, the large mass of the panels could contribute to a reduction of the natural frequencies of some modes under the threshold value of 16.7 Hz.

This chapter presents an analysis of the dynamic characteristics of APC cladding. The first section summarizes the studies of the experimental natural frequencies of four APC panels installed on the BNCS building. These results are used to validate numerical models of panels and connections in SAP2000. Finally, key features of panels and connections are varied to understand the possible range of natural frequencies for the main modes of APC panels. It is noted that, from a dynamic point of view, APC cladding can be considered formed by many separate units, each one comprised by one panel and its connections (Figure 6.1a). The panel can be seen as a 2D element, while each connection acts as a translational spring. As a result, each panel-connection unit can be represented as a multi degree of freedom system, in which the mass is that of the panel, while the global stiffness is created by a combination of the stiffness of panel and connections (Figure 6.1b). With respect to the plane of the panel, the three axes of movement of the system can be identified as in-plane vertical (IP_v), in-plane horizontal (IP_h) and out-of-plane (OP).

6.1 Past Studies

Only a handful of studies focusing on the dynamic characterization of APC cladding was performed in the past. With the goal of understanding if earthquake motions could be amplified in the panels, Memari et al. (2004) created models of two panels on ABAQUS using brick elements for the panel, shell elements for the flat parts of the connections, and beam elements for the steel rods in

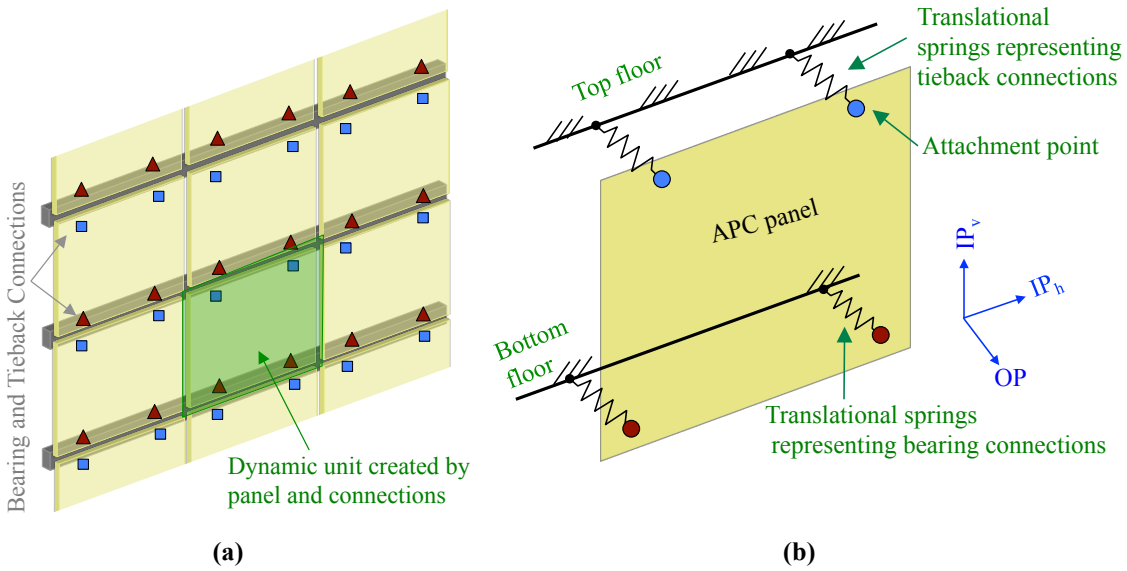

Figure 6.1. Representation of the panel and connections as dynamic units (a) installed on a building and (b) as a multi-degree of freedom system

flexing tieback connections. The concrete was assigned the nominal f'_c of 5000 psi and E of 4300 ksi. The first panels consider was a 20'x7'x6'' spandrel panel connected to a 2'10'' beam with bearing connections at top and tieback connections at the bottom. The model ,which was composed by 11600elements and 17871 nodes, revealed three main modes of vibrations in the $IP_{,h}$, $IP_{,v}$ and OP direction at 45.63, 55.60, and 13.04 Hz, respectively. The second panel considered was a 12'x6'x6'' floor-to-floor panel with two 9.5'' long flexing tiebacks at the top, and two bearing connections at the bottom. The flexing connections used in this case are similar to those used in the BNCS project, while the bearing connections differed substantially. In fact, in this case they were created using a simple angle bolted to a panel embed and to a structural element. Figure 6.2a and b show the model of tieback and bearing connections, respectively. The three main natural frequencies in the $IP_{,h}$, $IP_{,v}$ and OP directions were identified in this case at 5.43, 19 and 5.4 Hz, respectively. Figure 6.2c shows the main $IP_{,h}$ mode identified.

A second research program was performed by Merrick et al. (2004). During this study, experimental natural frequencies of APC cladding were determined with vibration tests, and these values were compared to the natural frequencies obtained by numerical models. The numerical model of the panel was created in SAP2000, and reproduced the panel geometry, mass and support conditions.

This study showed a good correlation between experimental and analytical frequencies (Figure 6.3).

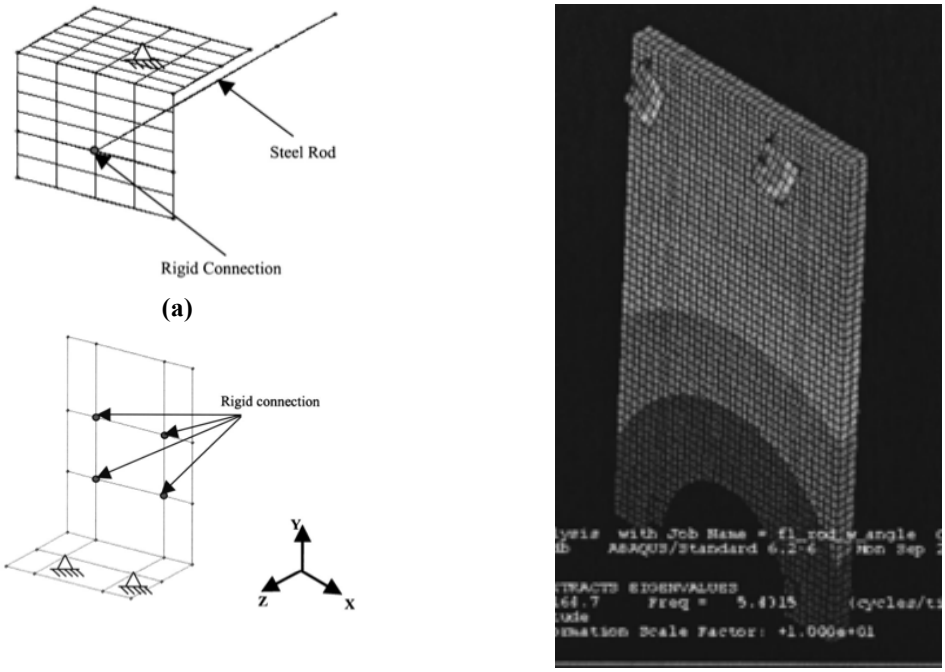

Figure 6.2. Model of the floor-to-floor panel created by Memari et al. 2004: (a) tieback connection, (b) bearing connection, and (c) $IP_{,h}$ mode of vibration (Courtesy of Memari et al. 2004)

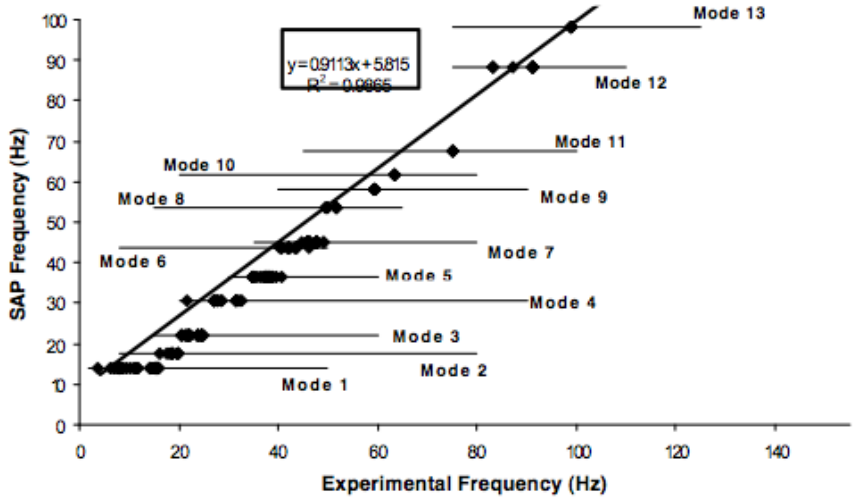

Figure 6.3. Comparison between experimental and numerical frequencies determined by Merrick et al. 2004 (Courtesy of Merrick et al. 2004)

6.2 Dynamic Behavior of APC Cladding Installed on the BNCS Building: Experimental Results

The natural frequencies of four panels installed on the BNCS building were determined through the spectral analysis of accelerations recorded in the panels and building floors. For the OP panels 4ES and 5ES, only east-west (OP) accelerations were analyzed, while for the IP panels 4SE and 5SE both the east-west (IP) and vertical accelerations were studied. The results presented are relative to the white noise run before the beginning of the FB test phase. The following steps are performed to process the raw acceleration data and determine the natural frequencies of the panels:

- The initial baseline of the signal is removed by subtracting to the entire time series the average of the first 500 samples;
- A short-time Fourier transform of the time series is created with the function "spectrogram" in Matlab. The length considered is 4096 samples and the window function used is the Blackman;
- The 4096 samples long Fourier transform is averaged to reduce the error and the absolute value (i.e. magnitude) is considered;
- A smoothing spline is fit to this data to extract the peaks. The spline is not shown in the following plots for clarity.

Frequencies from 0 to 35 Hz are included. Even if vibrations with frequency close to 35 Hz are not likely to influence the seismic behavior of the panels, they are still presented to support the validation of the numerical model. Results are shown separately for each panel, and then a cross comparison is used to reveal the natural frequencies of each of the panels.

6.2.1 OP panels: 5ES and 4ES

Each of the OP panel under consideration was instrumented with an east-west accelerometer at the top and bottom of the window opening, as shown in Figure 6.4a. Figure 6.4b shows the frequency spectrum obtained from the sensors installed on panel 5ES and the floors it was attached to. Up to a frequency of 4 Hz, the responses of panel and roof slab align. Between the frequencies of 4 and 6.5 Hz, the bottom of the panel exhibits the same frequency response of the roof, while the response of the top of the panel is amplified. For frequencies larger than 6.5 Hz, the panel amplifies the response of the floors. Peaks at

7.9 and 16 Hz are identified at the top of the opening, while at its bottom the peaks were at 7.9, 16.0, 20.3 and 31.8 Hz. Figure 6.4c shows the same results for panel 4ES. It is noted that the scale of the vertical axis is different, since the amplitude of vibration in this panel was smaller. Up to a frequency of 6.5 Hz, there is no amplification of acceleration, and the bottom of the panel exhibits the same behavior as the bottom slab. At a frequency of 7 .5-8 Hz, the bottom of the panel shows amplification compared to the bottom slab, and the top of the panel amplified accelerations compared with the top. Smaller peaks at either one or both the locations were recorded at 9.9, 12.9, 16.5, 20.4, 21.6, and 29.1 Hz.

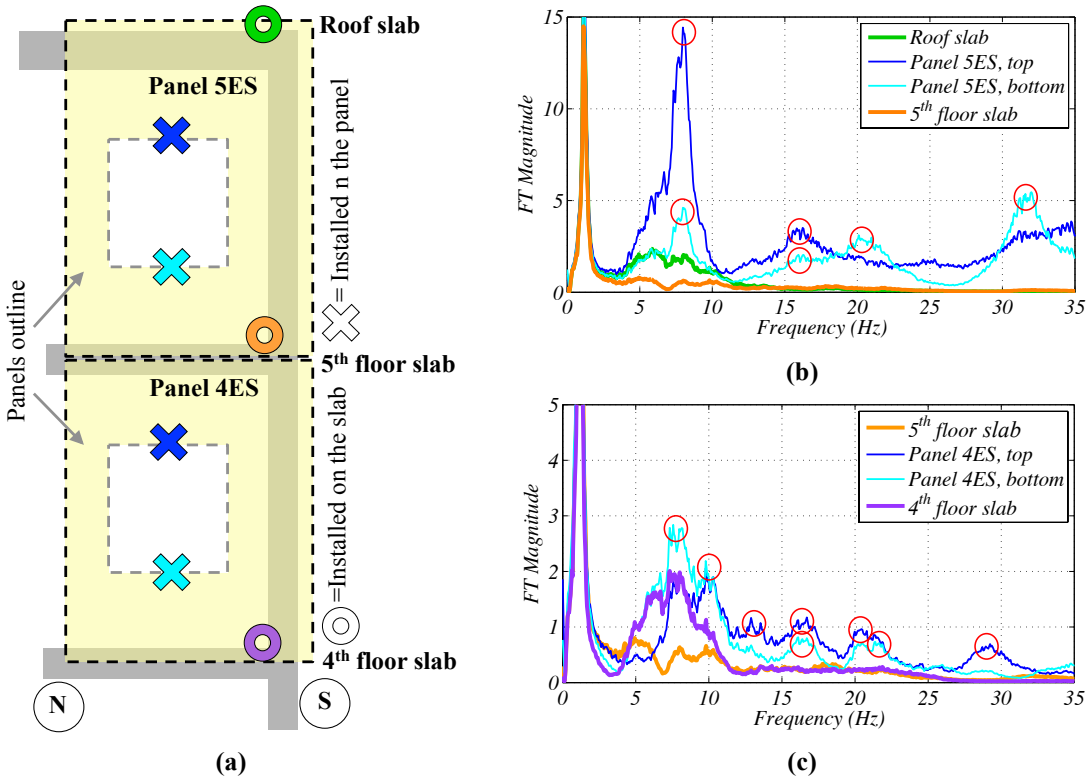

Figure 6.4. (a) Location of the accelerometers in the OP panels under consideration (elevation view) and spectral analysis for (a) panel 5ES and (b) panel 4ES

Panels 4ES and 5ES exhibit a significantly different behavior, even if they were installed close to each other and had similar features. The reason for this difference is not clear, but it can be attributed to the fact that the two panels were characterized by:

1. Different mass. Panel 4ES was shorter and thus lighter than panel 5ES. However, this difference was not substantial (0.5 kips);

2. Different boundary conditions. There were two main differences in boundary conditions between panels 4ES and 5ES. This first was the different type of tieback connection: while 5ES had a snug sliding connection, panel 4ES has a short flexing connections. The presence of a snug sliding connection could have contributed to more vibrations passing onto the panel, due to the larger surface of contact, while the flexing connection of panel 4ES could have damped the vibration to the panel. In addition, while the upper side of panel 5ES was completely free, that of panel 4ES was connected to the bottom of panel 5ES through caulking in the joint;
3. Different stiffness. This was due to the different type of tieback connection;
4. Different input motions. In fact, panel 5ES received input from roof and 5th floor, while panel 4ES from the 5th floor and 4th floor. It is noted that understanding the influence of the input motions is complicated by the fact that the input to the panel form the building was received at four distinct points.

6.2.2 IP panels: 5SE and 4SE

Panels 5SE and 4SE were instrumented with east-west accelerometers at their top and at the mid-height of their window opening. In addition, vertical accelerometers were installed at the eastern and western edge of each panel. Figure 6.5a shows the exact location of these sensors and their direction. One of the vertical accelerometers did not work properly, and thus it is not presented in this figure. Figure 6.5b shows the frequency spectrum of the east-west acceleration recorded in panel 5SE at the two locations, and compares it to that of its top and bottom slab. Up to 8 Hz, the frequency response of the panel is very similar (but slightly amplified) to that of the bottom slab. The response is actually smaller than that of the roof slab up to a frequency of 9 Hz. Several peaks in the panel response can be identified at higher frequencies. Namely, peaks at both locations can be seen at 9.8, 13.9 and 20.4 Hz, while the peak at 24.0 Hz is found only at the top of the panel.

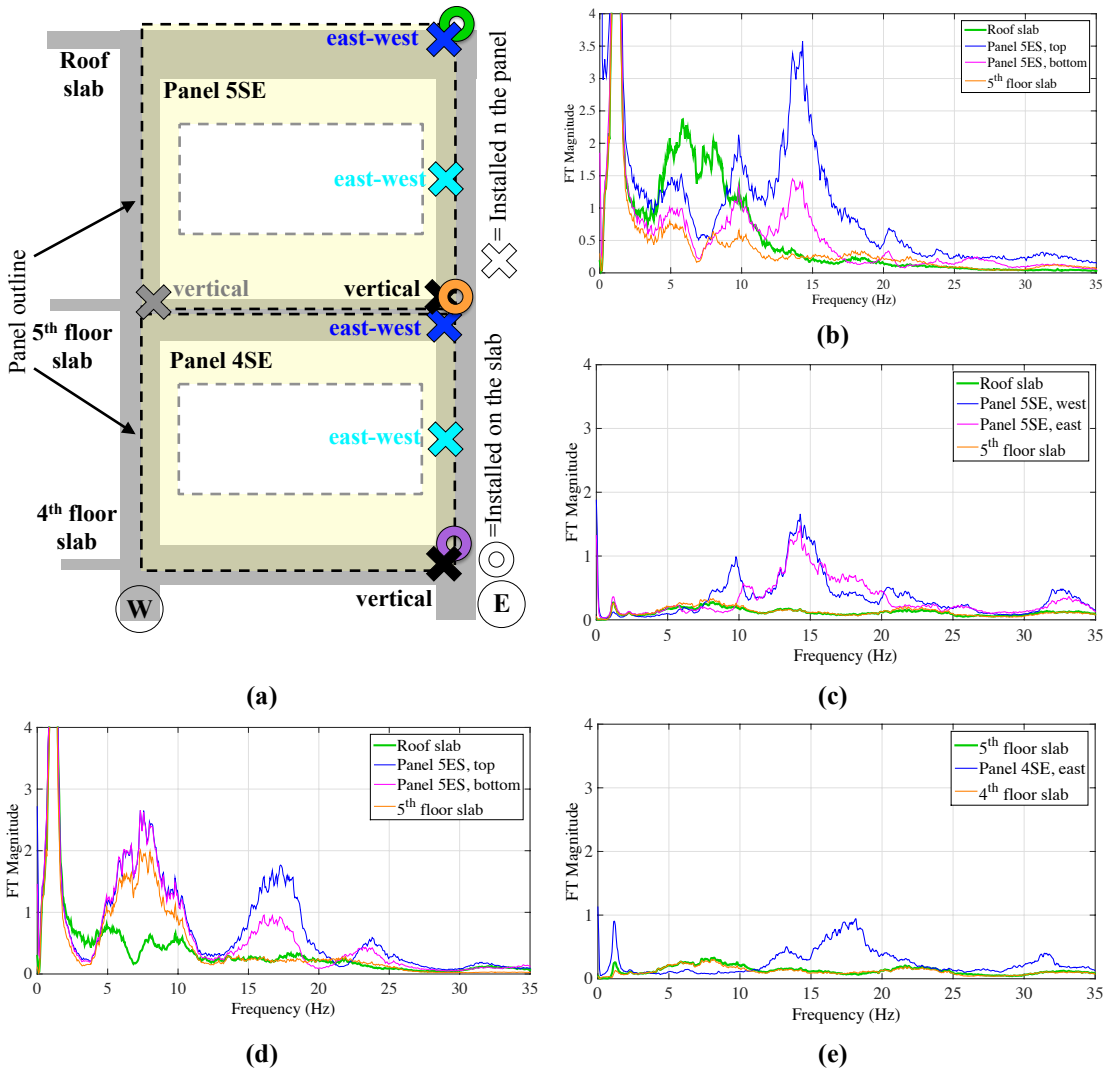

Figure 6.5. (a) Location of the accelerometers in the IP panels under consideration and spectral analysis for panel 5SE in the (a) east-west and (b) vertical direction, and for panel 4SE in the (d) horizontal and (e) vertical directions

Figure 6.5c shows the same results for vertical accelerations. In this case, the response of the panel is similar or smaller to that of the building up to 7.6 Hz. A first peak is identified at around 10 Hz, while a larger peak is found at 14.1 Hz. The fact that this peak is present in both vertical and horizontal accelerations can lead to the hypothesis that this frequency is associated to a rocking-type motion. Smaller peaks at either one of the locations are identified at 15.8, 17.9, 19.8, and 20.6 Hz. A last peak in the frequency response of the vertical accelerations can be found at 32.7 Hz. Since this peak seems particularly pronounced and it is almost absent in the horizontal accelerations, it can be associated with a vertical mode of the panel.

Figure 6.5d shows the same results for the east-west accelerations of panel 4SE. In this case, the frequency response at the top and mid-height of the panel is only slightly amplified compared to that of the bottom slab up to 12 Hz. This seems to confirm that in the in-plane direction the panel moves rigidly with the bottom slab. However, it is possible to identify some peaks in the response of the panel at higher frequencies, namely at 17.5 and 23.7 Hz. The frequency spectrum of the vertical accelerations (Figure 6.5e) reveals a first peak at 13.3 Hz, while the largest peak is at 17.7 Hz. This has a correspondence to one of the vibrations recorded in the IP direction, suggesting again a rocking-type motion. For the same reasons explained for panel 5SE, the peak at 31.5 Hz can be associated to a vertical mode of the panel.

6.2.3 Summary

The study presented in the previous sections shows that, in many instances, vibrations at the same frequency were present in the slabs and different panels. This phenomenon could have several explanations:

1. Some of the panels had the same natural frequency. This is a reasonable hypothesis for panels 4ES and 5ES for example, since they had similar characteristics;
2. The vibration was associated with one panel, and it propagated to other panels, since they were close to each other;
3. The vibration was created by a higher mode of the building.

To shed light on this issue, it was decided to conduct a cross-comparison of the peaks in the frequency spectrum of the east-west accelerations measured in the panels and adjacent slabs. Underling assumption is that the element originating a particular vibration shows a larger peak at that frequency. Figure 6.6 shows this cross-comparison, and it was created extracting the peaks in Fourier transform showed in the previous sections for panels and slabs. The vertical axis uses a logarithmic scale, because of the large variation in peak amplitude. Peaks with magnitude smaller than one are not considered, because they are deemed to be unreliable. The horizontal axis is bound to the range of frequencies of interest for the panels, which the previous section showed to be 7-32 Hz.

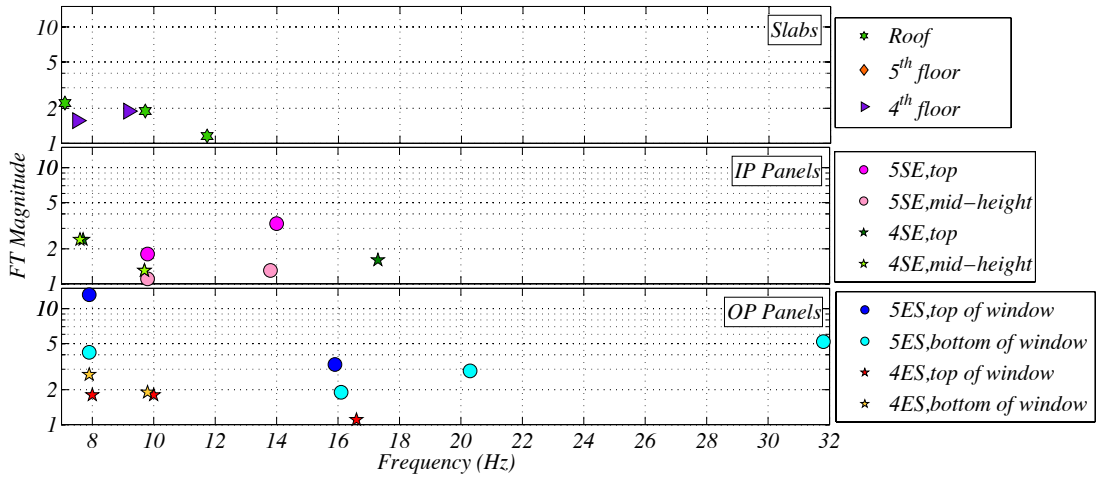

Figure 6.6. Cross comparison of the peaks in the Fourier transform observed at each location (FT=Fourier Transform)

Four main natural frequencies of panel 5ES can be identified at 7.9, 16, 20.3 and 31.8 Hz. Since panel 5ES moved mainly in the OP direction, and the accelerometers recording the motion were oriented in the east-west (OP) direction, it is likely that these frequencies are associated with OP modes. Results are less straightforward for panel 4ES. The first peak is observed at around 8 Hz, but its origin is uncertain. In fact, this vibration could have been originated by the propagation through the structure of the strong vibration of panel 5ES or by a higher mode of the building. This hypothesis is supported by the fact that peaks at this frequency are recorded also in panel 4SE and the slab. No clear conclusions can be drawn also in case of the vibration at 9.8 Hz, since peaks at a similar frequency and magnitude are present also in the roof and fourth floor slab, leading to the hypothesis that this vibration could be associated with a mode of the building. Finally, no clear conclusions can be made also for the vibration at 16.5 Hz, because this could have originated in panel 5ES, which vibrated strongly at a similar frequency. Hence, no modes can be clearly identified for panel 4ES using only experimental results. The frequency of the main mode of panel 5SE can be identified at 13.9 Hz, and it was already concluded that this mode is likely to be a rocking-type mode. This is consistent with the fact that panel 5SE is moving mainly in the IP direction, and that sensors recording the motion were east-west (IP) accelerometers. As for the vibration at around 10 Hz, nothing can be concluded since this vibration is present also in the slabs at the same magnitude. One mode can be identified for panel 4SE at 17.5 Hz, which was already identified as a rocking mode. No strong conclusions can be drawn from the peaks at

around 8 and 10 Hz, since these vibrations are very similar to those of the slab and other panels. Table 6.1 summarizes the experimental natural frequencies identified for each panels. To complete this table, the vertical modes found in the previous section are also added.

Table 6.1. Summary of natural frequencies determined experimentally for the panels under consideration

Panel	Experimental Frequency (Hz) [Mode type]			
5ES (OP)	7.9 [OP]	16 [OP]	20.3 [OP]	31.8 [OP]
4ES (OP)	-	-	-	-
4SE (IP)	17.5 [Rocking]	31.5 [Vertical]	-	-
5SE (IP)	13.9 [Rocking]	32.7 [Vertical]	-	-

6.3 Dynamic Behavior of APC Cladding Installed on the BNCS Building: Results From Numerical Models

Numerical models of panels 4ES, 5ES, 4SE and 5SE were created in SAP2000. These models had the following characteristics:

- The APC panel was modeled using thin shell elements with the thickness of the panels (5''). In terms of material properties for concrete, it was decided to use the nominal compressive strength f'_c of 5 ksi, a Young modulus E of 4030 ksi, and a weight per unit volume of 150 pcf;
- Bearing connections were modeled as translational springs with a different stiffness in each direction (OP, $IP_{,v}$ and $IP_{,h}$). The points of connections of the springs to the panel corresponded to the center of the bearing connections, as specified in the construction drawings;
- Simplified tieback connections were modeled using frame elements for the rods and thin shell elements for the connection plates. The properties of A36 steel were used for the steel parts (E=29000 ksi, f_y =36 ksi, f_u =58 ksi, weight per unit volume = 490 pcf). The panel-rod and rod-plate connections were assumed to be rigid; and
- The location of the tieback connections and springs representing the bearing connections was that specified in the construction drawings.

More details about the characteristics of each single model are presented in the pertinent

sections. The modal analysis was conducted using eigenvectors.

6.3.1 OP Panels

The first step of the modeling was the calculation of the stiffness of the bearing connections in the three directions. This was done with a separate model reproducing the bearings installed in the OP panels under consideration. The stiffness found in this fashion was then assigned to the springs representing the bearing connections in the panel model. Finally, the dynamic characteristics of the panel thus created were found.

Bearing Connections

Figure 6.7a shows a photograph of the bearing connection used in panel 4ES and 5ES, while Figure 6.7b presents the way in which it was modeled, which included:

1. A horizontal plate. This corresponds to the horizontal leg of the angle in the panel embed. The vertical leg of the angle is not considered since it can be assumed to move rigidly with the panel. The horizontal leg of the angle is modeled as a 14'' long, 5.25'' wide and 0.75'' thick plate;
2. Vertical side plates. These two plates are square plates 3.5'' long and 0.375'' thick. They are welded to the horizontal plate with 2'' long welds and to the slab embed with 3'' long welds;
3. Vertical back plate. This is 6'' long, 3.5'' high and 0.375'' thick. It is connected to the horizontal plate and slab embed with 5'' long welds; and
4. A bearing bolt. This has a diameter of 0.75'' and a total length of 3.5''.

The model contains in total 2 frame elements for the bolt and 106 thin shell elements with 370 edges for the plates. The boundary conditions are modeled as follows:

- Connection from the horizontal plate to the panel. The boundary conditions imposed at this location vary, since this is the edge where different forces and restrains are imposed to determine the stiffness of the connection in the three directions;
- Welds between the different steel parts. At these location, the elements connected are fixed each other;
- Welds to the slab embed. Nodes at the location of these welds are considered fix.

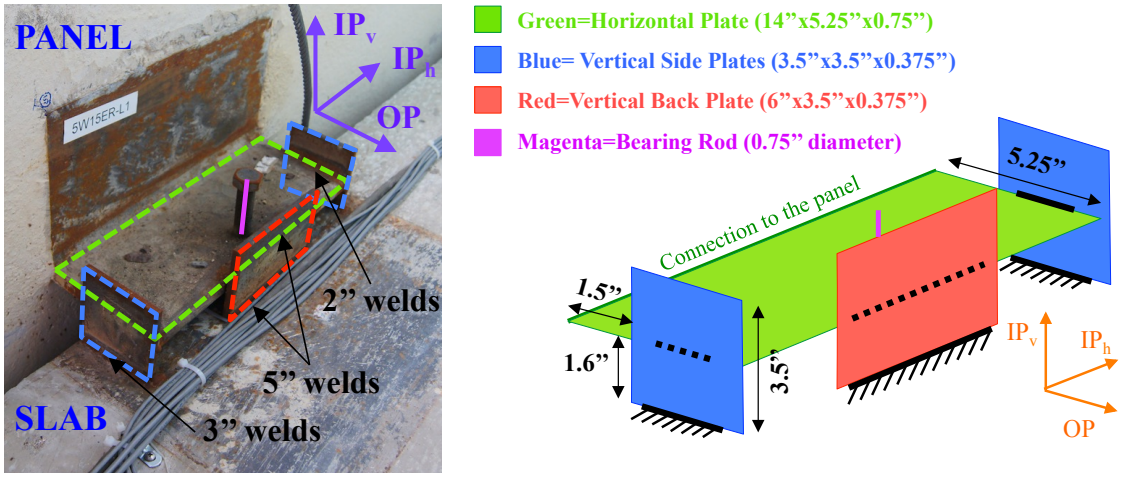

(a) (b)

Figure 6.7. Bearing connection in the OP panels: (a) photograph and (b) model

Translational stiffness of the bearing connections in each of the three directions is found and the force needed to create a unit displacement in the specified directions (while the movement in the other directions is restrained). This analysis, revealed the stiffness in the three directions as:

- k_{IPh}: 9600 kips/inch;
- k_{IPv}: 1690 kips/inch; and
- k_{OP}: 11000 kips/inch.

Figure 6.8 shows the deformed shape obtained by applying forces in each of the three directions. In the $IP_{,h}$ direction (Figure 6.8a), the main contributors to the stiffness are the back vertical plate and the horizontal plate deforming in their strong direction, and for this reason the stiffness is very large. In the $IP_{,v}$ direction (Figure 6.8b), the cantilevering section of the horizontal plate bending in its weak direction provides the largest contribution to the flexibility, and for this reason the stiffness in this direction is the lowest. In the OP direction (Figure 6.8c), the horizontal plate acting axially and the side plates deforming in their strong direction contributed to the large stiffness.

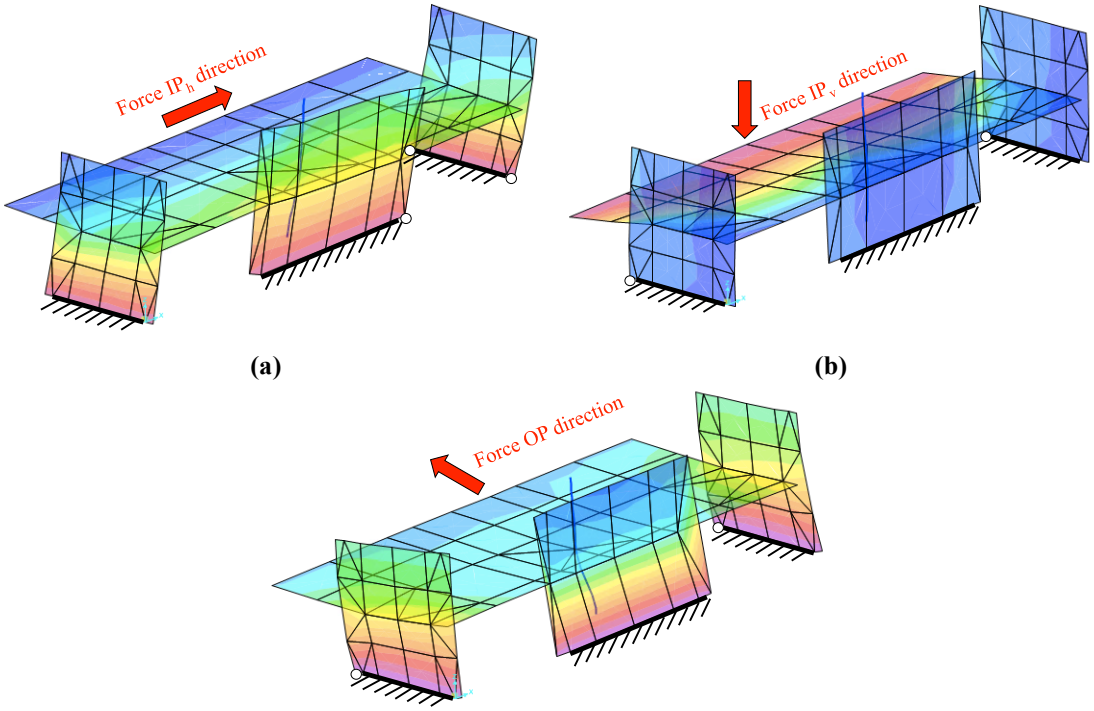

Figure 6.8. Deformation of the bearing connections for force applied in the (a) IP_h, (b) IP_v and (c) OP directions.

Panel 5ES

Figure 6.9 shows the SAP2000 model of panel 5ES, including the names given to each corner of the panel (A through D) to facilitate the discussion in this section. The panel in the model has the same geometry of the real panel, and it is composed by 105 rectangular thin shell elements. As already explained, bearing connections are modeled as translational springs, while the tiebacks are reproduced in a more detailed fashion.

Figure 6.10a and b show a photograph of the snug sliding tieback close corner A and its model, respectively. Three elements of this connection contributed to its flexibility and were reproduced in the model:

1. The vertical leg of the connection angle. This leg was 1’5’’ long, 5’’ tall and 0.5’’ thick and had a 1’x2’’ slot;
2. A cover plate which was 1’7’’ long, 3’’ tall and 0.375’’ thick;

   A sliding rod, which was 0.75’’ in diameter (0.65’’ effective diameter). The free length of the

rod was considered to be 0.5’’, corresponding to the thickness of the slotted plate.

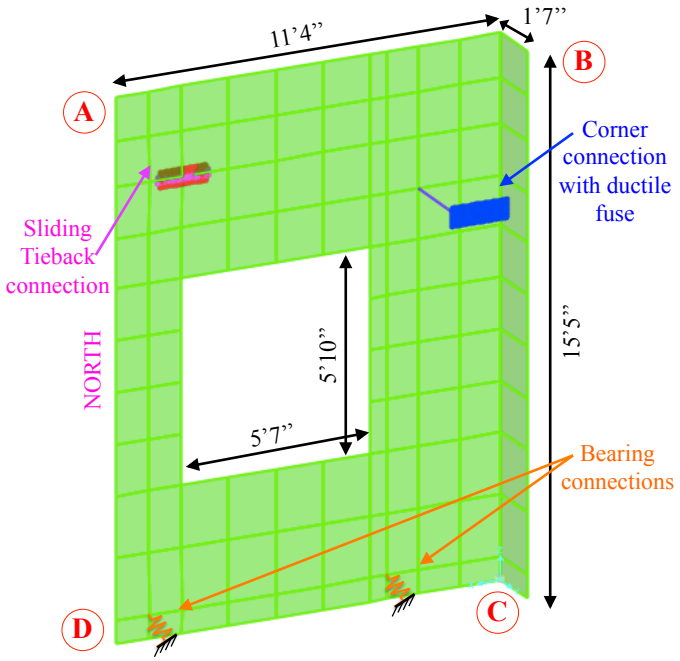

Figure 6.9. Model of panel 5ES

In terms of boundary conditions, the vertical plate was assumed to be fix at the top, at the point of continuity with the other leg of the angle, while the vertical and cover plate were considered rigidly connected in the overlapping areas. This second condition might not be generally accurate, since these two plates were not welded together and they were designed to slide during earthquake motions. However, this assumption was deemed reasonable for the goal of matching the numerical natural frequencies of the panel to the experimental ones obtained during the low-amplitude white noise test. In fact, it is unlikely that these two plates moved with respect to each other during this motion. In total, this connection was composed by one frame element reproducing the rod, 126 thin shell elements and 504 edges.

Figure 6.10c and d show a photograph and the model of the connection with ductile fuse close to corner B. This was considered composed by two main elements. This first is a ductile plate, which was 1’8.5’’ long, 7’’ tall and 0.75’’ thick and it was welded to the column embed through horizontal plates with 8’’ welds. The second was a coil rod. This rod was 1’’ in diameter and 2’5’’ long, and it was reproduced with its effective diameter of 0.88’’. In terms of boundary conditions, the ductile plate was

considered fixed at the location of the welds. The model used one frame element for the rod, and 120 rectangular area objects with 480 edges for the ductile plate.

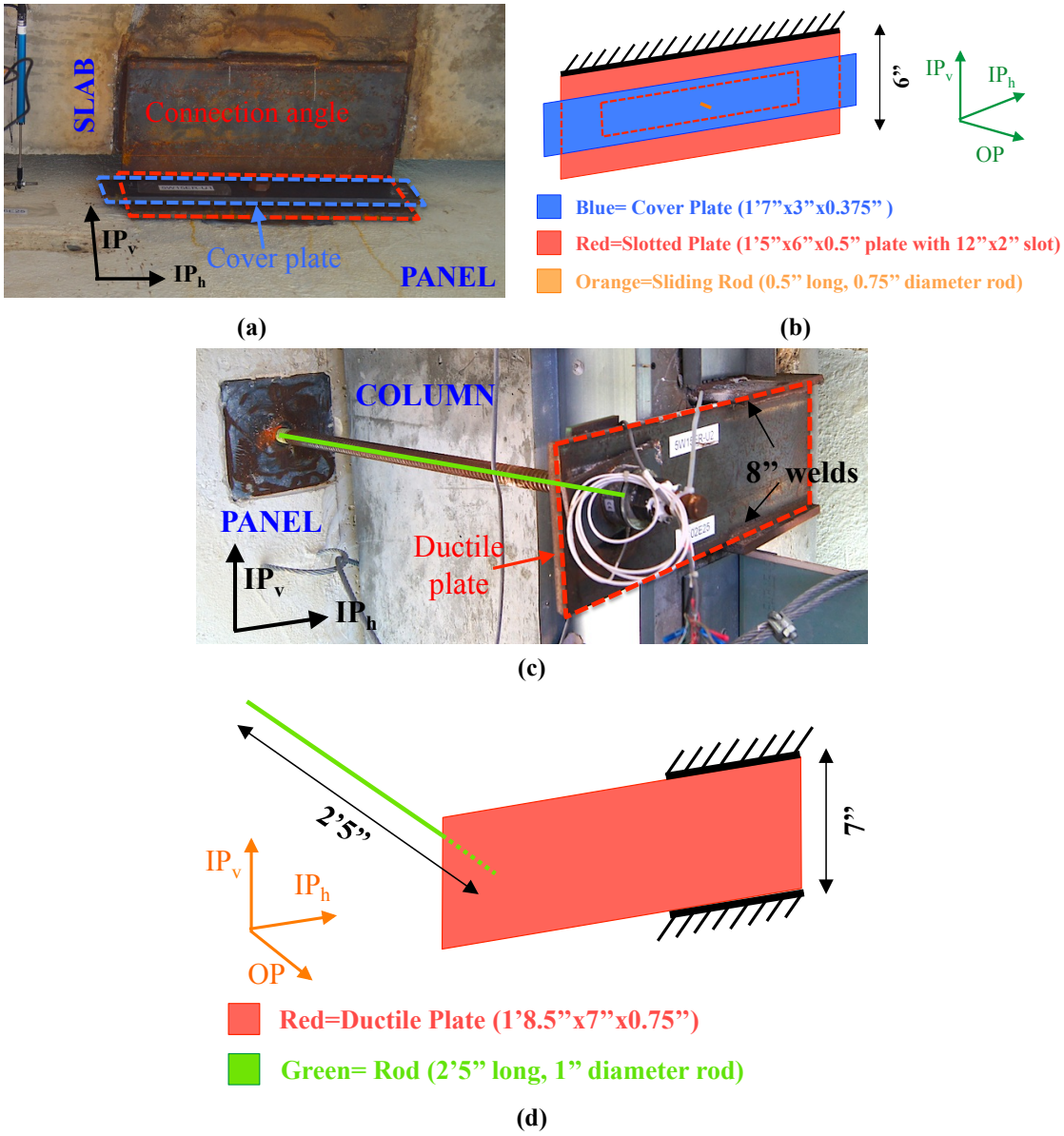

Figure 6.10. Connections in panel 5ES: photograph (a) and model (b) of the snug sliding tieback and photograph (c) and model (d) of the corner connection with ductile fuse

The following natural modes and frequencies were found, all of them involving OP bending deformation of the panel:

- Mode 1 (7.9 Hz), which involved mostly the folding of the corner AB of the panel, which was softer due to the presence of the ductile fuse connection (Figure 6.11a);

- Mode 2 (18.2 Hz), characterized by the OP deformation of the side of the panel between corners A and D (Figure 6.11b);
- Mode 3 (20.5 Hz), characterized by the vertical outward folding of the central part of the panel (Figure 6.11c); and
- Mode 4 (32.3 Hz), involving the folding of several parts of the panel in different directions (Figure 6.11d).

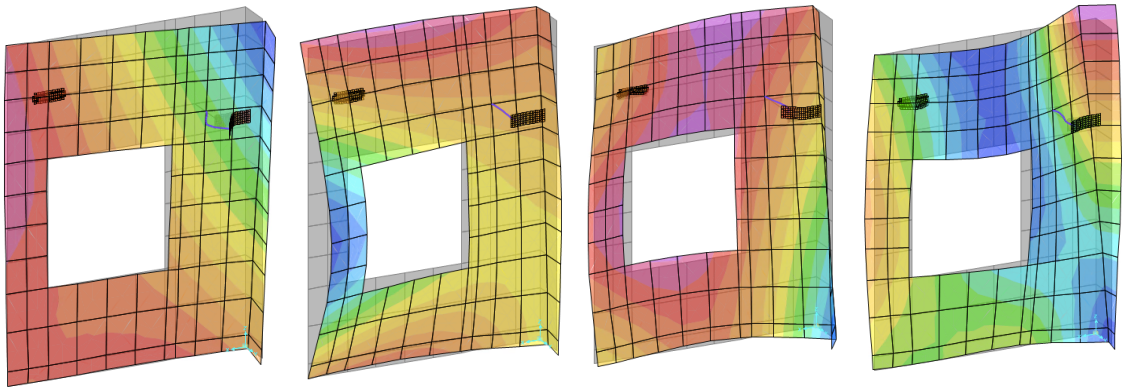

(a) **(b)** **(c)** **(d)**

Figure 6.11. Natural modes of panel 5ES predicted by the numerical model (the contour represent relative amplitude of displacement in the OP direction of the panel

Each of the frequencies determined numerically had a close correspondence to one of the experimental frequencies, as presented in Table 6.2. The first natural frequency is predicted perfectly, the second frequency has an error of 14%, while the error on the third and fourth frequencies is only 1%. It is noted that not only the model was able to capture the experimental frequencies, but it also created modal shapes congruent with the experimental ones. In fact, comparing the relative amplitude of the Fourier transform peaks for the accelerations recorded at the top and bottom of the window opening (Figure 6.4a), it is possible to conclude that the first two modes create a larger relative deformation of the top location, while the third and the fourth modes had larger relative displacements at the bottom location. This behavior is also predicted by the numerical model for the four mode shapes identified.

Table 6.2. Comparison of experimental and numerically estimated natural frequencies for panel 5ES

Mode	Experimental Frequency (Hz)	Numerical Frequency (Hz)	Difference (%)
1 (OP bending)	7.9	7.9	0
2 (OP bending)	16.0	18.2	14
3 (OP bending)	20.3	20.6	1
4 (OP bending)	31.8	32.4	2

Panel 4ES

Panel 4ES was very similar to panel 5ES, except for the fact that it was shorter and it had a short flexing tieback connection instead of a sliding ones. Hence, the two models were also the same except for these two differences. Figure 6.12 shows the model of panel 4ES. The flexing tieback connection was assumed composed by two elements:

- A vertical plate 7'' long, 4.5'' high and 0.5'' thick. This corresponds to the vertical leg of the connection angle;
- A 0.75'' diameter rod (0.65'' effective diameter) with a free length of 11''.

The vertical plate was fixed at its top. The model of the flexing connection was created using 1 frame element for the rod and 48 rectangular area elements with 192 edges for the vertical plate. In total, the model was composed by 2 frames, 250 thin shells and 1000 edges.

The OP bending modes calculated for panel 4ES where similar to those of panel 5ES (Figure 6.11), but the natural frequencies were at 9.1, 18.4, 21.4 and 34.3 Hz, slightly larger than those of panel 5ES. It is noted that panel 4ES had reduced mass compared to 5ES, but also reduced flexibility due to the presence of the flexing connection. In addition, the larger flexibility of the tieback connection contributed to the lowering of the frequency of the rocking mode to 17.9 Hz. Results from this numerical model were used to shed some light on the experimental results. Namely, it was possible to conclude that one of the two experimental peaks at either 8 or 10 Hz could be associated with the first natural frequency of the panel predicted at 9.1 Hz. As for the small peak at 16.5 Hz, it was possible to associate it with the second OP bending mode at 18.4 Hz.

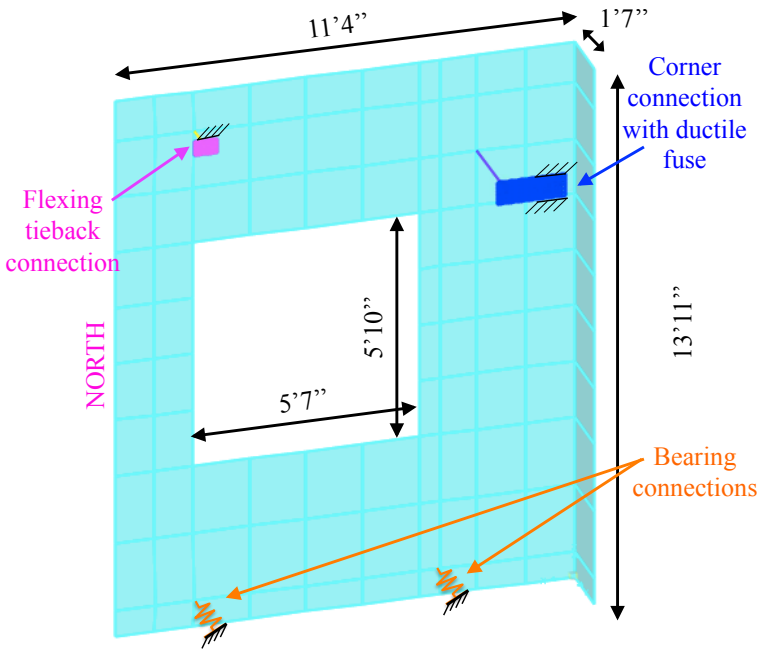

Figure 6.12. Model of panel 4ES

6.3.2 IP panels

In the case of the IP panels, an additional level of complexity was created by the complicated geometry of the bearing connections (see Figure 3.4a). Creating a simplified model of this connection to obtain its stiffness was not deemed feasible, and for this reason, it was decided to adopt the following values of stiffness:

- k_{IPh} and k_{OP}: these values were assumed to be the same as those of the bearing connections in the OP panels. This decision was considered appropriate since the stiffness in these directions was really large, and not expected to affect the behavior considerably;
- k_{IPv}: this was determined with a semi-empirical method. Namely, it was assumed that the stiffness of the vertical mode of vibration was associated only with the k_{IPv} of the bearing connections. Hence, it was possible to back-calculated k_{IPv} through the values of mass and the experimental natural frequency of the vertical mode.

Panel 4SE

Figure 6.13 shows the model of panel 4SE and its connections. Each of the four flexing tieback connections was composed by:

- A vertical plate 7'' long, 4.5'' high and 0.5'' thick, corresponding to the vertical leg of the angle used in the connection; and
- A 0.75'' diameter rod (0.65'' effective diameter). The free length of the rod used in the model was 11'' for the outer connections and 15'' for the inner ones.

Each flexing connection was modeled with one frame element for the rod, and 48 rectangular thin shell elements with 192 edges for the plate, which was considered fix at its top edge.

The vertical stiffness of the bearing connections was found through the following calculations:

$$\omega = 2\pi f = 2\pi \cdot 31.5 = 198 rad / \sec \quad \text{Eq. 6.1}$$

m=10000 lbm

$$k = \omega^2 m = 419482800 lbm / ft = 1014 kips / inch \quad \text{Eq. 6.2}$$

This total stiffness was divided equally between the two bearing connections, which were then assumed to have a k_{IPv} of 507 kip/inch per connection. In total, the panel was composed by four frame objects, and 182 rectangular thin shell objects with 728 edges.

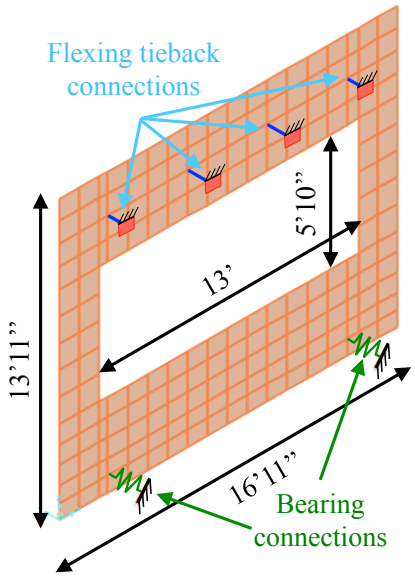

Figure 6.13. Model of panel 4SE

Through this numerical model, the following natural modes and frequencies were identified for panel 4SE:

- Mode 1 (14.2 Hz), an OP bending mode involving the bending of the panel around an

horizontal axis (Figure 6.14b);

- Mode 2 (15.5 Hz), a bending mode with movement around a vertical axis (Figure 6.14c);
- Mode 3 (18.4 Hz), the rocking mode (Figure 6.14c);
- Mode 4 (24.8 Hz), another bending mode involving especially the deformation of the sides (Figure 6.14d);
- Mode 5 (31.2 Hz), the vertical translation mode (Figure 6.14e).

The comparison between the experimental and numerical natural frequencies could be done only for the rocking mode, since the vertical mode was used to find the vertical stiffness of the bearing connections. The rocking mode shows a good comparison between the experimental and numerical results, confirming that the stiffness of the bearing connections utilized was a good approximation. Table 6.3 shows the comparison between experimental and numerical frequencies for this panel. It is noted that no OP modes were found experimentally, which makes sense considering that this panel moved mainly in the IP direction, and that the sensors were able to record only east-west (IP) motion.

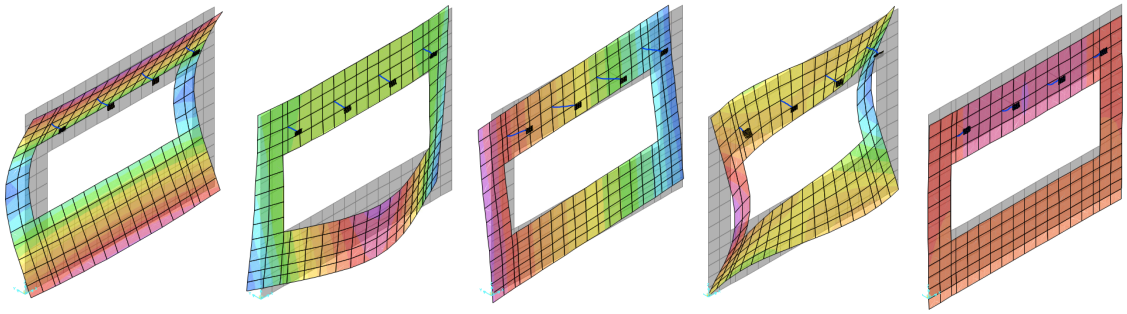

(a) **(b)** **(c)** **(d)** **(e)**

Figure 6.14. Natural modes of panel 4SE: (a) first OP bending mode- contour of OP displacement, (b) second OP bending mode- contour of OP displacements, (c) rocking mode-contour of vertical displacements, (d) third OP bending mode- contour of OP displacements, and (e) vertical translation mode- contour of vertical displacements

Table 6.3. Comparison of experimental and numerically determined natural frequencies for panel 4SE

Mode	Experimental Frequency (Hz)	Numerical Frequency (Hz)	Difference (%)
1 (OP bending)	-	14.2	-
2 (OP bending)	-	15.5	-
3 (Rocking)	17.5	17.9	+2
4 (OP bending)	-	24.8	-
5 (Vertical translation)	31.5	30.3	-4

Panel 5SE

The model of panel 5SE was very similar to that of panel 4SE, the only differences being the height of the panel (15''5' in this case) and the different length of the rods in the flexing connections. In this case, the free length of the rods was 15'' for the outer connections and 19'' for the inner ones. The same semi-empirical method adopted previously to determined the k_{IPv} of the bearing connections was utilized. Namely, the following calculations were performed:

$$\omega = 2\pi f = 2\pi \cdot 32.7 = 205 rad/\sec \quad \text{Eq. 6.3}$$

m=10800 lbm

$$k = \omega^2 m = 483287500 lbm/ft = 1174 kips/inch \quad \text{Eq. 6.4}$$

Hence, in this case the stiffness per connection was found to be 587 kips/inch. The modes predicted for this panel had a very similar shape to those of panel 5SE (Figure 6.14), with two additional OP bending modes being identified. Table 6.4 shows the comparison between numerical and experimental natural frequencies. As seen for panel 4SE, also in this case there was good agreement between the numerical and experimental frequency of the rocking mode, confirming the accuracy of the assumed vertical stiffness of the bearing connections.

Table 6.4. Comparison of experimental and numerical natural frequencies for panel 5SE

Mode	Experimental Frequency (Hz)	Numerical Frequency (Hz)	Difference (%)
1 (OP bending)	-	10.2	-
2 (Rocking)	13.9	15.1	+8
3 (OP bending)		15.2	
4 (OP bending)	-	22.2	-
5 (OP bending)	-	22.4	-
6 (OP bending)	-	28.7	-
7 (Vertical translation)	32.7	29.9	-8

6.3.3 Summary

The comparison between experimental and numerical natural frequencies revealed that an accurate numerical model of the panel can predict its main modes with great accuracy. This is especially true for OP bending modes, while the comparisons is less clear for IP modes, since the k_{IPv} of the bearing connections was found using some experimental data. Errors in the prediction of the natural frequencies were generally less than 5%, and had a maximum of 14%. Thanks to this study, it was possible to conclude that the dynamic behavior of panels is dominated by three types of modes:

1. OP bending modes: these modes were those with the lowest natural frequency. Several of these modes with different shapes were identified for each panel, and they dominated the response in the OP direction. However, the first OP bending mode generally accounts for the large mass participation factor;
2. Rocking mode: this mode dominates the IP-horizontal response of the panels; and
3. Vertical translation mode: this mode controls the vertical response of the panels and it was observed at very high frequencies (>30Hz).

6.4 Sensitivity Study

The goal of this study is to understand how different features of the panel influence its dynamic characteristics, and to provide a range for the natural frequencies of its three main modes of vibration. Several features of the cladding panels were changed during this study, namely:

- Stiffness of the connections. Detailed models of typical bearing and flexing tieback connections are used to determine their range of stiffness in the three directions. Sliding tiebacks are not considered since they are assumed to be similar to very stiff flexing connections. Subsequently, these values of stiffness are utilized in the global model of the panels to evaluate how they affect the dynamic behavior of the system;
- Mass and stiffness of the panel. The range of natural frequencies of the OP bending, rocking and vertical mode is found by analyzing the smallest and largest panel typically used in the field, with the stiffness of their connections varying from really large to very low. Both plain panels and panels with window openings are considered. It is noted that varying the geometry of the panel affects both its mass and stiffness. Subsequently, the influence of other factors affecting the stiffness of the panels is analyzed, to understand the further shift they might create in the natural frequencies. Namely, these variables are the locations of the connections and the Young modulus of concrete.

The panels are modeled as in the previous section, except for the fact that both bearing and flexing connections are reproduced using translational springs, whose stiffness is determined with a separate model. The modal analysis is performed using eigenvectors also in this case.

6.4.1 Variation of Stiffness of the Connections

Bearing Connections

The range of stiffness of bearing connections is obtained by modeling what can be considered the stiffest and the softest bearing connections in common use. Figure 6.15 shows the typical configuration of these connections, which is slightly different from what was used in the BNCS experiment. The range of dimensions of each of the components of the connection is obtained by APC cladding designers, namely these elements and their possible range of dimensions are:

- A horizontal plate, part of the panel embed. The width of the plate is considered constant at 6'' while its length and its thickness are varied from 6'' to 12'', and from 0.75'' to 1'', respectively. The cantilevering length of the plate is also varied from 1'' to 2'' to account for construction tolerances;

- Two angles on the sides of the horizontal plate, welded to the horizontal plate and structural embed. The length and height of these angles is varied from 3.5'' to 4'', and its thickness from 0.5'' to 0.375'';
- A 1'' diameter bearing bolt (0.88'' effective diameter).

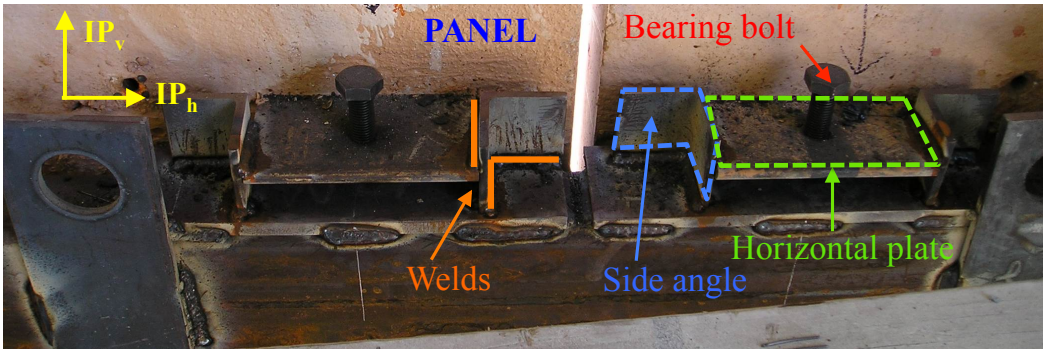

Figure 6.15. Photograph of typical bearing connections (Image courtesy of Glen Underwood-Clark Pacific)

Figure 6.16a and b show the details of the dimensions of the stiffest and softest bearing connection considered, respectively. These connections are modeled using the same material properties and boundary conditions used for the model of the bearing connections in the BNCS building. The model utilizes thin shell elements with the properties of A36 steel (E=29000 ksi), the elements are considered rigidly connected if welded together, and fixed restraints are applied at the bottom of the angles at the location of welds. The model of the stiffest bearing uses 1 frame element, 100 areas and 400 edges, while that of the softest connection is composed by 1 frame element, and 136 area elements with 544 edges. The stiffness in each direction is obtained as already explained in the case of the BNCS connections. The stiffest connections reveals the following values of stiffness:

- k_{IPh}=12050 kips/inch;
- k_{IPv}=12000 kips/inch; and
- k_{OP}=17200 kips/inch;

These values are very large, confirming the effectiveness of these types of connection in fixing the panel to the floor. The values of stiffness obtained for the softest bearing are:

- k_{IPh}=6750 kips/inch;
- k_{IPv}= 2352 kips/inch; and

- k_{OP}=9470 kips/inch;

Even in the case of the soft connection, the stiffness in the three directions is large. In both cases, the largest stiffness is observed in the OP direction, followed by the one in the IP_h direction. The stiffness in the IP_v direction is very large in the case of the stiff configuration, while it decreases by 80% in the case of the soft configuration. This is mainly due to the increment in cantilevering length of the horizontal plate.

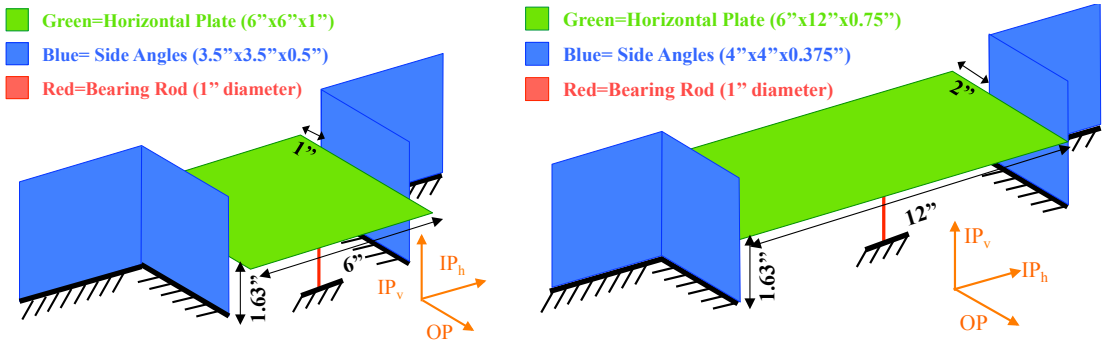

(a) **(b)**

Figure 6.16. Models of the (a) stiffest and (b) softest bearing connections

Flexing Tieback Connections

The goal of the study on flexing tieback connections is to determine their range of stiffness and to understand how their main features influence their stiffness. This objective is achieved by first considering the typical configuration of a flexing connection, and then varying some its main features. In its basic configuration, a flexing connection is considered to be composed by three elements (Figure 6.17a):

1. A vertical plate, corresponding to the vertical leg of the connection angle. This plate is assumed to be 7'' long, 5.5'' tall, and 0.5'' thick, with a 3'' diameter hole at its center for the installation of the rod. The plate is assumed to be fixed at its top, at the point of continuity with the other leg of the angle;
2. A washer. A typical geometry of 6''x3''x0.375'' is used, and it is placed centered with respect to the vertical plate;
3. The flexing rod. The effective diameter and the free length of the rod were considered.

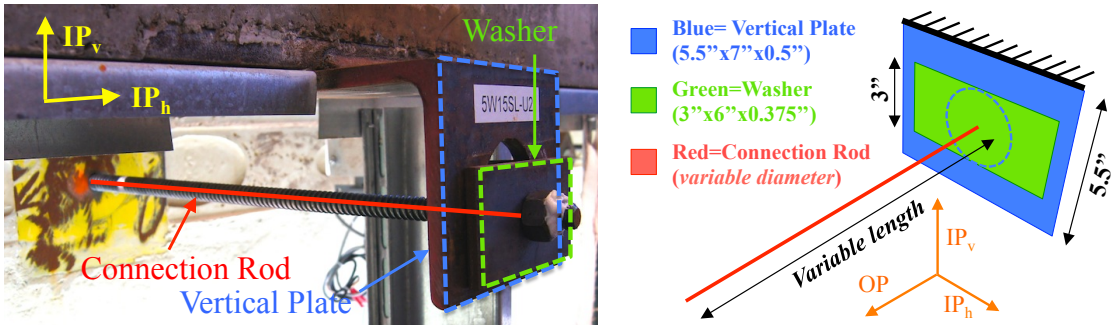

(a) (b)

Figure 6.17. Flexing tieback connections: (a) photograph and (b) model with typical dimensions

The following characteristics of the flexing connections are varied:

- The length and diameter of the rod. Diameters of 0.75'' and 1'' are considered, corresponding to effective diameters of 0.65'' and 0.88'', respectively. The free lengths analyzed are 7'', 11'', 15'' and 19'';
- The boundary conditions of the rod at the connection with the panel. In the first case, the rotations are restrained at both ends of the rod ("fix-fix" condition), while in the second case rotations are restrained only at the washer-rod connection, while they are allowed at the panel-rod interface ("fix-free rotations" condition).

The model thus created is composed by 637 thin shell elements and 2452 edges, while the number of frame elements considered varies from 7 to 19, depending on the rod length (each frame element was 1'' long). The stiffness in each direction is found as explained in the previous sections. Figure 6.18b-d show the deformed shape obtained for one of the configurations by applying force in one direction. These deformed configurations help identifying the sources of stiffness and flexibility in each direction: the flexibility in the IP directions is created mainly by the flexibility of the rod (Figure 6.18a-b), while the displacement in the OP direction involves mainly the bending deformation of the plate (Figure 6.18c).

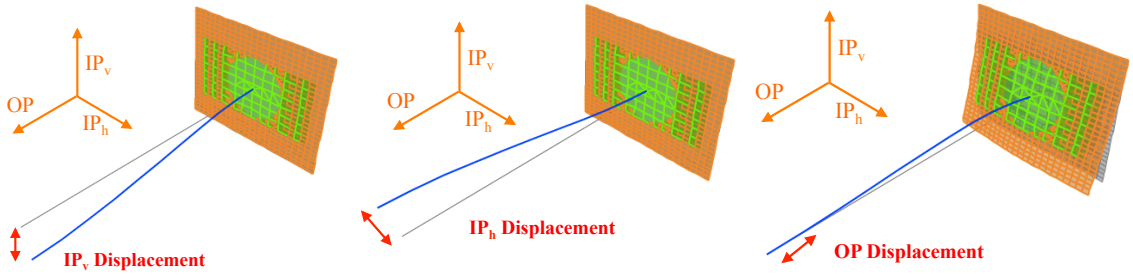

Figure 6.18. Model of flexing tieback connections: (a) original configuration showing the geometry, (b) deformation for IP vertical displacement, (c) IP horizontal displacement, and (d) out-of-plane displacement

Figure 6.19a shows that k_{OP} decreases linearly with decrement in rod diameter and length, because of the lower axial stiffness of a longer and thinner rod. However, it is not influenced markedly by the boundary conditions. The range of stiffness obtained for k_{OP} is 170-280 kips/inch. Figure 6.19b shows the variation of stiffness in the IP directions. $k_{IP,h}$ and $k_{IP,v}$ are generally very similar, since their main contributor is the rod, which behaves the same in the two directions. Their difference can be attributed to the plate, which gives a different contribution in the two directions. The range of stiffness obtained spans from 0.1 to 18 kips/inch.

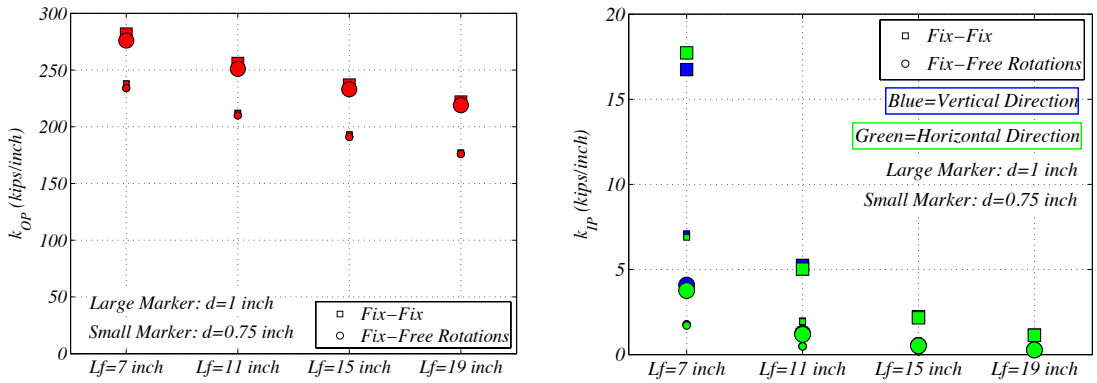

Figure 6.19. Variation of (a) k_{OP} and (b) k_{IP} of flexing connections

Effect of the Stiffness of the Connections on the Dynamic Characteristics of Panels

The different values of stiffness of the bearing and tieback connections found in the previous sections were integrated into a panel model, to understand how they influence its dynamic behavior. Namely, the goals of this study are to:

1. Understand the total range of variation of the frequencies of the three main modes of vibration created by the change in stiffness; and
2. Evaluate how each of the stiffness components affects the dynamic characteristics of the system.

The stiffness of the connections is varied among four values: the highest and the lowest obtained from the analysis of the connections, their average, and an extreme case in which the stiffness was reduced to 25% of the low value, and called "low bound" (Table 6.5). This last case reflects the possible use of connections softer than the typical ones, for instance in case of longer distances between the panel and the point of attachment to the structure. Even if a reduction of 75% might seem large, this is the same reduction observed for the bearing connections in the BNCS building with respect to the typical ones, and for this reason it was considered realistic. It is noted that $k_{IP,}$ and k_{IPh} of the flexing connections were assimilated into a global k_{IP}, since they were very similar. It was decided to consider an average size panel with the geometry of panel 4SE (mass=10.0 kips). However, only two outer tieback connections are used, since this configuration is more typical for a panel of this size. Figure 6.20 shows the model of the panel in this analysis, which was composed by 182 thin shell elements with 728 edges.

Table 6.5. Variation of the stiffness components considered in this study (the three directions OP, IP_h and IP_v refer to the global degrees of freedom of the panel)

Stiffness level	Bearing			Tieback	
	k_{OP} (kips/inch)	k_{IPh} (kips/inch)	k_{IPv} (kips/inch)	k_{OP} (kips/inch)	k_{IPh} and k_{IPv} (kips/inch)
High	17200	12050	12000	280	18
Average	13335	9400	7176	225	9
Low	9470	6750	2352	170	0.1
Low Bound	2367	1687	588	42.5	0.025

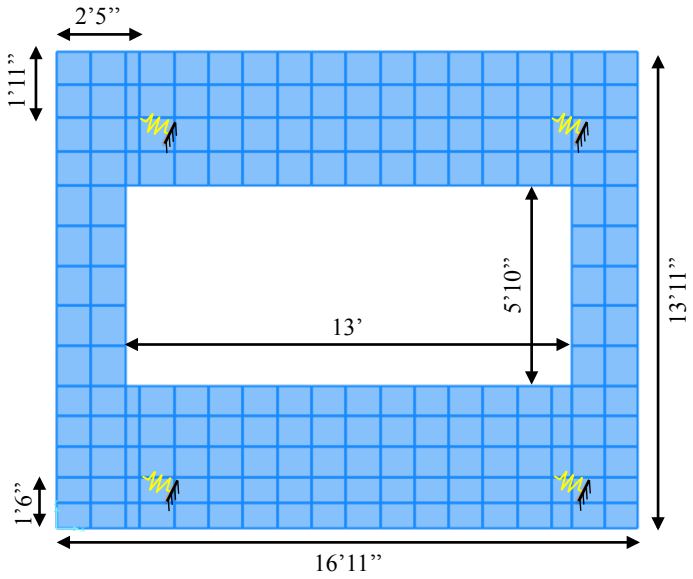

Figure 6.20. Model of the average size panel considered in the analysis (based on the geometry of panel 4SE)

To understand the total range of variation of natural frequencies and set a baseline, the stiffness of both bearing and tieback connections is varied between the high and the low bound values for all the connections at once. The first sector of Figure 6.21 named "baseline" shows the results from this analysis. The OP bending mode was not affected considerably by the stiffness of the connections in general, since it involves mainly the deformation of the panel itself. The decrement of stiffness from the highest to the lowest values created a decrement in frequency of only 1.6 Hz (from 12.9 Hz to 11.3 Hz, corresponding to -12%). The rocking mode presents a considerable change in frequency with the variation of the connection stiffness, namely its frequency varied from 29.4 Hz to 18.2 Hz (-38%). A large drop in the frequency with decrement in the stiffness of the connections was also observed for the vertical mode. Namely, this mode was at very large frequencies (~68-65 Hz), for large and average stiffness of the connections, while its frequency decreased to 32 Hz (- 52%) for the low bound value of the stiffness. It is noted that, even in this worst-case scenario, the frequency of this mode remained quite large.

A second analysis was performed to study the influence of each of the five components of stiffness on the total variation in frequency. Each stiffness component is initially set to the low value for all the connections, and then one by one each of them was varied from the high, to the average to the

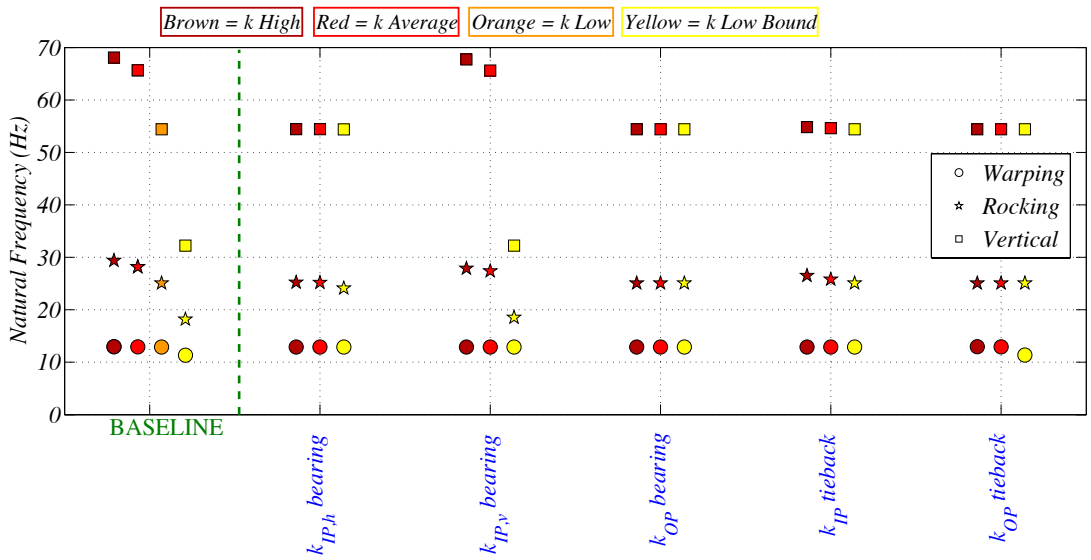

Figure 6.21. Variation of natural frequencies of the panels with change of stiffness of the connections

low bound value. Results from this study are shown in the second sector of Figure 6.21, where the x-axis indicates which stiffness component was varied. The plot shows that the only contribution to the change in frequency of the OP bending mode is the k_{OP} of the tieback connections, which affects the frequency only when set to the low bound value. This can be explained by the fact that the OP bending mode involves mainly OP deformation. The major contributor to the change in frequency of the rocking mode is the k_{IPv} of the bearings, while some minor influence is provided by the change in k_{IP} of the tiebacks and k_{IPh} of bearings. This is due to the fact that the rocking mode involves mainly vertical deformations of the bearings and horizontal deformation of the tieback connections, with only minor horizontal movement at the bearings. Finally, the plot shows that the vertical mode is influenced almost exclusively by the k_{IPv} of the bearing connections, with a minor contribution of the k_{IP} of the tiebacks. This is consistent with the type of motion produced by this mode, which involves vertical deformation of the bearing and tieback connections. The influence of k_{IP} of the tiebacks is relatively small because of their higher flexibility compared to that of the bearing connections.

6.4.2 Variation of the Mass and Stiffness of Panels

Geometry of the Panels

A variation of the geometry of APC panels creates both a change is mass and stiffness.

Namely, a less massive panel has also a reduced stiffness, due to the smaller size or the presence of window openings, while a larger panel tends to be stiffer. Consequently, the global effect of a change in geometry on the natural frequency of a mode is highly dependent on the specific characteristics of the modal shape. To understand the complex interaction between the variation of mass and stiffness, three analyses were conducted:

1. The largest and smallest plain panels commonly installed in the field are considered. The dimensions of such panels are obtained from engineers experienced in the design of APC cladding. This analysis had the goal of determining the effects of the size of panels on the natural frequencies of the three main modes of vibration;
2. Windows are added to these large and small panels to understand the effects of the reduction of mass and stiffness created by the openings;
3. The largest panel with windows is compared to an average size panel having half the mass but also a reduced stiffness. Goal of this third study was to provide further clarification on the relative effects of the variation of mass and stiffness.

These three analysis not only helps explain how the three main modes of vibration are affected by a change in the geometry of the panels, but they also lead to the determination of a general range of frequencies of the three main modes of vibration of the panels.

Figure 6.22a shows the geometry of the largest panel considered (weight =33.7 kips) and the location of its connections. The model used 450 thin shell elements with 1800 edges. Figure 6.22b shows the change in natural frequencies of the OP bending, rocking and vertical modes with variation of the stiffness of the connections. It is noted that in this and the following studies the values of the stiffness is varied from “high” to “low bound” for all the connections at once. The frequency of the OP mode mode is at 12.2 Hz for high stiffness of the connections, and it presents only a small variation in case of average and low stiffness. However, the frequency drops to 8.6 Hz (-30%) in case the low bound stiffness is used. The frequency of the rocking varies between 48.8 and 16.07 Hz (-67%), meaning that for low stiffness of the connection the motion of this massive panel could be activated during an earthquake. The frequency of the vertical mode remains higher for all the values of the

connection stiffness considered, namely in between 75.7 and 22.16 Hz (-70%). Figure 6.22c shows the geometry selected for the small panel (mass=6.25 kips). The model was created using 144 thin shell elements with 576 edges. Figure 6.22d shows that in this case, all the main modes have generally large frequencies due to the low mass of the panel. Namely, the OP bending mode is at 22.9 Hz for very stiff connections while it drops to 16.1 Hz for soft connections (-30%). The rocking and vertical modes are at very large frequencies for all the values of stiffness considered. Namely, the rocking mode varies from 79.4 to 26.7 Hz (-69%) and the vertical mode is in the range between 134 and 41.8 Hz (-69%). In this case, only the OP bending mode is likely be activated during an earthquake if very soft connections are used.

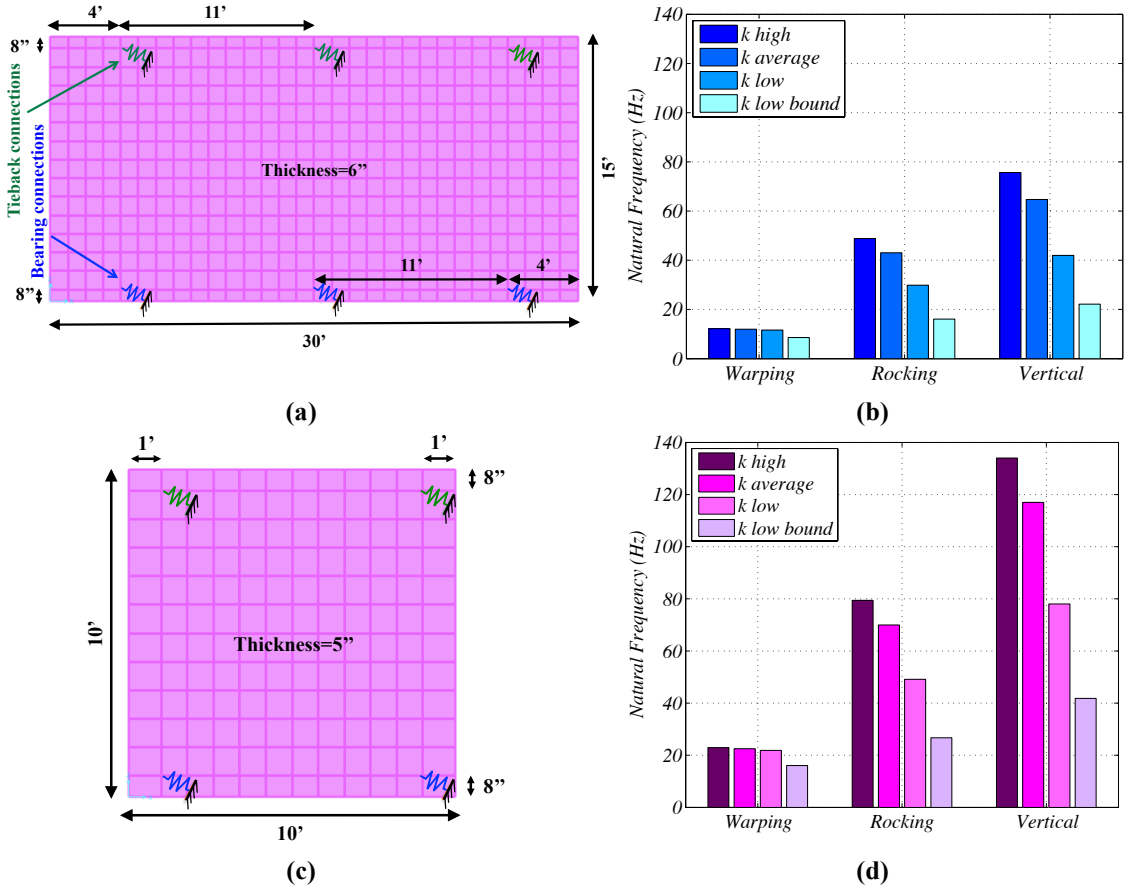

Figure 6.22. Large panel without windows: (a) geometry and (b) variation of frequency, and large panel with two windows: (c) geometry and (d) variation of frequency

In the following analysis, window openings comprising of a 30% of opening area are added to the largest and smallest panel previously considered (Figure 6.23). This value of opening area was

chosen because it creates windows of typical size for the panels under consideration. The addition of the openings generated a drop in the mass of the panels to 23.5 kips and 4.44 kips for the large and small panel, respectively. The addition of windows openings has two competing effects of the natural frequencies: it tends to increase the frequency by lowering the mass of the panels, and it tends to decrease the frequency by decreasing its stiffness. The relative importance of these two effects determines whether the global frequency of the panel is reduced of increased.

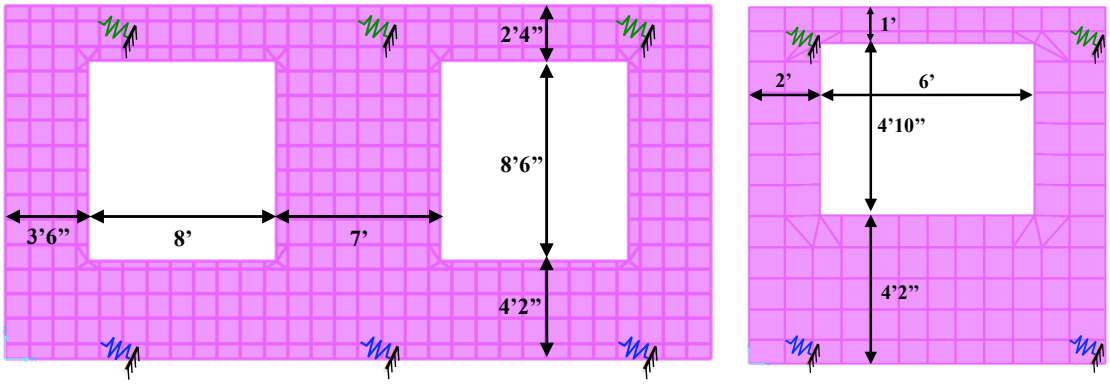

Figure 6.23. Geometry of the (a) large and (b) small panels with the addition of the window openings

Figure 6.24a shows the effect of the addition of the window opening on the OP bending mode for the two panels. It is noted that the 1:1 lines creates two quadrants: in the upper left quadrant the frequency of the panel with windows is larger than that of the same panel without window, meaning that the effect of the reduction of mass in predominant. The reverse happens in the second quadrant, where the predominant effect is the reduction in stiffness. Since the OP bending mode involves mainly a deformation of the panels, both the reduction of the mass and stiffness had a large effect, and the plot shows that, for the higher values of the connection stiffness, the two effects compensate and the frequency of the mode does not change considerably. However, when the stiffness of the connection gets to the low bound value, the frequency of this mode become larger in the case of panel with the window opening, meaning that the effect of the reduction in mass prevails. This is caused by the fact that the global stiffens of the panel is determined by a combination of the stiffness of panels and connections. When the flexibility of the connections is very large, it controls the final response, which is then relatively less sensitive to the flexibility of the panel, and more to its mass. The total range of

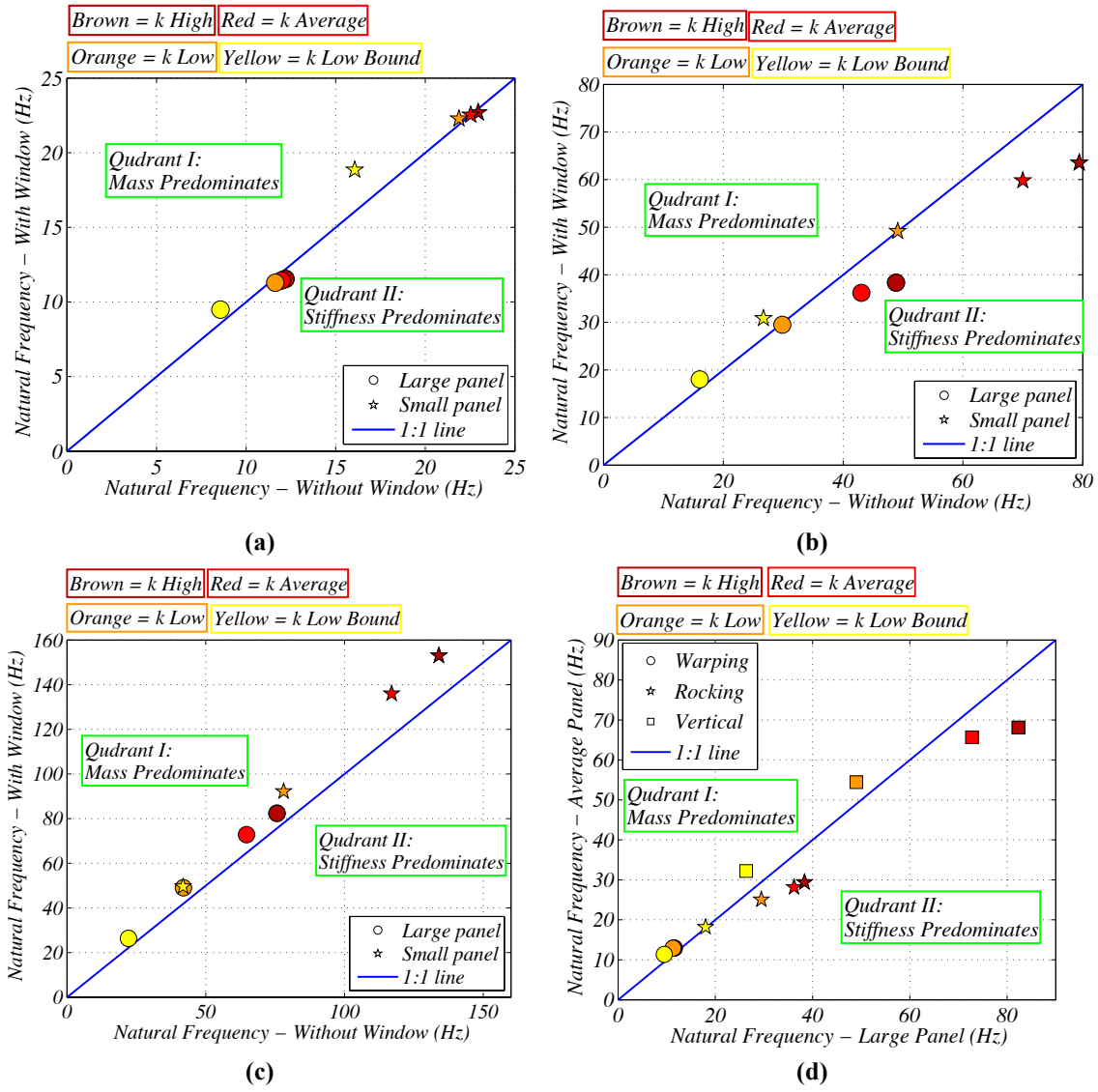

Figure 6.24. Comparison of the natural frequencies of the panels with and without windows for the (a) the OP bending mode, (b) the rocking mode, and (c) the vertical mode and (d) comparison of natural frequencies for the large panels with windows and the average size panel with windows

frequencies for this mode becomes 9.5-11.5 Hz for the large panels and 18.8-22.7 Hz for the small panel.

Figure 6.24b shows the same results for the rocking mode. Generally, this mode is more sensitive to the reduction in stiffness, especially at high stiffness, while the effect of the change in mass and stiffness compensate at low stiffness of the connections. This can be explained by the fact that, when the connections are really stiff, the deformed mode involved also a deformation of the panels, which is much easier in the presence of window openings. The total range of natural frequency for the

panel when window openings are present is 18-38.3 Hz for the large panels and 30.8-63.5 Hz for the small panels.

Figure 6.24c presents the same results for the vertical mode. In this case the reduction of mass created by the addition of the window openings creates an increment of the frequency in all cases considered for both panel sizes, hence the effect of the reduction of mass is always predominant. This can be explained by the fact that this mode involves an almost rigid movement of the panel in this case, and thus the stiffness if mainly the one provided by the connection, while it is not affected by the stiffness of the panel itself. The range of frequency of this mode is very high, at 26.3-82.3 Hz for the large panels and 49.6-153 Hz for the small panel.

To further clarify the relative effects of mass and stiffness for each mode, a cross comparison between an average size panels (Figure 6.20) and the large panel with windows (Figure 6.23) was conducted. The first panel has less than half the mass (m=10.0 kips) but it is also less stiff due to its geometry, while the largest panels was more massive (m=23.5 kips) and stiffer. Figure 6.24d presents such comparison. Even if the mass of the large panel is more that double, the frequency of the OP bending mode is similar in the two cases, meaning the change is stiffness and mass compensate each other. For the rocking mode, the frequency is higher in the case of the largest panels, meaning that the increment is stiffness is more relevant that the increment in mass. As for the vertical mode, there are different results depending of the stiffness of the connections. At low stiffness, the panel tends to move rigidly, thus the influence of the increment in mass is predominant and the less massive panel has a higher frequency. However, at higher stiffness of the connection this mode involves more deformation of the panel, thus the effect of the increment in stiffness in larger, and the stiff-massive panels has the higher frequency.

In conclusion, the geometry of the panel influences the frequency of the modes by both changing its mass and frequency, and the following general observations can be made:

- OP bending mode. This mode is highly influences both by the mass and stiffness of the panels, and in many cases the two effects compensated each other and lead to similar frequencies. This was observed for the same panel with and without windows, and in the comparison between

panel 4SE and the massive panels with windows.

- Rocking mode. This mode is influence more by the change in stiffness than by the change in mass. In fact, the addition of windows tends to create a decrement in the frequency, and the softer-lighter panel 4SE had lower frequencies respect to a large-stiff panel.
- For the vertical mode, results depend more on the mass of the panel. This was especially true in case of the addition of windows to the same panel, which created panels with higher frequency. However, the comparison between panel 4SE and the larger-stiffer panel revealed that this might now always be the case: in connections are very stiff and thus the panel is more subjected to deformation, the influence o the stiffness might predominate and create an increment in the frequency even for increased mass.

Figure 6.25 summarizes the variation in natural frequencies of the main modes for the case considered: small panel (with and without window opening), average size panels and large panel. The total range of the stiffness was:

- OP bending mode: 8.6-22.9 Hz;
- Rocking mode: 16.1-79.4 Hz; and
- Vertical mode: 22.16-153.1 Hz.

The vertical mode is the one presenting more variability, but the OP bending mode is the more likely to be activated during and earthquake.

Variation of the Location of the Connections

The location of tieback and bearing connection on an average size panel was varied to determine its influence on the main modes of a panel. The model of panel 4SE was used, as already presented (Figure 6.20). The stiffness of the connections was varied from high to the low bound. Four different location of the connections were chosen (named Case 1 through Case 4) and they are shown in Figure 6.26a. It is noted that in this analysis there was not only a change in the frequency of the modes, but also a significant change in the modal shape, making the analysis of the results more complicated. Figure 6.26b summarizes the change in natural frequency for the four cases considered.

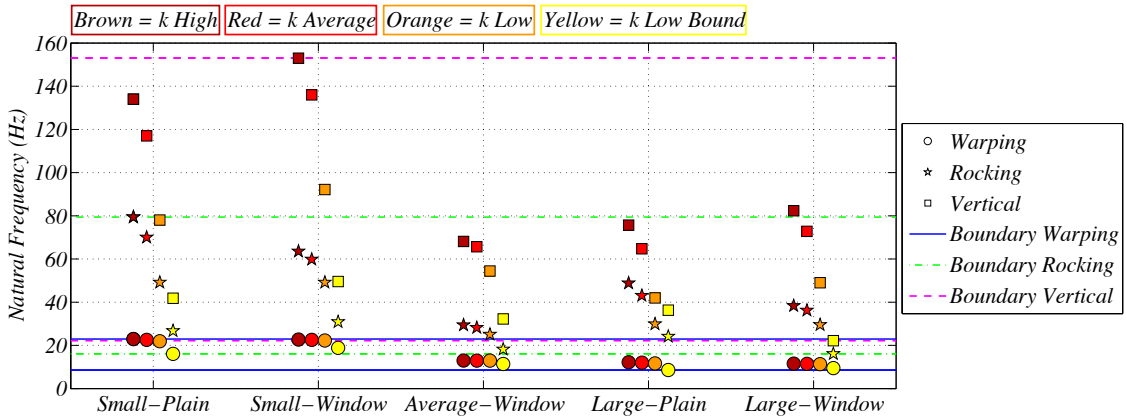

Figure 6.25. Change in the natural frequencies of the panels with variation of the geometry of the panels

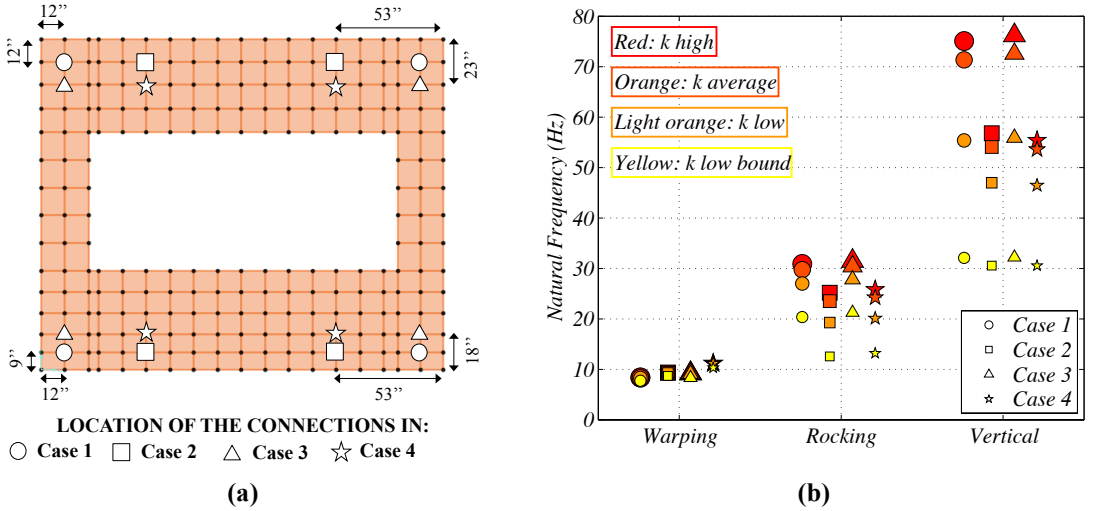

Figure 6.26. (a) location of the connections in the four cases considered and (b) influnce of the location on the frequency of the modes considered

The OP bending mode presents a reduction in frequency in case the connections are placed on the outer edge of the panel and a higher stiffness in case 4, when they are placed more at the center. The frequency of the mode varied from 8.3 Hz in case 1 to 11.1 Hz in case 4 (+33%). Clearly the change is due to the fact that allowing more free space for the panel to deform reduces its stiffness hence its frequency. The rocking mode is characterized by a lowing of the frequency from ~27.5 Hz in case 1 and 3 to ~19.7 Hz (-28%) in case of case 2 and 4. Difference of these sets of cases was the horizontal location of the connection. Clearly, the decrement in frequency is due to the to the decrement in the arm of the connections in case 2 and 4, which facilitates motion and makes the rocking motion of the panel

easier (i.e. softer). The same trend is observed for the case of the vertical mode but at higher frequencies. In this case the change in frequency from ~55.7 Hz in case 1 and 3 to ~46.7 Hz in case 2 and 4 (-16%) was due to a variation in modal shape (Figure 6.27). From the deformed modal shape, it is possible to observe that, when the connections are far apart, the vertical movement is more rigid, probably because of the influence of the vertical concrete elements acting axially. However, when the connections are further from the edges, each section of the panel can more freely bend, thus softening the behavior.

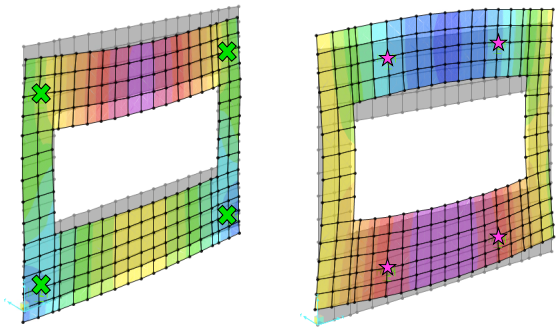

(a) **(b)**

Figure 6.27. Vertical modes in (a) case 3 and (b) case 4

Variation of Concrete Properties

In this third study, it was decided to analyze the influence of concrete stiffness by applying a variation factor on the original stiffness (E=4030 ksi). Two cases considered extreme are assumed, namely:

- Softer concrete (e.g. caused by cracking). The variation factor applied to E was assumed to be 0.35, as suggested by ACI for wall elements. This is clearly a really extreme value. To facilitate a comparison, an intermediate variation factor of 0.7 was also considered;
- Stiffer concrete. In this case it was considered an increment in stiffness due to the normal process of gaining of strength of concrete in time. Assuming that over time the strength gain of concrete could reach 1.2 (Nilson et al. 2004), and considering a concrete mix of 6000 psi at 28 days, this concrete could reach a strength of 7200 psi with time. The resulting E would be 4800 ksi, corresponding to a variation factor of 1.2.

  The analysis was run considering a low value of stiffness for the connections and the original

location of the connections. Figure 6.28 shows that varying the stiffness of concrete lead to a variation of the frequency of the OP bending mode between +8% (15.5 Hz) and -40% (8.5 Hz). The rocking motion varied from +6.3% to -34.9% from the original value, with its frequency varying from 25.1 to 16.3 Hz. The rocking motion varied between 56.4 Hz (+4%) and 38.7 Hz (-29%) and it remained at large frequencies for all the cases considered.

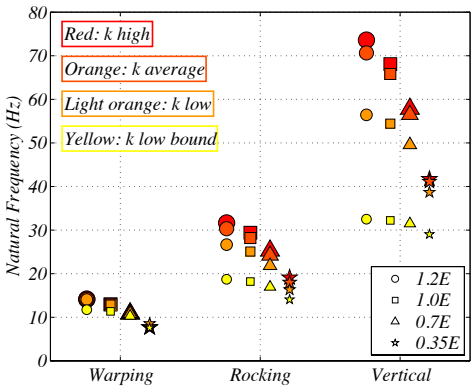

Figure 6.28. Variation of the three main modes of vibration with the variation of concrete properties

6.5 Summary Remarks

The following conclusions can be drawn from the studies performed in this chapter:

- Numerical models reproducing APC panels and connections can capture with reasonable accuracy their dynamic characteristics, importantly for OP bending modes (sections 6.1 and 6.2);
- Bearing connections have a very high stiffness in the OP and IP_h directions, while the stiffness in the IP_v direction could reach relatively low values when the supporting structure is further from the panel. In contrast, flexing connections have a low stiffness in the IP direction, while a higher stiffness in the OP direction.
- For the typical range of stiffness of the connections, there are three main modes controlling the response: a bending mode in the OP direction, a rocking mode in the IP_h direction and a vertical model which dominated the IP_v response;
- Modes of vibration are specific to the particular geometry of the panel, which can vary greatly in the field. For this reason, a case-by-case analysis is useful to determine the dynamic

characteristics of the APC system. In this work, sensitivity studies were performed to obtain general trends of behavior. Namely, the influence on the frequency of the three main modes of vibration of the stiffness of the connections (from high to extremely low cases), their location, and the concrete properties was analyzed for a panel of average dimensions. Subsequently, models of the largest and smallest possible panels with and without windows were created to study the effect of the panel size on natural frequencies. The following general trends were observed:

1. First OP bending mode. This is generally the mode at the lowest frequency and thus the one with the most potential to be activated during an earthquake. For an average size panel, the range of frequencies obtained by changing the variables under consideration one at a time was 8.3 – 15.5 Hz. The frequency of this mode was not affected excessively by the stiffness of the connections, except for the k_{OP} of tiebacks, which created a small drop in frequency (~ 6% in the case considered). The largest reduction of the natural frequency of vibration of this mode was obtained by changing the location of the connections. In fact, it was in this case that the panel reached its minimum possible frequency of 8.3 Hz. Even if the determination of a quantitative trend is not possible since it is highly depended on the specific panel geometry, from a qualitative point of view it can be concluded that lower frequencies are obtained in case the connections are further from each other and the panel has more free space to deform. The reduction of Yong modulus of the concrete also greatly affected this mode, for a total range of variation between 8.5 and 15.5 Hz. In the case of the largest panel considered, the total frequency range of this mode varied from 8.5 to 12.2 Hz depending on the stiffness of the connections (including both the solid panels and the panel with windows). The frequency of this mode becomes very large for small panels, with a total range of frequencies from 16.1 and 22.9 Hz. In conclusion, since in many cases the natural frequency of the OP bending mode is below 16.7 Hz, it is not always accurate to consider the panels to be “rigid” elements in this direction of motion, and thus assign a component amplification factor of 1.0 (ASCE 2010);

2. Rocking mode. For an average size panel, it was found that this mode has high frequency, generally larger than the threshold value of 16.7 Hz. For the average size panel considered, the total range of frequencies obtained by changing the variables under consideration one at a time was 16.3 – 29.4 Hz. First of all, a reduction of the k_{IPv} of the bearings and k_{IPh} of the tiebacks to extremely low values showed able to create a reduction in the frequency of the mode from ~29 Hz to ~18 Hz. The change in the position of the connections was also able to create considerable change in frequency (19.3-27.8 Hz). From a qualitative perspective, if connections are located closer to the vertical centerline of the panel, the frequency of this mode is reduced. This effect is created by the reduction in the arm between the connections. Reducing the stiffness of concrete also created a considerable variation in the frequency of this mode, for a total range of 16.3 - 26.6 Hz. In the case of a very large panel without windows, the total range of frequencies obtained is between 24.1 and 48.8 Hz, while the presence of two window openings in the same panel creates a decrement in the frequency, for a total range between 18 and 38.3 Hz. In case of the small possible panel, frequencies of this mode are really high for all the considered stiffness of the connections. Namely the frequency varies between 26.7 and 79.4 Hz for the plain panel and 30.8 and 63.5 Hz for the panel with the window opening. Since the natural frequencies of the rocking mode is mostly larger than 16.7 Hz, it is reasonable to consider the panels “rigid” when moving in the in-plane horizontal direction;
3. Vertical translation mode. This mode is generally characterized by very high frequencies. For the average size panel considered, the frequency of this mode remained above 30 Hz in all the cases. Namely, a variation in the range of stiffness of the connections, created a range of frequencies between 32.2 and 68.1 Hz. Varying the location of the connections showed to have some effect on the frequency of this mode, with a possible reduction from ~56 Hz to ~ 47 Hz in case of connections closer to the vertical center axis of the panel. This was attributed to a change in the modal shape. The variation of the stiffness of the concrete created a range of natural frequencies of 56.4 to 38.7 Hz. In case of the very large

panels, the total range of frequency was 82.3 to 26.4 Hz, while for the smaller panels it was between 153 Hz and 41. 8 Hz, clearly way too large to be affected by earthquake motion. Thus, when moving in the in-plane vertical direction, an APC panel can be classified as “rigid”.

Further practical conclusions drawn for this study include:

- If stiff connections are used: only OP bending modes are likely to be activated during an earthquake. A model of the specific geometry of the panel can lead to the determination of the natural frequencies of these modes;
- If OP bending modes are a concern: an increment in the value of k_{OP} of the tiebacks can create an increment in the frequencies of these modes. In addition, locating the connections closer to each other and leaving less space available for the deformation of the panels can also help creating stiffness;
- If bearing connections with a lower k_{IPv} are used (this can be the case for a larger distance between the building and the panels): the rocking mode can lower to frequencies possibly activated during an earthquake. If this is a concern, placing the connections further from the vertical centerline of the panel or using tieback with larger k_{IPh} can provide more stiffness to the system;
- If very small panels are used: it is unlikely that any of the modes can be activated during an earthquake, unless very low stiffness of the connections are used. This could lead to the activation of the OP bending mode

ACKNOLEDGEMENTS

Chapter 6 reproduces content and images of the material as it appears in the Proceedings of the ATC-SEI conference 2015. Pantoli, E., and Hutchinson T. C., 2015. “Experimental and Analytical Study of the Dynamic Characteristics of Architectural Precast Concrete Cladding.” Proceedings, ACT-SEI, 2nd conference on improving the seismic performance of existing buildings and other structures, December 10-12, San Francisco, CA. The author of the dissertation is the principal author of the above cited papers.

Chapter 7

Accelerations in APC Panels During Service Level Earthquakes

Buildings can behave in very different ways when subjected to small and large earthquake motions. During service level earthquakes, modern buildings are thought to remain mostly within the linear elastic range of behavior, with the response dominated by the first mode, especially for short buildings. During larger earthquakes, such as the design level earthquake, buildings are intended to undergo plastic deformation. In this case, the building response is also influenced by higher modes, whose frequency can also shift due to softening of the structure. Early research on nonstructural components often did not take into account this difference in response, leading to possible errors in the calculation of both the structural and component amplifications of input accelerations.

In this dissertation, separate studies are conducted for low intensity service level earthquakes and higher intensity design basis earthquakes. In the former case, the building remains elastic, while building inelastic response is considered in the latter case. This chapter presents the results of the first study. It is noted that understanding the behavior of nonstructural components in service level earthquakes, and thus starting to apply the principles of performance-based design to nonstructural components, is very important to create resilient buildings, which can remain fully functional after small earthquakes.

In this chapter, a linear model of the BNCS building incorporating one APC panel modeled as a single-degree-of-freedom (SDOF) system is created in SAP2000 (CSI 2013). This model is first validated using the experimental results, and then it is used to perform parametric studies aimed at understanding the amplification of accelerations in APC panels with the variation of the dynamic characteristics of the panels, their location and the input motion considered. Results from these studies are compared to the present suggestions in ASCE-7 (ASCE 2010). It is noted that this study focuses exclusively on the BNCS building because of the large amount of experimental data available.

7.1 Description of Building and Panel Models

7.1.1 Building Model

Geometry of the Elements

The geometry of the building was described in Chapter 3 of this dissertation. This building was modeled considering its beams, columns, walls and slabs. Columns and beams were modeled with frame objects aligned with the geometric centerline of the member, and assigned with their actual cross section. Namely, columns were modeled as rectangular 26''x18'' sections, with the long direction being in the direction of motion. Beams were also modeled as rectangular sections 28'' tall and 12'' wide, while the cladding beams at the upper stories were 18''x18''. A total of 78 frame objects were used.

Slabs and elevator walls were modeled as thin shell objects with their actual thickness (8'' and 5'', respectively). Such a strategy is reasonable for two-dimensional elements with thickness less than 1/5 or 1/10 of the span. A total of 319 thin shell elements were utilized. In totality, 434 nodes were used. Both the base of columns and elevator walls were considered fixed. The foundation was not explicitly modeled. The detailed geometry of a typical floor is presented in Figure 7.1. It in noted that the roof did not have the elevator opening.

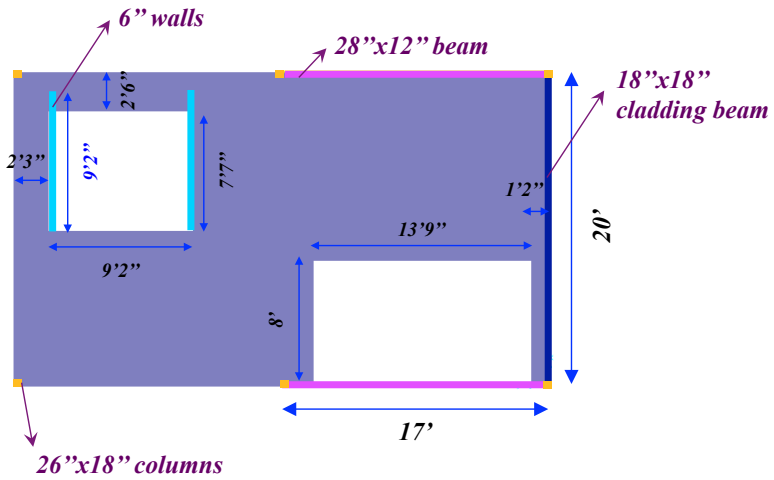

Figure 7.1. Detailed geometry of the plan view for a typical floor

Material Properties

After the creation of the building model, the material properties had to be attributed to each of the building members. Since the building model was linear, the key material property is the Young

modulus E, which in this case is defined as a function of the unconfined compressive strength of the concrete f'$_c$ as defined by Chang and Mander (1994):

$$E = 185000 f_c'^{3/8} \quad \text{Eq. 7.1}$$

Where f'$_c$ needs to be in psi. The values of f'$_c$ for each member was found with compression tests on concrete performed at the beginning of the testing sequence. Since different elements of the building revealed very similar f'$_c$, it was decided to group these elements together and assign to this group the average f'$_c$. The four groups of structural elements with similar concrete properties were:

- Columns and walls at the first level;
- Columns and walls at the upper levels;
- Beams and slabs at the second, third and fourth floors;
- Beams and slabs at the fifth floor and roof.

The average f'$_c$ and the corresponding E for each group are presented in Table 7.1. Figure 7.2 shows the building model, presenting only the frame elements in part a, and only the thin shell elements in part b.

Table 7.1. Concrete properties for different structural elements

Element	f'$_c$ (ksi)	E (ksi)
Columns and walls at the first level	7.91	5357
Columns and walls at the upper levels	8.44	5489
Beams and slabs at the second, third and fourth floors	7.04	5128
Beams and slabs at the fifth floor and roof	8.17	5423

Distribution of Additional Vertical Weight and Horizontal Inertial Masses

Additional vertical weights and horizontal inertial masses had to be added to the model to account for the nonstructural components (summarized in Chen et al. 2013a) and the regions of the slab outside of the centerline of the beams (Figure 7.3a). The following considerations about vertical weights were made:

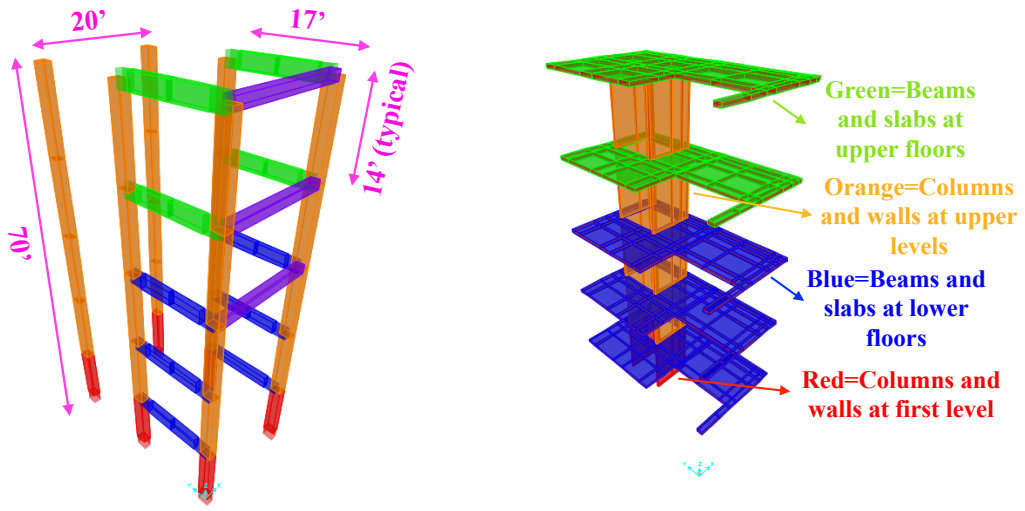

(a) (b)

Figure 7.2. Model of the BNCS building: (a) frame elements and (b) thin shell elements used for walls and floor component showing the color code used for each group of elements having the same material properties. Note that the model frame elements are shown apart from the shell elements only for clarity

- The weight of the stairs was applied to the slab, at the points corresponding to the attachments of the flights and landing to the floors;
- The weight of the elevator was distributed among the two elevator walls;
- The weight of the cooling tower and air handling unit was applied on the roof slab at the location of the centerline of each piece of equipment;
- The weight of the penthouse was lumped at four locations in the roof slab;
- The vertical weight of the balloon framing rested on the foundation, and thus it was not included;
- The vertical weight of each cladding panel was lumped in the bottom slab at a point underneath the center of the panel;
- The weight of the ceilings, partition walls, equipment and others was lumped at the center of the floor;
- The weight of the parts of the slab on the outside of the centerline of the beams was added as a lumped weight at the centerline of the corresponding side of the building (Figure 7.3a).

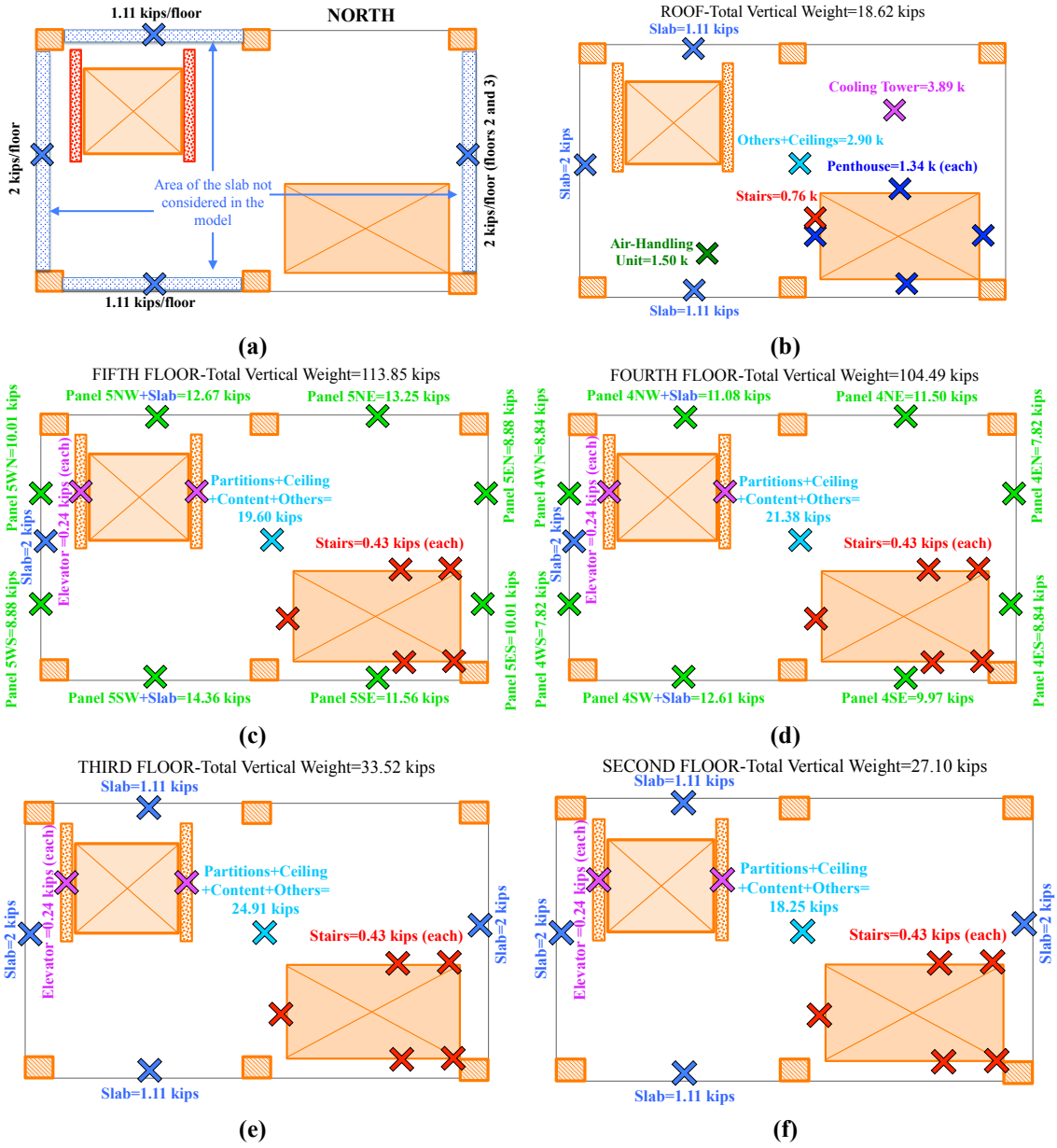

Figure 7.3. (a) Additional mass created by the slab, and distribution of vertical weights at (b) roof, (c) fifth, (d) fourth , (e) third, and (f) second floor ("X" denoted mass placement)

The exact location of all additional vertical weights at each floor is presented in Figure 7.3b-f. Figure 7.4 presents a summary of how the inertia masses were attributed at each floor. The horizontal inertial masses of partition walls, content, ceilings, elevator, stairs and additional portions of the slab were considered similarly as that of the vertical weights. The horizontal inertial mass of the cladding panels required some special consideration, since it is distributed differently in the OP and IP horizontal direction, namely:

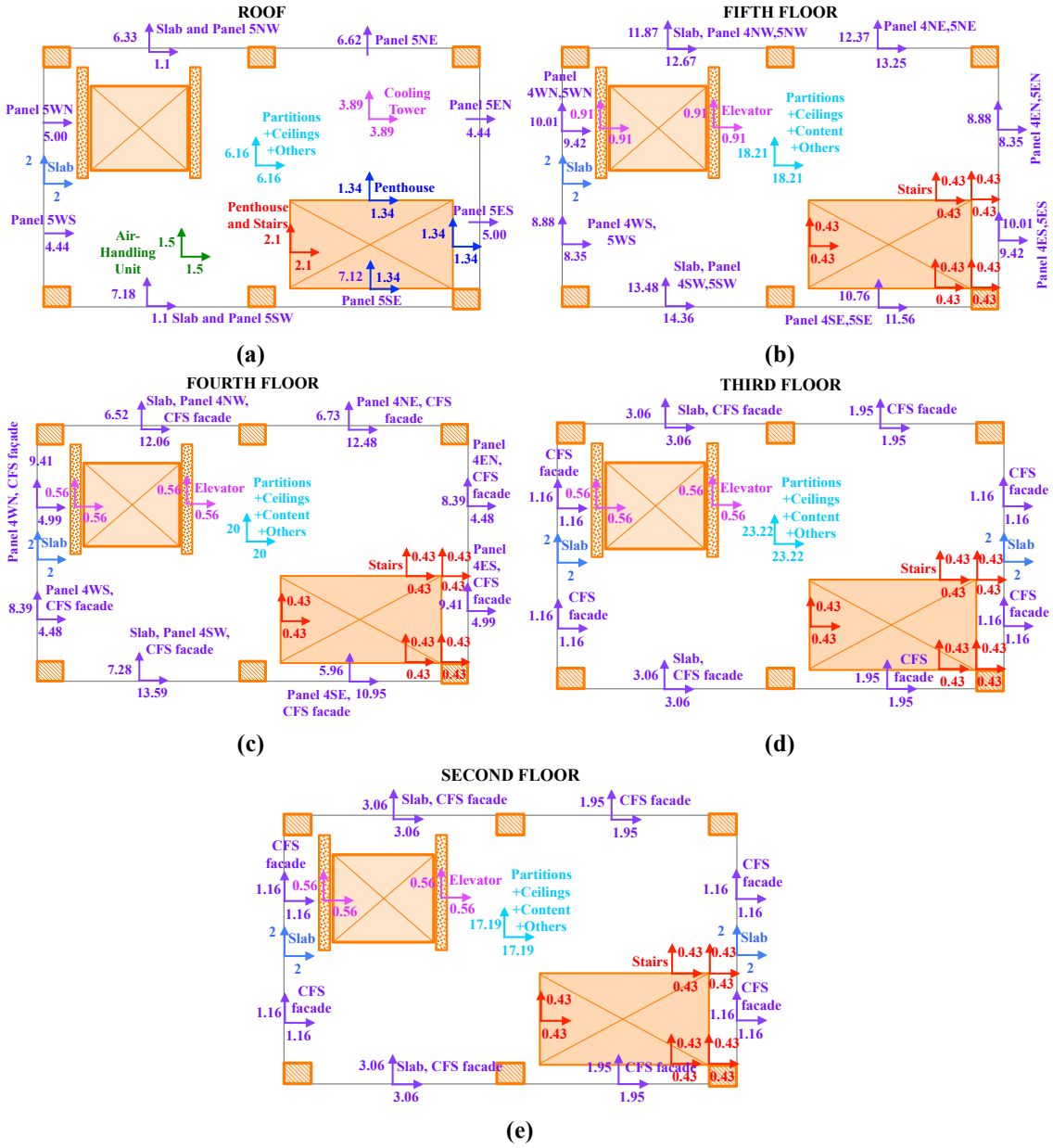

Figure 7.4. Distribution of horizontal inertial masses at (a) roof, (b) fifth, (c) fourth , (d) third, and (e) second floors (units: kips)

- OP direction of the panel: the mass was equally divided, i.e. half to the top and half to the bottom slab;
- IP direction of the panel: the mass was assigned to the bottom slab. Both translational masses in all directions and rotational masses around the north south axis were added.

The inertial horizontal mass of the cold-formed steel façade was also assigned to the floors. Its

total mass (37.34 kips) was distributed to the floors proportionally to their tributary area, namely it was divided among floor four (6.22 kips), floor three (12.44 kips), and floor two (12.44 kips), while the mass attributed to floor one was not considered as this rested on the shake table. At each floor, the mass was lumped as 8 points, two per side of the building, with each location having a lumped mass proportional to its tributary length. This was considered a feasible representation of the mass distribution, and it was consisted with the distribution of masses from the APC cladding.

7.1.2 Comparison of the Dynamic Characteristics of the Building: Numerical Model and Test Results

The building model was first of all validated via comparison between experimental and numerical natural frequencies and mode shapes. The experimental natural frequencies were determined with data recorded during white noise tests conducted before the starting of the BI seismic testing sequence by Astroza et al. (2013). It is noted that, for the scope of this validation, it was decided to use the average natural frequencies among those obtained with different system identification methods as investigated in Astroza et al. (2013). The numerical natural frequencies were found by performing modal analysis using the Ritz vectors in the SAP2000 model. Table 7.2 and Figure 7.5 present the comparison between experimental and numerical natural frequencies. The error in the natural frequency was within 30% for all the modes (with an average error of ~20%), with the numerical natural frequencies lower than those determined experimentally. As the masses are known to be accurate, this implies that, at the beginning of the testing sequence and for very low amplitude input motions, the physical building was stiffer than the present numerical model. This is most likely attributed to the stiffness provided by the partition walls and other multiply attached nonstructural components, which are not considered in this model. Figure 7.6 presents the first three numerical natural modes.

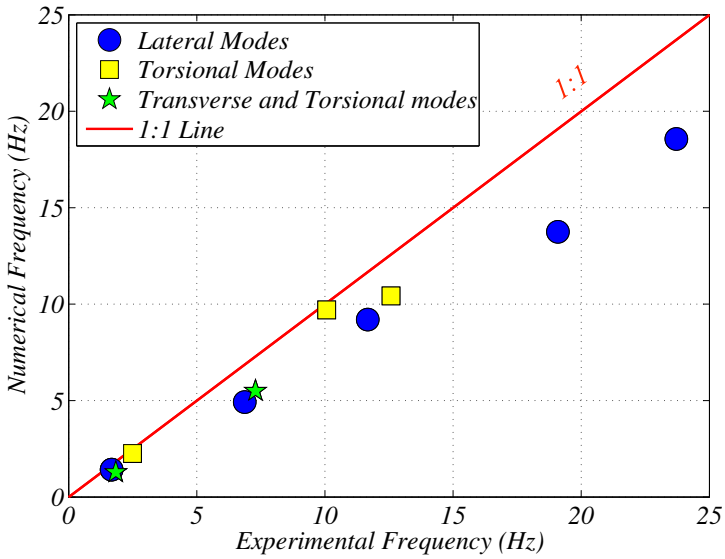

Figure 7.5. Comparison of natural frequencies obtained experimentally and numerically. (Includes values found at white noise with 1% and 1.5%g RMS)

Table 7.2. Summary of the comparison between experimental and numerical results

Mode #	Mode Type	Experimental frequency range (Hz)*	Experimental frequency (mean)* (Hz)	Numerical frequency (Hz)	Difference (%)
1	First Longitudinal	1.55-1.83	1.68	1.42	-15%
2	Transverse and Torsional	1.81-1.90	1.84	1.30	-29%
3	Torsional	2.39-2.52	2.49	2.26	-9%
4	Second Longitudinal	6.68-7.04	6.87	5.00	-27%
5	Second lateral and Torsional	6.94-8.00	7.29	5.53	-24%
6	Second Torsional	9.82-10.38	10.07	9.73	-3%
7	Third Longitudinal	11.50-11.92	11.67	9.32	-20%
8	Third Torsional	12.35-12.76	12.58	10.48	-17%
9	Fourth Longitudinal	18.81-19.42	19.09	13.85	-27%
10	Fifth Longitudinal	23.50-24.44	23.71	18.60	-22%

* From Astroza et al. 2013

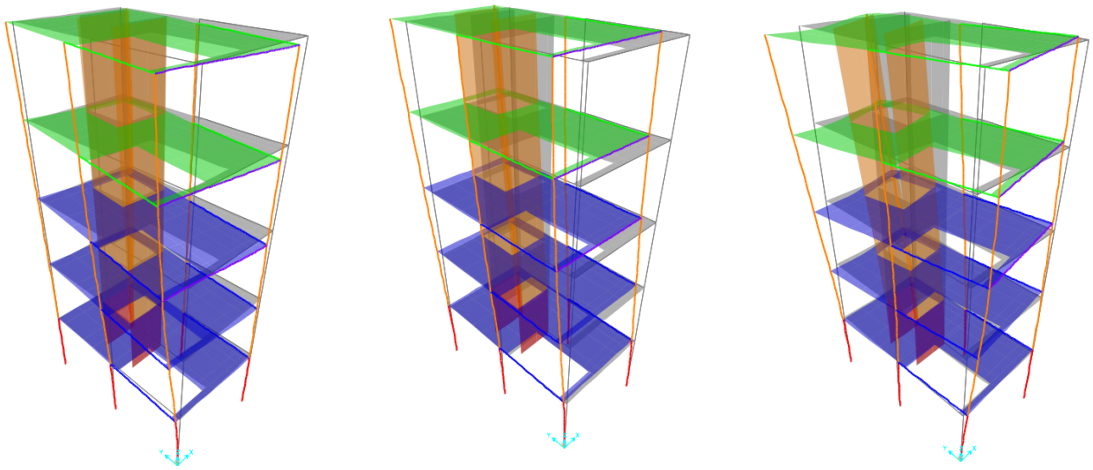

(a) (b) (c)

Figure 7.6. First three natural modes: (a) first torsional, (b) first longitudinal, and (c) first transverse and torsional as predicted with the linear elastic model in SAP2000

Figure 7.7 shows the comparison between the experimental and numerical first mode, which dominates the response of the building. The elevation view of the east-west displacement of the SE column (Figure 7.7a) shows that the numerical model predicts some additional stiffness at the lower levels, which have smaller modal displacement compared to the reality. However, the modal displacements are correct at the upper stories. The plan view of the displacements at the roof (Figure 7.7b) shows that the model predicts more twisting of the building compared to the experimental values.

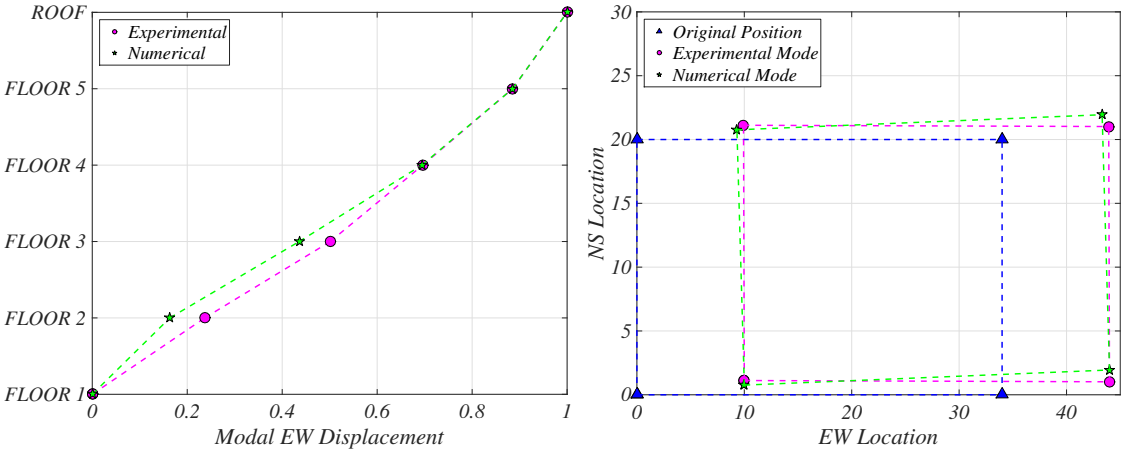

(a) (b)

Figure 7.7. Comparison of the experimental and numerical first mode: (a) modal EW displacement and (b) displacement at the roof

7.1.3 Reduction of Stiffness in the Building Members

It is well documented in the literature that cracking in concrete members creates a significant reduction of their stiffness. Cracking not only occurs during earthquakes, but might happen also under gravity loads, and once stiffness is lost, it is never regained (Priestley 2003). Many design codes recognize this problem, and solve it by suggesting the application of reduction factors to the gross-section stiffness. For example the New Zealand code specifies reduction factors of the gross moment of inertia of 0.35 for beams, and between 0.4 and 0.7 for columns (NZS 3101-2 1995), while ACI-318 code proposes 0.35 for beam, 0.7 for columns, 0.7 for un-cracked walls, 0.35 for cracked walls and 0.25 for flat plates and slabs (ACI-318 2011). A set of reduction factors was also proposed by Pauley and Priestley in 1992, namely these were 0.4 for rectangular beams (range: 0.3-0.5) and 0.6 for columns with low axial load (range: 0.5-0.7).

For the scope of this study, reduction factors were applied only to the values of the Young modulus. These were varied to obtain the same numerical and experimental values of the natural frequency of the first longitudinal mode during the low-amplitude input seismic motions (FB1 and FB2). The natural frequency of the first longitudinal mode during these first two tests was 1.05 Hz (0.95 second period), as presented by Chen et al. (2015). Different reduction factors were applied to the E of the four groups of structural elements presented in Table 7.1, and are shown in Table 7.3. The reduction factors were determined considering the suggestions from previous studies, and the fact that more cracking, thus a smaller reduction factor, was likely present at the lower level. Namely, the following reduction factors were found to create the best match between experimental and numerical results:

- Columns and walls at the first level: 0.65;
- Columns and walls at the upper floors: 0.7. This is the upper value suggested, which is consistent with the fact that the degree of damage at this point was still low;
- Beams and slabs at the lower floors: 0.45;
- Beams and slabs at upper floors: 0.5. This is the upper limit of the reduction factor suggested.

These reduction factors indicate a frequency of the first mode at 1.05 Hz, matching exactly that obtained during the experiment. Table 7.4 presents the full comparison between natural frequencies

obtained with the original and reduced stiffness.

Table 7.3. Original and reduced concrete stiffness

Element	E original (ksi)	E reduced (ksi) (% reduced)
Columns and walls at the first level	5357	3482 (65)
Columns and walls at the upper levels	5489	3842 (70)
Beams and slabs at the second, third and fourth floors	5128	2307 (45)
Beams and slabs at the fifth floor and roof	5423	2711 (50)

Table 7.4. Comparison between the natural frequencies obtained with the original stiffness and reduced stiffness

Mode #	Mode Type	Numerical frequency with original E (Hz)	Numerical frequency with reduced E (Hz)
1	First Longitudinal	1.42	1.05
2	Transverse and Torsional	1.30	0.99
3	Torsional	2.26	1.74
4	Second Longitudinal	5.00	3.82
5	Second lateral and Torsional	5.53	4.34
6	Second Torsional	9.73	7.73
7	Third Longitudinal	9.32	7.28
8	Third Torsional	10.48	8.45
9	Fourth Longitudinal	13.85	10.89
10	Fifth Longitudinal	18.60	14.93

7.1.4 Model of APC Panels

One panel at a time was sequentially incorporated in the building model. Each panel was modeled as a SDOF system with an EW translational mass at the center and two link elements connecting the mass to the top and bottom floor (Figure 7.8). The mass was that of the panel itself, while the stiffness of the two springs were selected to obtain the desired natural frequency of the panel, no local damping is considered at the spring-mass location. By modeling the panel in this way and incorporating it into the building model, it was possible to create excitation to the panels from

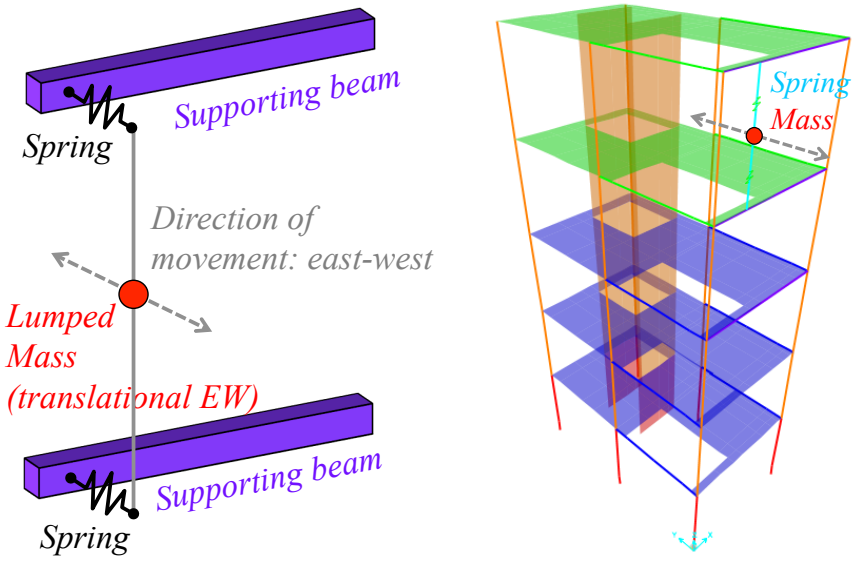

Figure 7.8. Schematic of the building and panel model

both the top and bottom floors. This is very important, and it was ignored in many studies performed in the past on nonstructural components, which determined the amplification of the components using floor response spectra.

Two panels were considered in this study: panels 4ES and panel 5ES, which were alternatively added to the building model. These were selected because they were the only OP panels instrumented with accelerometers, and thus making the validation of the model possible. It was decided not to consider in this study the two IP panels instrumented with accelerometers (4SE and 5SE) for three main reasons:

1. The study of the dynamic characteristics of APC cladding revealed that only the OP bending mode is likely to be activated in an earthquake, since the numerical frequencies of the IP modes are generally very large;
2. During FB1 and FB2, analysis of the response spectra of the IP panels 4SE and 5SE showed that the natural vibrations of the panels was not activated. This confirmed what observed in point 1, and also made the validation of the panel behavior difficult;
3. The comparisons of floor and panels accelerations recorded during the BNCS experiments for the FB motions revealed that the range of amplification in OP panels is larger than that in IP

panels. This can be seen comparing the results in Figure 7.9 and Figure 7.10. When considering the peak accelerations in the panel and bottom floors, the amplifications are from 1.05 to 2 for OP panels, while they are only from 1 to 1.85 for IP panels. When the peak panel accelerations are compared to the accelerations at the top floors, the amplification factors vary from 0.95 to 1.65 for OP panels and from 0.9 to 1.35 for IP panels. Thus, it was concluded that results found considering the OP panel can be extended to include IP panel while still being

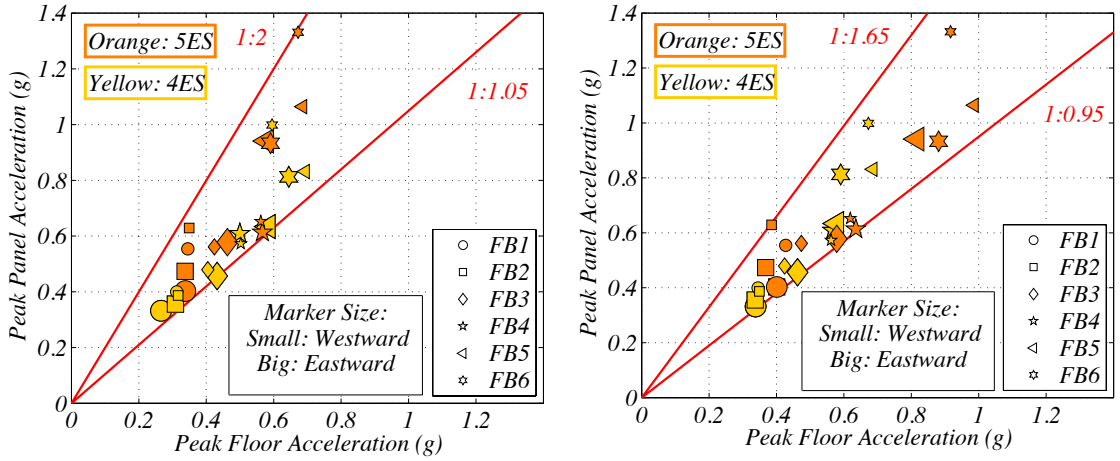

Figure 7.9. Peak floor accelerations versus peak panel accelerations for OP panels considering the (a) bottom floor and (b) top floor

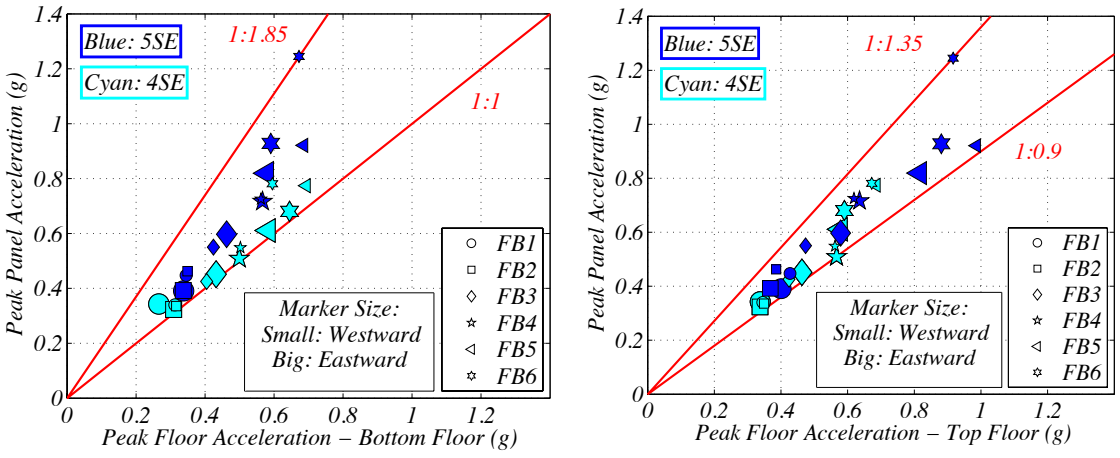

Figure 7.10. Peak floor accelerations versus peak panel accelerations for IP panels considering the (a) bottom floor and (b) top floor

conservative. It is important to notice that the values of peak accelerations in the IP panels in case of panel 4SE and 5SE might be larger than what normally expected, since the bearing connections were much softer that those normally used.

7.2 Validation of the Numerical Model - Linear Dynamic Analysis

The goal of this section is to determine the values of damping minimizing the difference between the results of the numerical linear dynamic analysis and those found in the experiment for the panel and its top and bottom floors. Both the time history of accelerations and floor response spectra were considered. Since this chapter focuses on linear elastic behavior, it was decided to validate the model by comparing the response of the building and the panel during FB1 and FB2, during which the system remained quasi-elastic. A separate validation was performed for the model with panel installed at the fifth and fourth levels. The experimental time histories of accelerations were obtained by applying a baseline correction and a low-pass filter (4^{th} order Butterworth with cutoff frequency at 25 Hz) to the raw data. The numerical time histories were found in SAP2000 with the modal solution using the Ritz vectors previously determined. When this solution method is used, damping can be attributed separately to each of the natural frequency. The input motion to the numerical model was the time history of acceleration at the first floor of the building in the east-west direction (averaged between the recordings at the four corners). The input and output signals were both sampled at 250 Hz (sampling period of 0.004 seconds). After finding the damping ratios and validating the model for FB1 and FB2, a comparison of the results for FB3 is also presented. Test FB3 is treated differently in that damage accumulated during FB1 and FB2, thus the response during FB3 can be assumed nonlinear, and the natural frequency of the building began to shift due to softening of the structure.

7.2.1 Optimal Damping Ratios during FB1 and FB2 – Panel 5ES

When the model of panel 5ES was included in the building model, a stiffness of 66 kips/inch had to be attributed to the springs to have a natural frequency of the panel model corresponding to the experimental one of 7.9 Hz. In case of FB1, the following values of optimal damping were determined:

1. Damping of the first mode of the building: 9%. This value dominates the structural response and provides a very good comparison of the response spectra of the floors at low frequencies;

2. Damping of the second and third longitudinal modes: 13%. The numerical model predicted a relatively large influence of these higher lateral modes, and for this reason a larger damping had to be added;
3. All the other modes: 4%. Specifically, this created a good comparison at the natural frequency of the panel.

The comparisons of the time histories of accelerations and displacements, pseudo acceleration spectrum and pseudo displacement spectrum for the roof and fifth floor during FB1 are presented in **Figure 7.11** through Figure 7.14. For all these cases, there is a good comparison between numerical and experimental results.

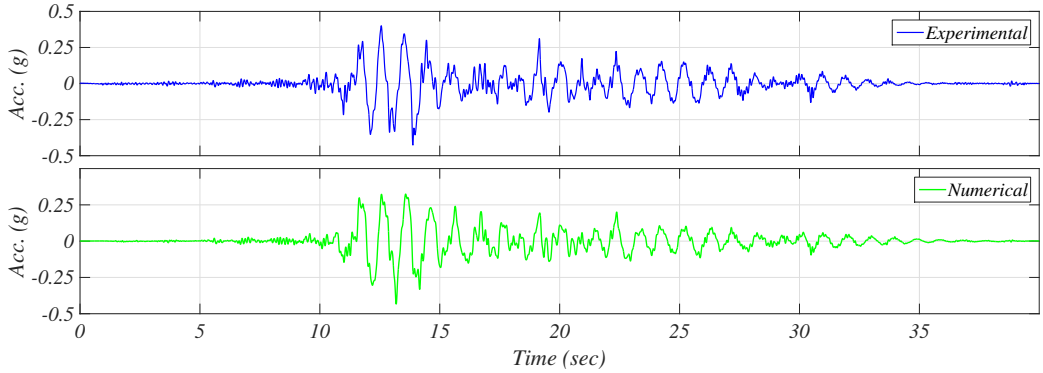

(a)

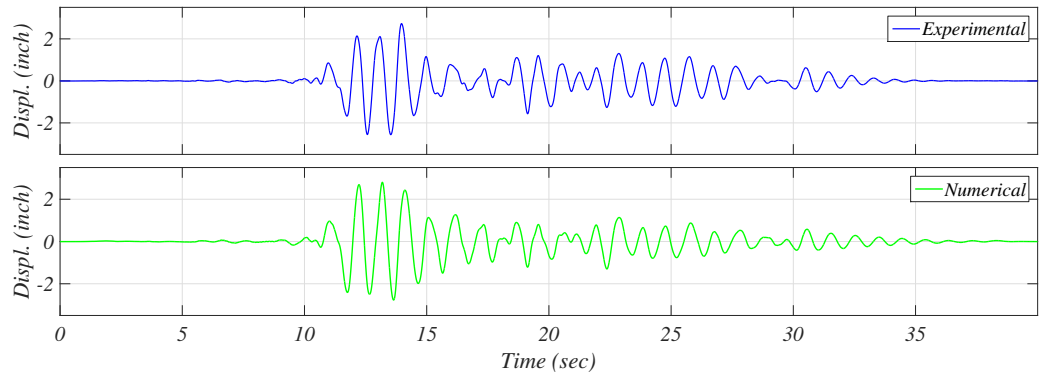

(b)

Figure 7.11. Comparison between experimental and numerical results for the model with panel 5ES during FB1: (a) time history of absolute accelerations, and (b) time history of relative displacements for the SE corner of the roof

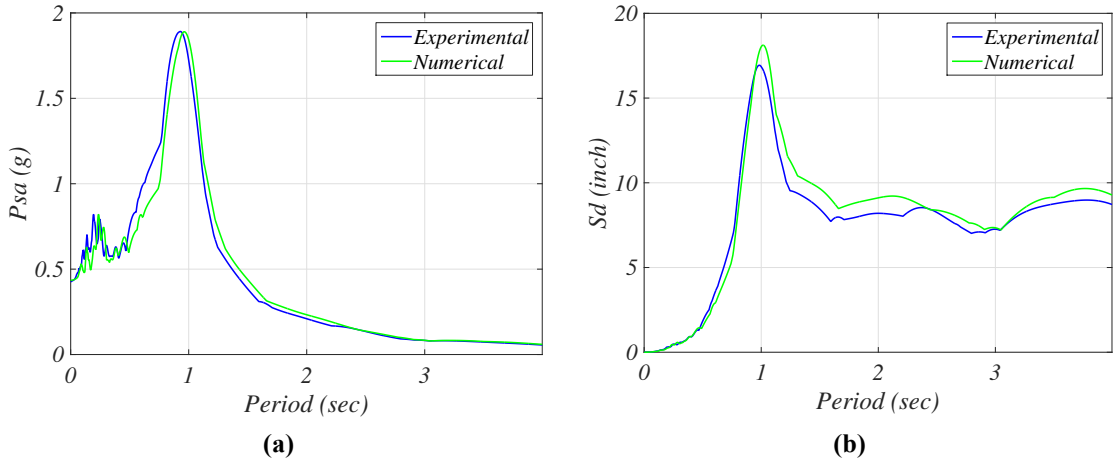

(a) **(b)**

Figure 7.12. Comparison of experimental and numerical results for the model with panel 5ES during FB1: (a) pseudo acceleration spectrum and (b) displacement spectrum for the SE corner of the roof

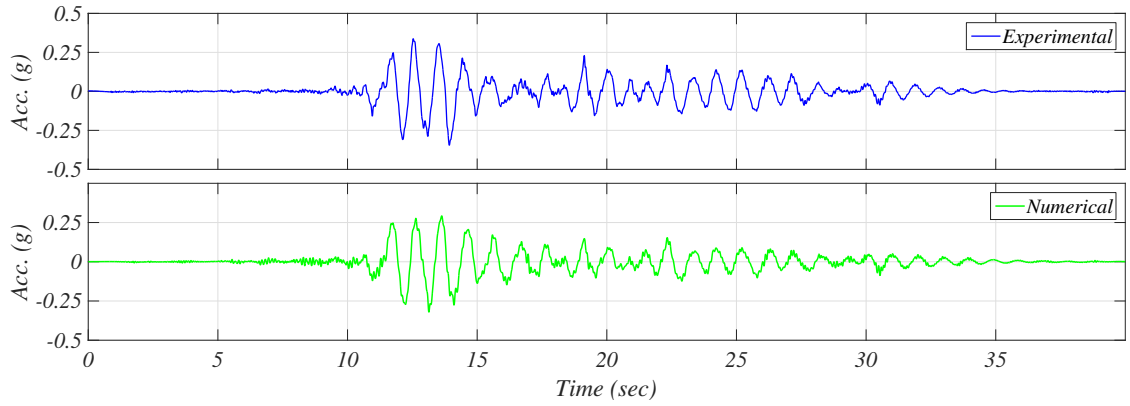

(a)

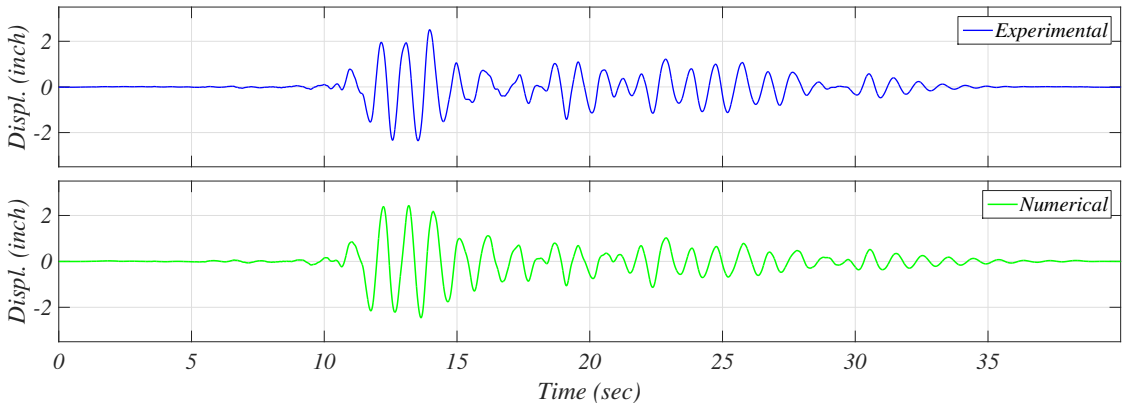

(b)

Figure 7.13. Comparison between experimental and numerical results for the model with panel 5ES during FB1: (a) time history of absolute accelerations, and (b) time history of relative displacements for the SE corner of the fifth floor

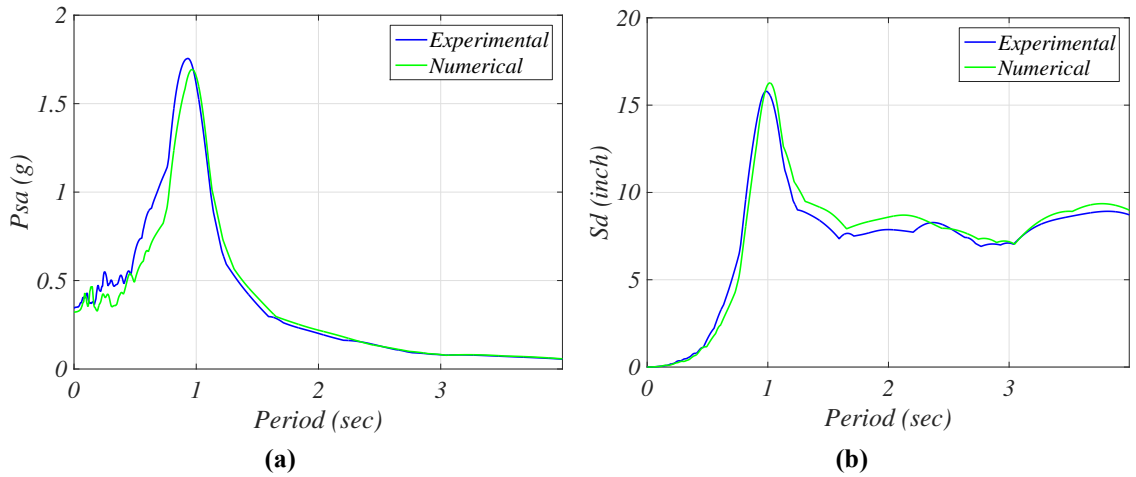

Figure 7.14. Comparison of experimental and numerical results for the model with panel 5ES during FB1: (a) pseudo acceleration spectrum and (b) displacement spectrum for the SE corner of the fifth floor

Figure 7.15 shows the comparisons of the time history of accelerations in panel 5ES. Results are very similar for positive accelerations, while negative peaks are larger in the experimental case. Figure 7.16 presents the pseudo acceleration and displacement spectra for the panel. Comparison is still good, and it can be noticed that the model is able to reproduce the resonance of the panel.

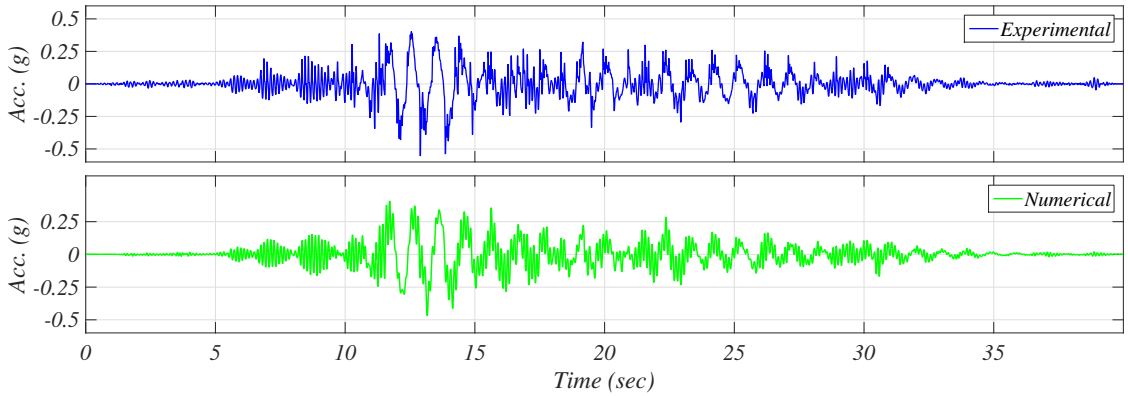

Figure 7.15. Comparison of experimental and numerical time histories of accelerations for panel 5ES during FB1

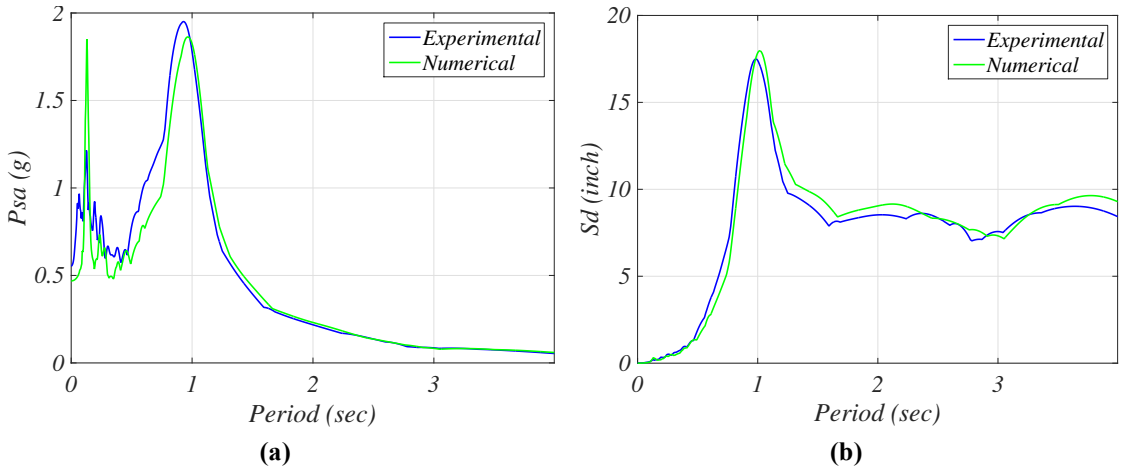

Figure 7.16. Comparison of experimental and numerical results for panel 5ES during FB1: (a) pseudo acceleration spectrum and (b) displacement spectrum

A procedure similar to that used for FB1 was used to determine the results for FB2. Very similar results were obtained, except that a lower damping at the first mode of response of the building was identified. This is expected since FB1 and FB2 were of similar in amplitude. The optimal damping ratios were:

1. Damping ratio of the first longitudinal mode: 4%;
2. Damping to the second and third longitudinal modes: 13%;
3. Damping of the other modes: 4%.

Figure 7.17 through Figure 7.20 present a comparison of experimental and numerical results for the roof and fifth floor during FB2. Time histories of accelerations are very similar, and the model can also predict the resonance-type behavior of the panel, which is quite visible between about seconds 30 and 35. Time histories of acceleration, pseudo acceleration and displacement spectrum for panel 5ES are shown in Figure 7.21 and Figure 7.22. Time histories are reasonably similar, and also in this case the model is more accurate in the prediction of positive peaks. Comparison of spectral values is promising, with the peak showing the resonance of the panel being similar for both experimental and numerical results.

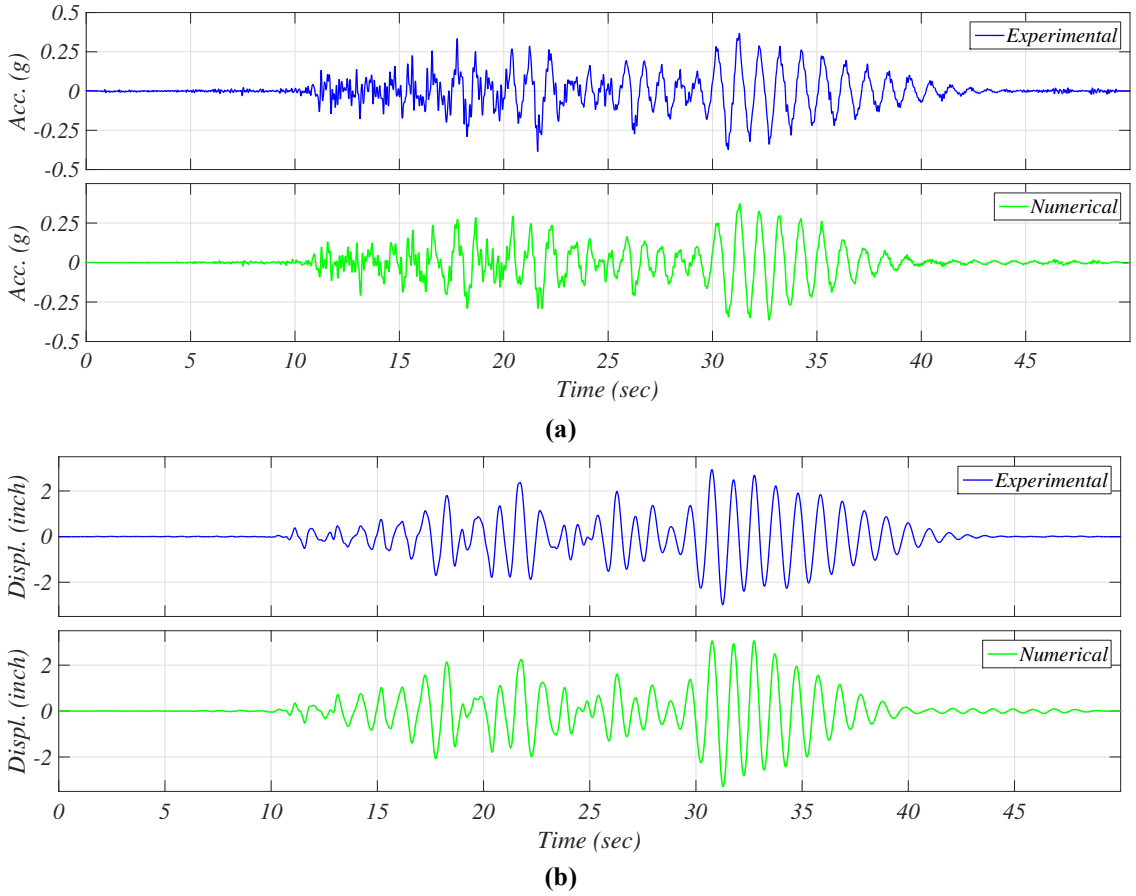

Figure 7.17. Comparison between experimental and numerical results for the model with panel 5ES during FB2: (a) time history of absolute accelerations, and (b) time history of relative displacements for the SE corner of the roof

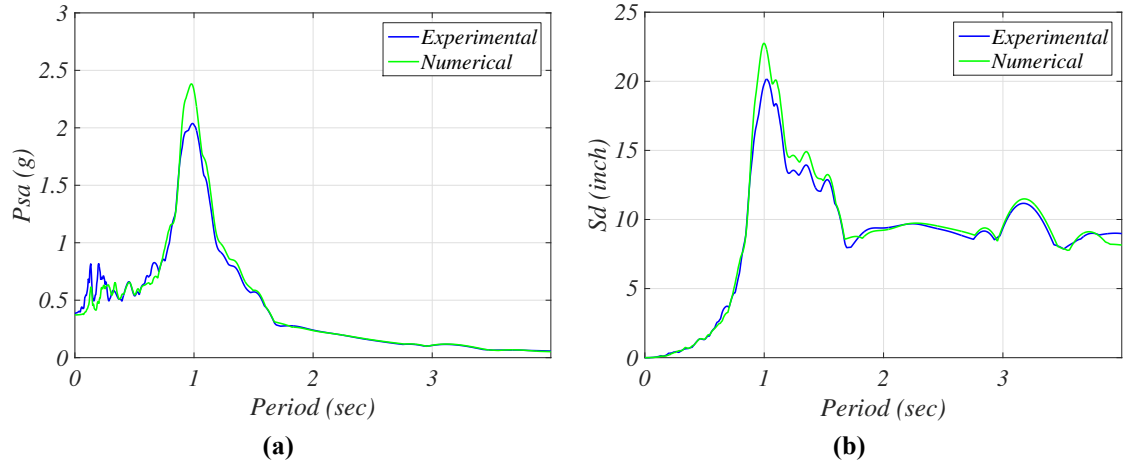

Figure 7.18. Comparison of experimental and numerical results for the model with panel 5ES during FB2: (a) pseudo acceleration spectrum and (b) displacement spectrum for the SE corner of the roof

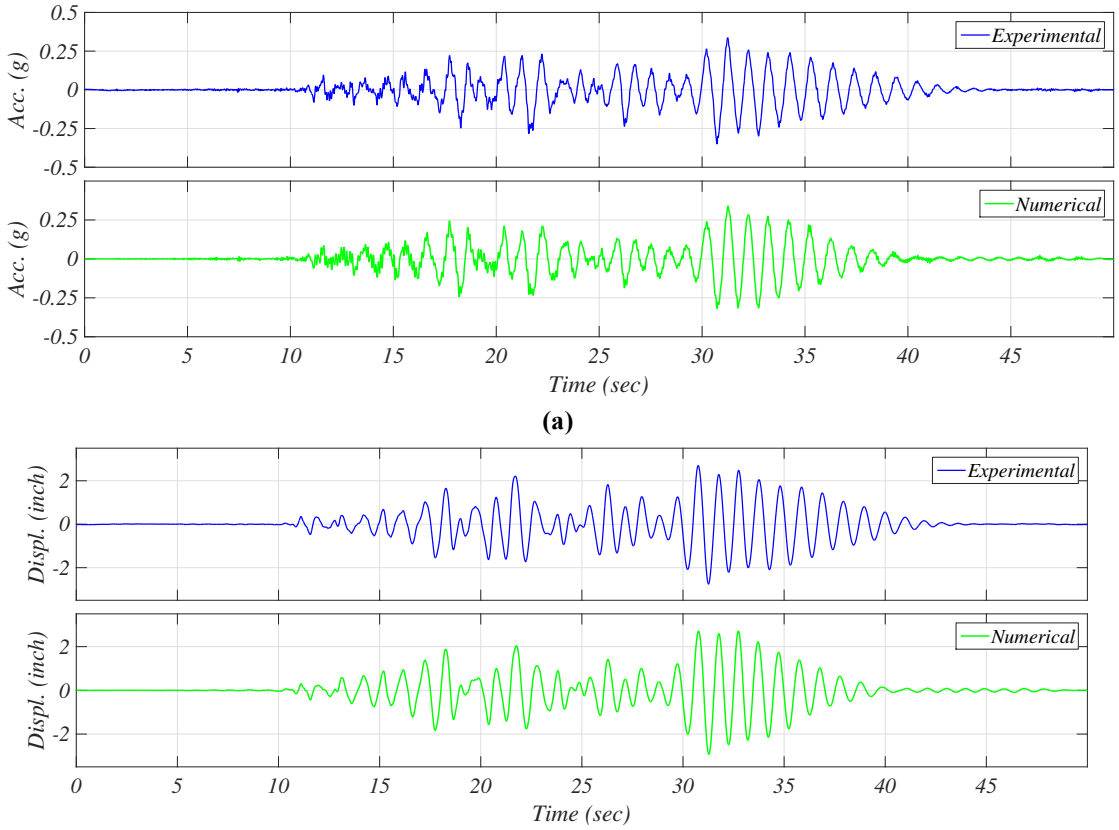

Figure 7.19. Comparison between experimental and numerical results for the model with panel 5ES during FB2: (a) time history of absolute accelerations, and (b) time history of relative displacements for the SE corner of the fifth floor

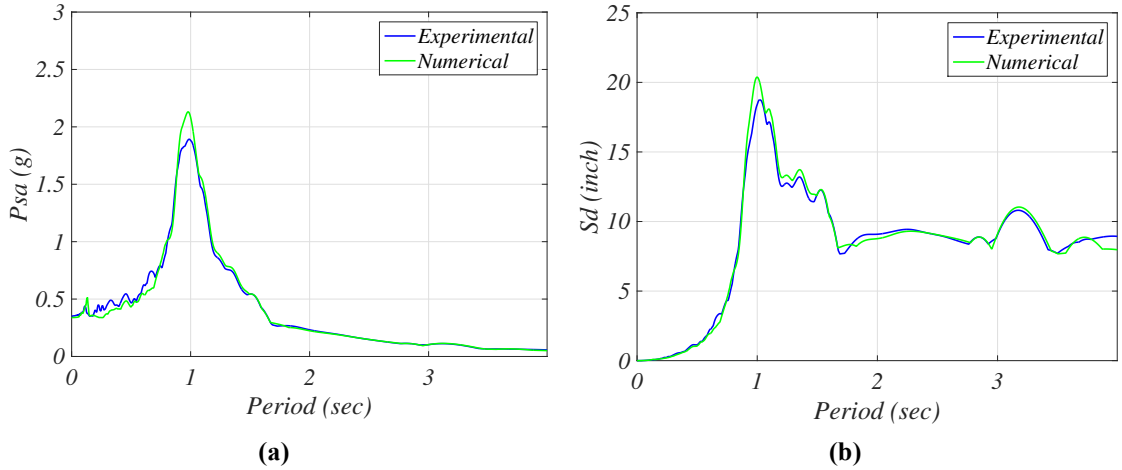

Figure 7.20. Comparison of experimental and numerical results for the model with panel 5ES during FB2: (a) pseudo acceleration spectrum and (b) displacement spectrum for the SE corner of the fifth floor

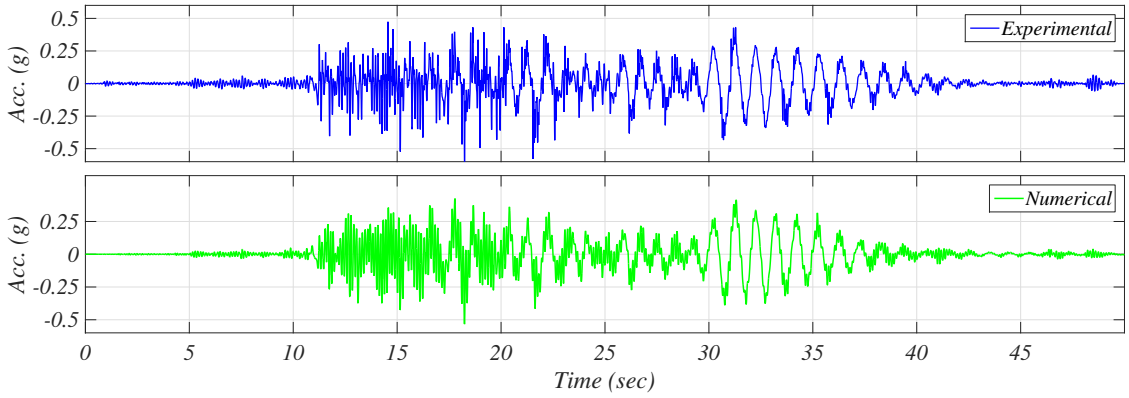

Figure 7.21. Comparison of time histories of accelerations between experimental and numerical results for panel 5ES during FB2

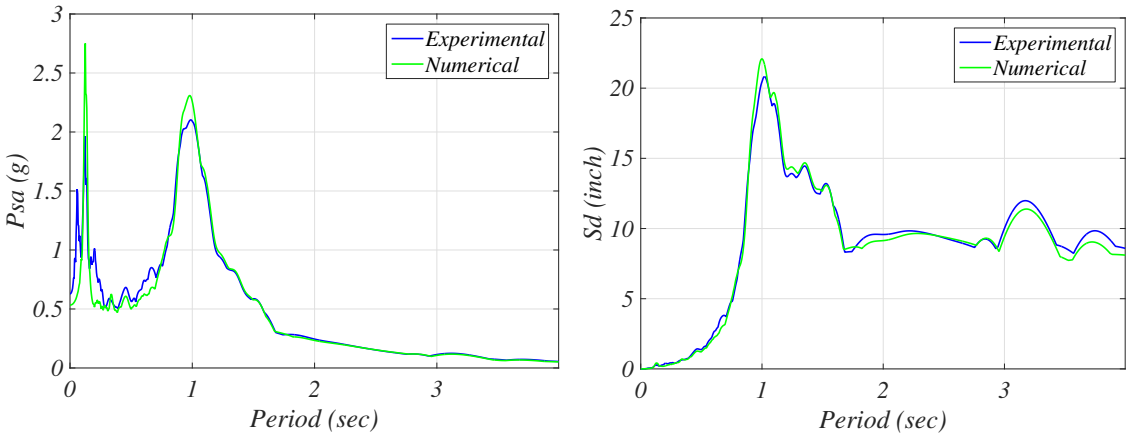

(a) **(b)**

Figure 7.22. Comparison of experimental and numerical results for panel 5ES during FB2: (a) pseudo acceleration spectrum and (b) displacement spectrum

7.2.2 Determination of Damping Ratios for FB1 and FB2 – Panel 4ES

The same analyses were run for the model including panel 4ES instead of 5ES. In this case, the natural frequency of the panel was 9.1 Hz, and the stiffness of the spring that created this frequency was 76 kips/inch. Since the panel was at the fourth level, the optimal damping was determined by minimizing the errors relative to the accelerations in the fifth and fourth floors and those in panel 4ES. For FB1 the best match was found for the following damping ratios:

1. Damping of the first mode of the building: 8%;
2. Damping of the second and third longitudinal modes: 13%;
3. All the other modes: 4%.

These values are very similar to those found for the first model. Figure 7.23 till Figure 7.26

present the comparison of the experimental and numerical relevant structural response, while Figure 7.27 and Figure 7.28 present the results relative to panel 4ES during FB1. Also in this case, comparisons are very good.

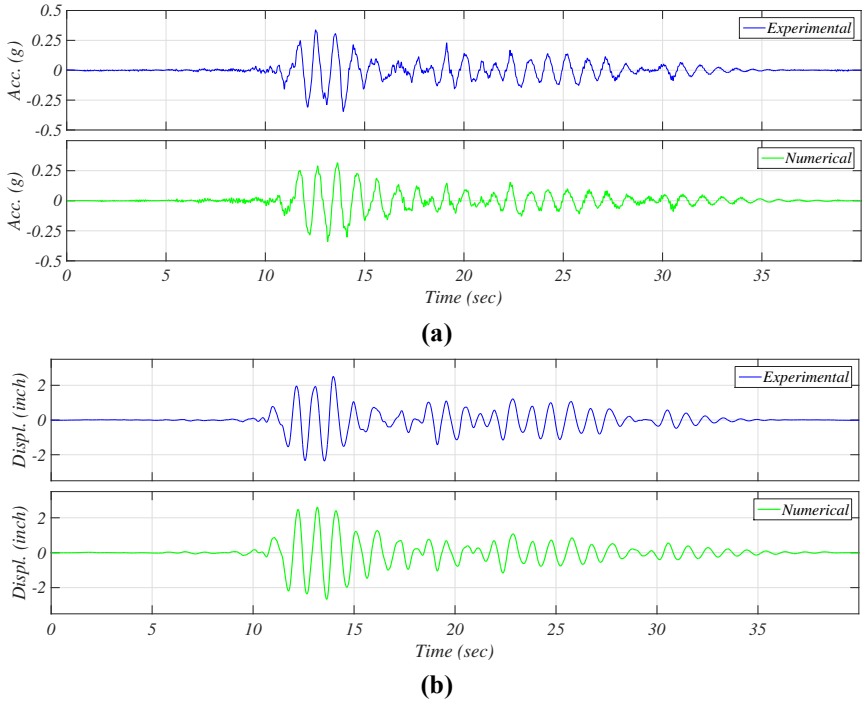

Figure 7.23. Comparison between experimental and numerical results for the model with panel 4ES during FB1: (a) time history of absolute accelerations, and (b) time history of relative displacements for the SE corner of the fifth floor

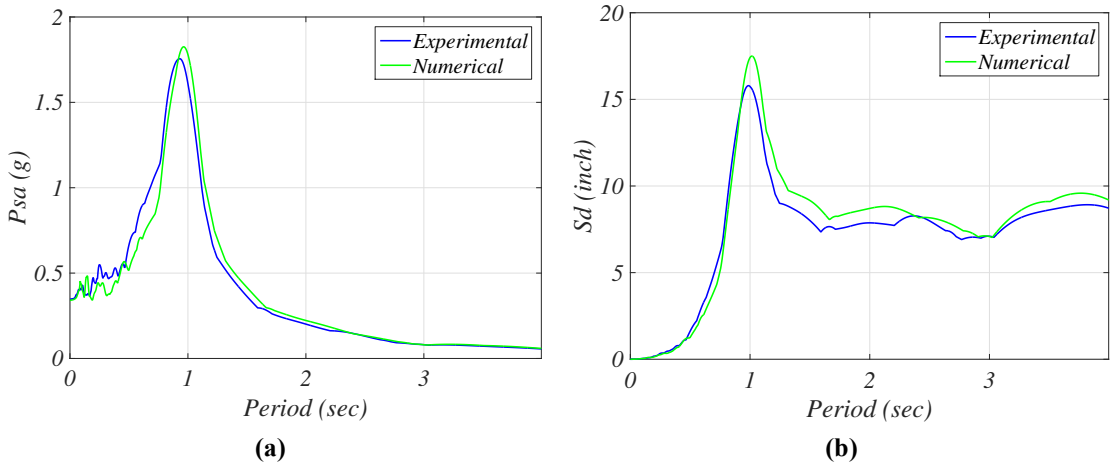

Figure 7.24. Comparison of experimental and numerical results for the model with panel 4ES during FB1: (a) pseudo acceleration spectrum and (b) displacement spectrum for the SE corner of the fifth floor

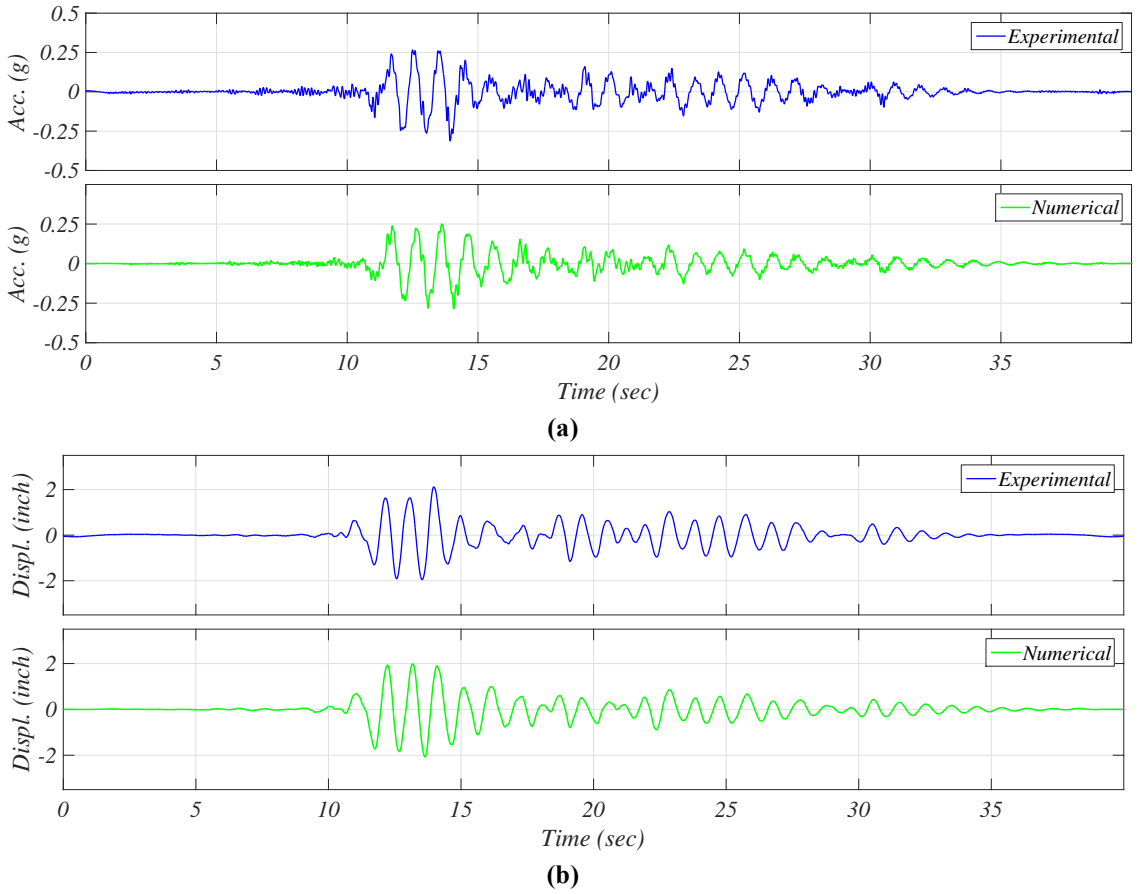

Figure 7.25. Comparison between experimental and numerical results for the model with panel 4ES during FB1: (a) time history of absolute accelerations, and (b) time history of relative displacements for the SE corner of the fourth floor

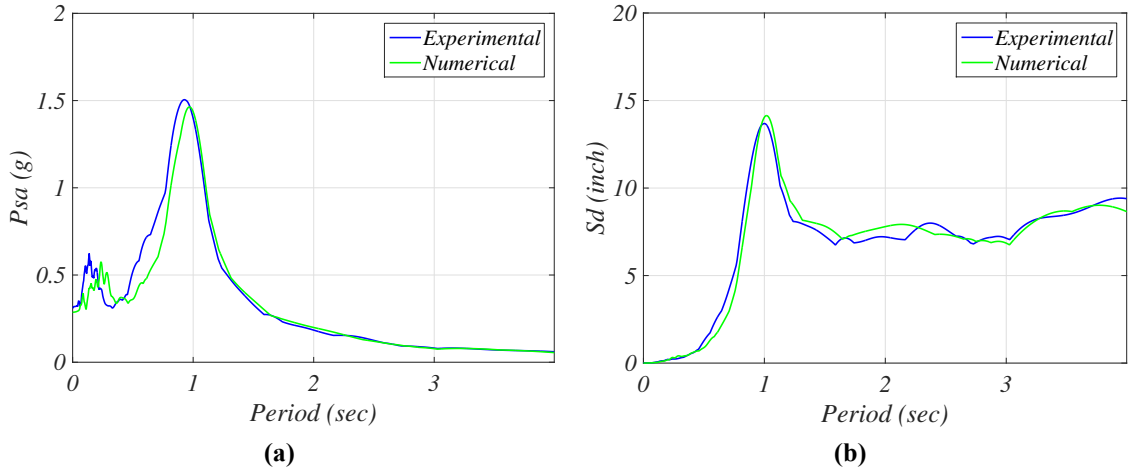

Figure 7.26. Comparison of experimental and numerical results for the model with panel 4ES during FB1: (a) pseudo acceleration spectrum and (b) displacement spectrum for the SE corner of the fourth floor

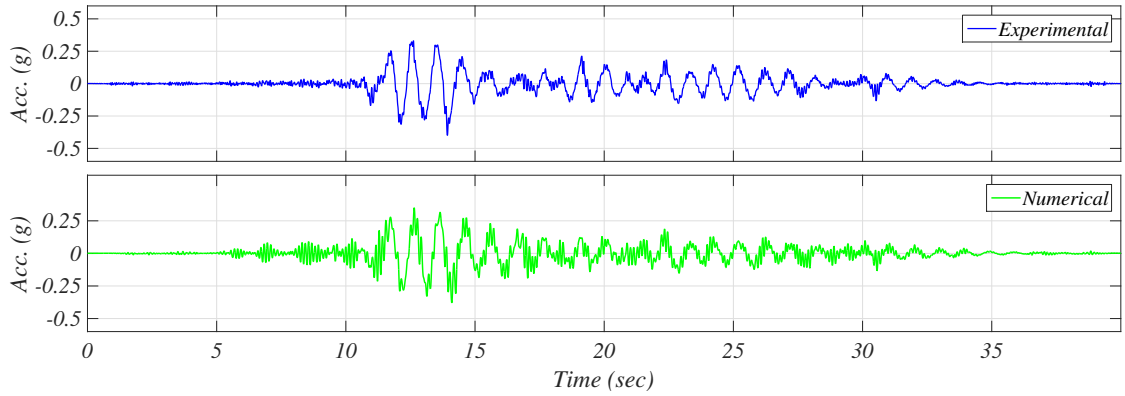

Figure 7.27. Comparison of time histories of accelerations between experimental and numerical results for panel 4ES during FB1

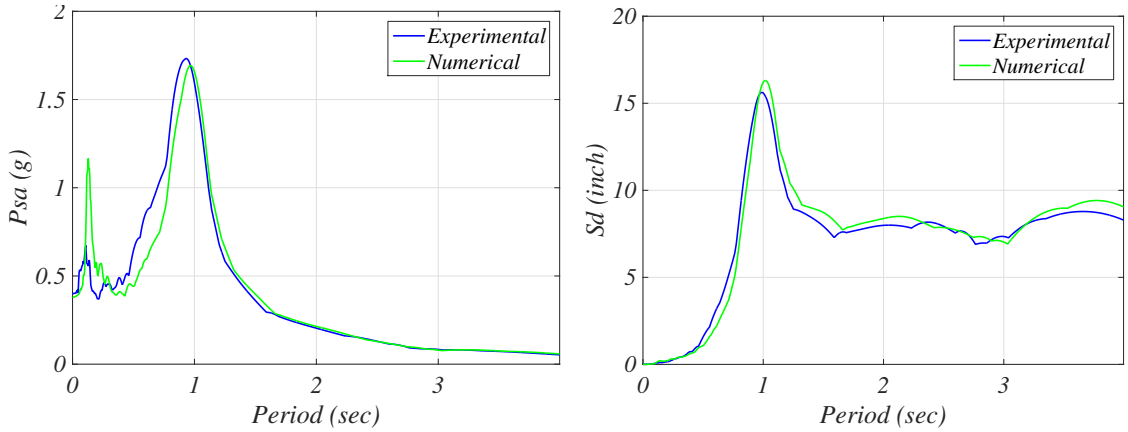

(a) **(b)**

Figure 7.28. Comparison of experimental and numerical results for panel 4ES during FB1: (a) pseudo acceleration spectrum and (b) displacement spectrum

The optimal damping for FB2 for the model including panel 4ES was deemed to be the same as the one used when the panel is installed at the fifth level (4% for all the modes, except second and third longitudinal modes damped at 13%). Comparisons relative to the fifth and fourth floors are presented in Figure 7.29 to Figure 7.32 and show a good agreement between numerical and experimental results. The same can be said for results relative to panel 4ES presented in Figure 7.33 and Figure 7.34.

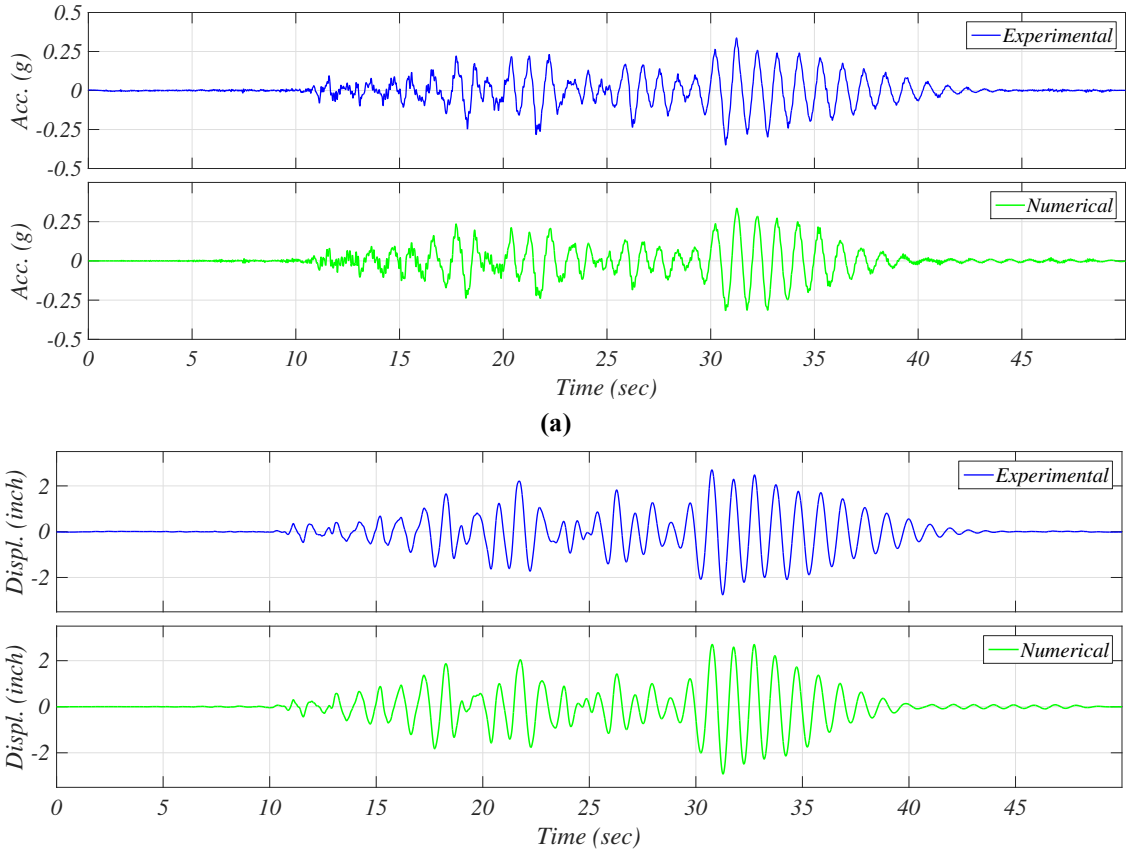

Figure 7.29. Comparison between experimental and numerical results for the model with panel 4ES during FB2: (a) time history of absolute accelerations, and (b) time history of relative displacements for the SE corner of the fifth floor

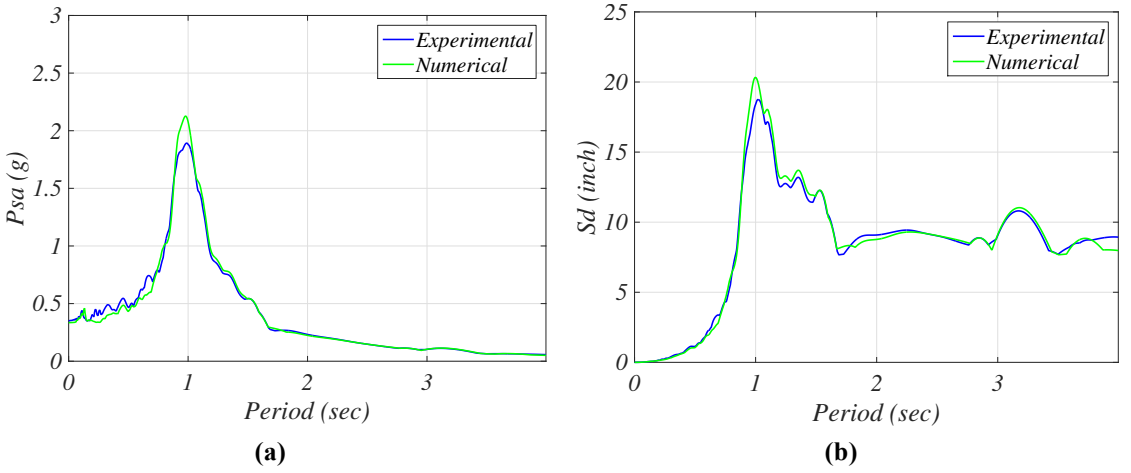

Figure 7.30. Comparison of experimental and numerical results for the model with panel 4ES during FB2: (a) pseudo acceleration spectrum and (b) displacement spectrum for the SE corner of the fifth floor

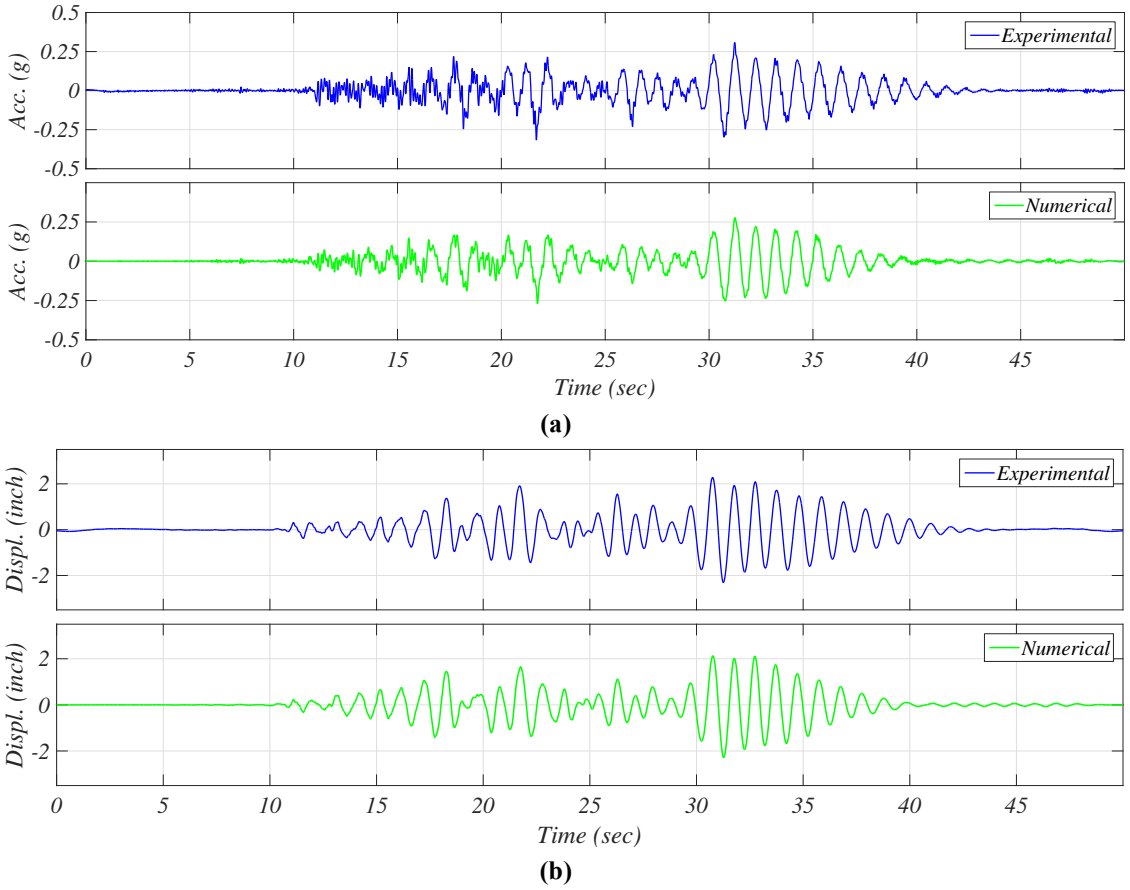

Figure 7.31. Comparison between experimental and numerical results for the model with panel 4ES during FB2: (a) time history of absolute accelerations, and (b) time history of relative displacements for the SE corner of the fourth floor

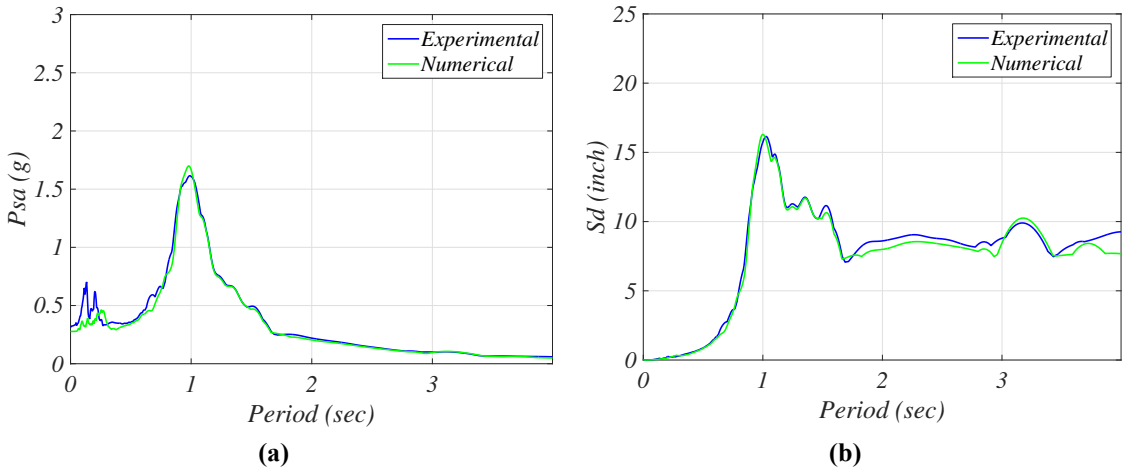

Figure 7.32. Comparison of experimental and numerical results for the model with panel 4ES during FB2: (a) pseudo acceleration spectrum and (b) displacement spectrum for the SE corner of the fourth floor

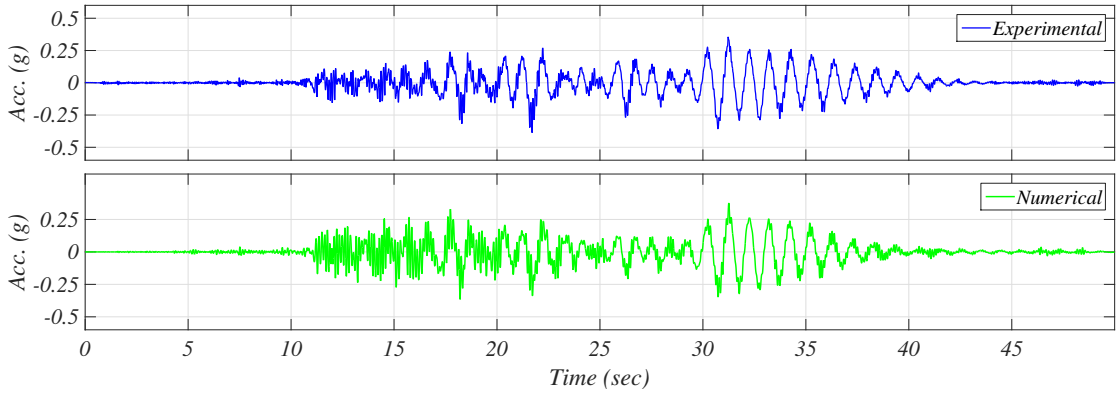

Figure 7.33. Comparison of time histories of accelerations between experimental and numerical results for panel 4ES during FB2

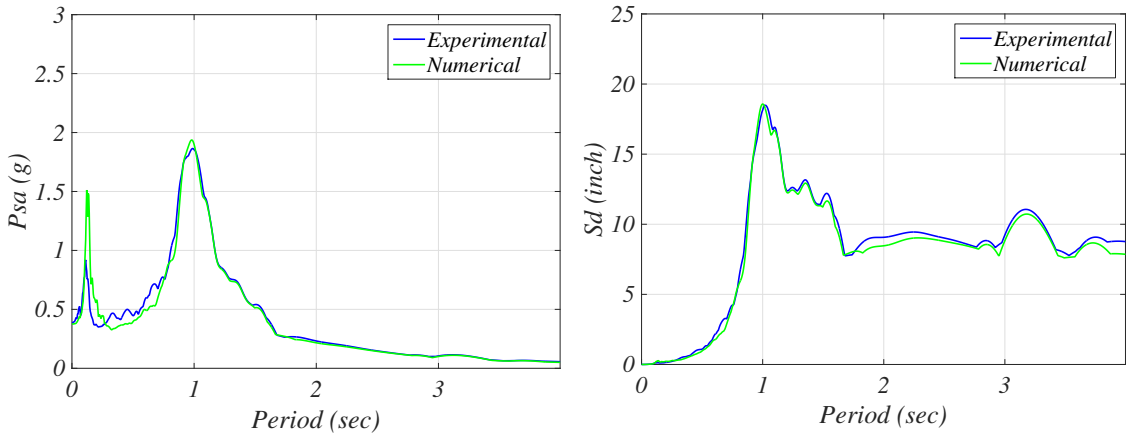

(a) **(b)**

Figure 7.34. Comparison of experimental and numerical results for panel 4ES during FB2: (a) pseudo acceleration spectrum and (b) displacement spectrum

7.2.3 Comparison of Numerical and Experimental Damping Ratios

Experimental values of damping ratios during white noise were found with different system identification methods by the previously cited study by Astroza et al. (Astroza et al. 2013). The range of values of damping ratios and their average for the first four modes are presented in Table 7.5. It is noted that the white noise motions were smaller in amplitude compared to FB1 and FB2, which are used to validate the model. The first longitudinal mode has an experimental damping ratio of 4.4%, similar to that of the optimal value of 4% for FB2. However, this value is smaller than that on 9% optimizing the comparison for FB1. This higher damping can be caused by more damage occurring during FB1, since it was the first FB motion. The experimental values of damping remained around 2-4% for higher modes, while in the model a value of 13% had to be used. This large influence of the higher modes in

the numerical model is considered just a numerical effect.

Table 7.5. Experimental damping ratios for the first four modes found by Astroza et al. 2013 (including those for the white noise with 1% and 1.5% rms)

Mode #	Mode Type	Range (%)	Average (%)
1	First Longitudinal	4.1-6.2	4.4
2	Transverse and Torsional	1.1-4.1	2.9
3	Torsional	2.0-3.5	2.6
4	Second Longitudinal	0.7-7.7	3.5

7.2.4 Comparison of Numerical and Experimental Results: Peak Accelerations

Figure 7.35 presents the plot of the experimental versus numerical (with optimal damping) peak accelerations in the floors and panels during motions FB1 and FB2. The percentage errors in prediction in each of the cases is shown in Figure 7.36. These figures confirm that the comparison between experimental and numerical results is generally good, with percentage errors smaller than 20% in all the cases. Experimental accelerations tend to be larger than the numerical ones. Errors are larger for panel 5ES during FB1, while smaller for panel 4ES during FB1. The larger errors in the prediction of peak acceleration in panel 5ES during both FB1 and FB2 is attributed to the presence of high frequencies in the experimental results (15 – 25 Hz) that the model cannot reproduce.

7.2.5 Comparison of Numerical and Experimental Results: Component Amplification Factors

Figure 7.37 presents the comparison between experimental and numerical values of the component amplification factor a_p. The percentage error is calculated as the experimental value minus the numerical value divided by the experimental value multiplied by 100, and it is reported in Figure 7.38. Errors remain smaller than 20% also in this case, except for the $a_{p,top}$ in the Eastward direction for panel 5ES during FB1, for which the error is 25%. The values of a_p are more uniformly located around the 1:1 line compared to the values of peak accelerations.

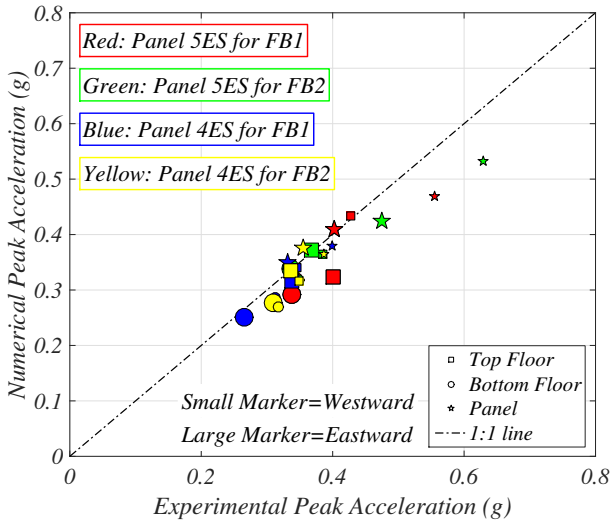

Figure 7.35. Comparison between numerical and experimental EW peak accelerations

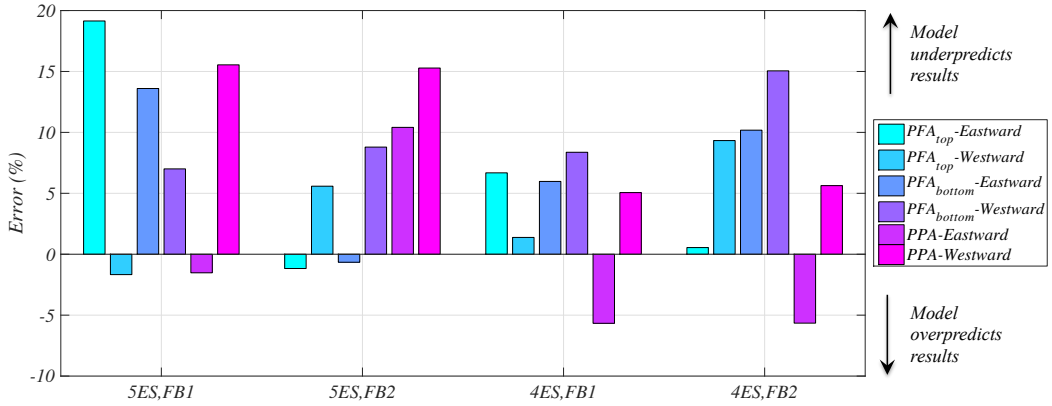

Figure 7.36. Percentage of error in the prediction of EW peak accelerations

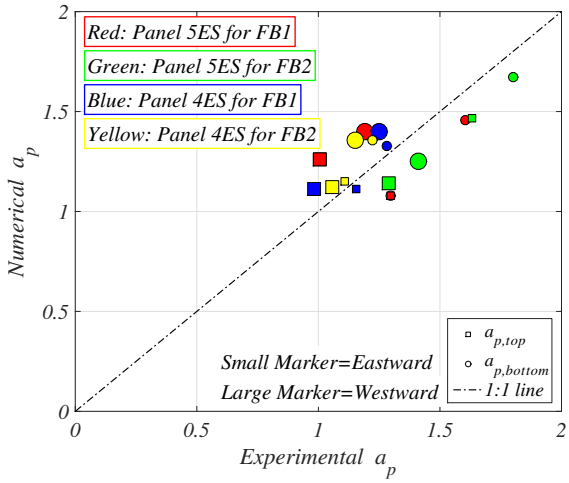

Figure 7.37. Comparison between numerical and experimental values of a_p

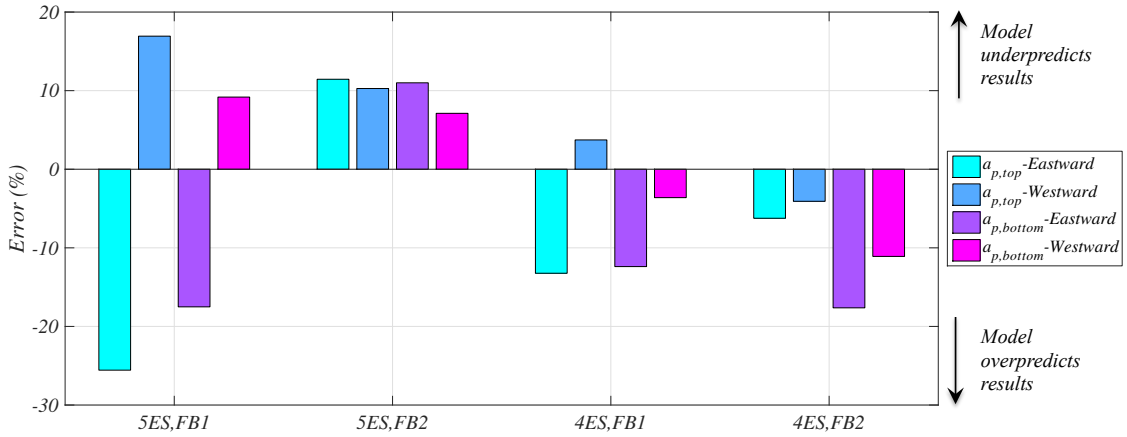

Figure 7.38. Percentage of error in the prediction of a_p

7.2.6 Comparison for FB3

A comparison of the experimental and numerical results was performed also for FB3. The value of damping adopted was 4% for all the modes except 13% for the second and longitudinal modes, the same of FB2. This motion can be considered at the upper limit of a service level motion, with PIDR reaching almost 1%. This motion was not spectrally matched like FB1 and FB2. Figure 7.45 though Figure 7.50 are relative to the model with panel 5ES. Figure 7.45a shows the comparison between the experimental and numerical values of the acceleration at the roof. The comparison is generally good, except for seconds 30-40. The predicted peak acceleration in the positive directions are still good, with an experimental value of 0.58 g and a numerical value of 0.55g, resulting in a prediction error of -5%. A larger prediction error is observed for the negative accelerations, for which the experimental peak is only -0.47 g while the numerical is -0.61 g, resulting in an error of +30%. Part of the error is caused by the softening of the building during FB3. Figure 7.45b shows the time history of relative displacements at the roof. As seen in the case of the accelerations, also in this case the comparison is better in the positive than in the negative direction. Figure 7.46 shows the comparison between experimental and numerical results in terms of pseudo acceleration and displacement spectrum. The softening of the building is clearly visible in these plots. Results are still consistent for the pseudo acceleration spectrum, while they get larger for the displacement spectrum. Figure 7.41 and Figure 7.42 show the same comparison for the bottom floor. Experimental and numerical values of peak accelerations and displacements show good results, even if problems in the time history remain for seconds 30 to 40 of

the time history. Figure 7.43 and Figure 7.44 show the comparison of the time history and spectral values of panel 5ES. Except for the effects of the softening of the building, comparisons are quite good. In terms of peak accelerations in the panel, the peaks are 0.58 g and -0.56 g in the experimental case and 0.52 g and -0.64 g in the numerical case, resulting in errors of -10% and +14% respectively.

The same results relative to the model with panel 4ES re presented in Figure 7.45-Figure 7.50. The same trends observed previously can be seen:

- The is a good comparison between peak accelerations and displacements;
- The time histories show errors between seconds 30 and 40;
- The spectral responses show the softening of the building, and the agreement for the results in better for accelerations than displacements.

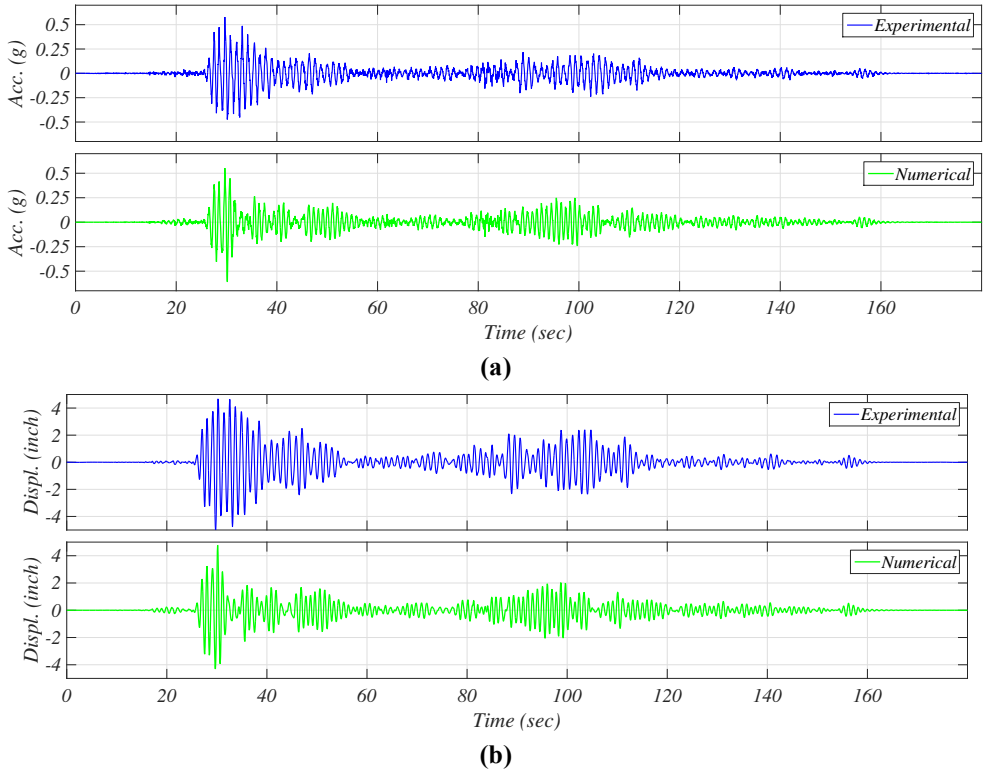

Figure 7.39. Comparison between experimental and numerical results for the model with panel 5ES during FB3: (a) time history of absolute accelerations, and (b) time history of relative displacements for the SE corner of the roof

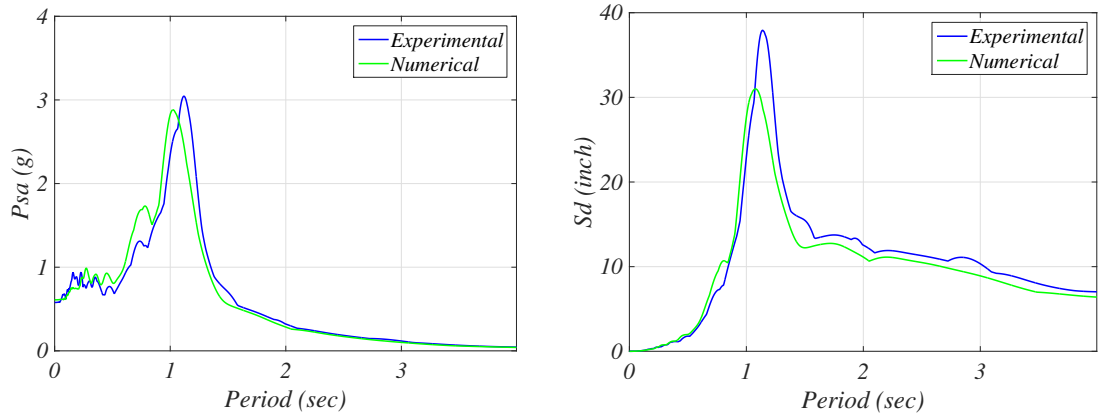

(a) **(b)**

Figure 7.40. Comparison of experimental and numerical results for the model with panel 5ES during FB3: (a) pseudo acceleration spectrum and (b) displacement spectrum for the SE corner of the roof

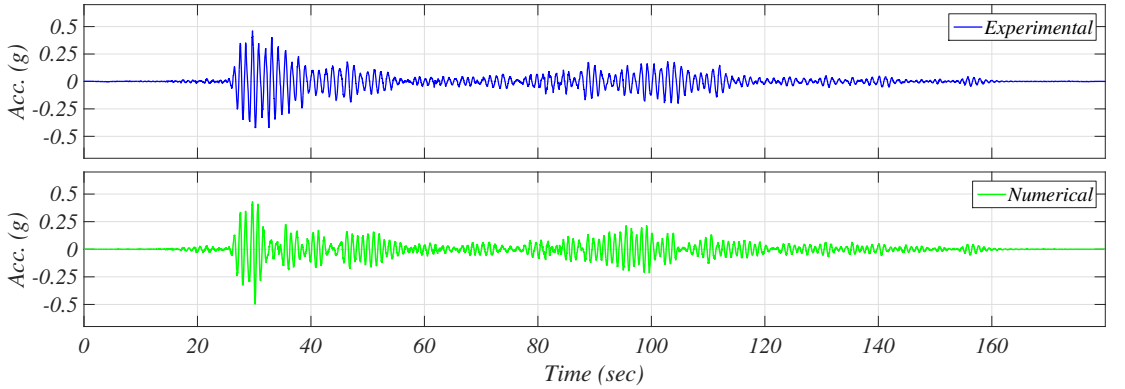

(a)

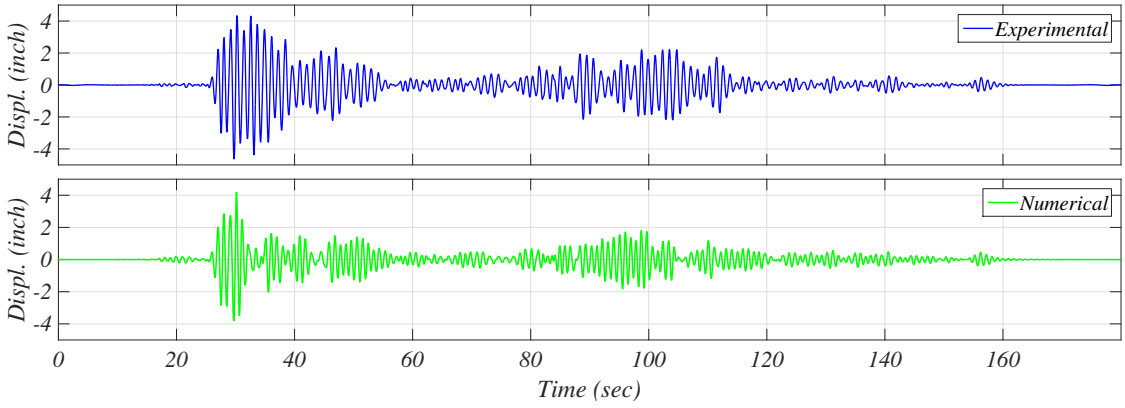

(b)

Figure 7.41. Comparison between experimental and numerical results for the model with panel 5ES during FB3: (a) time history of absolute accelerations, and (b) time history of relative displacements for the SE corner of the fifth floor

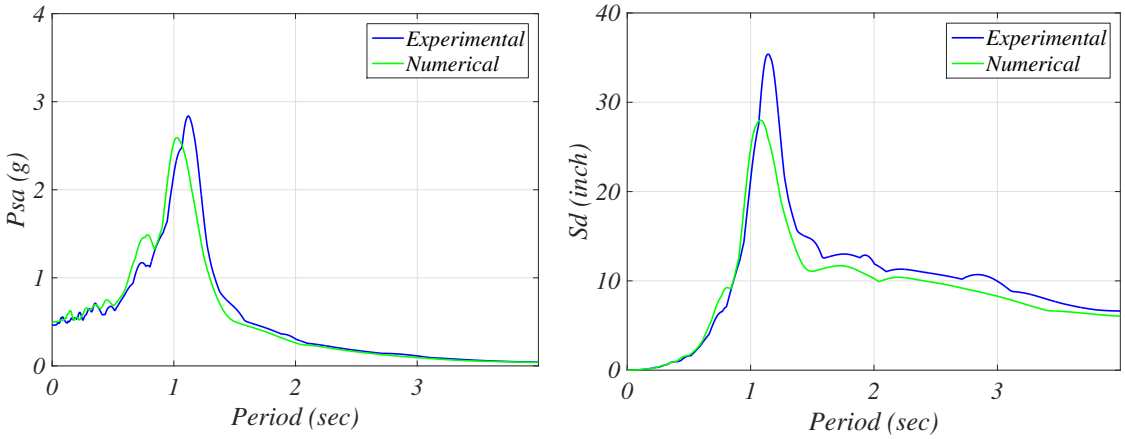

(a) **(b)**

Figure 7.42. Comparison of experimental and numerical results for the model with panel 5ES during FB3: (a) pseudo acceleration spectrum and (b) displacement spectrum for the SE corner of the fifth floor

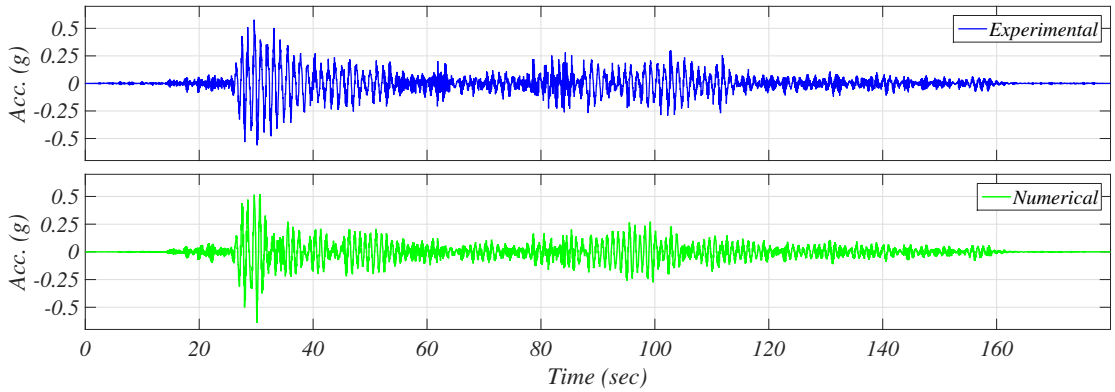

Figure 7.43. Comparison of time histories of accelerations between experimental and numerical results for panel 5ES during FB3

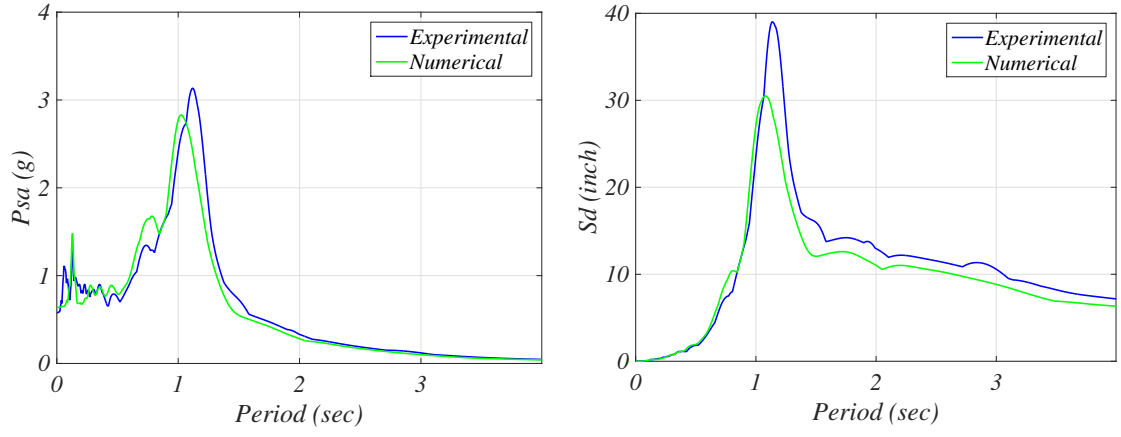

(a) **(b)**

Figure 7.44. Comparison of experimental and numerical results for panel 5ES during FB3: (a) pseudo acceleration spectrum and (b) displacement spectrum

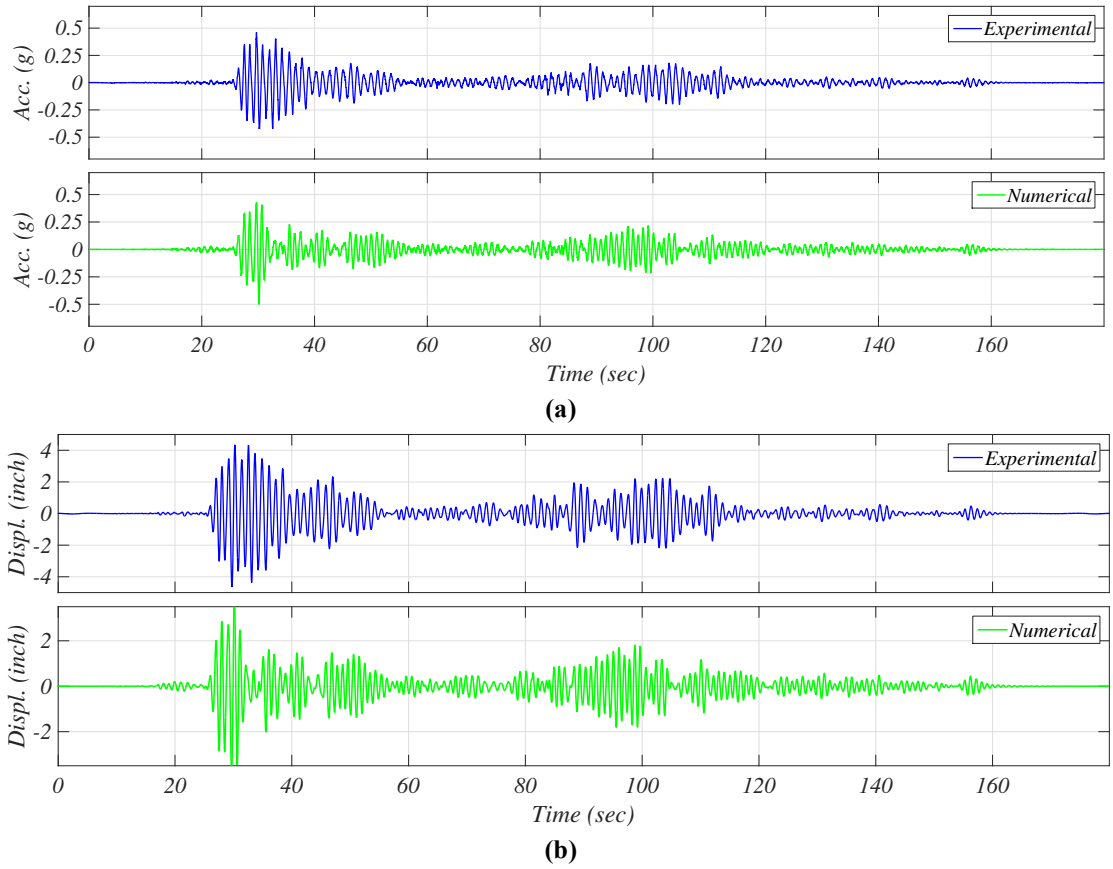

Figure 7.45. Comparison between experimental and numerical results for the model with panel 4ES during FB3: (a) time history of absolute accelerations, and (b) time history of relative displacements for the SE corner of the fifth floor

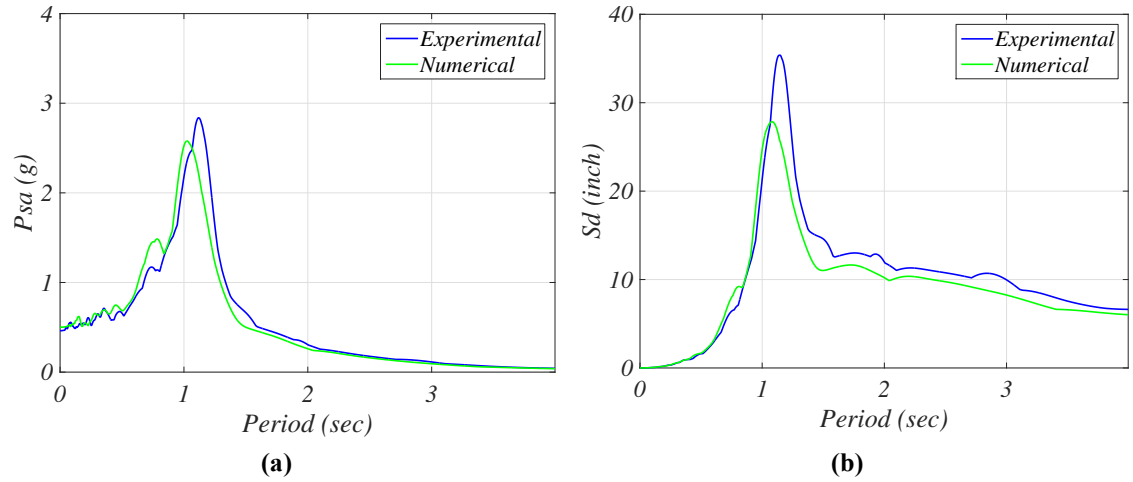

Figure 7.46. Comparison of experimental and numerical results for the model with panel 4ES during FB3: (a) pseudo acceleration spectrum and (b) displacement spectrum for the SE corner of the fifth floor

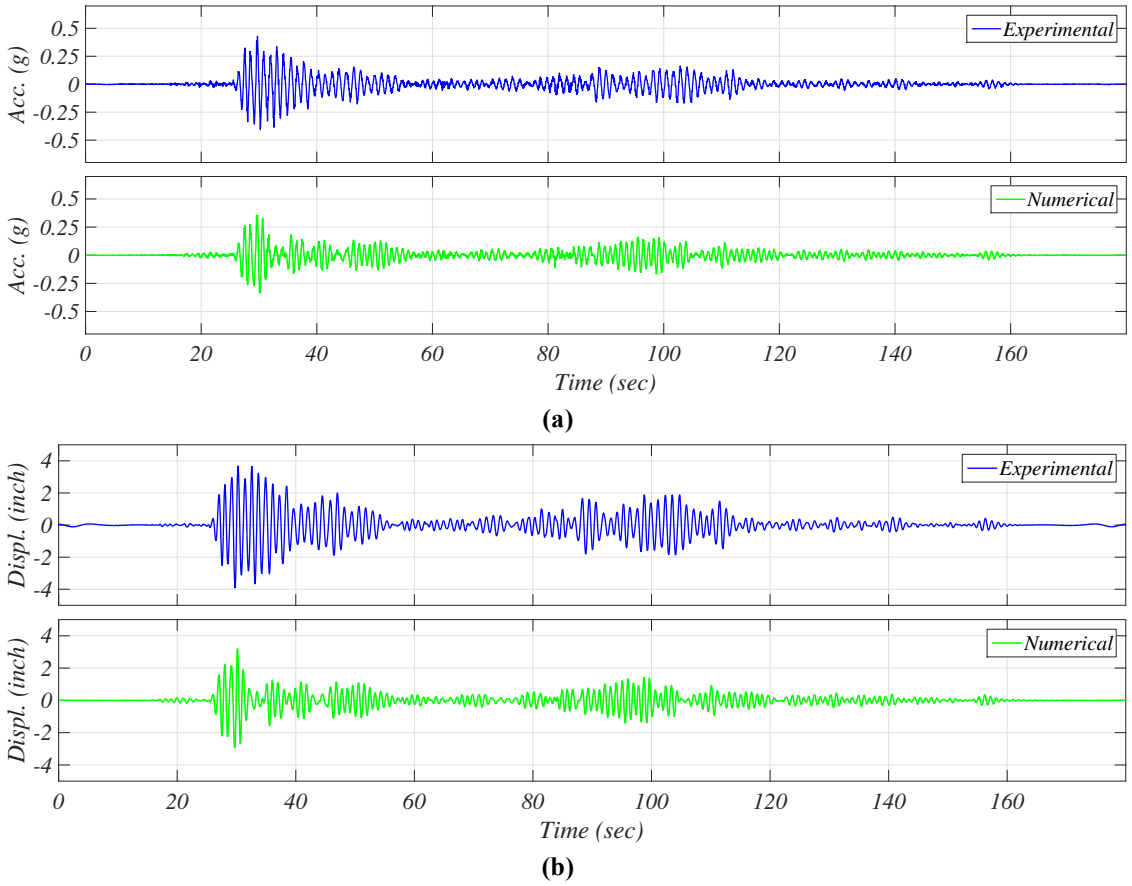

Figure 7.47. Comparison between experimental and numerical results for the model with panel 4ES during FB3: (a) time history of absolute accelerations, and (b) time history of relative displacements for the SE corner of the fourth floor

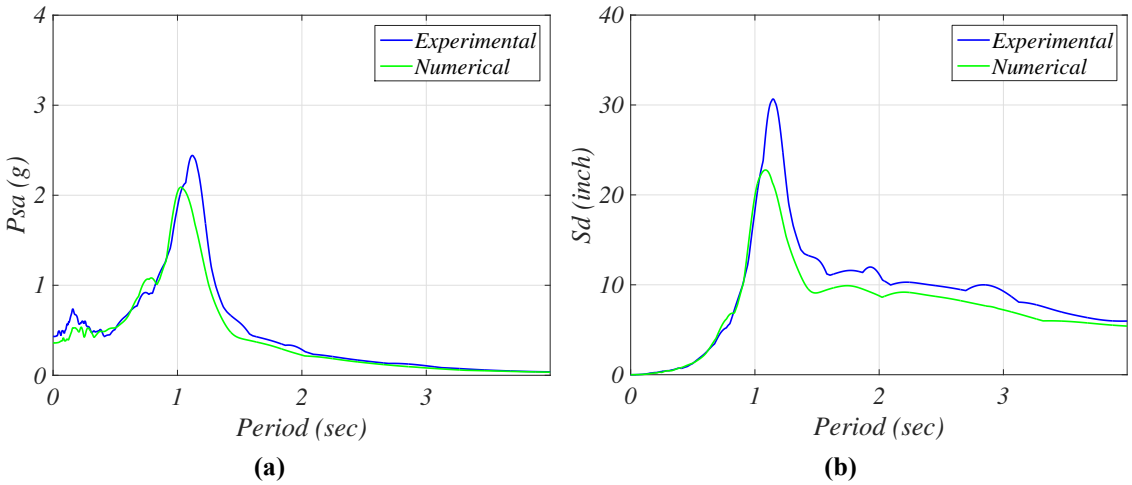

Figure 7.48. Comparison of experimental and numerical results for the model with panel 4ES during FB3: (a) pseudo acceleration spectrum and (b) displacement spectrum for the SE corner of the fourth floor

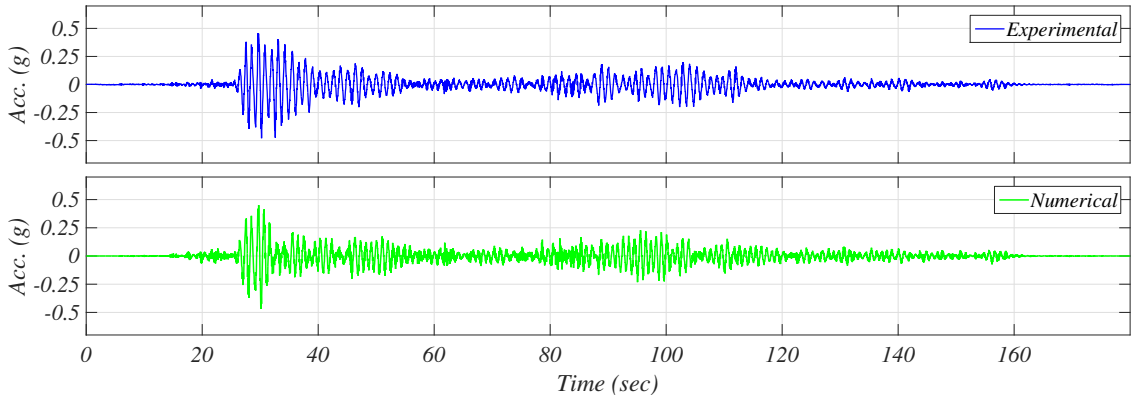

Figure 7.49. Comparison of time histories of accelerations between experimental and numerical results for panel 4ES during FB3

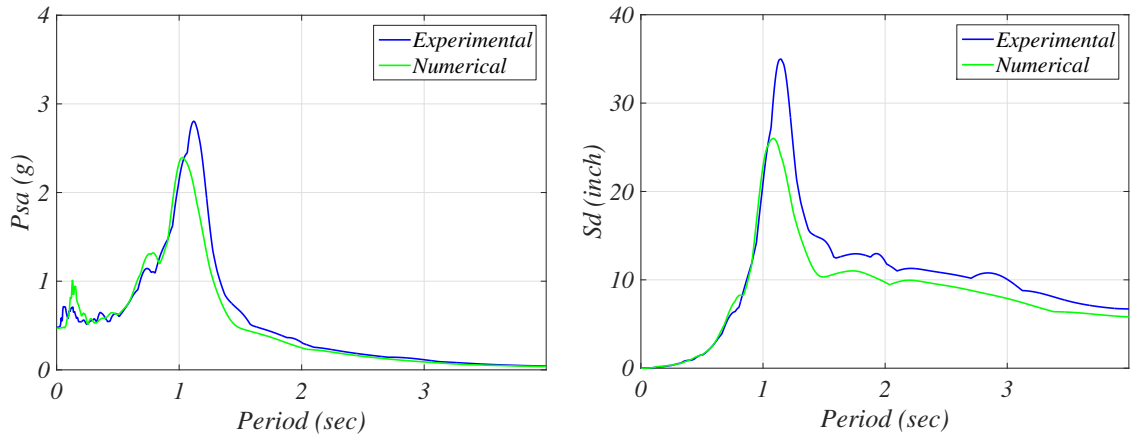

(a) **(b)**

Figure 7.50. Comparison of experimental and numerical results for panel 4ES during FB3: (a) pseudo acceleration spectrum and (b) displacement spectrum

7.3 Parametric Analysis

The goal of this analysis is to understand the accelerations developed in an APC panel during a service level earthquake with the variation of its natural frequency, location and input motion. Linear dynamic analyses are run using the building-panel model described in the previous sections, with the damping values that optimized the results for FB2 (4% damping for all the modes except 13% for the second and longitudinal modes). The following parameters are varied in this analysis:

- Input motion. Eighteen input ground motions were selected from the PEER ground motion database (http://ngawest2.berkeley.edu) and spectrally matched to the service-level spectrum (25% of the maximum credible earthquake spectrum). In addition, the experimental results

from FB1, FB2 and FB3 are also included;

- Location of the panel. This is varied between the location of 5ES and 4ES;
- Natural frequency of the panel. This is set at 8, 11 and 14 Hz. These values were selected since they are typical of average size panels, as determined in Chapter 6. The values of stiffness used in the model to achieve natural frequency of 8,11 and 14 Hz were 68, 130 and 240 kips/inch for panel 5ES and 57, 117 and 221 kips/inch for panel 4ES, respectively. The experimental results are relative to the experimental natural frequency of the panels (7.9 Hz for 5ES and 9.1 Hz for 4ES).

7.3.1 Quantities of Interest

The first quantity of interest studied is the seismic coefficient C_p, defined as:

$$C_p = \frac{F_p}{W_p} \qquad \text{Eq. 7.2}$$

Since the seismic coefficient is the ratio between the seismic force and the seismic weight, it can be inferred that it corresponds to the acceleration of the component divided by the gravity acceleration. C_p is found in the model by extracting the peak acceleration of the SDOF representing the panel. Thus, one value of C_p is obtained per panel. C_p can be seen as the multiplication of three factors:

1. Peak ground acceleration (PGA) which can be expressed in g or as a fraction of S_{DS};
2. Amplification of the acceleration in the structure a_s. Since the APC cladding is attached to two floors, two different amplification coefficients can be defined relative to each panel:

$$a_{s,top} = \frac{PFA_{topfloor}}{PGA} \qquad \text{Eq. 7.3}$$

$$a_{s,bottom} = \frac{PFA_{bottomfloor}}{PGA} \qquad \text{Eq. 7.4}$$

Where PFA is the peak floor acceleration at a certain floor;

3. Component amplification factor a_p. As seen for a_s, also in this case it is possible to defined a_p relative to the top and bottom floor as:

$$a_{p,top} = \frac{PPA}{PFA_{topfloor}} \qquad \text{Eq. 7.5}$$

$$a_{p,bottom} = \frac{PPA}{PFA_{bottomfloor}} \qquad \text{Eq. 7.6}$$

Where PPA is the peak panel acceleration of the panel. Since then panel is modeled as a SDOF system, each panel has a single values of PPA, and this is considered constant along the height of the panel. This is clearly an approximation, since the acceleration of the panel is not actually constant, due to the deformability of the panels.

Figure 7.51a shows a summary of the accelerations involved in the study on an APC panel: the peak ground acceleration, peak floor accelerations for top and bottom floor and the peak panel acceleration PPA (corresponding with C_p when expressed in g). When these accelerations are divided by the peak ground acceleration, it is possible to determine the amplification factors along the height of the building (Figure 7.51b). $a_{s,top}$ and $a_{s,bottom}$ are the structural amplification factors, while the total amplification of the panel can be found by multiplying a_s by a_p. It is noted that the peaks are the maximum of the absolute value extracted from the time history and are not correlated in time.

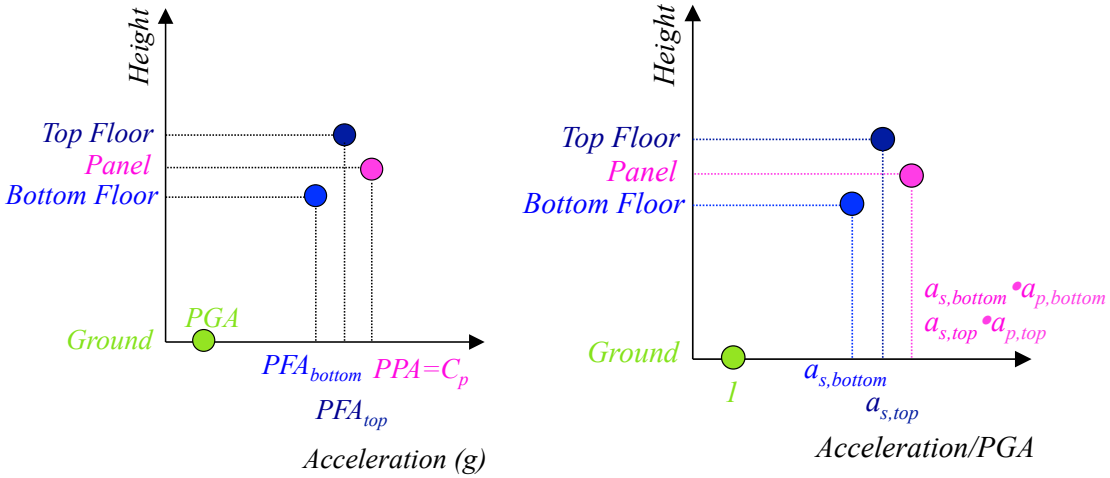

Figure 7.51. Schematic showing the (a) accelerations and (b) amplification factors involved in the study of APC panels

7.3.2 Code Limits for the Quantities of Interest

The quantities of interest explained above can be identified within the ASCE-7 (ASCE 2010)

formula to determined F_p, as shown in Figure 7.52. It is noted that the values of C_p found in the formula of the code includes also the response modification factors R_p, which reduces the force to account for the ductility of the element. In this study I_p is considered always equal to 1.0. The values of R_p and the other quantities of interest for the roof, fifth floor and fourth floor are summarized in Table 7.6, which considered the S_{DS} of 1.4 (Chen at al. 2015). It is noted that, the F_p of each connection is found considering the height of its attachment to the structure to find the structure amplification factor. Thus, in each panel the top connections are designed with the forces relative to the upper floor and the bottom connections are relative to the bottom floor.

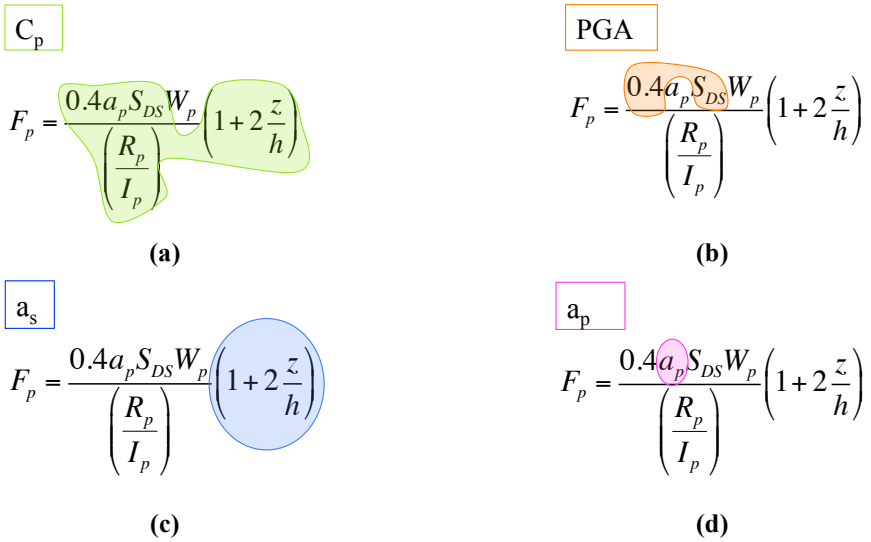

Figure 7.52. Components of the code formula to determine F_p which represent the (a) the seismic coefficient, (b) the peak ground acceleration, (c) amplification of acceleration in the structure, and (d) the component amplification factor

7.3.3 Input Motions

Characteristics of the Input Motions

In addition to experimental motions FB1, FB2 and FB3, eighteen additional seismic input motions were selected from the PEER Ground Motion Database. Of these eighteen motions, six were from strike-slip fault earthquakes, six from normal fault earthquakes and six from oblique fault earthquakes. The motions selected have different duration, distance from the epicenter and shear wave velocity of the soil were. These motions were spectrally matched to the 42-year return period earthquake, which was created by scaling the maximum credible earthquake (MCE) by a factor of 0.25,

Table 7.6. Summary of the code limits for the different quantities considered

Quantity	Element	Floor	Value
PGA	-	-	$0.4S_{DS}$=0.4*1.4=0.56 g
a_s	-	Roof	3
		Fifth	2.6
		Fourth	2.2
a_p	Fastener	All	1.25
	Body	All	1
R_p	Fastener	All	1
	Body	All	2.5
C_p	Fastener	Roof	2.1
		Fifth	1.82
		Fourth	1.54
	Body	Roof	0.67
		Fifth	0.58
		Fourth	0.49

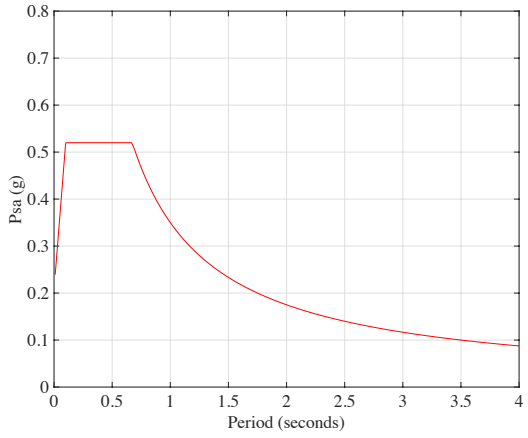

Figure 7.53. Target spectrum for service level earthquake

and it is shown in Figure 7.53. The matching was performed between a maximum and minimum period of 1.425 and 0.028 seconds, respectively. The maximum was dictated by the ASCE-7 code suggestion of matching the period up to 1.5 times the main period of the building. In this case the elastic period of the building was 0.95 seconds, leading to a maximum period suggested by the code of 1.425. The decision relative to the minimum value was dictated by the fact that focus of this study are the

nonstructural components, which are more sensitive to low periods.

RSPmatch09 was used to spectrally match the motion (Fouad and Rathje 2012). Some of the main features of the matched motions are presented in this section. For clarity of explanation, these results are presented separately for earthquakes generated by a strike-slip, reverse and normal fault. The general characteristics of the strike-slip fault earthquakes are presented in Table 7.7. For each of the six strike-slip motions, this table presented the name of the earthquake during which it was recorded, the country where it happened, its magnitude M_w, the station name and code indicating the orientation of the motion, the distance from the point of rupture R_{rup}, the duration D_{95}, and the shear wave velocity V_{30} of the soil. The table shows the variety of characteristics of these motions, with R_{rup} varying from 12 to 79 km, D_{95} spanning from 10 to almost 40 seconds, and V_{30} varying roughly from 200 to 720 m/sec.

Table 7.7. Characteristics of the strike-slip earthquake motions selected: earthquake, country, magnitude, station, R_{rup}, D_{95}, and V_{30}

Earthquake event [date]	Country	M_w	Station name [Record Name]	R_{rup} (km)	D_{95} (sec)	V_{30} (m/sec)
Darfield 09/04/10	New Zealand	7.0	LSRC [LSRCN15W]	79	23	561
El-Mayor Cucapah 04/10/10	Mexico	7.2	Bonds Corner [BRC360]	32	38	223
Imperial Valley 10/15/79	U.S. (CA)	6.5	Calipatria Fire Station [CAL225]	24	25	205
Manjil 06/21/90	Iran	7.4	Abbar [ABBAR—L]	12	29	723
Tottori 10/06/00	Japan	6.0	OKY004 [OKY004EW]	19	15	475
Trinidad 11/08/80	U.S. (CA)	7.2	Rio Dell Overpass [RDW270]	76	10	311

Table 7.8 presents other characteristics of the spectrally matched motions, such as PGA, spectral response at short periods (S_s), spectral response at 1 second (S_1), peak floor acceleration (PFA) and peak interstory drift ratio (PIDR) created by the motion in the building. The values of PGA, S_s and S_1 are very similar because the motions are spectrally matched. The values of the peak structural

responses are obtained with results from the model and are also similar, with PFA between 0.51 and 0.61 g and PIDRs between 0.67 and 0.76%. Figure 7.54 presents the time history and pseudo-acceleration spectrum for the spectrally matched motions.

Table 7.8. Characteristics of the strike-slip motions selected and structural response: PGA, S_S, S_1, PFA and PIDR

Earthquake	PGA (g)	S_S (g)	S_1 (g)	PFA (g)	PIDR (%)
Darfield	0.30	0.50	0.34	0.58	0.73
El-Mayor Cucapah	0.29	0.5	0.36	0.54	0.74
Imperial Valley	0.25	0.53	0.36	0.51	0.67
Manjil	0.24	0.49	0.35	0.52	0.72
Tottori	0.24	0.48	0.34	0.56	0.75
Trinidad	0.26	0.49	0.35	0.62	0.76

Table 7.9,Table 7.10and Figure 7.55, present the same results for the normal fault earthquake. In this case R_{rup} varies from 6.8 to 59.6 km, D_{95} spans from 5 to 32 seconds, and V_{30} varies from 240 to 680 m/sec. The values of PGA, S_s and S_1 are very similar because the motions are spectrally matched. PFAs vary from 0.44 g to 0.61 g, while PIDRs change from 0.66 to 0.77%.

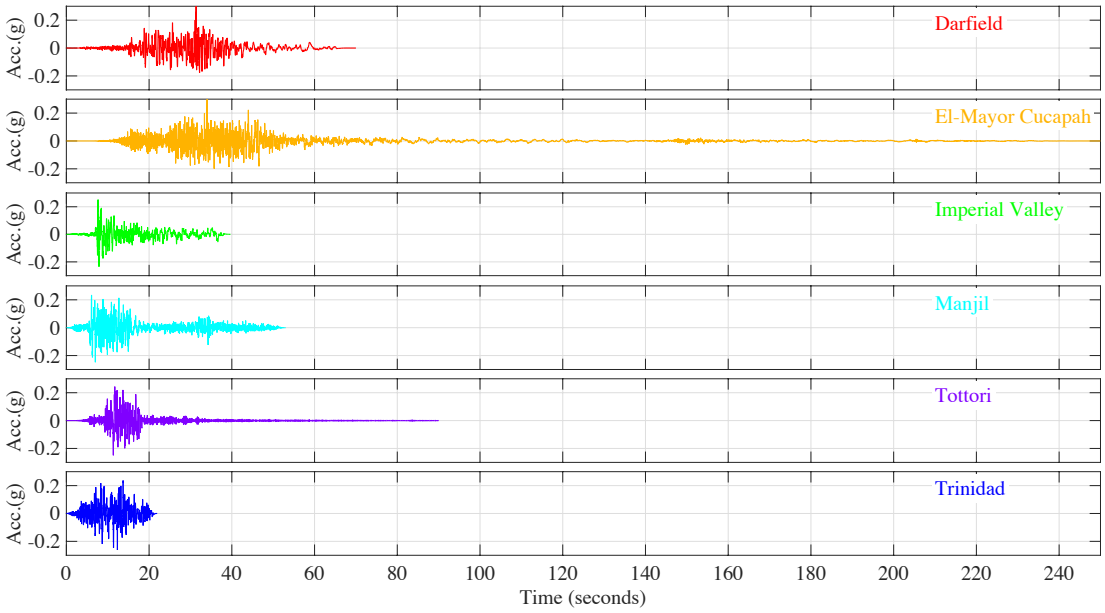

(a)

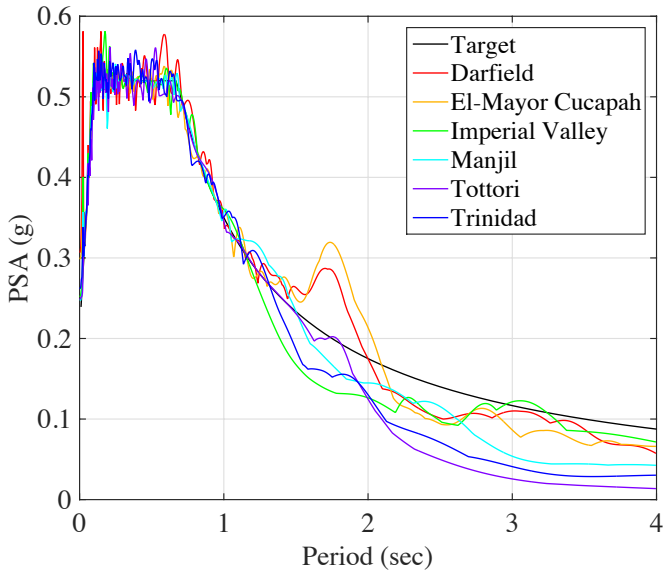

(b)

Figure 7.54. Matched strike-slip motions: (a) time histories and (b) pseudo-acceleration spectra

Table 7.9. Characteristics of the normal fault earthquake motions selected: earthquake, country, magnitude, station, R_{rup}, D_{95}, and V_{30}

Earthquake event [date]	Country	M_w	Station name [Record Name]	R_{rup} (km)	D_{95} (sec)	V_{30} (m/sec)
Anza 10/30/01	U.S. (CA)	4.9	La Quinta - Bermudas & Durango [QB090.AT2]	28	5	360
Dinar 10/05/95	Turkey	6.4	Cardak [CAR076.AT2]	44	13	428
Irpinia 11/23/80	Italy	6.9	Torre del Greco [TDG000.AT2]	59	32	593
L'Aquila 04/06/09	Italy	6.3	L'Aquila - V. Aterno -Colle Grilli [FA030XTE.AT2]	6	8	685
Northwest China 01/27/97	China	5.8	Jiashi [JIA000.AT2]	27	14	240
Umbria 09/26/97	Italy	6.0	Castelnuovo-Assisi [A-CSA000.AT2]	17	28	293

Table 7.10. Characteristics of the normal fault motions selected and structural response: PGA, S_S, S_1, PFA and PIDR

Earthquake	PGA (g)	S_S (g)	S_1 (g)	PFA (g)	PIDR (%)
Anza	0.217	0.503	0.363	0.52	0.68
Dinar	0.231	0.535	0.313	0.44	0.66
Irpinia	0.213	0.552	0.319	0.55	0.77
L'Aquila	0.229	0.550	0.347	0.61	0.70
Northwest China	0.194	0.569	0.352	0.52	0.69
Umbria	0.306	0.522	0.349	0.57	0.68

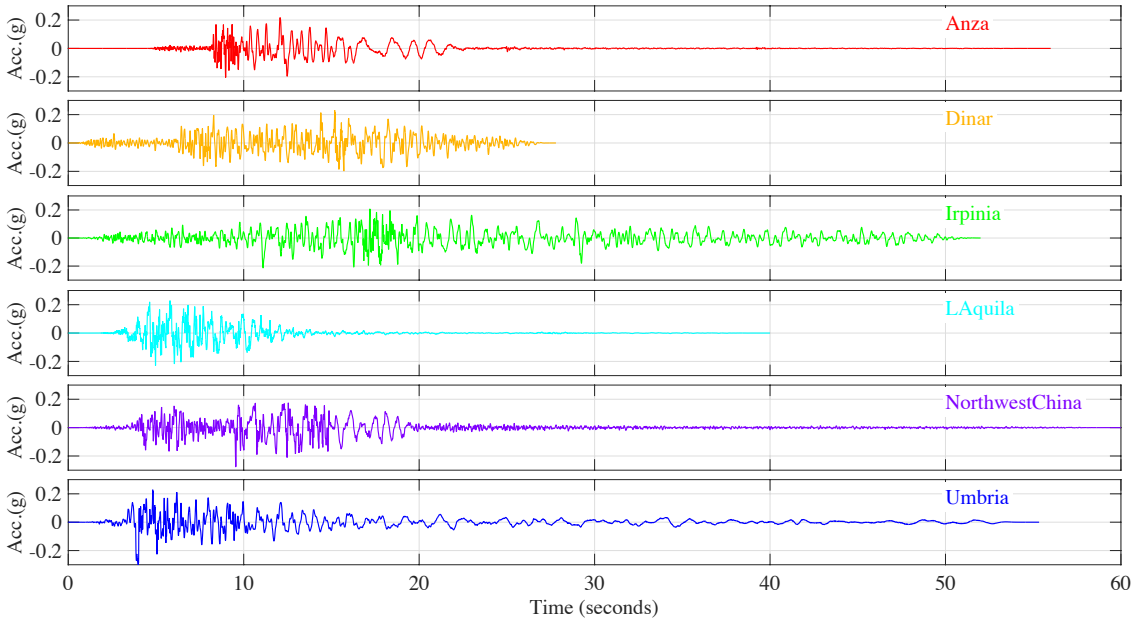

(a)

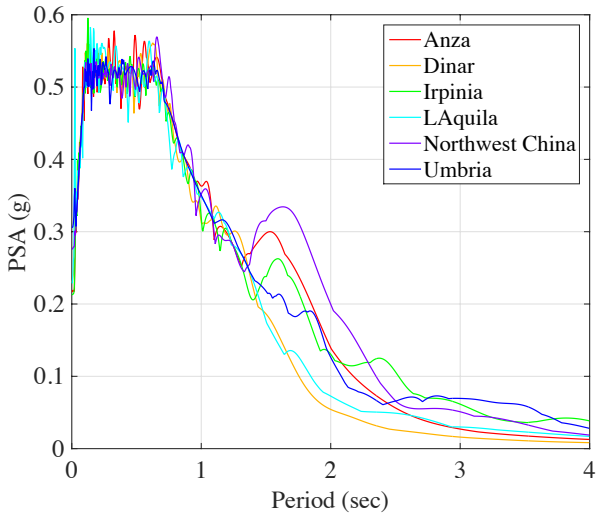

(b)

Figure 7.55. Matched normal fault earthquake motions: (a) time histories and (b) pseudo-acceleration spectra

Table 7.11, Table 7.12 and Figure 7.56 present the result for the motions from a reverse fault earthquake. R_{rup} varies from 7 to 47 km, D_{95} spans from 10 to 80 seconds, and V_{30} varies from 200 to 900 m/sec. PFAs vary from 0.49 g to 0.59 g, while PIDRs change from 0.67 to 0.75%. More information about the original and scaled earthquake motions are presented in Appendix A.

Table 7.11. Characteristics of the reverse fault earthquake motions selected: earthquake, country, magnitude, station, R_{rup}, D_{95}, and V_{30}

Earthquake event [date]	Country	M_w	Station name [Record Name]	R_{rup} (km)	D_{95} (sec)	V_{30} (m/sec)
Cape Mendocino 04/25/92	U.S. California	7.0	College of the Redwoods [CRW270.AT2]	31	15	492
Chichi 09/21/99	Taiwan	7.6	CHY004 [CHY004-N]	47	80	271
Iwate 06/14/08	Japan	6.9	Mizusawaku Interior O ganecho [44B71EW.AT2]	7	40	413
Loma Prieta 10/17/89	U.S. California	6.9	Piedmont Jr High School Grounds [PJH045.AT2]	73	12	895
Niigata 10/23/04	Japan	6.6	NIG018 [NIG018EW.AT2]	25	70	198
Whittier 10/01/87	U.S. California	6.0	Bell Gardens – Jaboneria [JAB207.AT2]	17	10	267

Table 7.12. Characteristics of the reverse fault motions selected and structural response: PGA, S_S, S_1, PFA and PIDR

Earthquake	PGA (g)	S_S (g)	S_1 (g)	PFA (g)	PIDR (%)
Cape Mendocino	0.236	0.534	0.337	0.59	0.71
Chichi	0.291	0.517	0.354	0.49	0.68
Iwate	0.248	0.523	0.353	0.50	0.74
Loma Prieta	0.294	0.504	0.349	0.57	0.67
Niigata	0.227	0.519	0.332	0.55	0.76
Whittier	0.231	0.506	0.331	0.52	0.73

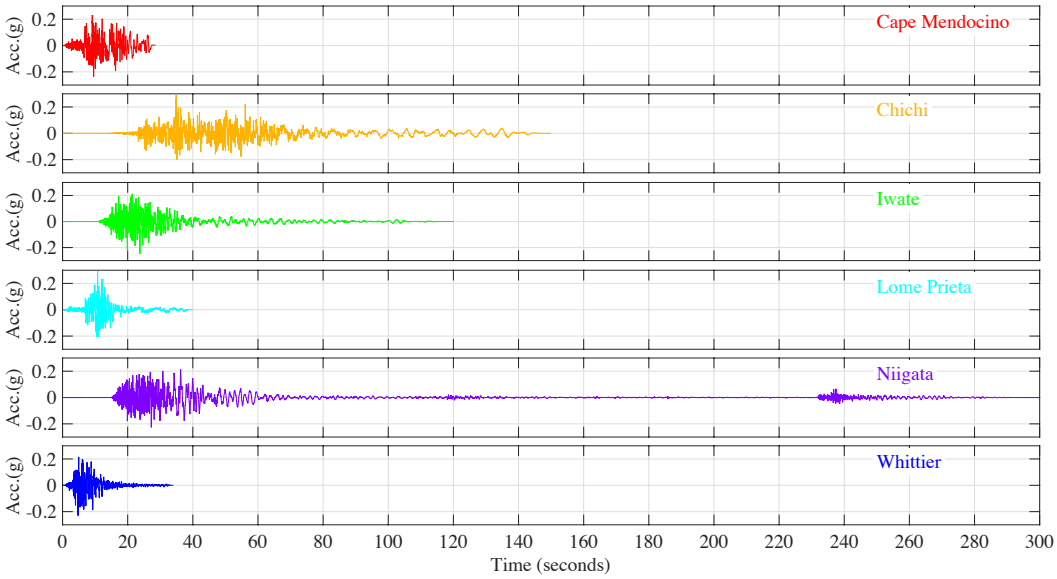

(a)

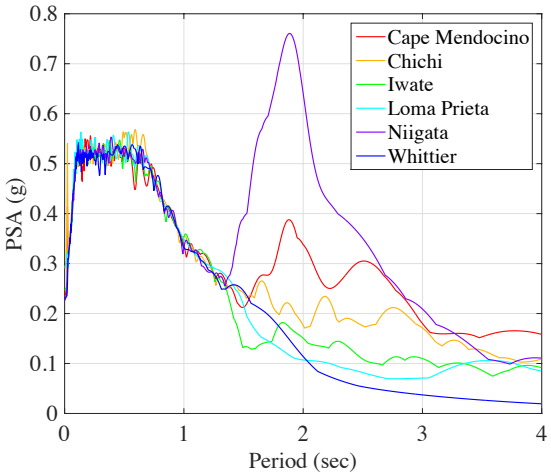

(b)

Figure 7.56. Matched reverse fault earthquake motions: (a) time histories and (b) pseudo-acceleration spectra

7.3.4 Results: Seismic Coefficient C_p

Figure 7.57 presents the values of C_p found during the analysis for panels having a natural frequency of 8, 11 and 14 Hz installed at the fifth and fourth levels, and compares them with the code limits for body and fasteners of the connections. The markers showing the results are presented at the location of the mass of the SDOF (mid-height of the panel), however these values are considered constant along the height of one panel. Thus, the C_p relative to each panel can be compared to the code limits relative to the top and bottom floors. The different color of dots represents the different natural

frequency of the panels considered, the purple triangle represents the experimental results, while the green and blue stars show the average and 95th percentile of the distribution, respectively. The code limits for body and fastener elements of the connections are presented with a cyan and black line, respectively.

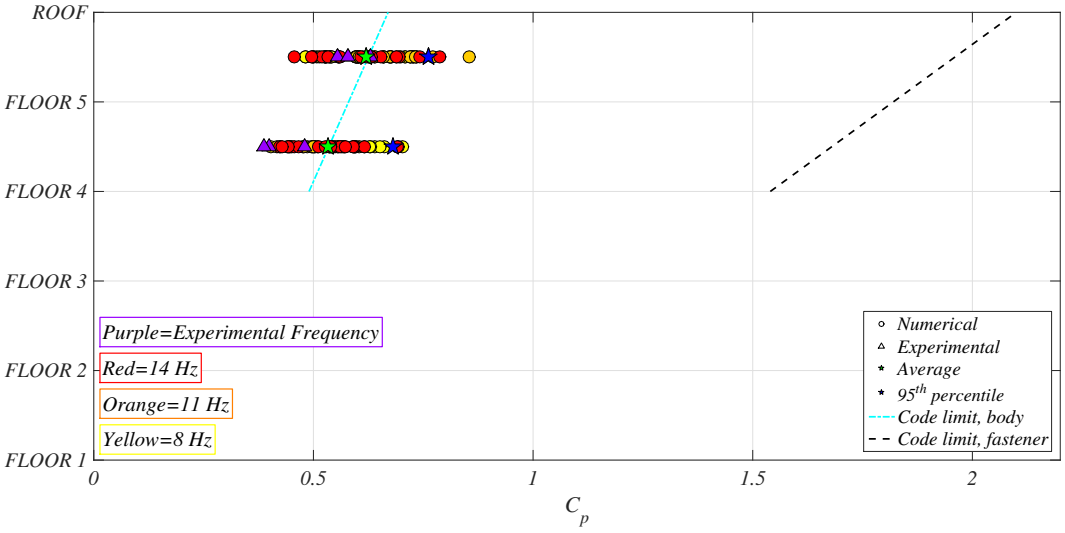

Figure 7.57. Values of the seismic coefficient C_p for panels installed at the fourth and fifth level

As expected for a service level earthquake, the achieved C_p are well below the code limit for fastener elements. However, this is not the case for the ductile body elements. For the panel at the fifth level, C_p varies from 0.45 to 0.85. The 95th percentile of the distribution is 0.76, while the average is 0.62. The code limit of C_p for body elements of 0.67 for the top floor represents the 70% percentile of the distribution. This means that, in the case of top connections, the actual force is larger than the design force F_p in 30% of the cases. This value might seem large, however the 95th percentile of the distribution is only 1.13 times F_p, thus spread damage it is still not expected. The code limit of 0.58 for the fifth floor represents the 35th percentile of the distribution of the fifth floor panel, meaning that for the bottom connections, the actual force is larger than the design force in 65% of the cases. In this case the 95th percentile is 1.31 times the code limit.

For panels installed at the fourth level, the values of C_p vary from 0.38 to 0.70, with an average of 0.53 and a 95th percentile of 0.68. The code limit for the top floor of 0.58 represents again the 70th percentile of the distribution, while the limit for the bottom floor of 0.49 represent the 35th percentile.

The value of the 95th percentile are 1.17 and 1.38 times those of the code limits for the top and bottom floor, respectively. Thus, these results are similar to those observed for the panel at the fifth level.

The previous observations lead to the conclusions that during a service level earthquake the forces developed in the connections are similar to the design level forces for ductile elements. The situation is different for connections to the bottom and top floors of a panel. In fact, when a building movement is dominated by the first mode, a panel connected to two floors is "pulled" by the top floor and "slowed down" by the lower floor. This is not taken into account by the code. As a consequence, the values provided by the code are particularly unconservative for the design of the bottom connections of the panel. However, in common panel configurations, the bottom of the panels are attached to the building with bulky bearing connections, thus the possibility of damage to these is considered unlikely. Damage could be expected in case the bottom of the panel has tiebacks instead of bearing connections.

7.3.5 Results: Structure Amplification Factor and Component Amplification Factor

Figure 7.58 shows the numerical and experimental results relative to a_s, including the mean and 95th percentile of the distribution and the code limits for the roof, fifth and fourth floor. The values of a_s for each earthquake were found by extracting the peak of the absolute value of the time history of accelerations. The plot shows that the code values are very close to 95th percentile of the distribution. The plot also shows that in this case the distribution of a_s along the height of the building is roughly linear. The 95th percentile of the distribution of a_s obtained in this study can be found by changing the formula in the code to:

$$a_s = 1 + 1.7\frac{z}{h} \qquad \text{Eq. 7.7}$$

The value of 1.7 obtained from the distribution is very similar to the value of 2 proposed by the code, which provides an overestimation by a factor of 1.17. It is noted that the values obtained in this analysis and those provided by the code *should not be consistent,* since this analysis refers to service level motions, while that in the code is relative to design level earthquakes.

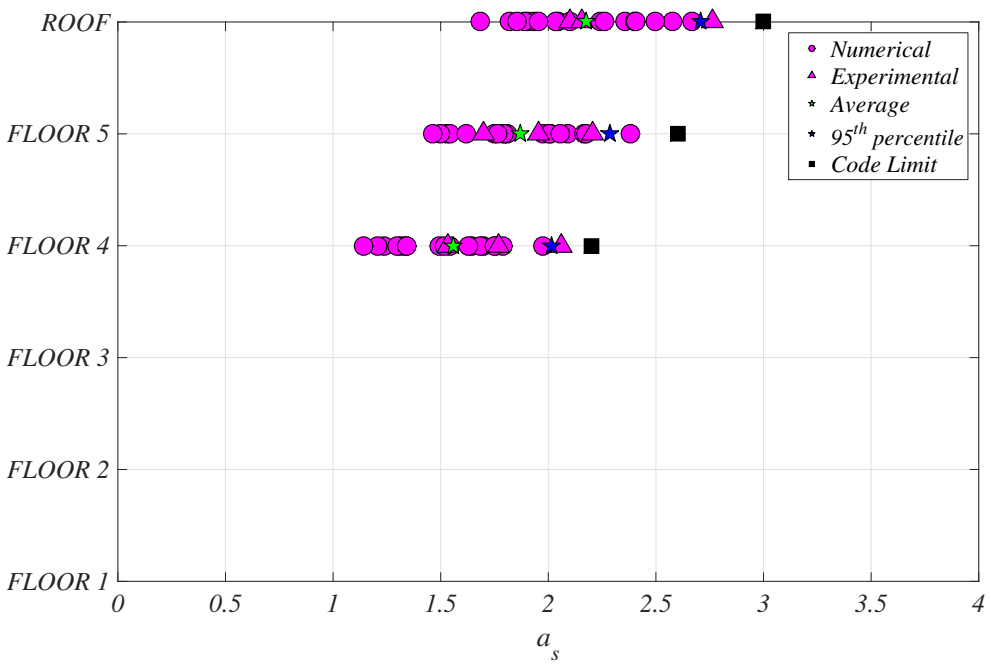

Figure 7.58. Values of the structural amplification factor for the ground motions considered

Results of the analysis for the component amplification factor a_p are presented in Figure 7.59. Both the values of $a_{p,top}$ and $a_{p,bottom}$ are presented, and they are shown close to the top and bottom floors, respectively. This distribution shows a great scatter in the results. At the fifth level $a_{p,bottom}$ varies from 1.11 to 1.68 while $a_{p,top}$ varies from 0.9 to 1.63. Hence, the panel acceleration could be less than that of the top floor, but it is always more than that of the bottom floor. The 95th percentile of the distribution is at 1.6 for $a_{p,bottom}$ and 1.41 for $a_{p,top}$. When the panel is installed at the fourth level, the values of $a_{p,bottom}$ are larger, while those of $a_{p,top}$ are smaller. In fact, $a_{p,bottom}$ varies from 1.10 to 1.77, with 95th percentile at 1.72, while $a_{p,top}$ spans from 0.90 to 1.43, with 95th percentile at 1.38. Clearly, these values are far from the limits of 1 and 1.25 set by the code for the a_p of body and fastener elements of the connections.

Table 7.13 shows the values of mean and 95th percentile of $a_{p,topn}$ and $a_{p,bottom}$ for panels of the three frequencies considered. Maximum amplification is reached for a panel of natural frequency of 8 Hz for the fourth level and 11 Hz for the fifth level. This might seem counterintuitive, since it might be assumed that panels with lower natural frequencies always provide larger amplification. However, the level of amplification depends also on the modal shape of the building mode close to the panel frequency. In this case, the natural mode of the building mode at a frequency closer to 8 Hz has a node

at the mid height of the fifth level, thus explaining the difference of amplification at 8Hz for panels 4ES and 5ES.

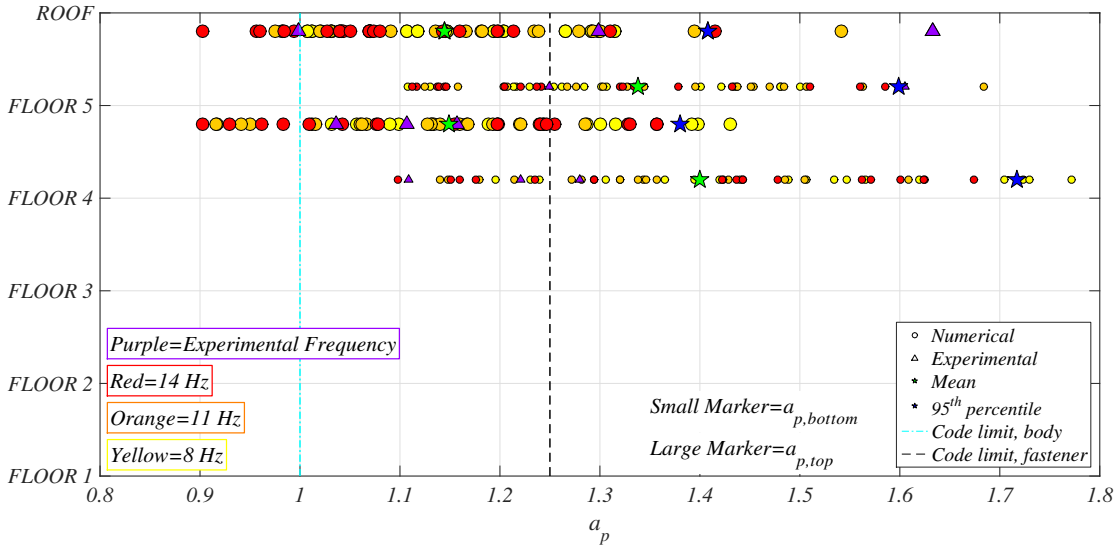

Figure 7.59. Values of $a_{p,bottom}$ and $a_{p,top}$

Table 7.13. Mean and 95th percentile of $a_{p,top}$ and $a_{p,bottom}$ for panels with different natual frequencies

	Panel 4ES			Panel 5ES		
	8 Hz	11 Hz	14 Hz	8 Hz	11 Hz	14 Hz
Mean $a_{p,bottom}$	1.48	1.34	1.41	1.31	1.38	1.28
Mean $a_{p,top}$	1.20	1.10	1.15	1.13	1.18	1.09
95th percentile $a_{p,bottom}$	1.75	1.57	1.65	1.49	1.63	1.57
95th percentile $a_{p,top}$	1.42	1.27	1.36	1.31	1.48	1.37

7.4 Limitation of This Study

While this study presents a one-of-a-kind analysis focusing exclusively on APC cladding, there are several limitations, mostly related to simplifications in the analysis. First of all, the stiffness of the structural elements in the building model is kept constant, and does not take into account any softening created by earthquake motions. The stiffening effects of the nonstructural components (cladding, partitions etc.) on the building is also ignored, and their masses are lumped at discrete locations. An important limitation is the simplification of panels as SDOF systems, with all the mass concentrated at the center of the panel. This assumption, which was made to simplify the problem and possibly extend

the results to panels with different geometries, is not very accurate. This is true especially for OP panels, since OP bending modes include deformation of the panels. The stiffness of the two links connecting the mass of the SDOF system to the top and bottom floors is the same. This is generally not the case, due to the difference between bearing and tieback connections. This assumption is adopted again to simplify the analysis and allow extension of the results to different types of panels. Possible nonlinearities in either the building or panels are not considered. Finally, these results are relative only to the BNCS building, while further studies are suggested to understand how the panels might behave while attached to different types of buildings

7.5 Summary Remarks

This chapter presents an analysis of the forces developed in APC cladding connections during a service level earthquake, and their comparison with the limit proposed by the ASCE-7 code (ASCE 2010). To achieve this, a model of the BNCS building including two panels considered SDOF systems is created. The two panels selected are 5ES and 4ES, which move in the OP direction and are located at the fifth and fourth level, respectively. The numerical results are compared with experimental data obtained for the service level motions during the BNCS experiment. Subsequently, the model is used to perform a parametric study. The main parameters considered during this study are:

1. Input motion characteristics. Eighteen additional motions scaled to match the target spectrum for the service level earthquake are considered;
2. The natural frequency of the panel. The frequencies considered are 8 Hz, 11 Hz and 14 Hz.

This study shows that, because during service level earthquakes the building motion is dominated by its first mode, APC panels are excited by larger accelerations at their top. Thus, the amplification of acceleration in the panels tends to be larger compared to the bottom floor, since the top floor pulls the panel forward, while the bottom tends to restrain it. Consequently, it is important to distinguish between $a_{p,top}$ and $a_{p,bottom}$, and to recognize that $a_{p,bottom}$ is larger than $a_{p,top}$.

The design force for fastener elements is much larger than the forces achieved during service level motions in all the case considered, as expected. However, the design force for body elements of

the connections could be smaller than the achieved one, due to the reduction of F_p by the arbitrary factor R_p. This is the case especially for the bottom of the panel, due to the pulling effects of the top floor. The parametric analysis performed reveals that the actual seismic coefficient C_p might be larger than its design value for the body elements in the top connections in 30% of the cases, and 65% for the bottom connections. The 95^{th} percentile of the distribution of C_p is between about 1.1 and 1.3 times the code limits for the top and bottom floors, respectively. This could potential have negative consequences, since it might lead to damage in the panels during small earthquakes. However, the parts of the system with larger differences between actual and design forces are the connection at the bottom of the panels. These are generally very bulky bearing connections, which are not expected to be damaged at forces of 1.3 times F_p. However, this might not be the case if tiebacks are connected at the bottom of the panel.

Analysis relative to the structure and component amplification factors were also performed. The value of a_s was found to increase linearly along the height of the building, with values very similar to those provided by the design code. The component acceleration factors are larger than the code prescription for both body and fastener elements. In this analysis the 95^{th} percentile of $a_{p,bottom}$ was around 1.6, while that of $a_{p,top}$ was around 1.4.

ACKNOLEDGEMENTS

Chapter 7 reproduces content and images of the material currently in preparation. Pantoli, E., Hutchinson, T.C. “Seismic accelerations developed in APC cladding panels” (tentative title). The author of the dissertation is the principal author of the above cited papers.

Chapter 8

Acceleration Sensitive Design of Connections Under the Design Earthquake

When subjected to design level earthquakes, modern buildings are expected to dissipate energy, typically resulting in damage to key structural components. Thus, their behavior will be different compared to that observed during service level motions, during which the structure remains mostly linear elastic. One of the major differences is the potential influence of the higher modes of the building, both in terms of deformed shape and predominant frequency. This might be very relevant when analyzing nonstructural components such as APC cladding. In fact, since the panels are connected at two floors, changes in the building deformed shape creates a variation in the way the panel is excited, while changes in the predominant natural frequency of the building could shift more energy close to the natural frequency of the panels themselves. Recall that this may be as low as 8 Hz for out of plane (OP) modes.

While the previous chapter focused on the analysis on the behavior of APC cladding during service level earthquakes, this chapter focuses on the study of its behavior during design level motions. The procedure is similar to that of the previous chapter. In fact, the same building model and panels are considered. However, the building model is modified to account for the nonlinearities expected during a design level motion. After describing in detail the properties of nonlinear elements assumed in the model, two validations of the model results are presented. The first is a pushover analysis, and the second involves comparison of the results of nonlinear dynamic analysis with the experimental results from test FB5, which is considered a design level earthquake. This second validation is also used to determine the optimal damping ratios. The last part of this chapter summaries the results from a parametric study during which eighteen additional earthquake motions matched to the design spectrum were run on the model. As seen in the previous chapters, the values of C_p, a_s and a_p are analyzed and compared to the limits provided in the code.

8.1 Description of the Nonlinear Numerical Model

The same building model of the BNCS building used in the previous chapter was used in this case with the following modifications:

- Nonlinear elements, in the form of plastic hinge elements. Plastic hinges are added at the base of each column at the first floor and the ends of each beam (Figure 8.1a). Fiber hinges are assigned at the base of the column, while lumped plasticity hinges are assigned to the beams. The hinges in the beams are modeled as a deformation controlled, in which only the moment around the horizontal axis of the section is considered nonlinear. This choice is made since the normal force and the moment in the other direction remains small. When this type of hinge is selected, SAP2000 requires the assignment of its the moment-rotation curve (specified using five points) and the hysteresis type. Those are discussed for the beam at each floor in the pertinent sections below;

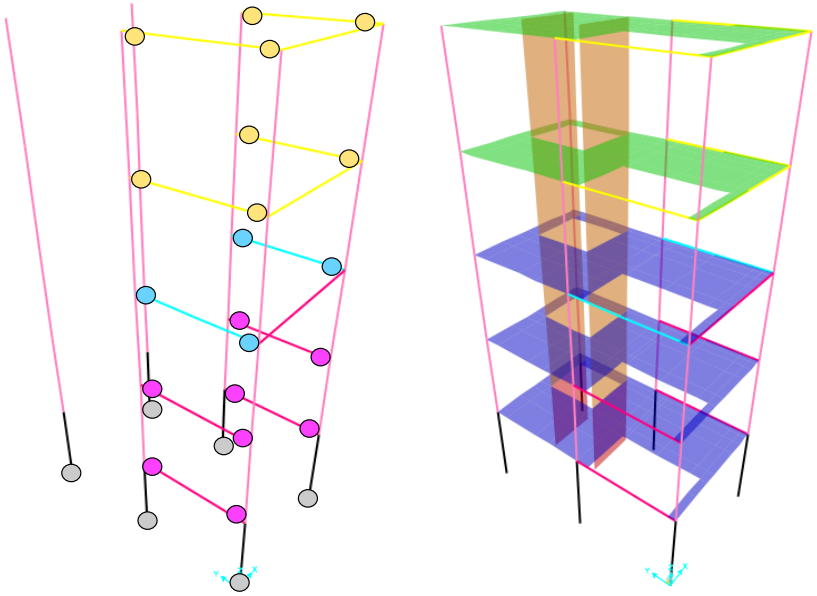

(a) **(b)**

Figure 8.1. Nonlinear model: (a) location of the nonlinear elements and (b) model showing the different material properties used for linear elastic elements (color codes indicates the different material properties)

- The stiffness of the elastic elements was further reduced. As seen in the previous chapter, the reduction factors are applied to the Young modulus of concrete. The stiffness reduction factors are considered the minimum suggested by the literature in Section 7.1.3, and they are presented in Table 8.1. The stiffness of the concrete in the prestressed beam at the fourth floor was not reduced, since the potential for cracking is restrained by the prestressing;
- The base of the elevator wall was considered pinned. This is a minor change and does not have considerable effects on the results.

Table 8.1. Concrete properties used for linear elements in the nonlinear model

Element	E original (ksi)	Reduction factor	E reduced (ksi)
Columns at the first level	5357	0.4	2142
Walls at the first level	5357	0.35	1874
Columns at the upper levels	5489	0.4	2195
Walls at the upper levels	5489	0.35	1921
Beams at the second and third	5128	0.3	1538
Beams at the fourth floor	5128	0.5	2564
Slabs at the second, third and fourth floor	5128	0.25	1282
Beams at the fifth floor and roof	5423	0.3	1626
Slabs at the fifth floor and roof	5423	0.25	1355

8.1.1 Plastic Hinges in the Columns at the First Floor

Figure 8.2a shows the exact geometry of a typical column, which was 26'' in the longitudinal direction (direction of motion) and 18'' in the transverse direction. At each location the appropriate material property was used to define the fiber, as explained below. Two different types of longitudinal bars were used in the column: at the corners #9 Grade 60 steel while at the edges #6 Grade 75 steel. Figure 8.2b shows the geometry of the section in the section designer tool in SAP2000.

Material Properties

The four materials used in this section were:

- #9 Grade 60 reinforcing bar (Park model). Results from tensions tests in the #9 steel indicate a f_y of 69 ksi and f_u of 119 ksi, but strain data were not available. Since stress-strain data from

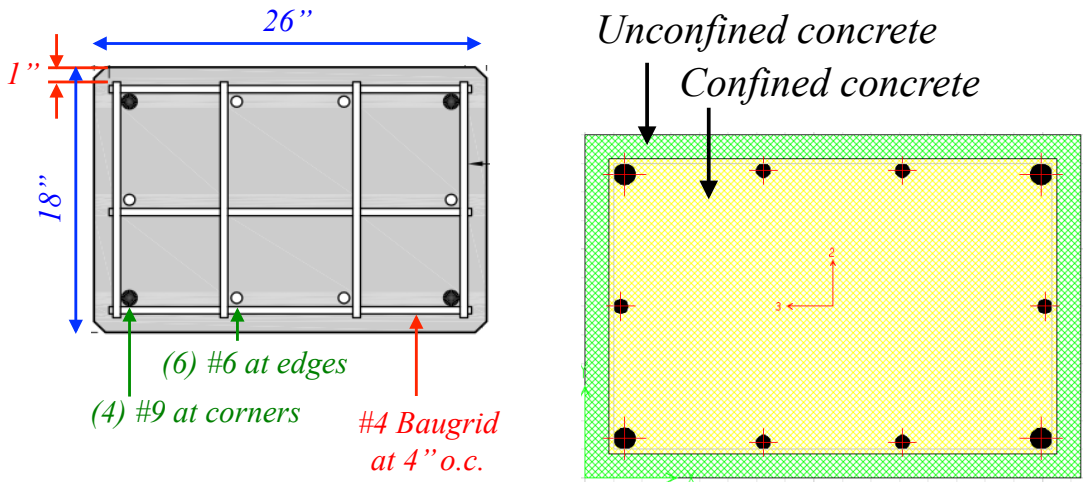

Figure 8.2. Cross section of a column: (a) geometry and (b) model in the section designer tool in SAP2000

another batch of #9 used were available, it was decided to use strain values form this second batch. It is noted that this batch of steel was provided by the same manufacturer at the same time, and both types of steel were grade 60. The values of strain assumed in the model were 0.01 inch/inch at the onset of hardening and 0.12 inch/inch at the ultimate point. These values of strain are consistent with what reported in the literature for A706 grade 60 steel (Nilson et al. 2004, Paulay and Priesley 1992). The hysteresis type selected was kinematic, as suggested by the SAP manual for metals (CSI 2013);

- #6 grade 75 bar (Park model). As for the the #9 bar, also in the case of the #6 bars only the values of yield and ultimate stresses were available from mill certificate (f_y = 84 ksi, f_u =118 ksi). In this case typical values of yield and ultimate strain for grade 75 steel were used (ε at the onset of hardening of 0.0035 inch/inch and ultimate strain of 0.105 inch/inch) (Nilson et al. 2004). The hysteresis type selected was kinematic (more information about material properties can be found in Chen et al. 2013a);
- Unconfined concrete. The compressive behavior of concrete was modeled using the Mander model on SAP2000, with the ultimate stress of 7.91 ksi and strain at peak stress of 0.0023 inch/inch found from laboratory testing. The ultimate strain of unconfined concrete was

assumed as 0.004 inch/inch. The tensile strength of the unconfined concrete was 0.67 ksi. The Takeda hysteresis loop was selected;

- The behavior of confined concrete was determined through the section designer tool in SAP2000. These calculations take into account the type of transverse reinforcement in the columns, which was created by #4 baugrids spaced at 4'' on center and having four and three legs in the longitudinal and transverse direction, respectively. Baugrids are different than normal transverse reinforcement since they are welded. Laboratory tests providing stress-strain data were performed on two baugrids, and they revealed consistent results for f_y of 81 ksi and f_u of 91 ksi. The Park model for steel was adopted also in this case to represent the monotonic behavior. A strain at the onset of hardening of 0.0025 inch/inch and an ultimate strain capacity of 0.056 inch/inch were adopted. It is noted that the final strain is low, but the value of 5.6% is consistent –and actually slightly larger- than what was reported on the mill certificate (between 4.22% and 5.48%). The requirement specified on the mill certificate is 4% and all the baugrids tested met this limit. The stress-strain behavior of the confined concrete was found through the section designer function of SAP2000, and results show a ultimate strength of 10.79 ksi and a strain at peak stress of 0.0067 inch/inch. The ultimate strain of the confined concrete was found with the formula proposed by Paulay and Prislety (1992) as:

$$\varepsilon_{ccu} = 0.004 + \frac{1.4\rho_s f_{yh}\varepsilon_{sm}}{f'_{cc}} = 0.0106 inch/inch \qquad \text{Eq. 8.1}$$

This value was lower than expected, because of the lower ultimate strain of the transverse reinforcement. These models used for concrete were verified with theoretical calculations performed using Chang and Mander (1994) and the comparison revealed good (Appedix B). The Takeda hysteresis type was selected for this material.

Figure 8.3 presents the stress-strain curve for all the reinforcing bars used in the column, while Figure 8.4 presents the model of the confined and unconfined concrete. The length of the length of the plastic hinge l_p was determined with the formula provided by Paulay and Priestley (1992):

$$l_p = 0.08l + 0.15 d_b f_y = 25"$$ Eq. 8.2

Where d_b is the diameter of the reinforcing bar, and l is the length of the structural elements.

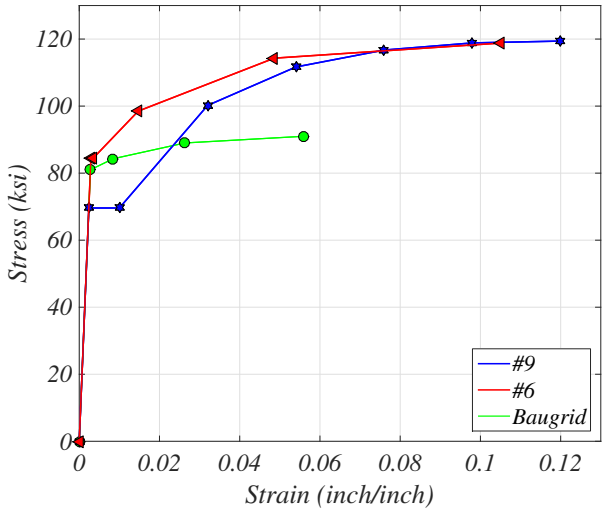

Figure 8.3. Models of the steel used in the columns

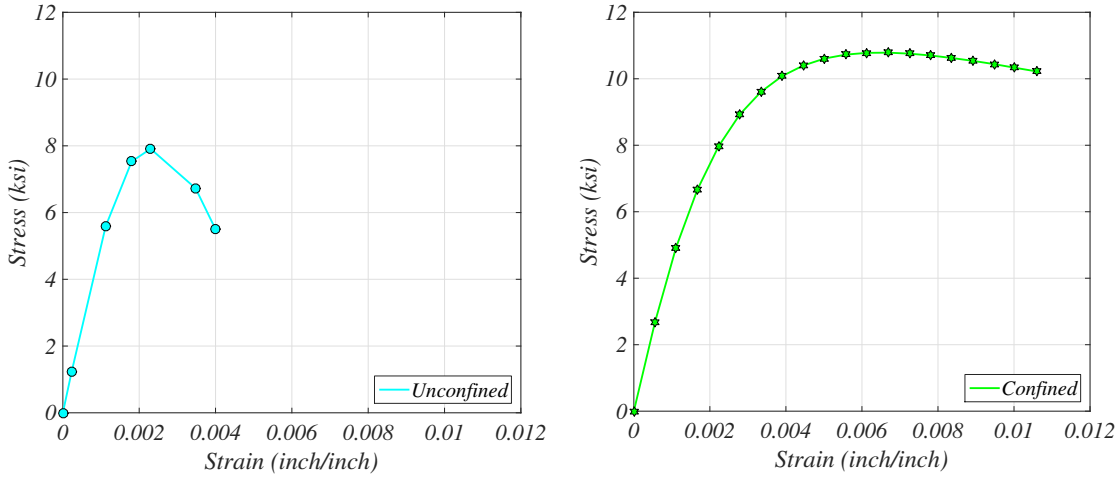

(a) **(b)**

Figure 8.4. Model of the concrete used in the column (compression only): (a) unconfined, (b) confined

Axial Force-Moment (P-M) Interaction Diagram

The axial force-moment (P-M) yield and ultimate interaction curves are shown in Figure 8.5. The two curves were created by identifying the yield and ultimate points of the moment-curvature plot at different level of normal forces using the section designer tool in SAP2000. The values presented were checked with theoretical calculations presented in Appendix B.

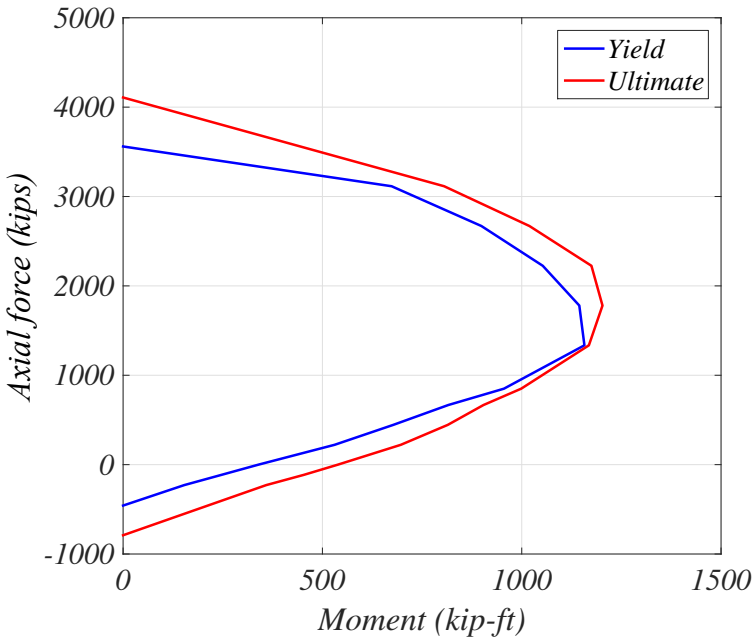

Figure 8.5. P-M interaction diagram for the columns of the building

8.1.2 Plastic Hinges in the Beam at Floor Two and Three

The beams at the second and third floor of the BNCS building had the geometry shown in Figure 8.6a and were characterized by the presence of high strength steel in the longitudinal direction. The beam was 28'' high and 12'' high, it had four longitudinal #7 bars of high-strength grade 100 steel and the transverse reinforcement was composed of #4 grade 60 bars.

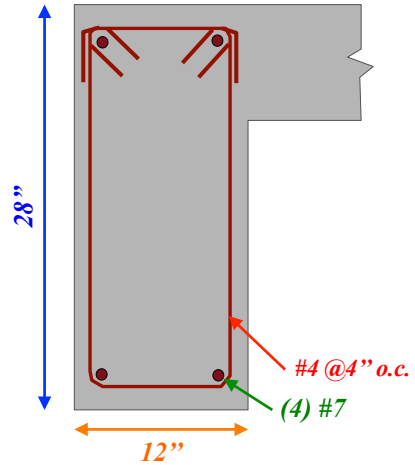

Figure 8.6. Geometry of the beams installed at the second and third floors

Material Properties

Tension tests on longitudinal reinforcing bars used in the beams were performed. These revealed an average f_y of 128 ksi, an average f_u of 159 ksi. To build the Park model for steel, a strain at the onset of hardening of 0.0071 inch/inch and ultimate strain of 0.05 inch/inch were used (Figure 8.7). Tension tests were performed also on the batch of #4 bars used as transverse reinforcement, and it was determined that the yield strength was 69 ksi, the ultimate strength was 99 ksi and the ultimate strain was 0.19 inch/inch. For the Park model, the onset of strain hardening was considered to be 0.003 inch/inch, which was the value allowing a better comparison with the stress-strain data from tension tests (Figure 8.8). The comparison of Figure 8.7 and Figure 8.8 shows that, while the longitudinal bars had larger ultimate stress, they also had smaller ultimate strain compared to the transverse reinforcement, as expected for high strength steel.

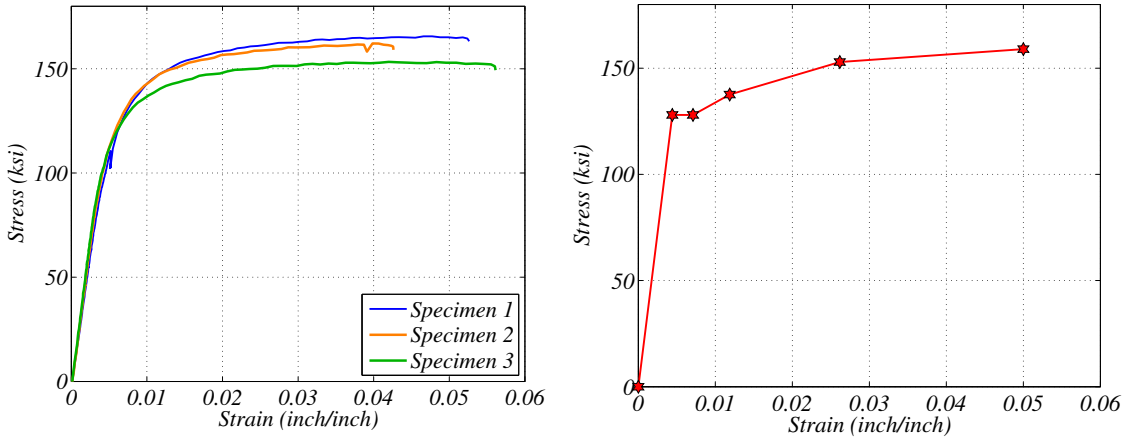

Figure 8.7. Grade 100 #7 bars used in the beams at the second floor: (a) results from tension tests and (b) Park model used on SAP2000

Strength of the unconfined concrete at these floors was determined with compression tests on concrete cylinders executed at the beginning of the BNCS testing sequence, which revealed a f'_c of 7.04 ksi. The strain at peak strength was 0.0023 inch/inch. The same ultimate strain of 0.004 inch/inch was considered (Figure 8.9a). The tensile strength was determined to be 0.63 ksi. The properties of the confined concrete were found through the section designer tool in SAP2000 and checked theoretically (Appendix B) and led to a f'_{cc} of 7.28 ksi, ε_{cc} of 0.0027 inch/inch. and ε_{cu} of 0.023 inch/inch (Figure 8.9b). In this case not much strength is added by confining the concrete due to the lack confinement in

the vertical direction, since no intermediate hoops were used along the height of the beam (Figure 8.6).

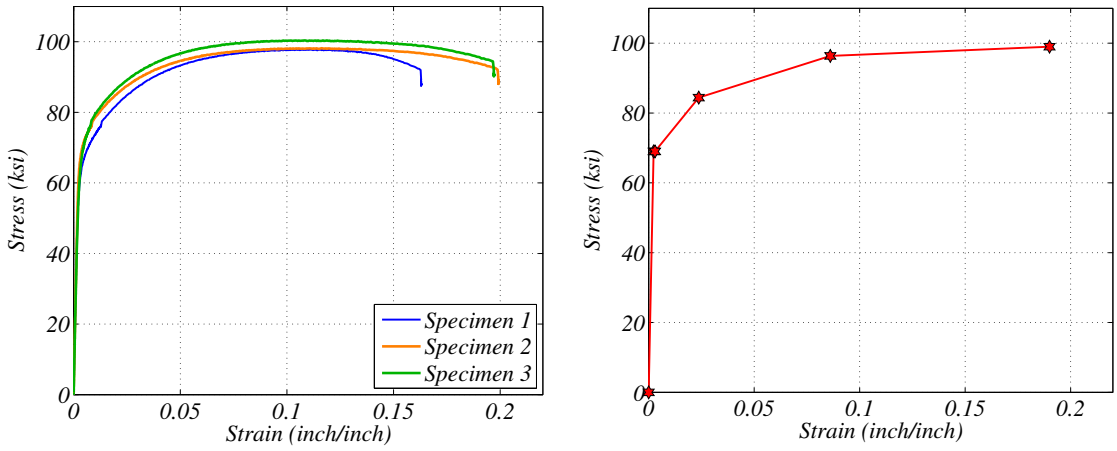

Figure 8.8. Grade 60 #4 bars used in the beams at the second and third floor: (a) results from tension tests and (b) Park model used on SAP2000

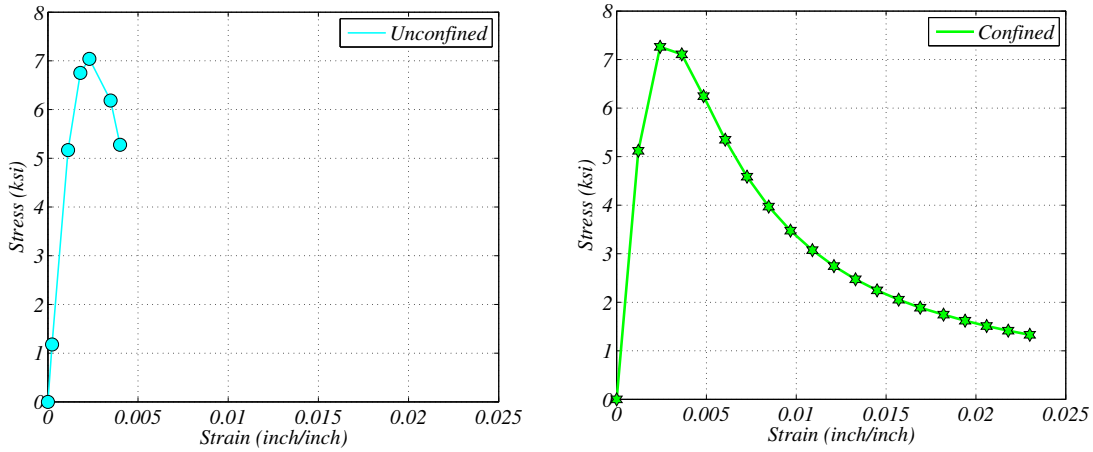

Figure 8.9 Model of the concrete in compression used in the beam at the second floor: (a) unconfined, (b) confined

Plastic Hinge Properties: Moment Curvature and Hysteresis

The moment curvature behavior of the section was obtained from the section designer tool in SAP2000 considering a zero normal force and it is shown in Figure 8.10a. Relevant points are shown at the yielding of the steel, the onset of steel hardening, spalling of unconfined concrete and failure of the steel. The values of moments showed in Figure 8.10a were validated through theoretical calculations, as presented in Appendix B. The length of the plastic hinge with the same formula used previously as:

$$l_p = 0.08l + 0.15 d_b f_y = 33"$$ Eq. 8.3

With this length and the moment-curvature plots it was possible to find the moment-rotation curve characterizing the plastic hinge model, as presented in Figure 8.10b.

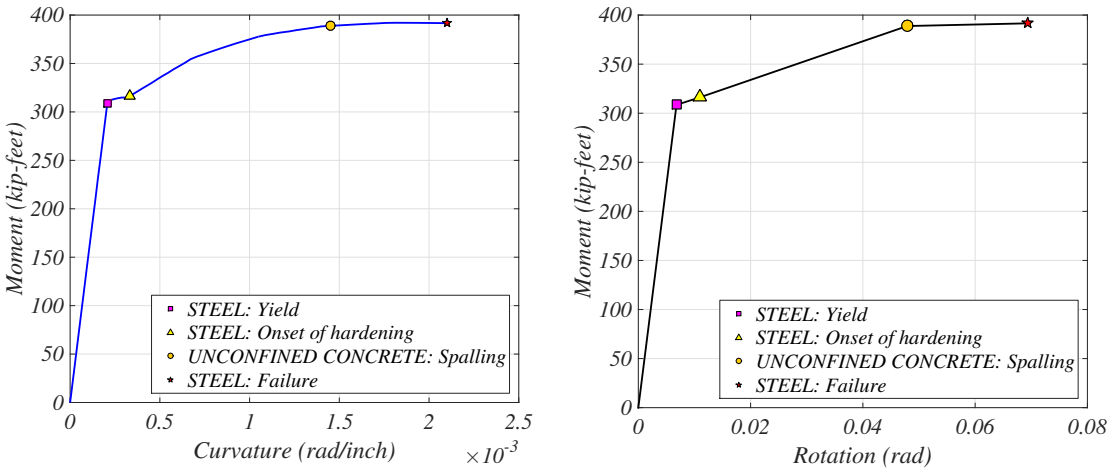

(a) **(b)**

Figure 8.10. Behavior of the hinge in the beam at the second floor: (a) moment curvature obtained from the section designer tool with relevant points and (b) simplified hinge behavior

The pivot hysteresis loop was selected. This model is similar to the Takeda one, but it allows the inclusion of strength degradation (Dowell et al. 1998). It is based on the observation that in reinforced concrete unloading and reloading is directed to specific points (called pivots) (CSI 2015). Five additional parameters need to be added when the pivot hysteresis is selected:

- α_1 indicated the pivot point for unloading from positive force;
- α_2 is the same as α_1 but for negative force;
- β_1 locates the pivot point for reverse loading from zero to positive force;
- β_2 is the same as β_1 but for negative force;
- η determined the amount of degradation of the elastic slope after plastic deformation and it in in between 0 and 10.

The hysteresis loop thus obtained is presented in Figure 8.11. The values of the first four parameters were calculated from the values of the axial load ratio and the longitudinal steel ratios thanks to the tables presented in Dowell et al. 1998 ($\alpha_1=\alpha_2=5.9$, $\beta_1=\beta_2=0.54$). The parameter η was set to 5, which is in between the extreme values of 0 and 10. This selection was made because of the lack of

more accurate information.

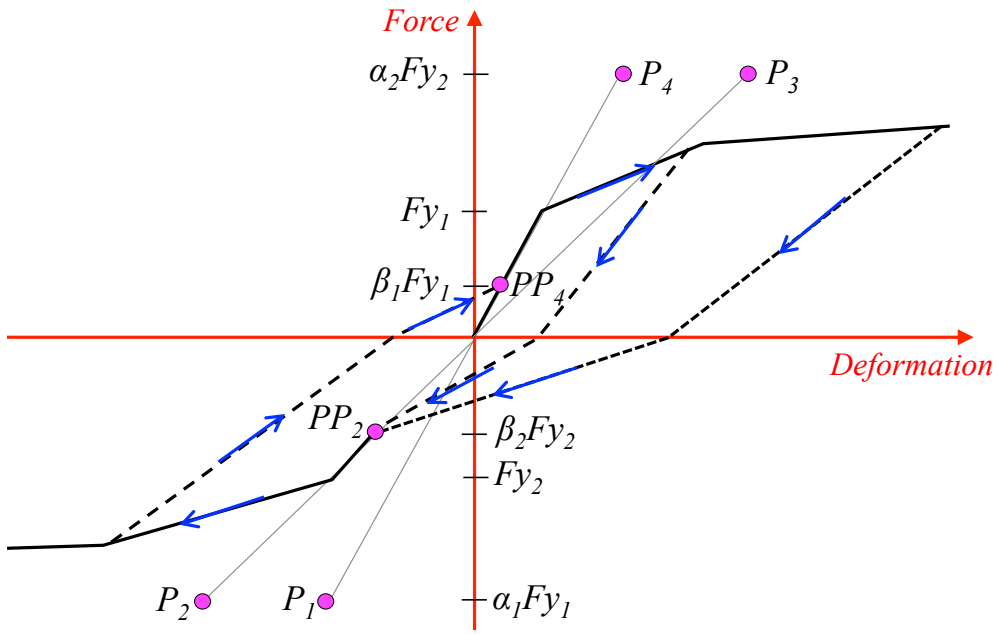

Figure 8.11. Pivot hysteresis model (reproduced from CSI 2015)

8.1.3 Plastic Hinges on Floor Four Beams

Figure 8.12a presents the geometry of the beams at this floor. A special type of beam characterized by a ductile connector (DDC) was used at this floor. In addition, the beam was post-tensioned with a force of 132 kips. The section was modeled in the section designer tool in SAP 2000 by using the DDC rods instead of the reinforcing bar in the section. It is noted that, while these sections were designed to have the same moment capacity as the ones in the previous floors, this changed during construction, since a different diameter of the rod had to be used.

Material Properties

The ductile connector was constructed with grade 60 steel. Tensile tests on this particular batch were not executed, but similar tests were performed by Chang et al. (2008), and they revealed the f_y of 60 ksi, f_u of 91 ksi, strain at the onset of hardening of 0.015 inch/inch and an average ultimate strain of 0.18 inch/inch. The transverse reinforcement was created with grade 60 #4 bars. The mill certificates of these bars showed values of 63 ksi for f_y and 93 ksi for f_u. As for the strain at the onset of hardening and final strain, the values of 0.003 and 0.19 inch/inch used for the similar #4 batch at the lower level beams was used. The Park model of stress-strain for both transverse and longitudinal displacement of the

reinforcing bars is shown in Figure 8.12b. The type of concrete used at this floor as similar properties of those used at floor two and three. The stress-strain behavior of the confined concrete was obtained from the section designer tool and compared to theoretical calculations (Appendix B), and it is shown in Figure 8.13.

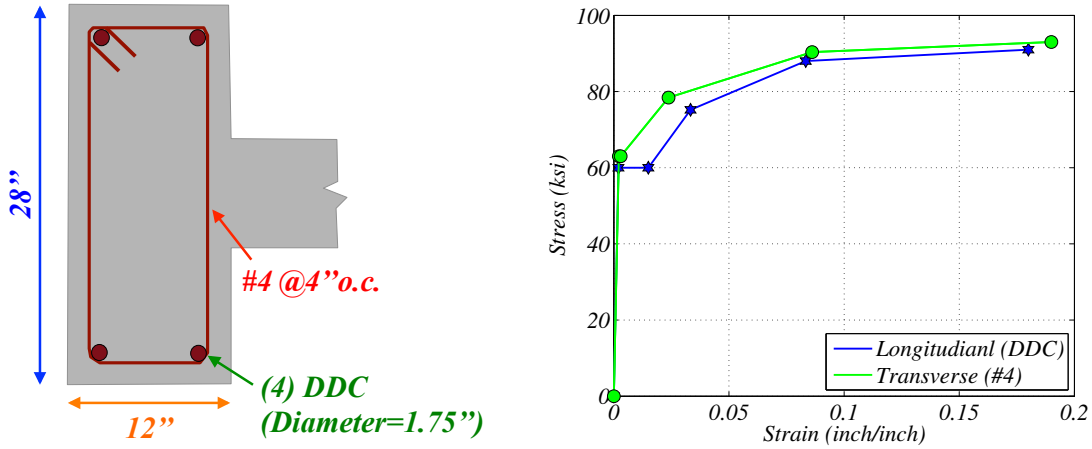

Figure 8.12. Beam installed at the fourth floor: (a) geometry and (b) model of longitudinal and transverse steel

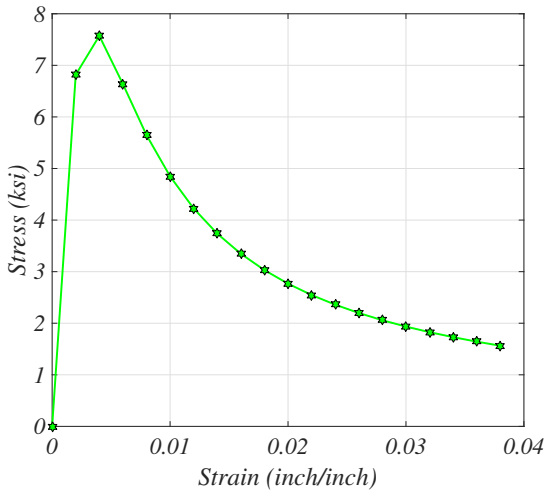

Figure 8.13. Model of confined concrete for the beam at the fourth floor

Plastic Hinge Properties: Moment Curvature and Hysteresis

The moment curvature was created with the section designer tool in SAP2000 for a section with normal force applied equal to the post-tensioning. The moment curvature resulting from this analysis is shown in Figure 8.14a. The flat section at around 0.0013 inch/inch curvature corresponds to

the lost in strength of confined concrete after its peak strength is reached. The length of the plastic hinge was calculated to be 32'' using the same formula as in the previous sections. This length allowed determining the characteristic moment-rotation curve for the beam at this floor (Figure 8.14b). The parameters attributed to the pivot hysteresis were found as explained previously and were $\alpha_1=\alpha_2=7.5$, $\beta_1=\beta_2=0.64$ and $\eta=5$.

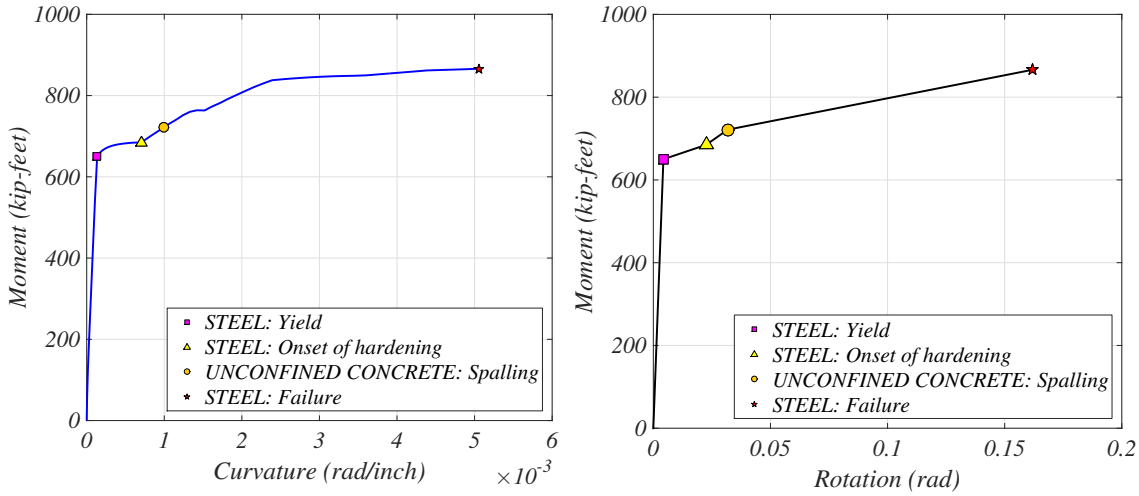

Figure 8.14. Behavior of the hinge in the beam at the fourth floor: (a) moment curvature obtained from the section designer tool with relevant points and (b) moment-rotation curvature attributed to the hinge

8.1.4 Plastic Hinges on Fifth Four Beams

Beams at this floor had the same geometry of the beam at the fourth floor, with the difference that this beam was not post-tensioned.

Material Properties

The properties of the steel at this section was the same as the one seen at the fourth floor. As for the concrete, the f'_c of the unconfined concrete at this floor was 8.17 ksi, and its ultimate strain was assumed to be at 0.004 inch/inch. For the confined concrete f'_{cc} was 8.7 ksi, number that was calculated first through the section designer tool in SAP 2000, and then confirmed with theoretical calculations presented in Appendix B. The ultimate strain was found at 0.034 inch/inch. The final stress-strain curves for both the unconfined and confined concrete result similar to those presented in the previous sections.

Plastic Hinge Properties: Moment Curvature and Hysteresis

The moment curvature found with the section designer tool in SAP2000 is shown in Figure 8.15a. This curve was obtained considering zero normal force, since the beam at this floor was not post-tensioned. Since the value of the normal force were small, the moment capacity in this case is also smaller. The length of the plastic hinge is the same as determined for the beam at the fourth floor. in Figure 8.15b presents the moment-rotation curve attributed to the section. The parameters attributed to the pivot hysteresis were determined as explained in the sections above, as $\alpha_1=\alpha_2=7.8$, $\beta_1=\beta_2=0.72$ and $\eta=5$.

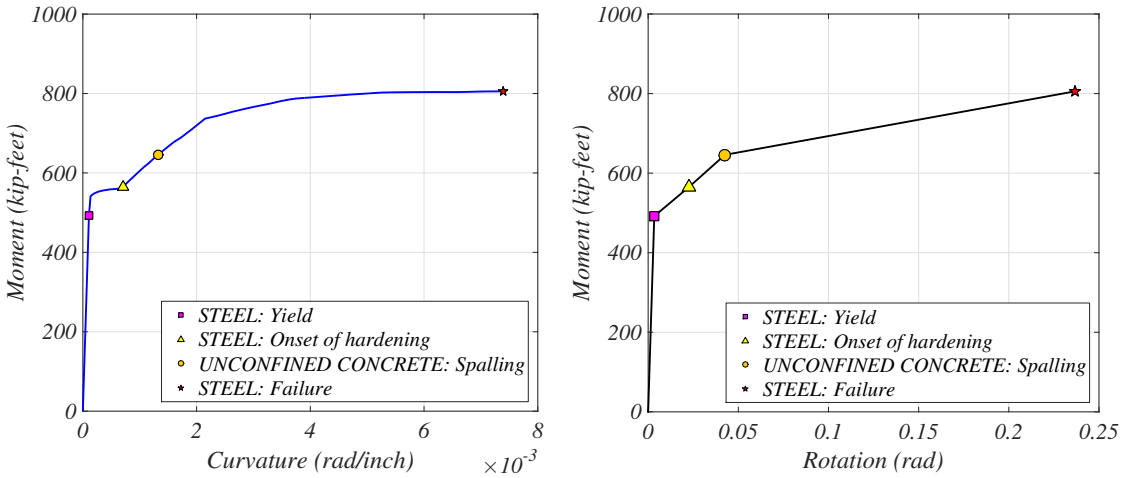

Figure 8.15. Behavior of the hinge in the beam at the fifth floor: (a) moment curvature obtained from the section designer tool with relevant points and (b) simplified hinge behavior

8.1.5 Beams at the Roof

The beam at the roof was a commonly used beam, characterized by four #7 longitudinal bars top and bottom and two sets of rectangular hoops. Its geometry is presented in Figure 8.16.

Material Properties

The properties of the longitudinal steel were available from mill certificates, and indicated a f_y of 73 ksi and f_u of 97 ksi. The stress-strain data were not available, and for this reason the results from a #6 bar of the same type of steel provided by the same manufacturer was used to provide information of the strain. This indicated a strain at the onset of hardening of 0.007 inch/inch and ultimate strain of 0.15 inch/inch. Stress-strain data was also not available for the transverse reinforcement, but mill certificates

indicated a f_y of 66 and f_u of 100 ksi. These results were very similar to the #4 bars used at floors two and three, and for this reason the same model was used. The properties of the unconfined concrete at this floor were at same as those at the fifth floor. The properties of the confined concrete were obtained considering the reinforcement of this section, and have a f'_{cc} of 8.8 ksi, a ε_{cc} of 0.0028 inch/inch and an ε_{cu} of 0.053 inch/inch.

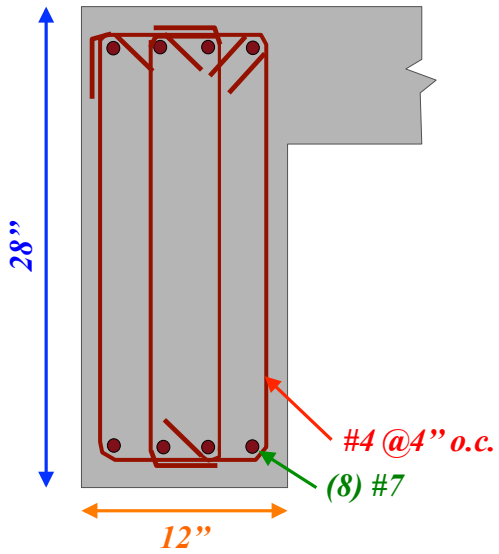

Figure 8.16. Geometry of the beams at the roof

Plastic Hinge Properties: Moment Curvature and Hysteresis

Figure 8.17a presents the moment curvature obtained for this section from the section designer tool in SAP2000. The length of the plastic hinge was 26''. Through the moment curvature plot and the plastic hinge length it is possible to find the moment-rotation curve assigned to the hinge in the building model (Figure 8.17b). The parameters attributed to the pivot hysteresis were $\alpha_1=\alpha_2=6.5$, $\beta_1=\beta_2=0.64$ and $\eta=5$, found as explained previously. The moment capacity was similar to that of the lower floors, as intended by design. Table 8.2,Table 8.3 and Table 8.4 present a summary of the properties of longitudinal steel, transverse steel and concrete for all the sections considered.

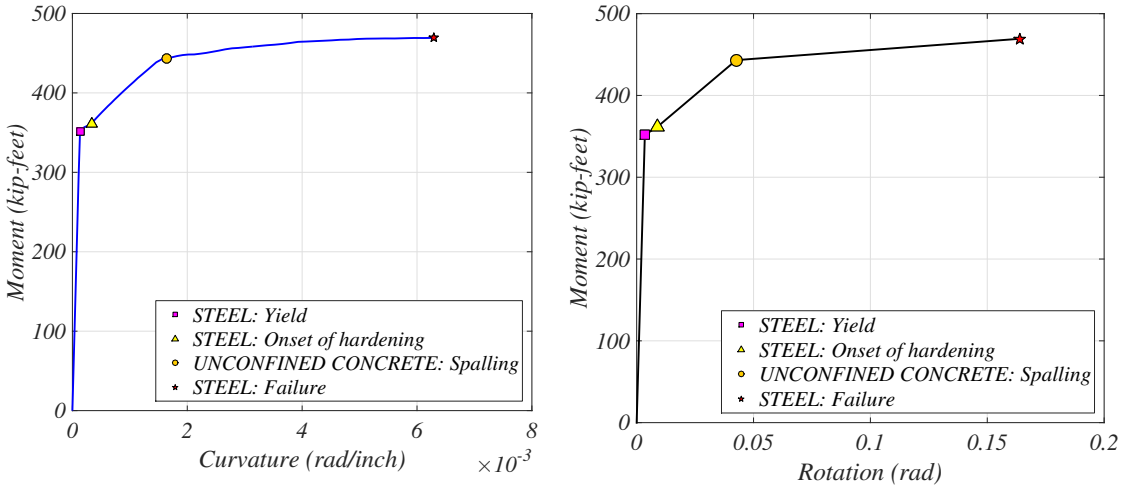

(a) **(b)**

Figure 8.17. Behavior of the hinge in the beam at the roof: (a) moment curvature obtained from the section designer tool with relevant points and (b) moment-rotation behavior attributed to the hinge

Table 8.2. Summary of the properties of longitudinal reinforcement (results from laboratory tests and can be found in Chen et al. 2013a and b)

Element	Bar diameter (size)	Stress			Strain		
		f_y (ksi)	f_u (ksi)	Source	ε_{oh} (inch/inch)	ε_u (inch/inch)	Source
Columns	1.128 (#9)	69	119	Laboratory Tests	0.01	0.12	Similar batch (#9)
Columns	0.75 (#6)	84	118	Mill Certificate	0.0035	0.105	Nielsen et al. 2004
Beams-floors 2 and 3	0.875 (#7)	128	159	Laboratory tests	0.0071	0.05	Laboratory tests
Beams - floor 4 and 5	1.75 (DDC)	60	91	Chang et al. 2008	0.015	0.18	Chang et al. 2008
Beams - Roof	0.875 (#7)	73	97	Mill Certificate	0.007	0.15	Similar batch (#6)

Table 8.3. Summary of the properties of transverse reinforcement

Element	d_b (inch)	Stress			Strain		
		f_y (ksi)	f_u (ksi)	Source	ε_{oh} (inch/inch)	ε_u (inch/inch)	Source
Column	0.5	81	91	Laboratory tests	0.0025	0.056	Laboratory tests
Beams-floor 2 and 3	0.5 (#4)	69	99	Laboratory tests	0.003	0.19	Laboratory tests
Beams-floor 4	0.5 (#4)	63	93	Mill Certificate	0.003	0.19	Similar batch
Beams-floor 5	0.5 (#4)	66	100	Mill Certificate	0.003	0.19	Similar batch
Beams-roof	0.5 (#4)	66	100	Mill certificate	0.003	0.19	Similar batch

Table 8.4. Summary of properties of concrete (unconfined and confined)

Element	Unconfined				Confined		
	f'c (ksi)	ε_c (inch/inch)	ε_{cu} (inch/inch)	E_c (ksi)	f'_{cc} (ksi)	ε_{cc} (inch/inch)	ε_{ccu} (inch/inch)
Column-first floor	7.91	0.0023	0.004	5357	10.8	0.0067	0.0106
Beam-Floor 2	7.04	0.0023	0.004	5128	7.28	0.0027	0.023
Beam-Floor 3	7.04	0.0023	0.004	5128	7.26	0.0027	0.023
Beam-Floor 4	7.04	0.0023	0.004	5128	7.58	0.004	0.038
Beam – Floor 5	8.17	0.0023	0.004	5423	8.77	0.0036	0.034
Beam - Roof	8.17	0.0023	0.004	5423	8.79	0.0028	0.053

8.2 Pushover Analysis

The first analysis conducted with the nonlinear model was a pushover analysis, which is a common tool for the seismic performance evaluation of buildings. Pushover analysis is a nonlinear static analysis in which the building is pushed sideways until it reaches a failure point. The deformed shape at which the structure is pushed, or "load pattern" is intended to represent the distribution of inertia forces during an earthquake, and it is generally that of the predominant mode of vibration of the building. However, using the first mode can be an unreasonable for structures whose motion is largely affected by higher modes, such as high-rise buildings, while it is considered reasonable for low rise structures (two to five stories). Because of the height of the BNCS building, the pushover analysis is thought to be able to provide a reasonable assumption, at least up to test FB5. It is noted that during test FB6, the results showed a very large influence of higher modes. The following parameters were used in the pushover analysis on SAP 2000:

- The initial load at step zero of the analysis was considered the one given by the deal loads. It is noted that these are relatively small compared to those obtained by the pushover analysis, since this is a relatively light building;
- The load pattern applied followed the shape of the first lateral mode in the longitudinal direction;
- Only P-Delta were considered as geometric non-linearities;
- The load was applied in displacement controlled in the longitudinal direction of the building. The displacements checked where the conjugate ones. The SAP2000 manual specifies that using the conjugate displacement in particularly important when the displacement of the joint whose displacement is controlled is affected by non-linearlities. The conjugate displacement is the weighted average of the displacement of all the joints, where the weight used is the load on that node. When hinges start yielding, thus changing the deformation pattern, the conjugate displacement adjusts and find a monotonically increasing displacement component to control. In this case, the conjugate displacement is used to determine whether the load should be increased or decreased. The node whose displacement was controlled was the node at the

center of the roof, and the maximum displacement applied was 50'' (total drift ratio at the roof=6%). It is noted that this node is always used to determine how far the structure should move, even if the displacement used for the control is the conjugate one;

- Save at multiple states (save positive increments only);
- Nonlinear solution control: default values were used. These parameters were initially changed to check the stability of the solution, and the brought back to their initial value.

8.2.1 Pushover Curve

The pushover curves for the building in the westward and eastward directions are presented in Figure 8.18. First of all, it can be noted that these curves are quite symmetrical, which is expected in this case, since the frame supporting the horizontal loads is symmetric. It is noted that there are asymmetries in the floor of the building (location of the walls, elevator and stair opening) but these are less influential in this case. The behavior of the building is linear till a total drift or roughly 0.5%, while it starts to exhibit larger nonlinearities at a drift around 1%.

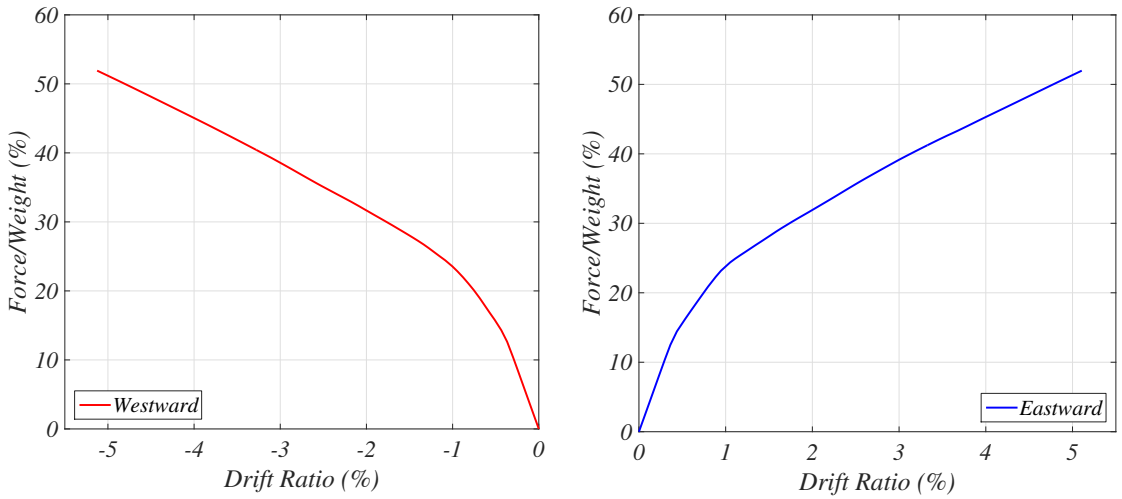

Figure 8.18. Pushover curves in the (a) westward and (b) eastward directions

The curves in both directions are very steep compared to what one might expect. This behavior is attributed to the fact that many elements in the building remain elastic, thus controlling the post yield stiffness of the structure. To understand which of the linear elastic elements control the post yield stiffness of the building, the stiffness of each of the linear elastic elements was reduced selectively to

30% of their initial values. The results are presented in Figure 8.19. When the stiffness of beams and columns is reduced, the initial stiffness varies, however the final stiffness does not change considerably. When the stiffness of the wall is reduced, the pushover curve does not change considerably, confirming that the walls do not have a lot of effect on the behavior. The element controlling the post-yield stiffness of the curve is clearly the slab. This is due to the fact that the slab is connected to the beams, thus it can limit their deformation. While this clearly a limitation of this model, it was decided not to change the stiffness of the slab and to keep it that same as suggested by the code values.

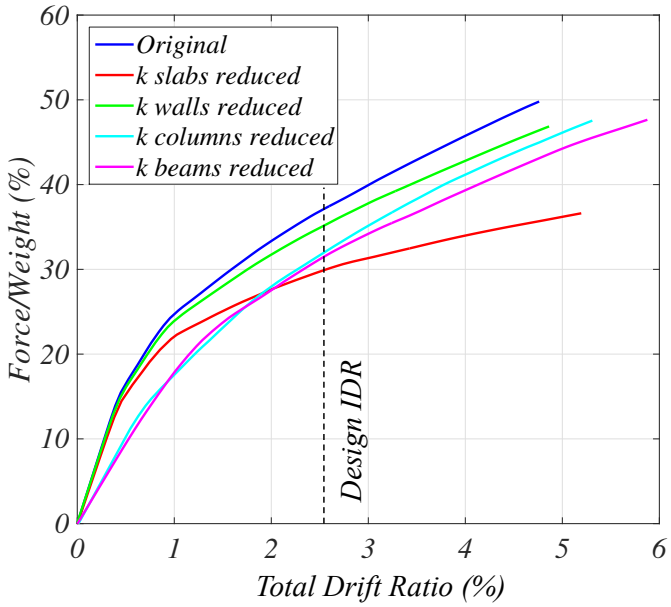

Figure 8.19. Pushover curved obtained by reducing selectively the stiffness of the linear elastic elements

8.2.2 Effect of P-Delta

Figure 8. 20 presents a comparison of the pushover curves in the eastward direction with and without the inclusion of P-Delta effects. For this building, considering the P-Delta effects does not have a large influence in the results. In fact, they reduce the maximum force from 57% to 50% of the weight and they reduce the maximum drift from 5.1% to 4.7% (this is due to the fact that the analysis stop at the first failure of a plastic hinge). The reason for the small influence of the P-Delta can be attributed to the fact that this building was relatively light.

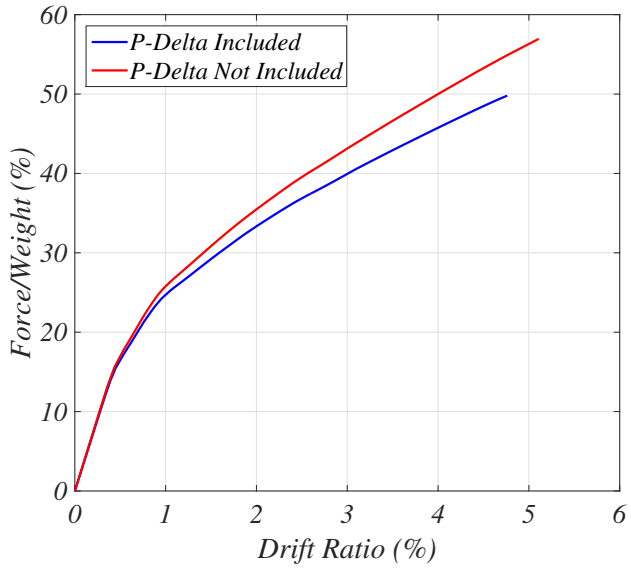

Figure 8. 20. Comparison of the pushover curve in the eastward direction with and without P-Delta effects

8.2.3 Behavior of Hinges in the Columns at the First Floor

Figure 8.21 presents the P-M behavior of the three columns in the southern frame during westward pushover. Before the start of the pushover, the three columns carry similar loads, with the column in the central portion of the building being larger. The load in the south-west (SW) column is beginning of the pushover, the load in south-east (SE) column decreases, that in the south central (SC) column increases, and the load in the western column increases only slightly. This is due to the fact that the SW column is not part of the main frame, and connected to it only by the thin slab. After yield is reached in the columns, each of them tends to lose moment carrying capacity temporarily. After this, the tension in the eastern column increases drastically, and it approaches the ultimate surface at a moment of ~300 kips-inch. The normal force in the western column increases after yielding, probably to help the SC column supporting the load, since this column yields as well. The final moments in the SW and SC columns are around 800 and 1000 kips-inch, respectively. Failure is reached first by the column with most compression.

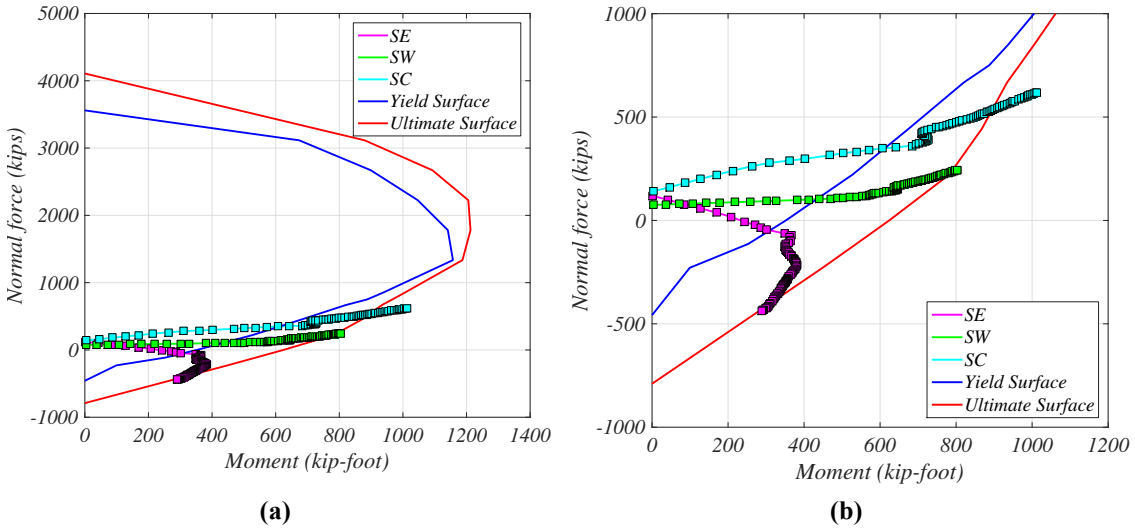

Figure 8.21. P-M behavior of hinges in the columns of the southern frame for pushover in the westward direction (data point represent the points found by the analysis in SAP2000)

Very similar trends are observed for the northern frame (Figure 8.22). However, in this case the force in the western column exceeds that in the central columns. The difference between the southern and northern fame is due to the presence of the walls on this side of the building on the north edge. In fact, thanks to the stiffening effect of the walls, the slab in this case is able to transmit more force to the western column. On the southern side of the building this is not possible, since the slab is very flexible and it deforms, thus reducing the transmission of forces.

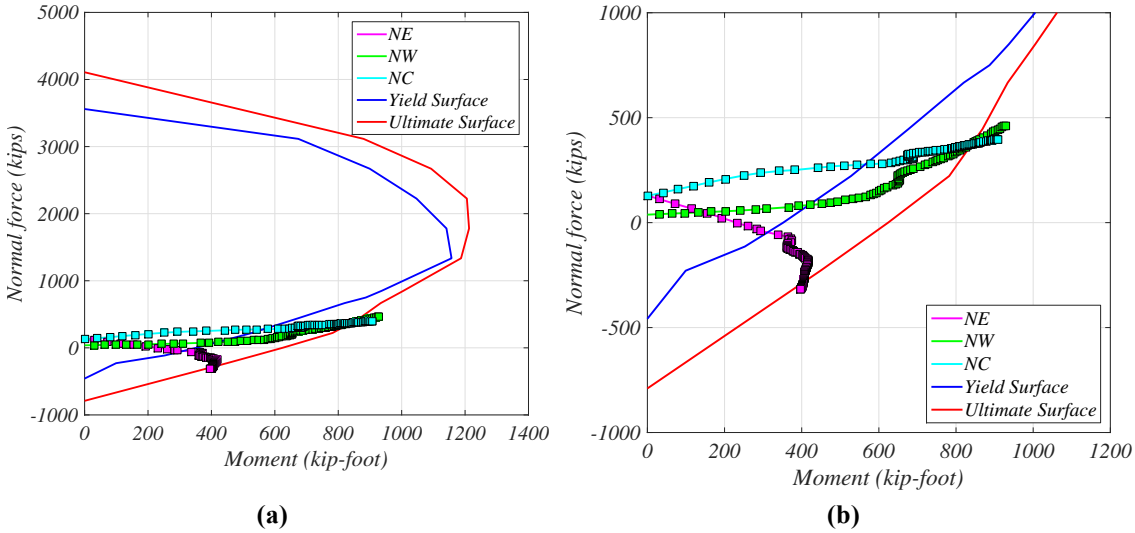

Figure 8.22. P-M behavior of hinges in the columns of the northern frame for pushover in the westward direction

Figure 8.23 and Figure 8.24 present the same results for the pushover in the eastward direction. Results are similar, except for the fact that in this case the eastern column is in compression and the central one is in tension. As noted for the southern frame in the pushover in the westward direction, the contribution of the western column remains minimal, due to the flexibility of the slab. Very interesting results are presented in Figure 8.24, which shows the results for the eastward pushover in the northern frame. In fact, in this case there is an increment in compression force in the eastern column, as expected, while both the central and western column support only a small amount of forces at large displacements. This is due again to the influence of the walls, which in this case end up absorbing part of the tension required to support the overturning moment. Failure is reached first of all by the column with the maximum compression as observed for the pushover in the westward direction.

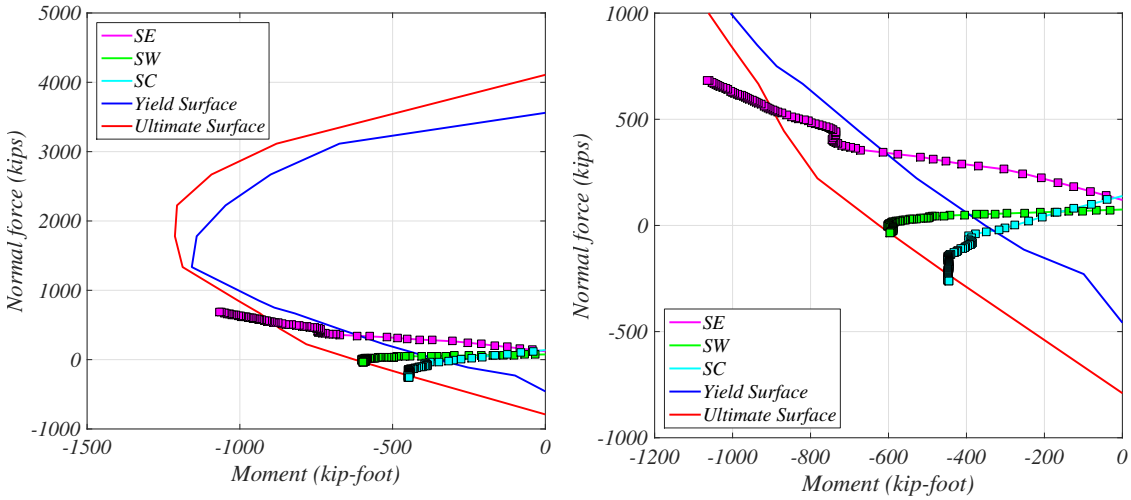

Figure 8.23. P-M behavior of hinges in the columns of the southern frame for pushover in the eastward direction

Results from this analysis can be summarized in the following points:

- In the southern frame, most of the normal force during motion is absorbed by the eastern and central column, while the western column does not contribute significantly due to the presence of the thin and flexible slab connecting it to the main frame. Small contribution is provided only at large displacements, during which this column follows the behavior of the central column;

- In the northern frame the presence of the walls changes the pattern of behavior seen in the southern frame in two main ways. First, they stiffen the slab thus helping carrying part of the force in the western column. In addition, they carry part of the normal force created by the overturning moment;
- The first column failing is the one with the maximum compression.

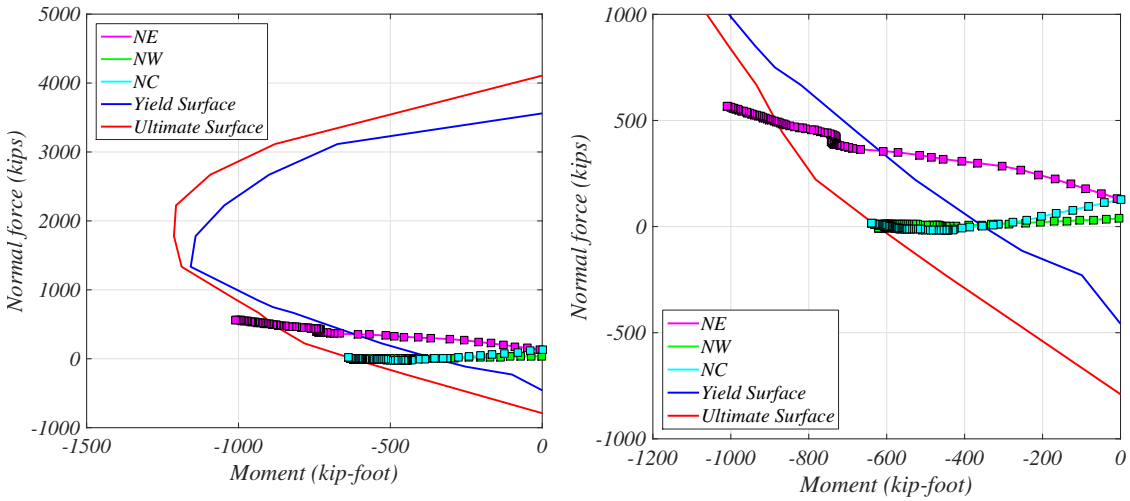

Figure 8.24. P-M behavior of hinges in the columns of the northern frame for pushover in the eastward direction

8.2.4 Behavior of Hinges in the Beams

Figure 8.25 presents the moment-plastic rotation of the hinges in the western edge of the beams in the southern frame obtained during the pushover in the eastward direction. This plot shows that the beams at floors two and three reach a similar level of rotation, and are the ones closer to failure. These results are consistent with the observed damage, since failure was reached first of all in the beams at the two lower floors. The PIDR at the first level for the failure point is at around 7.2% in both directions, which is larger than the PIDR of FB6, during which failure of many of the bar at the first two floors was observed. According to the model, the beam at the fourth floor barely reach concrete spalling, while for the one at the fifth floor the onset of steel hardening was not achieved. For the beams at the roof yielding of the steel is reached close to the failure point of the building. Results are similar for the pushover in the other direction.

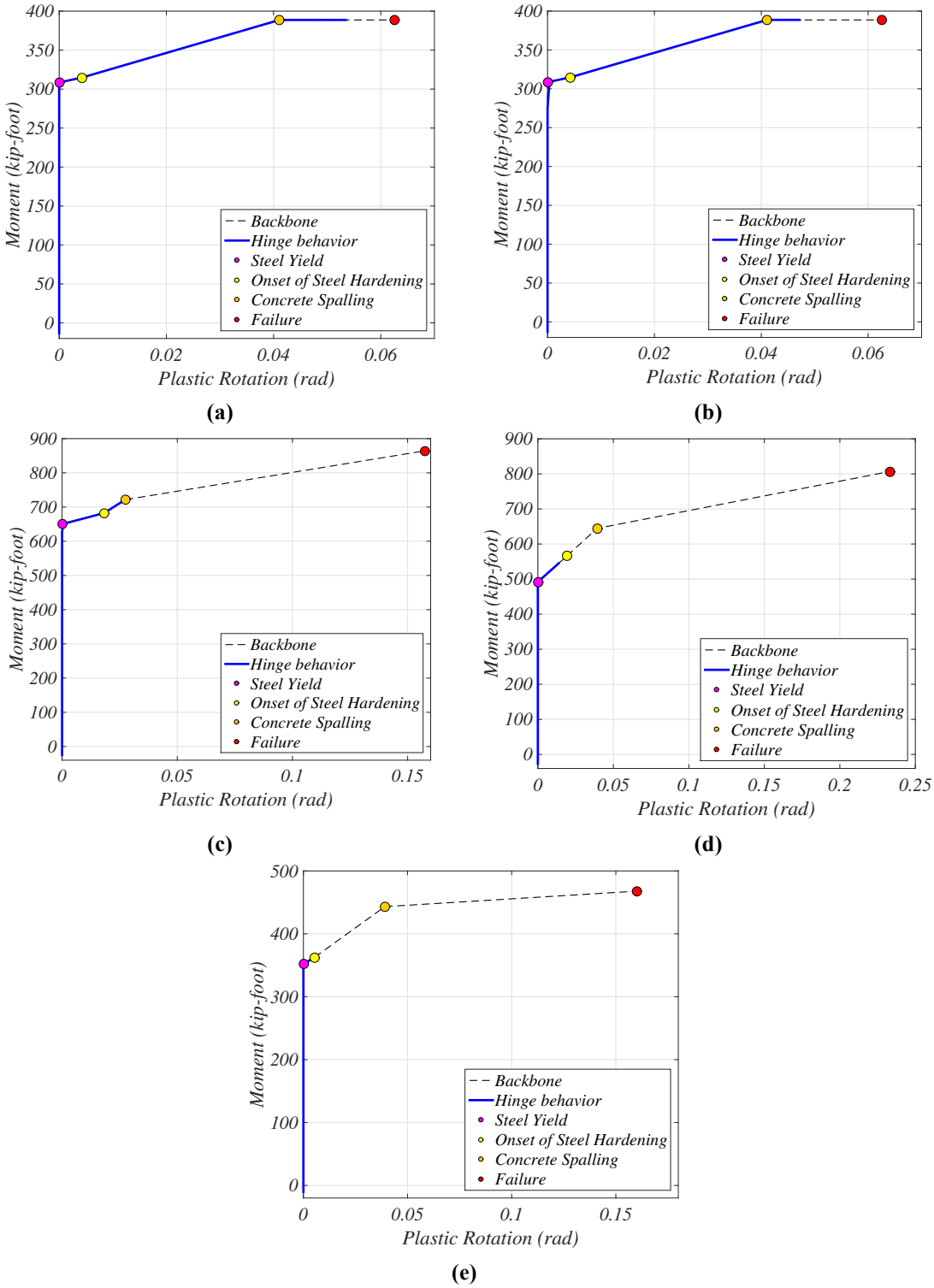

Figure 8.25. Behavior of the plastic hinges during the pushover in the eastward direction (the location selected in the western end of the southern frame)

8.2.5 Interstory Drift Ratios

The peak interstory drift ratios (PIDRs) obtained experimentally during the fixed-based motions were compared to the PIDRs obtained during the pushover analysis in the two directions, and are shown in Figure 8.26. The numerical PIDs shown in the plots are the ones providing the same global drift as the experimental one in the earthquake specified. The results for test FB1 are not presented since they are very similar to those for test FB2. The plot shows that the comparison up to FB4 is very good, in fact the model can capture the general shape of the building, with larger drifts at the second level, similar drifts at the first and third stories, and lower drifts at the upper levels. For these motions, the model tends to under predict the drifts at the two lower levels and overpredict that of the upper stories. One of the possible reasons is that the lower floors might have been softened already in the experiment during the previous series of earthquakes. Another plausible reason is the presence of the cladding panels at the two upper levels. In fact, these might have stiffened the upper levels, thus reducing their relative influence of the upper stories on the global drift.

In case of test FB5, the experimental and numerical results are still very close for drifts in the westward direction, in which the error is minimal. However, errors are larger for drifts in the eastward direction. Probably, this is due to some type of nonlinearity in the experiment that the model cannot capture.

Results for FB6 are not very consistent, except for the lower stories in the westward direction. In general, during FB6 the model over predicts the drifts at the uppers stories and under predicts those at the lower stories. Reasons for this include the fact that the model does not predict the fracture of the reinforcing bar in the beams at the lower stories and does not include the stiffening effects of cladding at the upper levels. This comparison allows to conclude that the model provides reasonable results up to PIDR of 2.3%. After this level, errors in the prediction might be expected.

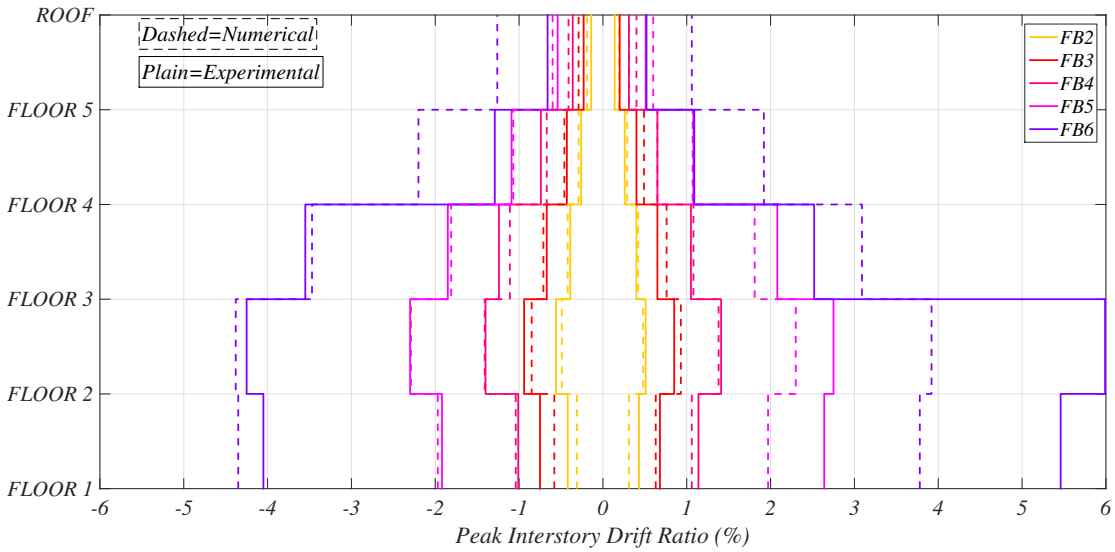

Figure 8.26. Comparison of experimental and numerical PIDR obtained during the pushover analysis for similar levels of roof drift

8.3 Nonlinear Dynamic Analysis – Validation of the Results

FB5 was run in the model to obtain the optimal value of damping and validate the results of the numerical model. This motion was selected because it can be considered the design level event. As done in the previous chapter, the models including panel 5ES and 4ES were run separately. It is noted that the stiffness assigned to the springs in the SDOF had to be changed to achieve the experimental natural frequencies, since the stiffness of the slab and beam supporting the SDOF was changed. In this case the value of stiffness attributed to the springs to obtained a natural frequency of 7.9 Hz for the panel on the fifth level and 9.1 Hz for the panel of the fourth floor was 83 kips/inch and 82 kips/inch, respectively.

8.3.1 Parameters for the Numerical Analysis

The analysis in SAP2000 was run as a nonlinear time history analysis solved with direct integration. The initial conditions were those created by the dead load of the structure. In terms of geometric nonlinearities, only P-Delta effects were considered. The solution method used was the Newmark method with the parameters gamma equal to 0.5 and beta equal to 0.25. The following nonlinear parameters were found to provide the best results:

- Maximum substep size: 0.004 seconds. It is noted that SAP 2000 reduces automatically the step size when needed in the analysis;
- Minimum substep size: 0 seconds;
- Maximum constant stiffness iterations per step: 100;
- Maximum Newton-Raphson iterations per step: 100;
- Iteration convergence tolerance (relative): 0.0001. This value provided stable results while still keeping the time of the analysis reasonable;
- Event lumping tolerance (relative): 0.01;
- Max line searches per iteration: 100;
- Line search acceptance tolerance (relative): 0.02;
- Line-search step factor: 1.618.

8.3.2 Optimal Damping

This analysis mainly consisted in determining the optimal values of damping. In SAP2000, only Rayleigh damping can be used, and four parameters can be set: two frequencies and the damping ratio to attribute to those frequencies. For the scope of this analysis, it was considered of interest to control the damping at three locations: the first mode of the building, the second mode of the building (since the model tended to over predict its influence), and the main mode of the panels. However, it was not possible to control the three of them directly, since the damping can be specified at only two frequencies. For this reason, it was decided to run the analysis with many different combination of damping ratios at different frequencies and the select the damping ratio minimizing the error in prediction of accelerations of the panel, its supporting floors, and the component amplification factors. Two separate validations had to be performed for the panels at the fifth and fourth levels, since they had different natural frequencies and thus the level of optimal damping was different.

Building Model with Panel 5ES

The selection of the damping parameters was controlled by the following considerations:

1. The model tends to underestimate the effect of the first mode of the building, thus the damping around the frequency of the first mode has to be kept low;

2. The model tends to overestimate the effect of the second lateral mode of the building, thus the damping at that frequency needs to be as large as possible;
3. If the damping at the frequency of the panel is too large, the natural mode of the panel cannot be activated, and the results for the panel acceleration are lower than the experimental ones.

Clearly, the second and third factors are contrasting and difficult to combine, since having a large damping in the second mode of the building increased also the damping at the panel mode.

The minimum errors in the prediction of accelerations for this model was found for the following values of damping:

- 1% at a frequency of 0.1 Hz;
- 3% at a frequency of 5 Hz.

The results plot of the damping at all frequencies is presented in Figure 8.27. The values of natural frequencies shown in this plot is the one obtained with Ritz vector analysis on the model, which does not take nonlinearities into account. The values of damping at the first and second later modes of the building and panel mode are 0.6%, 1.8% and 4.7%, respectively. A value of 4% damping at the frequency of the panel mode was optimal also for the linear model on the system (Chapter 7).

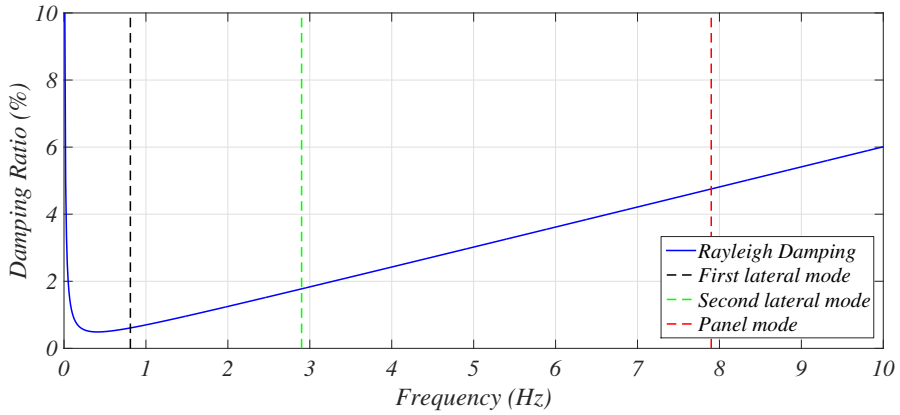

Figure 8.27. Optimal Rayleigh damping for the model with panel 5ES

Building Model with Panel 4ES

The same considerations made for the model with panel 5ES can be extended to the model including panel 4ES. However, in this case the optimal damping was achieved by imposing 1% damping at 0.1 Hz and 3% damping at 4 Hz (Figure 8.28). With these values of damping the

parameters, the damping at the first and second building modes and main panel modes were 0.7%, 2.2% and 6.8%, respectively. The larger optimal damping at the frequency of the panel for panel 4ES can be due to multiple reasons. First of all, the two panels had different boundary conditions. In fact, panel 5ES was free on the top while panel 4ES was caulked at all sides. Panel 5ES was also taller, thus allowing more movement at its top. Another reason for the lower damping needed for panel 5ES might also be that the excitation coming from the roof to panel 5ES was much larger than the excitation to panel 4ES from both the fifth and fourth floors. This could have resulted in a lower apparent value of the damping for panel 5ES.

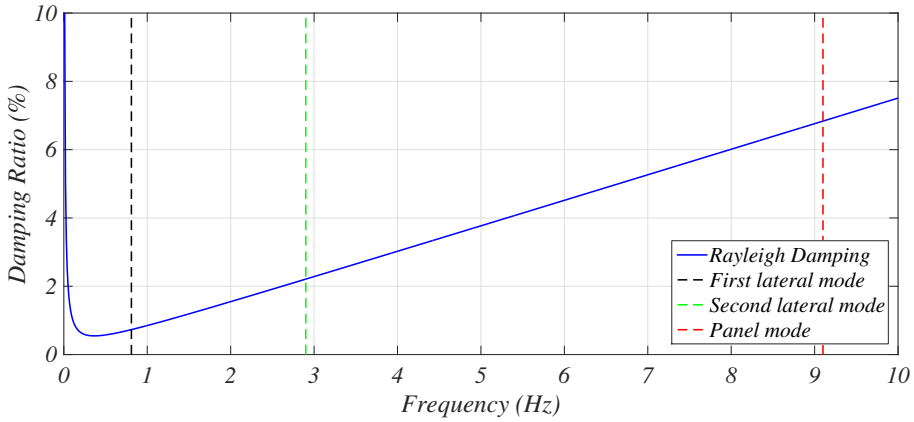

Figure 8.28. Optimal Rayleigh damping for the model with panel 4ES

8.3.3 Time History of Floor and Panel Accelerations

Building Model with Panel 5ES

Figure 8.29 and Figure 8.30 show the comparison between numerical and experimental accelerations in the roof and fifth floor for FB5. The experimental and numerical time histories generally compare well with each other. However, the model is not capable of catching some of the peaks in acceleration, such as those at around second 55. The comparison of the pseudo spectral accelerations for both floors show that the natural periods of the main modes of the building are very similar in the experimental and numerical case. However, the values of the pseudo accelerations at those periods are different. In fact, the model tends to under predict the influence of the first mode, while it over predicts the effect of higher modes, especially at the roof. It is noted that for both floors there is a very good agreement of the results at a period around 0.11-1.12 seconds, which is the natural

frequency of the panels.

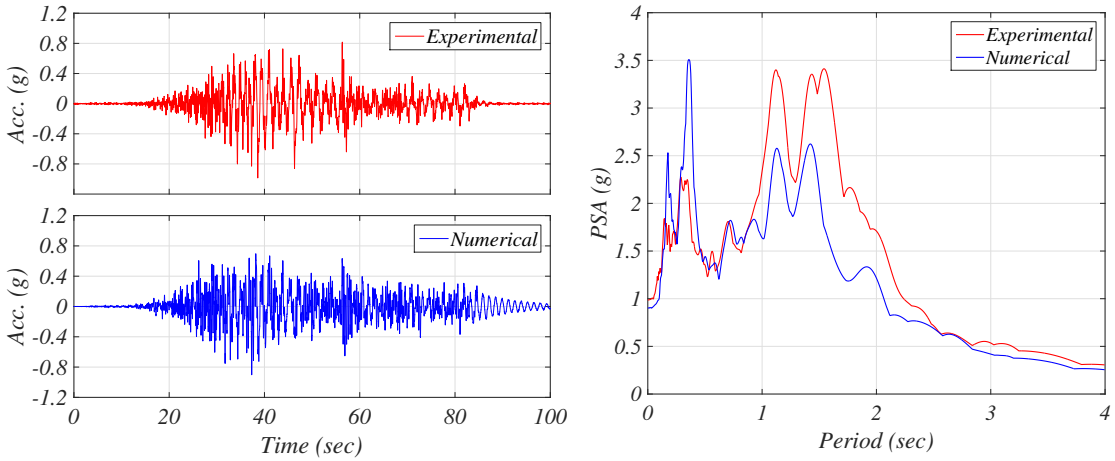

(a) **(b)**

Figure 8.29. Numerical and experimental accelerations at the roof for FB5: (a) time history and (b) pseudo acceleration spectra

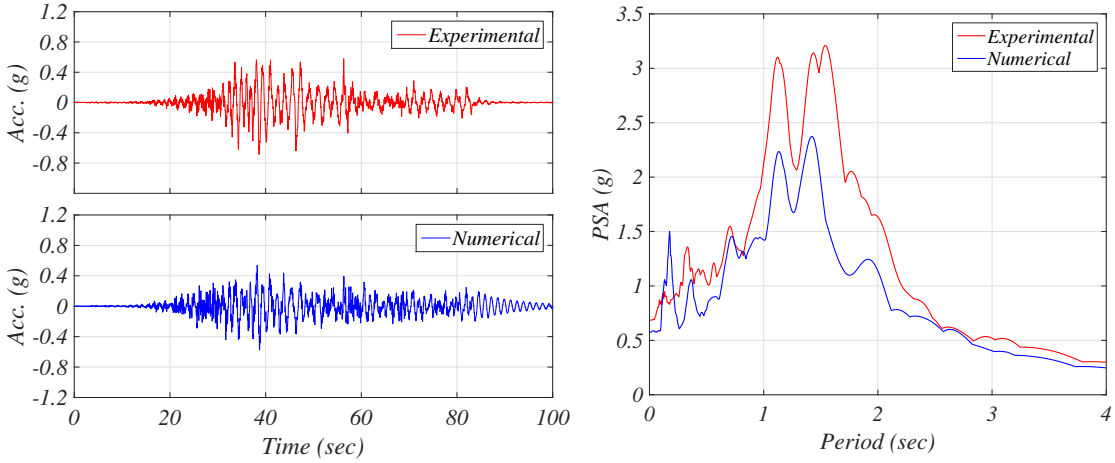

(a) **(b)**

Figure 8.30. Numerical and experimental accelerations at the fifth floor for FB5: (a) time history and (b) pseudo acceleration spectra

Figure 8.31 and Figure 8.32 present the comparison of the experimental and numerical values of the total drifts at the roof and fifth floor. Results in term of drifts present larger errors, with the model under predicting their values. This is expected since the mode under predicts low frequencies, which dominate the displacement response. This same patter of error can be seen both form the time histories and displacement spectrum. Even if drift errors are relatively large, this is not considered relevant for the scope of this study, which focuses on accelerations.

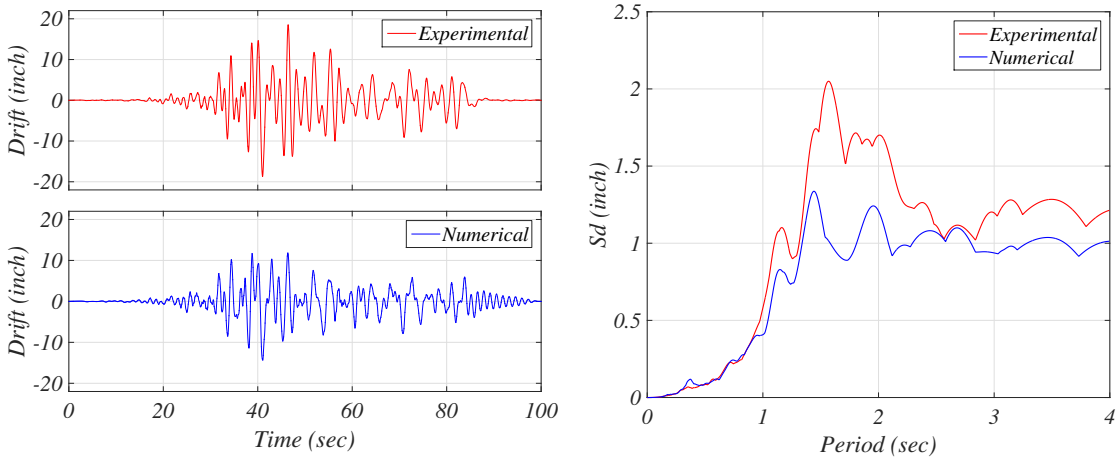

Figure 8.31. Numerical and experimental displacement at the roof for FB5: (a) time history and (b) displacement spectrum

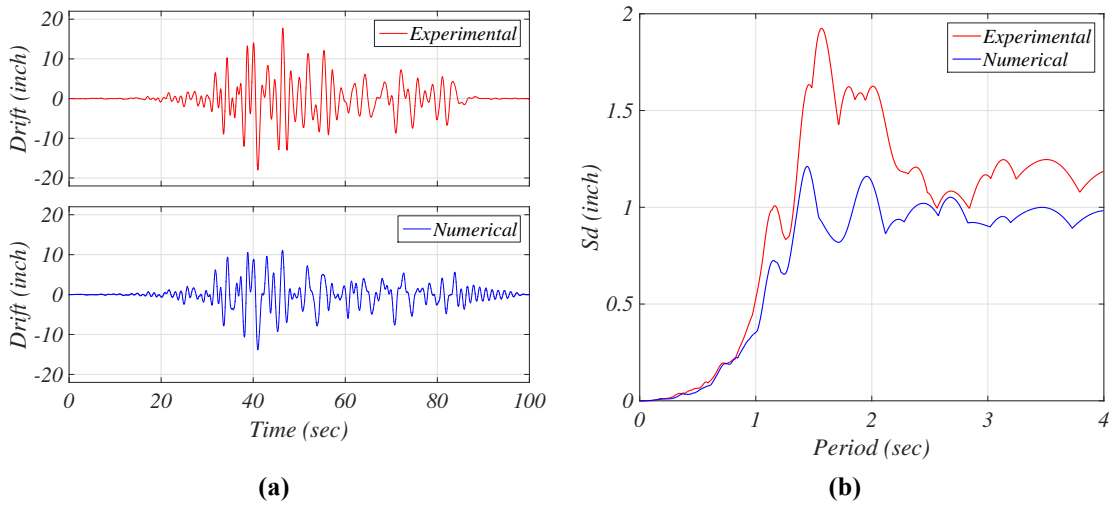

Figure 8.32. Numerical and experimental displacement at the fifth level for FB5: (a) time history and (b) displacement spectrum

Figure 8.33 presents the comparison of the time history and pseudo acceleration spectra for panel 5ES itself. As seen for the building, while there is a general agreement between the numerical and experimental time histories, there are still some discrepancies. For example, the model is not predicting the negative peaks at around second 40, the large positive peak at around second 55, and the decrement of accelerations at the end of the motion. However, there is good agreement in the spectral responses. In fact, the peak representing the panel response is well predicted. This peak is larger and sharper in the model. This is expected, since in reality the characteristics of the panels might change due to damage in

the panel, thus the energy shifts and the response is less sharp. It is noted that in the experiment there were also peaks in the spectral response at low periods/high frequencies. The origin of these is not clear, and the model cannot predict them. Table 8.5 presents the comparison between numerical and experimental peak accelerations and component amplification factors a_p. All errors remain smaller than 16% for the peak accelerations. The model tends to under predict the peak accelerations. Errors for components amplifications factors are even smaller (2% and 11%), with the model in this case slightly over predicting the experimental results.

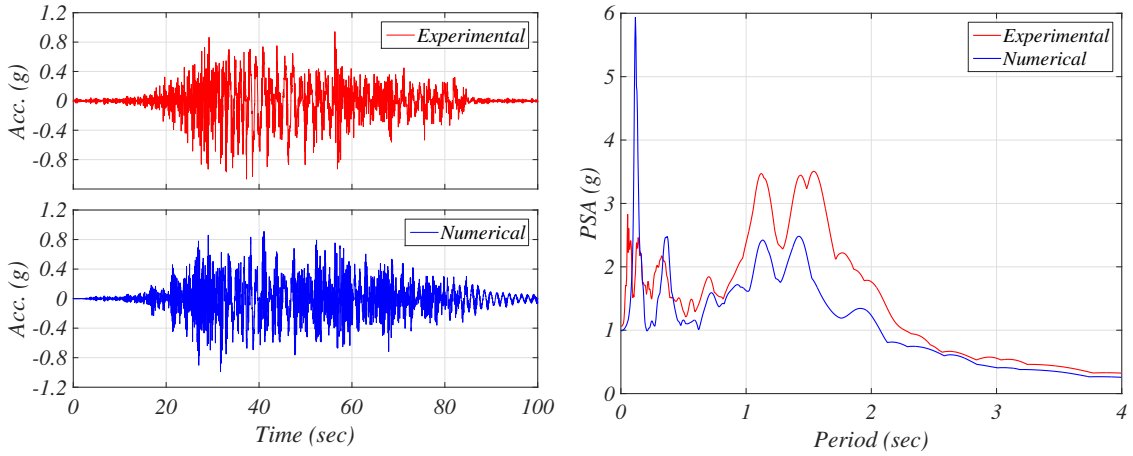

(a) **(b)**

Figure 8.33. Numerical and experimental accelerations in panel 5ES for FB5: (a) time history and (b) pseudo acceleration spectra

Table 8.5. Numerical and experimental values of PFA, $a_{p,top}$ and $a_{p,bottom}$ for model with panel 5ES

	Experimental Peak	Numerical Peak	Error (%)
Roof acceleration	0.99	0.9	-8.6
Fifth floor acceleration	0.69	0.57	-16.2
Panel acceleration	1.06	0.99	-6.9
$a_{p,top}$	1.08	1.10	+1.8
$a_{p,bottom}$	1.55	1.72	+11.0

Building Model with Panel 4ES

The comparison of experimental and numerical time history of acceleration and pseudo acceleration spectrum for the fifth floor and fourth floors are presented in Figure 8.34 and Figure 8.35.

It is noted that the comparison for the fifth floor needs to be presented again, since the damping values used in this second model change, thus even structural response might theoretically change. However, Figure 8.34 shows that the results remain consistent with what previously observed. Figure 8.35a shows that the accelerations in the fourth floor were better predicted in the positive than negative direction. The pseudo acceleration spectra in Figure 8.35b show an almost perfect match for periods lower than 1 second.

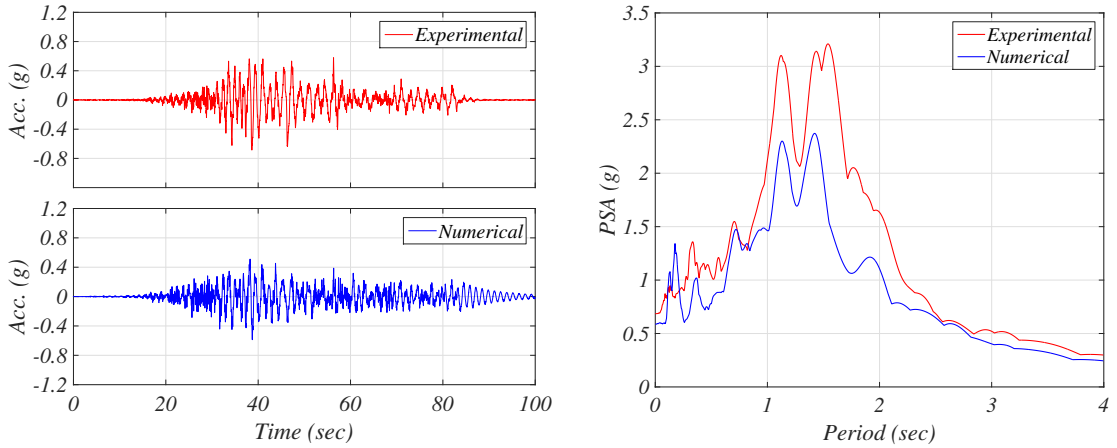

Figure 8.34. Numerical and experimental accelerations at the fifth for FB5: (a) time history and (b) pseudo acceleration spectra

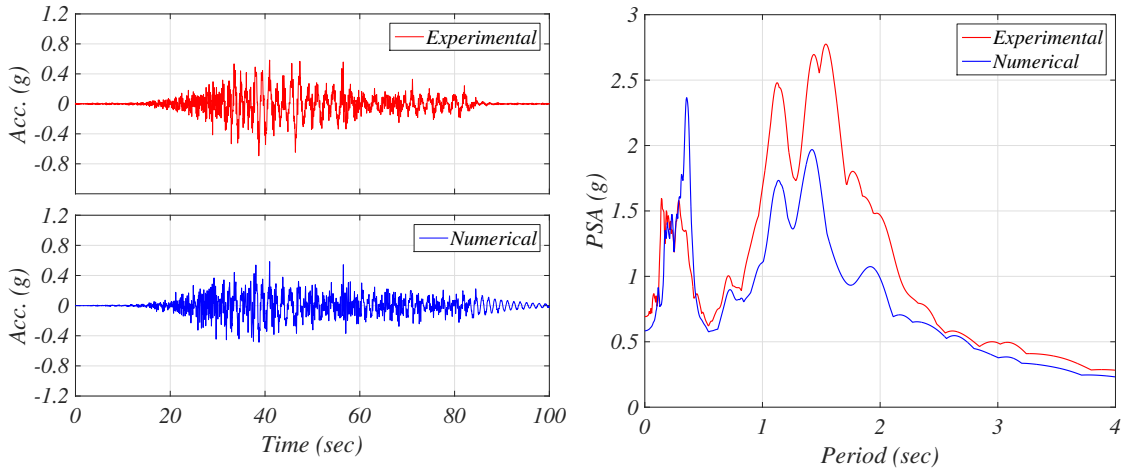

Figure 8.35. Numerical and experimental accelerations at the fourth floor for FB5: (a) time history and (b) pseudo acceleration spectra

The time history and spectrum of displacements at the fifth and fourth floors is presented in Figure 8.36 and Figure 8.37, respectively. Results are consistent with what previously observed. In fact, also in this case the total displacements are smaller in the model than in reality. The time histories of accelerations and pseudo acceleration spectrum for panel 4ES is shown in Figure 8.38. Both comparisons are good. Figure 8.38b shows that also in this case the model predicts a large spike close to the frequency of the panel (9.1 Hz). Very close to this peak there is in this case a second peak, which represents the third lateral mode of the building. The presence of a spike at this frequency in the panel shows that the third building mode includes also movement of the panel itself. Table 8.6 presents the values of PFA, PPA and a_p for the panel installed at the fourth floor and the errors in their prediction. The errors are always smaller than 18%. As observed previously, the model underestimates the peak accelerations of roughly 16%. The errors in the prediction of the component acceleration factors remain very small (~3%).

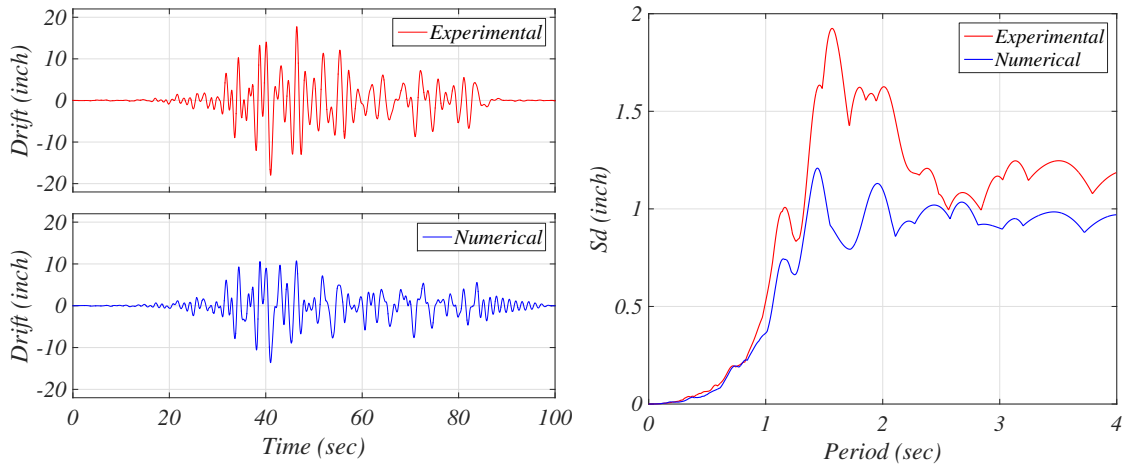

(a) **(b)**

Figure 8.36. Numerical and experimental displacement at the fifth floor for FB5: (a) time history and (b) displacement spectrum

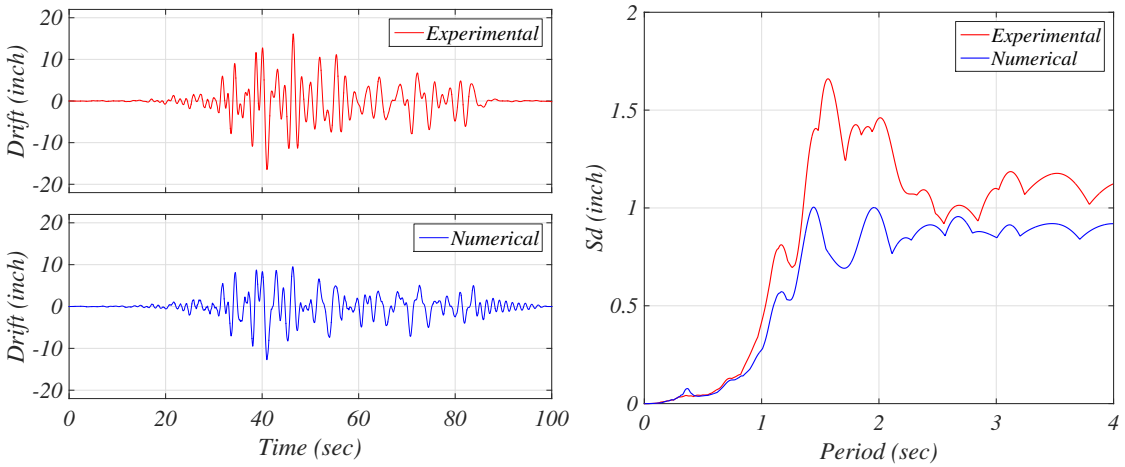

(a) (b)

Figure 8.37. Numerical and experimental displacement at the fourth floor for FB5: (a) time history and (b) displacement spectrum

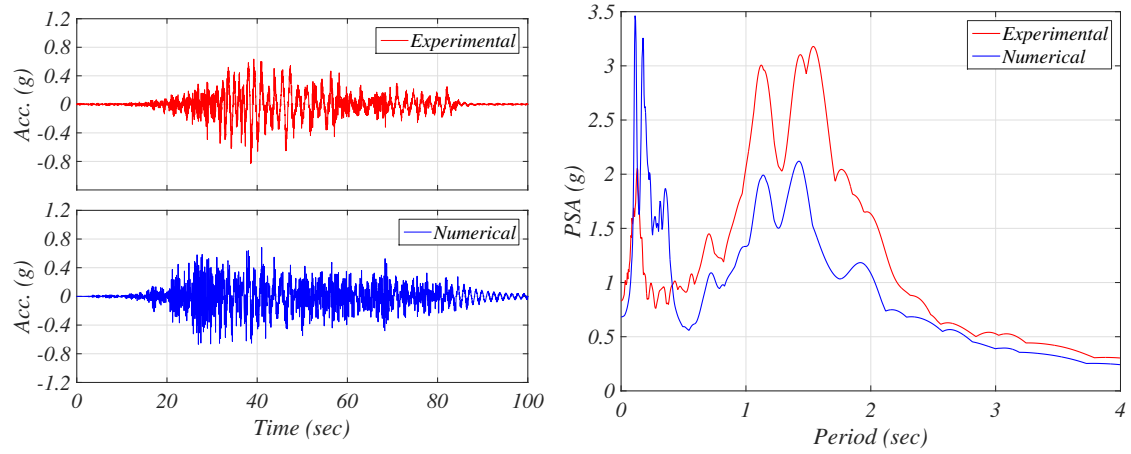

(a) (b)

Figure 8.38. Numerical and experimental accelerations in panel 4ES for FB5: (a) time history and (b) pseudo acceleration spectra

Table 8.6. Numerical and experimental values of PFA, $a_{p,top}$ and $a_{p,bottom}$ for model with panel 4ES

	Experimental Peak	Numerical Peak	Error (%)
Fifth floor acceleration	0.69	0.59	-14.3
Fourth floor acceleration	0.69	0.58	-15.8
Panel acceleration	0.83	0.68	-17.8
$a_{p,top}$	1.21	1.16	-4.1
$a_{p,bottom}$	1.20	1.17	-2.4

8.3.4 Behavior of the Plastic Hinges in the Columns at the First Floor

Figure 8.39 presents the moment-rotation behavior for the plastic hinges at the base of the column. The maximum numerical rotations in the column are around 0.007 radians, which is smaller than expected considering the PIDs reached during FB5 (~2.3%). There might be several reasons for this. First of all, the model tends to generally under predict displacements, as already explained in the previous sections. Another reason might be attributed to the fact that the columns in the experimental building were already damaged thus softer, while in the model they were assumed to start behaving at the full initial stiffness. In addition, the low stiffness attributed in the model to the part of the column remaining elastic might move part of the deformation to this section of the column instead of the plastic hinge. Even if rotations are smaller than expected, they are consistent with each other. In fact, each couple of columns aligned in the north-south direction present similar results, which is expected since they had similar levels of normal forces. The comparison of the P-M behavior of the southern columns with the P-M interaction surface is presented in Figure 8.40. This shows that all the columns reach the yield surface and after that their behavior started to change, with the normal force increasing or decreasing sharply depending on the direction of motion. This plot shows that the plasticization was larger for positive moments.

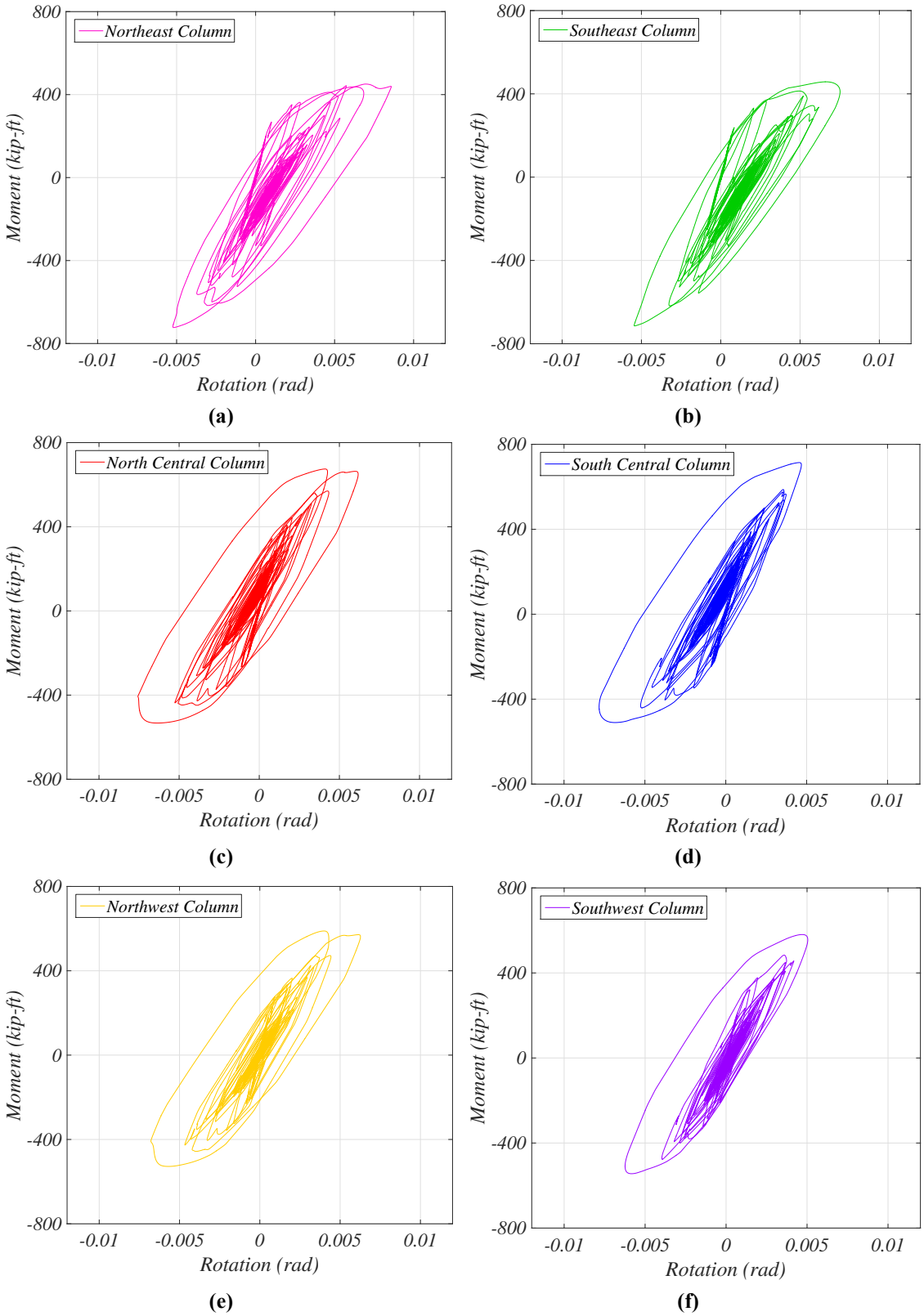

Figure 8.39. Moment-rotation at the base of the column of the first floor

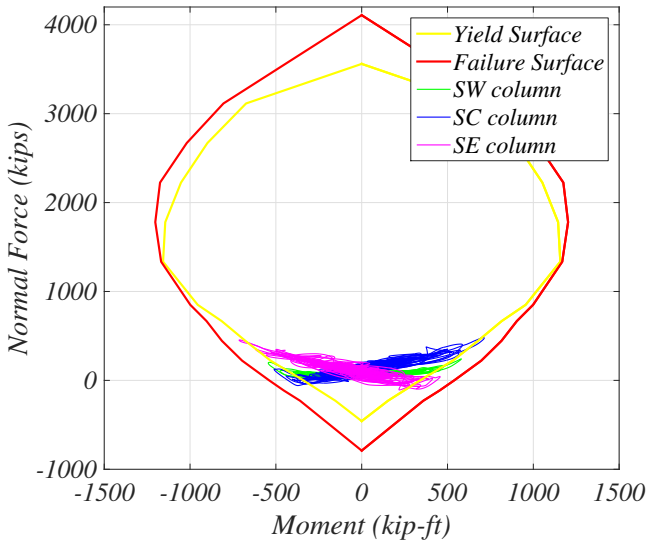

Figure 8.40. P-M interaction curves and P-M behavior of the columns during FB5 (numerical values)

8.3.5 Behavior of the Plastic Hinges in the Beams

Figure 8.41 shows the moment versus plastic rotation for the plastic hinges in the eastern side of the southern frame at floors two, three and four. According to the model, the beam reaching maximum plastic rotation was the one of the third floor, with a maximum of 0.01 radians of plastic rotation, while the one on the second floor reached a maximum plastic rotation of 0.09 radians. The elastic rotation for the beams at these floors can be found considering a plastic hinge length of 33'', and a yield strain of the longitudinal bars at 0.0044 inch/inch, and a distance between centerline of the bars at 25'' as:

$$rotation = \arctan\left(\frac{2 \cdot 0.0044 \cdot 33}{25}\right) = 0.012 rad \qquad \text{Eq. 8.4}$$

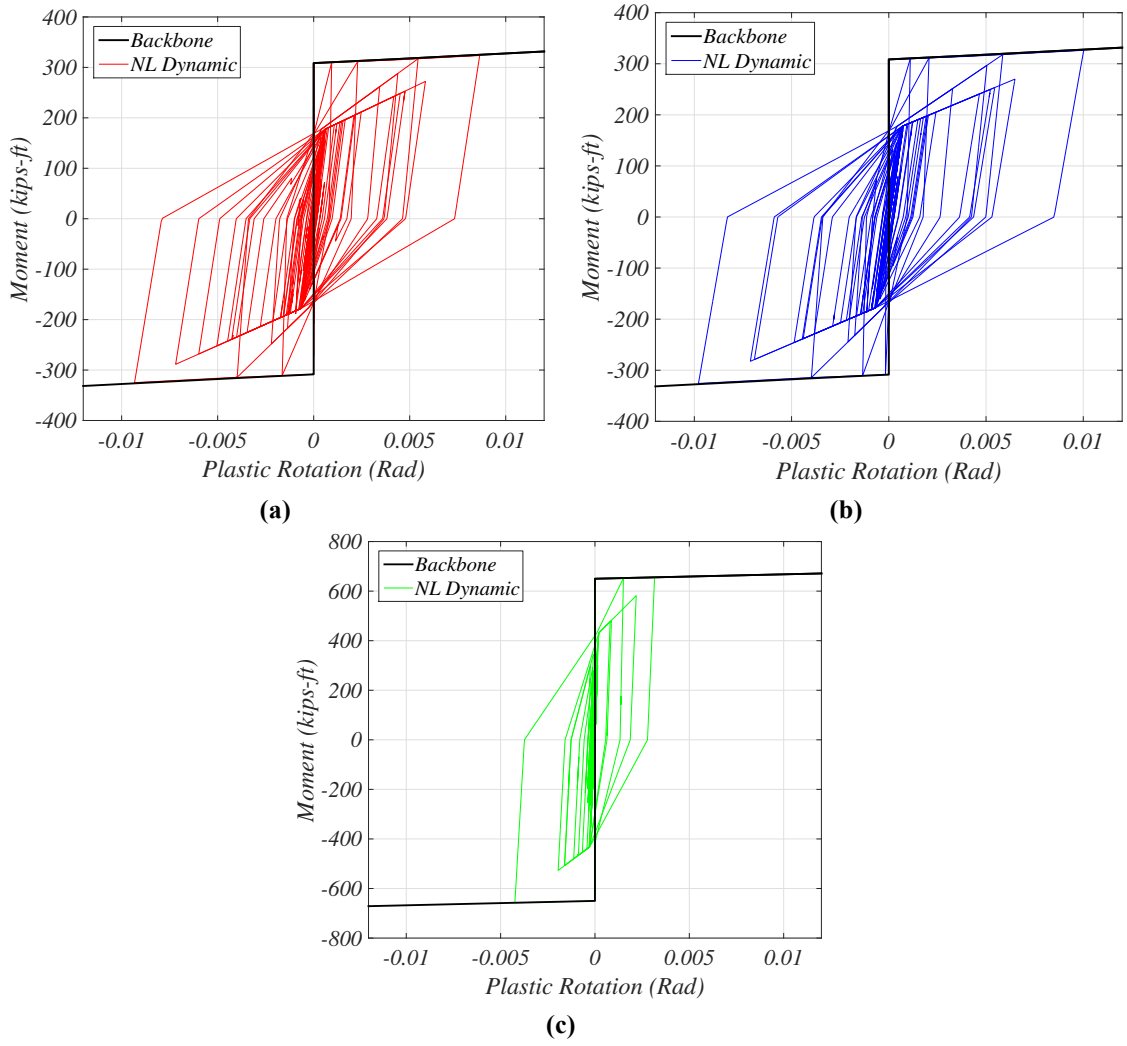

Figure 8.41. Moment versus plastic rotation for beams at floor (a) two, (b) three, (c) four

Adding the values of plastic and elastic rotation, the total value of the rotation reveals to be 0.022 radians for the beam at the third floor and 0.021 for that at the second floor. This value is close to the peak rotations determined experimentally of around 0.023 radians for both the second and the third floors (Figure 8.42). However, it is noted that the model does not capture the asymmetric behavior of the beam. In fact, in the model the beam elements is centered compared to the slab, while this is not the case in the real building, where for all floors except the floor the upper part of the beam is connected to the slab (see construction drawings in Chen et al. 2013b). According to the model, the beam at the fourth floor reached a plastic rotation of 0.004 radians. In this case the elastic rotation can be found considering a yield strain of 0.0002 inch/inch, a length of the plastic hinge of 32'' and a distance

between the centerline of the bars of 23'' as:

$$rotation = \arctan\left(\frac{2 \cdot 0.002 \cdot 32}{23}\right) = 0.005 rad \qquad \text{Eq. 8.5}$$

The total maximum rotation for the beam at this floor remained under 0.009 radians. This value is similar to the experimental peak of 0.012 radians. It is noted that this is the only case where the rotation is roughly symmetric in both the experimental and numerical case, since the beam was centered with respect to the slab. The values of plastic rotations for beams at the fifth floor and roof were close to zero, and are thus not reported. The experimental values in Figure 8.42 confirm that the rotations at these floors remained small.

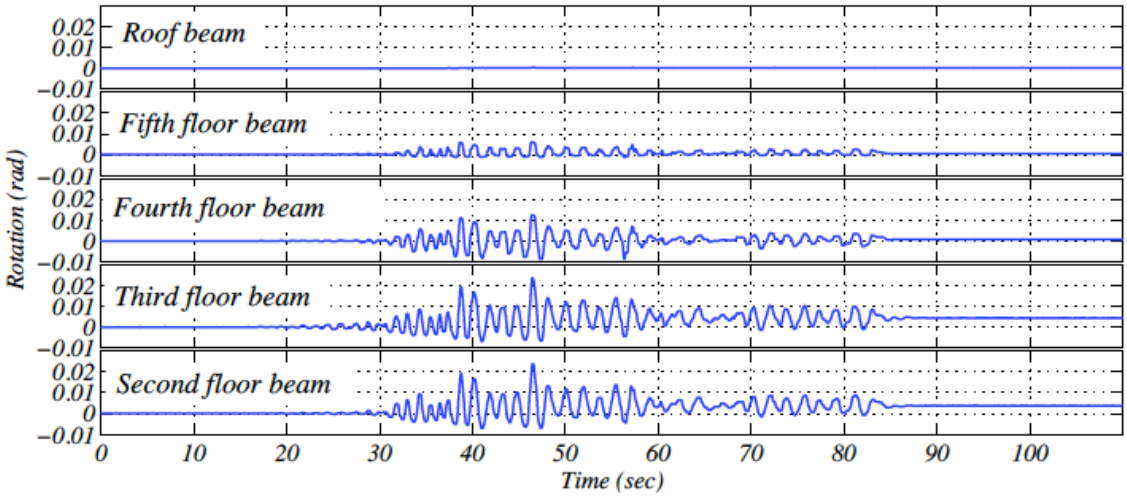

Figure 8.42. Rotation of the Western edge of the Northern frame beam during FB5 (Pantoli et al. 2013a)

8.3.6 Sensitivity Study of the Effect of Damping

To check the effect of damping on the results, it was decided to change by 20% and 40% each of the four parameters of the Rayleigh damping and check their effect on the peak accelerations in the floors and panel (for the building with 5ES). Figure 8.43 and Figure 8.44 report the results for the change of the first frequency (f_1) and damping ratio (ξ_1) of the Rayleigh damping. Not much change was created in this case by changing these values of plus and minus 40% and 20%. This could be attributed to the fact that these values were small, so the percentage change is also small in absolute terms. Figure 8.45 and Figure 8.46 present the same results for change in ξ_2 and f_2. In this case it can be

observed only a minor effect on the peak accelerations in the floors, probably to the influence of the higher modes. However, larger influence is observed for the peak acceleration in the panel. A -40% change in ξ_2 creates a change in the peak panel acceleration from 1 to 1.23 (+23%). The experimental peak is 1.06 g, thus the error remains limited (+16%). Changing ξ_2 of +40% creates a peak panel acceleration of 0.84 g, which is -16% compared to the numerical value with optima damping and a 20% error compared to the experimental results.

When f_2 is changed by -40% the numerical peak panel acceleration moves from 1 g to 0.78 g, which is -22% from the optimal numerical results and -26% compared to the experimental value. When f_2 is increased by 40%, the peak panel acceleration moves to 1.14 g, which is +14% compared to the optima numerical results and +7% compared to the experimental value. This study shows that the results are quite reliable and stable even with change in the damping parameters selected, especially because the errors compared to the experimental values remain within reasonable limits.

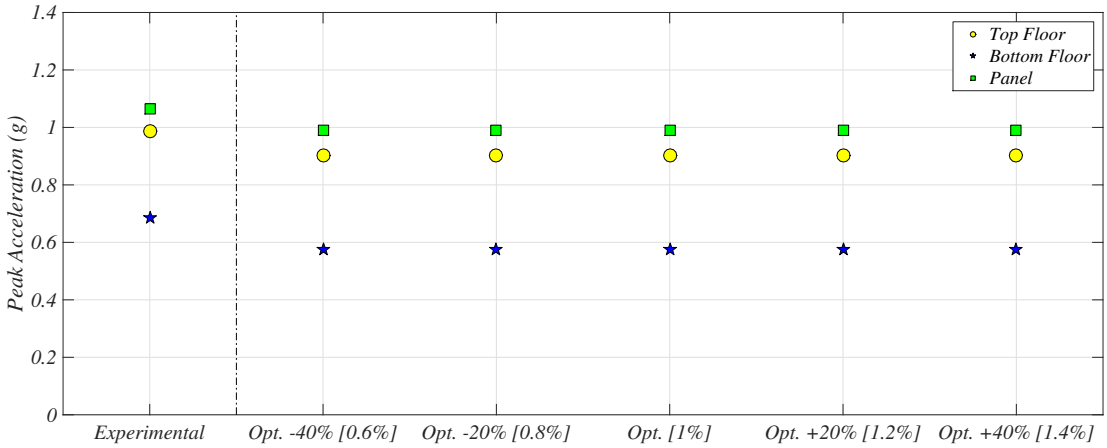

Figure 8.43. Change of peak acceleration with change in ξ_1

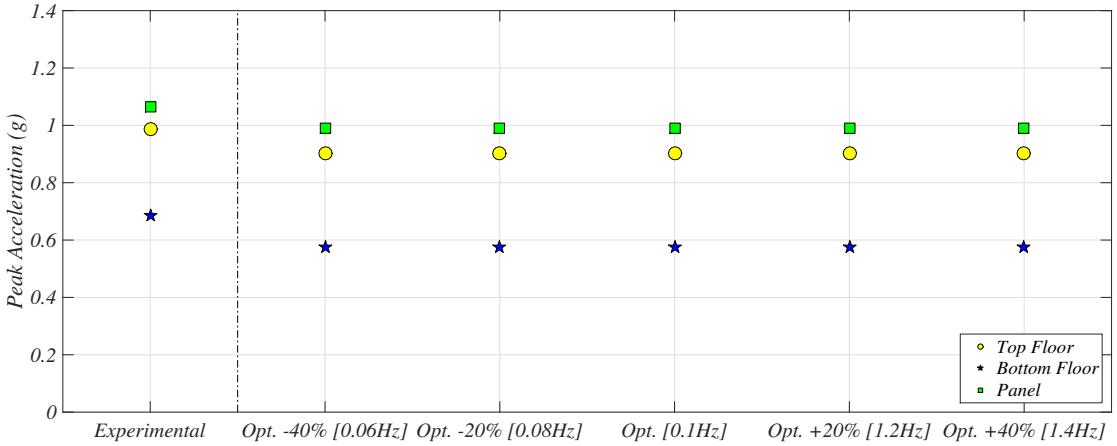

Figure 8.44. Change of peak acceleration with change in f_1

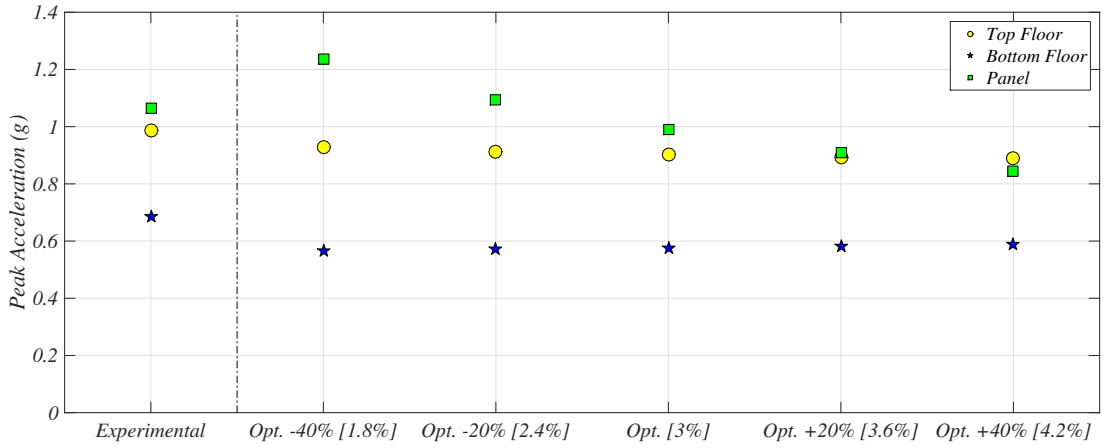

Figure 8.45. Change of peak acceleration with changed in ξ_2

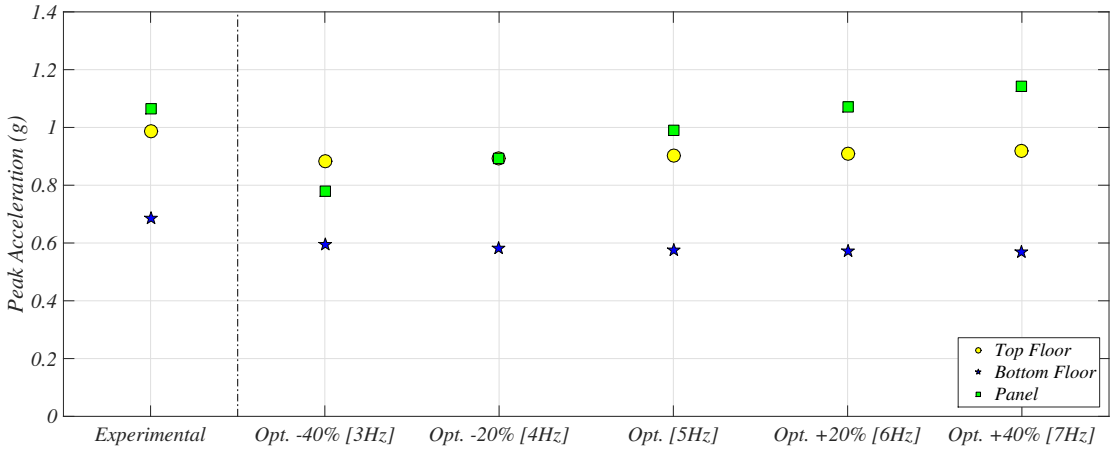

Figure 8.46. Change of peak acceleration with changed in f_2

8.4 Parametric Study

The analysis in this section is similar to that performed in the previous chapter, with the difference that the input motions are matched to the design level spectrum instead of the service level one. Results are also presented in a similar fashion as seen in Chapter 7. It is noted that in this case the experimental natural frequencies of the panels are kept constant throughout the study. In fact, increasing the frequency of the panels as done in chapter 8 would imply changing the values of the parameters in the Rayleigh damping, in order to keep the damping at the frequency of the panel similar. Thus would also create a further reduction of damping at the higher natural frequencies of the building, thus completely changing the structural response. The structural results thus obtained are considered too unreliable, and for this reason the frequency of panels is not changed.

8.4.1 Input Motions

The same original eighteen ground motions utilized in the previous chapter were used in this case. Information on the original motion is presented in Appendix A. These motions were matched to the design spectrum from periods of 0.028 seconds to 2.6 seconds, because of the considerations presented in the previous chapter. This sections shows the main characteristics of the matched motions and the structural response they create, while additional information about the matched motions are presented in Appendix A. As previously seen, also in this case the results are presented separately for the motions created by strike-slip, normal and reverse fault. This is done exclusively for clarity of explanation. Figure 8.47 shows the time history and pseudo acceleration spectra for the strike- slip motions considered. The values of PGA, S_s, S_1 for these motions and the main structural response they create in the building (in terms of PFA and PIDR) is presented in

Table 8.7. The values of PGA are discussed further in the section. The values of S_s are similar to each other, as expected for a match motion, and around 1.4 g. The values of S_1 are around 1 g. The average PIDR created by these motions is 2.2%, while the average PFA 0.92 g, close to the target design values of 2.5% PIDR and 0.7-0.8g PFA. The same results for the normal fault-generated motions are presented in Figure 8. 48 and Table 8.8. The results related to the input motions are very similar as expected. The average values of PIDR is still 2.2%, while the average value of PFA is slightly smaller

at 0.89 g. The values relative to a reverse fault generated motions are presented in Figure 8.49 and Table 8.9. All the results are similar.

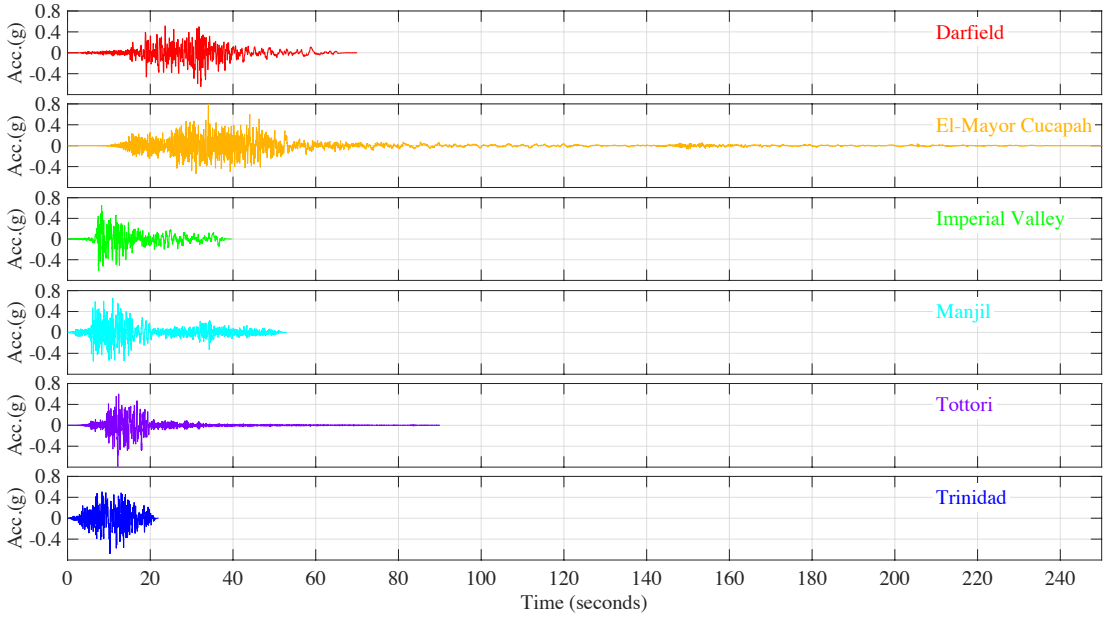

(a)

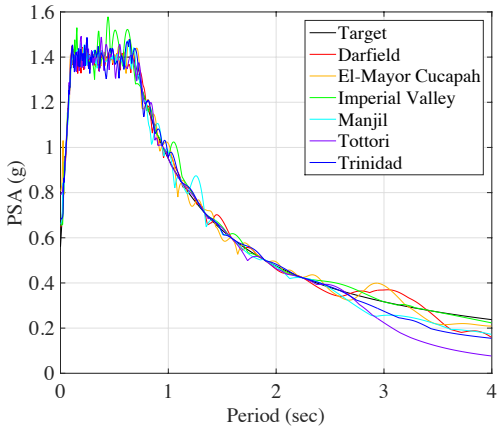

(b)

Figure 8.47. Strike-slip motions matched to the design spectrum: (a) time histories and (b) pseudo-acceleration spectra

Table 8.7. Characteristics of the match strike-slip motions and structural response: PGA, S_S, S_1, PFA and PIDR

Earthquake	PGA (g)	S_S (g)	S_1 (g)	PFA (g)	PIDR (%)
Darfield	0.65	1.42	0.96	0.91	1.95
El-Mayor Cucapah	0.81	1.41	1.02	0.89	2.01
Imperial Valley	0.65	1.40	0.98	0.83	2.55
Manjil	0.66	1.39	0.98	0.93	2.38
Tottori	0.79	1.35	0.95	0.84	2.51
Trinidad	0.68	1.38	0.95	1.14	2.67

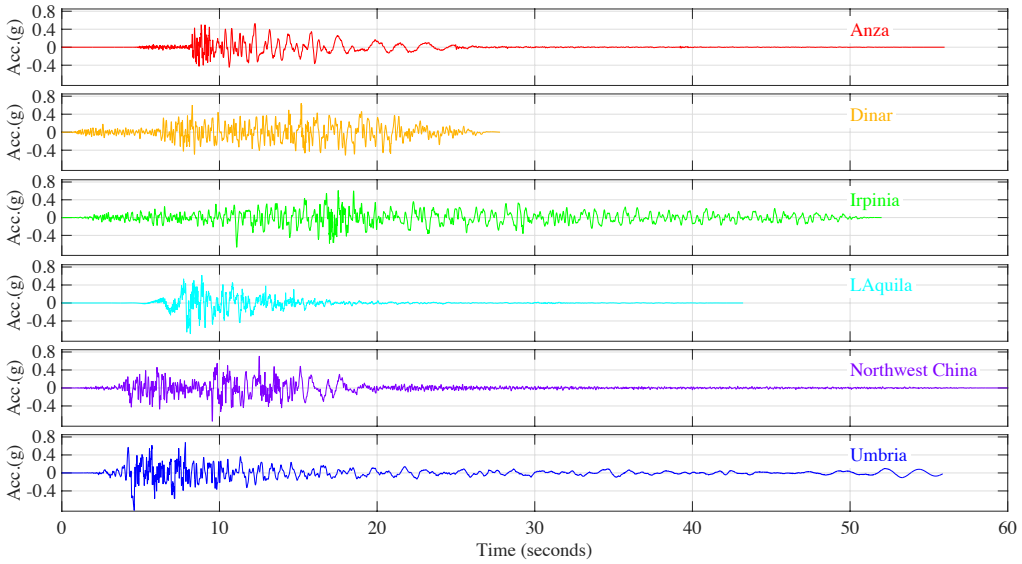

(a)

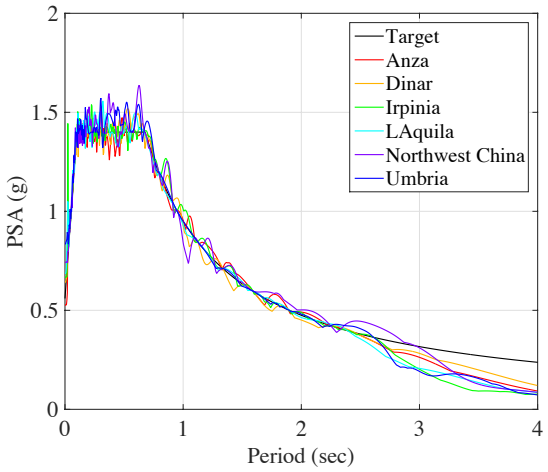

(b)

Figure 8. 48. Normal fault generated motions matched to the design spectrum: (a) time histories and (b) pseudo-acceleration spectra

Table 8.8. Characteristics of the normal fault motions and structural response PGA, S_S, S_1, PFA and PIDR

Earthquake	PGA (g)	S_S (g)	S_1 (g)	PFA (g)	PIDR (%)
Anza	0.53	1.3	0.95	0.91	2.38
Dinar	0.64	1.44	0.93	0.91	2.17
Irpinia	0.67	1.40	1.01	0.88	1.94
L'Aquila	0.68	1.47	0.93	0.91	2.23
Northwest China	0.74	1.49	0.84	0.91	2.13
Umbria	0.83	1.39	0.95	0.79	2.54

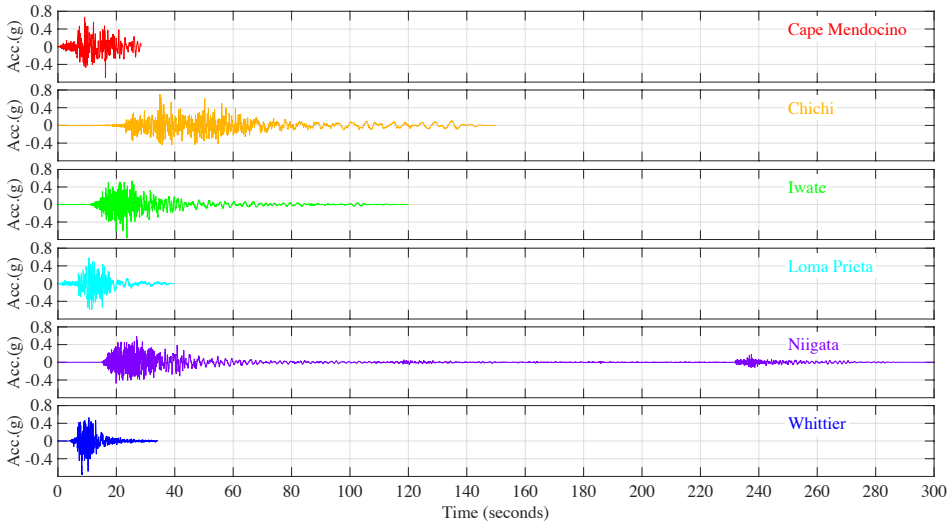

(a)

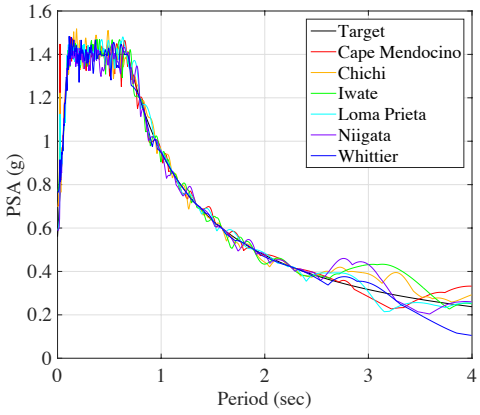

(b)

Figure 8.49. Reverse fault generated motions matched to the design spectrum: (a) time histories and (b) pseudo-acceleration spectra

Table 8.9. Characteristics of the reverse fault motions and structural response: PGA, S_S, S_1, PFA and PIDR

Earthquake	PGA (g)	S_S (g)	S_1 (g)	PFA (g)	PIDR (%)
Cape Mendocino	0.70	1.38	0.95	0.88	1.87
Chichi	0.70	1.37	0.96	0.97	1.96
Iwate	0.77	1.39	0.90	1.02	1.75
Loma Prieta	0.59	1.43	0.96	1.03	1.86
Niigata	0.59	1.35	0.95	1.04	2.17
Whittier	0.76	1.39	0.95	0.83	2.35

8.4.2 Results: Seismic Coefficient C_p

Figure 8.50 presents the values of the seismic coefficient C_p obtained in the experiment during test FB5 and through the numerical model for all the earthquakes considered. All the values of C_p thus considered are in between the code limit for body and fastener elements, meaning that yielding of ductile elements is possible, while none of the brittle elements is anticipated to fail. As seen in the previous chapter, only one value of C_p is obtained per panel, since the panel is simplified as a SDOF system. The value of C_p in the plot is presented at the location of the mass of the SDOF, but it is noted that it can be compared to the limits imposed by the code for both floors to which the panel is attached. For the fifth floor, C_p varies from 0.90 to 1.37, with the experimental value being close to the average of the distribution of 1.10. The 95^{th} percentile of the distribution is at 1.33, 2 times the limit for body of the connections at the upper floor and 2.3 times the limits for the body of the connections at the bottom floor. This 95^{th} percentile represents 63% and 73% of the code limit for fastener elements for the top and bottom floor, respectively. For the panel installed at the fourth level the value of C_p varies from 0.79 to 1.12, with the experimental value being code to the lower end of the distribution at 0.83. The 95^{th} percentile is 1.07, which in this case is 1.8 and 2.2 times the limit for the body elements connected to the top and bottom floors, respectively. This percentile is 58% and 69% the limit for fastener

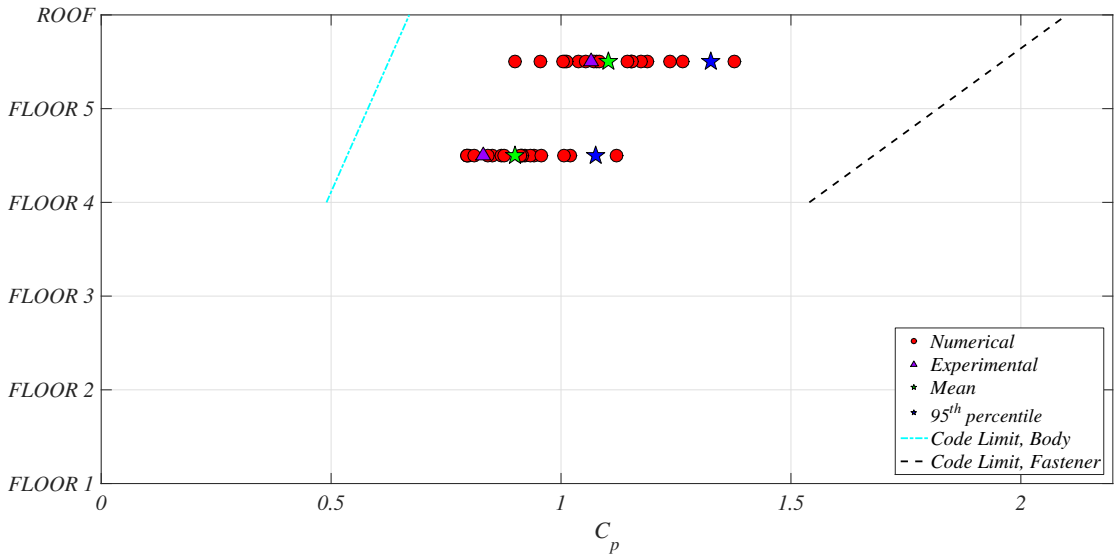

Figure 8.50. Values of the seismic coefficient C_p for panels installed at the fourth and fifth level during a design level motion

elements for the top and bottom floor, respectively. The 95th percentile of the distribution of C_p for the design level earthquake in this case are 1.7 and 1.6 times those obtained at the fifth and fourth levels during the service level motion. For both floors, one of the C_p values represents an outlier in the distribution. This point is created by different motions at each floor (Trinidad for the fifth floor and Whittier for the fourth level). Since the motions are spectrally matched, these larger peaks are probably not caused by the frequency content themselves, but by the way the motions at different frequencies combines in the SDOF. In summary, this plot shows that the limit values in the design code are safe, even if slightly conservative. Brittle (fastener) components are expected to reach roughly 60 to 70% of this design value C_p depending on which floor they are connected to. Yielding is expected in most ductile parts whose actual yield force is less than roughly two times F_p.

8.4.3 Results: Peak Floor Acceleration, Structure Amplification Factor and Component Amplification Factor

As seen in the previous chapter, also in this case the three components of C_p (a_s and a_p) are examined to better understand the results relative to the seismic coefficient C_p. Figure 8.51 presents the PFAs for the floors under consideration, with the PFA at the first floor representing the PGA. This plots clearly shows the influence of the higher modes of the building, with accelerations at the fifth floors smaller than the ground accelerations. This is due to the fact that the second lateral mode, which

dominates the response, has a node very close to the fifth floor. Accelerations at the fourth floor are slightly larger than those at the fifth floor, and similar to the ground accelerations. As well documented in the literature, the whiplashing effect of the higher modes can be observed in this case at the top of the building, where the acceleration is considerably larger than at the fifth and fourth floors. It is noted that the experimental value are consistent with the global distribution of the results explained above, and for all the upper floors they are in the upper half of the distribution, not far from the 95th percentile. The comparison between numerical and experimental values of PFA for FB5 shown in the previous section indicated that this model tend to under predict the PFAs of ~15%, which explains why the experimental values are close to the high-end of the distribution.

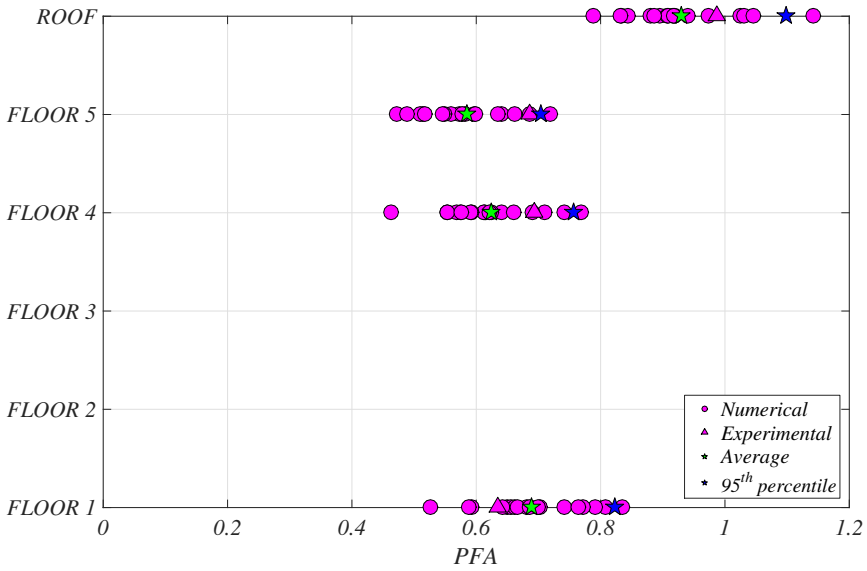

Figure 8.51. PGAs and PFAs at the fourth, fifth and roof level for the motions considered

The structural amplification factors a_s resulting from the PFA presented above and the code limit for a_s are shown in Figure 8.52. For both the fifth and fourth floors, the distribution of a_s have 95th percentiles close to the unity (1.13 and 1.07, respectively), showing that during the design level motion the damage at the lower floors protects the building from amplifying the acceleration excessively. Some amplification is still present at the top floor, with 95th percentile of the a_s at the roof of 1.76. The 95th percentile of the a_s at the roof, fifth and fourth floors are 58%, 41% and 51% of the code limits, respectively.

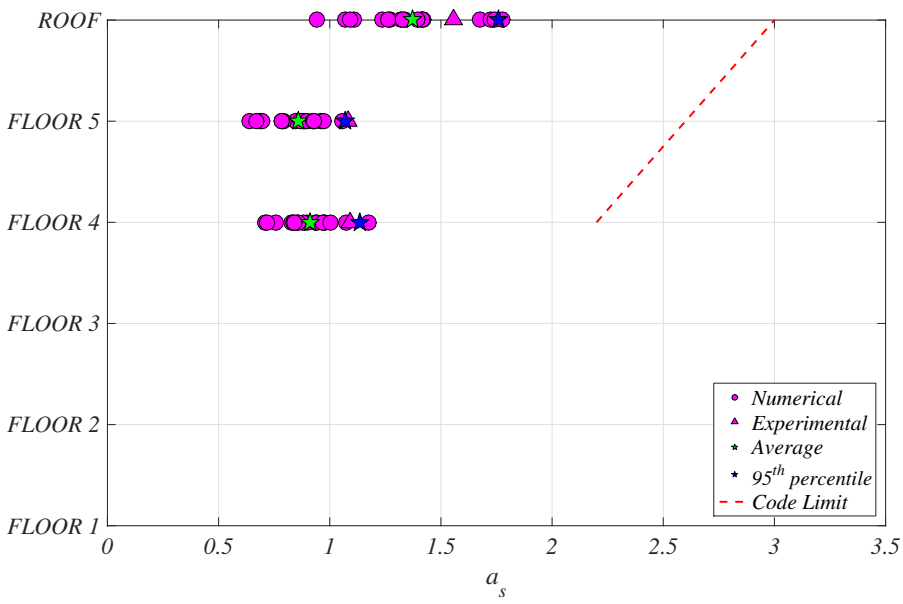

Figure 8.52. Structural amplification factors for the motions considered

Figure 8.51 and Figure 8.52 show that there are two possible inputs to the panels. If the panel is at intermediate height, the peak accelerations from top and bottom floors are similar. The values of the peaks do not provide information of the time history of accelerations at the top and bottom panels, which could move mainly in-phase or mainly out-of-phase. If the motion is out-of-phase (Figure 8.53a), not much amplification of accelerations in the panels in expected, since the panel gets pulled in opposite directions at the same time. Larger levels of amplification of acceleration are expected in case the motion is somehow in-phase (Figure 8.53b). When a panel is connected to two intermediate floors, the values of $a_{p,top}$ and $a_{p,bottom}$ are expected to be similar. The second case is for a panel installed at the roof, which is different since the roof might accelerate more than its lower floor, as shown in the figures above and well documented in the literature (see chapter 3). Thus, the roof can create a large pulling effect of the panel. $a_{p,bottom}$ is thus expected to be large, while $a_{p,top}$ is expected to be small, since the bottom floor is slowing down the acceleration of the panel (Figure 8.53c).

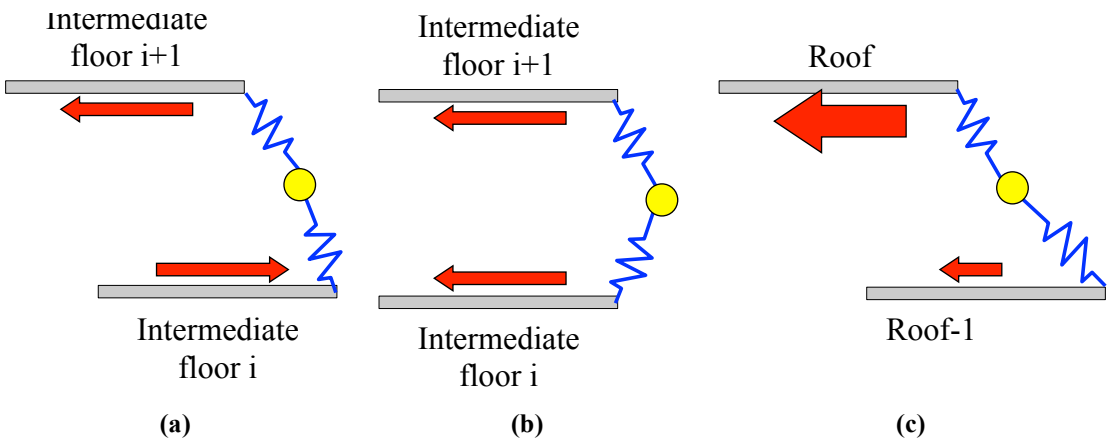

Figure 8.53. Possible excitations of the panel: (a) panel at intermediate levels moving out-of-phase, (b) panel at intermediate levels moving in-phase, and (c) panel attached to the roof

The values of $a_{p,bottom}$ and $a_{p,top}$ obtained from the analysis are presented in Figure 8.54, and they confirm the pattern explained above. For the fifth floor panel there is a large difference in results between $a_{p,bottom}$ and $a_{p,top}$, with the 95th percentile of the first being at 2.3, while the second being at 1.5. The values of $a_{p,top}$ and $a_{p,bottom}$ for panel 4ES are close to each other, and they have 95th percentiles of 2 and 1.7, respectively. It is noted that $a_{p,top}$ is larger than $a_{p,bottom}$ because the panel gets pulled more by the fourth floor, which has larger accelerations.

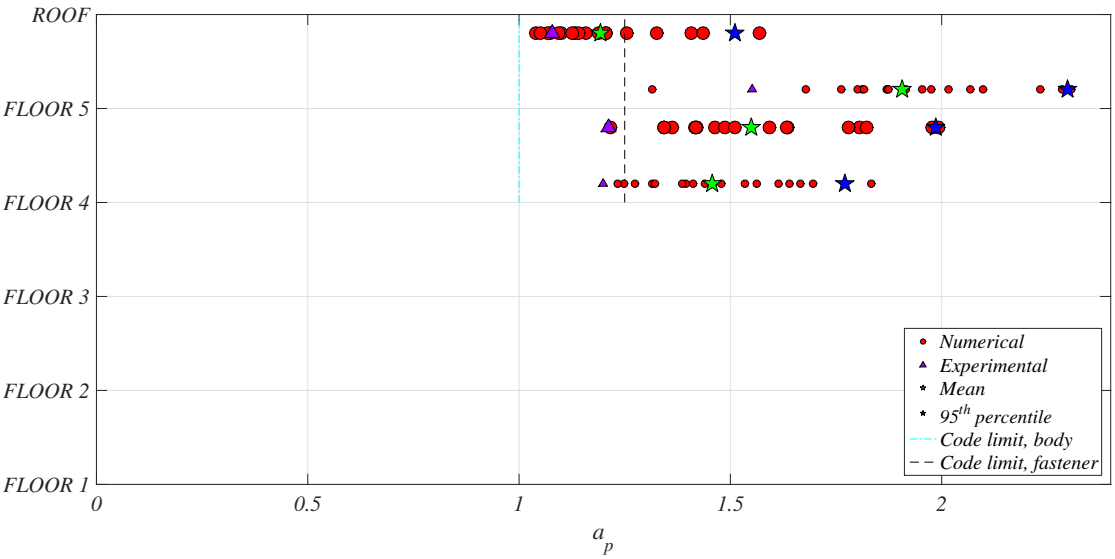

Figure 8.54. Values of $a_{p,top}$ and $a_{p,bottom}$ for the motions considered

In all the cases, a_p is larger than the code value of body of the connections of 1, confirming that the approximation of the panels as "rigid" nonstructural elements in not valid. The a_p values are also

generally larger than the code limit of 1.25 used for the fastener elements. The plot shows that the experimental values are in this case close to the lower bound of the distribution. This is partially due to the fact that the experimental PFA (which is at the denominator of the formula to determine a_p) are very close to the upper edge of the distribution. It is also noted that the validation of the model showed that the model tends to under predict the PFA and over predict the a_p (by a factor up to ~10%).

8.5 Limitations of the Study

Some of the limitations of this study, such as the fact that the panels are modeled as SDOF systems, are similar to those already presented in the previous chapters. However, the fact that this model is nonlinear creates further limitations. The main one is that the plasticity of the building is concentrated in the plastic hinges, while other elements remain linear elastic. This limitation is intrinsic in the software used, since SAP2000 allows to use material nonlinearities only in link/support elements, tension and compression limits in frame elements, and plastic hinges in frame elements (CSI, 2013). The stiffness of the elements remaining linear elastic (walls, slabs etc.) was selected based on results from literature. The results from the pushover analysis showed that the values assigned to the stiffness of the linear elastic elements, especially the slab, considerably influence the results.

Another limitation is related to the definition of the plastic hinges, for which the material properties were determined from laboratory experiments on the specific batch only in some cases, while in several cases information about the stress-strain behavior of the material had to be obtained from other sources.

Another limitation is related to the way the damping was assigned. In SAP2000, only Rayleigh damping can be used for the nonlinear dynamic analysis, and users are only free to assign four parameters: two frequencies of interest and the damping ratios at those two frequencies. This was a major limitation in this case, since the damping had to be kept low at the frequency of the panel (~8/9 Hz) to match the experimental results, but because of this the damping at the second mode of the building was also very low. For this reason, the model tends to under predict the effect of the first lateral mode while it over predicts the effects of the higher lateral modes. One of the main consequences of this error is the fact that the model under predict drifts, since these are dominated by

lower frequencies. Results from the pushover analysis show also that the BNCS building underwent some type of nonlinearity when moving in the eastward direction during FB5 that the model could not predict.

8.6 Summary Remarks

The study in this chapter has the goal of understanding the forces developing in the connections of APC cladding during a design level earthquake. A nonlinear model of the BNCS building including a panel moving in the OP direction and installed on either the fifth or fourth level was created in SAP2000, and validated with results from FB5. The prediction of the model had low errors, when compared with test results for accelerations in the floors and panel, and was then used for a parametric study, during which eighteen additional design level motions were considered.

This study reveals that the values of the seismic coefficient C_p in all the cases are in between the limits for the body and fastener elements of the connections assigned in the code, as intended. In fact, ductile elements are generally anticipated to yield during this type of motion, while brittle elements should be protected. The 95th percentile of the C_p distribution obtained is this study is roughly two times that of code limit for body elements. It is noted that many elements in the connections are selected also to facilitate constructability, and could thus be much stronger than what required by the code, thus not achieving yielding also at this large demands. In addition, yielding of one element in a connection limits further increment of forces, thus protecting all the other elements in the same connection. The C_p for fastener elements remains at roughly 60-70% of the code limits, thus providing a certain degree of conservatisms.

Even if results for the seismic coefficient are close to what the code intends, the analysis of the three components of C_p (a_s, a_p) show that these good results are obtained only by combining a series of errors. The structural amplification factor a_s reveals very different from the code prediction. In fact, the code prescribes a linear distribution of a_s varying from 1 at the first floor to 3.0 at the roof. However, the nonlinearities in the building increases the effects of the higher modes and also attenuates the floor accelerations, thus creating a very different behavior. For the building examined, the maximum a_s is achieved at the roof, with a 95th percentile of the distribution of a_s of only 1.76, less than 60% of the

prescribed value of 3.0. Larger discrepancies are observed at the fifth and fourth floors, where the 95th percentile of the distributions of a_s are close to 1.0, while the code prescribes 2.6 and 2.2, respectively. Thus, it can be inferred that the code is overly conservative in the prescription of a_s, especially for floors different than the roof, since accelerations in the roof tend to be larger because of the effects of the higher modes. Due to the difference in acceleration in the roof and intermediate floors, an APC panel can be subjected to two types of excitation. When connected to the roof, the larger pulling effect from this floor create higher values of $a_{p,bottom}$ and smaller values of $a_{p,top}$. When an APC panel is connected to two intermediate floors, whose peak accelerations are similar, the values of $a_{p,top}$ and $a_{p,bottom}$ are expected to be close to each other. The analysis confirms this pattern. In fact, at the top level the values of $a_{p,top}$ and $a_{p,bottom}$ have 95th percentiles at 1.5 and 2.3, respectively. At the fourth level, the values of $a_{p,top}$ and $a_{p,bottom}$ are similar, with 95th percentiles of the distributions at 2 and 1.7, respectively.

ACKNOLEDGEMENTS

Chapter 8 reproduces content and images of the material currently in preparation. Pantoli, E., Hutchinson, T.C. “Seismic accelerations developed in APC cladding panels” (tentative title). The author of the dissertation is the principal author of the above cited papers.

Chapter 9

Conclusions and Future Work

9.1 Motivation and Scope

Architectural precast concrete (APC) cladding is a type of façade used worldwide in a variety of buildings, such as residential, industrial and healthcare. APC panels often span from floor to floor, thus making this system sensitive to interstory drifts. However, different from many other components spanning multiple floors (such as pipes, metal stairs, cold-formed steel and glass façades), APC panels are very massive. The combination of these two features makes them quite unique among nonstructural components, since they can be equally sensitive to interstory drifts and accelerations.

The lack of specific research on this unique type of nonstructural component has several consequences. Importantly, design codes provide more qualitative rather than quantitative guidance for the drift-sensitive design of APC cladding. Consequently, engineers are left at their own devices when detailing panels and connections. In addition, the code does not consider properly the unique qualities of this system when calculating the design forces, which must be transmitted through the different components of the APC system. Unfortunately, instead, the code provides a unique value of the component amplification factor a_p. This ignores the fact that this system receives input motions from multiple, typically two, floors. As a consequence, this system might have two different values of amplification, one from the bottom and one from the top floor ($a_{p,bottom} \neq a_{p,top}$). In addition, the code prescribes a component amplification factor of 1.0, implying that this system is "rigid", meaning that its natural frequencies are larger than 16.7 Hz. While this assumption might be correct for lightweight façades, this is not the case for APC cladding. In fact, in the out-of-plane (OP) direction, the panels might be very flexible. This, in combination with the large mass of the panels, can lead to the presence of natural modes with low frequencies in the OP direction.

This research seeks to advance the knowledge of this unique type of nonstructural component, focusing on both drift and acceleration compatibility. The first part of this dissertation focuses on providing practical information to designers for the detailing of tieback connections and corner joints.

Findings on the seismic behavior of the tieback connections are based on three experimental programs. The first is a system level experiment conducted at the large outdoor shake table at the University of California, San Diego (UCSD), during which sixteen panels were installed on a full-scale five-story building. This structure was excited with a variety of earthquake input motions of varying intensity, while the building was in a base isolated or fixed base configuration. The other two experiments were component tests on sliding and flexing connections conducted at UCSD and San Jose State University (SJSU), respectively. The study of the behavior of corner joints is based on experimental data obtained from the system level tests program and a comparison numerical study of a chunk of a building with two corner panels colliding.

The second part of this research focuses on understanding the magnitude of accelerations, and thus forces, developed in APC cladding during earthquakes of various intensities. First, the primary natural modes and frequencies of typical APC cladding are identified. Then, APC panels are modeled as single degree of freedom (SDOF) systems and incorporated in a larger model of a building. This building-panel system model is subjected to suite of earthquake motions scaled to service and design level intensities. These results are then compared to the limits provided by the design code to identify possible shortcomings.

9.2 Research Uniqueness

This research is unique because of its focus on APC cladding, a subject that has received little attention in past efforts. This is a very distinct nonstructural component due to its mass and its connections to multiple floors, which make it very sensitive to both seismic drifts and accelerations. To improve the drift-compatible design of APC cladding, this research involved several tests on panels and connections, which provided a large and unique dataset. In fact, very few experiments on APC cladding panels were conducted in the past, and the BNCS project involved the only dynamic full-scale experiment in which stories were fully encased with APC cladding, thus completely capturing the interaction of the panels with the building and with each other. In addition, during this experiment, many different variables were considered. Unique are also the data from the component tests, since very few experiments like these were conducted in the past and, to the author's knowledge, none have

incorporated the variables considered herein.

To complement the experimental efforts, unique attribute of this dissertation was the consideration of accelerations imposed on APC cladding. Moreover, the numerical study of the dynamic characteristics of the panels performed in this research is the first complete study on the subject. Using the numerical models, the analysis of the accelerations developed in the panels during earthquakes is unique in that it considers a broad variety of features of the system: its natural frequency, the connections at two floors and its large mass. This fact, together with the presence of experimental data to validate the numerical results, make this study highly valuable to understand the accelerations developed in APC cladding during earthquake motions.

9.3 Major Findings

9.3.1. Drift-Compatible Design

Sliding Tieback Connections

The BNCS system level experiment and the components tests conducted at UCSD offer important insight into the seismic performance of sliding tieback connections. A key attribute of the system are the sliding plate washers. For example, both programs revealed that, when plate washer and nut are installed on each side of the slotted elements, the rod tends to bend prior to sliding. This bending creates a clamping force between the washers and the slotted plate prohibiting the intended sliding action. If short rods designed to slide are instead substantially bending, fracture of the rods may occur at low levels of interstory drift. A possible way to avoid this issue is to use snug sliding connections. In these tests, snug connections consistently demonstrated good behavior, since the rod is short and stiff and clamping force cannot develop absent the compression washer. Alternatively, an improved design of the sliding connections may require the elimination of the compression washer, rendering impossible for the clamping force to develop. These tests indicated however that in conjunction with removing the compression washer, a length over diameter ratio of less than 5.3 is essential to limit the potential generation of binding in the rod.

Flexing Tieback Connections

Results for the flexing tieback connections were obtained from the BNCS system level experiment and the component tests conducted at SJSU. First, it was observed that, as noted for the sliding connections, the response can manifest has a combination of sliding and bending behavior. In fact, during the BNCS experiment, long rods slid inside of oversized installation holes, thus showing residual deformation, even if no residual displacement in the panel was observed. The region of the rod behaving inelastically was very localized, approximately one or two diameters of the rod. This can be attributed to several factors, including the geometric complexity of the thread and the effect of cold working of the steel. During the component tests, a linear correlation was observed between the ratio of rod length to diameter normalized by the applied displacement ($L/d/\Delta$) and the number of cycles at fracture.

Corner Joints

During the BNCS experimental program, a new type of corner system was tested. This system allows the collision of the panels during large earthquakes, however prevents overload of the brittle parts of the connection by integrating a load-limiting element (in this case a steel plate) within the system. The BNCS experiment revealed that this new corner system performs best when combined with a butt-return joint at panel intersections, as this stiffens the panels thus avoiding cracking of the panels. A numerical model of the corner system was developed in SAP2000, and nonlinear analysis results from the use of this model revealed that allowing the collision between the panels can create large forces in all connections, even in the presence of a ductile fuse.

9.3.2. Acceleration Sensitive Design

Dynamic Properties of APC Cladding Panels

A study of the dynamic characteristics of APC panels considering geometries outside of the scope of the experimental program revealed that the movement of the panels is dominated by three modes. The in-plane vertical (IP_v) response is controlled by 1) a vertical mode, involving rigid displacement of the panel and vertical deformation of the connections. Due to the large stiffness of the bearing connections and panel in the IP_v direction, this mode has very large natural frequencies (more

than 30 Hz for all the cases considered). The movement in the in-plane horizontal (IP_h) direction is dominated by 2) a rocking mode. The natural frequencies of this mode are always larger than 16 Hz, thus it can be concluded that also in this case it is less likely that this mode will be activated during an earthquake. In the out-of-plane (OP) direction, the motion is controlled by 3) OP bending modes, whose natural frequency depends mainly on the geometry of the panels themselves and the OP stiffness of the connections. The natural frequency of the OP bending modes was as low as 8 Hz for the cases considered, thus these are the modes that are most likely to be activated during an earthquake.

Accelerations in APC Cladding Panels During Service Level Motions

During service level motions, the response of the building is generally dominated by the first natural mode, with peak floor accelerations (PFA) increasing roughly linearly from the ground to the roof. Because of this, APC panels receive a smaller input accelerations from the bottom floor compared to the top floor, and they tend to be "pulled forward" by the top floor, and "pulled back" by the bottom floor. Consequently, the component amplification factors a_p (defined as the peak panel acceleration divided by the peak floor acceleration) are larger when compared to the bottom floor than the top floor ($a_{p,bottom} > a_{p,top}$). For the BNCS building, it was found that $a_{p,bottom}$ and $a_{p,top}$ had 95th percentiles around 1.7 and 1.4, respectively. These values are larger than the recommended code values for a_p presently defined in ASCE 7-10 of 1.0 for body components and 1.25 for fastener elements.

The analysis performed revealed that the values of the seismic coefficient C_p could be larger than the code limit for ductile elements of the connections in several cases, however, especially for the connections at the bottom of the panel due to the pulling effects of the top floors. However, since the bottom of the panel is generally connected to floors with very bulky bearing connections, no damage should be expected at this location.

Accelerations in APC Cladding Panels During Design Level Motions

During design level earthquakes, most buildings are expected to sustain some level of damage and have a movement dominated by the first few modes of vibration. Structural amplifications factors a_s (defined as peak floor acceleration divided by peak ground acceleration) at the middle floors are close to each other, while they are larger at the roof. Because of this, the way in which APC cladding panels

can be excited depends on their locations. When panels are connected to two intermediate levels, the peak acceleration at their top and bottom floors are similar. In this case the $a_{p,bottom}$ and $a_{p,top}$ have also similar values. Analyses of the BNCS building reveal that these component amplification factors could vary from 1.2 to 2. For the panels connected to the roof, a large difference in $a_{p,bottom}$ and $a_{p,top}$ is expected. Namely, $a_{p,bottom}$ is likely to be large since the panel receives larger input at the roof level, while $a_{p,top}$ is expected to be small. For the panel placed at the top floor of the BNCS building, the values of $a_{p,bottom}$ spanned from 1.3 to 2.3, while $a_{p,top}$ had values from 1.0 to 1.6. The analysis revealed a large variability in the values of a_p, and the fact they could be larger than the code limit.

The analyses performed showed that the seismic coefficient C_p remains in between the code limit for the body and fastener elements of the connections in all cases, as intended by the design code. However, this result is obtained through the combination of over and under estimation of several factors. Namely, the amplification of acceleration in the structure a_s is overestimated by the code, while the component amplification factors a_p are underestimated.

9.4 Recommendations For Future Work

Research is still needed to improve our knowledge of the seismic behavior of APC cladding. Suggestions on future work include:

- Broadening the experimental database documenting the seismic behavior of APC panels. As mentioned in Chapter 1, there are many different configurations of APC cladding panels, including U-shaped, column covers, mullions and punched window wall panels. This research focused only on punched window wall panels. Similar system level tests should be conducted with other type of APC panel configurations;
- Testing tieback connections with a variety of details. APC cladding designers have great freedom when designing the panel connections, which has lead to a large variety of details used (see Chapter 1). Different connections will certainly have different limitations, thus it is important to test a broad variety of them to understand the optimal design;
- Understanding the behavior of windows in APC cladding panels. Unfortunately, during this research it was not possible to include within the test program glass panels, which are

generally installed within the in APC cladding system. Glass panels are brittle and thus highly susceptible to fracture during even minor earthquake shaking, thus incorporating them within future test programs would allow correlation between the glass fracture limit with the limit carried by APC panels

In addition to this work specific on APC cladding, research is still needed on other types of cladding systems, both in terms of drift-compatibility and forces. These façades include for example glass-fiber reinforced (GFRC) systems, glass façades, and steel curtain façades.

Bibliography

American Concrete Institute Committee 318, 318-11 (2011). "Building code requirements for structural concrete and commentary." ACI, Farmington Hills, MI.

American Institute of Steel Construction, 341, 341-10 (2010),."Seismic provisions for steel buildings." AISC, Chicago, IL.

American Society of Civil Engineers (2010). "ASCE 7-10 Minimum Design Loads for Buildings and Other Structures." ASCE, Reston, VA.

American Society of Civil Engineers (2005). "ASCE 7-05 Minimum Design Loads for Buildings and Other Structures." ASCE, Reston, VA.

Arnold, C. (2009). "Building Envelope Design Guide – Introduction." *Whole Building Design Guide*, <http://www.wbdg.org/design/env_introduction.php> (January, 2015).

Astroza, R., Ebrahimian, H., Conte, J. P., Hutchinson, T. C., and Restrepo, J. I. (2013). "Evolution of dynamic properties of a 5-story RC building during construction." *Topics in Dynamics of Civil Structures, Volume 4*, pp. 163-173, Springer, New York.

Applied Technology Council (1978). "ATC 3-06: Tentative Provisions for the Development of Seismic Regulations for Buildings." Applied Technology Council, Redwood City, CA.

Baird, A. (2014). "Seismic performance of precast concrete cladding systems." Doctoral dissertation, University of Canterbury, New Zealand.

Baird, A., Palermo, A., and Pampanin, S. (2013). "Controlling Seismic Response using Passive Energy Dissipating Cladding Connections." *Proc. 2013 NZSEE Conference,* Wellington, New Zealand, April 23-26.

Barid, A., Palermo, A., and Pampanin, S. (2012). "Experimental and numerical validation of seismic interaction between cladding systems and moment resisting frames." *Proc., 15th World Conference on Earthquake Engineering*, Lisbon, Portugal, September 24-28.

Baird, A., Palermo, A., Pampanin, S., Riccio, P., and Tasligedik, A. S. (2011). "Focusing on Reducing the Earthquake Damage to Facade Systems." *Bulletin of the New Zealand Society for Earthquake Engineering*, 44(2), pp, 108-120.

Belleri, A., Torquati, M., Marini, A., and Riva, P. (2016). "Horizontal cladding panels: in-plane seismic performance in precast concrete buildings." *Bulletin of Earthquake Engineering,* 14(4), pp. 1103-1129.

Belleri, A., Brunesi, E., Nascimbene, R., Pagani, M., Riva, P. (2014). "Seismic performance of precast industrial facilities following major earthquakes in the Italian territory*." Journal of Performance of Constructed Facilities,* 29(5), pp. 04014135.

Bournas, D. A., Negro, P., and Taucer, F. F. (2013). "Performance of industrial buildings during the Emilia earthquakes in Northern Italy and recommendations for their strengthening." *Bulletin of Earthquake Engineering*, 12(5), pp. 2383-2404.

Building Seismic Safety Council (1994). "NEHRP Recommended Provisions for the Development of Seismic Regulations for New Buildings." Washington, DC: Federal Emergency Management Agency.

Building Seismic Safety Council (1997). "NEHRP Recommended Provisions for the Development of Seismic Regulations for New Buildings." Washington, DC: Federal Emergency Management Agency.

Bruneau, M., Uang, C.M., and Whittaker, A. (1998). "Ductile design of steel structures", McGraw Hill.

Capozzi, V. (2009). "Comportamento sismico dei collegamenti nelle strutture prefabbricate." Doctoral dissertation, Università degli Studi di Napoli Federico II.

Chang, B. , Hutchinson, T. , and Englekirk, R. (2008). "Experimental seismic performance evaluation of innovative beam-column subassemblies." *Rep. SSRP 08/01*, Dept. of Structural Engineering, Univ. of California, San Diego.

Chang, G.A., and Mander, J.B., (1994). "Seismic Energy Based Fatigue Damage Analysis of Bridge Columns: Part 1 – Evaluation of Seismic Capacity," NCEER Technical Report No. NCEER-94-0006.

Chaudhuri, S. R., and Hutchinson, T. C. (2004). "Distribution of peak horizontal floor acceleration for estimating nonstructural element vulnerability." *Proc. of the 13th World Conference on Earthquake Engineering*, Vancouver, Canada, August 1-6.

Chen, M. C., Pantoli, E., Wang, X., Astroza, R., Ebrahimian, H., Hutchinson, T. C., Conte, J. P., Restrepo, J. I., Marin, C., Walsh, K., Bachman, R. E., Hoehler, M. S., Englekirk, R., and Faghihi, M. (2016) "Full-scale structural and nonstructural building system performance during earthquakes: Part I – specimen description, test protocol and structural response." *Earthquake Spectra*, 32(2), pp. 737-770.

Chen, M.C., Pantoli, E., Wang, X., Astroza, R., Ebrahimian, H., Mintz, S., Hutchinson, T. C., Conte, J. P., Restrepo, J. I., Meacham, B., Kim, J., and Park, H. (2013a). "BNCS Report #1: Full-scale structural and nonstructural building system performance during earthquakes and post-earthquake fire - specimen design, construction and test protocol." *Structural Systems Research Project Report Series, SSRP 13/9*, University of California San Diego, La Jolla, CA.

Chen, M. C., Pantoli, E., Wang, X., Mintz, S., Hutchinson, T. C., and Restrepo, J. I. (2013b). "BNCS Report #4: Full-scale structural and nonstructural building system performance during earthquakes and post-earthquake fire – construction details and technical specifications of specific subsystems." *Structural Systems Research Project Report Series, SSRP 13/12*, University of California San Diego, La Jolla, CA

Cheung, K. S. (2010). "Nonlinear Pushover Analysis of a One-Story Precast Concrete Cladding System." Master's Thesis, San Jose State University.

Craig, J.I., Leistikow, R., Fennell, C.J. (1988). "Experimental Studies of the Performance of Precast Concrete Cladding Connections." *Proc., 9th World Conference on Earthquake Engineering*, Tokyo-Kyoto, Japan, August 2-9, pp. 201-206.

Crosbie, M. J. (2005). "Curtain Walls." Birkhäuser Architecture.

Computer and Structures Inc. (2015). "CSI Analysis reference manual." Berkeley, CA.

Computer and Structures Inc. (2013). “CSI Analysis reference manual.” Berkeley, CA.

Department of Defense Tri-Services Seismic Design Committee, (1982) "Seismic Design for Buildings." *Technical Manual TM No. 5-809-10/NAVFAC P-355/ AFM 88-3*, Joint Departments of the Army, the Navy and the Air Force, U.S. Government Printing Office, Washington, D.C..

Di Croce, M., Di Ludovico, M., Di Sarno, L., Fico, R., Longo, A., Magliulo, G., Manfredi, G., and Prota, A. (2012). “Terremoto dell’Emilia: report preliminare sui danni registrati a Pieve di Cento (BO), Camposanto (MO), Medolla (MO) e Crevalcore (BO) in seguito agli eventi sismici del 20 e 29 maggio 2012 Rilievi e Verifiche di Agibilità del 30 e 31 maggio 2012.” Reluis.

Dowell, R. K., Smith, J. W., and Hutchinson, T. C. (2008). “Floor and attached component seismic amplification factors from nonlinear time-history analysis.” *Proc. of the 13th World Conference on Earthquake Engineering*, Vancouver, Canada, August 1-6.

Dowell, R. K., Seible, F., and Wilson, E. L. (1998). “Pivot hysteresis model for reinforced concrete members.” *Structural Journal*, 95(5), pp. 607-617.

Drake, R. M., and Bragagnolo, L. J. (2000). “Model code design force provisions for elements of structures and nonstructural components.” *Earthquake spectra*, 16(1), pp. 115-125.

EERI (2010). “The El Mayor-Cucapah, Baja California Earthquake April 4, 2010, An EERI Reconnaissance Report.” *Earthquake Engineering Research Institute*, Oakland, California.

Ercolino, M., Coppola, O., Petrone, C., and Magliulo G. (2012). “Report sui danni registrati a Mirandola (MO) in seguito all’evento sismico del 29 maggio 2012.” Reluis.

Ercolino, M., Coppola, O., Petrone, C., and Magliulo G. (2012). “Report sui danni registrati a San Felice sul Panaro (MO) in seguito agli eventi sismici del 20 e 29 maggio 2012.” Reluis.

FEMA E-74 (2011). “Reducing the Risks of Nonstructural Earthquake Damage: A Practical Guide.”

Fathali, S., and Lizundia, B. (2011). “Evaluation of current seismic design equations for nonstructural components in tall buildings using strong motion records.” *The Structural Design of Tall and Special Buildings*, 20(S1), pp. 30-46.

Fintel, M. (1986). “Performance of precast and prestressed concrete in Mexico earthquake.” Prestressed Concrete Institute, Chicago, IL.

Fouad, L. and Rathje, E. M. (2012), "RSPMatch09," Available at: <https://nees.org/resources/rpsmatch09>.

Gaiotti, R., Smith, B.S. (1992). “Stiffening of Moment-Resisting Frame by Precast Concrete Cladding.” *PCI Journal*, 37(5), pp. 180-92.

Ghosh S.K., and Cleland N.M. (2012). “Performance of Precast Concrete Building Structures.” *Earthquake Spectra*, 28(S1), pp. S349–S384.

Gjelvik, A. (1973). “Interaction between Frames and Precast Panel Walls.” *Journal of the Structural Division*, 100(ST2), pp. 405-426.

Goodno, B.J., E1-Gazairly, L., Hsu, C.C., and Craig, J.I. (1992). "Use of Advanced Cladding Systems for Passive Control of Building Response in Earthquakes." *Proc., 10th World Conference on Earthquake Engineering*, Madrid, Spain, July 19-24, pp. 4195-4200.

Goodno, B., Craig, J., and Zeevaert-Wolff, A. (1989). "The Mexico Earthquake of September 19, 1985-Behavior of Heavy Cladding Components." *Earthquake Spectra*, 5(1), pp. 195-222.

Goodno, B. J., and Palsson, H. (1986). "Analytical studies of building cladding." *Journal of structural engineering*, 112(4), pp. 665-676.

Goodno, B.J., Will, K.M., and Palsson, H. (1980). "Effect of Cladding on Building Response to Moderate Ground Motion." *Proc., 7th World Conference on Earthquake Engineering*, Istanbul, Turkey, September 8-13, pp. 449-456.

Henry, R. M., and Roll, F. (1986). "Cladding-frame interaction." *Journal of Structural Engineering*, 112(4), pp. 815-834.

Henry, R.M., Goodspeed, C.H., and Calvin, D.L. (1989). "A Simplified Box-Frame Model for Structural Cladding Panels." *Proc., Architectural Precast Concrete Cladding - Its Contribution to Lateral Resistance of Buildings*, Chicago, IL, November 8-9, pp. 62-79.

Hobelmann, J.P., Schachter, M., and Cooper, M.C. (2012). "Architectural precast concrete panel systems used for lateral-force resistance." *PCI journal*, 57(1), pp. 124-134.

Horii, S., Oka, S., Inukai, M., Kohno, K., Sakamoto, I., and Seike, T. (1995). "A report on the damages of precast concrete curtain walls by the 1995 hyogo-ken nanbu earthquake." PCSA, Tokyo, Japan.

Horne, J. P., and Burton, H. (2003). "Investigation of code seismic force levels for hospital equipment. In Proceedings of Seminar on Seismic Design, Retrofit, and Performance of Non-structural Components." ATC-29, Vol. 2.

Hutchinson, T.C., Pantoli, E., McMullin, K. M., Hildebrand, M., and Underwood, G. (2014). "Seismic Drift Compatibility of Architectural Precast Concrete Panels and Connections: A Design Guide for Engineers." *Structural Systems Research Project Report Series, SSRP 14/16*. University of California San Diego, La Jolla, CA.

Hutchinson T., Restrepo J., Conte J., and Meacham B. (2013). "Overview of the building nonstructural components and systems (BNCS) project." *Proc. ASCE Structures Congress*, Pittsburgh, PA, May 2-4, pp.1485-1498.

International Conference of Building Officials (1927). "1927 Uniform Building Code." Whittier, CA.

International Conference of Building Officials (1935). "1935 Uniform Building Code." Whittier, CA.

International Conference of Building Officials (1988). "1988 Uniform Building Code." Whittier, CA.

Igusa, T., and Der Kiureghian, A. (1985). "Dynamic characterization of two-degree-of-freedom equipment-structure systems." *Journal of engineering mechanics*, 111(1), pp. 1-19.

International Code Council (2012). "2012 International building code." Country Club Hills: ICC, IL.

Iverson, J.K., and Hawkins, N.M. (1994). "Performance of Precast/Prestressed Concrete Building Structures During Northridge Earthquake." *PCI Journal*, 39(2), pp. 38-55.

Kehoe, B. (2014).”Defining rigid vs. flexible nonstructural components.” *Proceeding 10th US national conferences on earthquake engineering*, Anchorage, Alaska, July 21-25.

Kehoe, B., and Freeman, S.A., (1998). “A critique of procedures for calculating seismic design forces for nonstructural elements.” ATC 29-1.

Kelly, J.M. (1982). "The Influence of Base Isolation on the Seismic Response of Light Secondary Equipment." Report No. UCB/EERC-81/17, Earthquake Engineering Research Center, University of California, Berkeley, CA.

Kemeny, Z.A., and Lorant, J. (1989). “Energy Dissipating Elastomeric Connections.” *Proc., Architectural Precast Concrete Cladding - Its Contribution to Lateral Resistance of Buildings*, Chicago, IL, November 8-9, pp. 287-199.

Kim, J.K., Meacham, B.J. and Park., H. (2013). “Full-Scale Structural and Nonstructural Building System Performance during Earthquakes and Post-Earthquake Fire: Fire Test Program and Preliminary Outcomes.” Worcester Polytechnic Institute, Worcester, MA.

Lepage, A., Shoemaker, J. M., and Memari, A. M. (2012). “Accelerations of nonstructural components during nonlinear seismic response of multistory structures*.” Journal of Architectural Engineering*, 18(4), pp. 285-297.

Magliulo, G., Ercolino, M., Petrone, C., Coppola, O., and Manfredi, G. (2013). “The Emilia earthquake: the seismic performance of precast RC buildings.” *Earthquake Spectra*, 30(2), pp. 891-912.

Mandelli Contegni, M., Palermo, A., and Toniolo, G. (2007). “Strutture prefabbricate: schedario dei collegamenti.” Available at <http://www.reluis.it/>

Maneetes, H., and Memari, A. M. (2009). “Finite element modeling of reinforced concrete cladding panels.” *Electronic Journal of Structural Engineering*, 9, pp. 62-72.

McMullin, K. M. (2014). “Experimental testing of coil rod under flexural loading for push-pull connections on architectural precast concrete.” Report to the Charles Pankow Foundation.

McMullin, K. M., Ortiz, M., Patel, L., Yarra, S., Kishimoto, T., Stewart, C., and Steed, B. (2012). “Response of Exterior Precast Concrete Cladding Panels in NEES-TIPS/NEESGC/E-Defense Tests on a Full Scale 5-Story Building.” *Proc., 2012 ASCE Structures Congress*, Chicago, IL, May 29-31, pp. 1069-1079.

McMullin, K., Wong, Y., Choi, C., Chan, K. (2004). “Seismic performance of precast concrete cladding connection.” *Proc., 13th World Conference on Earthquake Engineering,* Vancouver, Canada, August 1-6.

Medina, R. A., Sankaranarayanan, R., and Kingston, K. M. (2006). “Floor response spectra for light components mounted on regular moment-resisting frame structures.” *Engineering structures*, 28(14), pp. 1927-1940.

Memari, A. M., Maneetes, H., Bozorgnia, Y. (2004). “Study of the effect of near-source vertical ground motion on seismic design of precast concrete cladding panels.” *Journal of architectural engineering*, 10(4), pp. 167-184.

Merrick, D., McMullin, K., Hildebrand, M., and Kwong, A. (2003). “In-Situ Vibration Characteristics of Precast Cladding Panels.” *Proc., ASCE Structure Congress*, Seattle, WA, May 29-June 1.

Meyyappa, M., Goodno, B. J., Fennell, C. J. (1988). "Modeling and Performance of Precast Cladding Connections." *Proc., Computing in Civil Engineering: Microcomputers to Supercomputers*, Alexandria, VA, March 29-31, pp. 208-218.

Miranda, E., and Taghavi, S. (2005). "Approximate floor acceleration demands in multistory buildings. I: Formulation." *Journal of structural engineering*, 131(2), pp. 203-211.

Miranda, E., and Taghavi, S. (2009). "A comprehensive study of floor acceleration demands in multi-story buildings." *Proc. ATC/SEI 2009 Conference on Improving the Seismic Performance of Existing Buildings and Other Structures*, San Francisco, CA, December 9-11, pp. 616-626.

Miyamoto International (2009). "L'Aquila, Italy, Earthquake Field Investigation Report." West Sacramento, CA.

Mohammadi, M. E. (2014). "Inelastic Analysis of Seismic Loading of Precast Concrete Cladding Using Commercially Available Software." Master's Thesis, San Jose State University.

Murray, S. C. (2009). "Contemporary Curtain Wall Architect." Princeton Architectural Press.

NEES Ground Motion Database. Available at: http://ngawest2.berkeley.edu

New Zealand Standard NZS 3101: Part 1 (1995), "Code of practice for the design of concrete structures", New Zealand Standards Association, Wellington, New Zealand

Nilson, A. H., Darwin, D., and William, C.D. (2004). "Design of concrete structures", McGraw-Hill Higher Education.

NZNSEE- New Zealand National Society for Earthquake Engineering (2007). "Architectural Design for Earthquake: A Guide to the Design of Non-structural Elements." NZNSEE, Wellington, New Zealand.

Pall, A.S. (1989). "Friction-Damped Connections for Precast Concrete Cladding." *Proc., Architectural Precast Concrete Cladding - Its Contribution to Lateral Resistance of Buildings*, Chicago, IL, November 8-9, pp. 300-309.

Pantoli, E., Hutchinson, T. C., McMullin, K. M., Underwood, G. A., and Hildebrand, M. J., 2016. "Seismic-drift-compatible design of architectural precast concrete cladding: Tieback connections and corner joints." *PCI Journal*, July-August, 38-52.

Pantoli, E., Chen, M. C., Wang, X., Astroza, R., Ebrahimian, H., Hutchinson, T. C., Conte, J. P., Restrepo, J. I., Marin, C., Walsh, K., Bachman, R. E., Hoehler, M. S., Englekirk, R., and Faghihi, M. (2016). "Full-scale structural and nonstructural building system performance during earthquakes: part II – NCS damage states." *Earthquake Spectra*, 32(2), pp. 771-794.

Pantoli, E., and Hutchinson T. C., 2015. "Experimental and Analytical Study of the Dynamic Characteristics of Architectural Precast Concrete Cladding." *Proceedings, ACT-SEI, 2nd conference on improving the seismic performance of existing buildings and other structures*, December 10-12, San Francisco, CA.

Pantoli, E., Hutchinson, T., Underwood, G. A., and Hildebrand M., (2014). "Seismic behavior of sliding push-pull connections in architectural precast concrete panels." *Proc. Façade Tectonics Conference*, January 9-12, Los Angeles, CA.

Pantoli, E., Chen, M., Wang, X., Astroza, R., Mintz, S., Ebrahimian, H., Hutchinson, T., Conte, J. P., Restrepo, J. I., Kim, J., Park, H., and Meacham (2013a). "BNCS report #2: full-scale structural and nonstructural building system performance during earthquakes and post-earthquake fire – test results." *Structural Systems Research Project Report Series, SSRP 13/10*, University of California San Diego, La Jolla, CA.

Pantoli, E., Chen, M., Hutchinson, T., and Restrepo, J. (2013b). "BNCS Report #3: Full-scale structural and nonstructural building system performance during earthquakes and post-earthquake fire – camera and analog sensor details." *Structural Systems Research Project Report Series, SSRP 13/11*, University of California San Diego, La Jolla, CA.

Pantoli, E., Chen, M., Hutchinson, T., Underwood, G. A., and Hildebrand M. (2013c). "Shake table testing of a full-scale five-story building: seismic performance of precast concrete cladding panels." *Proc., Compdyn*, Kos Island, Greece, June12–14.

Pantoli, E., Hutchinson, T., Underwood, G. A., and Hildebrand M. (2013d). "Shake table testing of a full-scale five-story building: seismic performance of precast concrete cladding panels." *Proc., PCI convention*, Grapevine, TX, September 21-24.

Park, R., and Pauley, T. (1975). "Reinforced concrete structures." John Wiley & Sons.

Paulay, T., and Priestley, M.J.N. (1992). "Seismic design of reinforced concrete and masonry buildings". Wiley.

PCI-Precast/Prestressed Concrete Institute, PCI MNL 120 (2010). "PCI Design Handbook-Precast and Prestressed Concrete." PCI, Chicago, IL.

PCI-Precast/Prestressed Concrete Institute, PCI MNL 122 (2007). "PCI Architectural precast concrete manual," PCI, Chicago, IL.

PCI-Precast/Prestressed Concrete Institute. "Discover the freedom of precast concrete." PCI, Chicago, IL.

Pinelli, J. P., Craig, J. I., and Goodno, B. J. (1995). "Energy-based seismic design of ductile cladding systems." *Journal of Structural Engineering*, 121(3), pp. 567-578.

Pinelli, J.P., Craig, J.I., Goodno, B.J., and Hsu, C.C. (1993). "Passive Control of Building Response Using Energy Dissipating Cladding Connections." *Earthquake Spectra*, 9(3), pp. 529-546.

Pinelli, J.P., and Craig, J.I. (1989). "Experimental Studies on the Performance of Mexican Precast Cladding Connections." *Proc., Architectural Precast Concrete Cladding - Its Contribution to Lateral Resistance of Buildings*, Chicago, IL, November 8-9, 159-176.

Prefabbricazione.web 2014a <http://www.prefabbricazione-web.it/Notizia/3928/Soluzioni_per_la_prefabbricazione:_la_staffa_per_pannelli_orizzontali___EDIL_P.O..html>

Prefabbricazione.web 2014b <http://www.prefabbricazione-web.it/Notizia/3167/Staffa_per_pannelli_verticali___EDIL_P.V..html>

Priestley, M.J.N., 2003. "Myths and fallacies in earthquake engineering." IUSS press, Padova, Italy.

Qu, B., Goel, R. K., and Chadwell, C. B. (2014). "Evaluation of ASCE/SEI 7 provisions for determination of seismic demands on nonstructural components." *Proc. Tenth U.S. National Conference on Earthquake Engineering*, Anchorage, (AK), July 21-25.

Raths C.H. and Mulholland G.R. (1989). "Non-load bearing precast concrete panel shear wall type behavior", *Proc., Architectural Precast Concrete Cladding - Its Contribution to Lateral Resistance of Buildings*, Chicago, IL, November 8-9, pp. 217-230.

Rihal, S.S. (1988). "Earthquake Resistance and Behavior of Heavy Facades/Claddings and Connections in Medium-Rise Steel-Framed Buildings." *Proc., 9th World Conference on Earthquake Engineering*, Tokyo-Kyoto, Japan, August 2-9, pp.207-212.

Rodriguez, M. E., Restrepo, J. I., and Carr, A. J. (2002). "Earthquake-induced floor horizontal accelerations in buildings." *Earthquake engineering and structural dynamics,* 31(3), pp. 693-718.

Sack, R.L., Beers, R.J., and Thomas, D.L. (1989). "Seismic Behavior of Architectural Precast Concrete Cladding." *Proc., Architectural Precast Concrete Cladding - Its Contribution to Lateral Resistance of Buildings*, Chicago, IL, November 8-9, pp. 141-158.

Sielaff, B. J., Nielsen, R. J., and Schmeckpeper, E. R. (2005). "Evolution of design Code requirements for exterior elements and connections." *Earthquake Spectra*, 21(1), pp. 213-224.

Singh, M. P., Moreschi, L. M., Suárez, L. E., and Matheu, E. E. (2006a). "Seismic design forces. I: Rigid nonstructural components." *Journal of structural engineering*, 132(10), pp. 1524-1532.

Singh, M. P., Moreschi, L. M., Suárez, L. E., and Matheu, E. E. (2006b). "Seismic design forces. II: Flexible nonstructural components." *Journal of structural engineering*, 132(10), pp. 1533-1542.

Soong, T. (1995). "Seismic behavior of nonstructural elements- state-of-the-art report." *Proc. 10th European Conference on Earthquake Engineering*, Vienna, Austria, August 28-September 2.

Soong T, Chen G, Wu Z, Zhang R-H, and Grigoriu M. (1993). "Assessment of the 1991 NEHRP Provisions for Nonstructural Components and Recommended Provisions." National Center for Earthquake Engineering Research, Technical Report NCEER-93-0003.

Taly, N. (1988). "The Whittier Narrows, California Earthquake of October 1, 1987 - Performance of Building at California State University, Los Angeles." *Earthquake Spectra*, 4(2), pp. 277-317.

Thiel, C.C., Elsesser, E., Lindsay, J., Kelly, T., Bertero, V.V., Filippou, F., McCann, R. (1986). "Seismic Energy Absorbing Cladding System A Feasibility Study*." Proc., ATC-17 Seminar and Workshop on Base Isolation and Passive Energy Dissipation*, San Francisco, CA, March 12-14, pp. 251-260.

Toniolo, G., and Colombo, A. (2012). "Precast concrete structures: the lessons learned from the L'Aquila earthquake." *Structural Concrete*, 13(2), pp. 73-83.

SteelConstruction. "Inflill walling." *SteelConstruction.info* ,, Available at: <http://www.steelconstruction.info/Infill_walling> (January 2016)

Uchida, N., Aoygai, T., Kawamura, M., and Nakagawa, K. (1973). "Vibration test of steel frame having precast concrete panels." *Proc., 5th World Conference on Earthquake Engineering*, Rome, Italy, June 25-29, pp. 1167-1177.

Vigener, N., and Brown, M. A. (2012). "Building design envelope – curtain walls." *Whole Building Design Guide*, <http://www.wbdg.org/design/env_fenestration_cw.php> (January 2014).

Villaverde, R. (2009). "Fundamental concepts of earthquake engineering." CRC press, Tylor & Francis Group, Boca Raton, Florida.

Villaverde, R. (1997). "Seismic design of secondary structures: state of the art." *Journal of structural engineering*, 123(8), pp. 1011-1019.

Wang, X., Astroza, R., Huchinson, T., Conte, J., and Bachman, R. (2014). "Seismic Demands on Acceleration-Sensitive Nonstructural Components Using Recorded Building Response Data–Case Study." Proc. Tenth US National Conference on Earthquake Engineering, Anchorage, AK, July 21-25.

Wang, M. L. (1987). "Cladding performance on a full scale test frame." *Earthquake spectra*, 3(1), pp. 119-173.

Wieser, J., Pekcan, G., Zaghi, A. E., Itani, A., and Maragakis, M. (2013). "Floor accelerations in yielding special moment resisting frame structures." *Earthquake Spectra*, 29(3), pp. 987-1002.

Appendix A

Input Ground Motions Used in Parametric Analysis

Eighteen ground motions were selected from the NEES Ground Motion Database to be used in the parametric analysis in Chapter 7 and 8. These motions were scaled to match the 42-year return period spectrum in Chapter 7 and the design spectrum in Chapter 8. This appendix presents detailed information on the original motions, and information about the scaled motions more detailed than what is presented in the respective chapters. Since these motions were selected from a strike-slip fault, reverse fault, and six from normal fault generated earthquake, it is decided to present separate results for each of these cases. It is noted that this is done only for clarity.

A.1 Original motions

General information about these motions is presented in Table 7.7. The time history of the original ground acceleration, velocities and displacements is shown in Figure A.1,Figure A.2, and Figure A.3, while Figure A.4 presents the pseudo acceleration, pseudo velocity and displacement spectra for these same motions. Table A.1 shows the values of PGA, S_s and S_1 for these motions.

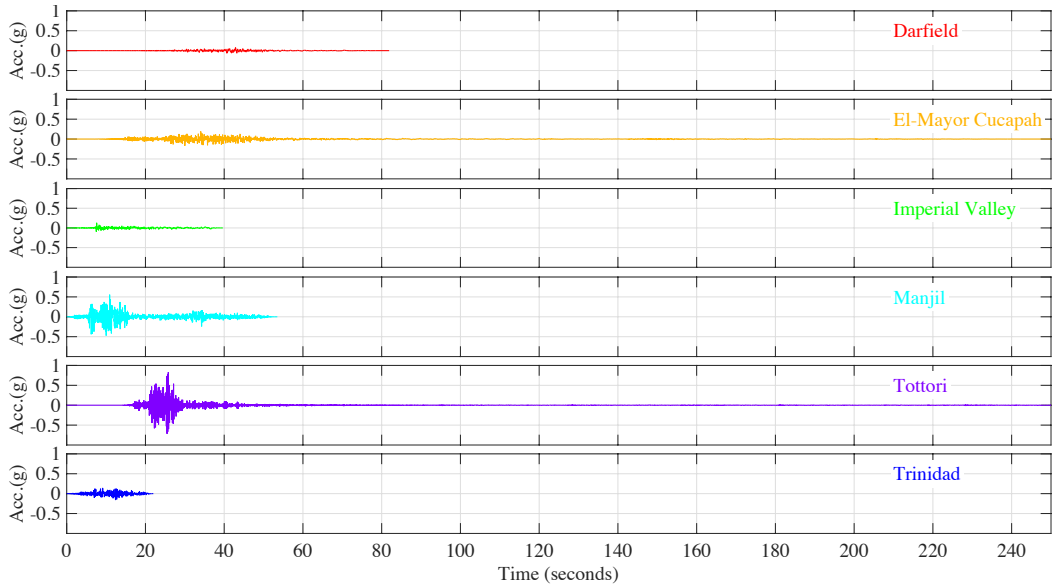

Figure A.1. Acceleration of the un-scaled motions from strike-slip fault generated motions

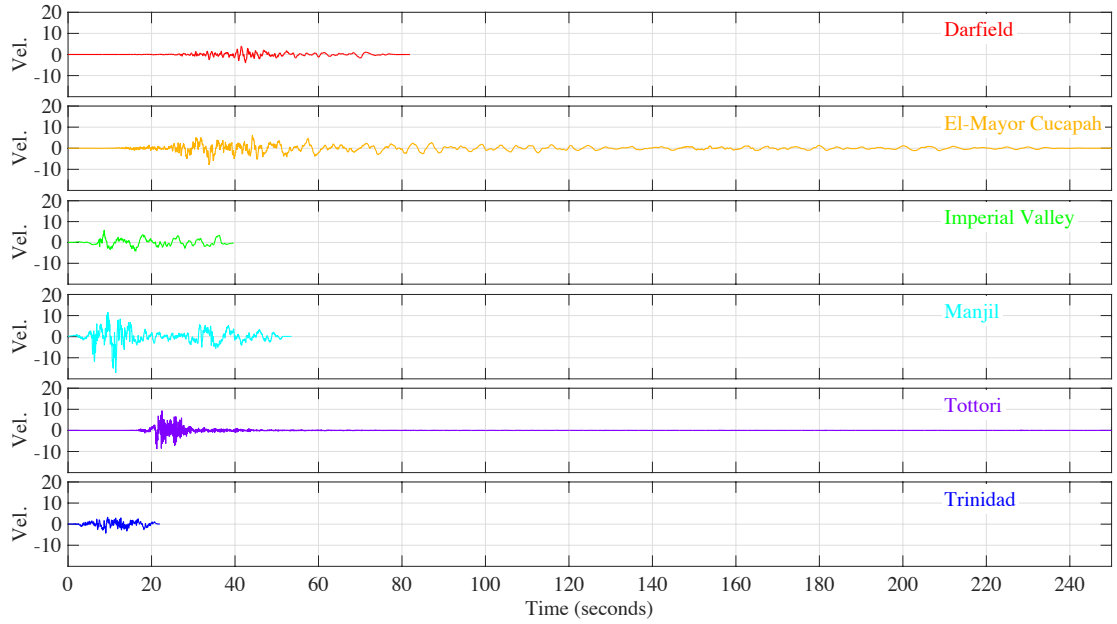

Figure A.2.Velocities of the un-scaled motions from strike-slip fault generated earthquakes (Units: inch/sec)

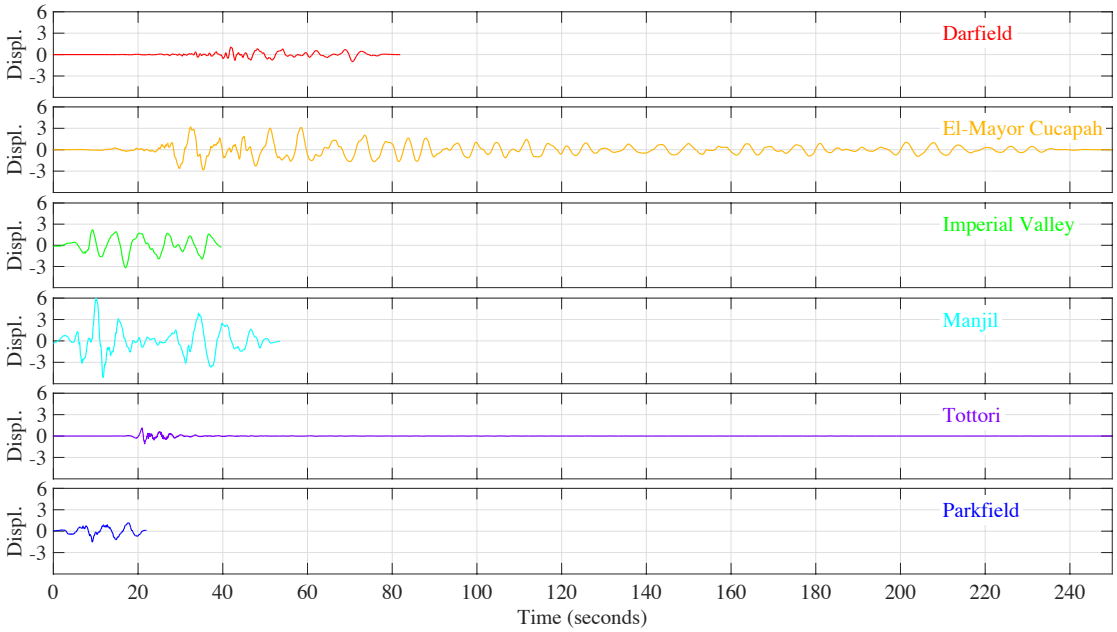

Figure A.3. Displacements of the un-scaled motions from strike-slip fault generated earthquakes (Units: inch)

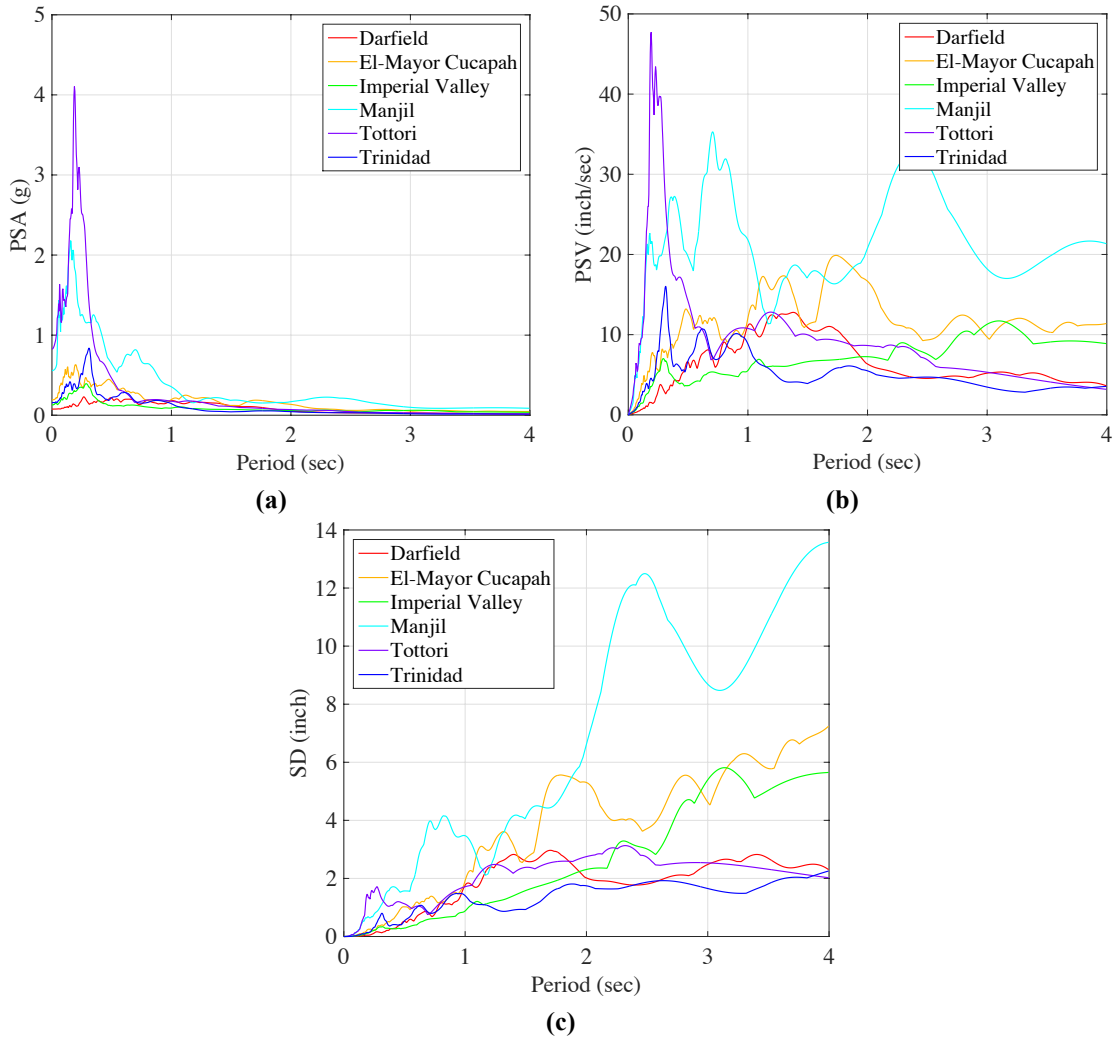

Figure A.4. (a) pseudo acceleration, (b) pseudo velocity, and (c) displacement spectrum for the original motions from strike-slip fault originated motions

Table A.1. Values of PGA, S_s and S_1 for the original strike-slip fault motions

Earthquake	PGA	S_s	S1
Darfield	0.076	0.118	0.180
El-Mayor Cucapah	0.192	0.631	0.196
Imperal Valley	0.128	0.296	0.089
Manjil	0.557	1.747	0.354
Tottori	0.828	3.500	0.175
Trinidad 1980	0.156	0.351	0.143

The time history of the original motions from reverse fault in terms of ground acceleration, velocity and displacement are presented in Figure A.5, Figure A.6, and Figure A.7. For these same motions, Figure A.8 present the pseudo acceleration, velocity and displacement spectra, while Table A.2 presents a summary of the PGA, S_s and S1 of the original motions.

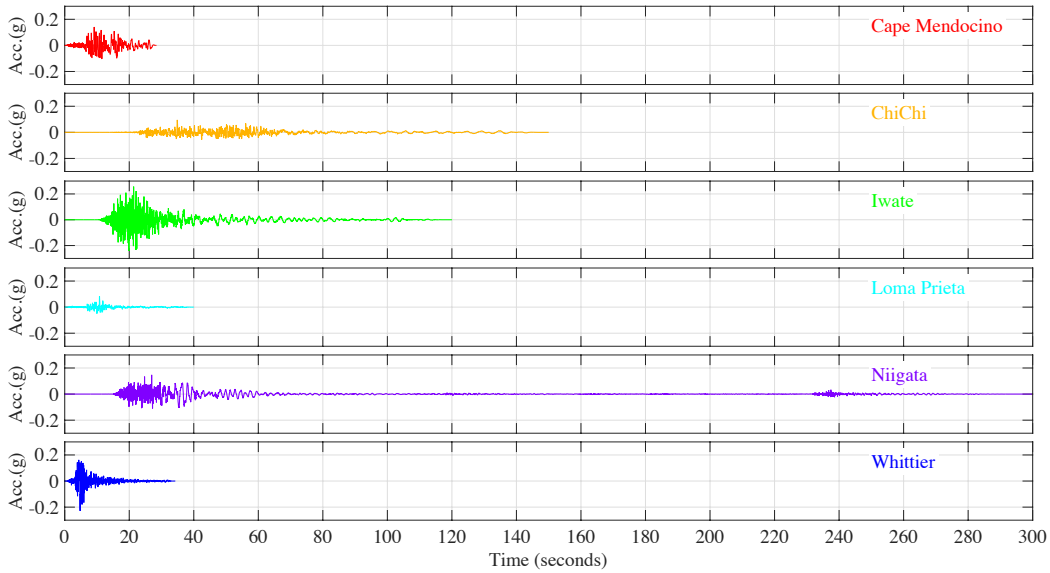

Figure A.5. Time history of accelerations for the original reverse fault motions selected

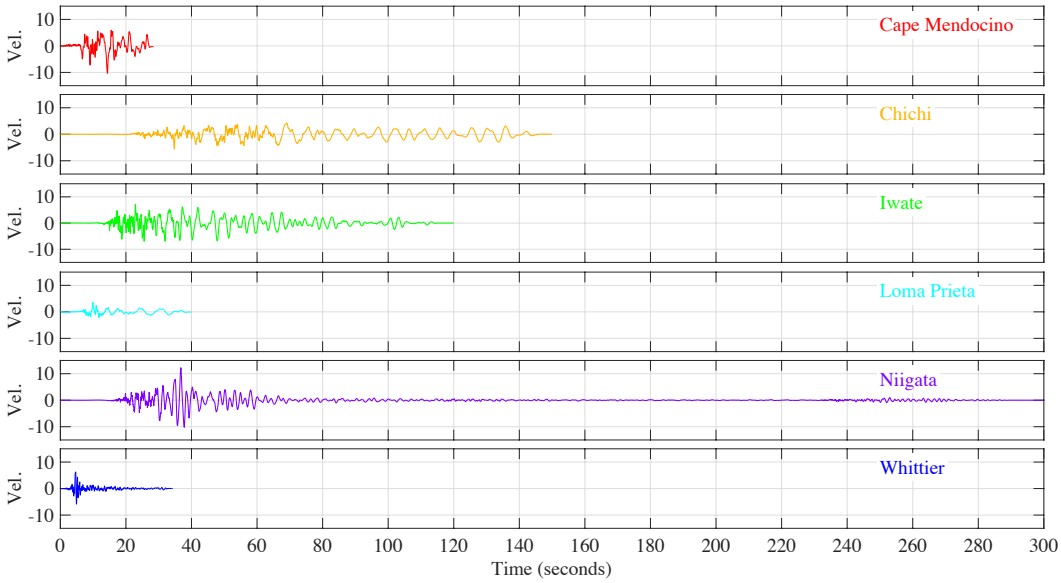

Figure A.6. Time history of original velocities for the reverse fault generated motions (Units: inch/sec)

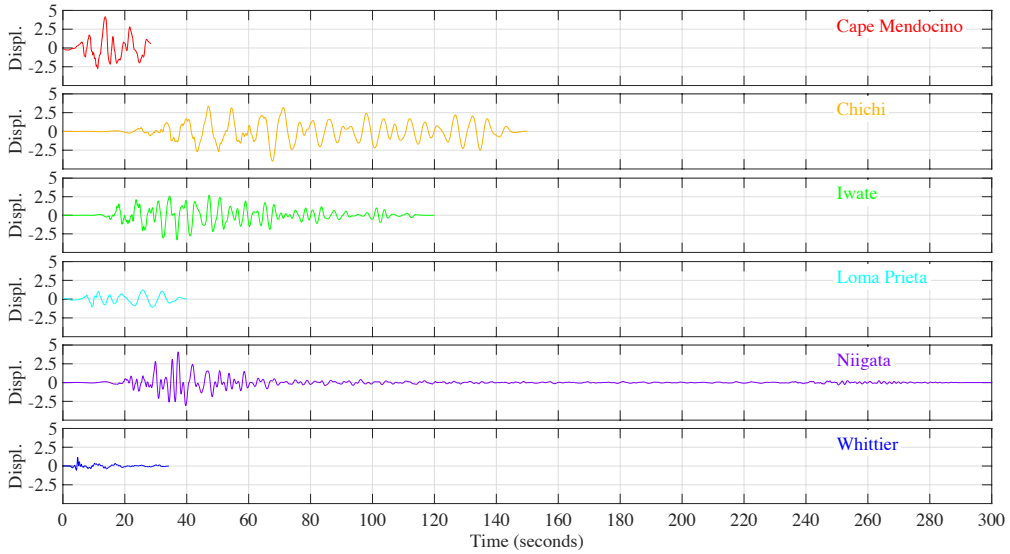

Figure A.7. Time history of original displacement for the reverse fault generated motions selected (Units: inch)

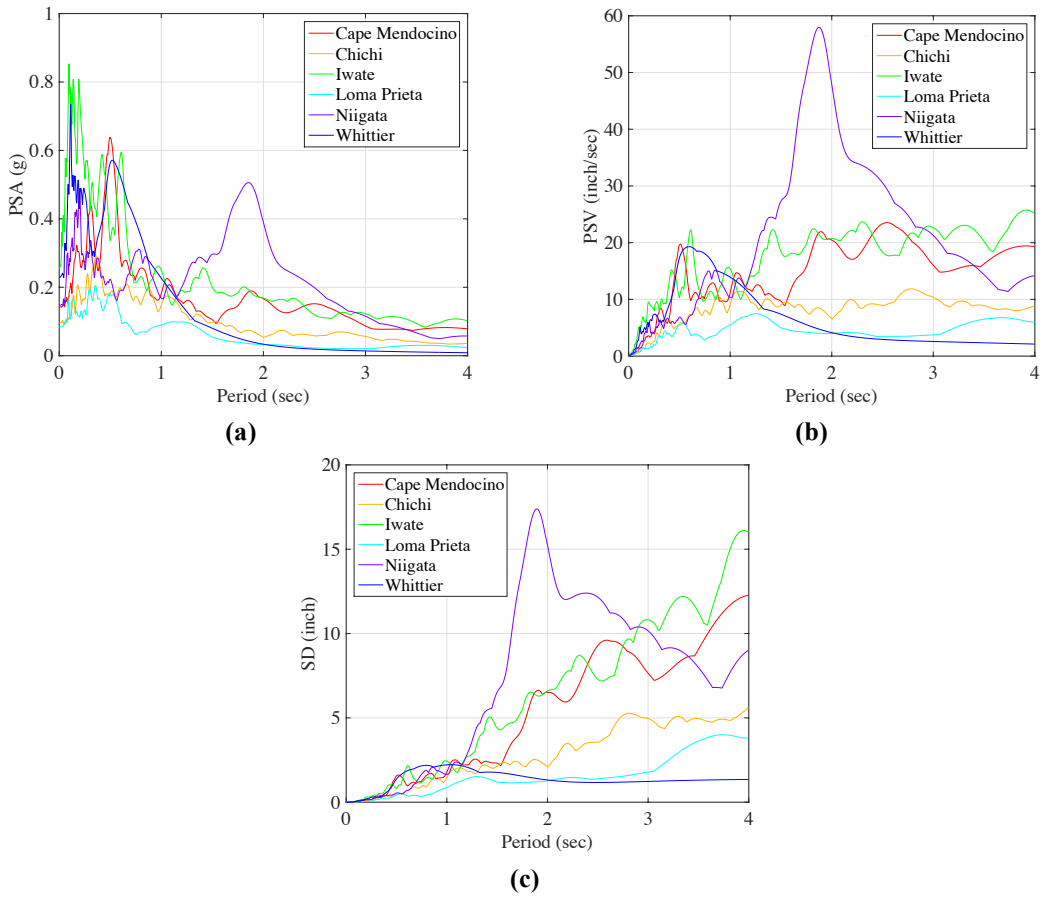

Figure A.8. (a) pseudo acceleration, (b) pseudo velocity, and (c) displacement spectrum for the original motions from reverse fault originated earthquakes

Table A.2. Values of PGA, S_s and S_1 for the original reverse fault motions

Earthquake	PGA	S_s	S_1
Cape Mendocino	0.1411	0.288	0.182
Chichi	0.095	0.185	0.147
Iwate	0.257	0.761	0.250
Loma Prieta	0.083	0.112	0.089
Niigata	0.147	0.481	0.168
Whittier	0.229	0.446	0.226

The time history of the original motions from reverse fault in terms of ground acceleration, velocity and displacement are presented in Figure A.9, Figure A.10, and Figure A.11. For these same motions, Figure A.12 present the pseudo acceleration, velocity and displacement spectra, while Table A.3 presents a summary of the PGA, S_s and S1 of the original motions.

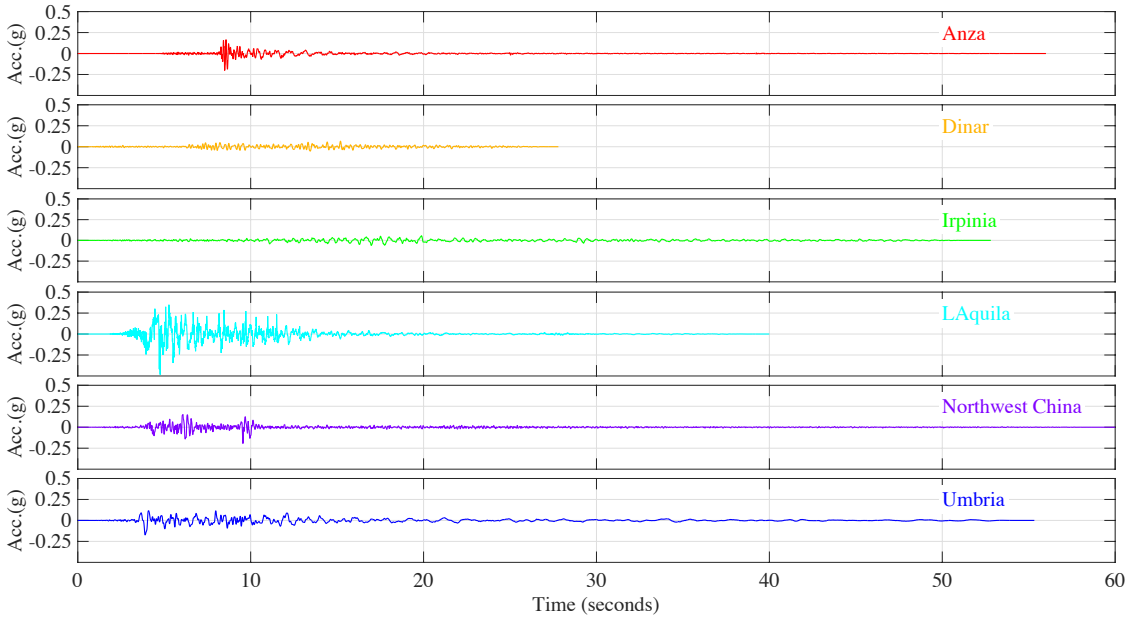

Figure A.9. Time history of original accelerations for the normal fault generated motions

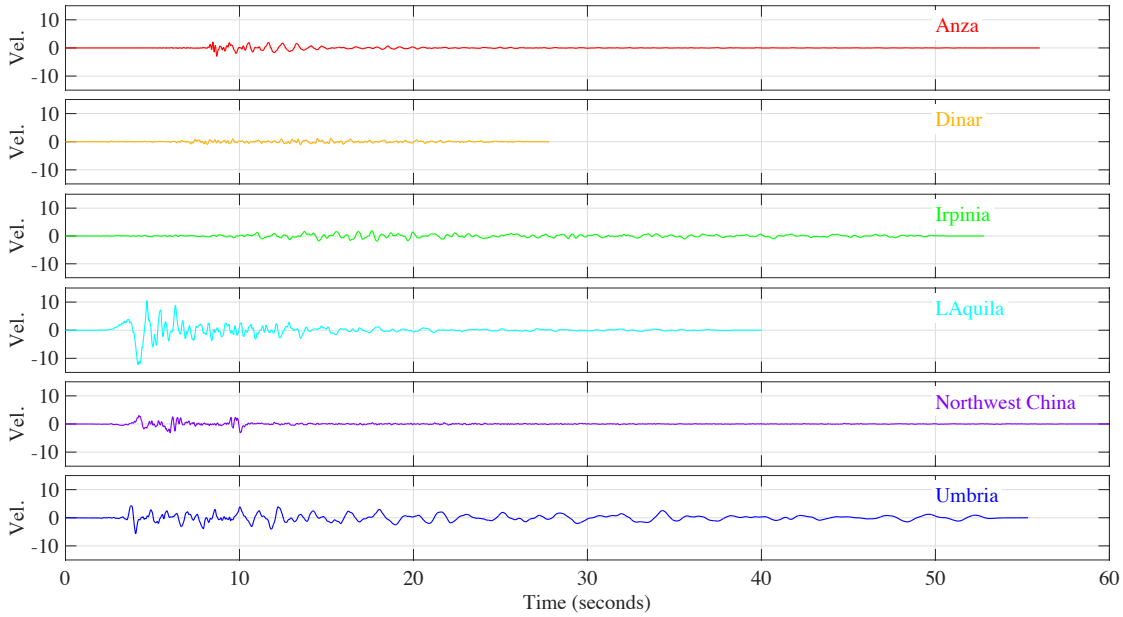

Figure A.10. Time history of original velocity for the normal fault generated motions (Units: inch/sec)

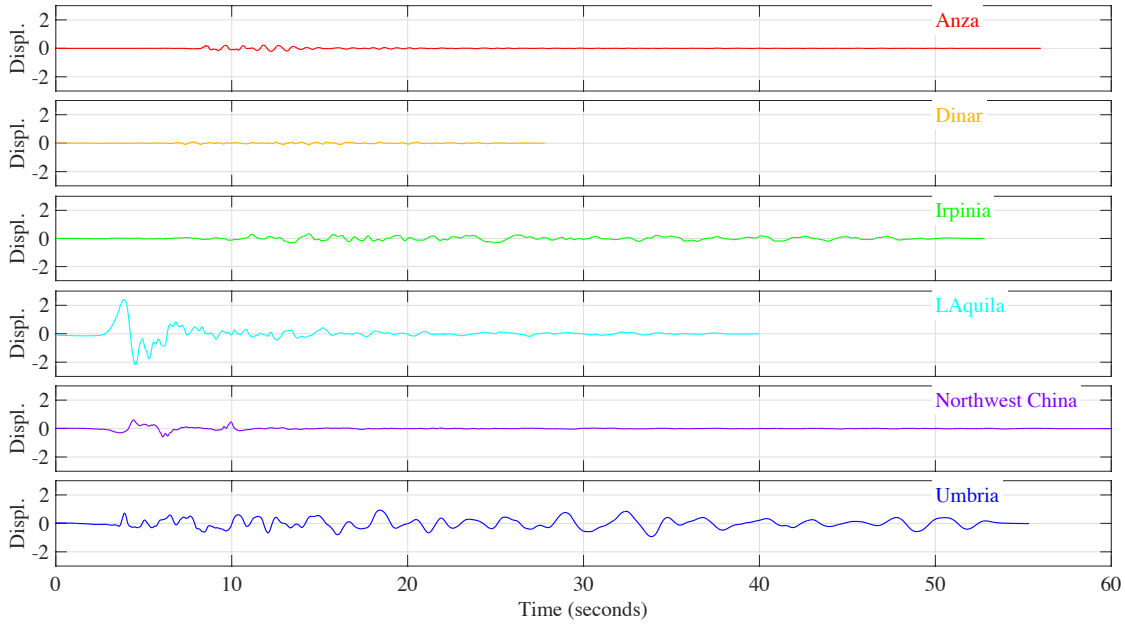

Figure A.11. Time history of original displacement for the normal fault generated motions (Units: inch)

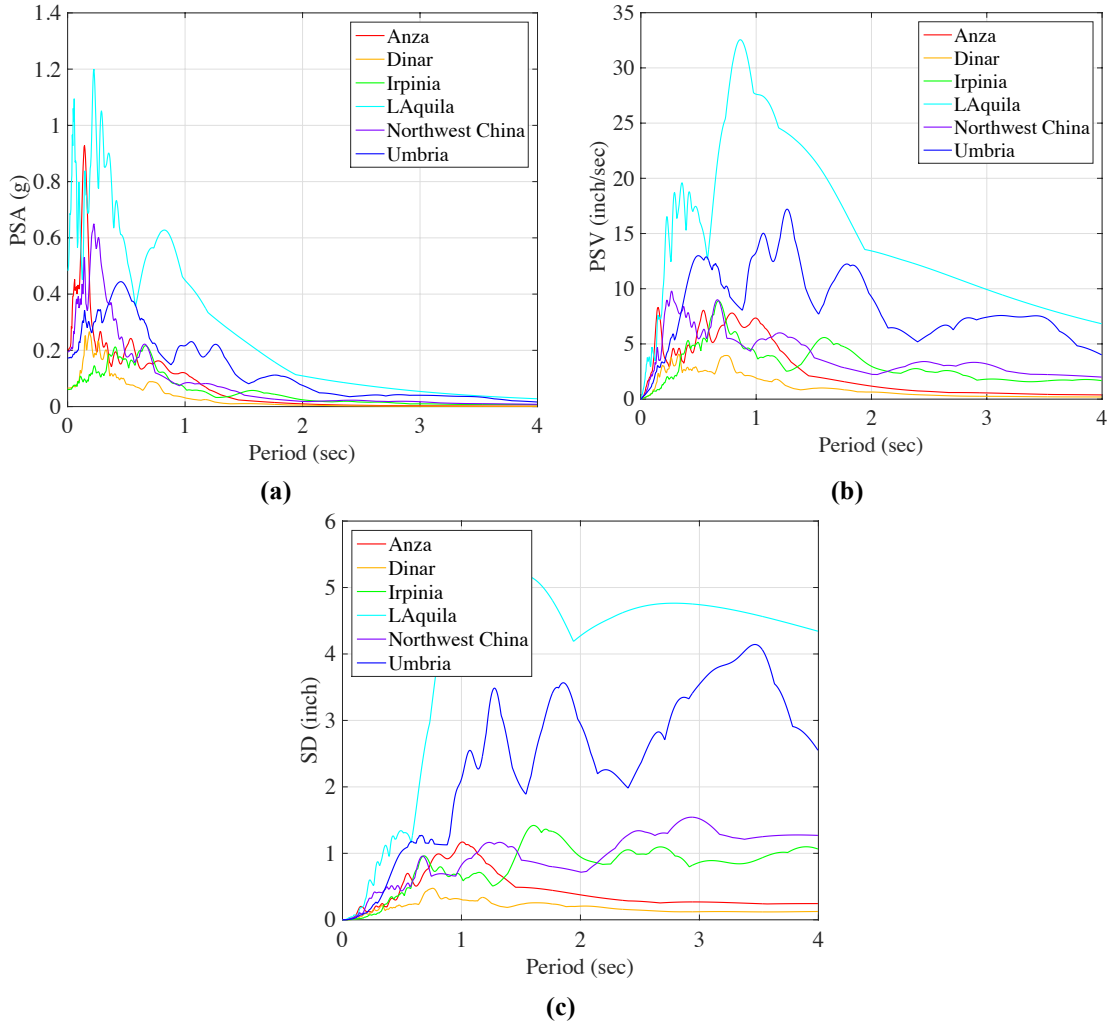

Figure A.12. (a) pseudo acceleration, (b) pseudo velocity, and (c) displacement spectrum for the original motions from normal fault originated earthquakes

Table A.3. Values of PGA, S_s and S_1 for the original normal fault motions

Earthquake	PGA	S_s	S_1
Anza	0.202	0.323	0.119
Dinar	0.065	0.243	0.031
Irpinia	0.060	0.119	0.065
L'Aquila	0.483	0.89	0.449
Northwest China	0.194	0.569	0.084
Umbria	0.173	0.266	0.216

A.2 Motions Scaled to Service Level (Chapter 7)

Figure A.13,Figure A.14, and Figure A.15 present the time history of accelerations, velocities and displacements for the matched motions from a strike slip fault, while Figure A.16 shows the pseudo acceleration, pseudo velocity and displacement spectra for the same motions. The values of the relevant ground parameters (PGA, S_s, S_1) and peak structural response were already presented in Table 7.7. The time history of the matched motions from reverse fault in terms of ground acceleration, velocity and displacement are presented in Figure A.17, Figure A.18, and Figure A.19. For these same motions, Figure A.20 presents the pseudo acceleration, velocity and displacement spectra.

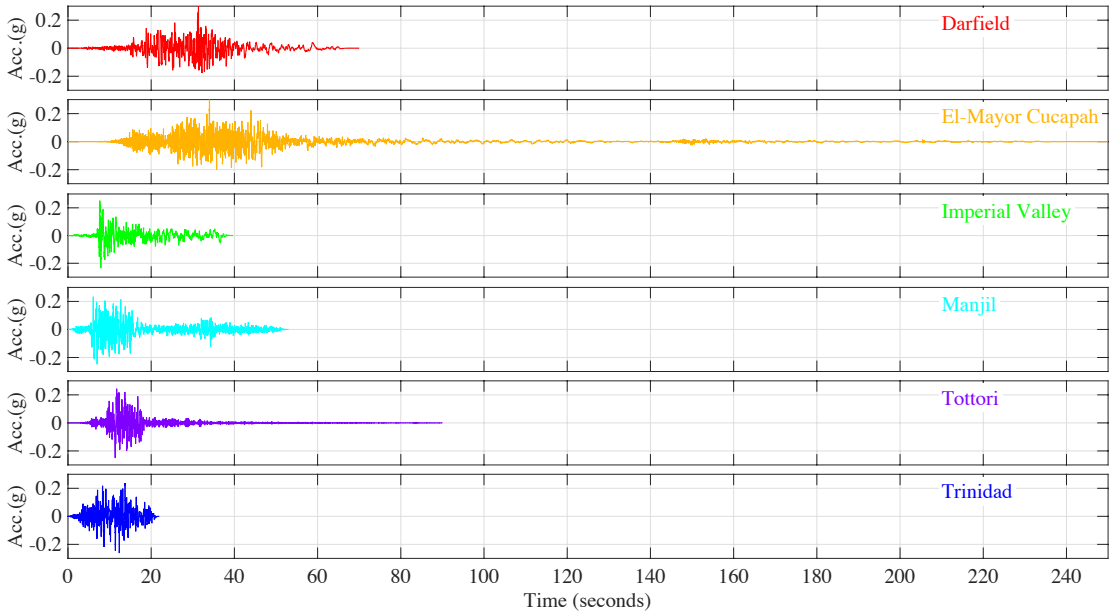

Figure A.13. Acceleration of the scaled motions from strike-slip fault generated earthquakes

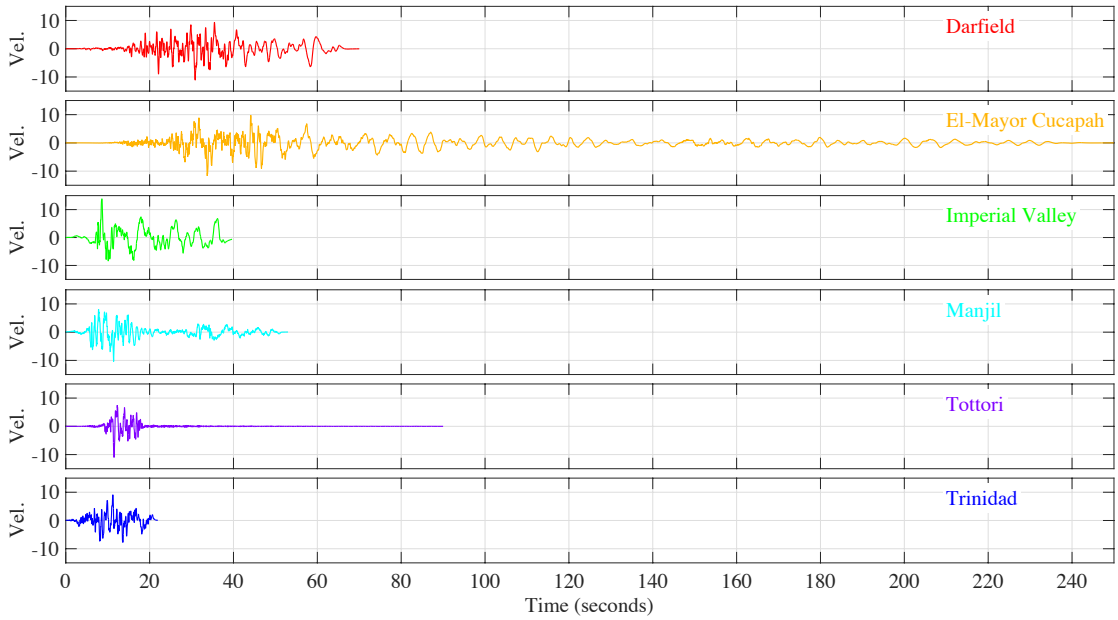

Figure A.14. Velocities of the scaled motions from strike-slip fault generated earthquakes (Units: inch/sec)

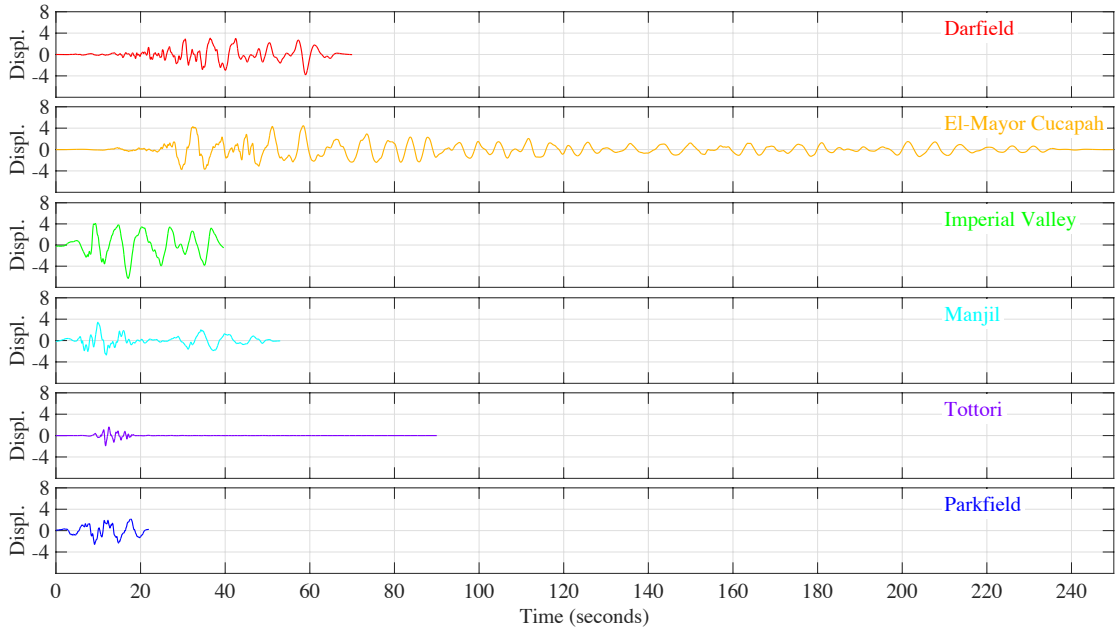

Figure A.15. Displacements of the scaled motions from strike-slip fault generated earthquakes (Units: inch)

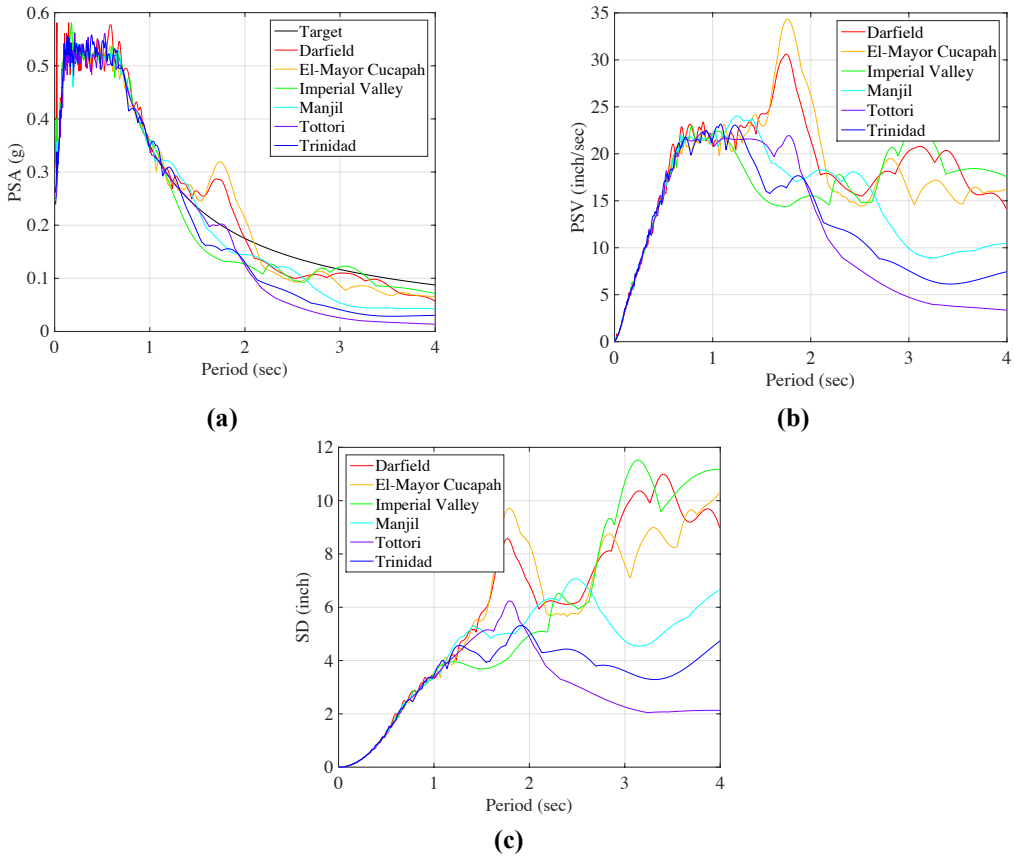

Figure A.16. (a) pseudo acceleration, (b) pseudo velocity, and (c) displacement spectrum for the motions from strike-slip fault originated earthquakes matched to the 42-year return spectrum

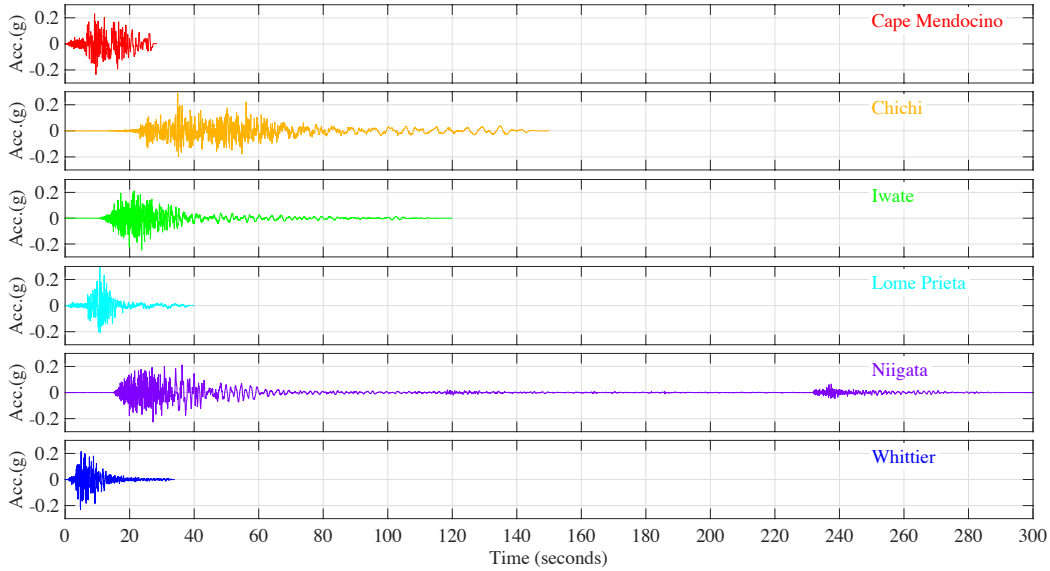

Figure A.17. Time history of acceleration for the motions from reverse fault matched to the 42 year return period earthquake

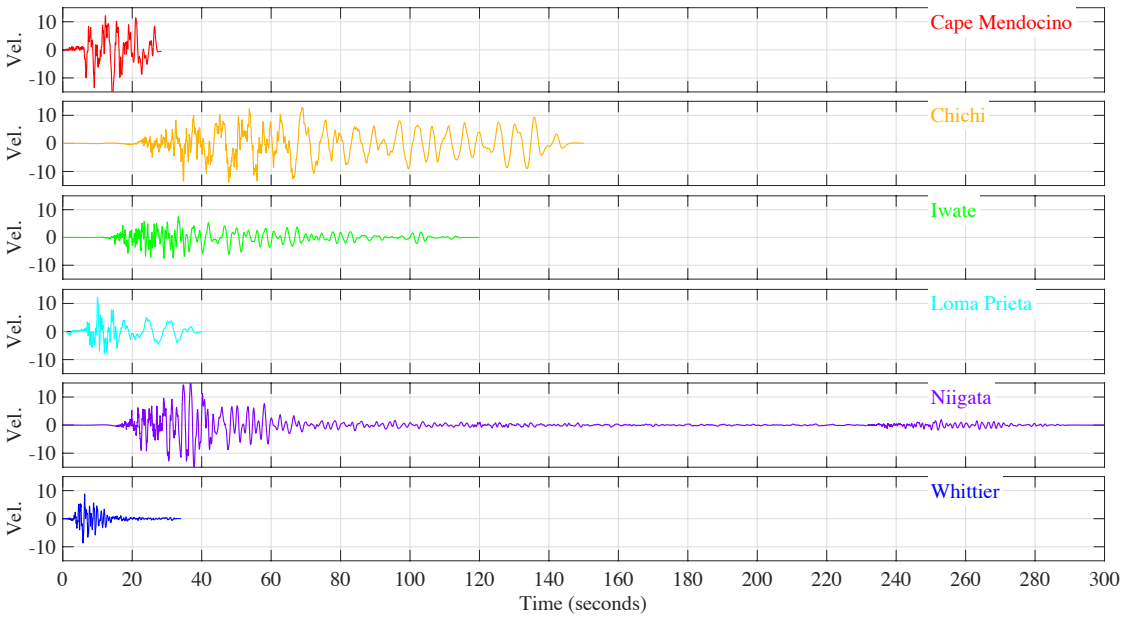

Figure A.18. Time history of velocities for the motions from reverse fault matched to the 42 year return period earthquake (units: inch/sec)

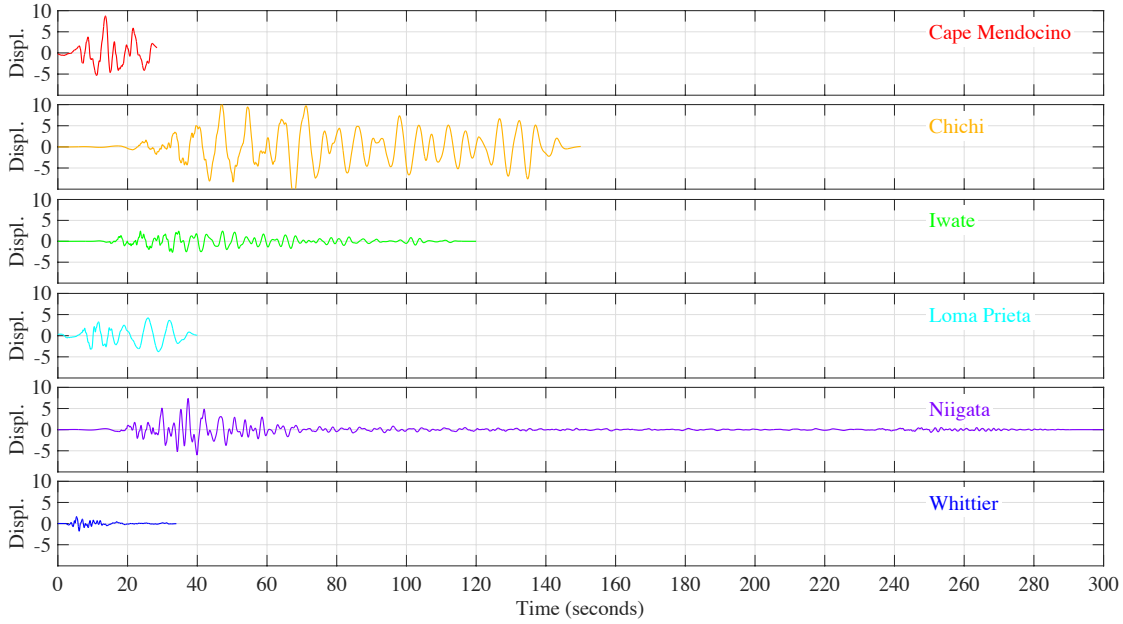

Figure A.19. Time history of displacements for the motions from reverse fault matched to the 42 year return period earthquake (units: inch)

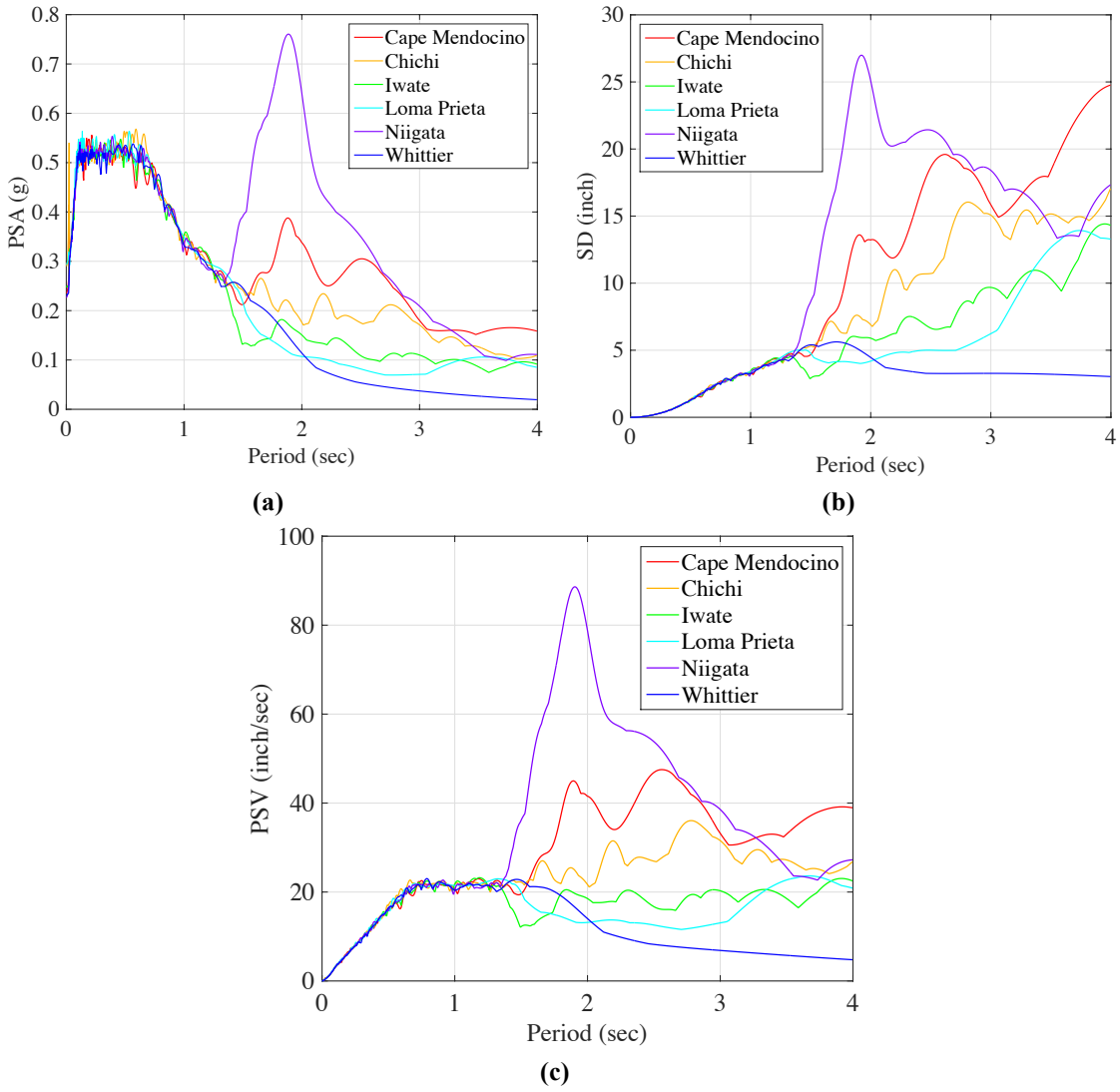

Figure A.20. (a) pseudo acceleration, (b) pseudo velocity, and (c) displacement spectrum for the motions from reverse fault originated earthquakes matched to the 42-year return spectrum

Figure A.21, Figure A.22, and Figure A.23 show the time history of accelerations, velocities and displacements for the matched motions from a strike slip fault, while Figure A.24 shows the pseudo acceleration, pseudo velocity and displacement spectra for the same motions. The values of the relevant ground parameters (PGA, S_s, S_1) and peak structural response were already presented in Table 7.9.

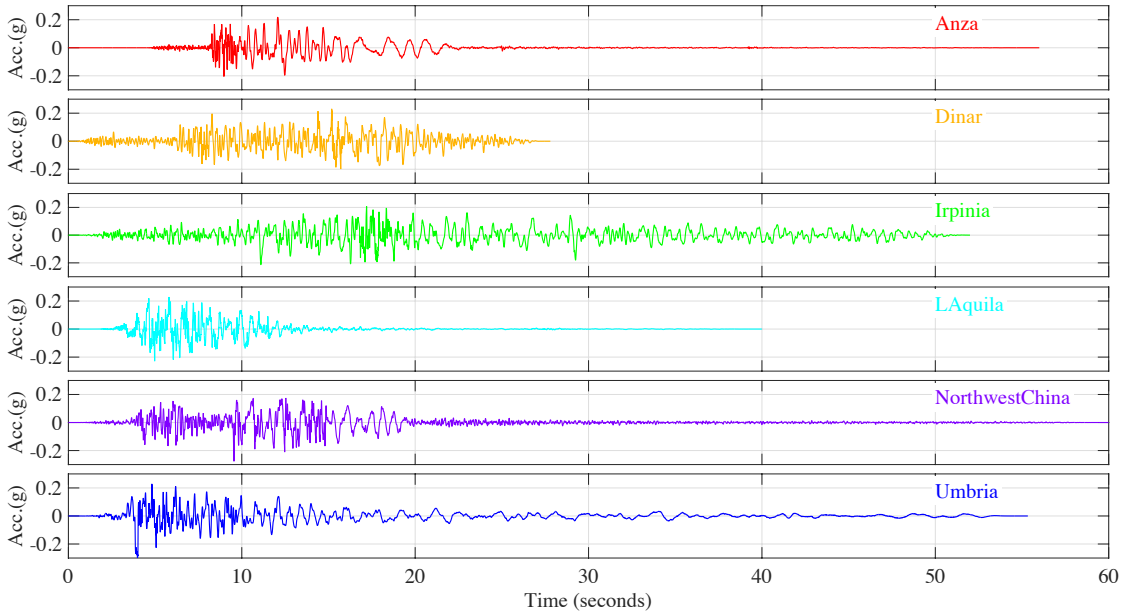

Figure A.21. Time history of acceleration for the normal fault generated motions matched to the 42-year return spectrum

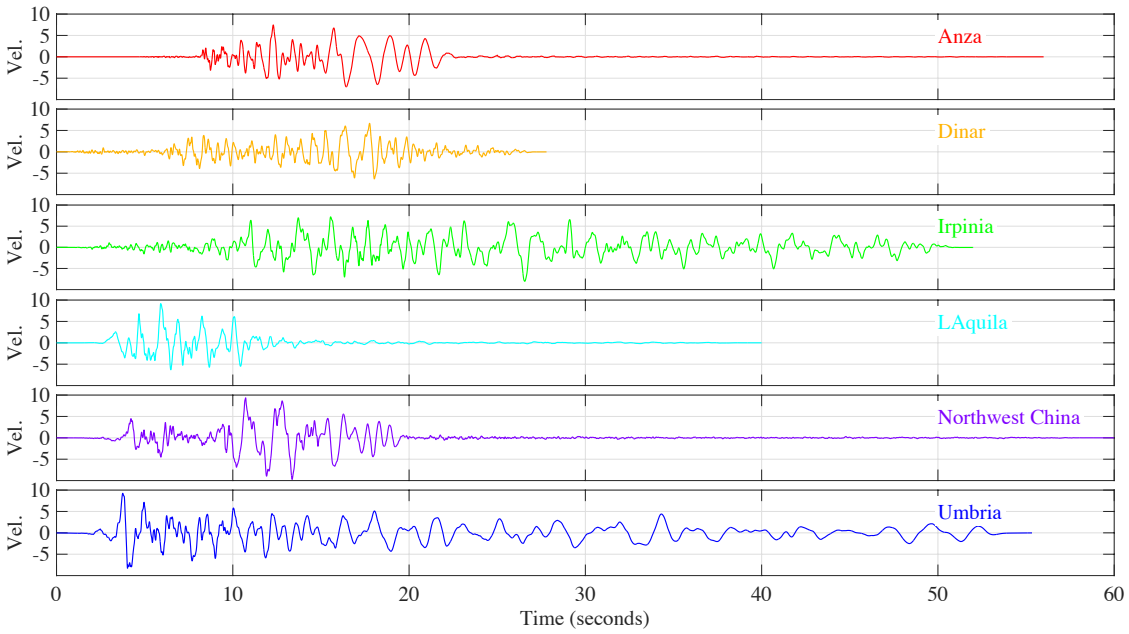

Figure A.22. Time history of velocities for the motions from normal fault matched to the 42 year return period earthquake (units: inch/sec)

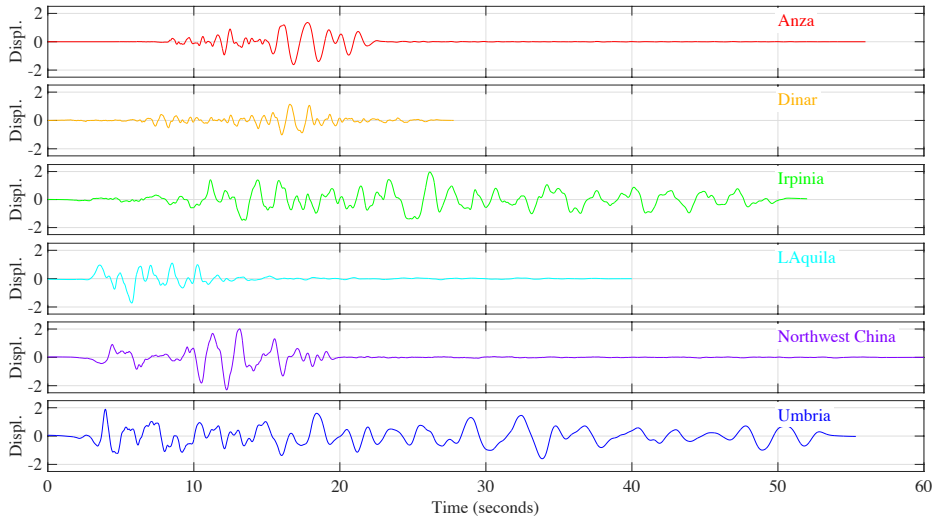

Figure A.23. Time history of displacements for the motions from normal fault matched to the 42 year return period earthquake (units: inch)

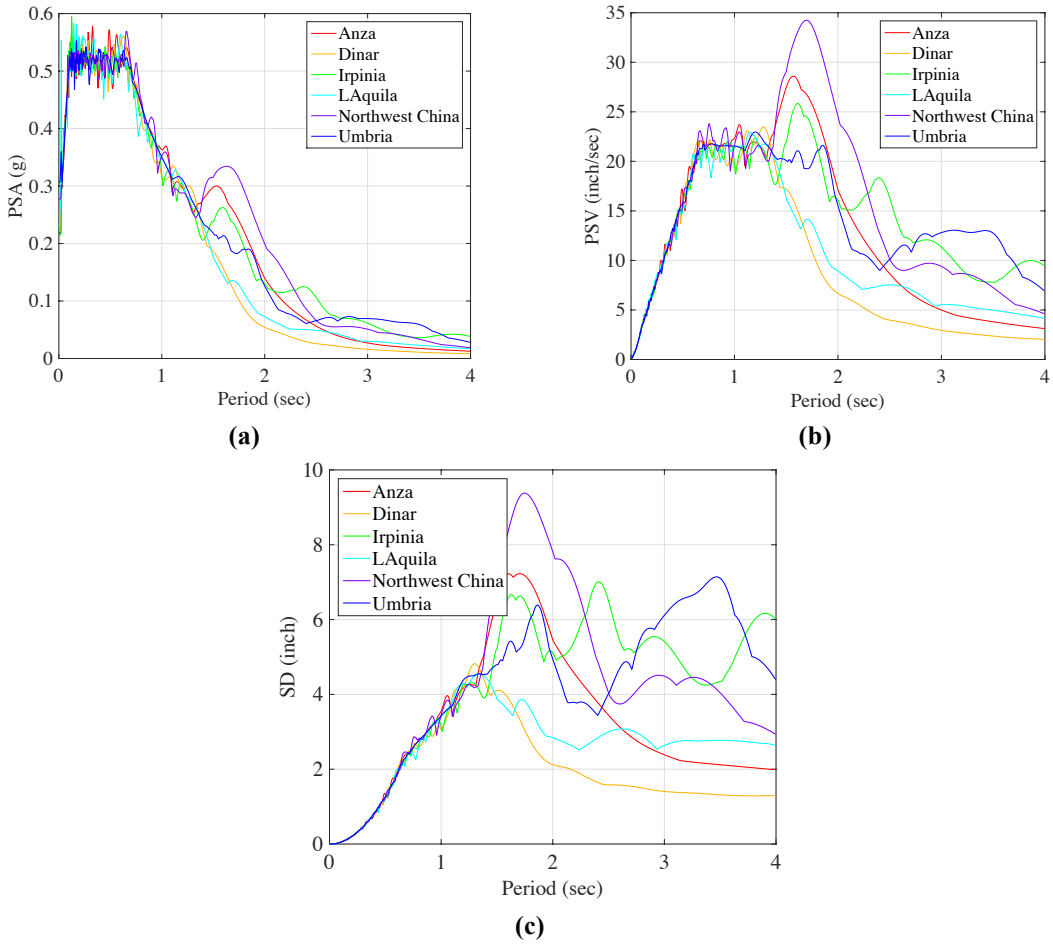

Figure A.24. (a) pseudo acceleration, (b) pseudo velocity, and (c) displacement spectrum for the motions from normal fault originated earthquakes matched to the 42-year return spectrum

A.3 Motions Scaled to Design Level (Chapter 8)

The relevant time histories and spectral responses (acceleration, velocity, displacements) relative to motions from a strike-slip fault earthquake are presented in Figure A.25 through Figure A.28. The time histories for the reverse fault generated motions are presented in Figure A.29, Figure A.30, and Figure A.31, while Figure A.32 presents the spectral information for the same motions. Figure A.33, Figure A.34, and Figure A.35 present the time histories of acceleration, velocity and displacement for the normal fault generated motions, and Figure A.36 presents the pseudo acceleration, pseudo velocity and displacement spectra for these same motions.

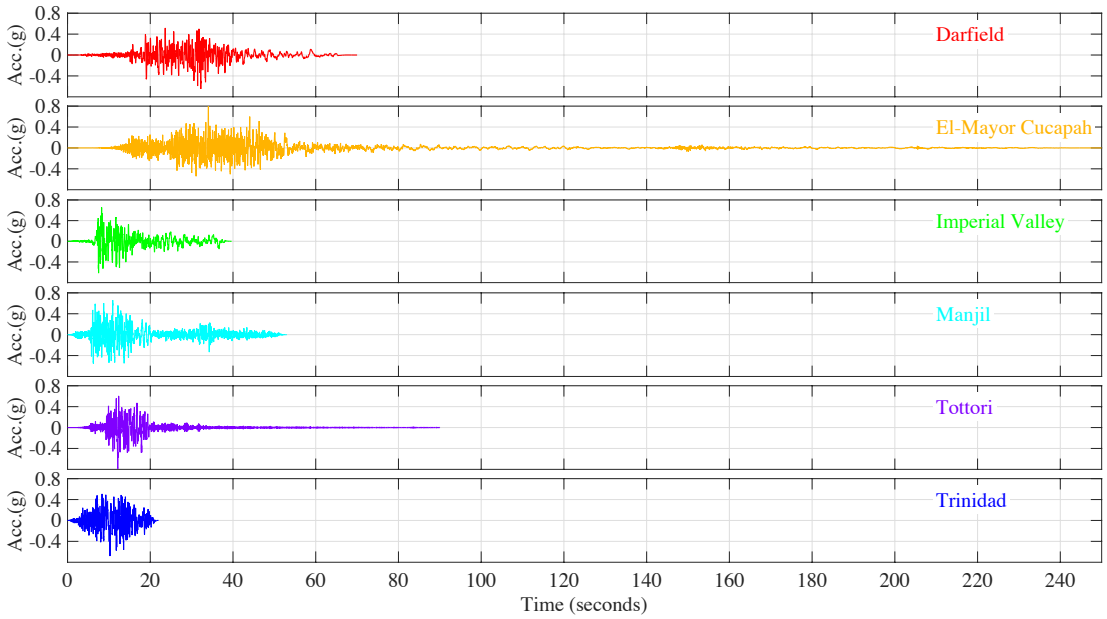

Figure A.25. Time history of accelerations for the strike-slip generated earthquakes matched to the design level spectrum

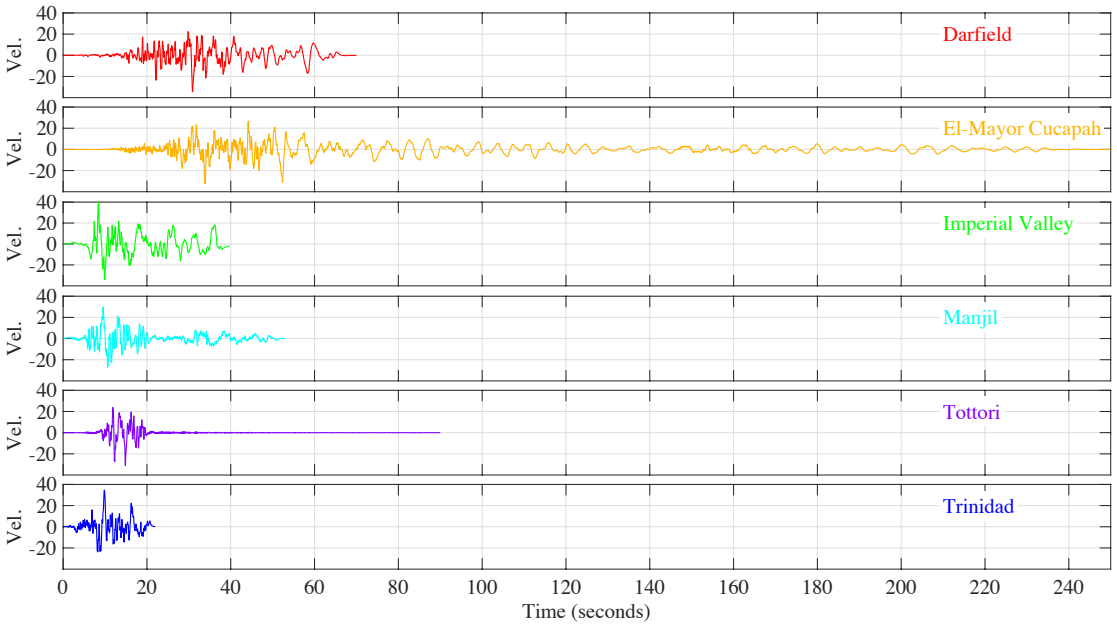

Figure A.26. Time history of velocities for the motions from strike-slip fault generated earthquakes matched to the design spectrum (units: inch/sec)

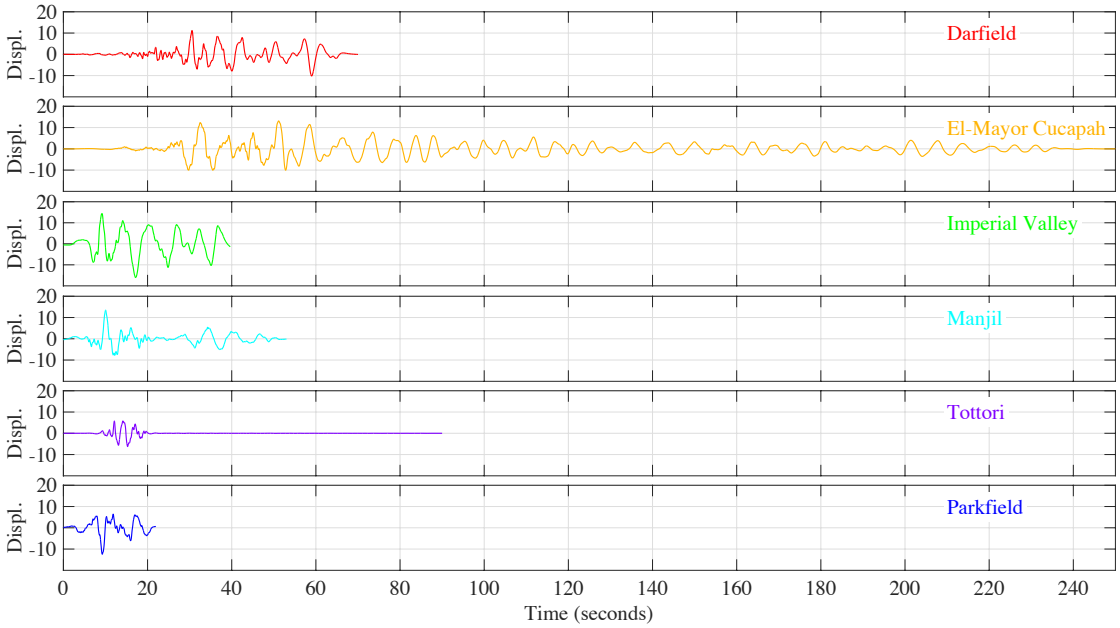

Figure A.27. Time history of displacement for the motions from strike-slip fault generated earthquakes matched to the design spectrum (units: inch)

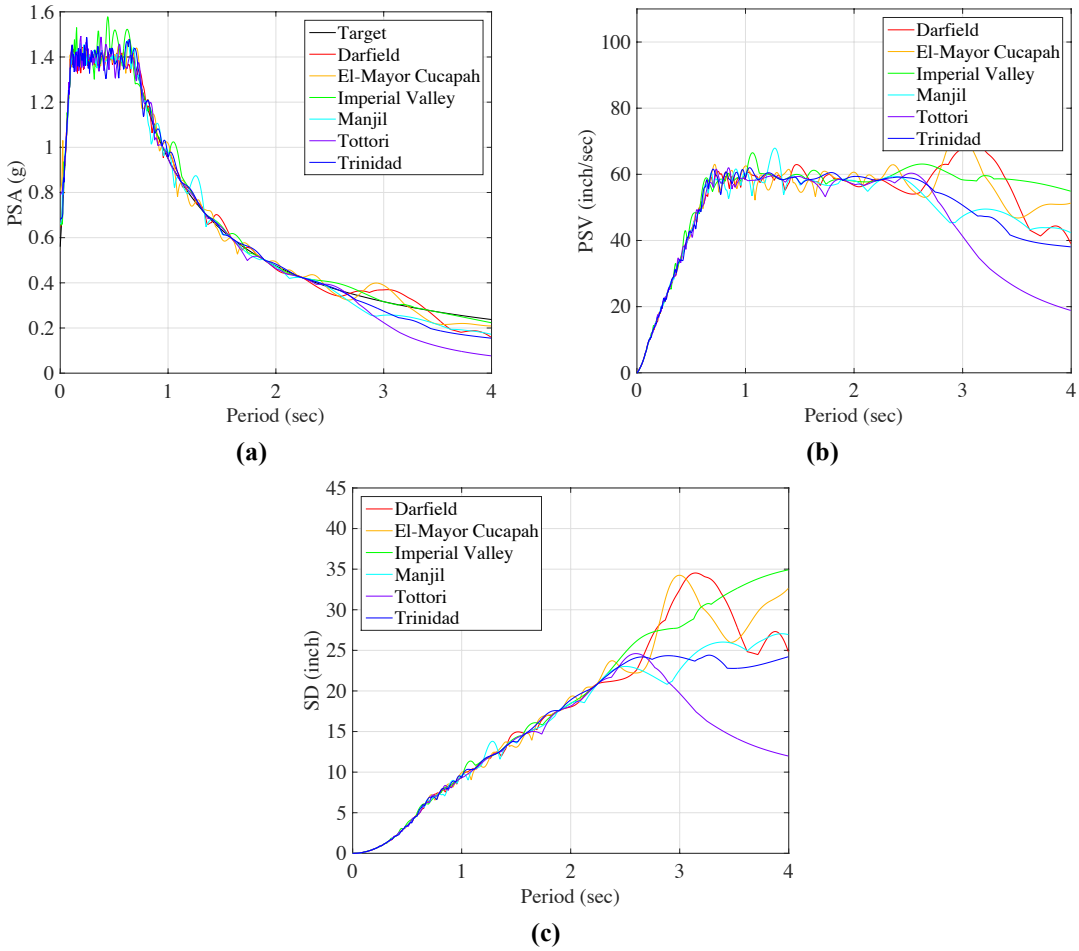

Figure A.28. (a) pseudo acceleration, (b) pseudo velocity, and (c) displacement spectrum for the motions from strike-slip fault originated earthquakes matched to the design spectrum

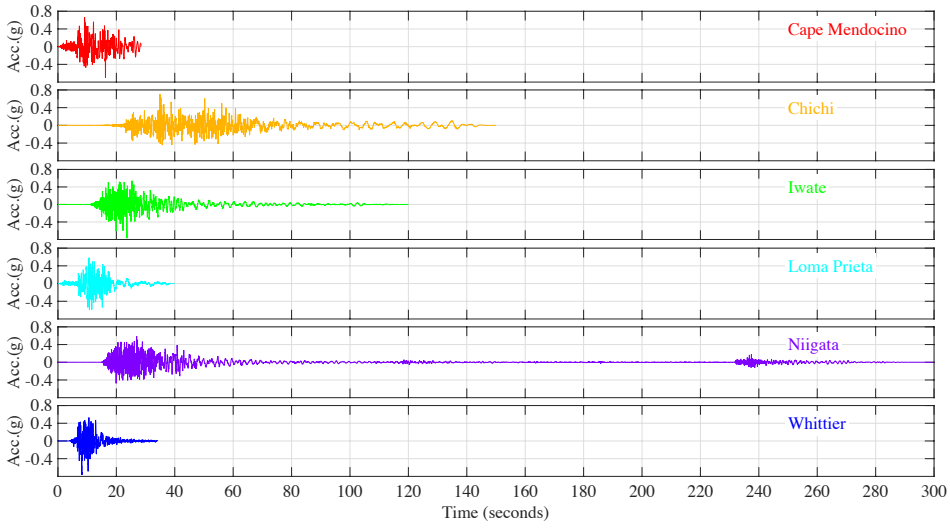

Figure A.29. Time history of accelerations for the reverse fault generated earthquakes matched to the design level spectrum

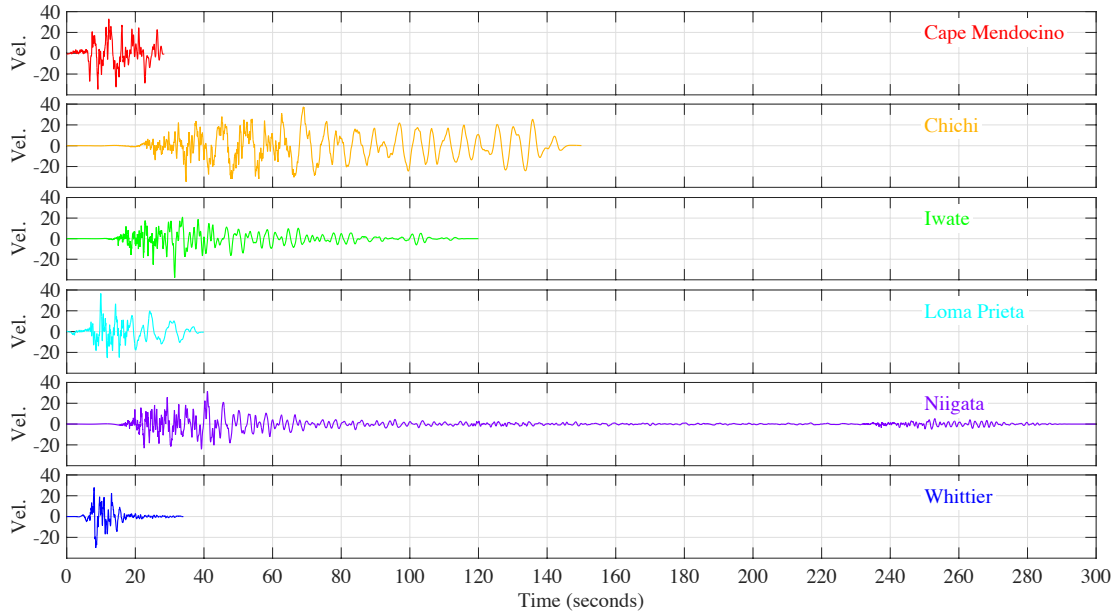

Figure A.30. Time history of velocities for the motions from reverse fault generated earthquakes matched to the design spectrum (units: inch/sec)

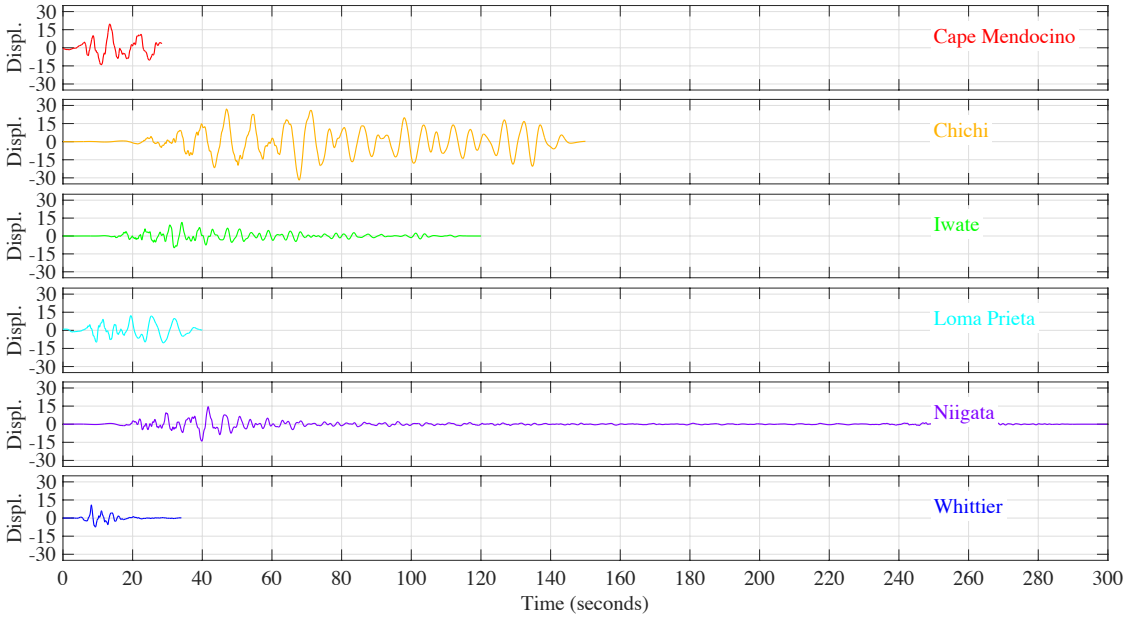

Figure A.31. Time history of displacements for the motions from reverse fault generated earthquakes matched to the design spectrum (units: inch)

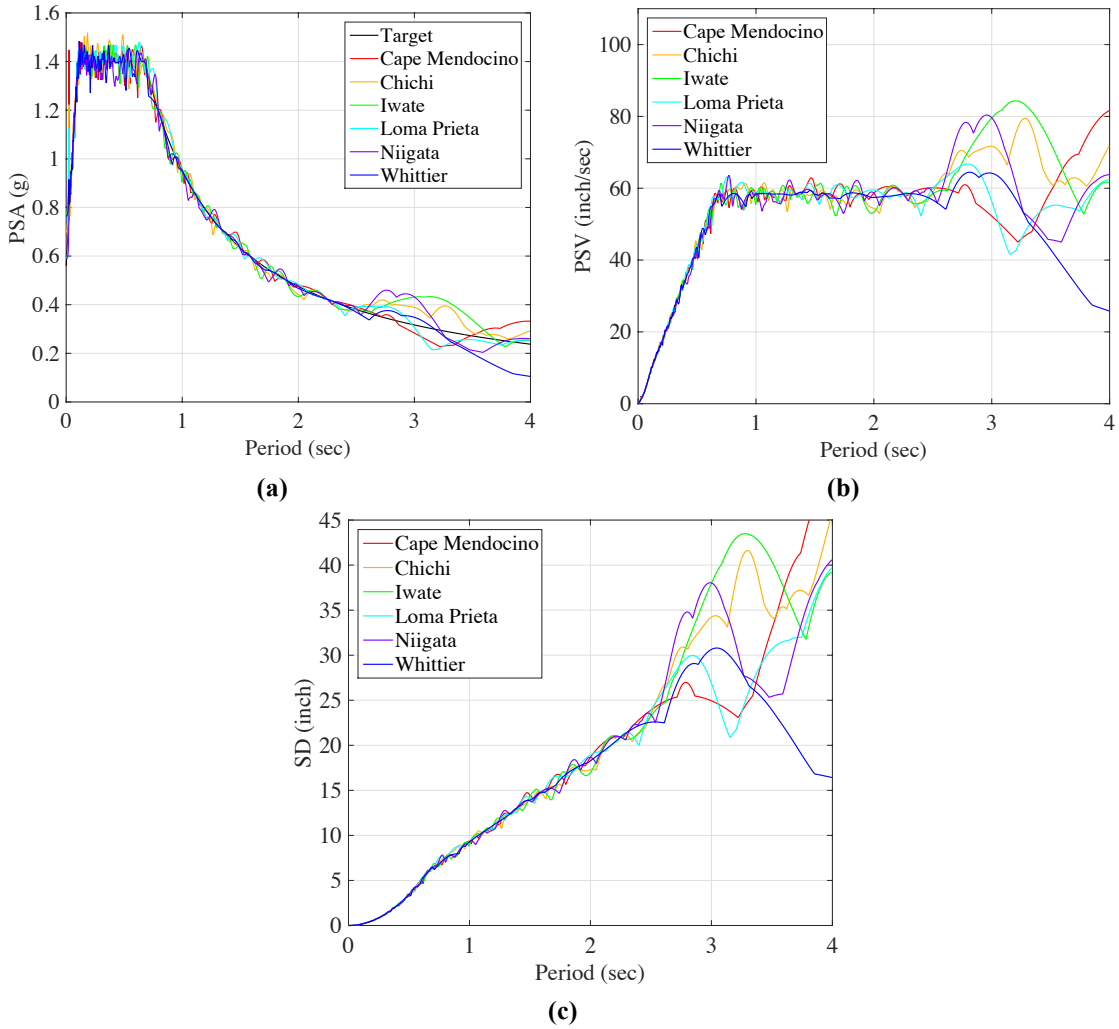

Figure A.32. (a) pseudo acceleration, (b) pseudo velocity, and (c) displacement spectrum for the motions from reverse fault originated earthquakes matched to the design spectrum

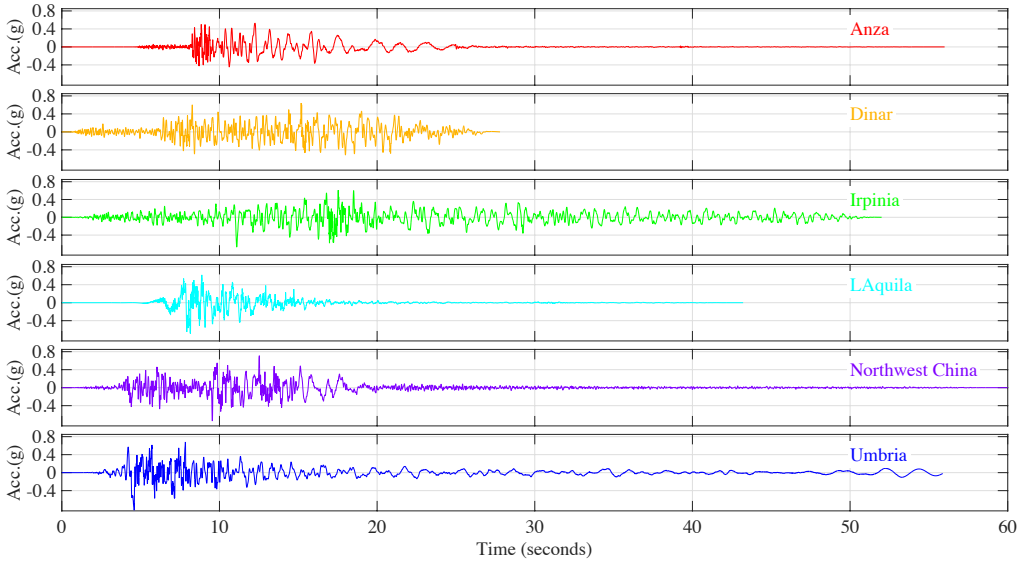

Figure A.33. Time history of accelerations for the normal fault generated earthquakes matched to the design level spectrum

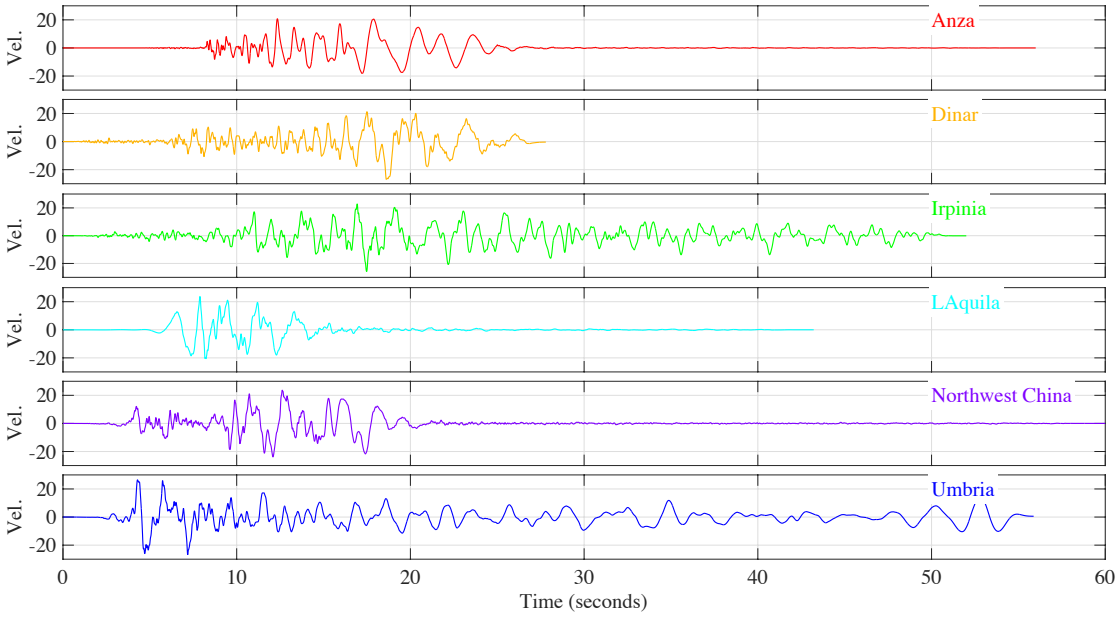

Figure A.34. Time history of velocities for the normal fault generated earthquakes matched to the design level spectrum (units: inch/sec)

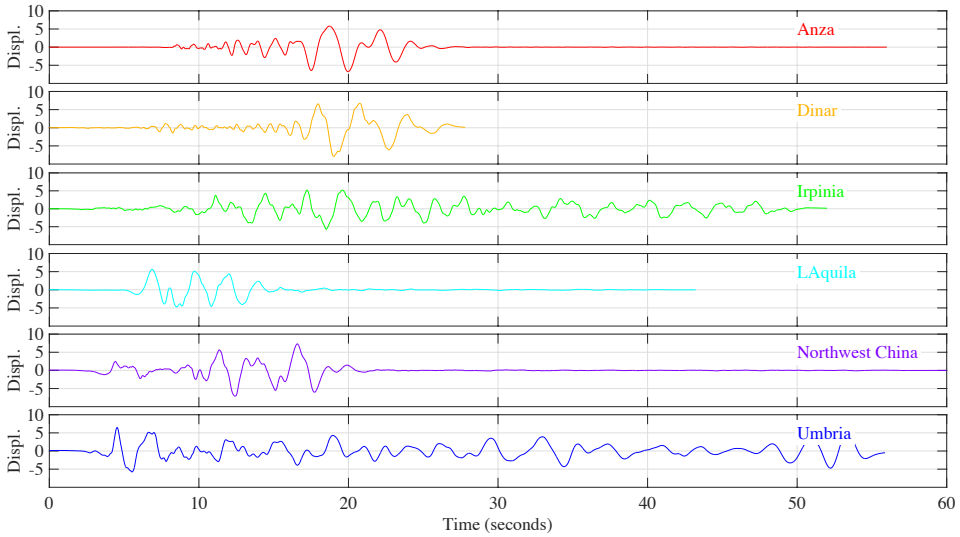

Figure A.35. Time history of displacements for the normal fault generated earthquakes matched to the design level spectrum (units: inch)

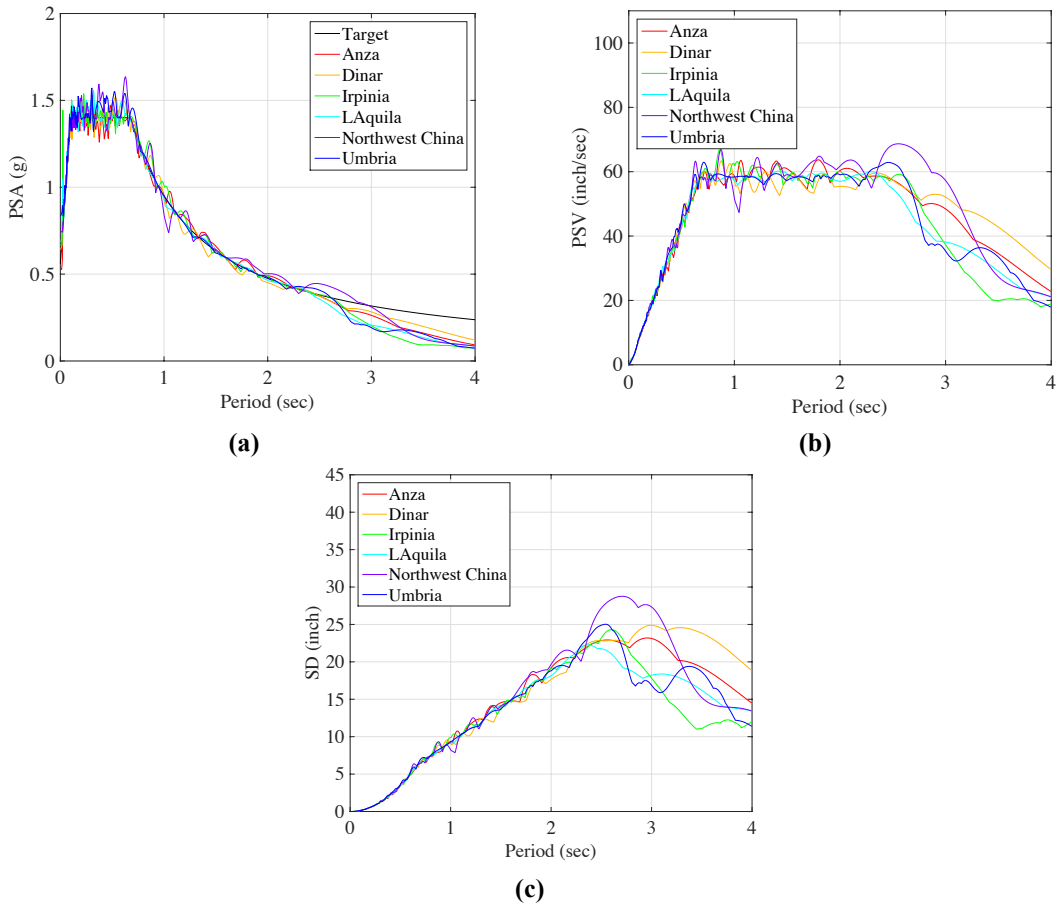

Figure A.36. (a) pseudo acceleration, (b) pseudo velocity, and (c) displacement spectrum for the motions from reverse fault originated earthquakes matched to the design spectrum

Appendix B

Chapter 8– Theoretical Calculations

B.1 First Floor Columns

B.1.1 Behavior of Confined Concrete

The properties of confined concrete determined on SAP2000 were validated with numerical calculations using the procedure proposed by Chang and Mander in 1994. Figure B.1 shows the relevant dimensions of the column, where b_c and d_c indicate the dimensions of the confined core and w_x and w_y are the width of the parabolic areas of unconfined concrete.

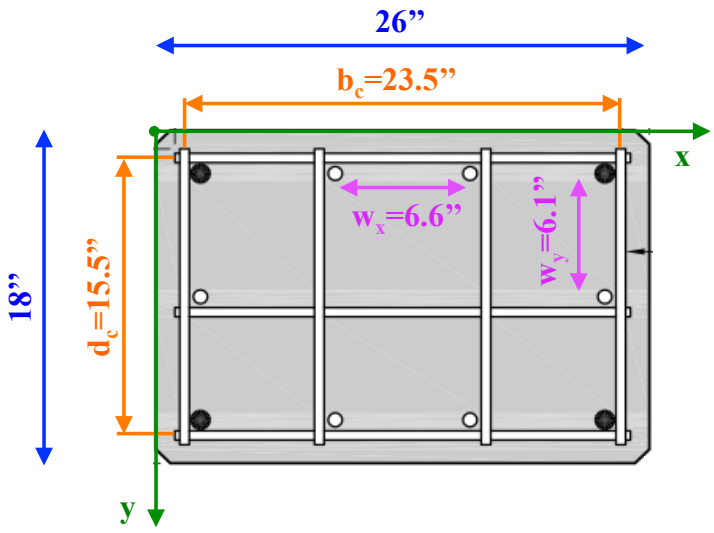

Figure B.1. Relevant dimensions of the concrete column

The procedure to find f'_{cc} involves the calculation of the following:

1. Area of the confined core A_{cc}, which is the area of the concrete within the center lines of the perimeter hoops. In this case the area of longitudinal steel A_{ls} is determined by the sum of the area of 4 #9 bars and 6 #6 bars, which provide an area of 6.64 inch^2.

   $$A_{cc} = b_c d_c - A_{st} = \quad 357.61\ inch^2$$

   A_{cc} can also be found with the formula:

   $$A_{cc} = A_c(1-\rho_{cc}) = 23.5 \cdot 15.5 \cdot \left(1 - \frac{6.64}{23.5 \cdot 15.5}\right) = 364.25 \cdot \left(1 - \frac{6.64}{364.25}\right) = 357.61 inch^2$$

Where A_c is the area of core of section enclosed by the center lines of the perimetral hoops, and ρ_{cc} is the ratio of area of longitudinal reinforcement to area of core of section;

2. Area of the parabolas inside which the concrete in not properly confined. In this case there are four parabolic areas in the y direction (w_y=6.1'') and six in the x direction (w_x=6.6''), where w is the clear distance between adjacent bars. The ineffectively confined area in the x direction A_{ix} and in the y direction A_{iy} are:

$$A_{ix} = 6 \cdot \frac{w_x^2}{6} = 6 \cdot \frac{6.6^2}{6} = 43.56\ inch^2$$

$$A_{iy} = 4 \cdot \frac{w_y^2}{6} = 4 \cdot \frac{6.1^2}{6} = 24.80\ inch^2$$

3. Effectively confined area A_e incorporating the areas non confined in elevation based on the clear vertical space between hoops s'. In this case the spacing on center is 4'', meaning that the clear distance is 3.5'':

$$A_e = \left(b_c d_c - A_{ix} - A_{iy}\right)\left(1 - 0.5\frac{s'}{b_c}\right)\left(1 - 0.5\frac{s'}{d_c}\right) =$$

$$= (364.2 - 43.56 - 24.8)\left(1 - 0.5\frac{3.5}{23.5}\right)\left(1 - 0.5\frac{3.5}{15.5}\right)$$

$$= 295.8 \cdot 0.925 \cdot 0.887 = 242.7\ inch^2$$

4. Confinement effectiveness coefficient k_e for rectangular hoops:

$$k_e = \frac{A_e}{A_{cc}} = \frac{242.7}{357.6} = 0.679$$

5. In case there is different reinforcement in the two directions, it is possible to defined the reinforcement ratios in the two direction ρ_x and ρ_y, considering that in the x direction there are 3 #4 hoops for a total area A_{sx} of 0.6 inch^2 and in the y direction there are four legs for a total area A_{sy} of 0.8 inch^2. In this case s represent the centerline-to-centerline vertical distance between the hoops:

$$\rho_x = \frac{A_{sx}}{sd_c} = \frac{0.6}{4 \cdot 15.5} = 0.0097$$

$$\rho_y = \frac{A_{sy}}{sb_c} = \frac{0.8}{4 \cdot 23.5} = 0.0085$$

6. The effective lateral confining stresses in the x and y direction can be found considering that the yield stress of the hoops f_{yh} in 81 ksi:

$$f'_{lx} = k_e \rho_x f_{yh} = 0.679 \cdot 0.0097 \cdot 81 = 0.533\ ksi$$

$$f'_{ly} = k_e \rho_y f_{yh} = 0.679 \cdot 0.0085 \cdot 81 = 0.467\ ksi$$

7. Calculation of the parameters (Simplified as Proposed by Chang and Mander in 1994):

$$\bar{x} = \frac{f'_{l1} + f'_{l2}}{2f'_c} = 0.0633$$

$$r = \frac{f'_{l1}}{f'_{l2}} = \frac{0.467}{0.533} = 0.876$$

$$A = 6.8886 - (0.6069 + 17.275r)e^{-4.989r} = 6.8886 - (15.74) \cdot 0.0126 = 6.69$$

$$B = \frac{4.5}{\frac{5}{A}(0.9849 - 0.6306e^{-3.8939r}) - 0.1} - 5$$

$$= \frac{4.5}{0.747(0.9849 - 0.02) - 0.1} - 5 = \frac{4.5}{0.62} - 5 = 2.25$$

$$f_l = \frac{f'_{l1} + f'_{l2}}{2} = \frac{0.533 + 0.467}{2} = 0.5$$

8. Calculation of k_1:

$$k_1 = A\left(0.1 + \frac{0.9}{1 + B\bar{x}}\right) = 6.69\left(0.1 + \frac{0.9}{1.14}\right) = 5.93$$

9. Find f'_{cc}:

$$f'_{cc} = f'_{c0} + k_1 f_l = 7.9 + 4.796 \cdot 0.5 = 10.8 ksi$$

10. ε_{cc} was found with equations from equations 3.81a and b Chang and Mander (1994), namely:

$$k_2 = 5k_1 = 29.7$$

$$\varepsilon_{cc} = \varepsilon_{c0}(1 + k_2\bar{x}) = 0.0023(1 + 29.7 \cdot 0.0633) = 0.0066\ inch/inch$$

The stress-strain curve could be determined with what suggested by Chang and Mander 1994 in equation 3.17:

11. $y = \frac{f_c}{f'_{cc}} = \frac{nx}{1+\left(n-\frac{r}{r-1}\right)x+\frac{x^r}{r-1}}$

Where r is the factor controlling the descending branch of the curve. This was assumed as the one proposed by Mander 1988 as:

$$r = \frac{E_c}{E_c - E_{\sec}}$$

where:

E_c is the tangent modulus of elasticity of concrete and can be found using MPa as:

$$E_c = 5000\sqrt{f'_{c0}}\,(MPa) = 5355ksi$$

E_{sec} is the secant E for confined concrete and it is defined as:

$$E_{\sec} = \frac{f'_{cc}}{\varepsilon_{cc}} = \frac{10.8}{0.066} = 1636ksi$$

$$r = \frac{5355}{5355 - 1636} = 1.44$$

According to Chang and Mander 1994, the parameter n can be assumed as:

$$n = \frac{r}{r-1} = \frac{1.44}{1.44-1} = 3.27$$

$$n = \frac{E_c \varepsilon'_{cc}}{f'_{cc}} = \frac{5355 \cdot 0.0058}{10.3} = 3.01$$

$$r = \frac{n}{n-1} = \frac{3.01}{3.01-1} = 1.4975$$

12. The approximate value of the strain at the crushing of the concrete core can be determined with the formula from Pauley and Priseley (1992) as:

    $\varepsilon_{ccu} = 0.004 + 1.4\rho_s f_{yh} \epsilon_{sm} / f'_{cc}$

    Where in this case:

    - The ratio of the volume of transverse confining steel to the volume of the confined concrete area ρ_s can be found as the sum of ρ_x and $\rho_y = 0.0182$;
    - ε_{sm} is the steel strain at maximum tensile stress for the transverse reinforcement and it can be found as 0.033 inch/inch;

      Thus:

      $\varepsilon_{ccu} = 0.004 + 1.4 \cdot 0.0182 \cdot 81 \cdot 0.033/10.8 = 0.0103\ inch/inch$

This value is smaller than expected because of the low ductility of the transverse reinforcement. The comparison between the behavior of confined concrete found theoretically and the

one on SAP2000 is shown in Figure B.2, and it shows a very good comparison.

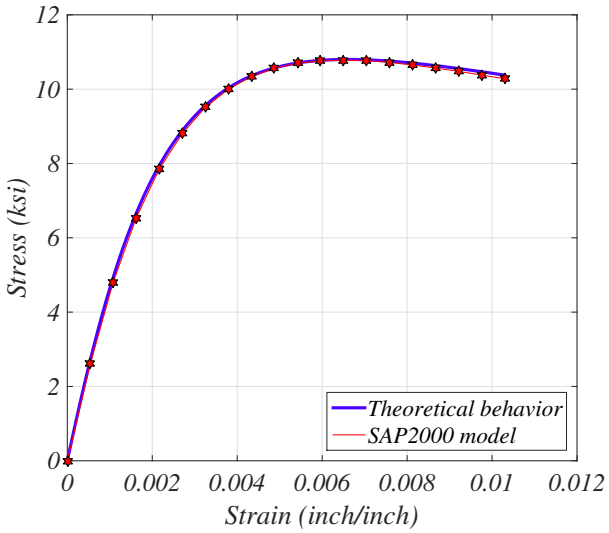

Figure B.2. Comparison of the model of confined concrete found theoretically and in SAP2000

B.1.2 P-M Interaction Surface (Yield and Ultimate)

To verify the pushover results, it was advised to create both the yield and ultimate interaction surface. The values of the curve were found with the section designer tool in SAP2000 by changing the normal force applied to the section and recording the yield and ultimate moment. Some of the relevant values obtained in SAP2000 are checked with the following theoretical calculations.

Pure Compression

The yielding point in case of pure compression of the section can be found considering that the yield strain in the section is 0.0024 inch/inch. At this strain the stress in the confined concrete is 8.4 ksi, while the stress in the unconfined concrete is considered zero since the peak stress is already surpassed, thus:

$$P_{y,compression} = d_c \cdot b_c \cdot f_c + A_{st} \cdot f_y = 15.5 \cdot 23.5 \cdot 8.4 + 6.64 \cdot 69 = 3523 kips$$

The ultimate values of stress for the concrete is 10.3 ksi, which happens at a strain of 0.01 inch/inch. At that strain, the stress in the longitudinal steel is 69 ksi. Thus the ultimate force can be found as:

$$P_{u,compression} = 15.5 \cdot 23.5 \cdot 10.3 + 6.64 \cdot 69 = 4200 kips$$

Both there values are very similar to those obtained in SAP2000.

Pure Tension

In the case of tension, only the steel acts and thus the yield and ultimate forces can be found as:

$$P_{y,tension} = A_{st} \cdot f_y = 6.64 \cdot 69 = 458 kips$$

$$P_{u,tension} = A_{st} \cdot f_y = 6.64 \cdot 119 = 790 kips$$

These values are the same as found in SAP2000.

Balances Failure

The balanced failure was check for the yield surface only. It was calculated thought the common procedure obtained with equilibrium considerations, as explained by Park and Pauley (1975), considering that:

- c= neutral axis depth;
- a=β_1c=0.85c is the width of the stress block;
- d= distance between the most compressed fibers and the centroid of the steel in tension (Figure B.3b);
- d'= distance between the most compressed fibers and the centroid of the steel in compression tension (Figure B.3b);
- d''=distance between the plastic centroid and the centroid of the steel in tension. In this case the plastic centroid is at the center of the section, since the section is symmetrically reinforced (Figure B.3b).

Considering the cracking of the concrete at the strain of 0.004 inch/inch, the depth of the concrete stress block a can be found as:

$$a = \frac{0.004E_s}{f_y + 0.004E_s}\beta_1 d = \frac{0.004 \cdot 29000}{69.6 + 0.004 \cdot 29000} 0.85 \cdot 23.94 = 12.72\ inch$$

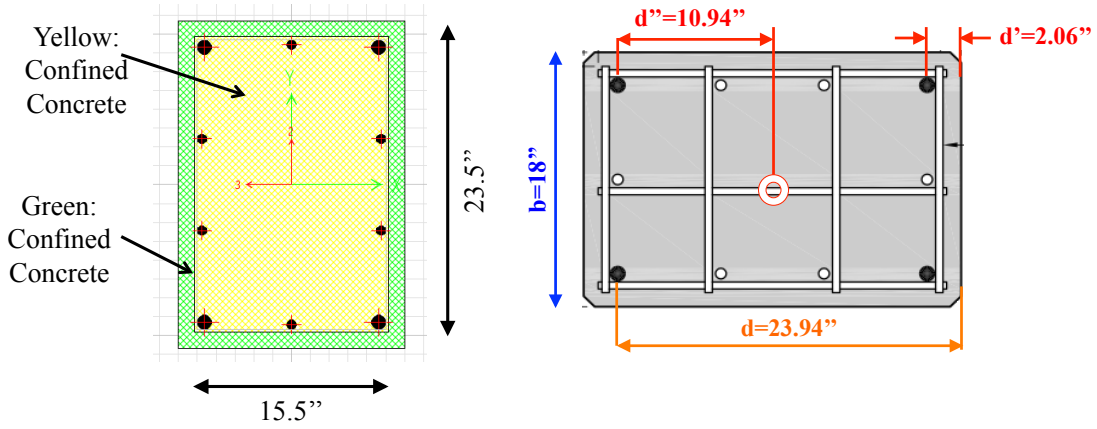

Figure B.3. Cross section of the column: (a) in the section designer tool in SAP2000 and (b) showing main dimensions used in the calculations

From this value, it is possible to find the compression force in case of the balanced failure P_b:

$$P_b = 0.85 \cdot f_c' \cdot a \cdot b = 0.85 \cdot 7.9 \cdot 12.72 \cdot 18 = 1537\ kips$$

And from there the maximum moment $P_b e_b$, where e_b is the eccentricity of the load:

$$P_b e_b = P_b(d - d'' - 0.5a) + A_s' f_y (d - d') =$$

$$= 1537(23.94 - 10.94 - 0.5 \cdot 12.72) + 2.44 \cdot 69.6 \cdot (23.94 - 2.06)$$

$$= 1537 \cdot 6.64 + 3715 = 13921\ kip - inch$$

Lastly, the strain in the tension steel ε_s needs to be checked to make sure it is above yield strain ε_y:

$$c = \frac{a}{\beta_1} = \frac{12.72}{0.85} = 14.96\ inch$$

$$\varepsilon_y = \frac{f_y}{E_s} = \frac{69.6}{29000} = 0.0024\ inch/inch$$

$$\varepsilon_s = 0.004 \frac{c - d'}{c} = 0.004 \frac{12.9}{14.96} = 0.0034\ inch/inch$$

Since the strain in the tension steel is larger than the yield strain, it is confirmed that the tension steel is yielded. The values of the balanced fracture of P_b of 1537kips and M_b of13921 kips-inch are very similar to one of the point found in the interaction diagram in the model. It is clearly confirmed that the interaction diagram presented in SAP2000 is working properly.

B.2 Beams on the Second and Third Floor

The same procedure adopted to model the column was used to model the beams at floor two. These beams had the geometry shown in Figure B.4 and were characterized by the presence of high strength steel in the longitudinal direction. The beam was 28'' high and 12'' high, it had four longitudinal #7 bars made of high-strength steel and the transverse reinforcement was made of #4 Grade 60 bars.

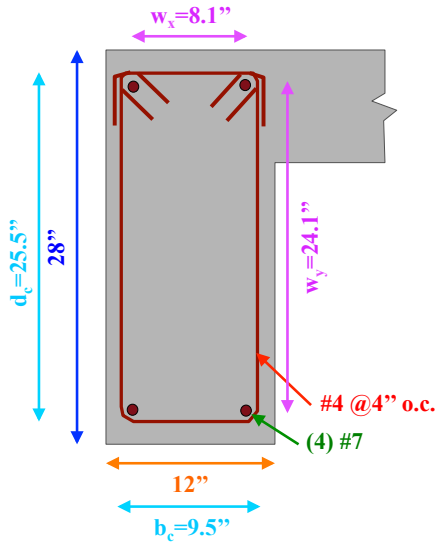

Figure B.4. Geometry of the beams at the second floor

B.2.1 Confined Concrete

The behavior the unconfined concrete was determined with SAP2000 and checked with the calculations explained above and repeated here for this beam:

1. $A_{cc} = b_c d_c - A_{st} = \quad 240 \text{ inch}^2$
2. $A_{ix} = 2 \cdot \frac{w_x^2}{6} = 2 \cdot \frac{8.1^2}{6} = 21.9\ inch^2$; $A_{iy} = 2 \cdot \frac{w_y^2}{6} = 2 \cdot \frac{24.1^2}{6} = 193.6\ inch^2$
3. $A_e = \left(b_c d_c - A_{ix} - A_{iy}\right)\left(1 - 0.5\frac{s'}{b_c}\right)\left(1 - 0.5\frac{s'}{d_c}\right) =$

   $= (242.25 - 21.9 - 193.6)\left(1 - 0.5\frac{3.5}{9.5}\right)\left(1 - 0.5\frac{3.5}{22.5}\right)$

   $= 26.75 \cdot 0.81 \cdot 0.93 = 20.34\ inch^2$
4. $k_e = \frac{A_e}{A_{cc}} = \frac{20.34}{240} = 0.084$

5. $\rho_x = \frac{A_{sx}}{sd_c} = \frac{0.4}{4 \cdot 25.5} = 0.0039$

   $\rho_y = \frac{A_{sy}}{sb_c} = \frac{0.4}{4 \cdot 9.5} = 0.01$

6. $f'_{lx} = k_e \rho_x f_{yh} = 0.084 \cdot 0.0039 \cdot 69 = 0.023\ ksi$

   $f'_{ly} = k_e \rho_y f_{yh} = 0.084 \cdot 0.01 \cdot 69 = 0.062\ ksi$

7. $\bar{x} = \frac{f'_{l1} + f'_{l2}}{2 f'_c} = 0.006$

   $r = \frac{f'_{l1}}{f'_{l2}} = \frac{0.023}{0.061} = 0372$

   $A = 6.8886 - (0.6069 + 17.275r)e^{-4.989r} = 5.79$

   $B = \frac{4.5}{\frac{5}{A}(0.9849 - 0.6306e^{-3.8939r}) - 0.1} - 5 = 2.22$

   $f_l = \frac{f'_{l1} + f'_{l2}}{2} = \frac{0.033 + 0.057}{2} = 0.0423\ ksi$

8. $k_1 = A\left(0.1 + \frac{0.9}{1 + B\bar{x}}\right) = 5.72$

9. Find f'_{cc}

   $f'_{cc} = f'_{c0} + k_1 f_l = 7.28\ ksi$

10. $k_2 = 5k_1 = 28.61$

11. $\varepsilon_{cc} = \varepsilon_{c0}(1 + k_2 \bar{x}) = 0.0027\ inch/inch$

    Clearly, there is only a small gain in ultimate stress and strain. This is because the effectively confined area is really small due to the lack of intermediate transverse reinforcement.

12. $\varepsilon_{ccu} = 0.004 + 1.4 \rho_s f_{yh} \epsilon_{sm} / f'_{cc} = 0.04$ inch/inch

On SAP2000, it was not possible to input this large value, because the addition of this value would not allow the other parameters of the confined concrete to work properly. Because of this issue, the maximum value of ε_{ccu} that would still allow the concrete model to work correctly was determined as ε_{ccu}=0.023 inch/inch.

B.2.2 Moment Curvature Curve

Values at certain locations of the moment curvature were checked. The checks performed

consisted in determining the nominal moment M_n and the plastic moment M_p with the common calculations presented by McGregor and Wright (2004). The following formulas were considered

$$T = A_s F_y$$

$$C_c = 0.85 f_c^{'} b a$$

$$C_s = E_s \varepsilon_s^{'} A_s^{'}$$

The value of a was found with the following equations:

$$(0.85 f_c^{'} b) a^2 + (0.003 E_s A_s^{'} - A_s f_y) a - (0.003 E_s A_s^{'} \beta_1 d^{'}) = 0$$

$$\beta_1 = 1.05 - 0.05 \frac{f_c^{'}(psi)}{1000}$$

$$M_n = C_c \left(d - \frac{a}{2} \right) + C_s \left(d - d' \right)$$

Where d is the distance between the compression fibers and the centroid of the steel in tension and d' is the distance between the compression fibers and the centroid of the steel in compression. In this case it was found that:

M_n=3828 kip-inch

This is very similar to the yield moment of the approximate model 3696 kip-inch. The maximum moment at large deformation was found considering both steel in tension and compression at the maximum stress. With this assumptions it is possible to find a M_p=4579 kip-inch, very similar to the maximum of the model of 4692 kips-inch.

B.3 Beams on the Fourth and Fifth Floor

Figure B.5 presents the geometry of the beam at the fourth and fifth floors. The difference between them was that the one at the fourth floor was post-tensioned, while the one at the fifth floor was not. The procedure for the determination of f'_{cc} follows these steps:

1. $A_{cc} = b_c d_c - A_{st} = \quad 232.63\ inch^2$
2. $A_{ix} = 2 \cdot \frac{w_x^2}{6} = 2 \cdot \frac{4^2}{6} = 5.33\ inch^2$

$$A_{iy} = 2 \cdot \frac{w_y^2}{6} = 2 \cdot \frac{23.2^2}{6} = 179\ inch^2$$

3. $A_e = \left(b_c d_c - A_{ix} - A_{iy}\right)\left(1 - 0.5\frac{s'}{b_c}\right)\left(1 - 0.5\frac{s'}{d_c}\right) = 43.7 inch^2$

4. $k_e = \frac{A_e}{A_{cc}} = 0.187$

5. $\rho_x = 0.0039\ and\ \rho_y = 0.0105$

6. $f'_{lx} = k_e \rho_x f_{yh} = 0.05\ ksi$

   $f'_{ly} = k_e \rho_y f_{yh} = 0.134\ ksi$

7. $\bar{x} = \frac{f'_{l1} + f'_{l2}}{2 f'_c} = 0.0131$

   $r = \frac{f'_{l1}}{f'_{l2}} = 0.372$

   $A = 6.8886 - (0.6069 + 17.275r)e^{-4.989r} = 5.79$

   $B = \frac{4.5}{\frac{5}{A}(0.9849 - 0.6306e^{-3.8939r}) - 0.1} - 5 = 2.224$

   $f_l = \frac{f'_{l1} + f'_{l2}}{2} = \frac{0.046 + 0.247}{2} = 0.092\ ksi$

8. $k_1 = 5.64$

9. $f'_{cc} = f'_{c0} + k_1 f_l = 7.56\ ksi$

10. $\mathrm{k_2} = 5\mathrm{k_1} = 28.21$

11. $\varepsilon_{cc} = \varepsilon_{c0}(1 + \mathrm{k_2}\bar{\mathrm{x}}) = 0.00315$ inch/inch

12. $\varepsilon_{ccu} = 0.004 + \frac{1.4\rho_s f_{yh}\epsilon_{sm}}{f'_{cc}} = 0.038\ inch/inch$

Beams at the fourth and fifth floor differ for the fact that the one on the fourth floor was post-tensioned, while the one on the fifth floor was not, and the type of concrete was also different. Since the geometry was the same, only the last points of the calculations changed as follows:

13. $f'_{cc} = f'_{c0} + k_1 f_l = 8.72\ ksi$

14. $\varepsilon_{cc} = \varepsilon_{c0}(1 + \mathrm{k_2}\bar{\mathrm{x}}) = 0.00308$ inch/inch

15. $\varepsilon_{ccu} = 0.004 + \frac{1.4\rho_s f_{yh}\epsilon_{sm}}{f'_{cc}} = 0.034\ inch/inch$

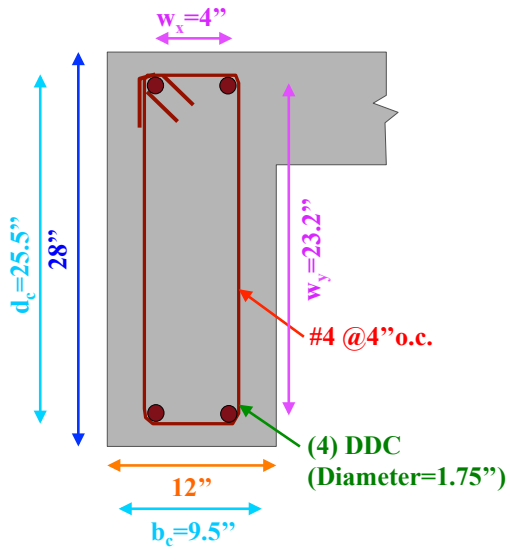

Figure B.5. Geometry of the beams at the fourth and fifth floors

B.4 Beams at the Roof

Figure B.6 presents the geometry of the beam at the roof. The results from SAP2000 were complemented with the following, which allow the determination of f'$_{cc}$ and ε_{cc}:

1. $A_{cc} = b_c d_c - A_{st} = \quad 237.45\ inch^2$

2. $A_{ix} = 6 \cdot \frac{w_x^2}{6} = 6 \cdot \frac{3^2}{6} = 9\ inch^2$

$$A_{iy} = 2 \cdot \frac{w_y^2}{6} = 2 \cdot \frac{23.2^2}{6} = 179\ inch^2$$

3. $A_e = \left(b_c d_c - A_{ix} - A_{iy}\right)\left(1 - 0.5\frac{s'}{b_c}\right)\left(1 - 0.5\frac{s'}{d_c}\right) = 40.9 inch^2$

4. $k_e = \frac{A_e}{A_{cc}} = 0.172$

5. $\rho_x = 0.0039$

$$\rho_y = 0.021$$

6. $f'_{lx} = k_e \rho_x f_{yh} = 0.044\ ksi$

$$f'_{ly} = k_e \rho_y f_{yh} = 0.239\ ksi$$

7. $\bar{x} = \frac{f'_{l1} + f'_{l2}}{2 f'_c} = 0.0173$

$$r = \frac{f'_{l1}}{f'_{l2}} = 0.186$$

$$A = 6.8886 - (0.6069 + 17.275r)e^{-4.989r} = 5.37$$

$$B = \frac{4.5}{\frac{5}{A}(0.9849 - 0.6306e^{-3.8939r}) - 0.1} - 5 = 3.46$$

$$f_l = \frac{f'_{l1} + f'_{l2}}{2} = \frac{0.046 + 0.247}{2} = 0.142\ ksi$$

8. $k_1 = 5.10$

9. $f'_{cc} = f'_{c0} + k_1 f_l = 8.89\ ksi$

10. $\mathrm{k_2} = 5\mathrm{k_1} = 25.51$

11. $\varepsilon_{cc} = \varepsilon_{c0}(1 + \mathrm{k_2}\bar{x}) = 0.00332$ inch/inch

12. $\varepsilon_{ccu} = 0.004 + \frac{1.4\rho_s f_{yh}\epsilon_{sm}}{f'_{cc}} = 0.053\ inch/inch$

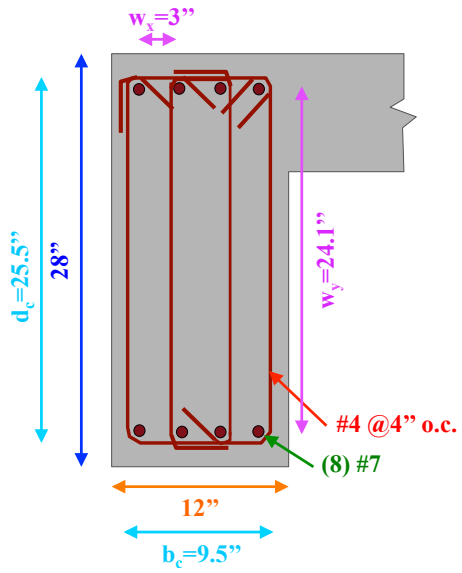

Figure B.6. Geometry of the beams at the roof